Lectures in Paleomagnetism, 2005
by Lisa Tauxe

Citation:
http://earthref.org/MAGIC/books/Tauxe/2005/

May 30, 2005

Chapter 1

The Physics of Magnetism

Suggested Supplemental Reading

For background:

pp 1-4: Butler (1992)

Chapters on magnetism from your favorite college physics book for review.

To learn more:

Chapter 1: Jiles (1992)

Chaper 1: Cullity (1972)

In this lecture we will review the basic physical principles behind magnetism. We will be using primarily the Système International (SI) units that are based on meters-kilograms-seconds. There are other sytems of units that are important in magnetism and the most prevalent of these (electromagnetic units of the cgs system) will be covered later in the lecture.

1.1 What is a magnetic field?

Magnetic fields, like gravitational fields, cannot be seen or touched. We can feel the pull of the Earth's gravitational field on ourselves and the objects around us, but we do not experience magnetic fields in such a direct way. We know of the existence of magnetic fields by their effect on objects such as magnetized pieces of metal, naturally magnetic rocks such as lodestone, or temporary magnets such as copper coils that carry an electrical current. If we place a magnetized needle on a cork in a bucket of water, it will slowly align itself with the local magnetic field. Turning on the current in a copper wire can make a nearby compass needle jump. Observations like these led to the development of the concept of magnetic fields.

Electric currents make magnetic fields, so we can define what is meant by a "magnetic field" in terms of the electric current that generates it. Figure 1.1a is a picture of what happens when we pierce a flat sheet with a wire carrying a current i. When iron filings are sprinkled on the sheet, the filings line up with the magnetic field produced by the current in the wire. A circle tangential to the field is shown in Figure 1.1b, which illustrates the *right-handrule* (see inset to Figure 1.1b). If your right thumb points in the direction of (positive) current flow (the direction opposite the flow of the electrons), your fingers will curl in the direction of the magnetic field.

The magnetic field $\mathbf{H}$ points at right angles to both the direction of current flow and to the radial unit vector $\mathbf{r}$ in Figure 1.1b. The magnitude of $\mathbf{H}$ is proportional to the strength of the current i. In the simple case illustrated in Figure 1.1b the magnitude of $\mathbf{H}$ is given by Ampère's

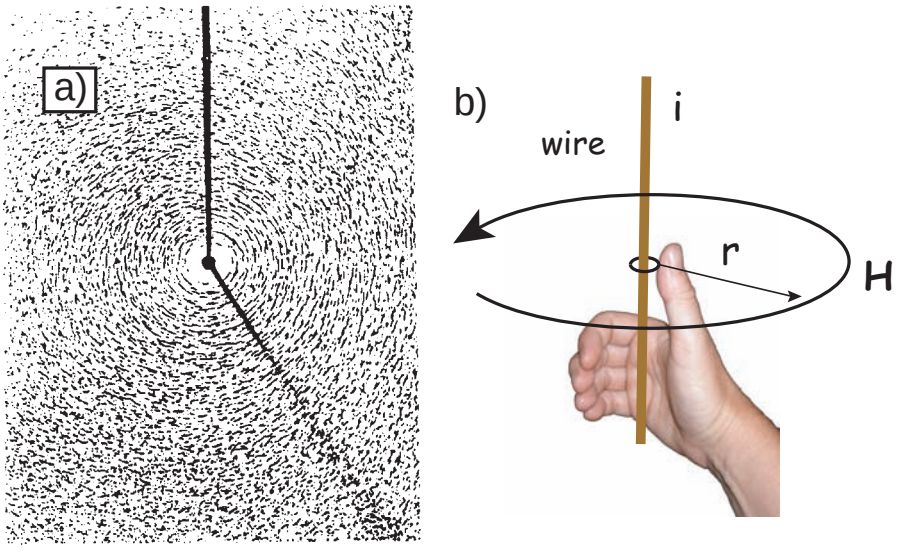

Figure 1.1: a) Distribution of iron filings on a flat sheet pierced by a wire carrying a current i. b) Relationship of magnetic field to current for straight wire. [Iron filings picture from Jiles (1992).]

law:

$$H = \frac{i}{2\pi r}.$$

So, now we know the units of $\mathbf{H}$: Am^{-1}.

Ampère's Law in its most general form is one of Maxwell's equations of electromagnetism: In a steady electrical field, $\nabla \times \mathbf{H} = \mathbf{J}_f$, where $\mathbf{J}_f$ is the electric current density. In other words: The curl (or circulation) of the magnetic field is equal to the current density. The origin of the term "curl" for the cross product of the gradient operator with a vector field is suggested in Figure 1.1a in which the iron filings seem to curl around the wire.

1.2 Magnetic moment

We have seen that an electrical current in a wire produces a magnetic field that curls around the wire. If we bend the wire into a loop with an area πr^2 that carries a current i, as shown in Figure 1.2a, the current loop creates the magnetic field shown by pattern of the the iron filings. This magnetic field is that same as the field that would be produced by a magnet with a magnetic moment $\mathbf{m}$ shown in Figure 1.2b. This moment is created by the current i and also depends on the area of the current loop (the bigger the loop, the bigger the moment), hence $\mathbf{m} = i\pi r^2$. The moment created by a set of loops (as shown in Figure 1.2c is the sum of the n individual loops, i.e.:

$$\mathbf{m} = ni\pi r^2. \tag{1.1}$$

So, now we know the units of $\mathbf{m}$: Am^2.

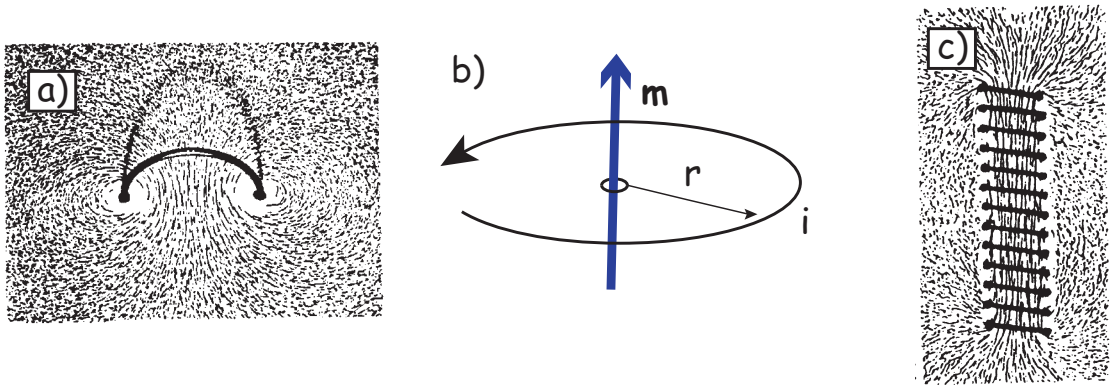

Figure 1.2: a) Iron filings show the magnetic field generated by current flowing in a loop. b) The magnetic field of a current loop with current i and area πr^2 is the same as one produced by a magnet with moment $\mathbf{m}$. c) The magnetic field of loops arranged as a solinoid is the sum of the contribution of the individual loops. [Iron filings pictures from Jiles (1992).]

1.3 Magnetic flux

The magnetic field is a vector field because at any point the field has both direction and magnitude. Consider the field of a bar magnet made visible by iron filings as shown in Figure 1.3. The direction of the field at any point is given by the arrows while the strength depends on how close the field lines are to one another. The magnetic field lines are known as "magnetic flux". The density of flux lines is one measure of the strength of the magnetic field: the magnetic induction $\mathbf{B}$.

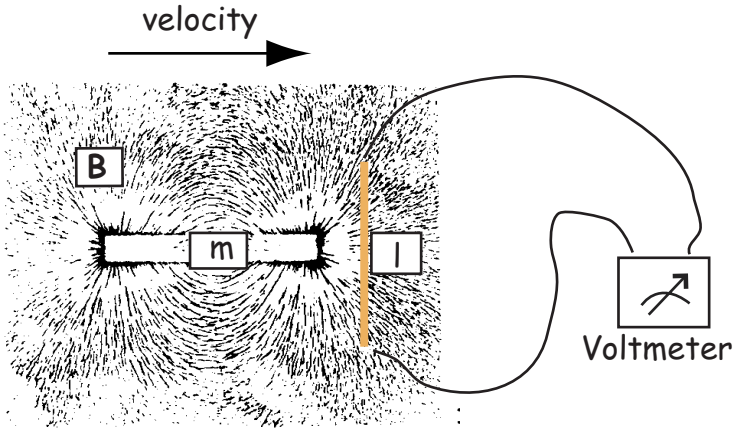

Figure 1.3: A magnetic moment $\mathbf{m}$ makes a vector field $\mathbf{B}$ made visible by the iron filings. If this field moves with velocity $\mathbf{v}$, it generates a voltage V in an electrical conductor of length l. [Iron filings picture from Jiles (1992).]

Magnetic flux density (i.e., magnetic induction) can therefore be quantified when a conductor moves through it. Magnetic induction can be thought of as something that creates a potential

difference with voltage V in a conductor of length l when the conductor moves relative to the magnetic induction B with velocity $\mathbf{v}$ (see Figure 1.3): $V = vlB$. From this we can derive the units of magnetic induction: the tesla (T). One tesla is the magnetic induction that generates a potential of one volt in a conductor of length 1 meter when moving 1 meter per second. Ergo, 1 T = 1 V $\cdot$ s $\cdot$ m^{-2}.

Another way of looking at this is that if magnetic induction ($\mathbf{B}$) is the flux density, this must be the flux Φ per unit area. So an increment of flux $d\Phi$ is the field B times the increment of area dA. The area here is the length of the wire l times its displacement ds in time dt. The instantaneous velocity is $dv = ds/dt$ so or $d\Phi = BdA$ and the rate of change of flux is:

$$\frac{d\Phi}{dt} = (\frac{ds}{dt})Bl = vBl = V. \tag{1.2}$$

Equation 1.2 is known as Faraday's law and in its most general form is the fourth of Maxwell's equations. We see from this equation that the units of magnetic flux must be a volt-second which is unit in its own right, the weber (Wb). The weber is defined as the amount of magnetic flux which, when passed through a one-turn coil of a conductor carrying a current of one ampere, produces an electric potential of one volt. This definition suggests a means to measure the strength of magnetic induction and is the basis of the "fluxgate" magnetometer.

1.4 Magnetic energy

A magnetic moment $\mathbf{m}$ has a *magnetostatic energy* (E_m) associated with it. This is the energy that tends to align compass needles with the magnetic field (see Figure 1.4. This energy is given by $\mathbf{m} \cdot \mathbf{B}$ or $mB\cos\theta$ where m and B are the magnitudes of $\mathbf{m}$ and $\mathbf{B}$, respectively. Magnetic energy has of joules.

1.5 Magnetization and magnetic susceptibility

Magnetization $\mathbf{M}$ is a moment per unit volume (units of Am^{-1}) or per unit mass (Am^{2}kg^{-1}). Subatomic charges such as protons and electrons can be thought of as tracing out tiny circuits and behaving as tiny magnetic moments. They respond to external magnetic fields and give rise to an induced magnetization. The relationship between the magnetization induced in a material $\mathbf{M}_I$ and the external field $\mathbf{H}$ is defined as:

$$\mathbf{M}_I = \chi_b \mathbf{H}. \tag{1.3}$$

The parameter χ_b is known as the *bulk magnetic susceptibility* of the material; it can be a complicated function of orientation, temperature, state of stress, time scale of observation and applied field but is often treated as a scalar.

Certain materials can produce magnetic fields in the absence of external magnetic fields (i.e., they are permanent magnets). As we shall see later in the course, these so-called "spontaneous" magnetic moments are also the result of spins of electrons which, in some crystals, act in a coordinated fashion, thereby producing a net magnetic field. The resulting magnetization can be fixed by various mechanisms and can preserve records of ancient magnetic fields. This *remanent magnetization* forms the basis of the field of paleomagnetism and will be discussed at length in the rest of this class.

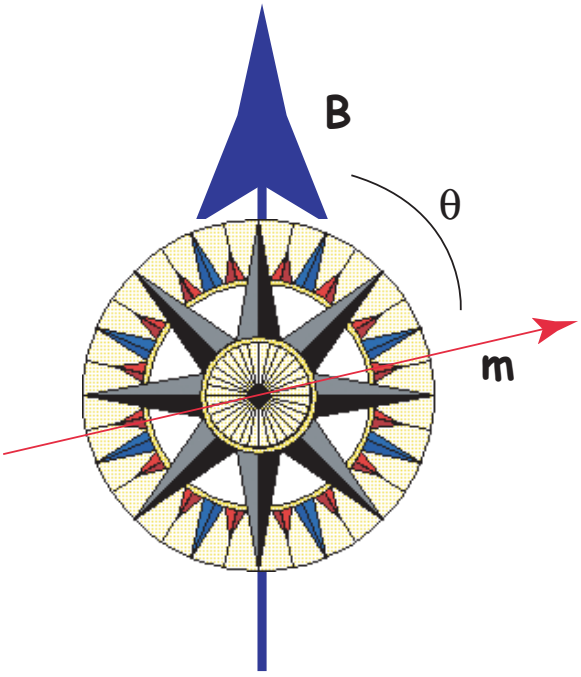

Figure 1.4: A magnetic moment **m** of for example a compass needle, will tend to align itself with a magnetic field **B**. The aligning energy is the magnetostatic energy which is greatest when the angle between the two vectors θ is at a maximum.

1.6 Relationship of B and H

From the foregoing discussion, we see that **B** and **H** are closely related. In paleomagnetic practice, both **B** and **H** are referred to as the "magnetic field". Strictly speaking, **B** is the induction and **H** is the field, but the distinction is often blurred. The relationship between **B** and **H** is given by:

$$\mathbf{B} = \mu_o(\mathbf{H} + \mathbf{M}). \tag{1.4}$$

where μ_o is a parameter known as "the permeability of free space". In the SI system, μ_o has dimensions of henries per meter and is given by $\mu_o = 4\pi \times 10^{-7}\mathrm{H} \cdot \mathrm{m}^{-1}$.

1.7 A brief tour of magnetic units in the cgs system

So far, we have derived magnetic units in terms of the Système International (SI). In practice, you will notice that in many laboratories and in the literature people frequently use what are known as cgs units, based on centimeters, grams and seconds. You may wonder why any fuss would be made over using meters as opposed to centimeters because the conversion is trivial. With magnetic units, however, the conversion is far from trivial and has been the source of confusion and many errors. So, in the interest of clearing things up, we will briefly outline the cgs approach to magnetic units.

The derivation of magnetic units in cgs is entirely different from SI. The approach we will take here (see Cullity, 1972) starts with the concept of a magnetic pole with strength p. By analogy

to Coulomb's law, the force between two poles p_1, p_2 instead of with current loops as we did for SI units. Coulomb's Law states that the force between two charges (q_1, q_2) is:

$$F_{12} = k\frac{q_1 q_2}{r^2} \tag{1.5}$$

where r is the distance between the two charges. In cgs units, the proportionality constant k is simply unity, whereas in SI units it is $\frac{1}{4\pi\epsilon_0}$ where $\epsilon_0 = \frac{10^7}{4\pi c^2}$ and c is the speed of light in a vacuum (hence $\epsilon_0 = 8.859 \cdot 10^{-12}$ $\mathrm{AsV^{-1}m^{-1}}$). [You can see why many people really prefer cgs but we are not allowed to publish in cgs in AGU journals so we just must grin and bear it!]

For magnetic units, we use pole strength p_1, p_1 in units of "electrostatic units" or esu, so Equation 1.5 becomes

$$F = \frac{p_1 p_2}{r^2}$$

Force in cgs is in units of dynes (dyn) so,

$$F = 1\mathrm{dyn} = \frac{1\mathrm{g\ cm}}{s^2} = \frac{1\ \mathrm{esu}^2}{cm^2}$$

so 1 unit of pole strength is rather awkwardly 1 $\mathrm{gm}^{1/2}$ $\mathrm{cm}^{3/2}$ s^{-1}. Of course there are no isolated magnetic poles in nature, only dipoles, but the concept of a unit of pole strength lies at the heart of cgs magnetic units.

A magnetic pole, as an isolated electric charge, will create a magnetic induction $\mu_o H$ in the space around it. One unit of field strength (defined as one "oersted" or Oe) is the unit of field strength that exerts a force of one dyne on a unit of pole strength. The relationship between force, pole and field is written as:

$$F = p\mu_o H.$$

So, a pole with one pole strength, placed in a one Oe field is acted on by a force of one dyne. This is the same force that it would experience if placed one centimeter away from another pole with one pole strength. Hence, the field of this monopole must be one oersted at one centimeter away, and fall off as $1/r^2$.

Returning to the lines of force idea developed for magnetic fields earlier, let us define the oersted to be 1 line of force per square centimeter. Imagine a sphere with a radius r surrounding the magnetic monopole. The surface area of such a sphere is $4\pi r^2$. The sphere is a unit sphere ($r = 1$), the field strength at the surface is 1 Oe, then there must be 4π lines of force passing through it.

Proceeding to the notion of magnetic moment, from a cgs point of view, we start with a magnet of length l with two poles of strength p at each end. Placing the magnet in a field $\mu_o\mathbf{H}$, we find that it experiences a torque Γ proportional to $p, l, \mathbf{H}$ such that

$$\Gamma = pl \times \mu_o\mathbf{H}. \tag{1.6}$$

Recalling our earlier discussion of magnetic moment, you will realize that pl is simply the magnetic moment m. The units of torque are energy, which are ergs in cgs, so the units of magnetic moment are ergs/oersted. We therefore define the "electromagnetic unit" (emu) as being one erg/oersted. [Some use emu to refer to the magnetization (volume normalized moment, see above), but this is incorrect.]

You will have noticed the use of the parameter μ_0 in the above treatment - a parameter missing in Cullity (1972) and in many books and articles using the cgs units. The reason for this is that μ_0 is unity in cgs units and simply converts from oersteds ($\mathbf{H}$) and gauss ($\mathbf{B}$) which are therefore used interchangeably. It was inserted in this derivation to remind us that there IS a difference and that the difference becomes very important when we convert to SI because μ_0 is not unity, but 4π x 10^{-7}! For conversion between commonly used cgs and SI paramters, please refer to Table 1. 1.

Table 1.1: Conversion between SI and cgs units.

Parameter	SI unit	cgs unit	Conversion
Magnetic moment ($\mathbf{m}$)	Am^2	emu	1 A m^2 = 10^3 emu
Magnetization ($\mathbf{M}$)	Am^{-1}	emu cm^{-3}	1 Am^{-1} = 10^{-3} emu cm^{-3}
Magnetic Field ($\mathbf{H}$)	Am^{-1}	Oersted (oe)	1 Am^{-1} = 4π x 10^{-3} oe
Magnetic Induction ($\mathbf{B}$)	T	Gauss (G)	1 T = 10^4 G
Permeability of free space (μ_0)	Hm^{-1}	1	4π x 10^{-7} Hm^{-1} = 1
Susceptibility (χ)			
total ($\frac{\mathbf{m}}{\mathbf{H}}$)	m^3	emu oe^{-1}	1 m^3 = $\frac{10^6}{4\pi}$ emu oe^{-1}
by volume ($\frac{\mathbf{M}}{\mathbf{H}}$)	-	emu cm^{-3} oe^{-1}	1 S.I. = $\frac{1}{4\pi}$ emu cm^{-3} oe^{-1}
by mass ($\frac{\mathbf{m}}{m} \cdot \frac{1}{\mathbf{H}}$)	m^3kg^{-1}	emu g^{-1} oe^{-1}	1 m^3kg^{-1} = $\frac{10^3}{4\pi}$emu g^{-1} oe^{-1}

1 H = kg $m^2A^{-2}s^{-2}$, 1 emu = 1 G cm^3, $B = \mu_o(H + M)$, 1 T = kg A^{-1} s^{-2}

1.8 The magnetic potential

An isolated electrical charge produces electrical fields that begin at the source (the charge) and spread (diverge) outward (see Figure 1.5a). Because there is no return flux to an oppositely charged "sink", there is a net flux out of the dashed box shown in the figure. The "divergence" of the electrical field is defined as $\nabla \cdot \mathbf{E}$ which quantifies the net flux (see supplement to Chapter 1 for more). In the case of the field around an electric charge, the divergence is non-zero.

Magnetic fields are different from electrical fields in that there is no equivalent to an isolated electrical charge; there are only pairs of "opposite charges", or magnetic *dipoles*. Therefore, any line of flux starting at one magnetic pole, returns to its sister pole and there is no net flux out of the box shown in Figure 1.5b; the magnetic field has no divergence (Figure 1.5b). This property of magnetic fields is another of Maxwell's equations: $\nabla \cdot \mathbf{B} = 0$.

We have already seen that the curl of the magnetic field ($\nabla \times \mathbf{H}$) depends on the current density which is not always zero. Therefore, magnetic fields cannot generally be represented as the gradient of a scalar field. However, in the special case away from electric currents, the magnetic field can be written as the gradient of a scalar field that is known as the *magnetic potential* ψ_m, *i.e.*,

$$\mathbf{H} = -\nabla\psi_m.$$

The presence of a magnetic moment $\mathbf{m}$ creates a magnetic field which is the gradient of a scalar field. We also know that the divergence of the magnetic field is zero, hence $\nabla^2\psi_m = 0$. This is LaPlace's equation which is the starting point for spherical harmonic analysis discussed briefly in Lecture 2.

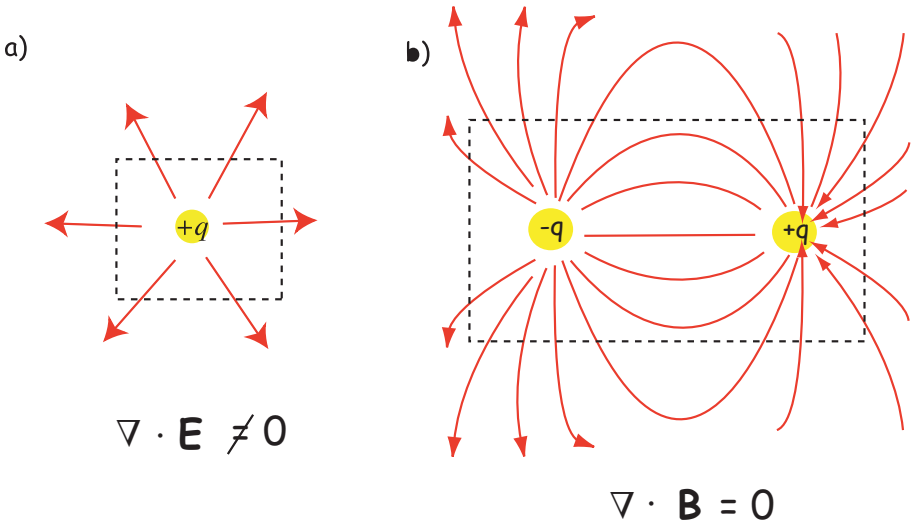

Figure 1.5: a) An electric charge produces a field that diverges out from the source. There is a net flux out of the dashed box, quantified by the divergence ($\nabla \cdot \mathbf{E}$), which is is proportional to the magnitude of the sources inside the box. b) there are no isolated magnetic charges, only dipoles. Within any space (e.g., the dashed box) any flux line that comes in, goes out. The divergence of such a field is zero, i.e., $\nabla \cdot \mathbf{B} = 0$.

The magnetic potential ψ_m is a function the vector $\mathbf{r}$ with radial distance r and angle θ from the moment. Given a *dipole moment* $\mathbf{m}$, the solution to LaPlace's equation for the simple case of a magnetic field produced by $\mathbf{m}$ is:

$$\psi_m = \frac{\mathbf{m} \cdot \mathbf{r}}{4\pi r^3} = \frac{m \cos\theta}{4\pi r^2}. \tag{1.7}$$

The radial and tangential components of $\mathbf{H}$ at P (Figure 1.6) are:

$$H_r = -\frac{\partial \psi_m}{\partial r} = \frac{1}{4\pi}\frac{2m\cos\theta}{r^3},$$

and

$$H_\theta = -\frac{1}{r}\frac{\partial V_m}{\partial \theta} = \frac{m\sin\theta}{4\pi r^3},$$

respectively.

1.9 The geodynamo

Maxwell's equations tell us that electric and changing magnetic fields are closely linked and can effect each other. Moving an electrical conductor through a magnetic field will cause electrons to flow, generating an electrical current. This is the principal of electric motors. In Figure 1.7 we see a design for a machine that will turn mechanical energy into magnetic field energy. The rotating disk is made of metal. As the disk turns in the presence of an initial magnetic field, the electrons scurry at right angles to the field, generating an electric potential (Figure 1.7b). The

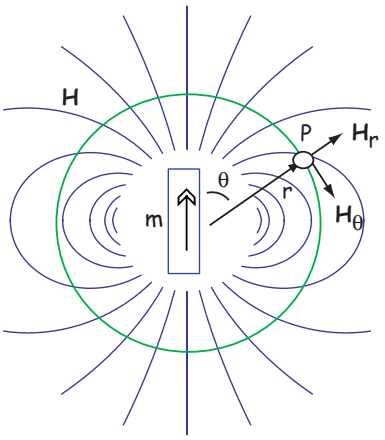

Figure 1.6: Field **H** produced at point P by a magnetic moment **m**. $\mathbf{H}_r$ and $\mathbf{H}_\theta$ are the radial and tangential fields respectively.

brush connection allows a current to flow through the wire wound into a coil, in turn generating a magnetic field. If the rotating disk is spun in the right direction, the magnetic field will be in the same sense as the initial field, amplifying the effect and generating a much larger magnetic field. More complicated setups using two disks whose fields interact with one another generate chaotic magnetic behavior that can switch polarities even if the mechanical motion remains steady. While a very poor analogue for the Earth's magnetic field, it demonstrates that moving electrical conductors can generate a magnetic field. In the Earth of course the moving electrical conductor is the molten iron outer core.

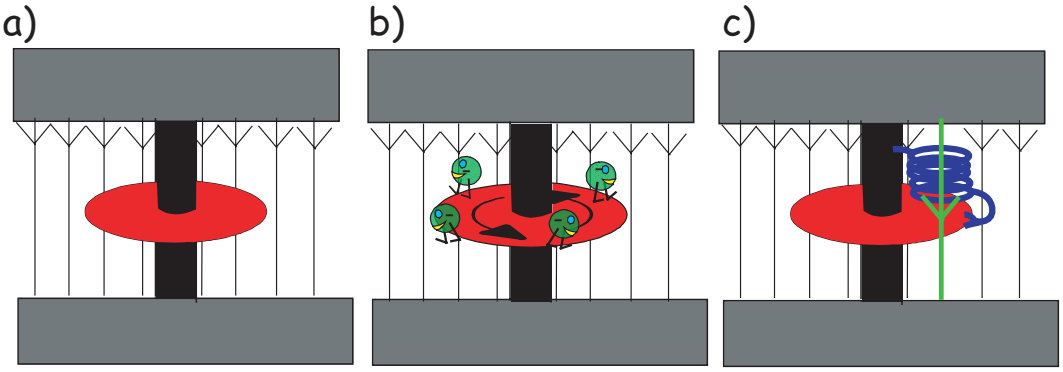

Figure 1.7: The Faraday disk dynamo. a) An initial field is produced by the electromagnet (thin arrows). The red disk is a conducting plate. b) When the conducting plate is rotated, electric charge moves perpendicular to the magnetic field setting up an electric potential between the inner conducting rod and the outer rim of the plate. c) When the conducting plate is connected to a coil wound such that a current produces a magnetic field in the same direction as the initial field, the magnetic field is enhanced. (Figure drawn with help from Philip Staudigel).

Appendix

In this appendix we will review the basic math concepts necessary to understand the chapter on magnetism. We will start with basic vector math and then review useful operators grad, div and curl.

A Vectors

A1 Addition

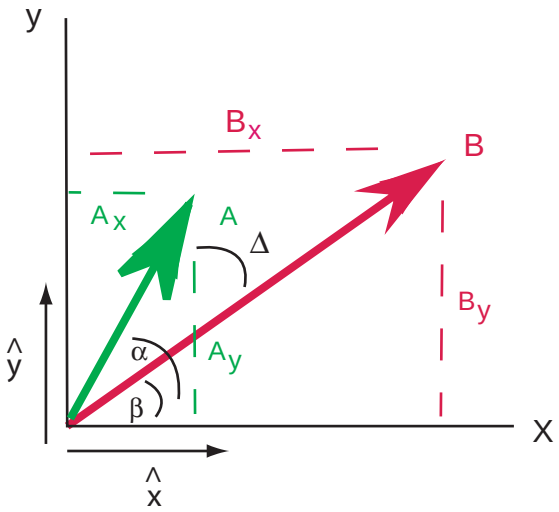

Figure A1: Vectors **A** and **B**, their components $A_{x,y}$, $B_{x,y}$ and the angles between them and the X axis, α and β. The angle between the two vectors is α -β = Δ. Unit vectors in the directions of the axes are $\hat{x}$ and $\hat{y}$ respectively.

To add the two vectors (see Figure A1) **A** and **B**, we break each vector into components $A_{x,y}$ and $B_{x,y}$. For example, $A_x = |A| \cos\alpha, A_y = |A| \sin\alpha$ where $|A|$ is the length of the vector **A**. The components of the resultant vector **C** are: $C_x = A_x + B_x, C_y = A_y + B_y$. These can be converted back to polar coordinates of magnitude and angles if desired.

A2 Subtraction

To subtract two vectors, compute the components as in addition, but the components of the vector difference **C** are: $C_x = A_x - B_x, C_y = A_y - B_y$.

A3 Multiplication

There are two ways to multiply vectors. The first is the dot product whereby $\mathbf{A} \cdot \mathbf{B} = A_x B_x + A_y B_y$. This is a scalar and is actually the cosine of the angle between the two vectors if the **A** and **B** are taken as unit vectors (assume a magnitude of unity in the component calculation.

The other way to perform vector multiplication is the cross product (see Figure A2), which produces a vector orthogonal to both **A** and **B** and whose components are given by:

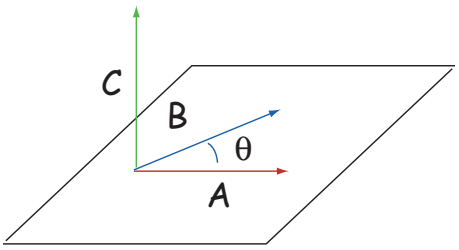

Figure A2: Illustration of cross product of vectors A and B separated by angle θ to get the orthogonal vector C.

$$C = \det \begin{vmatrix} \hat{x} & \hat{y} & \hat{z} \\ A_x & A_y & A_z \\ B_x & B_y & B_z \end{vmatrix}.$$

To calculate the determinant, we follow these rules:

$$C_x = A_y B_z - A_z B_y, C_y = A_z B_x - A_x B_z, C_z = A_x B_y - A_y B_x.$$

or

$$C_i = A_j B_k - A_k B_j \qquad i \neq j \neq k$$

A4 Change of coordinates

In paleomagnetism, we often have to change coordinate systems, from say sample coordinates to geographic, or to correct for tilting of the geological units. The way to do this in a simple 2-D case is illustrated in Figure A3. Given the vector shown in Figure A3a, that is oriented at an angle α from the $\mathbf{X}_1$ axis. To change to a second set of axes $\mathbf{X}'_1, \mathbf{X}'_2$, we first have to define a set of coefficients called "direction cosines". For example, the direction cosine a_{12} is the cosine of the angle between the old X_1 and the new X'_2, α_{12}. We can define four of these direction cosines to fully describe the relationship between the two coordinate systems:

$$\begin{aligned} a_{11} &= \cos\alpha_{11}, a_{21} = \cos\alpha_{21}, \\ a_{12} &= \cos\alpha_{12}, a_{22} = \cos\alpha_{22}. \end{aligned}$$

The first subscript always refers to the old system and the second refers to the new.

To find the new coordinates x'_1, x'_2 from the old, we just have:

$$\begin{aligned} x'_1 &= a_{11}x_1 + a_{12}x_2, \\ x'_2 &= a_{21}x_2 + a_{22}x_2. \end{aligned}$$

In three dimensions we have:

$$\begin{aligned} x'_1 &= a_{11}x_1 + a_{12}x_2 + a_{13}x_3, \\ x'_2 &= a_{21}x_2 + a_{22}x_2 + a_{23}x_3, \\ x'_3 &= a_{31}x_2 + a_{32}x_2 + a_{33}x_3, \end{aligned}$$

A short cut notation to this is: $x'_i = a_{ij}x_j$. This just means that for each axis i, just sum through the j's for all the dimensions.

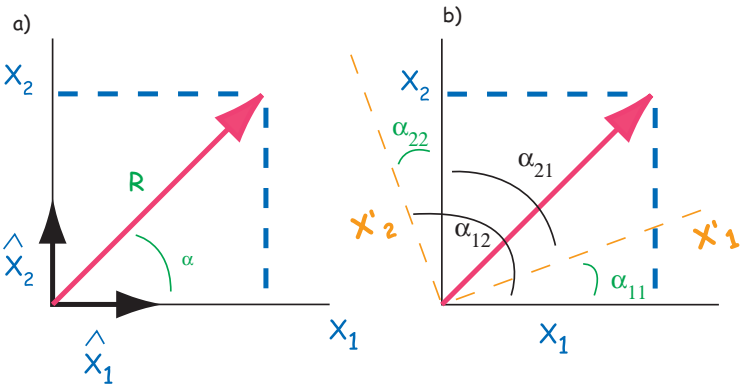

Figure A3: Transformation of axes. a) Definition of vector in one set of coordinates, x_1, x_2. b) Definition of angles relating old X axes to new X'.

B Upside down triangles

B1 Gradient, ∇

We often wish to differentiate a function along three orthogonal axes. For example, imagine we know the topography of a ski area (see Figure B1). For every location (in say, X and Y coordinates), we know the height above sea level. This is a scalar function. Now imagine we want to build a ski resort, so we need to know the direction of steepest descent and the slope (red arrows in Figure B1).

Figure B1: Illustration of the relationship between a vector field (direction and magnitude of steepest slope at every point, e.g., red arrows) and the scalar field (height) of a ski slope.

To convert the scalar field (height versus position) to a vector field (direction and magnitude of greatest slope) mathematically, we would simply differentiate the topography function. Let's say

we had a very weird two dimensional, sinusoidal topography such that $z = f(x) = \sin x$ with z the height and x is the distance from some marker. The slope in the x direction ($\hat{x}$), then would be $\hat{x}\frac{d}{dx}f(x)$. If $f(x, y, z)$ were a three dimentional topography then the gradient of the topography function would be:

$$(\hat{x}\frac{\partial}{\partial x}f + \hat{y}\frac{\partial}{\partial y}f + \hat{z}\frac{\partial}{\partial z}f)$$

For short hand, we define a "vector differential operator" to be a vector whose components are

$$\nabla = (\hat{x}\frac{\partial}{\partial x}, \hat{y}\frac{\partial}{\partial y}, \hat{z}\frac{\partial}{\partial z}).$$

This can also be written in polar coordinates:

$$\nabla = \frac{\partial}{\partial r}, \frac{\partial}{r\partial\theta}, \frac{\partial}{r\sin\theta\partial\phi}$$

Just as the direction and magnitude of maximum slope of the topography is a the gradient of the scalar function of height, the magnetic field is the gradient of a scalar function of something we will define as the magnetic potential. In Lecture 1, we said that the magnetic field **H** is the gradient of a scalar potential field ψ_m, or

$$\mathbf{H} = -\nabla\psi_m.$$

This means that for a simple dipolar field:

$$\psi_m = \frac{\mathbf{m}\cdot\mathbf{r}}{4\pi r^3}$$

We can derive the radial component of the field as:

$$H_r = \frac{\partial\psi_m}{\partial r} = \frac{1}{4\pi}\frac{2m\cos\theta}{r^3}$$

and the tangential component as:

$$H_\theta = \frac{-1}{r}\frac{\partial V_m}{\partial\theta} = \frac{m\sin\theta}{4\pi r^3}.$$

B2 Divergence

The divergence of a vector function (e.g. **H**) is written as:

$$\nabla\cdot\mathbf{H}$$

The trick here is to treat ∇ as a vector and use the rules for dot products described in the section A of this appendix. In cartesian coordinates, this is:

$$\nabla\cdot\mathbf{H} = \hat{x}\frac{\partial H_x}{\partial x} + \hat{y}\frac{\partial H_y}{\partial y} + \hat{z}\frac{\partial H_z}{\partial z}.$$

Like all dot products, the divergence of a vector function is a scalar.

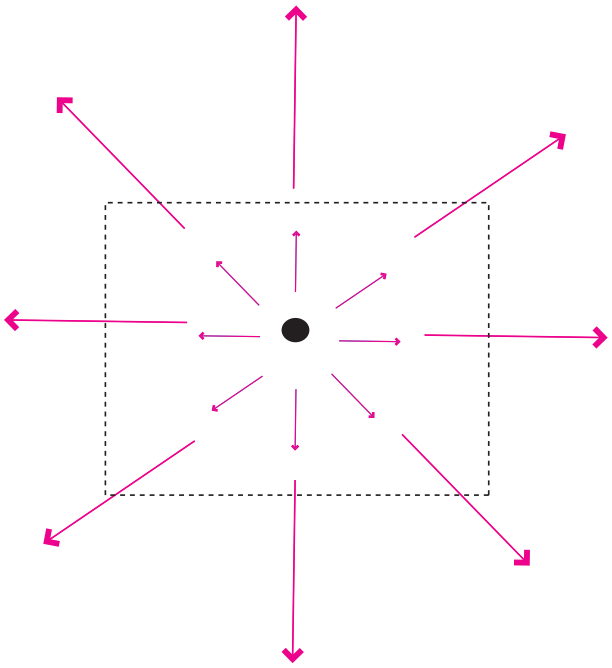

Figure B2: Example of a vector field with a non-zero divergence.

B3 Geometrical interpretation of divergence

The name divergence is well chosen because $\nabla \cdot \mathbf{H}$ is a measure of how much the vector field "spreads out" (diverges) from the point in question. In fact, what divergence quantifies is the balance between vectors coming in to a particular region versus those that go out. The example in Figure B2 depicts a vector function whereby the magnitude of the vector increases linearly with distance away from the central point. An example of such a function would be $v(r) = r$. The divergence of this function is:

$$\nabla \cdot v = \frac{\partial}{\partial r} r = 1$$

(a scalar). There are no arrows returning in to the dashed box, only vectors going out and the non-zero divergence quantifies this net flux out of the box.

Now consider Figure B3, which depicts a vector function that is constant over space, i.e. $v(r) = k$. The divergence of this function is:

$$\nabla \cdot v = \frac{\partial}{\partial r} k = 0.$$

The zero divergence means that for every vector leaving the box, there is an equal and opposite vector coming in. Put another way, no net flux results in a zero divergence. The fact that the divergence of the magnetic field is zero means that there are no point sources (monopoles), as opposed to electrical fields that have divergence related to the presence of electrons or protons.

B4 Curl

The curl of the vector function $\mathbf{B}$ is defined as $\nabla \times \mathbf{B}$. In cartesian coordinates we have

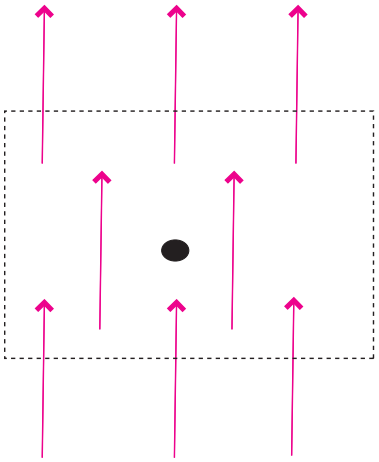

Figure B3: Example of a vector field with zero divergence.

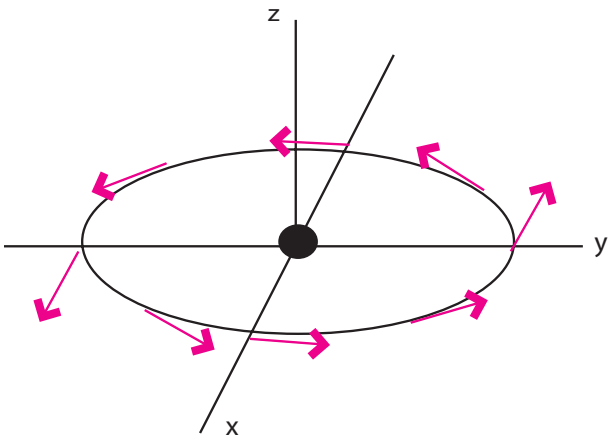

Figure B4: Example of a vector field with non-zero curl.

$$\nabla \times \mathbf{B} = \hat{x}(\frac{\partial}{\partial y}B_z - \frac{\partial}{\partial z}B_y) + \hat{y}(\frac{\partial}{\partial z}B_x - \frac{\partial}{\partial x}B_z) + \hat{z}(\frac{\partial}{\partial x}B_y - \frac{\partial}{\partial y}B_x).$$

Curl is a measure of how much the vector function "curls" around a given point. The function describing the velocity of water in a whirlpool has a significant curl, while that of a smoothly flowing stream does not.

Consider Figure B4 which depicts a vector function $v = -y\hat{x} + x\hat{y}$. The curl of this function is:

$$\nabla \times \ v = \det \begin{vmatrix} \hat{x} & \hat{y} & \hat{z} \\ \frac{\partial}{\partial x} & \frac{\partial}{\partial y} & \frac{\partial}{\partial z} \\ -y & x & 0 \end{vmatrix}.$$

or

$$\hat{x}(\frac{\partial}{\partial y}0 - \frac{\partial}{\partial z}x) + \hat{y}(\frac{\partial}{\partial x}0 - \frac{\partial}{\partial z}(-y)) + \hat{z}(\frac{\partial}{\partial x}x - \frac{\partial}{\partial y}(-y))$$
$$= 0\hat{x} + 0\hat{y} + 2\hat{z}$$

So there is a positive curl in this function and the curl is a vector in the $\hat{z}$ direction.

The magnetic field has a non-zero curl in the presence of currents or changing electric fields. In free space, away from currents (lightning!!), the magnetic field has zero curl.

Bibliography

Butler, R. F. (1992), *Paleomagnetism: Magnetic Domains to Geologic Terranes*, Blackwell Scientific Publications.

Cullity, B. (1972), *Introduction to Magnetic Materials*, Addison-Wesley Publishing Company.

Jiles, D. C. (1992), 'Numerical determination of hysteresis parameters for the modeling of magnetic properties using the theory of ferromagnetic hysteresis', *IEEE Transactions on Magnetics* **28**, 27–35.

Lectures in Paleomagnetism, 2005
by Lisa Tauxe

Citation:
http://earthref.org/MAGIC/books/Tauxe/2005/

May 30, 2005

Chapter 2

The Geomagnetic Field

Suggested Supplemental Reading

pp 3-7; 10-11: Butler (1992)

To learn more:

Chapters 1 & 2: Merrill et al. (1996)

2.1 The Earth's Magnetic Field

One of the major efforts in paleomagnetism has been to study ancient geomagnetic fields. Because human measurements only extend back a few centuries, paleomagnetism remains the only way to investigate ancient field behavior. Because of the application of paleomagnetism to geomagnetism, it is useful for students of paleomagnetism to understand something about the geomagnetic field. In this lecture we review the general properties of the Earth's present magnetic field.

The geomagnetic field is generated by convection currents in the liquid outer core of the Earth which is composed of iron, nickel and some unkown lighter component(s). The source of energy for this convection is not known for certain, but is thought to be partly cooling of the core and partly the bouyancy of the iron/nickel liquid outer core caused by freezing out of the pure iron inner core. Motions of this conducting fluid are controlled by the bouyancy of the liquid, the spin of the Earth about its axis and by the interaction of the conducting fluid with the magnetic field (in a horrible non-linear fashion). Solution of the equations for the fluid motions and resulting magnetic fields is a challenging computational task, but it is known that these motions act as a self-sustaining dynamo and create an enormous magnetic field.

2.1.1 Reference magnetic field

For many purposes, it is useful to have a compact representation of the the spatial distribution of the geomagnetic field for a particular time. It is often handy to have a mathematical approximation for the field along with estimates for rates of change such that field vectors can be accurately estimated at a given place at a given time (within a few hundred years at least). As we learned in Lecture 1, the magnetic field at the Earth's surface can be approximated by a scalar potential field, and this scalar potential field satisfies LaPlace's Equation:

$$\nabla^2 \psi_m = 0$$

This can be rewritten as:

$$\frac{1}{r}\frac{\partial^2}{\partial r^2}(r\psi_m) + \frac{1}{r^2 \sin\theta}\frac{\partial}{\partial\theta}(\sin\theta\frac{\partial\psi_m}{\partial\theta}) + \frac{1}{r^2 \sin^2\theta}\frac{\partial\psi_m}{\partial\phi^2} = 0$$

One solution to this equation is:

$$\psi_m = \frac{U(r)}{r}P(\theta)Q(\phi).$$

For the geomagnetic field, this is usually written as the scalar potential at radius r, co-latitude θ, longitude ϕ:

$$\psi(r,\theta,\phi) = \frac{a}{\mu_o}\sum_{l=1}^{\infty}\sum_{m=0}^{l} P_l^m(\cos\theta)\left[\left((g_e)_l^m\left(\frac{r}{a}\right)^l + (g_i)_l^m\left(\frac{a}{r}\right)^{l+1}\right)\cos m\phi + \left((h_e)_l^m\left(\frac{r}{a}\right)^l + (h_i)_l^m\left(\frac{a}{r}\right)^{l+1}\right)\sin m\phi\right], \quad (2.1)$$

where g and h are *gauss coefficients* calculated for a particular year and are given in units of nT, or magnetic flux (note the μ_o in the equation converting from tesla [B] to Am^{-1} [H]). The e and i subscripts indicate fields of external or internal origin and a is the radius of the Earth (6.371×10^6 m), μ_o is the permeability of free space (see Table 1.1 from Lecture 1) and the P_l^m's are proportional to the Legendre polynomials, normalized according to the convention of Schmidt (see suggested reading for more details). The Schmidt polynomials are increasingly wiggly functions of the argument $\cos\theta$.

We show three examples in Fig. 2.2 of the inclinations of the vector fields with their surface harmonics as insets. These are the axial ($m = 0$) dipole ($l = 1$), quadrupole ($l = 2$) and octupole ($l = 3$) terms whose contributions are determined by g_1^0, g_2^0 and g_3^0 respectively. The associated polynomials are:

$$P_1^0 = \cos\theta, \qquad P_2^0 = \frac{1}{4}(3\cos 2\theta + 1), P_3^0 = \frac{1}{8}(5\cos 3\theta + 3\cos\theta).$$

and are shown in Figure 2.1.

If the axial dipole field produced by the harmonic function in Fig. 2.2a were turned on its side with the north pole part pointing to the Greenwich meridian, the contribution would be determined by h_1^0 coefficient, and if it were at 90°E, it would be the h_1^1 coefficient. Therefore, the total dipole contribution would be the vector sum of the axial and two equatorial dipole terms or $\sqrt{{g_1^0}^2 + {h_1^0}^2 + {h_1^1}^2}$. The total quadrupole contribution ($l = 2$) combines five coefficients and the total octupole ($l = 3$) contribution combines seven coefficients.

In general, terms for which the difference between the subscript (l) and the superscript (m) is odd (e.g., the axial dipole g_1^0 and octupole g_3^0) produce magnetic fields that are asymmetric about the equator, while those for which the difference is even (e.g., the axial quadrupole g_2^0) have symmetric fields. In Fig. 2.2a we show the inclinations produced by a purely dipole field of the same sign as the present day field. The inclinations are all positive (down) in the northern hemisphere and negative (up) in the southern hemisphere. In contrast, inclinations produced by a purely quadrupolar field (Fig. 2.2b) are down at the poles and up at the equator. The map of inclinations produced by a purely axial octupolar field (Fig. 2.2c) are again asymmetric about the

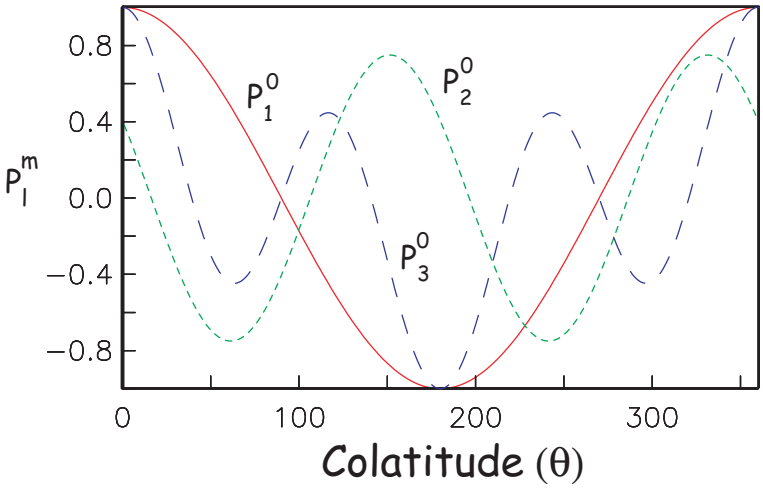

Figure 2.1: Schmidt polynomials

equator with vertical directions of opposite signs at the poles separated by bands with the opposite sign at mid-latitudes.

Getting back to observations of the geomagnetic field itself. It is a vector field, hence at every point, there is a direction and intensity (see Figure 2.3). A vector in three dimensions requires three parameters to define it fully no matter what coordinate system you choose. In cartesian coordinates these would be, for example, x, y, z or x_1, x_2 and x_3. Depending on the particular problem at hand, some coordinate systems are more suitable to use because they have the symmetry of the problem built into them. We will be using several coordinate systems in addition to the cartesian one and we will need to convert among them at will.

2.1.2 Components of magnetic vectors

The three elements of a magnetic vector that will be used most frequently are magnitude B (or sometimes H or M), declination D and inclination I, as shown in Figure 2.3. The convention used in this set of lectures is that axes are denoted $\mathbf{X}_1, \mathbf{X}_2, \mathbf{X}_3$, while the components along the axes are x_1, x_2, x_3. In the geographic frame of reference, positive $\mathbf{X}_1$ is to the north, $\mathbf{X}_2$ is east and $\mathbf{X}_3$ is vertically down in keeping with a right-hand rule; components of $\mathbf{B}$, for example, can alternatively be designated B_N, B_E, B_V.

From Figure 2.3 we see how to convert from the angular coordinate system of declination, inclination and total field magnitude to cartesian coordinate systems, using a little trigonometry, *i.e.*,

$$B_H = B\cos I = \sqrt{B_E^2 + B_N^2} \quad \text{and} \quad B_V = B\sin I = x_3. \tag{2.2}$$

The horizontal component can also be projected onto the North ($\mathbf{X}_1$) and East ($\mathbf{X}_2$) axes (the directions in which measurements are often made), *i.e.*,

$$B_N = x_1 = B\cos I\cos D \quad \text{and} \quad B_E = x_2 = B\cos I\sin D. \tag{2.3}$$

Equations 2.2 and 2.3 work equally well for components of magnetization.

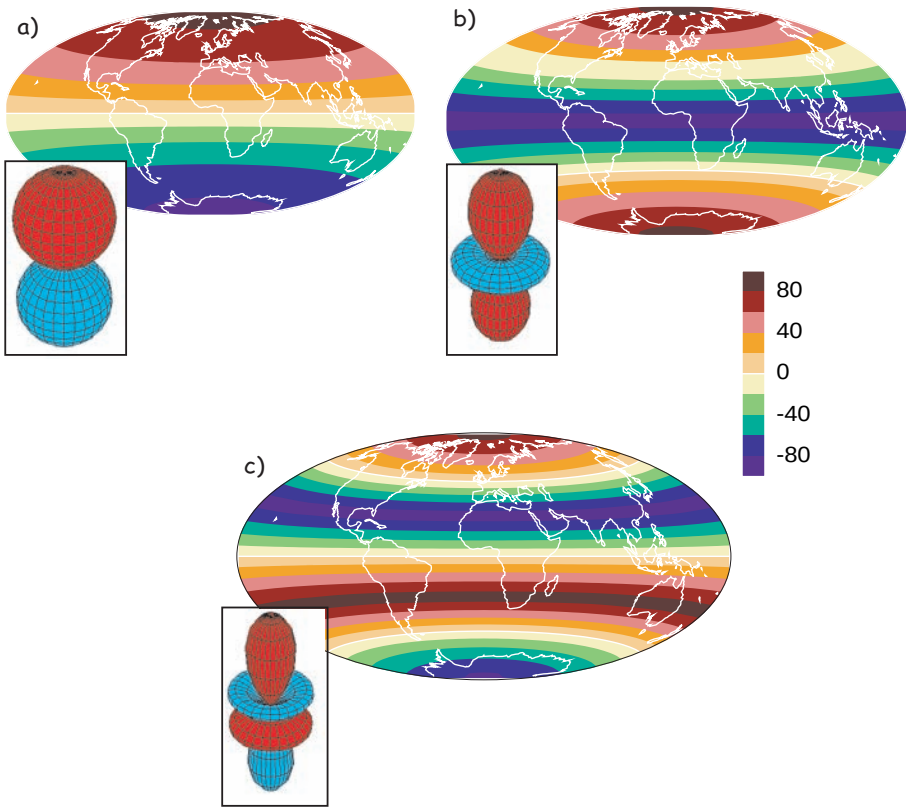

Figure 2.2: Examples of surface harmonics (insets) and maps of the associated patterns for global inclinations. a) Dipole, b) Quadrupole, c) Octupole. [Figure from Tauxe, 2005.]

If you have the cartesian coordinates of **B** (or **H** or **M**), they can be transformed to the geomagnetic elements D, I and B:

$$\begin{aligned} B &= \sqrt{x_1^2 + x_2^2 + x_3^2}, \\ D &= \tan^{-1}(x_2/x_1), \\ I &= \sin^{-1}(x_3/B). \end{aligned} \tag{2.4}$$

Be careful of the sign ambiguity of the tangent function. You may end up in the wrong quadrant and have to add 180°

Recalling Lecture 1 (including the appendix), once the scalar potential ψ_m is known, the components of the magnetic field can be calculated from the fact that $B = \nabla\psi_m$, so in spherical coordinates:

$$B_N = -\frac{1}{r}\frac{\partial\psi_m}{\partial\theta}, B_E = -\frac{1}{r\sin\theta}\frac{\partial\psi_m}{\partial\phi}, B_V = -\frac{\partial\psi_m}{\partial r}. \tag{2.5}$$

where r, θ, ϕ are radius, co-latitude (degrees away from the North pole) and longitude, respectively. Here, B_V is positive down B_N is positive to the north, the opposite of H_r and H_θ as defined in Lecture 1. Note that Equation 2.1 is in units of tesla, not Am^{-1}.

It is also true that if the magnetic vector field is known, the potential can be derived. In practice, the gauss coefficients for a particular reference field are estimated by least-squares fitting

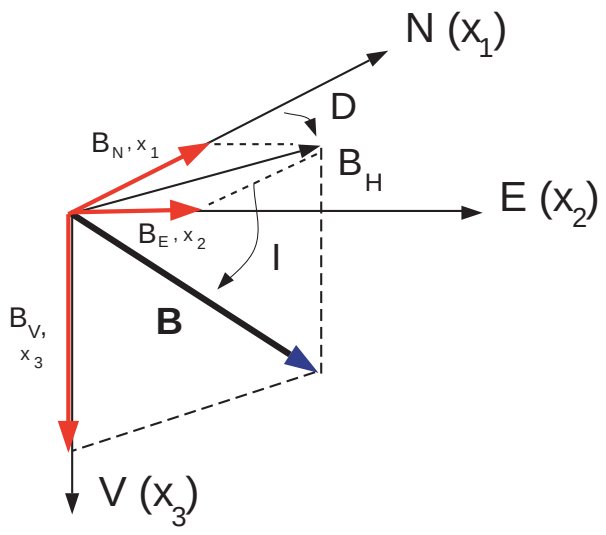

Figure 2.3: Components of the geomagnetic field vector **B**. B_H is the projection of the field vector **B** onto a plane tangent to the Earth's surface. B_H can be resolved into north and east components (B_N and B_E). B_V is the projection onto the vertical axis. D is measured clockwise from North and ranges from $0 \rightarrow 360°$. I is measured positive down from the horizontal and ranges from $-90 \rightarrow +90°$ (because field lines can also point out of the Earth). **M** or **H** can be substituted for **B** as needed.

of observations of the geomagnetic field. You need about 48 observations to estimate the coefficients out to about $L = 6$ reliably.

The gauss coefficients are determined by fitting Equations 2.5 and 2.1 to observations of the magnetic field made by magnetic observatories or satellite data for a particular time. The *International (or Definitive) Geomagnetic Reference Field* for a given time interval is an agreed upon set of values for a number of Gauss coefficients, and their time derivatives. IGRF (or DGRF) models and programs for calculating various components of the magnetic field are available on the Internet from the National Geophysical Data Center; the address is http://www.ngdc.noaa.gov.

In order to get a feel for the importance of the various gauss coefficients, take a look at Table 2.1 which has the gauss coefficients for the first six degrees from Olsen et al. (2000). The power at each degree is calculated by $R_l = \sum_m (l+1)[(g_l^m)^2 + (h_l^m)^2]$ (Lowes, 1974) and this is shown in Figure 2.4. It is clear that the lowest order terms (degree one) totally dominate the field consituting some 90% of the field. This is why the field can often be assumed to be equivalent to that created by a simple dipole at the center of the Earth.

It is also interesting to view the estimated geomagnetic elements from the IGRF for 1995. Using the values for a given reference field in Equations 2.1 and 2.5, we can calculate values of B, D and I at any location on Earth. Examples of maps made from such calculations using the IGRF for 1995 are shown in Figure 2.5. These maps demonstrate that the field is a complicated function of position on the surface of the Earth.

The intensity values in Figure 2.5 are in general highest at the poles (~ 60 μT) and lowest near the equator (~ 30 μT), but the contours are not straight lines parallel to latitude as they would be for a field generated strictly by a geocentric axial dipole (GAD) such as that shown in Figure 2.6. Similarly, a GAD would produce lines of inclination that vary in a regular way from -90° to +90°

Table 2.1: International Geomagnetic Reference Field, 2000 from Olsen et al. (2000).

l	m	g(nT)	h (nT)	l	m	g(nT)	h (nT)
1	0	-29614.72	0	5	0	-216.82	0
1	1	-1727.74	5186.27	5	1	350.96	43.69
2	0	-2267.11	0	5	2	222.36	171.65
2	1	3071.78	-2477.69	5	3	-130.72	-133.88
2	2	1672.18	-457.63	5	4	-168.53	-40.26
3	0	1340.85	0	5	5	-11.83	106.79
3	1	-2289.53	-226.99	6	0	72.34	0
3	2	1252.52	296.26	6	1	67.76	-17.09
3	3	715.1	-492.28	6	2	73.98	63.84
4	0	935.35	0	6	3	-161.06	65.19
4	1	786.71	271.92	6	4	-5.13	-61.34
4	2	250.81	-231.63	6	5	17.03	1.33
4	3	-404.66	118.54	6	6	-90.53	44.11
4	4	109.91	-303.88				

at the poles, with 0° at the equator; the contours would parallel the lines of latitude. Although the general trend in inclination shown in Figure 2.5b is similar to this GAD model field, there is considerable structure to the lines, which again suggests that the field is not perfectly described by a geocentric bar magnet. If the field were simply that of a geocentric axial dipole (a GAD field), declination would be everywhere zero. This is clearly not the case, as is shown by the plots of declination in Figure 2.5c.

The beauty of using the geomagnetic potential field is that the vector field can be evaluated anywhere outside the source region. Figure 2.6a shows the lines of flux predicted from the 1980 IGRF within the mantle. From this we can see that the field becomes simpler and more dipolar as we move from the core mantle boundary to the surface.

Perhaps the most important result of spherical harmonic analysis for our purposes is that the field is dominated by the first order terms ($l = 1$) and the external contributions are very small. The first order terms can be thought of as geocentric dipoles that are aligned with three different axes: the spin axis (g_1^0) and two equatorial axes that intersect the equator at the Greenwich meridian (g_1^1) and at 90° East (h_1^1).

2.2 Geocentric Axial Dipole (GAD) and other poles

To first order, the field is very much like one that would be produced by a gigantic bar magnet located at the Earth's center and aligned with the spin axis. In Figure 2.6b, we show a cross section of the Earth with a dipolar magnetic field superimposed. If the field were actually that of a *geocentric axial dipole* (GAD), it would not matter which cross section we chose because such a field is rotationally symmetric about the axis going through the poles; in other words, the magnetic field lines would always point North. The angle between the field lines and the horizontal at the surface of the Earth (inclination I), however, would vary between zero at the equator and 90° at the poles. Moreover, the magnetic field lines would be more crowded together at the poles than

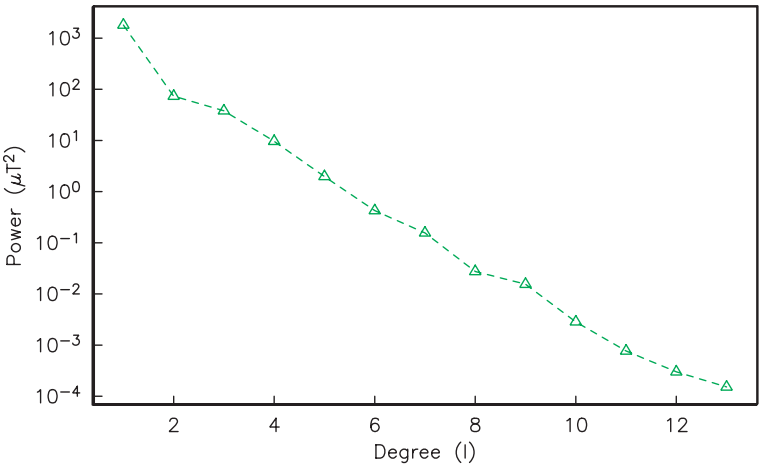

Figure 2.4: Power in of the geomagnetic field versus degree for the 2005 IGRF.

at the equator (the magnetic flux is higher at the poles) resulting in a polar field that would have twice the intensity of the equatorial field.

It turns out that when averaged over sufficient time, the geomagnetic field actually does seem on average to be that of a GAD field. This so-called *GAD model* of the field will serve as a useful crutch throughout our discussions of paleomagnetic data and applications.

The vector sum of the geocentric dipoles (g_1^0, h_1^0, h_1^1 in the IGRF) is a dipole that is currently inclined by 11° to the spin axis. The axis of this so-called *best-fitting dipole* pierces the surface of the Earth at the diamond in Figure 2.7. This point and its antipode are called *geomagnetic poles*. Points at which the field is vertical ($I = \pm 90°$ shown by a triangle in Figure 2.7) are called *magnetic poles*, or sometimes, *dip poles*. These poles are distinguished from the *geographic poles* where the spin axis of the Earth intersects its surface. The Northern geographic pole is shown by a dot in Figure 2.7. Averaging ancient magnetic poles over some 10,000 years gives what is known as a *paleomagnetic pole*.

Because the geomagnetic field is axially dipolar to a first order approximation, we can write:

$$\psi_m = \frac{1}{\mu_0} a g_1^0 \left(\frac{a}{r}\right)^2 P_1^0(\cos\theta) = \frac{1}{\mu_0} a g_1^0 \left(\frac{a}{r}\right)^2 \cos\theta = \frac{1}{\mu_0}\frac{B_o \cos\theta}{r^2}, \tag{2.6}$$

where B_o is $g_1^0 a^3$. Note that this will give units in tesla if g_1^0 is given in tesla (as gauss coefficients normally are) Thus, from Equation 2.6,

$$B_N = \mu_0 H_N = \frac{B_o \sin\theta}{r^3}, \quad B_E = 0, \quad \text{and} \quad B_V = \mu_0 H_V = \frac{2B_o \cos\theta}{r^3}. \tag{2.7}$$

Given some latitude λ on the surface of the Earth in Figure 2.6 and using the equations for B_V and B_N, we find that:

$$\tan I = \frac{B_V}{B_N} = 2\cot\theta = 2\tan\lambda. \tag{2.8}$$

This equation is sometimes called the *dipole formula* which shows that the inclination of the magnetic field is directly related to the co-latitude (θ) for a field produced by a geocentric axial dipole

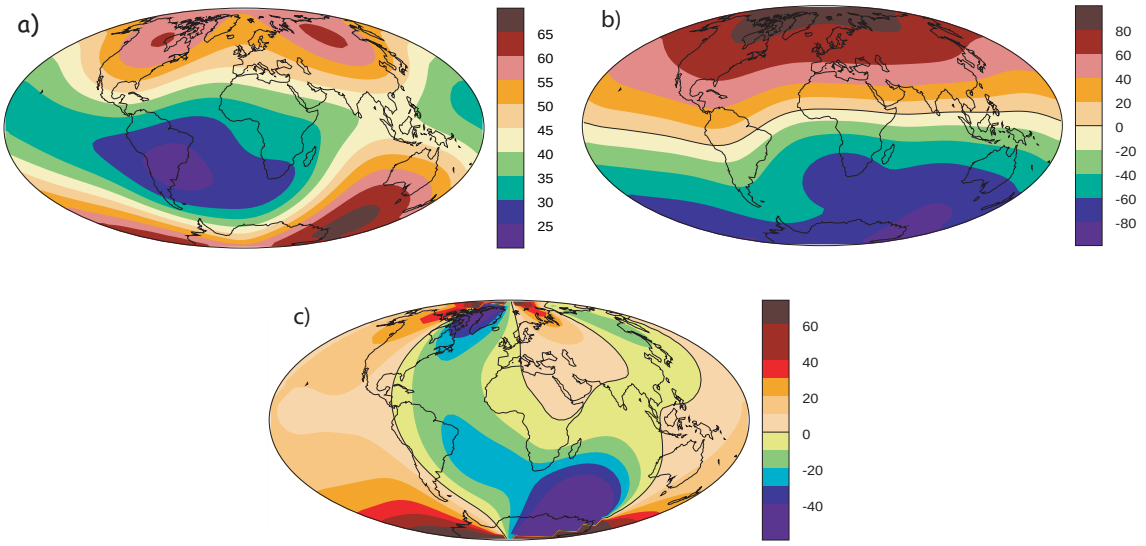

Figure 2.5: Maps of geomagnetic field of the IGRF for 1995 a) intensity in μT, b) inclination, c) declination.

(or g_1^0). The dipole formula allows us to calculate the latitude of the measuring position from the inclination of the (GAD) magnetic field, a result that is fundamental in plate tectonic reconstructions. The intensity of a dipolar magnetic field is also related to (co)latitude because:

$$B = (B_V^2 + B_N^2)^{\frac{1}{2}} = \frac{B_o}{r^3}(\sin^2\theta + 4\cos^2\theta)^{\frac{1}{2}} = \frac{B_o}{r^3}(1 + 3\cos^2\theta)^{\frac{1}{2}}\,. \tag{2.9}$$

The dipole field intensity has changed by more than an order of magnitude in the past and the dipole relationship of intensity to latitude turns out to be not useful for tectonic reconstructions.

2.3 Plotting magnetic directional data

Magnetic field and magnetization directions can be visualized as unit vectors anchored at the center of a unit sphere. Such a unit sphere is difficult to represent on a 2-D page. There are several popular projections, including the Lambert equal area projection which we will be making extensive use of in later chapters. The principles of construction of the equal area projection are covered in the appendix.

In general, regions of equal area on the sphere project as equal area regions on this projection, as the name implies. Plotting directional data in this way enables rapid assessment of data scatter. A drawback of this projection is that circles on the surface of a sphere project as ellipses. Also, because we have projected a vector onto a unit sphere, we have lost information concerning the magnitude of the vector. Finally, lower and upper hemisphere projections must be distinguished with different symbols. The paleomagnetic convention is: lower hemisphere projections use solid symbols, while upper hemisphere projections are open.

The dipole formula assumes that the magnetic field is exactly axial. Because there are more terms in the geomagnetic potential than just g_1^0, we know that this is not true. Because of the non-axial geocentric dipole terms, a given measurement of I will yield an equivalent *magnetic co-latitude* θ_m:

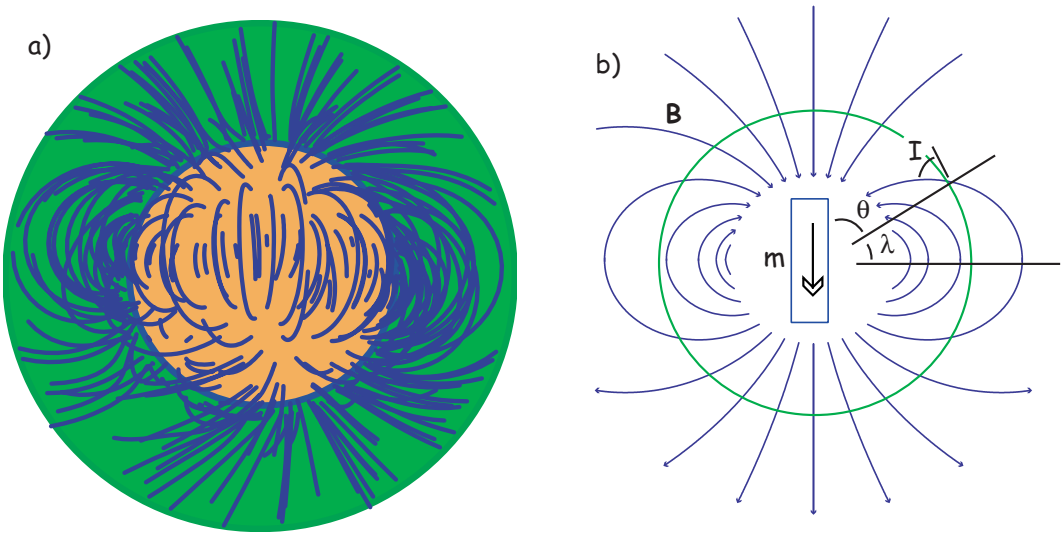

Figure 2.6: a) Predicted lines of flux for the 1980 IGRF. [Figure redrawn from R.L. Parker.] b) Orientations of magnetic field lines produced by a geocentric axial dipole m. λ and θ are latitude and co-latitude respectively. I is the local inclination at a particular point on the surface of the Earth.

$$\cot \theta_m = \tfrac{1}{2} \tan I. \tag{2.10}$$

Paleomagnetists often assume that θ_m is a reasonable estimate of θ and the validity of this assumption depends on several factors. We consider first what would happen if we took random measurements of the Earth's present field (see Figure 2.8). We randomly selected 200 positions on the globe (shown in Figure 2.8a) and evaluate the direction of the magnetic field at each site using the IGRF for 1995. These directions are plotted in Figure 2.8b using the paleomagnetic convention of open symbols pointing up and closed symbols pointing down. We also plot the inclinations as a function of latitude on Figure 2.8c. We see that, as expected from a predominantly dipolar field, inclinations cluster around the values expected for a geocentric axial dipolar field but there is considerable scatter and interestingly the scatter is larger in the southern hemisphere than in the northern one.

2.3.1 D', I' transformation

Often we wish to compare directions from distant parts of the globe. There is an inherent difficulty in doing so because of the large variability in inclination with latitude. In such cases it is appropriate to consider the data relative to the expected direction (from GAD) at each sampling site. For this purpose, it is useful to use the transformation proposed by (Hoffman 1984), whereby each direction is rotated such that the direction expected from a geocentric axial dipole field (GAD) at the sampling site is the center of the equal area projection. This is accomplished as follows:

Each direction is converted to cartesian coordinates (x_i) by:

Figure 2.7: The different magnetic poles. The triangle is the magnetic North Pole, where the magnetic field is straight down ($I = +90°$). The diamond is the geomagnetic North Pole, where the axis of the best fitting dipole pierces the surface. The dot is the geographic North Pole. The dashed line is the magnetic equator where $I = 0°$.

$$\begin{aligned} x_1 &= \cos D \cos I \\ x_2 &= \sin D \cos I \\ x_3 &= \sin I \end{aligned}$$

These are rotated to the new coordinate system (x_i', see appendix to Lecture 1) by:

$$\begin{aligned} x_1' &= (x_1^2 + x_3^2)^{1/2} \sin (I_d - \theta) \\ x_2' &= x_2 \\ x_3' &= (x_1^2 + x_3^2)^{1/2} \cos (I_d - \theta) \end{aligned}$$

where I_d = the inclination expected from a GAD field ($\tan I_d = 2 \tan \lambda$), λ is the site latitude, and θ is the inclination of the paleofield vector projected onto the N-S plane ($\theta = \tan^{-1}(x_3/x_1)$). The x_i' are then converted to D', I' by Equation 2.4. We see what happens to the directions shown in Figure 2.8b after the D', I' transformation in Figure 2.9. The latitudal dependence of the inclinations has been removed. Yet, it is a feature of the geomagnetic field that directions from a given latitude tend to be more scattered in the up-down directions than from side to side. This tendency for elongation in the directions is most extreme at the equator and least at the poles, where directions are more or less circularly symmetric.

2.3.2 Virtual Geomagnetic Poles

We are often interested in whether the geomagnetic pole has changed, or whether a particular piece of crust has rotated with respect to the geomagnetic pole. Yet, what we observe at a particular

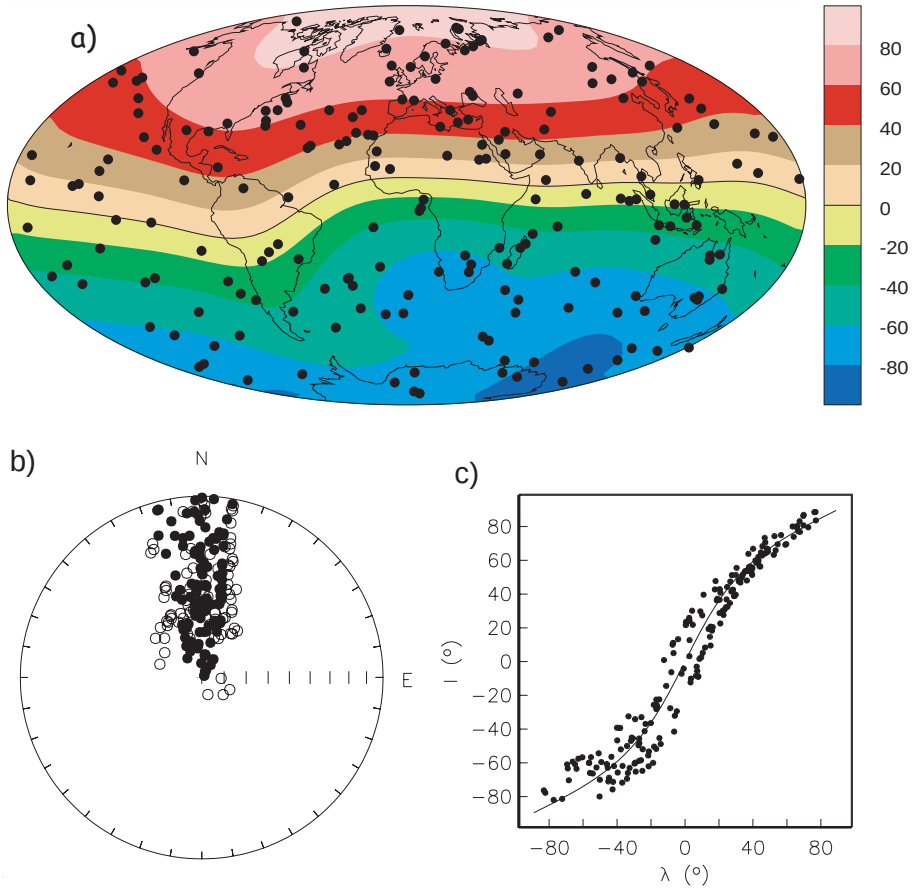

Figure 2.8: a) Hammer projection of 200 randomly selected locations around the globe. b) Equal area projection of directions of Earth's magnetic field as given by the IGRF evaluated for the year 1995 at locations shown in a). Open (closed) symbols indicate upper (lower) hemisphere. c) Inclinations (I) plotted as a function of site latitude (λ). The solid line is the inclination expected from the dipole formula (see text). Negative latitudes are south and negative inclinations are up.

location is the local direction of the field vector. Thus, we need a way to transform an observed direction into the equivalent geomagnetic pole.

In order to remove the dependence of direction merely on position on the globe, we imagine a geocentric dipole which would give rise to the observed magnetic field direction at a given latitude (λ) and longitude (ϕ). The *virtual geomagnetic pole* (VGP) is the point on the globe that corresponds to the geomagnetic pole of this imaginary dipole (Figure 2.10).

Paleomagnetists use the following conventions: ϕ is measured positive eastward from the Greenwich meridian and goes from $0 \rightarrow 360°$. θ is measured from the North pole and goes from $0 \rightarrow 180°$. Of course θ relates to latitude, λ by $\theta = 90 - \lambda$. θ_m is the magnetic co-latitude and is given by equation 2.10. Be sure not to confuse latitudes and co-latitudes. Also, be careful with declination. Declinations between 180° and 360° are equivalent to D - 360 ° and are counter-clockwise with respect to North.

The first step in the problem of calculating a VGP is to determine the magnetic co-latitude θ_m by equation 2.10 which is of course the dipole formula. The declination D is the angle from the

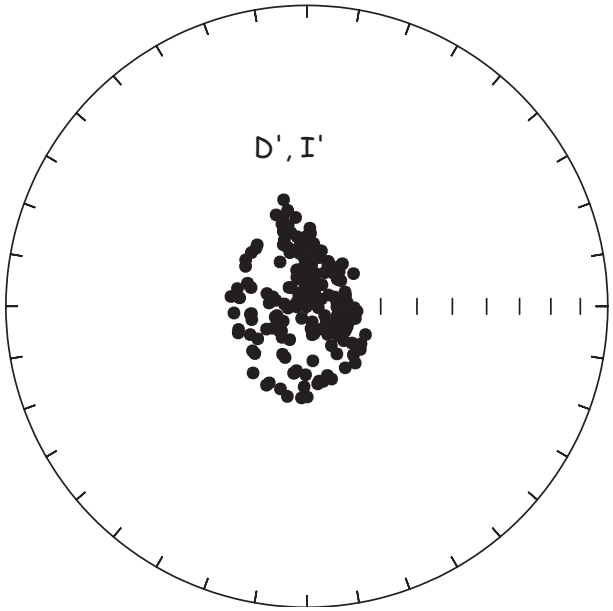

Figure 2.9: Directions from the Figure 13b transformed using the D', I' transformation.

geographic North Pole to the great circle joining S and P, and $\Delta\phi$ is the difference in longitudes between P and S, $\phi_p - \phi_s$. Now we use some tricks from spherical trigonometry as reviewed in the Appendix.

We can locate VGPs using the law of sines and the law of cosines. The declination D is the angle from the geographic North Pole to the great circle joining S and P (see Figure 2.10) so:

$$\cos\theta_p = \cos\theta_s \cos\theta_m + \sin\theta_s \sin\theta_m \cos D, \tag{2.11}$$

which allows us to calculate the VGP co-latitude θ_p. The VGP latitude is given by:

$$\lambda_p = 90 - \theta_p,$$

so $90 > \lambda_p > 0$ in the northern hemisphere and $0 < \lambda_p < 90$ in the southern hemisphere.

To determine ϕ_p, we first calculate the angular difference between the pole and site longitude $\Delta\phi$.

$$\sin\Delta\phi = \sin\theta_m \cdot \frac{\sin D}{\sin\theta_p}. \tag{2.12}$$

If $\cos\theta_m \geq \cos\theta_s \cos\theta_p$, then $\phi_p = \phi_s + \Delta\phi$. However, if $\cos\theta_m < \cos\theta_s \cos\theta_p$ then $\phi_p = \phi_s + 180 - \Delta\phi$.

Now we can convert the directions in Figure 2.8b to VGPs (Figure 2.11). The grouping of points is much tighter in Figure 2.11 than in the equal area projection because the effect of latitude variation in dipole fields has been removed.

If a number of VGPs are averaged together, the average pole position is called a "paleomagnetic pole". How to average poles and directions is the subject of another lecture, however.

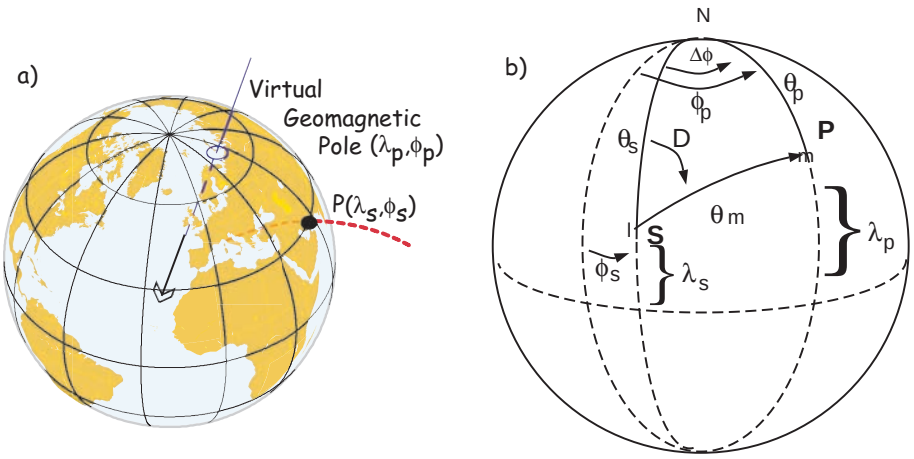

Figure 2.10: Transformation of a direction measured at S into a virtual geomagnetic pole position P, using principles of spherical trigonometry and the dipole formula. a) Illustration of the magnetic field line observed at position P and its associated VGP. b) More detailed view. Site S has latitude λ_s and longitude ϕ_s and a magnetic field direction D and I. The co-latitude of S is θ_s. $\Delta\phi$ is the difference in longitude between S and P and θ_p is the co-latitude of P. The direction can be transformed to an equivalent VGP (at P) with latitude λ_p and longitude ϕ_p as described in the text. The co-latitude of S with respect to P is the *magnetic co-latitude* θ_m. N is the geographic North Pole (the spin axis of the Earth).

2.3.3 Virtual Dipole Moment

As pointed out earlier, magnetic intensity varies over the globe in a similar manner as inclination. It is often convenient to express paleointensity values in terms of the equivalent geocentric dipole moment which would have produced the observed intensity at that (paleo)latitude. Such an equivalent moment is called the *virtual dipole moment* (VDM) by analogy to the VGP. First, the magnetic (paleo)co-latitude θ_m is calculated as before from the observed inclination and the dipole formula of equation 2.8, then following the derivation of equation 2.9,

$$\text{VDM} = \frac{4\pi r^3}{\mu_o} B_{ancient}(1 + 3\cos^2\theta_m)^{-\frac{1}{2}}. \tag{2.13}$$

Sometimes the site co-latitude as opposed to magnetic co-latitude is used in the above equation, giving a *virtual axial dipole moment* (VADM).

Appendix

In this appendix we will review the basic techniques necessary useful for understanding Lecture 2. In particular, we will cover plotting of equal area projections and spherical trigonometry.

A Equal area projections

The principles for how to make an equal area projection are shown in Figure A1. The point P corresponds to a D of 40° and I of 35°. D is measured around the perimeter of the equal area net

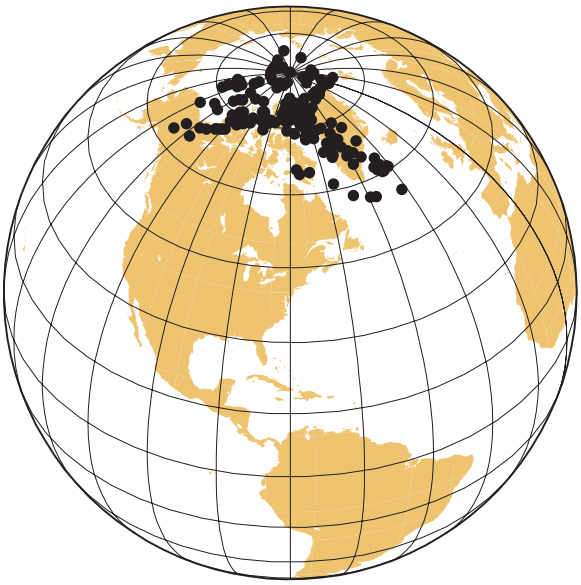

Figure 2.11: VGP positions converted from directions shown in Figure 2.8b.

and I is transformed as follows:

$$L = L_o\sqrt{(1 - |x_3|)}, \tag{A1}$$

where $L_o = 1/\sqrt{x_1^2 + x_2^2}$.

B Spherical trigonometry

In Figure B1, α, β and γ are the angles between the great circles labelled a, b, and c. On a unit sphere, a, b and c are also the angles subtended by radii that intersect the globe at the apices A, B, and C (see inset on Figure B1). Two formulae from spherical trigonometry come in handy in

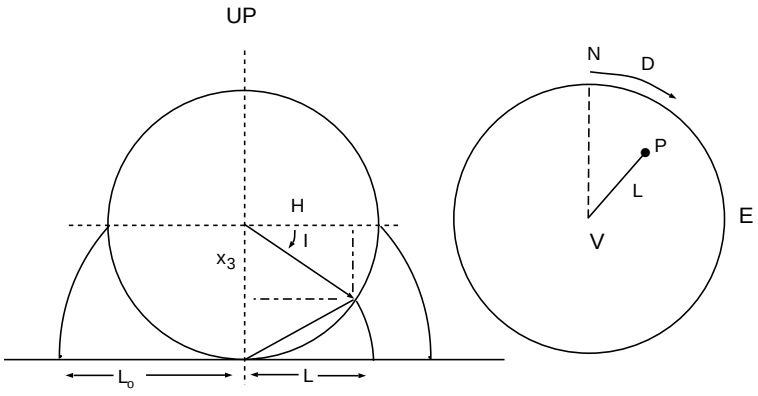

Figure A1: Construction of an equal area projection for a point P corresponding to a D of 40° and an I of 35°.

B. SPHERICAL TRIGONOMETRY

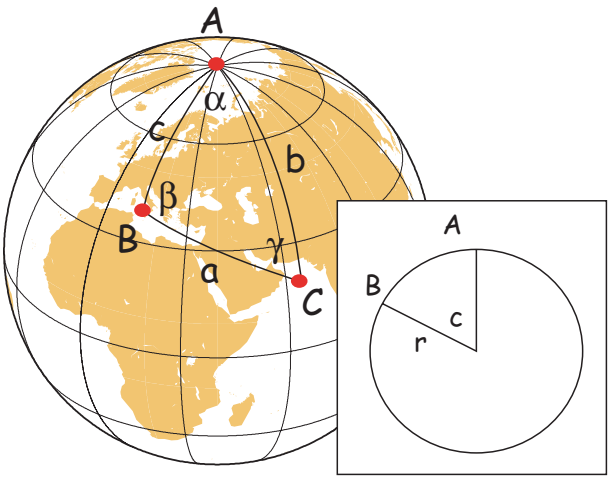

Figure B1: Rules of spherical trigonometry. a, b, c are all great circle tracks on a sphere which form a triangle with apices A, B, C. The lengths of a, b, c on a unit sphere are equal to the angles subtended by radii that intersect the globe at the apices, as shown in the inset. α, β, γ are the angles between the great circles.

paleomagnetism, the Law of Sines:

$$\frac{\sin\alpha}{\sin a} = \frac{\sin\beta}{\sin b} = \frac{\sin\gamma}{\sin c}, \tag{B1}$$

and the Law of Cosines:

$$\cos a = \cos b \cos c + \sin b \sin c \cos\alpha. \tag{B2}$$

Bibliography

Butler, R. F. (1992), *Paleomagnetism: Magnetic Domains to Geologic Terranes*, Blackwell Scientific Publications.

Hoffman, K. (1984), 'A method for the display and analysis of transitional paleomagnetic data', *J. Geophys. Res.* **89**, 6285–6292.

Lowes, F. (1974), 'Spatial power spectum of the main geomagnetic field and extrapolation to the core', *Geophys. J. R. Astron. Soc.* **36**, 717–730.

Merrill, R. T., McElhinny, M. W. & McFadden, P. L. (1996), *The Magnetic Field of the Earth: Paleomagnetism, the Core, and the Deep Mantle*, Academic Press.

Olsen, N., Sabaka, T. & Toffner-Clausen, L. (2000), 'Determination of the IGRF 2000 model', *Earth Planet. Sci. Lett.* **52**, 1175–1182.

Tauxe, L. (2005), 'Inclination flattening and the geocentric axial dipole hypothesis', *Earth Planet. Sci. Lett.* **233**, 247–261.

Lectures in Paleomagnetism, 2005
by Lisa Tauxe

Citation:
http://earthref.org/MAGIC/books/Tauxe/2005/

May 30, 2005

Chapter 3

Induced and Remanent Magnetism

Suggested Reading

For background:
pages 21-26 of Butler (1992)
For a review of basic quantum mechanics, see:
http://www.chemistry.ohio-state.edu/betha/qm/index.html, or
http://chemed.chem.purdue.edu/genchem/topicreview/bp/ch6/quantum.html
For some nice visualizations, see http://web.mit.edu/3.091/www/orbs/
General background in Statistical Mechanics (see, e.g.,
http://en.wikipedia.org/wiki/Statistical_mechanics)
To learn more:
Chapter 3.1 of O'Reilly (1984)
Chapter 2.1 to 2.7 in Dunlop and Özdemir (1997)

3.1 Introduction

In the last lecture we learned something of the present geomagnetic field. In order to study its past behavior, we are forced to use accidental records such as those left in rocks, sediments or archeological materials. But how are these materials magnetized and how are the magnetizations related to the magnetic field? This topic is the subject of the next few lectures.

Scientists in the late 19th century considered that it might be possible to exploit the magnetic record retained in rocks in order to study the geomagnetic field in the past. Early work in rock magnetism provided the theoretical and experimental basis for presuming that rocks might retain a record of past geomagnetic fields. There are several books and articles that describe the subject in detail (see e.g., the suggested readings). We present here a brief overview of theories on how rocks become and stay magnetized. We will begin with magnetism at the atomic level caused by electronic orbits and spins. Then we will see how electronic spins working in concert give rise to permanently magnetized substances (like magnetic minerals).

3.2 Magnetism at the atomic level

Substances generally respond to external magnetic fields by generating magnetic fields of their own; a few generate them spontaneously, in the absence of an external field. Therefore it is convenient

to separate the magnetization of a material **M** into two contributions: that which exists only in the presence of an external magnetic field (induced magnetization) and that which exists in zero external magnetic field (remanent magnetization).

As we learned in the first lecture, magnetic fields are generated by electric currents. At the atomic level, the electric currents are the motions of the electrons about the nucleus: the electronic orbit and the electronic spin. Let us first consider the role of the electronic orbit (see Figure 3.1).

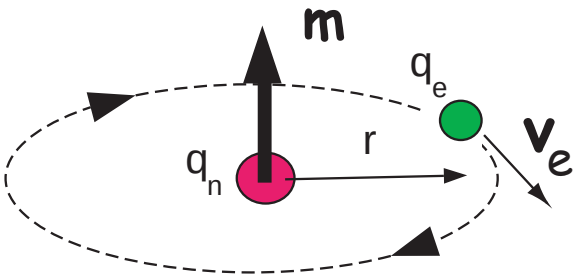

Figure 3.1: Orbital motion of electron with charge q_e and velocity v_e around the nucleus with charge q_n at a radius of r is like a current loop and generates moment **m**.

Classical physics (see Lecture 1) suggests that the magnitude of the moment generated by an orbiting electron is the current i times the area of the current loop πr^2 or $m = i\pi r^2$. The current is the charge per second:

$$i = \frac{q_e v_e}{2\pi r}$$

where v_e is the electronic velocity, so moment is:

$$m = i\pi r^2 = \pi r^2 \frac{q_e v_e}{2\pi r} = \frac{q_e v_e r}{2}. \tag{3.1}$$

The direction of **m** is given by the right hand rule (see Lecture 1 and remember that the charge of an electron is negative).

Quantum physics tells us the basic model just described cannot be. An electron zipping around a nucleus would be generating radio waves hence losing energy. It would eventually have to crash into the nucleus, which it appears not to do. In quantum mechanics, this is prevented by the fact that the angular momentum of the electron must be quantized and is an integer multiple of $h/2\pi$, where h is Planck's constant (6.63 x 10^{34} Js). In this view we have:

$$\mu_e v_e r = n \cdot \frac{h}{2\pi}$$

where μ_e is the mass of an electron (9.11 x 10^{-31} kg) and n is the energy level of the orbit. Solving for $v_e r$ and substituting into Equation 3.1, we find that the fundamental unit of magnetic moment of electrons ($n = 1$), termed the *Bohr magneton* (m_b), is given by:

$$m_b = \frac{h}{2\pi} \cdot \frac{q_e}{2\mu_e} = 9.27 \times 10^{-24} \frac{\text{kg m}^2}{\text{s}} \cdot \frac{\text{C}}{\text{kg}} = 9.27 \times 10^{-24} \text{A m}^2.$$

3.2. MAGNETISM AT THE ATOMIC LEVEL

The balance of the attractive force of the nucleus drawing the electron towards it and the centripetal "force" pushing the electon away is what keeps the charge in orbit. The attracive force between the nucleus (q_n) and the electron (q_e) is given by Coulomb's law:

$$F = \frac{kq_nq_e}{r^2},$$

where k is Boltzmann's constant, 1.381 x 10^{-23} JK^{-1}, and the centripetal "force" is given by:

$$F = \frac{\mu_e v_e^2}{r} = 2\pi\mu_e\omega^2 r,$$

where ω is the orbital frequency and remembering that $v = 2\pi\omega r^2$. Balancing these two competing forces and solving for ω gives a fundamental orbital frequency ω_o.

Recalling from Lecture 1 there is a torque $\mathbf{m} \times \mu_o\mathbf{H}$ on the electron in the presence of an external field $\mathbf{H}$, This torque changes the electronic orbit which creates a new balance of forces. The changed balance changes the orbital frequency, which in turn results in a changed magnetic moment. The sense of the change in moment is always to oppose the applied field. Therefore, the response of the magnetic moments of electrons creates an induced magnetization $\mathbf{M}_I$ that is observable outside the substance. As stated in Lecture 1, $\mathbf{M}_I$ is a function of the applied field $\mathbf{H}$, *i.e.*,

$$\mathbf{M}_I = \chi\mathbf{H}.$$

We also learned in Lecture 1 that the parameter χ is known as the *magnetic susceptibility*. The ratio $\mathbf{M}_I/\mathbf{H}$ for the response of the electronic orbitals is termed the *diamagnetic susceptibility* χ_d; it is negative, essentially temperature independent, and quite small (see Figure 3.2).

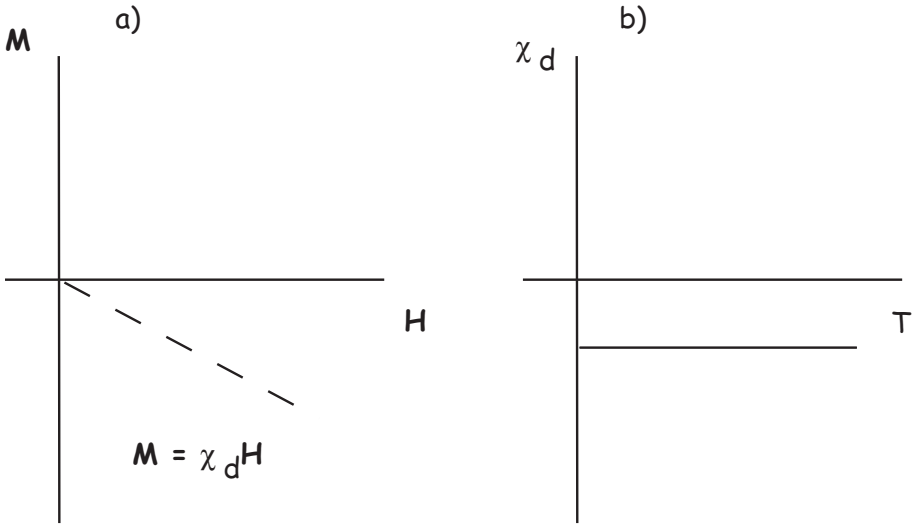

Figure 3.2: The diamagnetic response to externally applied magnetic fields. a) The magnetization $\mathbf{M}_I$ induced by a field $\mathbf{H}$ is inversely proportional to the field. b) The diamagnetic susceptibility is independent of temperature.

Diamagnetism is exhibited by all matter, arising as it does from the response of electronic orbitals to externally applied magnetic fields. In the absence of unpaired electronic spins, diamagnetic

susceptibility dominates the magnetic response. Common diamagnetic substances include quartz (SiO_2), calcite ($CaCO_3$) and water (H_2O). The mass susceptibility of quartz is -0.62 x 10^{-9} m^3kg^{-1} to give you an idea of the magnitudes of these things.

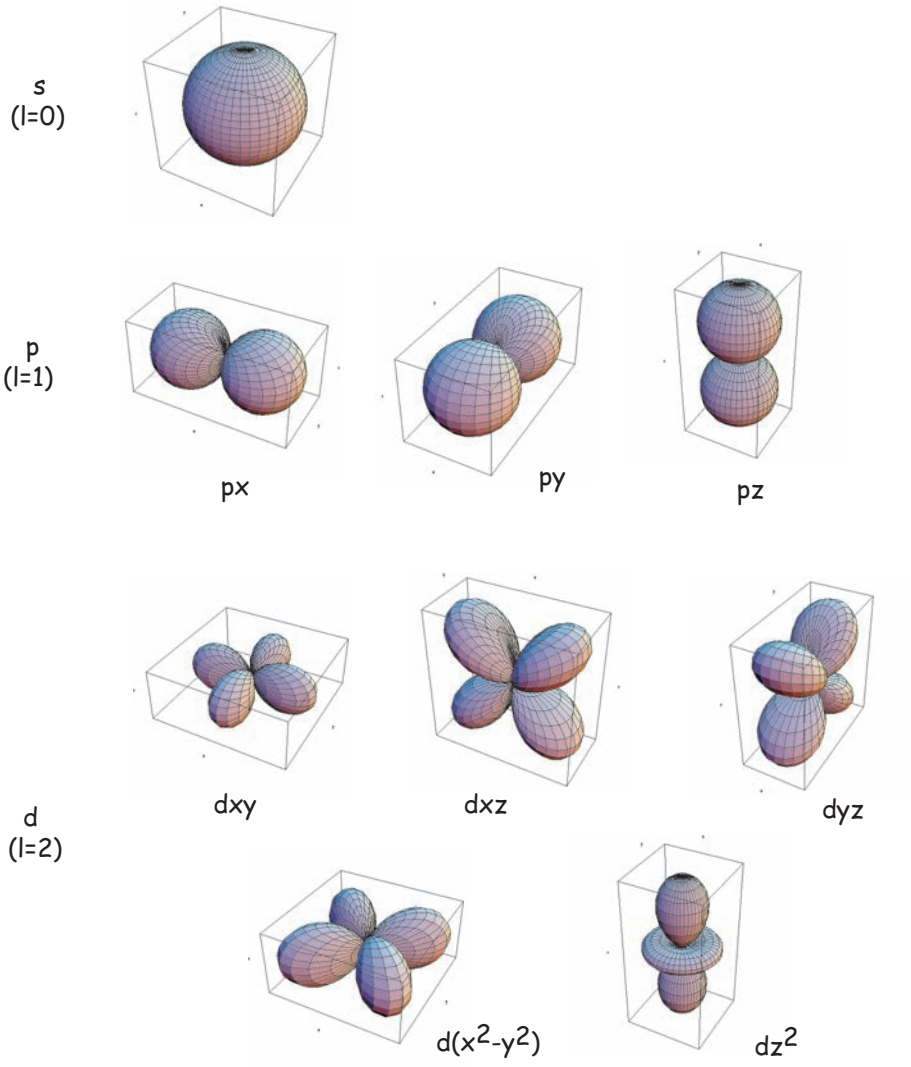

Figure 3.3: Schematic of surfaces of equal energy of the first three shells ($l = 1, 2, 3$). Modified from Alan Crosby's web site at http://solution.bu.edu/acrosby/orbitals/dxy.html.

3.2.1 Role of electronic spins

In most geological materials, the orbital contributions cancel out (they are "quenched") and the magnetization arises from the electronic spins. Electronic spins are a concept in quantum mechanics and have no easy to understand classical analogue. To understand spins, then, we have to review a few quantum mechanical principles.

Quantum mechanics describes the electronic structure of atoms in terms of the four quantum numbers n, l, m, s. The energy (size?) of a shell is given by n. The shape and orientation of the

shell is given by l and m respectively and the so-called "spin" is given by s which can be $\pm\frac{1}{2}$. Figure 3.3 shows surfaces of equal probability of finding electrons in several possible shapes and orientations of the first three shells (s, p, d).

Each level of increasing n has an increasing number of possible orbitals. For $n = 1$, we have only the $1s$ shell. For $n = 2$ we have the $2s$ orbital and three p orbitals. For now we don't really have to have a deep understanding of quantum mechanics, we may simply regard the quantum numbers as book keeping devices that specify how electronic orbitals are filled and the consequences for the magnetic properties of the material.

Electronic orbitals are filled according to three rules:

1) No two electrons may have the same set of quantum numbers. This is Pauli's exclusion principle. Because spin (s) can be $\pm\frac{1}{2}$, two electrons fit in one orbital. When a single electron occupies a given orbital, it is called "unpaired" and has a magnetic moment of 1 m_b.

2) Orbitals are filled in order of increasing energy. The energy state of a given orbital is dependent on the context (whether the atom is bound to other atoms or not), but in general they will be filled according to the scheme shown in Figure 3.4.

3) Electrons are added so that the atom has the spins as parallel as possible (Hund's rule). The scheme followed is shown in Figure 3.4. Notice that when filling the third energy level $(n = 3)$, all five d shells are filled up with one kind of spin (say, up, or $+\frac{1}{2}$), before the electrons begin to pair up. Also, because the energies of the shells change somewhat according to the context they are in, the $4s$ shell will actually give up an electron to a d shell, before the d shells begin to pair up. Hund's rule gives the atoms with some d shell electrons (the so-called "transition elements") the possibility of large magnetic moments.

Unpaired electronic spins behave as magnetic dipoles with a moment of one Bohr magneton. In the absence of an applied field, or in the absence of the ordering influence of neighboring spins which are known as *exchange interactions*, the spins are essentially randomly oriented. An applied field acts to align the spins which creates a net magnetization equal to $\chi_p \mathbf{H}$. χ_p is the *paramagnetic susceptibility*.

Each unpaired spin has a moment of one Bohr magneton $\mathbf{m}_b$. The elements with the most unpaired spins are the transition elements which are responsible for most of the paramagnetic behavior observed in rocks. For example, in Figure 3.4 we see that Mn^{25} has a structure of: $(1s^2 2s^2 2p^6 3s^2 3p^6) 3d^5 4s^2$, hence has 5 unpaired spins and a net moment of 5 m_b. Fe^{26} has a structure of $(1s^2 2s^2 2p^6 3s^2 3p^6) 3d^6 4s^2$ with a net moment of 4 m_b, In minerals, the transition elements are in a variety of oxidation states. Fe commonly occurs as Fe^{2+} and Fe^{3+}. When losing electrons to form ions, transition metals lose the 4s electrons first, so we have for example, Fe^{3+} with a structure of $(1s^2 2s^2 2p^6 3s^2 3p^6) 3d^5$, or 5 m_b. Similarly Fe^{2+} has 4 m_b and Ti^{4+} has no unpaired spins. Iron is the main magnetic species in geological materials, but Mn^{2+} (5 m_b) and Cr^{3+} (3 m_b) occur in trace amounts.

A useful model for paramagnetism was worked out by P. Langevin in 1905. Langevin theory is based on a few simple premises:

1) Each unpaired spin contributes a dipole moment.

2) In the absence of an applied field, the moments are essentially randomly oriented, *i.e.*, all directions are equally likely to occur.

3) An applied field acts to align the spins which creates a net moment.

4) There is competition between thermal energy kT (k is Boltzmann's constant and T is temperature in kelvin) and the magnetic energy E_m. Recalling Lecture 1 we know that E_m of a magnetic

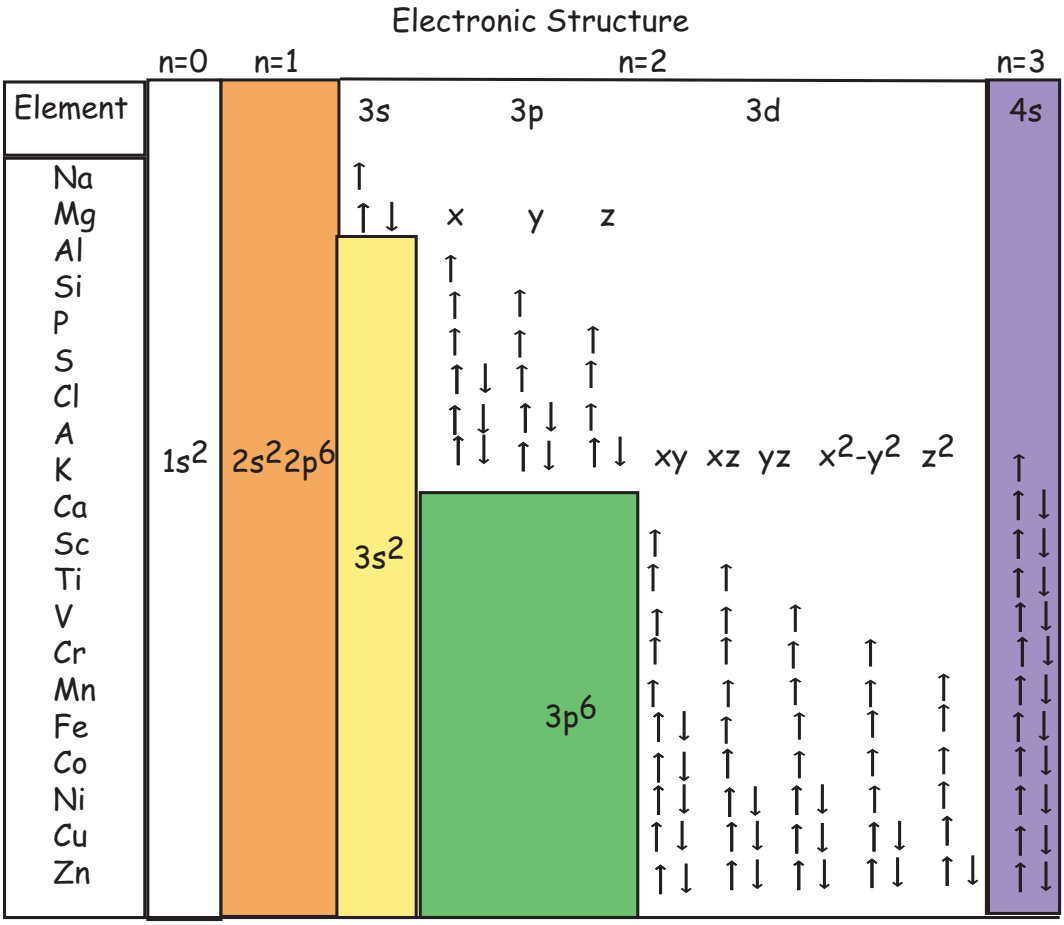

Figure 3.4: The electronic structure of the elements from Na to Zn.

moment $\mathbf{m}$ at an angle θ with an external magnetic field $\mathbf{H}$ is given by:

$$E_m = -\mathbf{m} \cdot \mu_o \mathbf{H} = -m\mu_o H \cos\theta. \tag{3.2}$$

Magnetic energy is at a minimum when the magnetic moment is parallel to the magnetic field. Using the principles of statistical mechanics, we find that the probability density of a given moment having energy E_m is:

$$P(E) \propto \exp\left(-E_m/kT\right). \tag{3.3}$$

This probability leads directly to the relationship:

$$\frac{M}{M_s} = [\coth\, a - \frac{1}{a}] = L(a). \tag{3.4}$$

The function enclosed in square brackets is known as the *Langevin function* which is derived in the Appendix. The magnetization, shown in Figure 3.5a, approaches saturation (in this case, M_s) when $m\mu_o H$ is some 10-20 times kT. When $kT >> m\mu_o H$, $L(a)$ is approximately linear

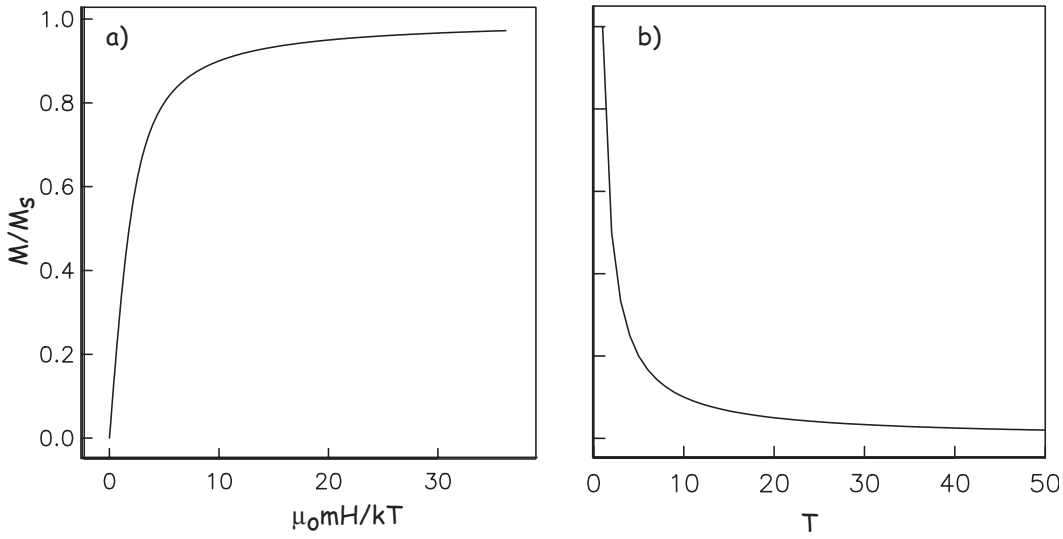

Figure 3.5: a) Paramagnetic magnetization (obtained from the Langevin function $L(a)$ versus $a = \mu_o mH/kT$. b) Paramagnetic magnetization as a function of temperature (Curie Law).

with a slope of $\sim 1/3$. At room temperature and fields up to many tesla, L(a) is approximately $\mu_o mH/3kT$. If the moments m are unpaired spins ($m = m_b$), then $M_s = Nm_b/v$, and:

$$\frac{M}{M_s} \simeq \frac{m_b \mu_o}{3kT} H.$$

Please note that we have neglected all deviations from isotropy including quantum mechanical effects as well as crystal shape, lattice defects, and state of stress. These complicate things a little, but to first order the treatment followed here a good assumption. We can rewrite the above equation as:

$$\frac{M}{H} = \frac{m_b \mu_o}{3kT} \cdot M_s = \frac{N m_b^2 \mu_o}{3kv} \cdot \frac{1}{T} = \chi_p. \tag{3.5}$$

To first order, paramagnetic susceptibility χ_p is positive, larger than diamagnetism and inversely proportional to temperature. This inverse T dependence (see Figure 3.5b) is known as Curie's law of paramagnetism. The paramagnetic susceptibility of, for example, biotite is 790 x 10^{-9} m^3 kg^{-1}, or about three orders of magnitude larger than quartz (and of the opposite sign!).

We have considered the simplest case here in which χ can be treated as a scalar and is referred to as the *bulk magnetic susceptibility* χ_b. In detail, magnetic susceptibility can be quite complicated. The relationship between induced magnetization and applied field can be affected by crystal shape, lattice structure, dislocation density, state of stress, etc., which give rise to possible anisotropy of the susceptibility. Furthermore, there are only a finite number of electronic moments within a given volume. When these are fully aligned, the magnetization reaches saturation. Thus, magnetic susceptibility is both anisotropic and non-linear with applied field.

3.3 Remanent magnetization

Some substances give rise to a magnetic field in the absence of an applied field. This magnetization is called *remanent* or *spontaneous* magnetization, and constitutes the phenomenon which is loosely known as *ferromagnetism (sensu lato)*. Magnetic remanence is caused by strong interactions between neighboring spins that occur in certain crystals.

The so-called *exchange energy* is minimized when the spins are aligned parallel or anti-parallel depending on the details of the crystal structure. Exchange energy is a consequence of the Pauli exclusion principle (no two electrons can have the same set of quantum numbers). In the transition elements, the **3d** orbital is particularly susceptible to exchange interactions because of its shape and the prevalence of unpaired spins, so remanence is characteristic of certain crystals containing transition elements with unfilled $3d$ orbitals.

In oxides, oxygen can form a bridge between neighboring cations which are otherwise too far apart for direct overlap of the $3d$ orbitals in a phenomenon known as superexchange. In Figure 3.6 the $2p$ electrons of the oxygen are shared with the neighboring $3d$ shells of the iron ions. Pauli's principle means that the shared electrons must be antiparallel to each of the electrons in the $3d$ shells. The result is that the two cations are coupled. In the case shown in Figure 3.6 there is an Fe^{2+} ion coupled antiparallel to an Fe^{3+} ion. For two ions with the same charge, the coupling will be parallel. Exchange energies are huge, equivalent to applying a field of the order of 1000 T. [The largest field available in the Scrips paleomagnetic laboratory is about 2.5 T, and that only fleetingly.]

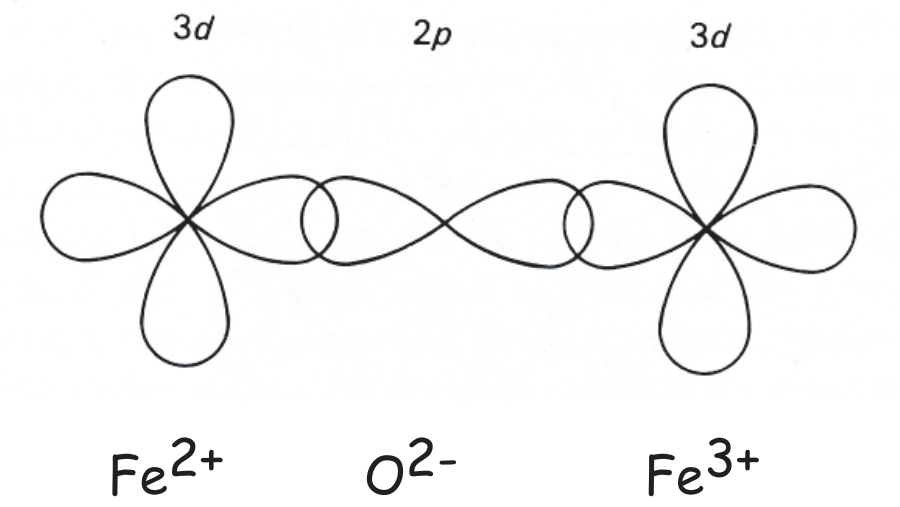

Figure 3.6: Exchange energy associated with overlapping orbitals. Example of super-exchange between the $3d$ orbitals of two iron cations through the $2p$ orbitals of the intervening oxygen anion. The two electrons in the $2p$ shells are, by necessity antiparallel. These are shared by the $3d$ shells, hence to two cations have anti-parallel spins. Modified from O'Reilly (1984).

As temperature increases, crystals expand and exchange becomes weaker. Above a temperature characteristic of each crystal type (known as the *Curie temperature* T_c), cooperative spin behavior disappears entirely and the material becomes paramagnetic.

While the phenomenon of ferromagnetism results from complicated interactions of neighboring

spins, it is useful to think of the ferromagnetic moment as resulting from a quasi-paramagnetic response to a huge internal field. This imaginary field is termed here the *Weiss molecular field* H_w. In Weiss theory, H_w is proportional to the magnetization of the substance, *i.e.*,

$$H_w = \beta M,$$

where β is the constant of proportionality. The total magnetic field that the substance experiences is:

$$H_{tot} = H + H_w = H + \beta M,$$

where H is the external field. By analogy to paramagnetism, we can substitute $a = \mu_o m_b(H_{tot})/kT)$ for H in Langevin equation:

$$\frac{M}{M_s} = L\left(\frac{\mu_o m_b(H + \beta M)}{kT}\right). \tag{3.6}$$

For temperatures above the Curie temperature T_c (i.e. $T - T_c > 0$) there is by definition no internal field, hence βM is zero. Substituting Nm_b/v for M_s, and using the low-field approximation for $L(a)$, Equation 3.6 can be rearranged to get:

$$\frac{M}{H} = \frac{\mu_o N m_b^2}{v3k(T - T_c)} \equiv \chi_f. \tag{3.7}$$

Equation 3.7 is known as the Curie-Weiss law and governs ferromagnetic susceptibility above the Curie temperature.

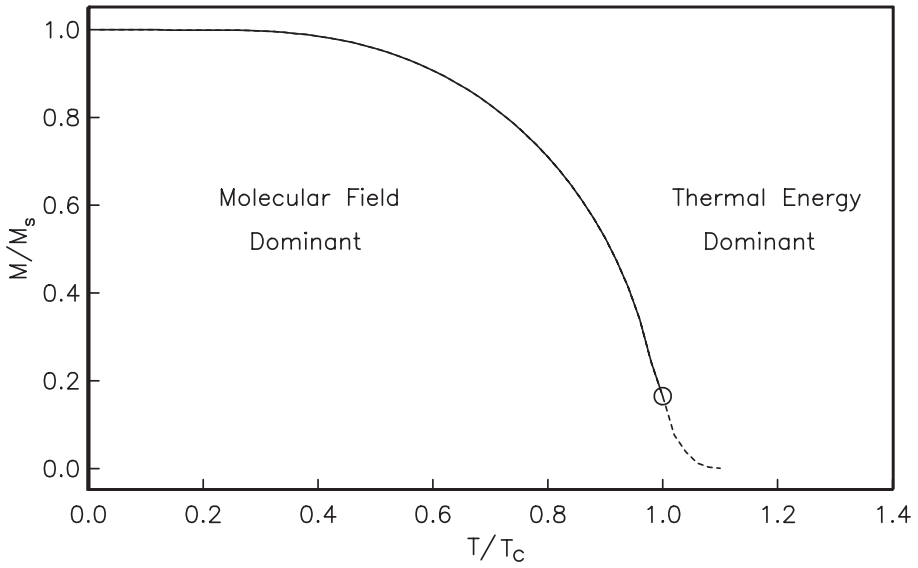

Figure 3.7: Behavior of magnetization versus temperature of a ferromagnetic substance.

Below the Curie temperature, we can neglect the external field H and get:

$$\frac{M}{M_s} = L(\frac{\mu_o m_b \beta M}{kT}).$$

Substituting again for M_s and rearranging, we get:

$$\frac{M}{M_s} = L(\frac{Nm_b^2\beta}{vkT} \cdot \frac{M}{M_s}) = L(\frac{T_c}{T} \cdot \frac{M}{M_s}), \tag{3.8}$$

where T_c is the Curie temperature and is given by:

$$T_c = \frac{Nm_b^2\beta}{vk}.$$

Equation 3.8 can be solved graphically or numerically and is sketched in Figure 3.7. Below the Curie temperature, exhange interactions are strong relative to the external field and the magnetization is governed by Equation 3.8. Above the Curie temperature, it follows the Curie-Weiss law (Equation 3.7).

We have treated ferromagnetism from a classical point of view and this is strictly incorrect as it results primarily from quantum mechanical phenomena. The primary difference between the classical derivation and the quantum mechanical one lies in the fact that in quantum mechanics, only certain angles of the magnetic moments are allowed, not all as in Langevin theory. In the end, the predictions of magnetization as a function of temperature are different in detail. However, the classical approach is sufficient for the purpose of understanding the rudiments of rock magnetism.

3.3.1 Types of ferromagnetism

As we have seen, below the Curie temperature, certain crystals have a permanent (remanent) magnetization resulting from the alignment of unpaired electronic spins over a large area within the crystal. Spins may be either parallel or anti-parallel; the sense of spin alignment is controlled entirely by crystal structure. The energy term associated with this phenomenon is the exchange energy. There are three categories of spin alignment: ferromagnetism (*sensu stricto*), ferrimagnetism and antiferromagnetism (see Figure 3.8).

In *ferromagnetism* (*sensu stricto*, Figure 3.8a), the exchange energy is minimized when all the spins are parallel, as occurs in pure iron. When spins are perfectly antiparallel (*antiferromagnetism*, Figure 3.8b), there is no net magnetic moment, as occurs in ilmenite. Occasionally, the antiferromagnetic spins are not perfectly aligned in an antiparallel orientation, but are canted by a few degrees. This *spin-canting* (Figure 3.8c) gives rise to a weak net moment, as occurs in hematite. Also, antiferromagnetic materials can have a net moment if spins are not perfectly compensated owing to defects in the crystal structure, as occurs in fine-grained hematite. The uncompensated spins result in a so-called *defect* moment (Figure 3.8d). We note in passing that the temperature at which spins become disordered in antiferromagnetic substances is termed the *Néel temperature*. In *ferrimagnetism*, spins are also aligned antiparallel, but the magnitudes of the moments in each direction are unequal, resulting in a net moment (Figure 3.8e).

Appendix

A Derivation of the Langevin function

Because we have made the assumption that there is no preferred alignment within the substance, we can assume that the number of moments ($n(\theta)$) between angles θ and $\theta + d\theta$ with respect to $\mathbf{H}$ is proportional to the solid angle $\sin\theta d\theta$ and the probability density function, *i.e.*,

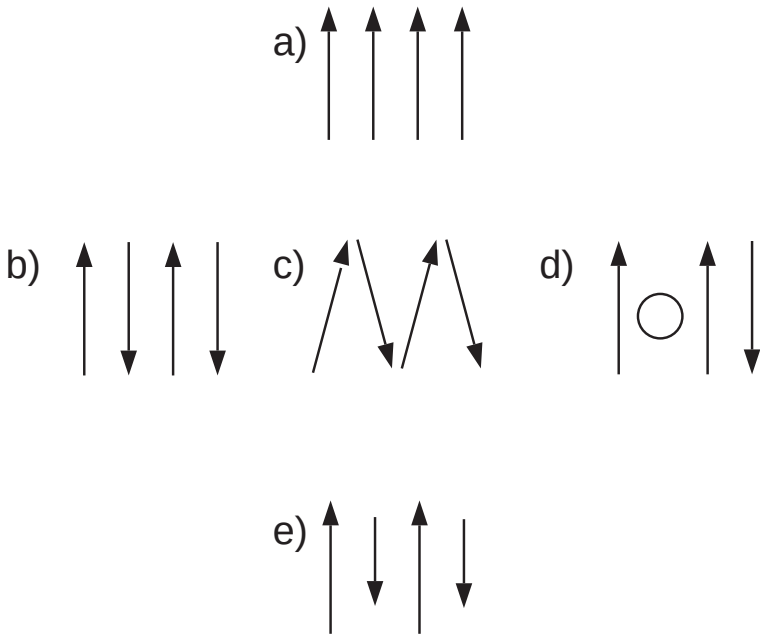

Figure 3.8: Types of spin alignment in ferromagnetism *(sensu lato)*: a) ferromagnetism (*sensu stricto*), b) antiferromagnetism, c) spin-canted antiferromagnetism, d) defect anti-ferromagnetism, e) ferrimagnetism.

$$n(\theta)d\theta \propto \exp\left(\frac{-E_m}{kT}\right)\sin\theta d\theta. \tag{A1}$$

When we measure the induced magnetization, we really measure only the component of the moment parallel to the applied field, or $n(\theta)m\cos\theta$. The net magnetization of a population of particles with volume v is therefore:

$$M_I = \frac{m_b}{v}\int_0^\pi n(\theta)\cos\theta d\theta. \tag{A2}$$

By definition, $n(\theta)$ integrates to N, the total number of moments, or

$$N = \int_0^\pi n(\theta)d\theta. \tag{A3}$$

The total saturation moment of a given population of N individual magnetic moments m is Nm. The saturation value of magnetization M_s is thus Nm normalized by the volume v. Therefore, the magnetization expressed as the fraction of saturation is:

$$\frac{M}{M_s} = \frac{\int_0^\pi n(\theta)\cos\theta d\theta}{\int_0^\pi n(\theta)d\theta}$$

$$= \frac{\int_o^\pi e^{(m\mu_o H\cos\theta)/kT}\cos\theta\sin\theta d\theta}{\int_o^\pi e^{(m\mu_o H\cos\theta)/kT}\sin\theta d\theta}.$$

By substituting $a = m\mu_o H/kT$ and $\cos\theta = x$, we write

$$\frac{M}{M_s} = N\frac{\int_{-1}^{1} e^{ax}xdx}{\int_{-1}^{1} e^{ax}dx} = (\frac{e^a + e^{-a}}{e^a - e^{-a}} - \frac{1}{a}), \tag{A4}$$

and finally

$$\frac{M}{M_s} = [\coth\ a - \frac{1}{a}] = L(a). \tag{A5}$$

Bibliography

Butler, R. F. (1992), *Paleomagnetism: Magnetic Domains to Geologic Terranes*, Blackwell Scientific Publications.

Dunlop, D. & Ozdemir, O. (1997), *Rock Magnetism: Fundamentals and Frontiers*, Cambridge University Press.

O'Reilly, W. (1984), *Rock and Mineral Magnetism*, Blackie.

Lectures in Paleomagnetism, 2005
by Lisa Tauxe

Citation:
http://earthref.org/MAGIC/books/Tauxe/2005/

May 31, 2005

Chapter 4

Magnetic anisotropy, magnetic domains and superparamagnetism

Suggested Reading

For background:
Chapter 3 (pp. 41-55) Butler (1992)
General background in Statistical Mechanics (see, e.g.,
http://en.wikipedia.org/wiki/Statistical_mechanics)
To learn more:
Chapter 2.8 & 5 Dunlop and Özdemir (1997)

4.1 Introduction

In Lecture 3 we learned that in some crystals electronic spins work in concert to create a spontaneous magnetization that remains in the absence of an external field. The basis of paleomagnetism is that these ferromagnetic particles carry the record of ancient magnetic fields. What allows the magnetic moments to come into equilibrium with the geomagnetic field and then what fixes that equilibrium magnetization into the rock so that we may measure it millions or even billions of years later? We will begin to answer these questions over the next few lectures.

We will start with the second part of the question: what fixes magnetizations in particular directions? The short answer is that certain directions within magnetic crystals are at lower energy than others. To shift the magnetization from one "easy" direction to another requires energy. If the barrier is high enough, the particle will stay magnetized in the same direction for very long periods of time - say billions of years. In this lecture we will address what causes and some of the consequences of these energy barriers.

4.2 The magnetic energy of particles

4.2.1 Magnetic moments and external fields

We know from experience that there are energies associated with magnetic fields. Just as a mass has a potential energy when it is placed in the gravitational field of another mass, a magnetic moment has an energy when it is placed in a magnetic field. We have seen this energy briefly in

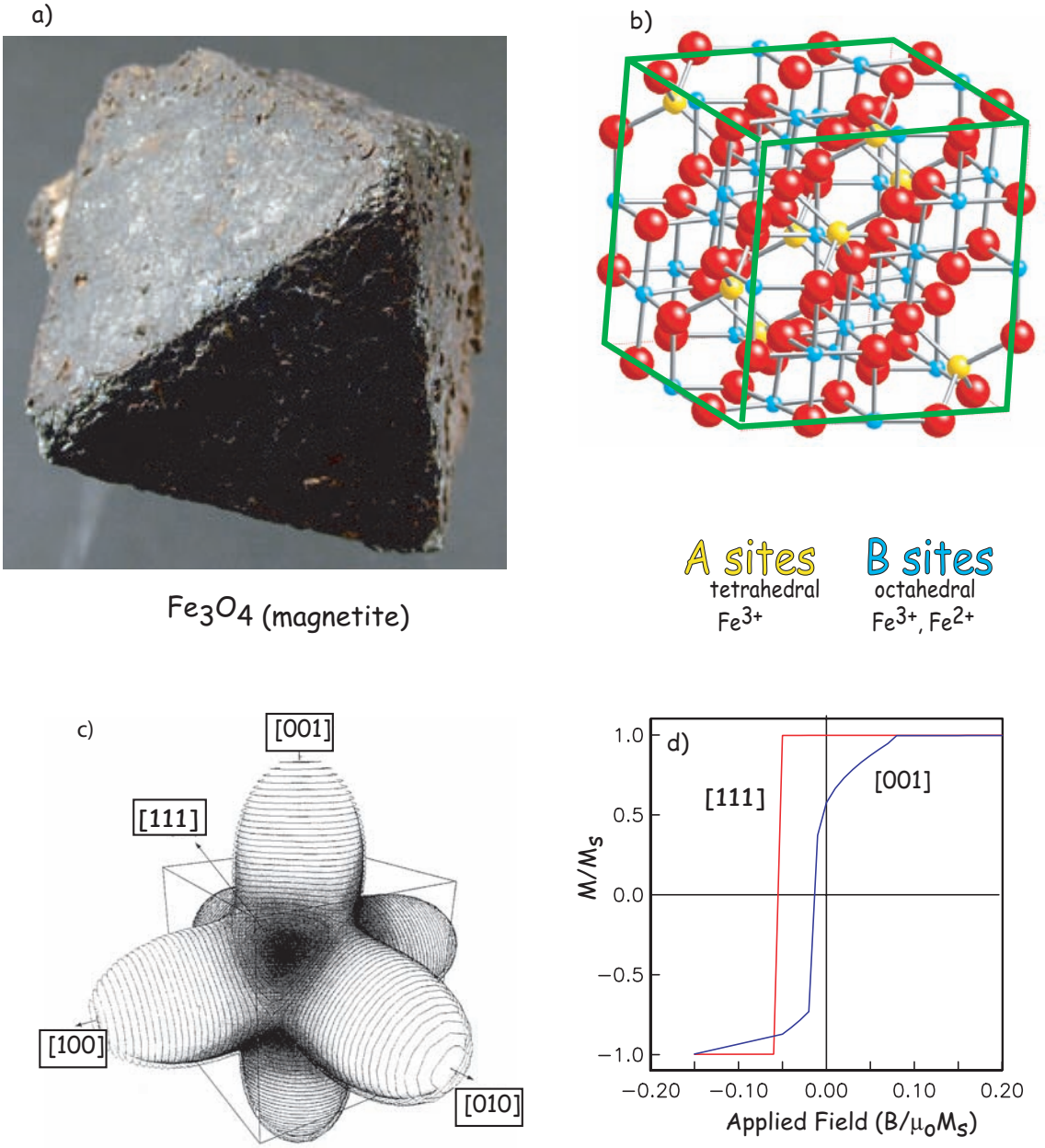

Figure 4.1: a) A magnetite octahedron. b) Internal crystal structure. Big red dots are the oxygen anions. The blue dots are iron cations in octahedral coordination and the yellow dots are in tetrahedral coordination. Fe^{3+} sits on the A sites and Fe^{2+} and Fe^{3+} sit on the B sites. c) Magnetocrystalline anisotropy energy as a function of direction within a magnetite crystal. The easiest direction to magnetize (the direction with the lowest energy) is along the body diagonal. (Redrawn from Williams and Dunlop, 1995.) d) Numerical simulation of the magnetization of a cube of magnetite as the applied field is brought down from saturation to zero, then changed sign and increased again in the opposite direction along two directions in the crystal. The magnetization when aligned with the body diagonal [111] direction (which is associated with the minimum energy state - see c) - is harder to change than along one of the "hard" directions (e.g. [001]).

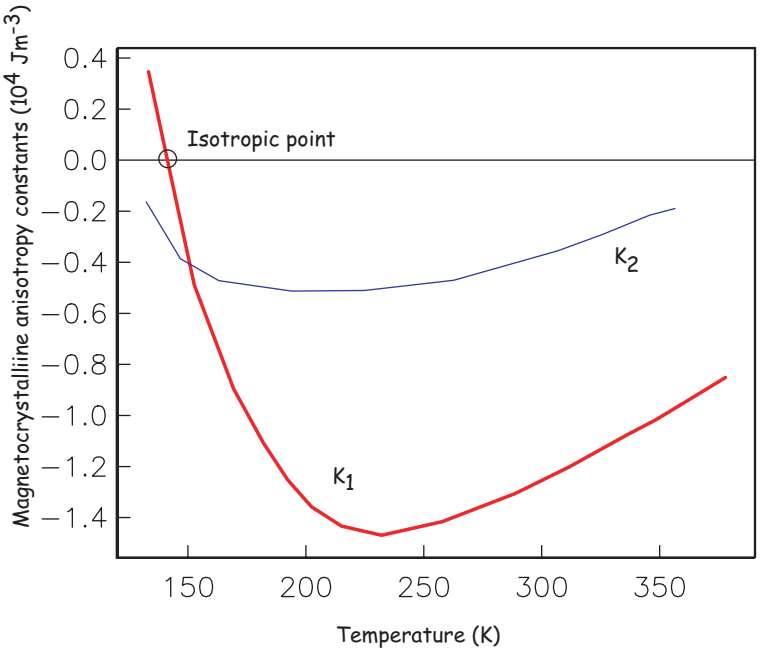

Figure 4.2: Variation of K_1 and K_2 of magnetite as a function of temperature. Redrawn from Dunlop and Özdemir (1997).

Lecture 3. This energy has many names, but here we will call it the "magnetostatic interaction energy density" (E_h):

$$E_h = -\mathbf{M} \cdot \mathbf{B}. \tag{4.1}$$

E_h is at a minimum when the magnetization $\mathbf{M}$ is aligned with the field $\mathbf{B}$. It is this energy that drives magnetic compass needles to seek the minimum energy state by aligning themselves with the ambient magnetic field.

4.2.2 Exchange energy

We learned in Lecture 3 that some crystalline states are capable of ferromagnetic behavior because of quantum mechanical considerations. Electrons in neighboring orbitals in certain crystals "know" about each other's spin states. In order to avoid sharing the same orbital with the same spin (hence having the same quantum numbers - not allowed from Pauli's exclusion principle), electronic spins in such crystals act in a coordinated fashion. They will be either aligned parallel or antiparallel according to the details of the interaction. This *exchange energy density* (E_e) is the source of spontaneous magnetization and is given for a pair of spins by:

$$E_e = -2J_e \mathbf{S}_i \cdot \mathbf{S}_j$$

where J_e is the "exchange integral" and $\mathbf{S}_i$ and $\mathbf{S}_j$ are spin vectors. Depending on the details of the crystal structure (which determines the size and sign of the exchange integral), exchange energy is at a minimum when electronic spins are aligned parallel or anti-parallel.

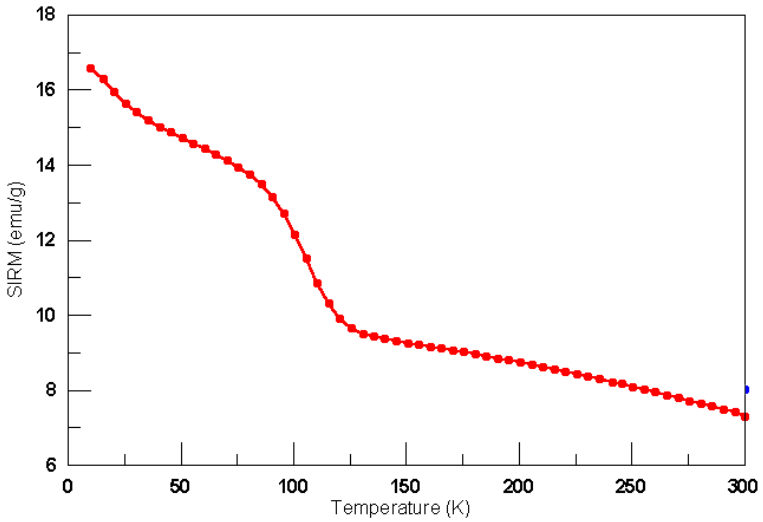

Figure 4.3: Magnetization curve for magnetite as a function of temperature. As the sample goes through the Verwey transition, a fraction of the magnetization is lost. Figure modified from the "Rock magnetic Bestiary" collection at the Institute for Rock Magnetism.

We define here a parameter that we will use later: the exchange constant $A = J_e S^2/a$ where a is the interatomic spacing. $A = 1.33$ x 10^{-11} Jm^{-1} for magnetite, a common magnetic mineral.

The $3d$ electronic orbitals within magnetic crystals are, unlike the s orbitals, anisotropic (recall Lecture 3). They "poke" in certain directions. Hence spins in some directions within crystals will be easier to coordinate than in others. We can illustrate this using the example of magnetite shown in Figure 4.1. Magnetite octahedra (Figure 4.1a), when viewed at the atomic level (Figure 4.1b) are composed of one ferrous (Fe^{2+}) cation, two ferric (Fe^{3+}) cations and four O^{2-} anions. Each oxygen anion shares an electron with two neighboring cations in a covalent bond.

In Lecture 3 it was mentioned that in some crystals, spins are aligned anti-parallel, yet there is still a net magnetization, a phenomenon known as "ferrimagnetism". This can arise from the fact that not all cations have the same number of unpaired spins. Magnetite, with its ferrous (4 m_b) and ferric (5 m_b) states is a good example. There are three iron cations in a magnetite crystal giving a total of 14 m_b to play with. This is HUGE. Magnetite is very magnetic, but not that magnetic! From Figure 4.1b we see that the ferric ions are all sitting on the tetrahedral (A) lattice sites and there are equal numbers of ferrous and ferric ions sitting on the octahedral (B) lattice sites. The A and B sites are aligned anti-parallel to one another because of super exchange (Lecture 3) so we have 9 m_b on the B sites minus 4 m_b on the A sites for a total of 5 m_b per unit cell of magnetite.

4.2.3 Magnetocrystalline anisotropy energy

The energy of moments aligned along different directions in magnetite is shown in Figure 4.1c. The bulges are in directions that have the highest energy ([001, 010, 100]). The lowest energy is along the body diagonal ([111] direction). The energy surface shown in Figure 4.1c represents the *magnetocrystalline anisotropy energy*, E_a. In a cubic crystal with direction cosines $\alpha_1, \alpha_2, \alpha_3$ (the cosines of the angles between the direction and the crystallographic axes [100, 010, 001]; see appendix to Lecture 1), the energy density is given by:

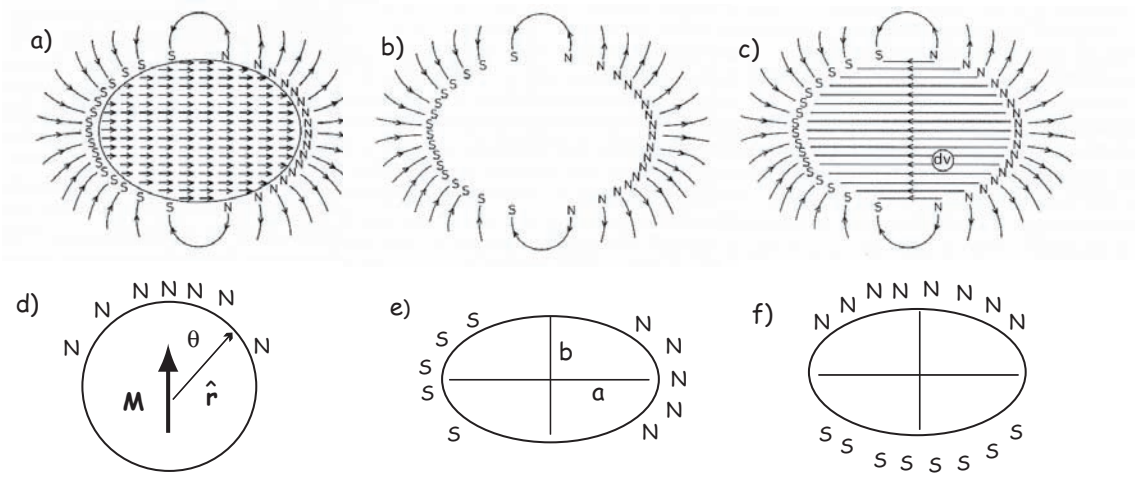

Figure 4.4: a) Internal magnetizations within a ferromagnetic crystal. b) Generation of an identical external field from a series of surface monopoles. c) The internal "demagnetizing" field resulting from the surface poles. (Redrawn from O'Reilly [1984]). d) Surface poles on a sphere. e) Surface poles on an ellipse, with the magnetization parallel to the elongation. f) Surface poles with the magnetization perpendicular to the axis of elongation.

$$E_a = K_1(\alpha_1^2\alpha_2^2 + \alpha_2^2\alpha_3^2 + \alpha_3^2\alpha_1^2) + K_2\alpha_1^2\alpha_2^2\alpha_3^2 \tag{4.2}$$

where K_1 and K_2 are empirically determined *magnetocrystalline anisotropy constants*. In the case of (room temperature) magnetite, K_1 is -1.35 x 10^4 Jm^{-3}. If you work through the magnetocrystalline equation, you will find that when K_1 is negative, E_a is at a minimum when it is parallel to the [111] direction (the body diagonal).

As a consequence of the magnetocrystalline anisotropy energy, once the magnetization is aligned with an easy direction, work must be done to change it. In Figure 4.1d we show the results of numerical simulations of the magnetization of a cube of magnetite as an applied field is brought from saturation to zero, then changed in sign and increased in the opposite direction. We show the results from two directions in the crystal. The magnetization aligned with the body diagonal [111] (associated with the minimum energy state - see Figure 4.1c) is harder to change than along one of the "hard" directions (e.g. [001]).

A useful parameter in characterizing the stability of a particular particle or assemblage of particles is the field that is required to drive the magnetizations out of the easy directions, over an energy barrier and into another easy direction. This field is called the flipping field, the coercive field or the coercivity (B_c or H_c depending on units), something we will consider in more detail in later lectures.

Cubic symmetry (as in the case of magnetite) is just one of many types of crystal symmetries. One other very important form is the uniaxial symmetry which can arise from crystal shape or structure. The energy density for uniaxial magnetic anisotropy is:

$$E_a = K_{u1} sin^2\theta + K_{u2} \sin^4\theta + ... \tag{4.3}$$

In this equation, when K_u is negative, the magnetization is constrained to lie perpendicular to the

axis of symmetry. When $K_u > 0$, the magnetization lies parallel to it.

An example of a mineral dominated by uniaxial symmetry is hematite. The magnetization of hematite is quite complicated, as we shall learn later, but one source is magnetization lies in the "spin-canting" (see Lecture 3) within the basal plane of a hexagonal crystal. Within the basal plane, the anisotropy constant is very low and the magnetization wanders fairly freely. However, the anisotropy energy away from the basal plane is high, so the magnetization is constrained to lie within the basal plane.

Because electronic interactions depend heavily on inter atomic spacing, magnetocrystalline anisotropy constants are a strong function of temperature (see Figure 4.2). In magnetite, K_1 changes sign at a temperature known as the "isotropic point". At the isotropic point, there is no large magnetocrystalline anisotropy. The large energy barriers that act to keep the magnetizations parallel to the body diagonal are gone and the spins can wander more freely through the crystal. Below the isotropic point, the energy barriers rise again, but with a different topology in which the crystal axes are the energy minima and the body diagonals are the high energy states.

At room temperature, electrons hop freely between the ferrous and ferric ions on the B lattice sites, so there is no order. Below about 120 K, there is an ordered arrangement of the ferrous and ferric ions. Because of the difference in size between the two, the lattice of the unit cell becomes slightly distorted and becomes monoclinic instead of cubic. This transition is known as the *Verwey transition*. Although the isotropic point (measured magnetically) and the Verwey transition (measured electrically) are separated in temperature by about 15^o, they are related phenomena (the ordering and electron hopping cause the change in K_1).

The change in magnetocrystalline anisotropy at low temperature can have a profound effect on the magnetization. In Figure 4.3 we show a typical (de)magnetization curve for magnetite taken from the "Rock magnetic bestiary" web site maintained at the Institute for Rock Magnetism: http://www.geo.umn.edu/orgs/irm/bestiary. There is a loss of magnetization at around 100 K. This loss is the basis for "low-temperature demagnetization" (LTD). However, some portion of the magnetization is always recovered after low temperature cycling (called the *low temperature memory*), so the general utility of LTD is somewhat limited.

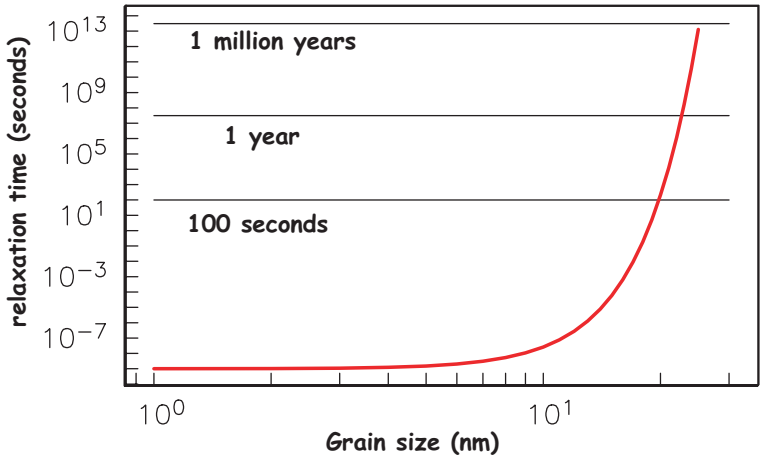

Figure 4.5: Relaxation time as a function of grain size in nanometers.

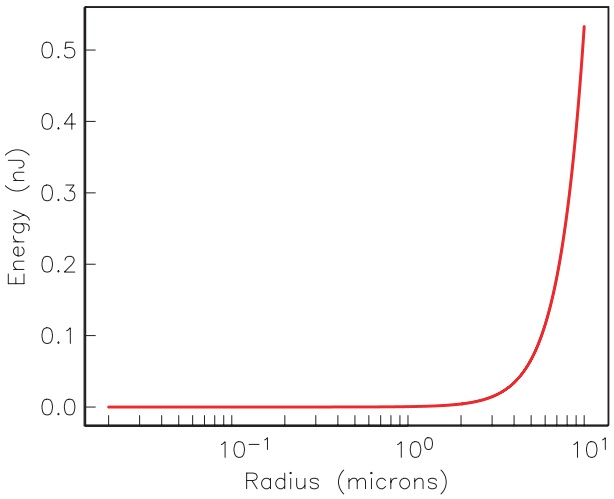

Figure 4.6: The self energy of a spherical particle of magnetite as a function of particle radius.

4.2.4 Magnetostriction - stress anisotropy

It is intuitively obvious that, because the exchange energy depends strongly on the details of the physical interaction between orbitals in neighboring atoms with respect to one another, changing the positions of these atoms will affect that interaction. Put another way, straining a crystal will alter its magnetic behavior. Similarly, changes in the magnetization can change the shape of the crystal by altering the shapes of the orbitals. This is the phenomenon of *magnetostriction*. The magnetic energy caused by the application of stress to a crystal be approximated by:

$$E_\sigma = -\frac{3}{2}\bar{\lambda}\sigma \sin^2\theta$$

where $\bar{\lambda}$ is an experimentally derived constant, σ is the stress, and θ is the angle of the stress with with respect to the c crystallographic axis. $\bar{\lambda}$ for magnetite is about 40 x 10^{-6}. Note the similarity in form of magnetostriction and uniaxial anisotropy giving rise to a single "easy axis" within the crystal.

4.2.5 Magnetostatic - or shape anisotropy

There is one more important source of magnetic anisotropy: shape. To understand how crystal shape controls magnetic energy, we need to understand the concept of the internal "demagnetizing field" of a magnetized body. In Figure 4.4a we show the magnetic vectors within a ferromagnetic crystal. These produce a magnetic field external to the crystal that is proportional to the magnetic moment (see Lecture 1). This external field is identical to a field produced by a set of "free poles" distributed over the surface of the crystal (Figure 4.4b). The surface poles don't just produce the external field, they also produce an internal field shown in Figure 4.4c. The internal field is known as the *demagnetizing field* H_d. H_d is proportional to the magnetization of the body and is sensitive to the shape. For the simple ellipsoid shown in Figure 4.4, the demagnetizing field is given by:

$$\mathbf{H}_d = -N\mathbf{M}$$

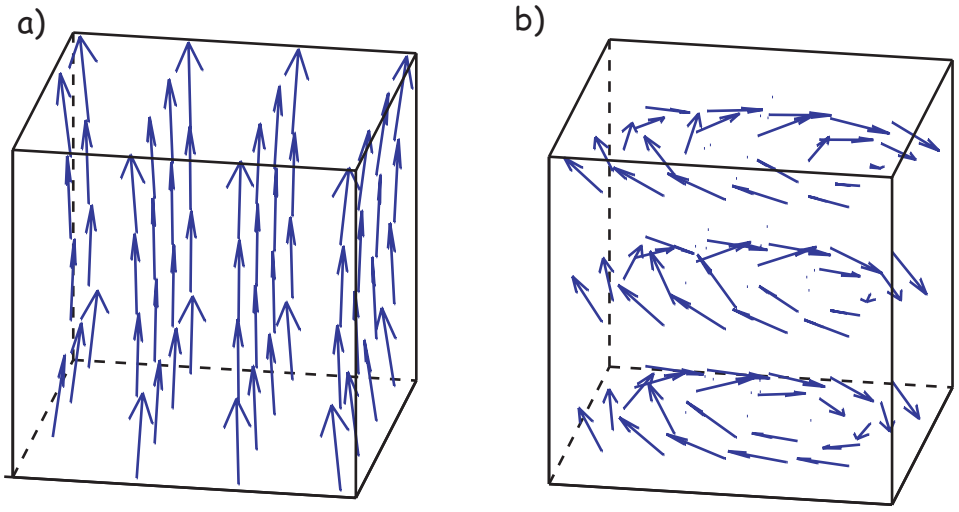

Figure 4.7: Possible non-uniform magnetization configurations that reduce self energy for magnetite with increasing particle widths. a) "Flower" state, b) "Vortex" state. (From Tauxe et al., 2002)

where N is a *demagnetizing factor* determined by the shape. For a sphere, the surface poles are distributed over the surface such that there are none at the "equator" and most at the "pole" (see Figure 4.4d). The expression for surface pole density is $\sigma_m = \mathbf{M} \cdot \hat{r}$. By using tricks of potential field theory in which we can pretend that the external field of a uniformly magnetized body is identical to that of a central dipole moment of magnitude $m = vM$ (where v is volume). At the equator of the sphere, $\mathbf{H}_d = -N\mathbf{M}$. The external field at the equator (remembering from Lecture 1) is given by

$$H_e = -\frac{m}{4\pi r^3}.$$

Also remembering that magnetization (in units of Am^{-1}) is the moment (in units of Am^2) per unit volume (in units of m^3) and the volume of a sphere is $\frac{4}{3}\pi r^3$, we have:

$$m = \frac{4}{3}\pi r^3 M,$$

so $H_d = -\frac{1}{3}M$, hence $N = \frac{1}{3}$.

Different directions within a non-spherical crystal will have different distributions of free poles (see Figures 4.4e,f), so N will depend on direction. In the case of an ellipsoid magnetized parallel to the elongation axis a (Figure 4.4e), the free poles are farther apart than across the grain, hence, intuitively, the demagnetizing field, which depends on $1/r^2$, must be less than in the case of a sphere. Thus, $N_a < \frac{1}{3}$. Similarly, if the ellipsoid is magnetized along b (Figure 4.4f), the demagnetizing field is stronger or $N_b > \frac{1}{3}$. In an ellipsoid there are three axes a, b, c, and $N_a + N_b + N_c = 1$ (in SI; in cgs units the sum is 4π).

Getting back to the anisotropy energy, that arising from the external field of the particle is called *magnetostatic energy* whose energy density equation is:

$$E_{ms} = \frac{1}{2}\mu_o N_a M^2 + \frac{1}{2}\mu_o (N_c - N_a) M^2 \sin^2\theta$$

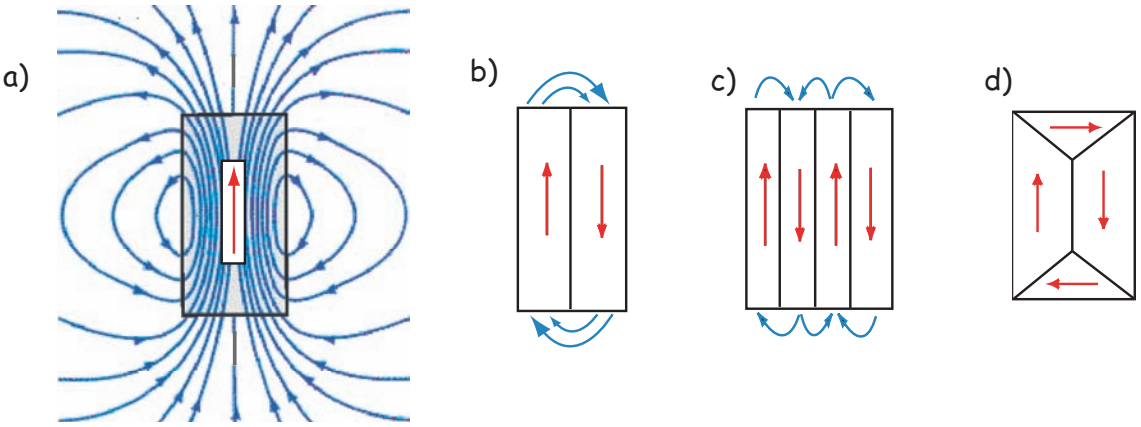

Figure 4.8: A variety of domain structures of a given particle. a) Uniformly magnetized (single domain). b) Two domains. c) Four domains in a lamellar pattern. d) Essentially two domains with two closure domains.

where N_c and N_a are the demagnetizing coefficients along the short and long axes respectively. This expression can be derived by "building" a magnetic particle and considering the potential energy gained by each volume dv as it is brought in ($-\mu_o \mathbf{M} dv \cdot \mathbf{H}_d$) and integrating. The $\frac{1}{2}$ appears in order to avoid counting each volume element twice and the v dissappears because all the energies we have been discussing are energy densities - the energy per unit volume. Note that the magnetostatic energy has a uniaxial form with the constant of uniaxial anisotropy - $K_u = \frac{1}{2}\Delta N \mu_o M^2$.

For a prolate ellipsoid $N_c = N_b$ and $a/c = 1.5$, $N_a - N_c = \sim 0.16$. Also, $N_a = \frac{1}{3}[1 - \frac{2}{5}(2 - \frac{b}{a} - \frac{c}{a})]$. The magnetization of magnetite is 4.8 x $10^5 \mathrm{Am}^{-1}$, so $K_u \simeq$ 2.3 x 10^4 Jm^3. This is somewhat larger than the absolute value of K_1 for magnetocrystalline anisotropy in magnetite (K_1= -1.35 x 10^4 Jm^{-3}), so the magnetization for even slightly elongate grains will be dominated by uniaxial anistropy controlled by shape. Minerals with low saturation magnetizations (like hematite) will not have shape dominated magnetic anisotropy, however.

4.2.6 Thermal energy

We have gone some way to answering some of the questions posed at the beginning of the lecture. It should be clear that it is the anisotropy energy which opposes change in the magnetic direction, preserving the magnetization for posterity. The related question of what allows the magnetization to come into equilibrium with the applied magnetic field, however, requires a little more work. The key is to find some mechanism which allows the moments to "jump over" magnetic anisotropy energy barriers and one answer is thermal energy E_T, given by:

$$E_T = kT$$

where kT is thermal energy (see Lecture 3).

Imagine a block of material containing a random assemblage of magnetic particles that are for simplicity uniformly magnetized and dominated by uniaxial anisotropy. Suppose that this block has some initial magnetization M_o and is placed in an environment with no ambient magnetic field. Anisotropy energy will tend to keep each tiny magnetic moment in its original direction and the magnetization will not change over time. With some thermal energy, certain grains will have

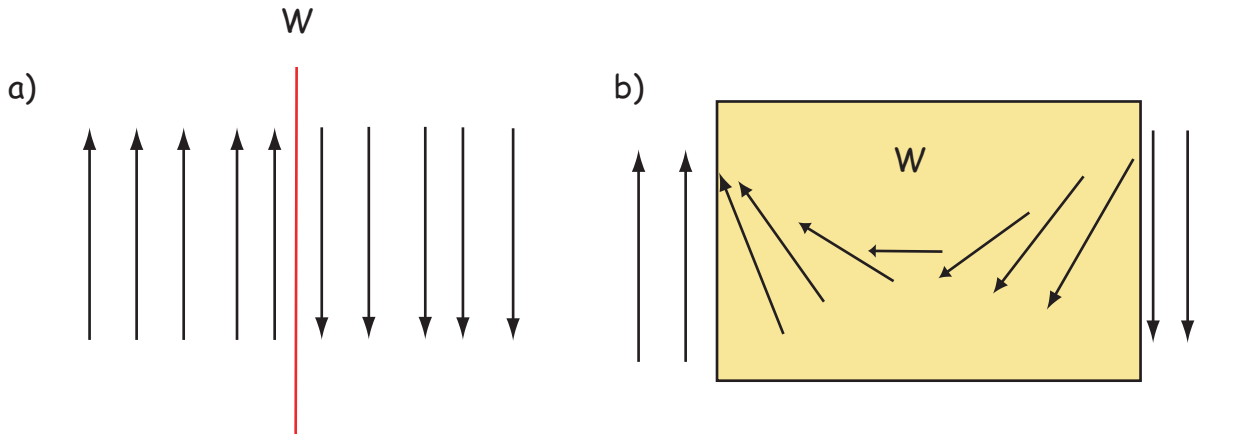

Figure 4.9: Examples of possible domain walls. a) There is a 180° switch from one atom to the next. The domain wall is very thin, but the exchange price is very high. b) There is a more gradual switch from one direction to the other [note: each arrow represents several 10's of unit cells]. The exchange energy price is lower, but there are more spins in unfavorable directions from a magnetocrystalline point of view.

sufficient energy to overcome the anisotropy energy and flip their moments to the other easy axis. Over time, the magnetic moments will become random.

We know from statistical mechanics that the probability of finding a grain with a given thermal energy is $P = \exp(-E_T/kT)$. So we may have to wait some time t for a particle to work itself up to having sufficient energy to flip over the energy barrier. Therefore, the magnetization as a function of time in this simple scenario will decay according to this equation:

$$M(t) = M_o \exp(\frac{-t}{\tau}) \tag{4.4}$$

where t is time and τ is an empirical constant called the *relaxation time* which is the time required for the remanence to decay to $1/e$ of M_o. This equation is the essence of what is called "Néel theory" (see, e.g., Néel, 1955).

The value of τ is a function of the competition between magnetic anisotropy energy and thermal energy. It is a measure of the probability that a grain will have sufficient thermal energy to overcome the anisotropy energy and switch its moment. Therefore in zero external field:

$$\tau = \frac{1}{C} \exp \frac{[\text{anisotropy energy}]}{[\text{thermal energy}]} = \frac{1}{C} \exp \frac{[Kv]}{[kT]}, \tag{4.5}$$

where C is a frequency factor with a value of something like 10^{10} s^{-1}. The anisotropy energy is given by the dominant anisotropy parameter K (either K_u, K_1, or λ) times the grain volume v. It is often convenient to use the relationship $K = \frac{B_c M_s}{2}$, which will be derived as a homework assignment.

Thus, the relaxation time is proportional to coercivity, and volume, and is inversely related to temperature. Relaxation time τ varies rapidly with small changes in v and T. There is a sharp transition between grains with virtually no stability (τ is on the order of seconds) and grains with stabilities of millions of years. To see how this works, we can take $K = K_1$ for magnetite and

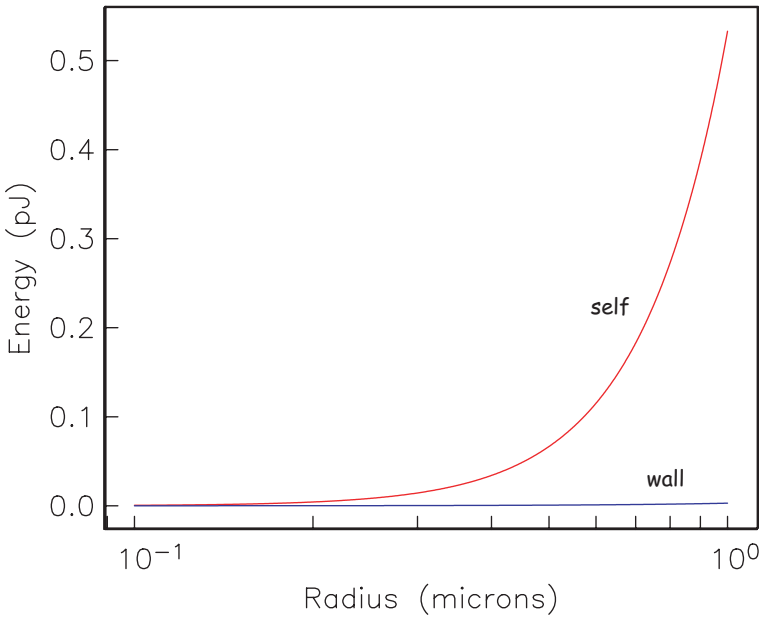

Figure 4.10: Comparison of "self" energy versus the energy of the domain wall in magnetite spheres as a function of particle size.

$v = d^3$ for the grain size of a cube of magnetite (see Figure 4.5). We have only considered equant particles of magnetite to construct Figure 4.5 so it is worth bearing in mind that Kv is a strong function of shape - the more elongate the particle, the higher the stability - a point we will return to at the end of the lecture.

Grains with $\tau \simeq 10^2 - 10^3$ seconds have sufficient thermal energy to overcome the anisotropy energy frequently and are unstable on a laboratory time-scale. In zero field, these grain moments will tend to rapidly become random and in an applied field, they tend to rapidly align with the field. The net magnetization is related to the field by a Langevin function (see Lecture 3). Therefore, this behavior is quite similar to paramagnetism, hence these grains are called *superparamagnetic* (SP). Such grains can be distinguished from paramagnets, however, because the field required to saturate the moments is typically much less than a tesla, whereas that for paramagnets can exceed hundreds of tesla.

4.3 Magnetic domains

4.3.1 Some theory

So far we have been discussing hypothetical magnetic particles that are uniformly magnetized. In Figure 4.4a we noted that there is an energy associated with the field generated by a magnetic particle. This *self energy* density is given by:

$$E_{self} = -\frac{1}{2}\mu_o \mathbf{M} \cdot \mathbf{H}_d = \frac{1}{2}\mu_o N M^2$$

It is interesting to consider how the self energy of a particle changes with volume. In a sphere with radius r microns (and volume $\frac{4}{3}\pi r^3$), we get the energy in joules as a function of volume in

Figure 4.6 by remembering that $M = 4.8$ x 10^5 Am^{-1} and $\mu_o = 4\pi$ x 10^{-7} Hm^{-1}.

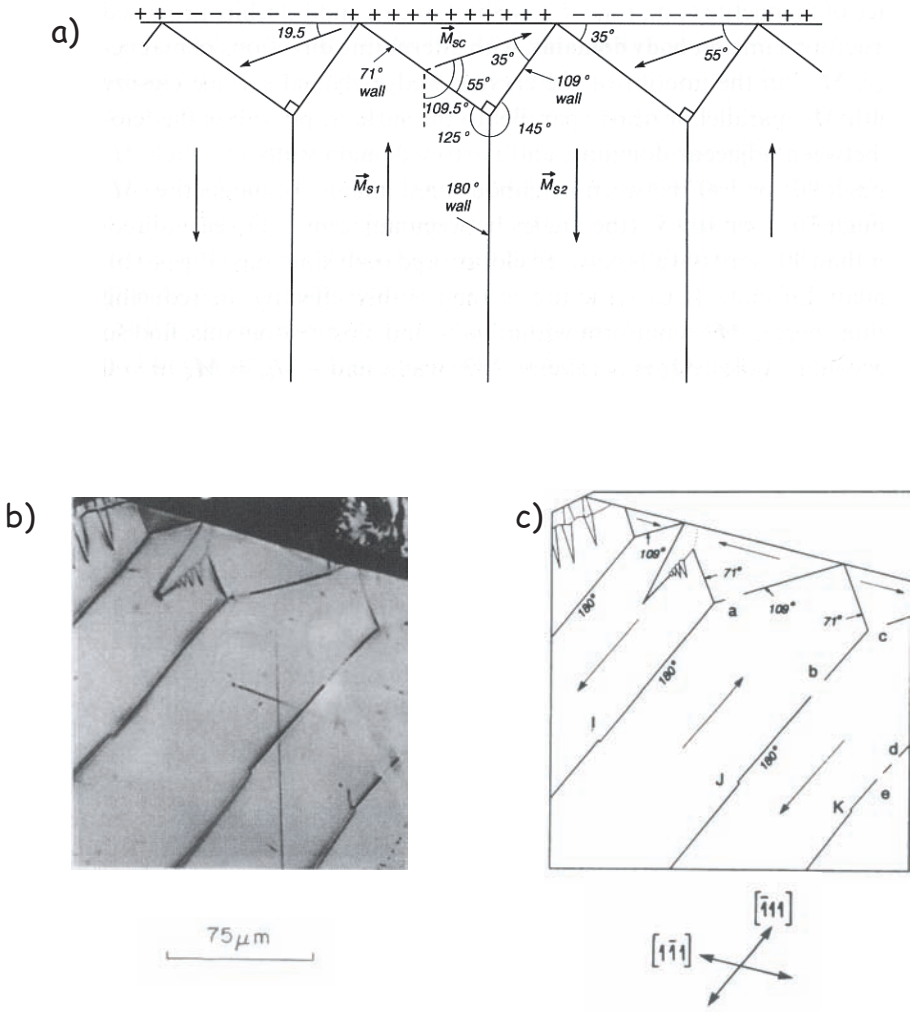

Figure 4.11: a) Theoretical predictions of possible domain structures for magnetite. b) Bitter patterns from an oriented polished section of magnetite. c) Interpretation of the magnetization. [Figures from Dunlop and Ozdemir (1997)].

Particles with strong magnetizations (like magnetite) have self energies that quickly become quite large. We have been learning about several mechanisms that tend to align magnetic spins. In fact in very small particles, the spins are essentially lined up. The particle is uniformly magnetized and is called *single domain* (SD). In larger particles (although still pretty small) the self energy exceeds the other exchange and magnetocrystalline energies and crystals have non-uniform states of magnetization.

There are many strategies possible for magnetic particles to reduce self energy. Numerical models (called micromagnetic models) can find internal magnetization configurations that minimize the energies discussed in the preceding sections. Micromagnetic simulations for magnetite particles (e.g. Schabes and Bertram, 1988) allow us to peer into the state of magnetization inside magnetic particles. These simulations give a picture of increasing complexity from so-called "flower"

(Figure 4.7a) to "vortex" states (Figure 4.7b) remanent states.

As particles grow even larger, they break into regions of uniform magnetization called *magnetic domains* separated by narrow zones of rapidly changing spin directions called *domain walls*. Magnetic domains can take many forms. We illustrate a few in Figure 4.8. The uniform case (single domain) is shown in Figure 4.8a. The external field is very large because the free poles are far apart (at opposite ends of the particle). When the particle organizes itself into two domains (Figure 4.8b), the external field is reduced by about a factor of two. In the case of four lamellar domains (Figure 4.8c), the external field is quite small. The introduction of *closure domains* as in Figure 4.8d reduces the external field to nothing.

$$n_d = Z \cdot \frac{b}{a} a^{\frac{1}{2}} \tag{4.6}$$

As you might already suspect, domain walls are not "free". If, as in Figure 4.9a, the spins simply switch from one orientation to the other abruptly, the exchange energy cost would be very high. One way to get around this to spread the change over several hundred atoms, as sketched in Figure 4.9b. The wall width δ is wider and the exchange energy price is much less. However, there are now spins in unfavorable directions from a magnetocrystalline point of view (they are in "hard" direction). Exchange energy therefore favors wider domain walls while magnetocrystalline anisotropy favors thin walls. With some work (see e.g., Dunlop and Özdemir, 1997, pp. 117-118), it is possible to come up with the following analytical expressions for wall width (δ_w) and wall energy per unit area ($\mathbf{E}_w$):

$$\delta_w = \pi \left(\frac{A}{K}\right)^{\frac{1}{2}}, E_w = 2\pi (AK)^{\frac{1}{2}}$$

where A is the exchange constant from before and K is the magnetic anisotropy constant (e.g., K_u or K_1). Plugging in values for magnetite given earlier we get $\delta_w = 0.28$ μm and $E_w = 2.3$ x 10^{-3}Jm^{-2}.

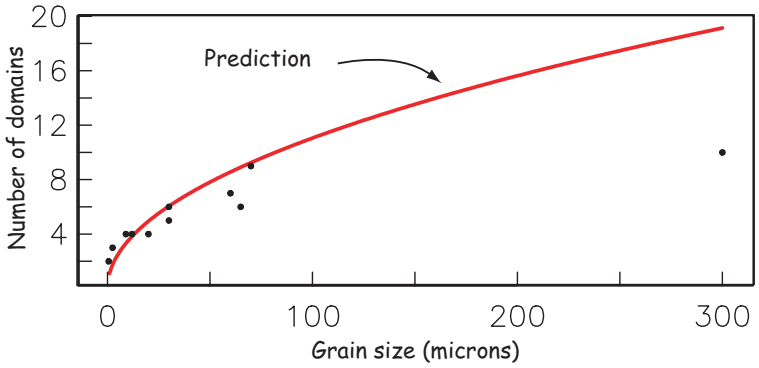

Figure 4.12: Number of domains in magnetite particles versus grain size. Solid curve: predicted values from theory (see text). Dots: data compiled by Özdemir and Dunlop (1997).

In Figure 4.10 we plot the self energy from Figure 4.6 and the wall energy from E_w for spheres of magnetite. We see that the wall energy in particles with radii of a few tenths of a micron is much less than the self energy, yet the width of the walls is also a few tenths of a micron. So the smallest wall is really more like the vortex state and it is only for particles closer to one micron in size that true domains separated by discrete walls are formed.

Finally, it is possible to predict the number of domains (n_d) in a given particle of magnetite. Assuming lamellar domains within cubes of magnetite, Dunlop and Özdemir (1997) derived the following equation:
where Z is a constant incorporating magnetostriction and wall energy and a and b are particle length and width as before. For magnetite, $Z \simeq 1.1 \times 10^3$. For a 100 μm equant grain of magnetite, then, we would expect to find 11 domains.

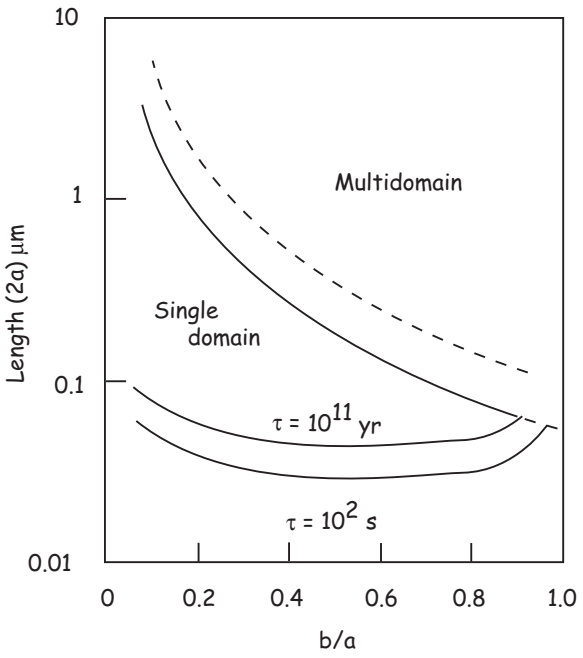

Figure 4.13: Expected domain states for various sizes and shapes of parallelopipeds of magnetite at room temperature. a and b are as in Figure 4.4. [Figure redrawn from Evans and McElhinny, 1969.]

4.3.2 Some experiments

How can we test the theoretical predictions of domain theory? Do they really exist? Are they the size and shape we expect? Are there as many as we would expect? In order to address these questions we require a way of "seeing" magnetic domains. Bitter (1931) devised a way for doing just that. Magnetic domain walls are regions with large stray fields (as opposed to domains in which the spins are usually parallel to the sides of the crystals to minimize stray fields). In the "Bitter technique" magnetic colloid material is drawn to the regions of high field gradients on highly polished sections allowing the domain walls to be observed.

We show an example of a photomicrograph taken from the interior of a large grain of magnetite (Dunlop and Özdemir, 1997). It appears that if great care is taken, domain walls of about the right size, shape and orientation can be found.

Özdemir and Dunlop (1997) compiled what they considered to be the "best" data on number of domains n_d observed in carefully sized magnetite grains. We replot their data compilation in Figure 4.12. Also shown is the prediction from Equation 4.6. There appear to be "too many"

domains for small grain sizes and "too few" for large grain sizes. In a seminal paper, Halgedahl and Fuller (1980) argued that there were far fewer domains than predicted for titanomagnetite, which they explained as arising from the fact that the energy to nucleate a domain wall from nothing had not been taken into account in the theory.

We are now in a position to pull together all the threads we have considered in this lecture and make a plot of what sort of magnetic particles behave as superparamagnets, which should be single domain and which should be multi-domain according to our simple theories. Evans and McElhinny (1969) made a beautiful plot (see Figure 4.13). There is virtually no SD stability field for equant magnetite; they are either SP or MD (multi-domain). As the width to length decreases (the particle gets longer), the stability field for SD magnetite expands. Of course micromagnetic modelling shows that there are several transitional states between uniform magnetization (SD) and MD, i.e. the flower and vortex remaent states, but Figure 4.13 or variations thereof (e.g. Butler and Banerjee, 1975) have enormous predictive power and continue to be used extensively.

Bibliography

Bitter, . (1931), *Phys. Rev* **38**, 1903–1905.

Butler, R. F. (1992), *Paleomagnetism: Magnetic Domains to Geologic Terranes*, Blackwell Scientific Publications.

Butler, R. F. & Banerjee, S. K. (1975), 'Theoretical single domain grain-size range in magnetite and titanomagnetite', *Jour. Geophys. Res.* **80**, 4049–4058.

Dunlop, D. & Ozdemir, O. (1997), *Rock Magnetism: Fundamentals and Frontiers*, Cambridge University Press.

Evans, M. E. & NcElhinny, M. W. (1969), 'An investigation of the origin of stable remanence in magnetite-bearing igneous rocks', *J. Geomag. Geoelectr.* **21**, 757–773.

Halgedahl, S. & Fuller, M. (1980), 'Magnetic domain observations of nucleation processes in fine particles of intermediate titanomagnetite', *Nature* **288**, 70–72.

Néel, L. (1955), 'Some Theoretical Aspects of Rock-Magnetism', *Adv. Phys* **4**, 191–243.

Özdemir, O. & Dunlop, D. J. (1997), *J. Geophys. Res* **102**, 20211–20224.

Schabes, M. E. & Bertram, H. N. (1988), 'Magnetization processes in ferromagnetic cubes', *J. Appl. Phys.* **64**, 1347–1357.

Tauxe, L., Bertram, H. & Seberino, C. (2002), 'Physical interpretation of hysteresis loops: Micromagnetic modelling of fine particle magnetite', *Geochem., Geophys., Geosyst.* **3**, DOI 10.1029/2001GC000280.

Williams, W. & Dunlop, D. (1995), 'Simulation of magnetic hysteresis in pseudo-single-domain grains of magnetite', *J. Geophys. Res.* **100**, 3859–3871.

Lectures in Paleomagnetism, 2005
by Lisa Tauxe

Citation:
http://earthref.org/MAGIC/books/Tauxe/2005/

May 31, 2005

Chapter 5

How rocks get and stay magnetized

Suggested Reading

For background:
Chapter 3 in Butler (1992)
http://assets.cambridge.org/052181/ 1198/excerpt/0521811198_excerpt.pdf
To learn more:
Chapters 8, 10,11, 13 in Dunlop and Özdemir (1997)

5.1 Introduction

In the last few lectures, we have begun to understand the magnetic remanence of single crystals in terms of minimizing exchange energy in crystal lattices. Without the anisotropy energy (the changes in energy states as a function of direction of magnetization within the crystal, the moments of individual grains would swing freely and would not retain a "memory" of the ancient field direction.

For paleomagnetism to work, we need some way to change the anisotropy energy from low enough to allow the magnetization to come into equilibrium with the ambient geomagnetic field to high enough that this equilibrium magnetization can be "frozen in" and be preserved for geological time scales.

5.2 The concept of dynamic equilibrium

Given that we live in a world that is above absolute zero and, down to the atomic level, everything is in motion, the state of the things is constantly changing. However, looking at the big picture, things often seem to be unchanging. Imagine for a moment a field full of sheep with a fence down the middle. The sheep can jump over the fence at will to get flowers on the other side and occasionally they do so. Over time, because the two sides are pretty much the same, the same number of sheep jump over in both directions, so if you were to count sheep on either side, the numbers would stay about the same. Now think about what would happen if it was raining on one side of the fence. More sheep would jump over to the sunny side than would jump to the rainy side and you might find over time, more sheep on the one side than the other (see Figure 5.1). These scenarios illustrate the concept of dynamic equilibrium.

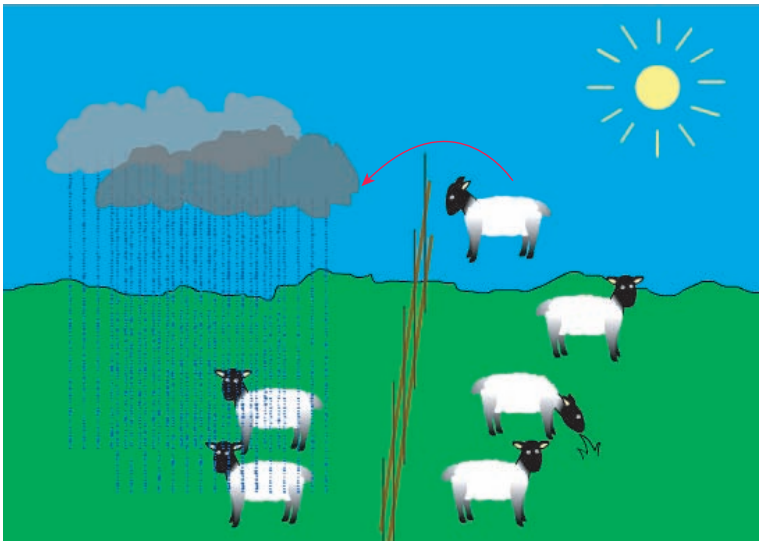

Figure 5.1: Illustration of dynamic equilibrium. If conditions on either side of the fence are equally pleasant, an equal number of sheep will be on either side of the fence, despite the fact that sheep are constantly jumping over the fence. If one side is preferrable (sunny rather than rainy), there will tend to be more sheep on the nicer side. (Drawing by Genevieve Tauxe.)

Returning to magnetism, a magnet with uniaxial anisotropy in the absence of a magnetic field will tend to be magnetized in one of two "easy" directions (see Lecture 4). In order to "jump over the fence" (the anisotropy energy) and get from one easy axis to another, a magnetic particle must have thermal energy in excess of the anisotropy energy. According to the Boltzmann distribution law, the probability of a given particle having an energy ϵ is proportional to $e^{-\epsilon/kT}$ where kT is the thermal energy (see Lecture 4). Therefore, it may be that at a certain time, the magnetic moment may have enough thermal energy for the electronic spins to overcome the energy barrier and flip the sense of magnetization from one easy axis to another.

If we had a collection of magnetized particles with some initial statistical alignment of moments giving a net remanence M_o, the random "fence jumping" by magnetic moments from one easy axis to another over time will eventually lead to the case where there is no net preference and the moment will have decayed to zero. The general concept of approach to equilibrium magnetization is the essence of what is known as Néel Theory, which we will discuss briefly in the following section.

5.3 Introduction to Néel Theory

The theoretical basis for how ancient magnetic fields might be preserved was established over fifty years ago with the Nobel Prize winning work of Néel (1949, 1955). The mechanism which controls the approach to magnetic equilibrium is relaxation time, which in the sheep analogy is the frequency of fence jumping. We defined relaxation time in Lecture 4 as:

$$\tau = \frac{1}{C} \exp \frac{[\text{anisotropy energy}]}{[\text{thermal energy}]} = \frac{1}{C} \exp \frac{[Kv]}{[kT]}, \tag{5.1}$$

where C is a frequency factor with a value of something like 10^{10} s^{-1}. Equation 5.1 is sometimes

called the *Néel equation*. In the "sheep in the rain" scenario, jumping over the fence into the rain required more motivation than jumping into the sun. It is also true that the energy barrier for magnetic particles to flip into the direction of the applied field B requires less energy than to flip the other way, so relaxation time must also be a function of the applied field. The more general equation for relaxation time is given by:

$$\tau = \frac{1}{C} \exp \frac{[Kv]}{[kT]} [1 - \frac{B}{B_c}]^2 \tag{5.2}$$

This lecture is concerned with magnetic remanences acquired mostly in the presence of the Earth's magnetic field, which is tiny compared to the coercivity of the minerals in question and so we will neglect the effect of B on τ in the following.

The anisotropy energy density is given by the dominant anisotropy constant K times the grain volume v. We learned in Lecture 4 that K for uniaxial shape anisotropy is K_u and is equal to $\frac{1}{2}\Delta N \mu_o M^2$. [We will learn in later lectures that the coercivity $B_c = \frac{2K_u}{M_s}$ which will come in handy later in this lecture.] Substituting into Equation 5.1 we get:

$$\tau = \frac{1}{C} \exp \frac{[\Delta N \mu_o M_s^2 v]}{[2kT]}, \tag{5.3}$$

where M_s is a strong function of temperature itself (see, e.g., Figure 3.8). We can see from Equation 5.3 that relaxation time is a function of magnetization, as well as volume and temperature, properties that we will return to later in the lecture and in future lectures through out the course.

5.4 Viscous Remanent Magnetization

We surmised earlier that if we placed a sample with a saturation magnetization in an environment with zero magnetic field, there would be no preference between directions along the easy axis, so the equilibrium magnetization M_e is zero. Equilibrium magnetization will be approached as individual particles flip their moments with no preferred direction (it is sunny everywhere), hence become increasingly random with respect to one another. Néel theory predicts that the magnetization of the sample will decrease according to the equation

$$M(t) = M_o \exp(\frac{-t}{\tau})$$

as shown in Figure 5.2a.

In the inset to Figure 5.3, the easy direction for the magnetization of the particle would be along its length (because of the dominance of shape anisotropy). Placing this particle in an external magnetic field results in a magnetostatic energy E_h of $-\mathbf{m} \cdot \mathbf{B} = -mb \cos\theta$, which is at a minimum when the moment is aligned with the field (see Lecture 4). Given an arbitrary θ, the difference in E_h between the two easy directions

$$\Delta E = 2(\mathbf{m} \cdot \mathbf{B}) = 2mB \cos\theta. \tag{5.4}$$

Because of the energy of the applied field E_h, the energy necessary to flip the moment from a direction with a high angle to the external field to the other direction with a lower angle is less than the energy necessary to flip the other way around. Therefore, a given particle will tend to spend more time with its moment at a favorable angle to the applied field than in the other

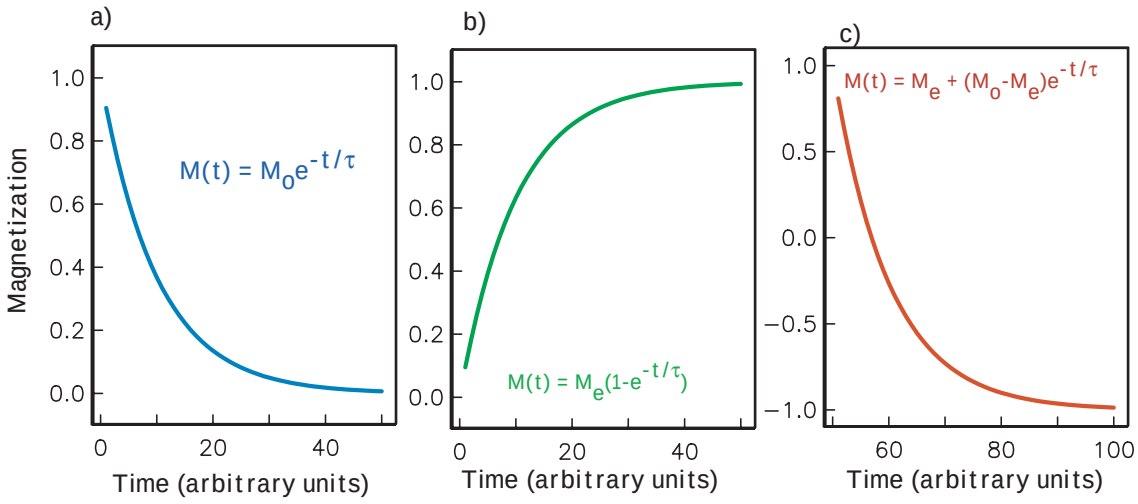

Figure 5.2: Magnetization versus time for a) Saturation remanence placed in zero field. b) Zero initial magnetization placed in a field. c) Magnetization placed in an antiparallel field.

direction. If we had a collection of such particles, the magnetization would tend to grow to some non-zero equilibrium magnetization. Therefore, if a specimen with zero initial remanence is put into a magnetic field, the magnetization $M(t)$ will grow to M_e by the complement of the decay equation:

$$M(t) = M_e(1 - e^{-t/\tau}) \tag{5.5}$$

as shown in Figure 5.2b. The magnetization that is acquired in this isochemical, isothermal fashion is termed *viscous remanent magnetization* or VRM. With time, more and more grains will have sufficient thermal energy to overcome anisotropy energy barriers and flip their magnetizations to an angle more in alignment with the external field.

The general case, in which the initial magnetization of a specimen is nonzero and the equilibrium magnetization is of arbitrary orientation to the initial remanence, the equation can be written as:

$$\mathbf{M}(t) = M_o + (\mathbf{M}_e - \mathbf{M}_o)(1 - e^{-t/\tau}) = \mathbf{M}_e + (\mathbf{M}_o - \mathbf{M}_e) \cdot e^{-t/\tau} \tag{5.6}$$

which grows (or decays) exponentially from $\mathbf{M}_o \rightarrow \mathbf{M}_e$ as $t \rightarrow \infty$ and the rate is not only controlled by τ, but also by the degree to which the magnetization is out of equilibrium (see Figure 5.2c).

Some short data sets appear to follow the relation $M(t) \propto \log(t)$. Many textbooks in fact suggest that VRM = S log t (see, e.g. Butler, 1992). Such a relationship suggests infinite remanence as $t \rightarrow \infty$, so cannot be true over a long period of time. S log t behavior can generally only be observed over a restricted time interval and closely spaced, long-term observations do not show a strict $\log(t)$-behavior.

VRM will therefore change as a function of time, and the relationship between the remanence vector and the applied field. Because relaxation time is also a strong function of temperature, VRM will grow more rapidly at higher temperature. When the relaxation time is short (say a few hundred seconds), the magnetization is essentially in equilibrium with the applied magnetic field. We have referred to these grains as being super-paramagnetic in earlier lectures.

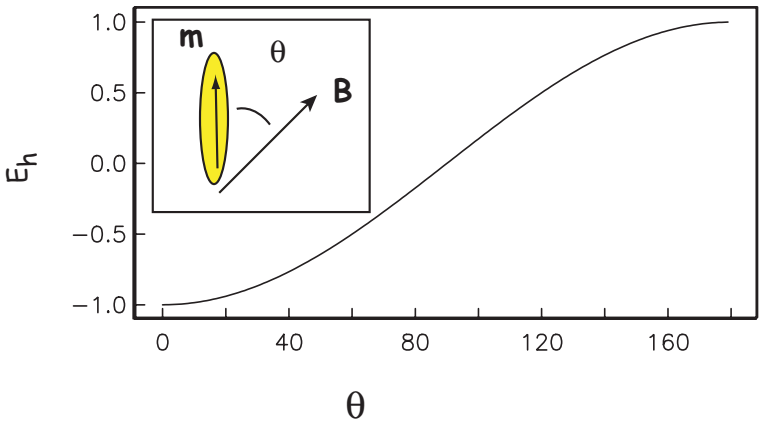

Figure 5.3: Variation of E_h as a function of the angle θ between magnetic moment **m** and applied field **B**.

5.5 Thermal Remanent Magnetization

From the Equation 5.3 we know that τ is a strong function of temperature. As described by Néel (1955), there is a very sharply defined range of temperatures over which τ increases from geologically short to geologically long time scales.

To calculate how relaxation time varies with temperature, we need to know how saturation magnetization varies with temperature. We found in Lecture 4 that to calculate this exactly is a rather messy process. However, the variation of saturation magnetization as a function of temperature can be reasonably well approximated by:

$$\frac{M_s(T)}{M_s(T_o)} = (\frac{T_c - T}{T_c})^\gamma$$

where T_c is the Curie Temperature and γ is about 0.43 for magnetite (see Dunlop and Özdemir [1997] for more details). Taking reasonable values for magnetite we can calculate the variation of relaxation time as a function of temperature for a cubic grain of width = 25 nm as shown in Figure 5.4. At room temperature, such a particle has a relaxation time of longer than the age of the Earth, while at a few hundred degrees, the grain is essentially superparamagnetic.

The temperature at which τ is equal to about $10^2 - 10^3$ seconds is defined as the *blocking temperature* T_b. At or above the blocking temperature, but below the Curie Temperature, a grain will be superparamagnetic. Further cooling increases the relaxation time such that the magnetization is effectively blocked and the rock acquires a *thermal remanent magnetization* or TRM.

Consider a lava flow which has just been extruded (see Figure 5.5). First, the molten lava solidifies into rock. While the rock is above the Curie Temperature, there is no remanent magnetization; thermal energy dominates the system. As the rock cools through the Curie Temperature of its magnetic phase, exchange energy becomes more important and the rock acquires a remanence. The magnetization, however, is free to track the prevailing magnetic field because anisotropy energy is still less important than the magnetostatic energy. The magnetic grains are superparamagnetic and the magnetization is in equilibrium with the ambient magnetic field.

The magnetic moments in the lava flow tend to flop from one easy direction to another, with a slight statistical bias toward the direction with the minimum angle to the applied field (Figure 5.5c).

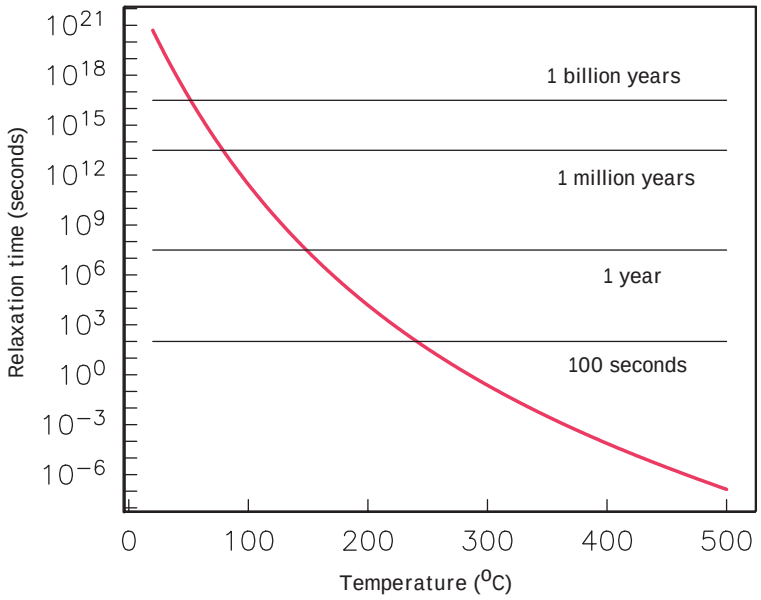

Figure 5.4: Variation of relaxation time versus temperature for a 25 nm width cube of magnetite.

Thus, the equilibrium magnetization of superparamagnetic grains is not fully aligned, but only slightly aligned, and the degree of alignment is a linear function of the applied field for low fields like the Earth's. The magnetization approaches saturation at higher fields (from ~ 0.2 T to several tesla, depending on the details of the source of anisotropy energy).

Recalling the energy difference between the two easy axes of a magnetic particle in the presence of a magnetic field (Equation 5.4), we can estimate the fraction of saturation for an equilibrium magnetization at a given temperature. Applying the Boltzmann distribution law to the theory of thermal remanence, we take ΔE from Equation 5.4 to be $2mB\cos\theta$, and the two states to be the two directions along the easy axis, one maximally parallel to and the other antiparallel to the applied field. The total number of particles N equals the sum of those aligned maximally parallel n_+ and those aligned maximally antiparallel n_-. So from the Boltzmann distribution we have

$$\frac{n_+}{n_-} = e^{2mB\cos\theta/kT}.$$

The magnetization of such a population, with the moments fully aligned is at saturation, or M_s. The magnetization at a given temperature $\mathbf{M}(T)$ would be the net moment or $n_+ - n_-$. So it follows that:

$$\frac{M(T)}{M_s} = \frac{n_+ - n_-}{n_+ + n_-},$$

With a little work this can be twisted into

$$\frac{1 - \exp\left[-2mB\cos\theta/kT\right]}{1 + \exp\left[-2mB\cos\theta/kT\right]}$$

which in turn can be boiled down to:

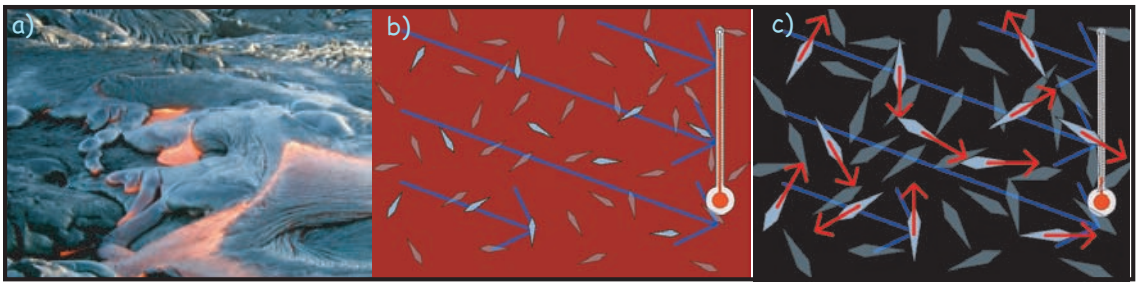

Figure 5.5: a) Picture of lava flow courtesy of Daniel Staudigel. b) While the lava is still well above the Curie temperature, crystals start to form, but are non-magnetic. c) Below the Curie temperature but above the blocking temperature, certain minerals become magnetic, but their moments continually flip among the easy axes with a statistical preference for the applied magnetic field. As the lava cools down, the moments become fixed, preserving a thermal remanence. [b) and c) modified from animation of Genevieve Tauxe available at: http://magician.ucsd.edu/Lab_tour/movs/TRM.mov.

$$\frac{M(T)}{M_s} = \tanh \frac{[mB\cos\theta]}{[kT]}$$

Now imagine that the process of cooling in the lava continues. The thermal energy will continue to decrease until the magnetic anisotropy energy becomes important enough to "freeze in" the magnetic moment wherever it happens to be. Thus, as the particles cool through their "blocking" temperatures, the moments become fixed with respect to further changes in field and to get the final magnetization for randomly oriented grains, we integrate over θ or:

$$\frac{M_{TRM}}{M_s} = \int_0^{90} \tanh \frac{[m_o B\cos\theta]}{[kT]} \cos\theta \sin\theta d\theta \tag{5.7}$$

where m_o is the grain moment at the blocking temperature. We show the behavior of TRM as a function of applied field for population of particles of width 70 nm whose blocking temperature is a 700 K in Figure 5.6. For values of B as small as the earth's ($\sim$ 20-60 μT), TRM is approximately linear with applied field.

Some things you should know about TRM

• The remanence of an assemblage of randomly oriented particles acquired by cooling through the blocking temperature in the presence of a field should be parallel to the orientation of that field.

• The intensity of thermal remanence should be linearly related to the intensity of the magnetic field applied during cooling (for Earth's field).

• In a rock, each grain has its own blocking temperature and moment. Therefore, by cooling a rock between two temperatures, only a portion of the grains will be blocked; the rock thus acquires a *partial thermal remanent magnetization* or pTRM.

• Three essential assumptions in certain paleomagnetic applications are 1) that each pTRM is independent of all others, 2) that a pTRM acquired by cooling through two temperatures can be removed by exposure to the same peak temperature and cooling in zero field, and 3) that pTRMs

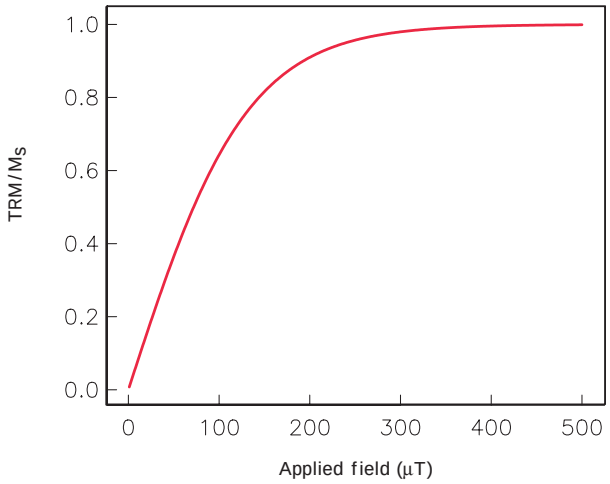

Figure 5.6: Relationship of TRM with respect to the applied field. The present Earth's field ranges in magnitude from $\sim$ 25 μT to $\sim$ 60 μT (see Lecture 2).

are additive; i.e. that the sum of individual pTRMs acquired between successive temperature steps is the same as that acquired when cooling over the entire interval.

Experimental results have tended to substantiate the theory outlined above for particles that are uniformly magnetized or nearly so. The behavior of grains that are vortex state or multi-domain appears to complicate the picture. Certain modifications have been made to accomodate the changing understanding of magnetic domains. The key difference between TRM in SD or flower state (F) populations and those with vortices (V) or domain walls (MD) is that the temperature at which a pTRM is frozen (the blocking Temperature T_b) is lower than the temperature for which the same pTRM is freed (the unblocking temperature T_{ub}) in V and MD grains but they are the same for SD and F grains. For further details on multi-domain TRM see e.g., Dunlop and Özdemir (1997).

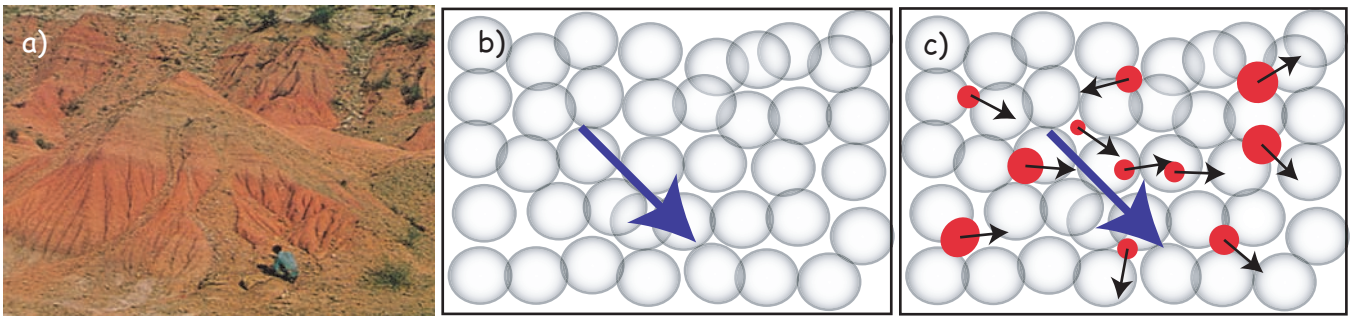

Figure 5.7: Grain growth CRM. a) Red beds of the Chinji Formation, Siwaliks, Pakistan. The red soil horizons have a CRM carried by pigmentary hematite. b) Initial state of non-magnetic matrix. c) Formation of superparamagnetic minerals with a statistical alignment with the ambient magnetic field (shown in blue).

5.6 Chemical Remanent Magnetization

As we will learn in more detail in the next lecture, magnetic mineralogy often changes after a rock is formed in response to changing environments. Red beds (see Figure 5.7a), a dominant sedimentary facies in earlier times, are red because of pigmentary hematite which grew at some point after deposition. Hematite is a magnetic phase and the magnetic remanence it carries when grown at low temperatures is a grain growth chemical remanent magnetization (g-CRM).

Magnetite is an example of a magnetic phase which is generally out of equilibrium in many enviroments on the Earth's surface. It tends to oxidize to another magnetic phase (maghemite) during weathering. As it changes state, the iron oxide may change its magnetic moment, acquiring an "alteration" chemical remanence (a-CRM).

The relationship of the new born CRM to the ambient magnetic field can be complicated. It may be largely controlled by the prior magnetic phase from whence it came, it may be strongly influenced by the external magnetic field, or it may be some combination of these factors. We will begin with the simplest form of CRM - the g-CRM.

Inspection of the Equation 5.3 for relaxation time reveals that it is a strong function of grain volume. A similar theoretical framework can be built for remanence acquired by grains growing in a magnetic field as for those cooling in a magnetic field. As a starting point for our treatment, consider a non-magnetic porous matrix, say a sandstone. As ground water percolates through the sandstone, it begins to precipitate tiny grains of a magnetic mineral (Figure 5.7c). Each crystal is completely isolated from its neighbors. For very small grains, the thermal energy dominates the system and they are superparamagnetic. When volume becomes sufficient for magnetic anisotropy energy to overcome the thermal energy, the grain moment is blocked and can remain out of equilibrium with the magnetic field for geologically significant time periods. Keeping temperature constant, there is a critical *blocking volume* below which a grain maintains equilibrium with the applied field and above which it does not. Thus the magnetization acquired during grain growth is controlled by the alignment of grain moments at the time that they growth through the blocking volume. Based on these principles, CRM should behave very similarly to TRM.

There have been a few experiments carried out with an eye to testing the grain growth CRM model and although the theory predicts the zeroth order results quite well (that a simple CRM parallels the field and is proportional to it in intensity), the details are not well explained, primarily because the magnetic field affects the growth of magnetic crystals and the results are not exactly analogous to TRM conditions (see e.g. Stokking and Tauxe, 1990a,b and Dunlop and Özdemir, 1997). Moreover, gCRMs acquired in changing fields can be much more complicated than a simple single generation, single field CRM.

Alteration CRM can also be much more complicated than simple g-CRM in a single field. Suffice it to say that the reliability of CRM for recording the external field must be verified (as with any magnetic remenance) with geological field tests and other tricks as described in future lectures.

5.7 Detrital Remanent Magnetization

In sedimentary environments, rocks become magnetized in quite a different manner than igneous bodies. Detrital grains are already magnetized, unlike igneous rocks which crystallize above their Curie Temperatures. Magnetic detrital particles can become aligned with the magnetic field while settling in the water column and when deposited retain a detrital remanent magnetization (DRM).

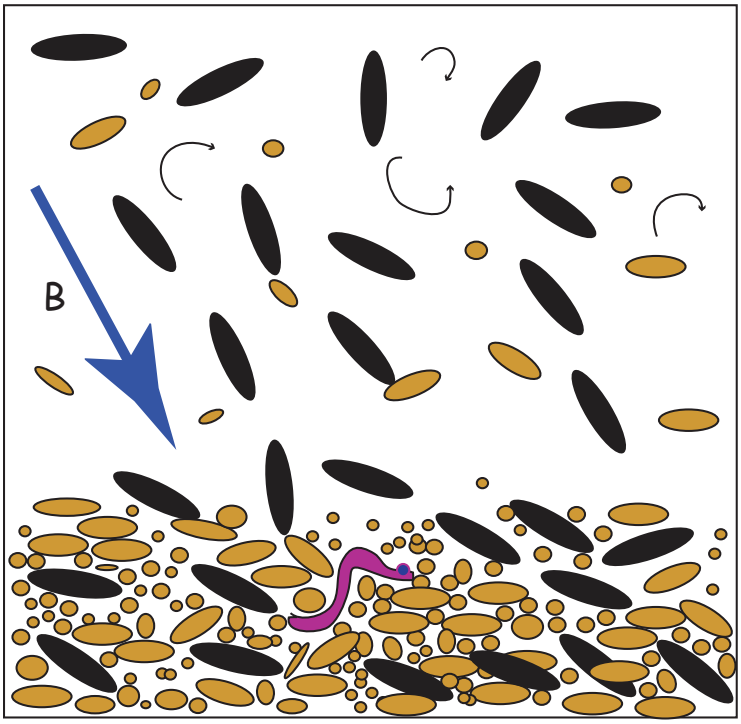

Figure 5.8: Schematic drawing of raditional view of the journey of magnetic particles from the water column to burial. Magnetic particles are black. (Redrawn from Tauxe, 1993.)

But particles may become re-aligned after depostion in a process called post-depositional remanent magnetization (pDRM) by the action of bioturbation, or other disturbances (see Figure 5.8).

The theoretical treatment of the behavior of magnetic particles in a viscous medium has been considered for decades (eg., Nagata, 1961). When placed in a viscous fluid, a magnetized particle is subjected to a hydrodynamic couple generated by fluid shear, a magnetic couple tending to align the magnetic moment with the ambient magnetic field, viscous drag and inertial forces tending to oppose motion and thermally inspired "Brownian" motions (e.g., Collinson, 1965).

Nagata (1961) considered theoretically the motion of magnetic particles in water. He started with the equation of motion for a magnetic particle with magnetic moment m suspended in water with moment of inertia I, with angle α with respect to the applied magnetic field B:

$$I\frac{d^2\alpha}{dt^2} = -\lambda\frac{d\alpha}{dt} - mB\sin\alpha, \tag{5.8}$$

where λ is the viscosity coefficient opposing the motion of the particle through the fluid. By neglecting the inertial term (which varies as r^5), Nagata (1961) solved Equation 1 as:

$$\tan\frac{\alpha}{2} = \tan\frac{\alpha_o}{2}e^{(-mBt/\lambda)} \tag{5.9}$$

where α_o is the initial angle between $\mathbf{m}$ and $\mathbf{B}$. Setting $\lambda = 8\pi r^3\eta$ where r is the particle radius and η is the viscosity of water ($\sim 10^{-3}$ kg m^{-1}s^{-1}) the time constant of Equation 5.9 over which an inital α_o is reduced to $1/e$ of its value is therefore:

$$\tau_d = \frac{\lambda}{mB} = \frac{6\eta}{MB} \tag{5.10}$$

where M is the volume normalized magnetization (see Lecture 1).

The fundamental problem that has plagued DRM theory for over four decades is that this time constant, for almost all reasonable values of m and B, is extremely short. Taking the value of magnetization for single domain magnetite of $M =\sim 4.8$ x 10^5 A/m and a particle with $r=$ 20 nm, we have m of $\sim$2 x 10^{-17} Am^2 (or 0.02 fAm^2). Placing this particle in a field of 30 μT, gives a value of τ_d of 40 μs. Even the magnetization for hematite ($M \sim$ 2000 A/m) results in a τ_d of a much less than a second at this field strength. So simple DRM theory predicts that sediments composed of isolated magnetic particles would have a saturation magnetization, insensitive to changing field strengths.

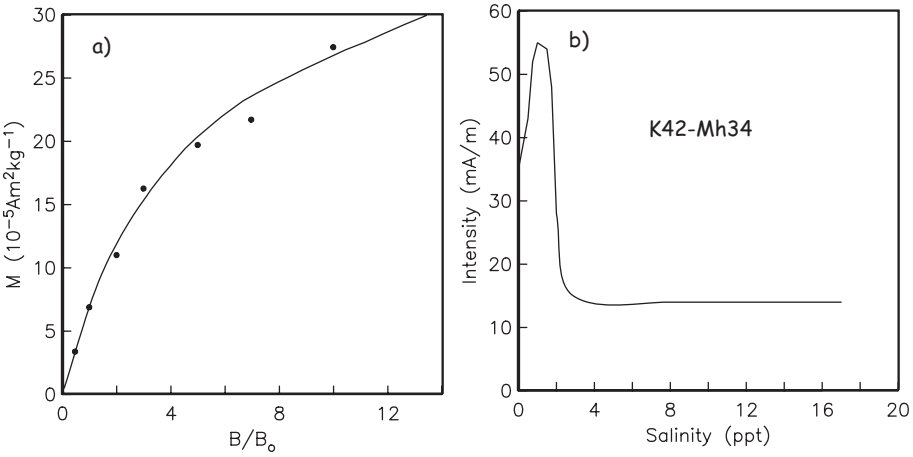

Figure 5.9: a) Depositional remanence verus applied field for redeposited glacial varves. B_o was the field in the lab. Data from Johnson et al. (1948). b) Relationship of DRM intensity and salinity for synthetic sediment composed of a mixture of kaolinte and maghemite. (Data of Van Vreumingen 1993.)

Simple theory notwithstanding, the first measurements of sedimentary paleointensity (Johnson et al., 1948) showed that DRM was not necessarily at saturation (see Figure 5.9a). The experimentally determined remanent magnetization was more or less linearly related to the field, for field strengths in the range of the Earth's and was orders of magnitude less than the saturation remanence.

Much subsequent thought about DRM theory has attempted to reconcile the simple prediction of saturation with the observational fact of a strong and nearly linear field dependence (for low fields) of DRM. There are two basic ways to accomplish this from a theoretical point of view:

- One can call on Brownian motion (e.g, Collinson, 1965) which would act to randomize magnetic moments through thermal agitation.
- Or one can hypothesize a lower value of M which would increase the time constant of alignment. For example, one can call on electrostatic and London-van-der-Waals forces which would lead to particles sticking together (flocculation) making larger particles with a lower net moment (e.g., Shcherbakov and Shcherbakova, 1983).

To estimate the size of particles effected by Brownian motion, Collinson (1965) balanced magnetic energy against thermal energy:

$$mB\alpha_o^2 = kT$$

where α_o is the Brownian deflection about the applied field direction, k is Boltzmann's constant (1.38 x 10^{23}J/°K) and T is the temperature in kelvin. Very small particles are superparamagnetic (SP) as opposed to single domain (SD) and do not contribute to the remanent magnetization, hence the lower grain size bound for Brownian motion is the SP/SD size threshold. To estimate the upper bound we need to know how remanent magnetization varies with grain size as well. It is now understood that the remanent states of magnetic particles like magnetite become increasingly complex as the multi-domain threshold is approached (see e.g., Schabes and Bertram, 1988).

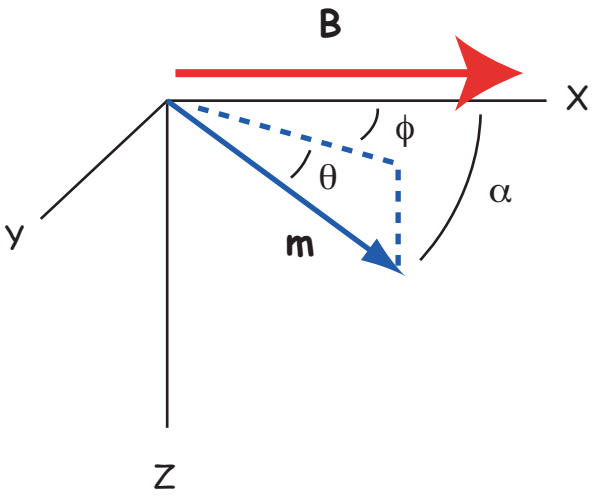

Figure 5.10: Coordinate system for magnetic particle in magnetic field.

So, for a "quick look" at the role of Brownian motion, we can take the end-member cases of a particle above the SP threshold, but still reasonably uniformly magnetized particle with radius r=20 nm and M of the M_s of magnetite. In this case, $m \sim 0.01$ fAm^2. At room temperature ($\sim$ 300 K) we have α_o >180° which would imply that the net moment of these particles would be completely dominated by thermal agitation. For a conservative upper bound of the effect of Brownian motion, we take a particle of radius $r = 0.2$ μm and assume a remanence of $\sim 0.1M_s$ or about 5 x 10^4 A/m based on numerical simulations. In this case $\alpha_o < 20°$. These approximate calculations suggest that particles of magnetite larger than a few tenths of a micron will not be effected by Brownian motion. Hence particles in the size range between the SP threshold and $\sim$ 0.1-0.2 μm may be dominated by Brownian motion *if they are isolated in a suspension of water, unattached to any other particles.* [Collinson (1965) arrived at a somewhat larger upper limit for Brownian motion using the experimental data available at the time and concluded that the linear dependence of DRM was probably controlled by Brownian motion.]

Several papers in the early 90's highlighted the role of water chemistry in controlling depositional remanence. Of particular interest here is the work of Van Vreumingen (1993), who investigated the effect of flocculation on the acquisition of depositional remanence.

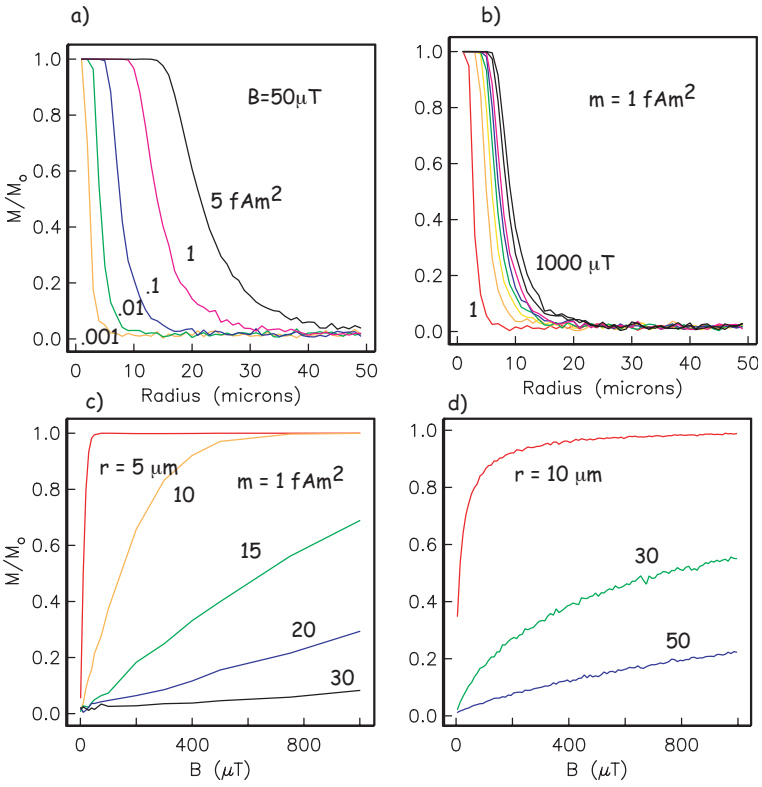

Figure 5.11: Results of numerical experiments of the flocculation model using the parameters: $l = 0.2$ m and the viscosity of water. M/M_o is the DRM expressed as a fraction of saturation. a) Holding B constant and varying $\bar{m}$ from 1 x 10^{-18} Am^2 to 5 x 10^{-15} Am^2 (fAm^2). Particles are essetially saturated up to 20 μm under these conditions. b) Holding $\bar{m}$ constant and varying B. For a given field strength, particles are either at saturation or randomly oriented, except for within a very narrow size range. c) Holding $\bar{m}$ constant and varying the applied field for a range of r. d) Same as c) but for distributions of r with the averages shown.

In Figure 5.9b we re-plot data from one of the van Vreumingen experiments. The data were obtained by depositing a synthetic mixture of kaolinite and maghemite under various conditions of salinity. There is an intriguing increase in intensity with small amounts of NaCl followed by a dramatic decrease with a plateau reached for salinities greater than about 4‰. Both the increase and the decrease can be explained in terms of flocculation, which is encouraged by increasing salinity. The initial increase could be due to maghemite particles adhering to the kaolinite hence reducing the effect of Brownian motion and the subsequent decrease could be caused by having larger flocs with decreased net moments, hence lowering the time constant of alignment.

Katari and Bloxham (2001) pursued the role of flocculation in the problem of DRM theory. They suggested that particles of magnetite are unlikely to be in isolation in many natural environments where small particles tend to flocculate or become incorporated into pellets held together by organic "glue". Drawing on the literature concerning the effect of aqueous chemistry on DRM in the laboratory which had demonstrated the profound effect of flocculation on DRM (see e.g., Figure 5.9b), they suggested that the appropriate value of m in Equation 5.9 was the net moment of the floc, far less than the moment of an isolated particle.

Katari and Bloxham (2001) use the empirical settling velocity v (in units of meters per second) as a function of floc radius (in units of meters) given by Gibbs (1985):

$$v = 1.1r^{0.78}$$

and then substitute $t = l/v$, where l is the settling distance, into a modified form of Equation 5.9. Here, we will just use the basic Nagata equation with the Gibbs settling velocity:

$$\tan(\alpha/2) \simeq \tan(\alpha_o)\exp(-mBl/8.8\pi\eta r^{3.78}) \tag{5.11}$$

Solving for α and then constraining the particle to follow the straightest path from the original coordinates (x, y, z) toward **B** (see Figure 5.10), one can calculate the new coordinates (x', y', z') of m by:

$$x' = \cos\alpha, y' = \sqrt{\frac{1-x'^2}{1+\frac{z^2}{y^2}}}, z' = y'\frac{z}{y}$$

From x', y', z' one can then calculate the new angles θ and ϕ as defined in Figure 5.10

Given a specified distribution of floc radii, one can evaluate the contribution of each size fraction separately and sum over all size fractions. The flocculation model assumes an initially random orientation of N individual flocs of θ_{oi}, ϕ_{oi} in a given size fraction $f(r)$ where $f(r)$ is the fractional contribution of a particular radius bin to the whole. Each floc is assigned the average moment $\bar{m}$. After settling through length l, the average magnetization for each size fraction will be:

$$M_x(r) = \bar{m}\sum_{i=1}^{N}\cos\theta_i\cos\phi_i f(r),$$

$$M_y(r) = \bar{m}\sum_{i=1}^{N}\cos\theta_i\sin\phi_i f(r),$$

$$M_z(r) = \bar{m}\sum_{i=1}^{N}\sin\theta_i f(r).$$

The contribution of each size fraction is normalized by $f(r)$. Hence, the total magnetization is the sum of each term

$$\bar{M}_x = \sum_r M_x(r), \bar{M}_y = \sum_r M_y(r), \bar{M}_z = \sum_r M_z(r).$$

The flocculation model can be used to predict DRM intensity behavior, given that settling length l, average magnetization $\bar{m}$, and the floc size distribution $f(r)$ are known. Following Katari and Bloxham (2001), we use the viscosity of water, a field of 50 μT, a settling length of 0.2 m and consider the effect of r and m. For the purposes of this numerical experiment, we sum the effect of 5550 particles with initial orientations that are uniformly distributed on a unit sphere.

The results of our numerical simulations are shown in Figure 5.11a whereby the DRM intensity M is shown as the fraction of saturation M_o as a function of radius and magnetic moment ranging from 5 fAm^2 to 0.001 fAm^2. For particles as strong as 5 fAm^2 (the nominal value chosen by Katari and Bloxham (2001) for their model), size fractions with radii up to some 15 μm are completely saturated. The critical radius r_{crit} below which magnetic grains achieve complete alignment decreases

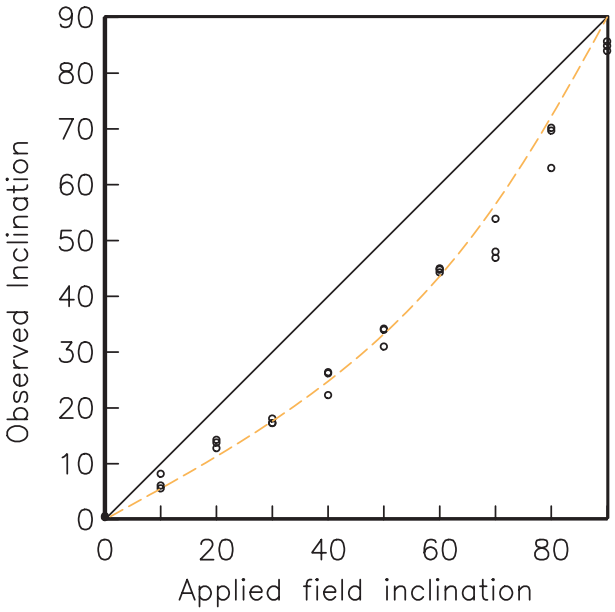

Figure 5.12: Applied field inclination versus remanent inclination for redeposited river sediments. [Data from Tauxe and Kent (1984).]

with decreasing m. At some point, Brownian motion will begin to have a randomizing effect on the net moment, so each of the curves shown in Figure 5.11a would have a drop off from saturation as the radius decreases to sub-micron sizes.

The effect of varying the applied field, while holding m constant at 1 fAm^2 is shown in Figure 5.11b. Increasing B increases the particle size over which saturation is achieved for a given value of m. Hence, field dependence of DRM is largely controlled by the fraction of the particles that are completely aligned with the field, which varies with B. This effect, when combined with the effect of Brownian motion may lead to a loss of fidelity of remanence at low fields.

Field dependence of DRM is also critically dependent on r as shown in Figure 5.11c. Here we chose a constant m and show DRM as a function of the applied field for various size fractions. Particles as small as 5 μm achieve complete alignment at very low fields. Particles of one micron (not shown) are insensitive to field intensity because they are completely aligned at field intensities like the Earth's.

In order to model sedimentary redeposition data, Katari and Bloxham (2001) used distributions of floc sizes, as is more likely in nature. We illustrate a few examples of DRM as a function of applied field for several different distributions in Figure 5.11d.

It is clear from the foregoing that the DRM model is capable of making specific and testable predictions which could be compared with carefully controlled laboratory redeposition data. The model or some close cousin can explain the general features of DRM including field dependency, but also might explain some of the sources of scatter observed in "real" paleointensity records. For example, in the cases where flocculation does NOT occur (perhaps in some lakes), DRM might not be expected to have a meaningful field dependence. This is because particles of magnetite larger than a few microns are magnetically unstable and the particles smaller than this are at saturation in a depositional setting. The contribution of Brownian motion which could dominate

the magnetization of smaller particles might compensate somewhat for this, but they would have to be volumetrically more important that the larger, saturated size fractions. Moreover, under low salinity conditions (most lakes), any change in salinity results in a large change in floc size, hence large changes in DRM.

There is also a profound dependence of DRM intensity on floc size which may vary as sediment flux and/or water chemistry changes. On the bright side, however, if the DRM model or some modified version can be verified, there is in fact the chance for finding absolute paleointensity under certain conditions.

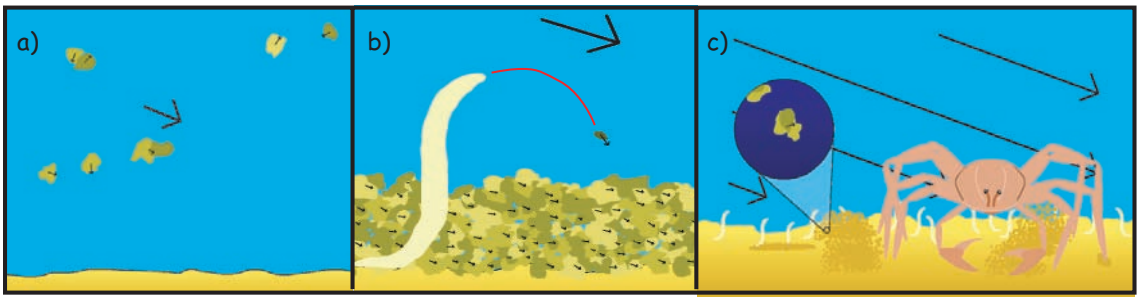

Figure 5.13: Model of Katari et al. (2000) for acquisition of DRM. a) Sedimentary particles flocculate in the water column resulting in large ($\sim$ 100 nm) particles with a lower net moment than a single homogeneous magnetic particle. b) The sediment can be ingested by organisms and excreted into the water column allowing fecal pellets to realign. c) Bioturbation by creatures crawling over the sediment water interface can resuspend particles, allowing them to realign. Below a critical depth, usually a few centimeters down, sediments are unlikely to be resuspended and join the "historical layer". Drawings modified from Genevieve Tauxe (http://magician.ucsd.edu/Lab_tour/labtour.html).

5.7.1 Inclination Error

Some sedimentary remanences show a remanence vector that is generally shallower than the applied field, a phenomenon known as *inclination error*. We show the results of a typical laboratory redeposition experiment in Figure 5.12. The tangent of the observed inclination is usually some fraction ($\sim$ 0.4-0.6) of the tangent of the applied field. Thus, inclination error is at a maximum at 45°and is negligible at high and low inclinations. Interestingly, many natural sediments (e.g. deep sea or slowly deposited lake sediments) display no inclination error. The worst cultprits appear to be sediments whose NRM is carried by detrital hematite, a flakey particle with a small saturation remanence.

It should also be noted that when squeezed in the laboratory to simulate compaction due to burial, the DRM becomes shallower and compaction related shallowing has been inferred in deep sea cores from $>$ 100 m depth (e.g., Anson and Kodama, 1987).

5.7.2 Post-depositional remanence

The general consensus of the paleomagnetic community is that DRM is reset below the sediment/water interface during bioturbation. It is my view that magnetic moments can only (re)align with the ambient magnetic field when they are either free or attached to flocs or pellets that are

sufficiently small to allow physical realignment. This basically means that the particles must be resuspended. Hence, physical reorientation can only take place in the uppermost sedimentary layer, in a zone that is frequently resuspended.

There are many articles in the literature suggesting that DRM is either heavily smoothed or is locked in at some depth. A close reading of the smoothing literature finds little in the way of experimental evidence for smoothing beyond a few centimeters and the deep lock-in literature is also severely flawed (see, e.g., Tauxe et al. 1996 and Katari et al., 2001). Considering for a moment the DRM model of Katari et al. (2000; see Figure 5.13 and 5.14). Remanence is acquired in the surface layer through initial settling of through resuspension by bioturbation, bottom currents, etc. The probibility of resuspension ranges from very low ($\sim$0%) in certain sedimentary sequences to very high (>99%) in others. In the latter case, there will be an increasing difference between the age of the sediments as measured by radiocarbon or stable isotopic tracers and the age of the magnetization itself, the magnetization being always acquired close to the sediment water interface, while the stable isotopic signature is fixed whenever the carbonate in the sediment formed. This difference has often been interpreted as a deep lock-in depth, while it is actually evidence of the opposite.

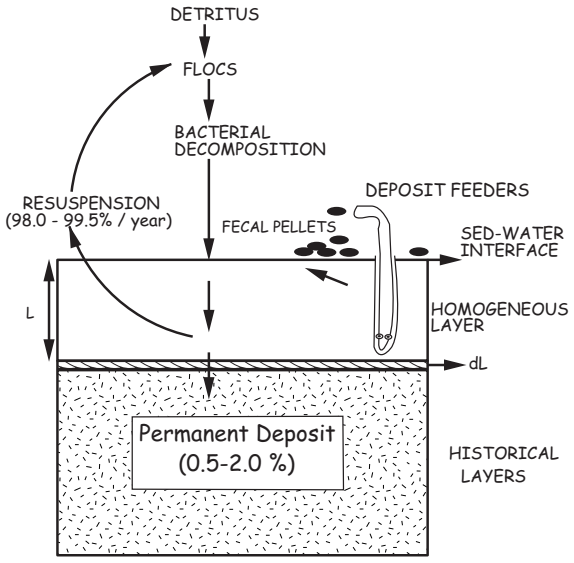

Figure 5.14: A simple model of detrital deep-sea sedimentation. Detrital particles are deposited at the sediment water interface, and then incorporated into the homogeneous layer of thickness L. The rate of deposition determines the rate at which a thin basal slice of the homogeneous layer of thickness dL gets incorporated into the historical layer. Magnetic particles in flocs or fecal matter will be reoriented in the homogeneous layer many times before they enter the permanent deposit. Once in the historical layer, no more realignment to changing magnetic field is possible. [Redrawn from Katari et al., 2000].

Summary of things you should know about DRM

• There has been much bru-ha-ha in the literature about the smoothing effect of bioturbation. In fact there is very little actual evidence in favor of extensive sedimentary smoothing.

• Be aware of the tendency to get shallow directions from several mechanisms: original sin (inclination error, *sensu strictu*) and compaction related effects.

• Post-depositional deformation can be difficult to see but can have a large effect on magnetic remanence. Hence, not all "excursions" are geomagnetic in origin.

• Be wary of sedimentary records that have not been thoughtfully sampled and analyzed.

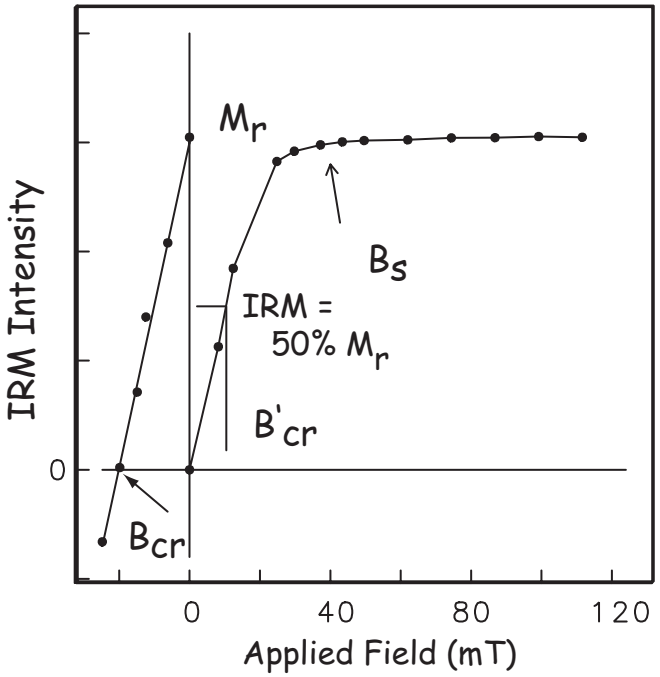

Figure 5.15: Acquisition of IRM by exposure to large magnetic fields. After saturation, the remanence remaining is M_r. One can then turn the sample around and applied smaller fields in the opposite direction to determine the field necessary to reduce the net remanence to zero. Two methods of estimating B_{cr} are shown.

5.8 Isothermal Remanent Magnetization

Examination of the Néel equation reveals an interesting dependence of relation time on the coercivity (see Lecture 4) of magnetic particles. We can therefore coax otherwise firmly entrenched particles to follow an applied field, if that field is larger than the coercivity. Exposing a particle to a large magnetic field, then, will allow magnetic particles whose coercivity is below that field to flip their magnetic moments to a direction at a more favorable angle to the applied field, resulting in a gain in magnetic remanence in that direction. This type of magnetic remanence is called an *isothermal remanent magnetization* or IRM.

In Figure 5.15 we illustrate the behavior of an initially demagnetized specimen as it is subjected to increasing impulse fields. The maximum IRM achieved is known as sIRM (saturation IRM) or M_r (and sometimes M_{rs}). After saturation, the specimen can be turned around and subjected to

increasingly large "back-fields". The field sufficient to remagnetize half of the moments (resulting in a net remanence of zero) is the "coercivity of remanence" (B_{cr} or H_{cr} depending on the magnetic units). Behavior of the laboratory IRM can be very useful in characterizing the magnetic mineralogy as we will learn in later lectures. IRM can also be acquired in nature by exposure to the high fields generated during lightning strikes. Such a remanence often results in scattered directions that are less stable but very much more intense than the original NRM.

There are many ways to estimate B_{cr}. The most common method is the *back-field method* illustrated in Figure 5.15. The sample is subjected to increasing instantaneous magnetic fields and measured until saturation is achieved. The sample is then turned around and subjected to a "back field" in small increments until the sIRM has been reduced to zero. The field at which the remanence is reduced to zero is B_{cr}. A second method would be to use the field required to impart an IRM that is half the intensity of the saturation remanence (B'_{cr}). Others will be introduced in later lectures.

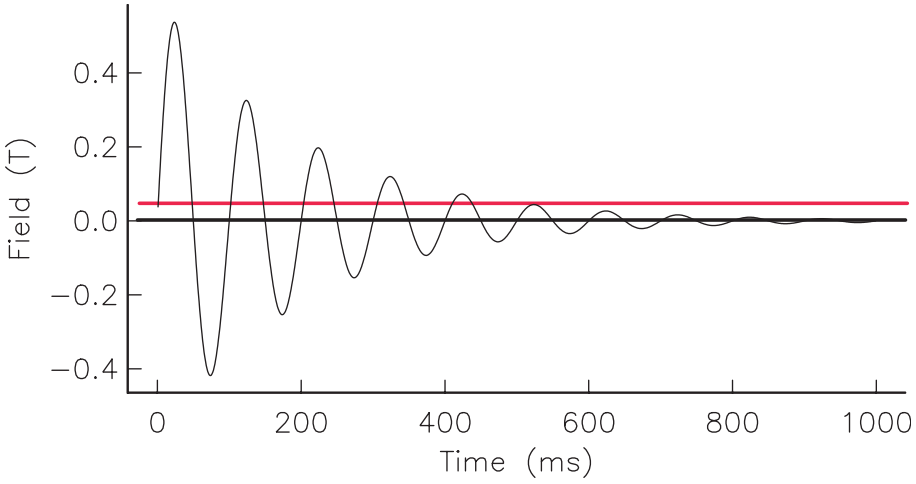

Figure 5.16: Acquisition of ARM in alternating magnetic field.

5.9 Natural Remanent Magnetization

A rock collected from a geological formation has a magnetic remanence which may have been acquired by a variety of mechanisms some of which we have described. The remanence of this rock is called *natural remanent magnetization* or NRM in order to avoid a genetic connotation in the absence of other compelling evidence. The NRM is often a combination of several components, each with its own history. The NRM must be picked apart and the various components carefully analyzed before origin can be ascribed. The procedures for doing this are described in later lectures.

5.10 Anhysteretic Remanent Magnetization

Another way to magnetize rocks (although not in nature) is to subject a sample to an alternating field (see Figure 5.16). Particles whose coercivity is lower than the peak oscillating field will flip and flop along with the field. These entrained moments will become stuck as the peak field gradually

decays below the coercivities of individual grains. Assuming that there is a range of coercivities in the sample, the low stability grains will be stuck half along one direction of the AF and half along the other direction; the net contribution to the remanence will be zero. This is the principle of so-called "alternating field demagnetization" which we will discuss in later lectures.

If there is a small DC bias field superposed on the alternating field, then there will be a statistical preference in the remagnetized grains for the direction of the bias field, analogous to TRM acquired during cooling. This net magnetization is termed the *anhysteretic remanent magnetization* or ARM.

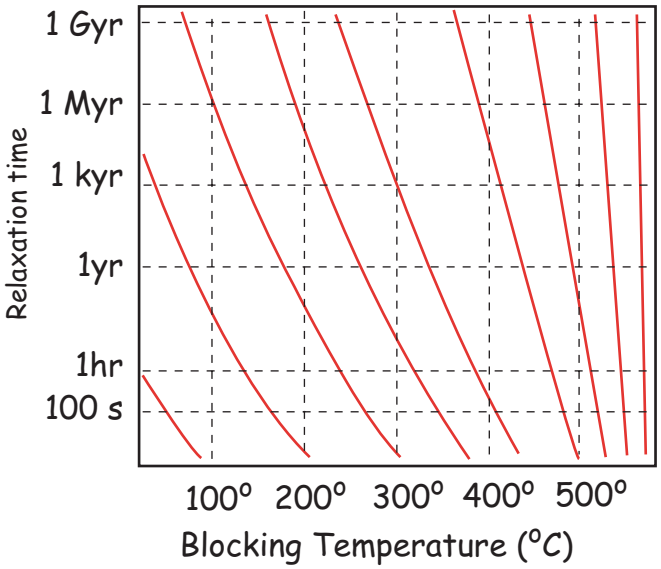

Figure 5.17: Theoretical nomogram relating relaxation time and blocking temperature for magnetite. [Redrawn from Pullaiah et al. 1975.]

5.11 Thermo-viscous Remanent Magnetization

Sometimes rocks are exposed to elevated temperatures for long periods of time (for example during deep burial). The grains with relaxation times (at the elevated temperature) shorter than the exposure time will have acquired a so-called thermo-viscous remanence. We know that

$$\tau = \frac{1}{C} \exp \frac{B_c M_s v}{2kT}$$

If we hold B_c, M_s and v constant, we could calculate the relationship of τ to temperature by:

$$T_1 \ln C\tau_1 = T_2 \ln C\tau_2$$

Of course B_c and M_s are also functions of temperature and we have in reality something more like

$$\frac{T_1 \ln C\tau_1}{M_s(T_1)B_c(T_1)} = \frac{T_2 \ln C\tau_2}{M_s(T_2)B_c(T_2)}$$

Using the theoretical relationships of $M_s(T)$ and $B_c(T)$ then, we obtain the following plots for τ versus T_b

5.11. THERMO-VISCOUS REMANENT MAGNETIZATION

Curves like those shown in Figure 5.17 allow us to predict what the blocking temperature of a viscous magnetization acquired over many years will be under laboratory (relaxation times of hundreds of seconds) would be.

Bibliography

Anson, G. L. & Kodama, K. P. (1987), 'Compaction-induced inclination shallowing of the post-depositional remanent magnetization in a synthetic sediment', *Geophys. J. R. astr. Soc.* **88**, 673–692.

Butler, R. F. (1992), *Paleomagnetism: Magnetic Domains to Geologic Terranes*, Blackwell Scientific Publications.

Collinson, D. W. (1965), 'DRM in sediments', *J. Geophys. Res.* **70**, 4663–4668.

Dunlop, D. & Ozdemir, O. (1997), *Rock Magnetism: Fundamentals and Frontiers*, Cambridge University Press.

Gibbs, R. (1985), 'Estuarine flocs: Their size, settling velocity and density', *J. Geophys. Res.* **90**, 3249–3251.

Johnson, E. A., Murphy, T. & Torreson, O. W. (1948), 'Pre-history of the Earth's magnetic field', *Terr. Magn. atmos. Elect.* **53**, 349–372.

Katari, K. & Bloxham, J. (2001), 'Effects of sediment aggregate size on DRM intensity: a new theory', *Earth Planet. Sci. Lett.* **186**(1), 113–122.

Katari, K., Tauxe, L. & King, J. (2000), 'A reassessment of post depositional remanenent magnetism: preliminary experiments with natural sediments', *Earth Planet. Sci. Lett.* **183**, 147–160.

Nagata, T. (1961), 'Rock Magnetism'.

Néel, L. (1949), 'Théorie du trainage magnétique des ferromagneétiques en grains fines avec applications aux terres cuites', *Ann. Geophys.* **5**, 99–136.

Néel, L. (1955), 'Some Theoretical Aspects of Rock-Magnetism', *Adv. Phys* **4**, 191–243.

Pullaiah, G., Irving, E., Buchan, K. & Dunlop, D. (1975), 'Magnetization Changes Caused by Burial and Uplift', *Earth Planet. Sci. Lett.* **28**, 133–143.

Schabes, M. E. & Bertram, H. N. (1988), 'Magnetization processes in ferromagnetic cubes', *J. Appl. Phys.* **64**, 1347–1357.

Shcherbakov, V. & Shcherbakova, V. (1983), 'On the theory of depositional remanent magnetization in sedimentary rocks', *Geophys. Surv.* **5**, 369–380.

Stokking, L. & Tauxe, L. (1990*a*), 'Multi-component magnetization in synthetic hematite', *Phys. Earth Planet. Inter.* **65**, 109–124.

Stokking, L. & Tauxe, L. B. (1990*b*), 'Properties of chemical remanence in synthetic hematite: testing theoretical predictions', *Jour. Geophys. Res.* **95**, 12639–12652.

Tauxe, L. (1993), 'Sedimentary records of relative paleointensity of the geomagnetic field: theory and practice', *Rev. Geophys.* **31**, 319–354.

Tauxe, L., Herbert, T., Shackleton, N. J. & Kok, Y. S. (1996), 'Astronomical calibration of the Matuyama Brunhes Boundary: consequences for magnetic remanence acquisition in marine carbonates and the Asian loess sequences', *Earth Planet. Sci. Lett.* **140**, 133–146.

Tauxe, L. & Kent, D. V. (1984), 'Properties of a detrital remanence carried by hematite from study of modern river deposits and laboratory redeposition experiments', *Geophys. Jour. Roy. astr. Soc.* **77**, 543–561.

van Vreumingen, M. (1993), 'The influence of salinity and flocculation upon the acquisition of remanent magnetization in some artificial sediments', *Geophys J Int* **114**, 607–614.

Lectures in Paleomagnetism, 2005
by Lisa Tauxe

Citation:
http://earthref.org/MAGIC/books/Tauxe/2005/

May 31, 2005

Chapter 6

Magnetic Mineralogy

Suggested Reading

For background:
Chapter 3 in Evans and Heller (2003)
To learn more:
Chapter 3 in Dunlop and Özdemir (1997)

6.1 Introduction

An essential part of every paleomagnetic study is a discussion of what is carrying the magnetic remanence and how the rocks got magnetized. For this, we need some knowledge of what the important natural magnetic phases are, how to identify them, how they are formed, and what their magnetic behavior is. In this lecture, we will cover a brief description of geologically important magnetic phases. Useful magnetic characteristics of important minerals can be found in Table 6.1.

Because iron is by far the most abundant transition element in the solar system, most paleomagnetic studies depend on the magnetic iron species: the iron-nickels (which are particularly important for extra-terrestrial magnetic studies), the iron-oxides such as magnetite, maghemite and hematite, the iron-oxyhydroxides such as goethite, and the iron-sulfides such as greigite and pyrrhotite. We are concerned here with the latter three since iron-nickel is very rare in terrestrial paleomagnetic studies.

6.2 Iron-oxides

Two solid solution series are particularly important in paleomagnetism: the ulvöspinel-magnetite and ilmenite-hematite series as shown on the ternary diagram in Figure 6.1. The apices of the ternary diagram are Fe^{2+} on the lower left, Fe^{3+} on the lower right and Ti^{4+} on the top. The oxides with these species are FeO (wustite), Fe_2O_3 (hematite or maghemite depending on structure) and TiO (rutile). Every point on the triangle represents a cation mixture or solution that adds up to one cation (hence the fractional formulae). Each of the solid arrows in Figure 6.1 (labelled Titanomagnetite and Hemoilmenite) represent increasing substitution of titanium into the crystal lattices of magnetite and hematite respectively. The amount of Ti substitution in titanomagnetites is denoted by "x", while substitution in the hemoilmenites is denoted by "y". Values for x and y range from 0 (magnetite or hematite) to 1 (ulvöspinel or ilmenite).

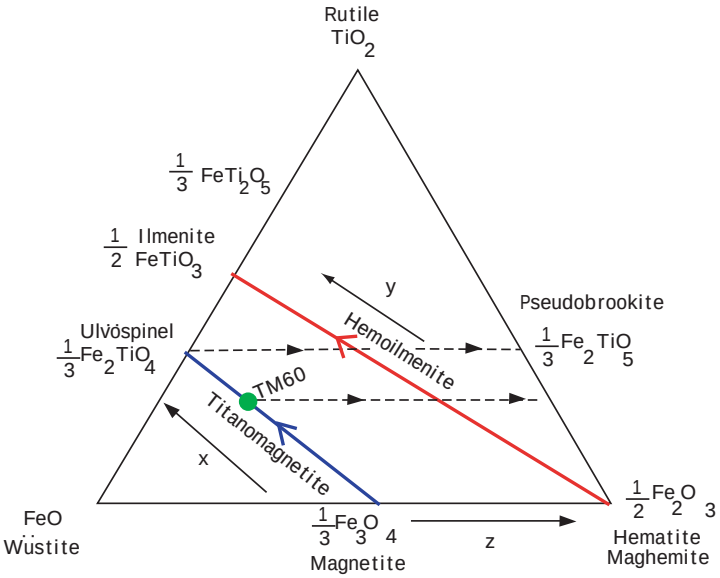

Figure 6.1: Ternary diagram for iron-oxides (modified from O'Reilly [1984]). The dashed lines with arrows indicate the direction of increasing oxidation (z). The solid lines are solid solution series.

Titanomagnetites $\mathbf{Fe_{3-x}Ti_xO_4}$

In earlier lectures on rock magnetism, we learned a few things about magnetite. As mentioned in Lecture 4, magnetite (Fe_3O_4) has an inverse spinel structure (AB_2O_4). The oxygen atoms form a face-centered cubic lattice into which cations fit in either octahedral or tetrahedral symmetry. For each unit cell there are four tetrahedral sites (A) and eight octahedral sites (B). To maintain charge balance with the four oxygen ions (O^{2-}), there are two Fe^{3+} ions and one Fe^{2+} ion. Fe^{3+} has five unpaired spins, while Fe^{2+} has four. As discussed earlier, each unpaired spin contributes one Bohr magneton ($\mathbf{m}_b$). The divalent iron ions all reside in the octahedral lattice sites, whereas the trivalent iron ions are split evenly between octahedral and tetrahedral sites: $Fe^{3+}|Fe^{3+}Fe^{2+}|O_4$. The A and B lattice sites are coupled with antiparallel spins and magnetite is ferrimagnetic. Therefore, the net moment of magnetite is (9-5=4) $\mathbf{m}_b$ per molecule (at 0 K).

Titanomagnetites can occur as primary minerals in igneous rocks. Magnetite, as well as various members of the hemoilmenite series, can also form as a result of high temperature oxidation. In sediments, magnetite often occurs as a detrital component, but it can also be produced by bacteria or authigenically during diagenesis.

Substitution of Ti^{4+}, which has no unpaired spins (see Lecture 3), has a profound effect on the magnetic properties of the resulting titanomagnetite. Ti^{4+} substitutes for a trivalent iron ion. In order to maintain charge balance, another trivalent iron ion turns into a divalent iron ion. The end members of the solid solution series are:

magnetite	ulvöspinel
$Fe^{3+}\|Fe^{3+}Fe^{2+}\|O_4$	$Fe^{2+}\|Fe^{2+}Ti^{4+}\|O_4$
$x = 0$	$x = 1$

Ulvöspinel is antiferromagnetic because the A and B lattice sites have the same net moment. When x is between 0 and 1, the mineral is called a titanomagnetite. If x is 0.6, the mineral is called

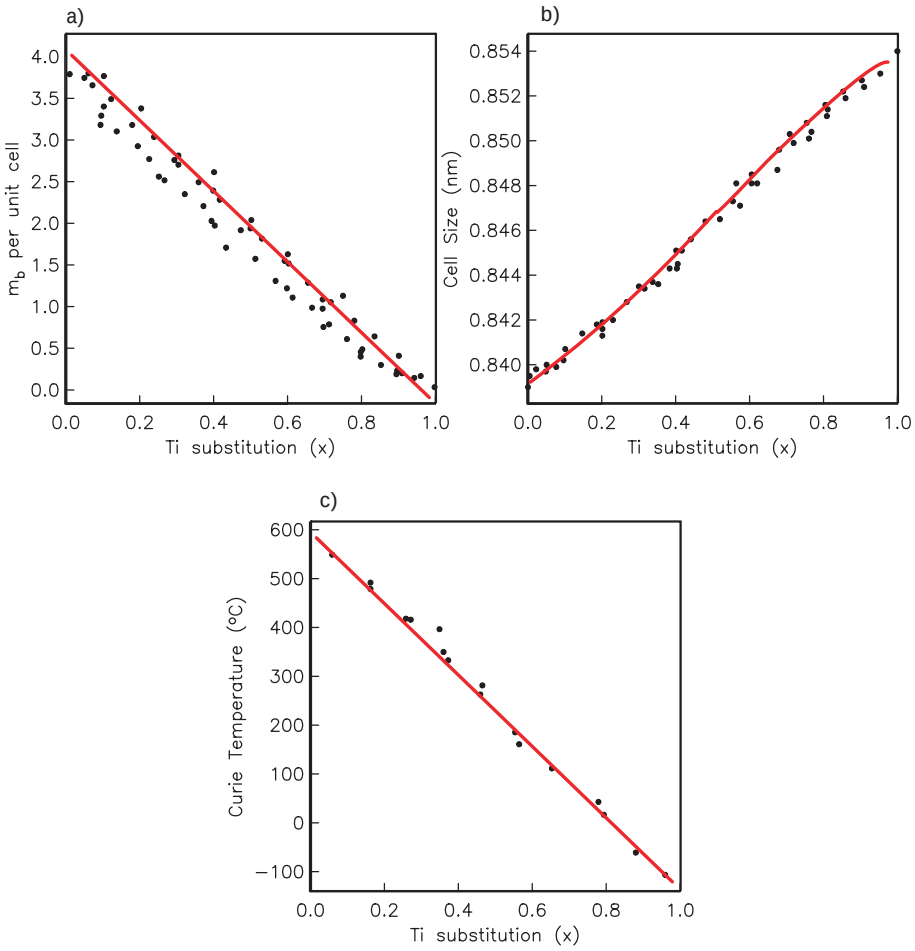

Figure 6.2: Variation of intrinsic parameters with titanium substitution in the titanomagnetite lattice. X is the degree of substitution from 0 (no Ti) to 1 (100% substitution). a) Variation of the magnetization expressed as Bohr magnetons per unit cell. b) Variation of cell lattice size. c) Variation of Curie temperature. (Data compiled by O'Reilly [1984].)

TM60.

The profound effect of titanium substitution on the intrinsic properties of titanomagnetite is illustrated in Figure 6.2. Because Ti^{4+} has no unpaired spins, the saturation magnetization decreases with increasing x (Figure 6.2a). The cell dimensions increase with increasing x (Figure 6.2b). As a result of the increased cell dimension, there is a decrease in Curie Temperature (Figure 6.2c). There is also a slight increase in coercivity (not shown).

The large M_s of magnetite (see Table 6.1) means that for deviations from equant grains as small as 10%, the magnetic anisotropy energy becomes dominated by shape. Nonetheless, aspects of the magnetocrystalline anisotropy provide useful diagnostic tests. The magnetocrystalline anisotropy constants are a strong function of temperature. On warming to ∼-100°C from near absolute zero, changes in these constants can lead to an abrupt loss of magnetization, which is known loosely as the *Verwey transition* (see Lecture 4). Identification of the Verwey transition suggests a remanence that is dominated by magnetocrystalline anisotropy. Furthermore the temperature at which it

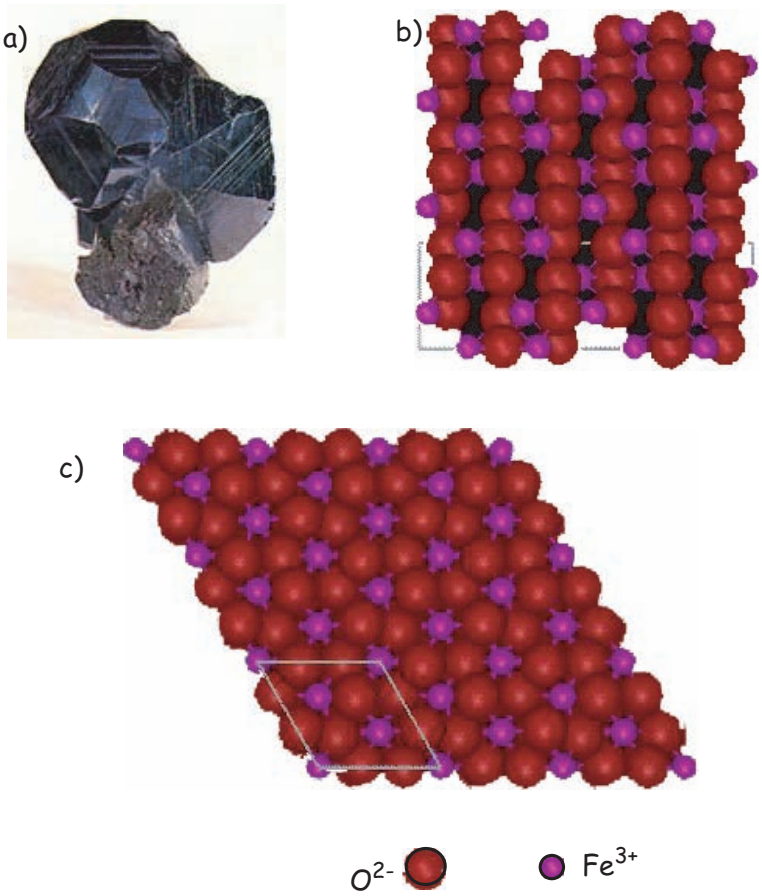

Figure 6.3: Hematite. a) photograph of specularite. b) Crystal structure of hematite. c) same as b) but rotated 90°.

occurs is sensitive to oxidation and the transition can be completely supressed by maghemitization (see Dunlop and Özdemir [1997]).

It should be noted that natural titanomagnetites often contain impurities (usually Al, Mg, Cr). These impurities also affect the magnetic properties. Substitution of 0.1 Al^{3+} into the unit cell of titanomagnetite results in a 25% reduction in M_s and a reduction of the Curie temperature by some 50°C. Substitution of Mg^{2+} into TM60 also results in a lower saturation magnetization with a reduction of some 15%.

6.2.1 *Hematite-Ilmenite* $Fe_{2-y}Ti_yO_3$

Hematite has a corundum structure (see Figure 6.3). It is rhombohedral with a pseudocleavage (perpendicular to the c axis) and tends to break into flakes. It is antiferromagnetic, with a weak parasitic ferromagnetism resulting from either spin-canting or defect ferromagnetism (see Lecture 3). Because the magnetization is a spin canted antiferromagnetism, the temperature at which this magnetization disappears is called the Néel Temperature instead of the Curie Temperature which is *sensu strictu* only for ferromagnetic minerals. The Néel temperature for hematite is approximately

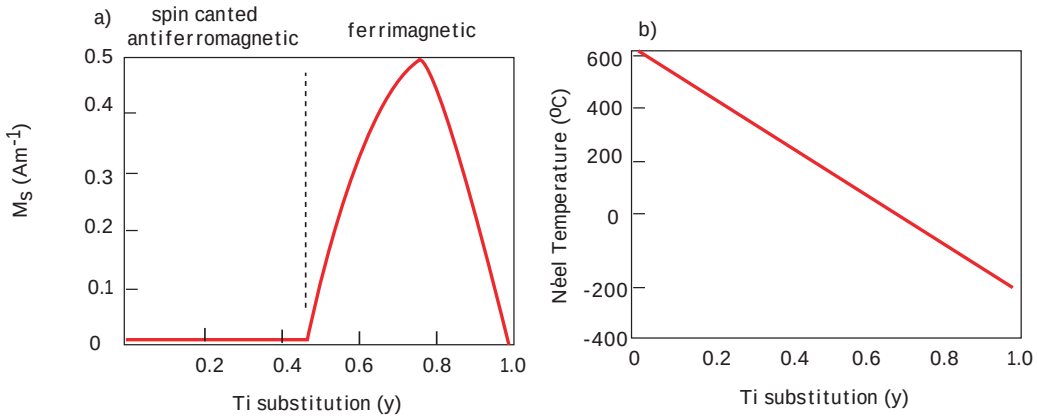

Figure 6.4: Variation of properties with Ti substitution in the titanohematite series. a) Variation of saturation magnetization. b) Variation of Nèel Temperature. (Redrawn from Butler, 1992).

685°C.

Above about -10°C (the *Morin transition*), the magnetization is constrained by aspects of the crystal structure to lie perpendicular to the c axis or within the basal plane. Below the Morin transition, spin-canting, but disappears and the magnetization is parallel to the c axis. This effect could be used to demagnetize the grains dominated by spin-canting: it does not affect those dominated by defect moments. Most hematites formed at low-temperatures have magnetizations dominated by defect moments, so the remanence of many rocks will not display a Morin transition.

Hematite occurs widely in oxidized sediments and dominates the magnetic properties of red beds. It occurs as a high temperature oxidation product in certain igneous rocks. Depending on grain size, among other things, it is either black (specularite) or red (pigmentary). Diagnostic properties of hematite are listed in Table 6.1.

The substitution of Ti into the lattice structure of αFe_2O_3 has an even more profound influence on magnetic properties than for magnetite. For $y = 0$ the magnetization is spin-canted antiferromagnetic, but when $y = 0.45$, the magnetization becomes ferrimagnetic (see Figure 6.4a). For small amounts of substitution, the Ti and Fe cations are distributed equally among the cation layers. For $y > 0.45$, however, the Ti cations preferentially occupy alternate cation layers. Remembering that the Ti^{4+} ions have no net moment, we can imagine that antiparallel coupling between the two sub-lattices results in ferrimagnetic behavior, as opposed to the equal and opposite style of anti-ferromagnetism.

6.2.2 Solid solution series

Above about 600°C, there is complete solid solution between magnetite and ülvospinel as well as between hematite and ilmenite along the two tracks in Figure 6.1. As the temperature goes down, ilmenite and titanohematite can exolve out of the crystals forming crystals with Ti-rich and Ti-poor lamellae (see Figure 6.5). Exolution is inhibited if the crystals cool rapidly so there are many metastable crystals with intermediate values of x or y in nature. A very common composition for magnetites in the ocean crust is 60% substituted with Ti. This is called TM60 (green dot in Figure 6.1.

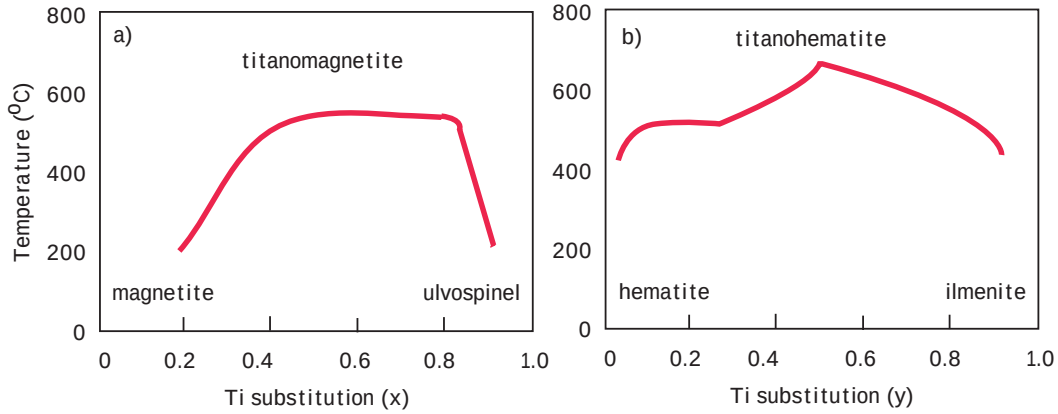

Figure 6.5: Phase diagrams for FeTi oxides. The composition is indicated by x or y. There is complete solid solution above the solid lines. Exolution begins as the temperature cools below the solid curves. a) Titanomagnetite series. b) Titanohematite series. (Redrawn from Dunlop and Özdemir, 1997).

Titanohematite particles with intermediate values of y have interesting properties from a paleomagnetic point of view. There is a solid solution at high temperatures, but as the temperatures drop the crystals exsolve into titanium rich and poor lamellae (see Figure 6.6). Figure 6.4 shows the variation in saturation magnetization and Néel temperature with Ti substitution. For certain initial liquid compositions, the exolution lamellae could have bands Ti-rich bands alternating with Ti-poor bands. If the Ti-rich bands have higher magnetizations, yet lower curie temperatures than the Ti-poor bands, the Ti-poor bands will become magnetized first. When the curie temperature of the Ti-rich bands is reached, they will become magnetized in the presence of the demagnetizing field of the Ti-poor bands, hence they will acquire a remanence that is antiparallel to the applied field. Because these bands have higher magnetizations, the net NRM will also be anti-parallel to the applied field and the rock will be *self-reversed*. This is fortunately very rare in nature.

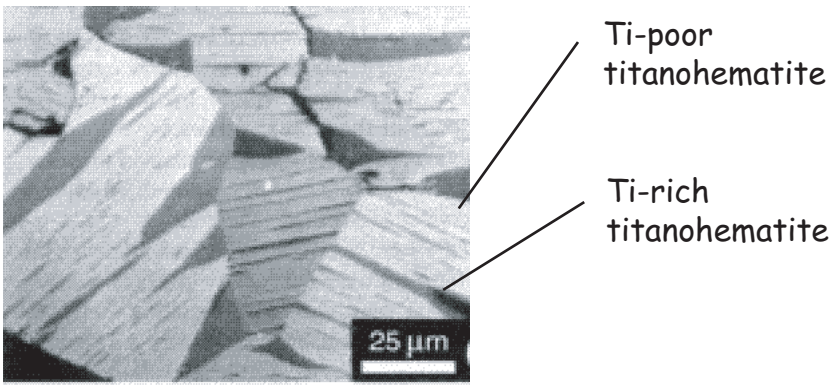

Figure 6.6: Photomicrograph of titanohematite exolution lamellae. Dark bands are Ti-rich (high magnetization, low T_c), light grey bands are Ti-poor (low magnetization, high T_c). (Modified from Maher and Thompson, 1999.)

6.2.3 Oxidation of (titano)magnetites to (titano)maghemites

Many minerals form under one set of equilibrium conditions (say within a cooling lava flow) and are later subjected to a different set of conditions (sea-floor alteration or surface weathering). They will tend to alter in order to come into equilibrium with the new set of conditions. Because the new conditions are often more oxidizing than then original conditions, compositions tend to move along the dashed lines in Figure 6.1. The degree of oxidation is represented by the parameter z.

While the solid solution between magnetite and ulvöspinel exists in principle, intergrowths of these two minerals are actually quite rare in nature because the titanomagnetites interact with oxygen in the melt to form intergrowths of low Ti magnetite with ilmenite. This form of oxidation is known as "deuteric" oxidation.

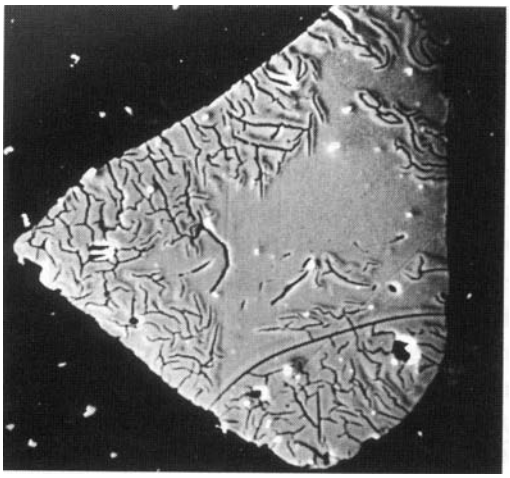

Figure 6.7: A magnetite crystal ($\sim$ 30 μm) undergoing maghemitization. Because of the change in volume, the crystal begins to crack. (From Gapeyev and Tsel'movich, 1988).

Low temperature oxidation will tend to transform a single phase spinel (titanomagnetite) into a new single phase spinel (titanomaghemite) by diffusion of Fe^{2+} from the lattice structure of the (titano)magnetite to the surface where it is converted to Fe^{3+}; titanomaghemite is a "cation-deficient" inverse spinel. Figure 6.7 shows a magnetite crystal in the process of becoming maghemite. The conversion of the Fe^{2+} ion means a loss in volume which results in characteristic cracking of the surface. There is also a loss in magnetization, a shrinkage of cell size and along with the tightening unit cell, an increase in Curie Temperature. These trends are shown for TM60 in Figure 6.8. Maghematization results in a much reduced Verwey transition (see Figure 6.9).

The (titano)maghemite structure is metastable and can invert to form the isochemical, but more stable structure of (titano)hematite, or it can be reduced to form magnetite. The two forms of Fe_2O_3 are distinguished by the symbols γ for maghemite and α for hematite. Inversion of natural maghemite is usually complete by about 350°C, but it can survive until much higher temperatures (for more details, see Dunlop and Özdemir, 1997). Also, it is common that the outer rim of the magnetite will be oxidized to maghemite, while the inner core remains magnetite.

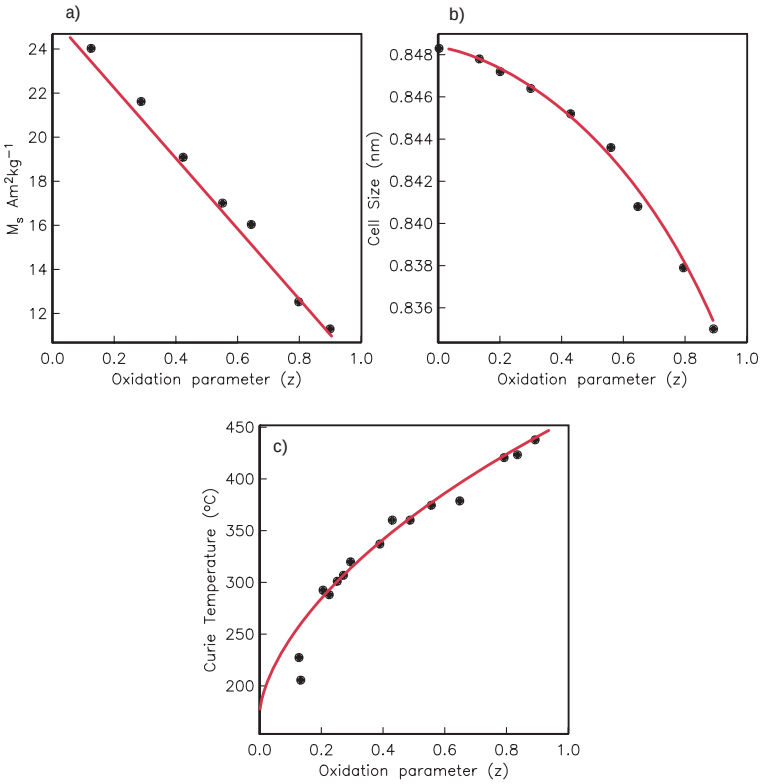

Figure 6.8: Variation of intrinsic parameters with oxidation in TM60. z is the degree of oxidation. a) Variation of the magnetization. b) Variation of cell lattice size. c) Variation of Curie temperature. (Data compiled by Dunlop and Özdemir [1997].)

6.3 Iron-oxyhydroxides and iron-sulfides

Of the many iron oxyhydroxides that occur in any abundance in nature, goethite (αFeOOH)is the most common magnetic phase. It is antiferromagnetic with what is most likely a defect magnetization. It occurs widely as a weathering product of iron-bearing minerals and as a direct precipitate from iron-bearing solutions. It is metastable under many conditions and dehydrates to hematite with time or elevated temperature. Dehydration is usually complete by about 325°C. It is characterized by a very high coercivity but a low Néel temperature of about 100–150°C. Diagnostic properties of goethite are listed in Table 6.1.

There are two iron-sulfides that are important to paleomagnetism: greigite (Fe_3S_4) and pyrrhotite (Fe_7S_8-$Fe_{11}S_{12}$). These are ferrimagnetic and occur in reducing environments. They both tend to oxidize to various iron oxides leaving paramagnetic pyrite as the sulfide component.

The Curie temperature of monoclinic pyrrhotite (Fe_7S_8) is about 325°C (see Figure 6.11a; Table 6.1). Monoclinic pyrrhotite undergoes a transition at $\sim$ 35 K, so low temperature measurements can be diagnostic for this phase (see Figure 6.10). Hexagonal pyrrhotite undergoes a structural transition from an imperfect antiferromagnet to a ferromagnet with much higher saturation magnetization at about 200°C. During a thermomagnetic experiment, the expansion of the crystal results in a large peak in magnetization just below the Curie Temperature (see Figure 6.11b). Mixtures of monoclinic and hexagonal pyrrhotite result in the behavior sketched in see Figure 6.11c. The

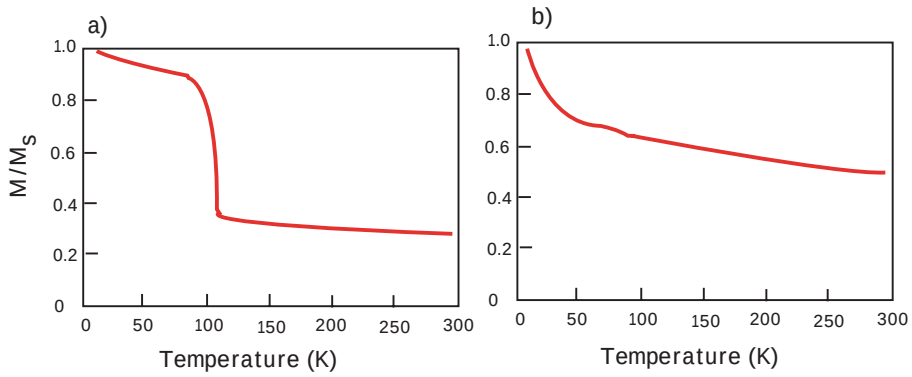

Figure 6.9: Effect of maghemitization on Verwey transition. a) Saturation remanence acquired at 10 K observed as it warms up for 37 nm soichiometric magnetite. b) Same but for partially oxidized magnetite. (Data from Özdemir et al., 1993).

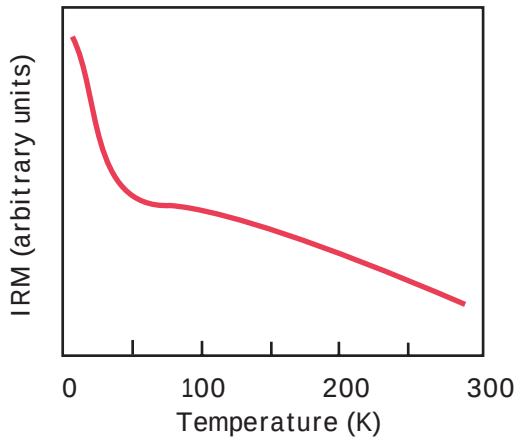

Figure 6.10: Low-temperature transition in monoclinic pyrhotite. (After Snowball and Torrii, 1999).

maximum unblocking temperature of greigite is approximately 330°C. Other diagnostic properties of greigite and pyrrhotite are listed in Table 6.1.

6.4 Occurence and alteration of FeTi oxides in igneous rocks

The composition and relative proportions of FeTi oxides, crystallizing from a silicate melt depend on a number of factors, including the bulk chemistry of the melt, oxygen fugacity and the cooling rate. The final assemblage may be altered after cooling. FeTi oxides are generally more abundant in mafic volcanic rocks (e.g. basalts) than silicic lavas (e.g., rhyolites). FeTi oxides can be among the first liquidus phases ($\sim$ 1000°C) in silicic melts, but in mafic lavas they generally are among the last phases to form ($\sim$1050°C), often with plagioclase and pyroxene.

Although there is considerable variability, the Ti (ulvöspinel) content of the titanomagnetite crystallizing from a melt generally is lower in more silicic melts (see solid black lines in Figure 6.12). Titanomagnetites in tholeiitic lavas generally have $0.5< x <0.8$ with an initial composition near

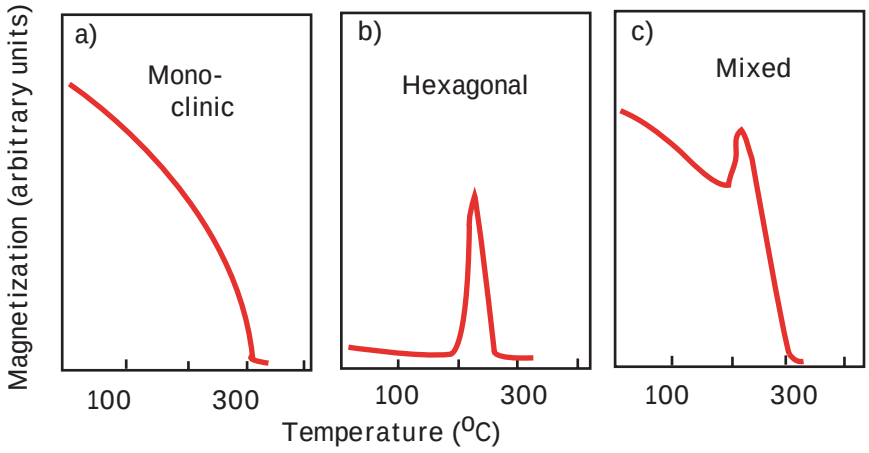

Figure 6.11: Thermomagnetic curves for a) monoclinic b) hexagonal and c) mixture of a) and b) pyrrhotite. (After Dekkers, 1988)

TM60 (x=0.6) characteristic for much of the oceanic crust. The range of rhombohedral phases (dashed red lines) crystallizing from silicate melts is more limited, $0.05 < y < 0.3$ for most lavas.

The final magnetic mineral assemblage in a rock is often strongly influenced by the cooling rate and oxygen fugacity during initial crystallization. As a first approximation, we distinguish slowly cooled rocks (which may undergo solid state exsolution and/or deuteric oxidation) from those in which the oxide minerals were rapidly quenched. As mentioned before, FeTi oxides in slowly cooled igneous rocks can exhibit exolution lamellae with bands of low and high titanium magnetites if the oxygen fugacity remains unoxidizing. This reaction is very slow, so its effects are rarely seen in nature.

The typical case in slowly cooled rocks is that the system becomes more oxidizing with increasing differentiation during cooling and crystallization. For example, both the dissociation of magmatic water and the crystallization of silicate phases rich in Fe will act to increase the oxidation state. This will drive compositions to higher z values (see Figure 6.1). The final assemblage typically consists of ilmenite lamellae and a nearly pure magnetite host because adding O_2 drives the reaction $Fe_2TiO_4 + O_2 \rightleftharpoons Fe_3O_4$ to the right. This process is known as *oxyexsolution*. Under even more oxidizing conditions, these phases may ultimately be replaced by their more oxidized counterparts (e.g., hematite, pseudobrookite).

Weathering at ambient surface conditions or mild hydrothermal alteration may lead to the development of cation deficient (titano)maghemites. This can either occur by addition of oxygen to the spinel phase with a corresponding oxidation of the Fe^{2+} to Fe^{3+} to maintain charge balance, or by the removal of some of the octahedral iron from the crystal structure.

6.5 Magnetic mineralogy of soils and sediments

Igneous rocks are the ultimate source for the components of sedimentary rocks, but biological and low-temperature diagenetic agents work to modify the igneous components and have a significant effect on magnetic mineralogy in sediments. As a result there is a virtual rainbow of magnetic mineralogies found in sediments. (Titano)magnetite coming into the sedimentary environment from an

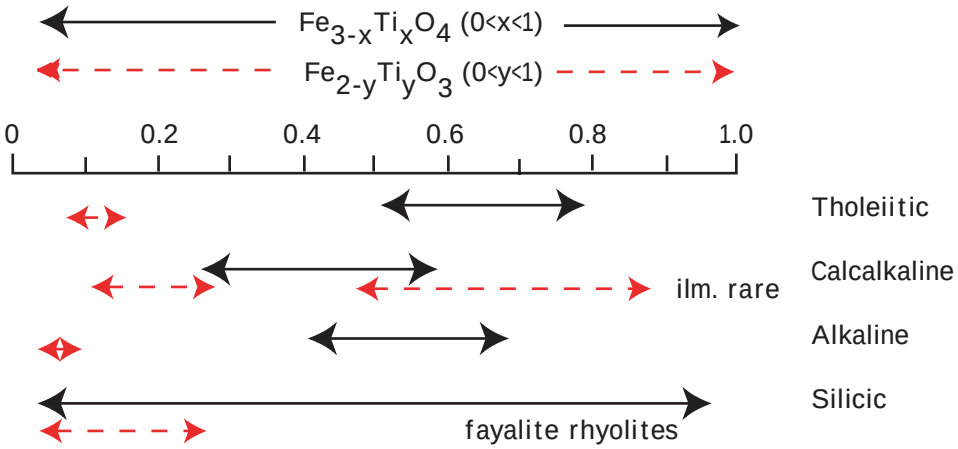

Figure 6.12: Occurence of FeTi oxides in igneous rocks. (Data from Frost and Lindsley, 1991).

igneous source may experience a change in pH and redox conditions that make it no longer the stable phase, hence may alter. Also, although the geochemistry of seawater is generally oxidizing with respect to the stability field of magnetite, pronounced changes in the redox state of sediments often occur with increasing depth as a function of the breakdown of organic carbon. Such changes may result in locally strongly reducing environments where magnetite may be dissolved and authigenic sulfides produced. Indeed, changes down sediment cores in the ferrimagnetic mineral content and porewater geochemistry suggest that this process is active in some marine sedimentary sequences. For example, dissolution of magnetite and/or production of non-magnetic sulfides may be responsible for the oft-seen decrease in various bulk magnetic parameters (e.g., magnetic susceptibility, IRM, ARM, etc.) with depth.

Some of the more spectacular magnetic minerals found in sediments are biogenic magnetites produced by magnetotactic bacteria (see Figure 6.13). The sizes and shapes of bacterial magnetite, when plotted on the Evans diagram from Lecture 3, suggest that magnetotactic bacteria form magnetite in the single domain grain size range - otherwise extremely rare in nature. It appears that bacterial magnetites are common in sediments, but their role in contributing to the natural remanence is still poorly understood.

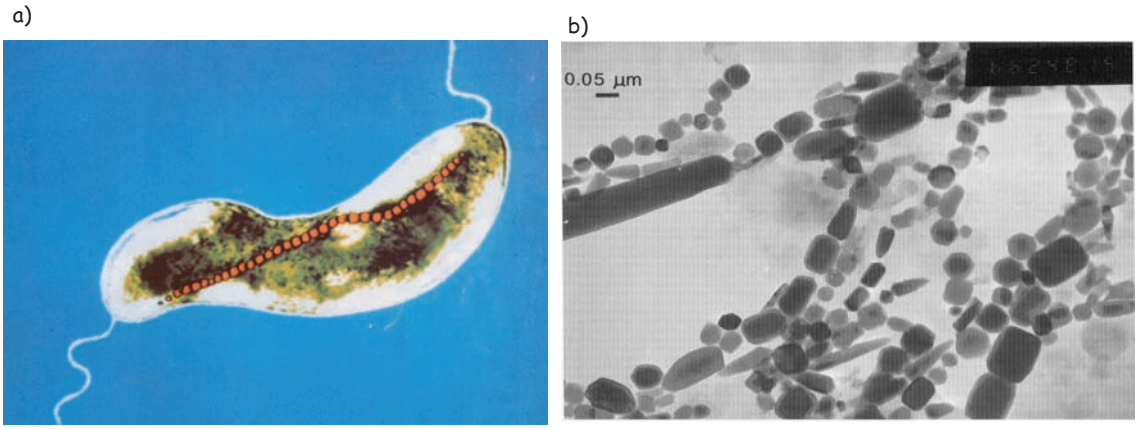

Figure 6.13: Photomicrographs of bacterial magnetites produced by magnetotactic bacteria. a) Intact magnetosome in living bacterium. (Fassbinder et al., 1990.) b) Chains recovered from ODP Site 1006D in the Bahamas (Hounslow in Maher and Thompson, 1999).

Table 6.1: Physical properties of magnetic minerals.

Magnetite	Fe_3O_4
Density = 5197 kg m^{-3}	Dunlop and Özdemir [1997]
Curie temperature = 580°C	Dunlop and Özdemir [1997]
Saturation Magnetization = 92 Am^2kg^{-1}	O'Reilly [1984]
Anisotropy Constant = -2.6 Jkg^{-1}	Dunlop and Özdemir [1997]
Volume susceptibility = $\sim$ 1 SI	O'Reilly [1984]
Typical coercivities are 10's of mT	O'Reilly [1984]
Verwey transition: 110-120 K	Özdemir and Dunlop [1993]
Cell edge = 0.8396 nm	Dunlop and Özdemir [1997]
Maghemite	γFe_2O_3
Density = 5074 kg m^{-3}	Dunlop and Özdemir [1997]
Curie temperature = 590-675°C	Dunlop and Özdemir [1997]
Saturation Magnetization = 74 Am^2kg^{-1}	Dunlop and Özdemir [1997]
Anisotropy Constant = 0.92 Jkg^{-1}	Dunlop and Özdemir [1997]
Verwey transition: suppressed	Dunlop and Özdemir [1997]
Breaks down to αFe_2O_3: between 250$\rightarrow$ 750°C	Dunlop and Özdemir [1997]
TM60	$Fe_{2.4}Ti_{0.6}O_4$
Density = 4939 kg m^{-3}	Dunlop and Özdemir [1997]
Curie temperature = 150°C	Dunlop and Özdemir [1997]
Saturation Magnetization = 24 Am^2kg^{-1}	Dunlop and Özdemir [1997]
Anisotropy Constant = 0.41 Jkg^{-1}	Dunlop and Özdemir [1997]
Coercivity $\sim$ 8 mT	Dunlop and Özdemir [1997]
Verwey transition: suppressed	Dunlop and Özdemir [1997]
Cell edge = 0.8482 nm	Dunlop and Özdemir [1997]
Hematite	αFe_2O_3
Density = 5271 kg m^{-3}	Dunlop and Özdemir [1997]
Néel temperature = 675°C	O'Reilly [1984]
Saturation Magnetization = 0.4 Am^2kg^{-1}	O'Reilly [1984]
Anisotropy Constant = 228 Jkg^{-1}	Dunlop and Özdemir [1997]
Volume susceptibility = $\sim$ 1.3 x 10^{-3} SI	O'Reilly [1984]
Coercivities vary widely and can be 10's of teslas	Banerjee [1971]
Morin Transition: $\sim$ 250-260 K (for $>$ 0.2 μm)	O'Reilly [1984]

Table 1 - continued

Goethite	αFeOOH
Density = 4264 kg m^{-3}	Dunlop and Özdemir [1997]
Néel temperature: 70 → 125°C	O'Reilly [1984]
Saturation Magnetization = 10^{-3} → 1 Am^2kg^{-1}	O'Reilly [1984]
Anisotropy Constant = 0.25 → 2 Jkg^{-1}	Dekkers [1989]
Volume susceptibility = ∼ 1 x 10^{-3} SI	Dekkers [1989]
Coercivities can be 10's of teslas	
Breaks down to hematite: 250 → 400°C	
Pyrrhotite	Fe_7S_8
Density = 4662 kg m^{-3}	Dunlop and Özdemir [1997]
Monoclinic:	
Curie temperature = ∼ 325°C	Dekkers [1989a]
Hexagonal:	
Curie temperature = ∼270°C	Dekkers [1988]
Saturation Magnetization = 0.4 -∼ 20 Am^2kg^{-1}	Worm et al. [1993]
Volume susceptibility = ∼ 1 x 10^{-3} → 1 SI	Collinson [1983];O'Reilly [1984]
Anisotropy Constant = 20 Jkg^{-1}	O'Reilly [1984]
Coercivities vary widely and can be 100's of mT	O'Reilly [1984]
Has a transition at ∼ 34 K	Dekkers et al. [1989]
	Rochette et al. [1990]
Hexagonal pyrrotite: transition near 200°	
Breaks down to magnetite: ∼ 500°C	Dunlop and Özdemir [1997]
Greigite	Fe_3S_4
Density = 4079 kg m^{-3}	Dunlop and Özdemir [1997]
Maximum unblocking temperature = ∼ 330°C	Roberts [1995]
Saturation Magnetization = ∼ 25 Am^2kg^{-1}	Spender et al. [1972]
Anisotropy Constant = -0.25 Jkg^{-1}	Dunlop and Özdemir [1997]
Coercivity 60→> 100 mT	Roberts [1995]
Has high M_r/χ ratios ∼ 70 x 10^3 Am^{-1}	Snowball and Thompson [1990]
Breaks down to magnetite: ∼ 270-350°C	Roberts [1995]

Bibliography

Banerjee, S. K. (1971), 'New grain size limits for paleomagnetic stability in hematite', *Nature Phys. Sci.* **232**, 15–16.

Butler, R. F. (1992), *Paleomagnetism: Magnetic Domains to Geologic Terranes*, Blackwell Scientific Publications.

Collinson, D. W. (1983), 'Methods in Rock Magnetism and Paleomagnetism'.

Dekkers, M. J. (1988), 'Magnetic properties of natural pyrrhotite Part I: behaviour of initial susceptibility and saturation magnetization related rock magnetic parameters in a grain-size dependent framework', *Phys. Earth Planet. Inter.* **52**, 376–393.

Dekkers, M. J. (1989*a*), 'Magnetic properties of natural goethite I. Grain size dependence of some low and high field related rock magnetic parameters measured at room temperature', *Geophys. Jour.* **97**, 323–340.

Dekkers, M. J. (1989*b*), 'Magnetic properties of natural pyrrhotite. II. High and low temperature behaviors of Jrs and TRM as a function of grain size', *Phys. Earth Planet. Inter.* **57**, 266–283.

Dekkers, M. J., Mattei, J. L., Fillion, G. & Rochette, P. (1989), 'Grain-size dependence of the magnetic behavior of pyrrhotite during its low temperature transition at 34 K', *Geophys. Res. Lett.* **16**, 855–858.

Dunlop, D. & Ozdemir, O. (1997), *Rock Magnetism: Fundamentals and Frontiers*, Cambridge University Press.

Evans, M. & Heller, F. (2003), *Environmental Magnetism: Principles and Applications of Enviromagnetics*, Academic Press.

Fassbinder, J., Stanjek, H. & Vali, H. (1990), 'Occurrence of magnetic bacteria in soil', *Nature* **343**, 161–163.

Frost, B. & Lindsley, D. (1991), The occurrence of Fe-Ti oxides in igneous rocks, *in* D. LIndsley, ed., 'Oxide Minerals: Petrologic and Magnetic Significance', Vol. 25 of *Reviews in Mineralogy*, Mineralogical Society of America, pp. 433–486.

Gapeyev, A. & Tsel'movich, V. (1988), 'Stages of oxidation of titanomagnetite grains in igneous rocks (in Russian)', *Viniti N. Moscow* **1331-B89**, 3–8.

Maher, B. A. & Thompson, R., eds (1999), *Quaternary Climates, Environments and Magnetism*, Cambridge University Press.

O'Reilly, W. (1984), *Rock and Mineral Magnetism*, Blackie.

Özdemir, O., Dunlop, D. J. & Moskowitz, B. M. (1993), 'The effect of oxidation of the Verwey transition in magnetite', *Geophys. Res. Lett.* **20**, 1671–1674.

Roberts, A. P. (1995), 'Magnetic properties of sedimentary greigite (Fe3S4)', *Earth Planet. Sci. Lett.* **134**, 227–236.

Rochette, P., Fillion, G., ei, J. L. M. & Dekkers, M. J. (1990), 'Magnetic transition at 30-34 Kelvin in pyrrhotite: insight into a widespread occurrence of this mineral in rocks', *Earth Planet. Sci. Lett.* **98**, 319–328.

Snowball, I. & Thompson, R. (1990), 'A stable chemical remanence in Holocene sediments', *Jour. Geophys. Res.* **95**, 4471–4479.

Snowball, I. & Torii, M. (1999), Incidence oand significance of magnetic iron sulphides inQuaternary sediments and soil, *in* B. Maher & R. Thompson, eds, 'Quaternary Climates, Environments and Magnetism', Cambridge University Press, pp. 199–230.

Spender, M. R., Coey, J. M. D. & Morrish, A. H. (1972), 'The magnetic properties and Mossbauer spectra of synthetic samples of Fe_3S_4', *Can. J. Phys.* **50**, 2313–2326.

Worm, H. U., Clark, D. & Dekkers, M. J. (1993), 'Magnetic susceptibility of pyrrhotite: grain size, field and frequency dependence', *Geophys. J. Int.* **114**, 127–137.

Lectures in Paleomagnetism, 2005
by Lisa Tauxe

Citation:
http://earthref.org/MAGIC/books/Tauxe/2005/

June 3, 2005

Chapter 7

Magnetic hysteresis

Suggested Reading

For background:
Butler (1992), pp 48-54
To learn more:
O'Reilly (1984), pp 69-87

7.1 Introduction

In Lecture 4 we discussed the energies that that control the state of magnetization within ferromagnetic particles. Particles will tend to find a configuration of internal magnetization directions that minimizes the energies (although meta-stable states with local energy minima or LEMs are a possibility). The longevity of a particular magnetization state has to do with the depth of the energy well that the magnetization is in and the energy available for hopping over energy barriers. We discussed a few basic configurations of the remanent magnetic state: uniform magnetization (single domain; SD), flower (F), vortex (V), and multi-domain (MD) states. We also mentioned the case in which thermal energy dominates: superparamagnetic (SP) particles.

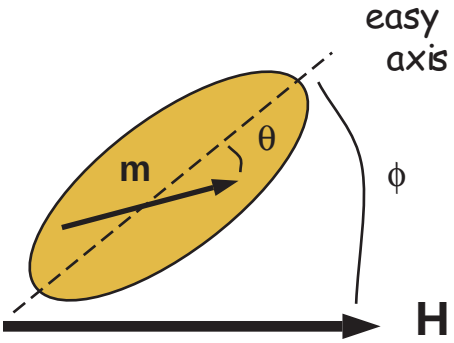

Figure 7.1: Sketch of a magnetic particle with easy axis as shown. In response to a magnetic field **H**, applied at an angle ϕ to the easy axis, the particle moment **m** rotates away from the easy axis, making an angle θ with the easy axis.

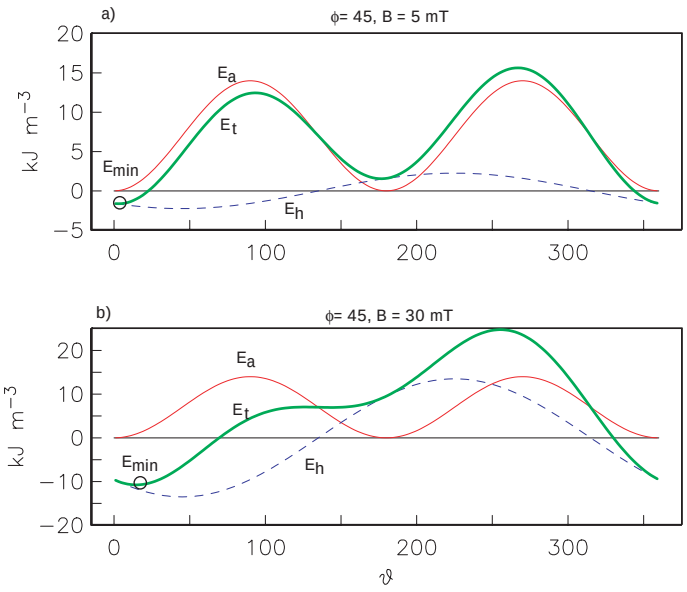

Figure 7.2: Variation of the anisotropy energy $E_a = K_u \sin^2\theta$, the interaction energy $E_h = -M_s B \cos(\phi - \theta)$ and the total energy $E_t = E_a + E_h$ as a function of θ for the particle shown in Figure 1. The θ associated with the minimum energy is indicated by E_{min}. a) $B = 5$ mT. b) $B = 30$ mT.

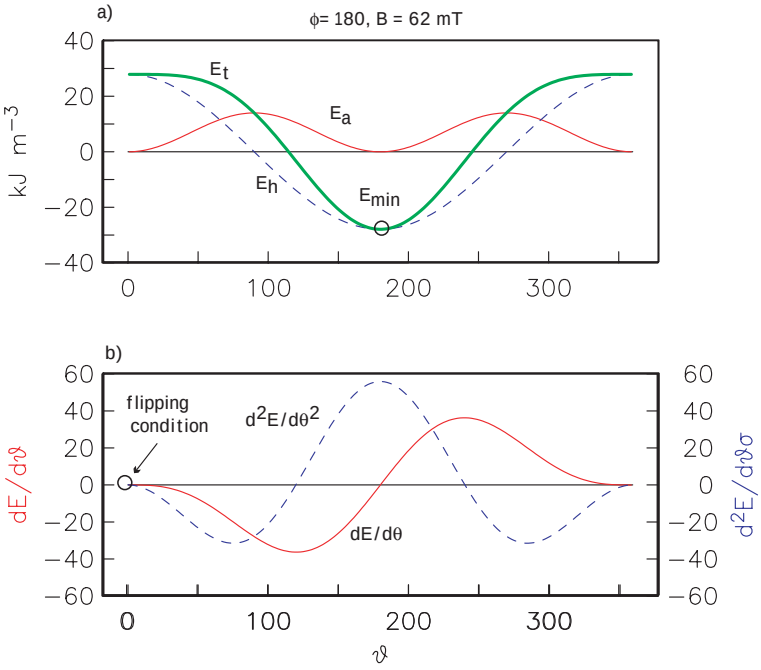

Figure 7.3: a) Variation of the anisotropy energy $E_a = K_u \sin^2\theta$, the interaction energy $E_h = -M_s B \cos\phi$ and the total energy $E_t = E_a + E_h$ as a function of θ for the particle shown in Figure 1. The field was applied with $\phi = 180°$ and was 62 mT in magnitude. The θ associated with the minimum energy is indicated by E_{min} and is 180°. b) Variation in first and second derivatives of the energy equation. The flipping condition of both being zero simulaneously is met.

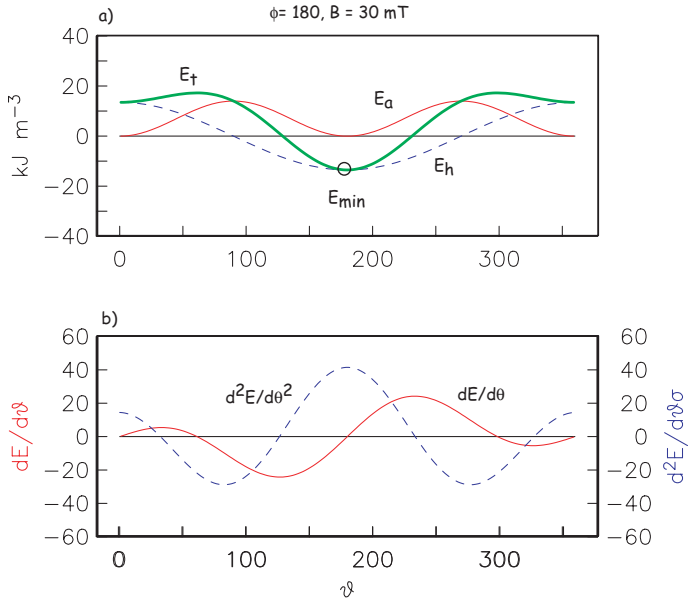

Figure 7.4: Same as previous figure, but the field was only 30 mT. The flipping condition is not met.

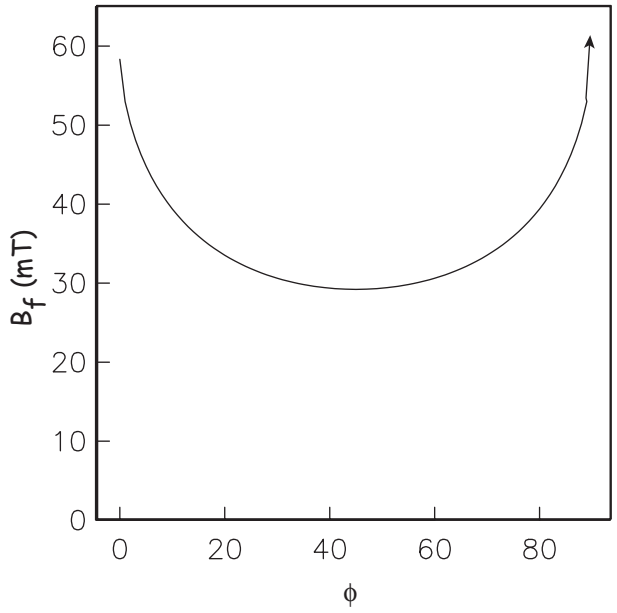

Figure 7.5: The flipping field B_f required to irreversibly switch the magnetization vector from one easy direction to the other in a single domain particle dominated by uniaxial anisotropy.

SP particles have sufficient thermal energy to easily overcome the various anisotropy energies; they come into equilibrium with whatever external field they are in within seconds. Particles with domain walls (multi-domain, or MD particles) also have low stability. It is relatively easy to move a wall around within crystals so the domains grow and shrink depending on the external field.

Quasi-uniformly magnetized (SD and F states) particles have a great deal of resistance to changes in the external field because the magnetization vectors have to jump over high energy barriers to change directions within the crystal. These particles require relatively high magnetic fields to overcome the anisotropy energy and change their magnetizations. Finally, vortex state particles are somewhere in between the extremes of uniformly magnetized particles and those with domain walls.

The ease with which particles can be "coerced" into changing their magnetizations in response to external fields can tell us much about the overall stability of the particles and perhaps also something about their ability to carry a magnetic remanence over the long haul. The concepts of long term stability, incorporated in the concept of relaxation time and the response of the magnetic particles to external magnetic fields are therefore linked through the anisotropy energy constant K (see Lecture 4). In this lecture we will discuss the behavior of magnetic particles in response to external magnetic fields.

7.2 The "flipping" field

Magnetic remanence is the magnetization in the absence of an external magnetic field. If we imagine a particle with a single "easy" axis - a so-called "uniaxial" particle, the magnetization in the absence of a magnetic field will be aligned along one of the directions parallel to the easy axis and θ, the angle between the magnetic moment $\mathbf{m}$ and the easy axis is zero (see Figure 7.1a). But if there is an external field applied at an angle ϕ to the easy axis, there will be a competition between the anisotropy energy (tending to keep the magnetization parallel to the easy axis) and the interaction energy (tending to line the magnetization up with the external magnetic field). We showed in Lecture 4 that the total magnetic energy density of such a particle is given by:

$$E_t = K_u \sin^2\theta - M_s B \cos(\phi - \theta) \tag{7.1}$$

The magnetic moment of a uniaxial single domain grain will find the angle θ that is associated with the minimum total energy (E_{min}; see Figure 7.2). For low external fields (e.g., 5 mT; Figure 7.2a), θ will be closer to the easy axis and for higher external fields (e.g., 30 mT; Figure 7.2b), θ will be closer to the applied field direction (ϕ).

When a magnetic field that is large enough to overcome the anisotropy energy is applied in a direction opposite to the magnetization vector, the moment will jump over the energy barrier and stay in the opposite direction when the field is switched off. The field necessary to accomplish this feat is called the *flipping field* (B_f) (also sometimes the "switching field"). Stoner and Wohlfarth (1948) showed that the flipping field can be found from the condition that $dE_t/d\theta = 0$ and $d^2E_t/d\theta^2 = 0$. We will call this the "flipping condition". The necessary equations can be found by differentiating Equation 7.1:

$$\frac{dE}{d\theta} = 2K_u \sin\theta\cos\theta - M_s B \sin(\phi - \theta), \tag{7.2}$$

and again

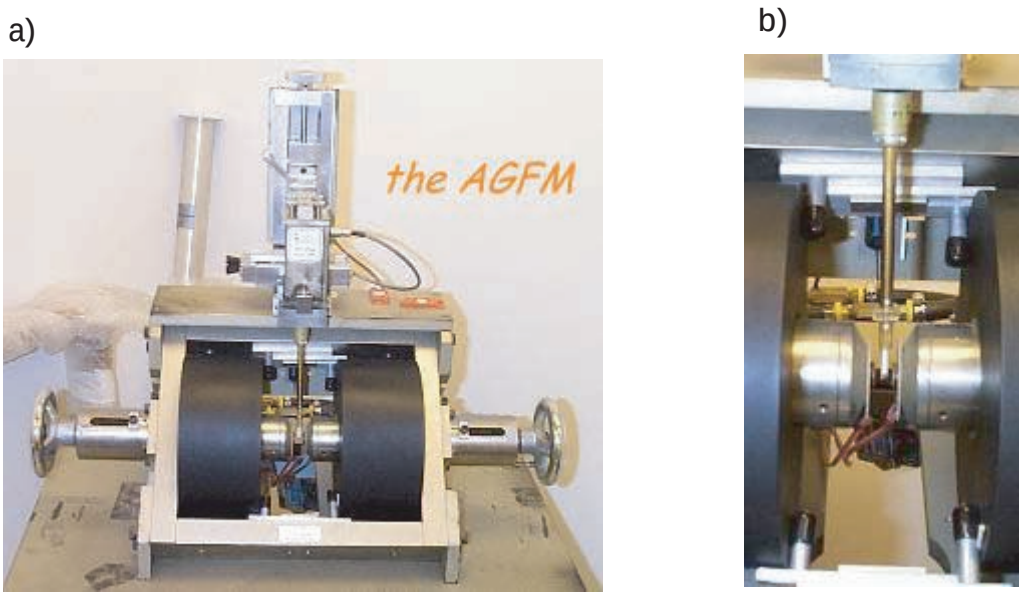

Figure 7.6: a) Micromag AGFM in the Scripps Paleomagnetic Laboratory. b) Blow up of measurement region.

$$\frac{d^2E}{d\theta^2} = 2K_u \cos(2\theta) + M_s B \cos(\phi - \theta). \tag{7.3}$$

Solving these two equations for B and using trigonometric trickery we get:

$$B_f = \frac{2K_u}{M_s}\frac{(1 - t^2 + t^4)^{\frac{1}{2}}}{1 + t^2} = \frac{2K_u}{M_s}\frac{1}{(\cos^{\frac{2}{3}}\phi + \sin^{\frac{2}{3}}\phi)^{\frac{3}{2}}} \tag{7.4}$$

where $t = \tan^{\frac{1}{3}}\phi$. Here we have the derivation for the so-called "intrinsic coercivity" (B_k) when the dominant magnetic anisotropy constant is K_u and ϕ is zero, $B_k = 2\frac{K_u}{M_s}$ (introduced as "coercivity" in Lecture 4).

Using the parameters for magnetite (K_u = 1.4 x 10^4 Jm^{-3} and M_s = 4.8 x 10^5 Am^{-1}) we get B_f = 58 mT. We plot the behavior of Equations 7.1 - 7.3 in Figure 7.3. We see that the minimum in E_t occurs at an angle of $\theta = 180°$ and that the first and second derivatives satisfy the flipping criterion by having a common zero crossing. There is no other field for which this is true (see, e.g., the case of a 30 mT field in Figure 7.4).

We show the flipping field B_f versus ϕ in Figure 7.5. For ϕ parallel to the easy axis (zero), B_f is 62 mT as we found before. B_f drops steadily as the angle between the field and the easy axis increases, until an angle of 45° when B_f starts to increase again. B_f is undefined when $\phi = 90°$, so when the field is applied at right angles to the easy axis, there is no field sufficient to flip the moment.

When a single domain, uniaxial particle is subjected to an increasing magnetic field the magnetization is gradually drawn into the direction of the applied field. If the flipping condition is not met, then the magnetization will return to the original direction when the magnetic field is

removed. If the flipping condition is met, then the magnetization undergoes an irreversible change and will be in the opposite direction when the magnetic field is removed.

7.3 Hysteresis loops

Now let us consider what happens to single particles when subjected to applied fields in the cycle known as the "hysteresis loop". Measurements of magnetic moment m as a function of applied field B are made on a variety of instruments, such as a vibrating sample magnetometer (VSM) or alternating gradient force magnetometer (AGFM; see Figure 7.6). In the AGFM, a sample is placed on a thin stalk between pole pieces of a large magnet. There is a probe mounted behind the sample that measures the applied magnetic field. There are small coils on the pole pieces that modulate the gradient of the applied magnetic field (hence alternating gradient force). The sample vibrates in response to changing magnetic fields and the amplitude of the vibration is proportional to the moment in the axis of the applied field direction. The vibration of the sample stalk is measured and calibrated in terms of magnetic moment. The magnetometer is only sensitive to the induced component of **m** parallel to the applied field $\mathbf{H}_o$, which is $m_{||} = m\cos\phi$ (because the off axis terms are squared and very small, hence can be neglected.) In the hysteresis experiment, therefore, the moment parallel to the field $m_{||}$ is measured as a function of applied field B.

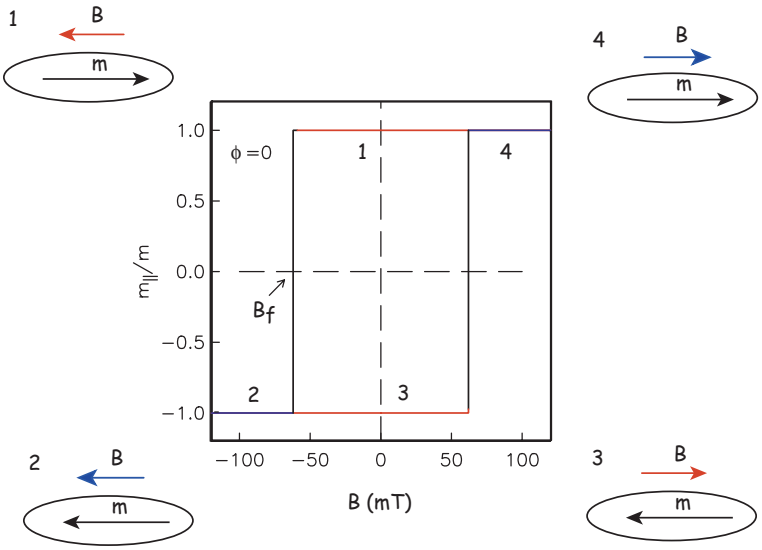

Figure 7.7: Moment measured for the particle ($\phi = 0°$) with applied field starting at 0 mT and increasing in the opposite directions along track #1. When the flipping field B_f is reached, the moment switches to the other direction along track #2. The field then switches sign and decreases along track #3 to zero, then increases again to the flipping field. The moment flips and the the field increases along track #4.

7.3.1 Uniaxial anisotropy

Imagine a single domain particle with uniaxial anisotropy. Because the particle is single domain, the magnetization is at saturation and, in the absence of an applied field is constrained to lie along

the easy axis. Now suppose we apply a magnetic field in the opposite direction (see track # 1 in Figure 7.7). When B reaches B_f in magnitude, the magnetization flips to the opposite direction (track #2 in Figure 7.7) and will not change regardless of how high the field goes. The field then is decreased to zero and then increased along track #3 in Figure 7.7 until B_f is reached again. The magnetization then flips back to the original direction (track #4 in Figure 7.7).

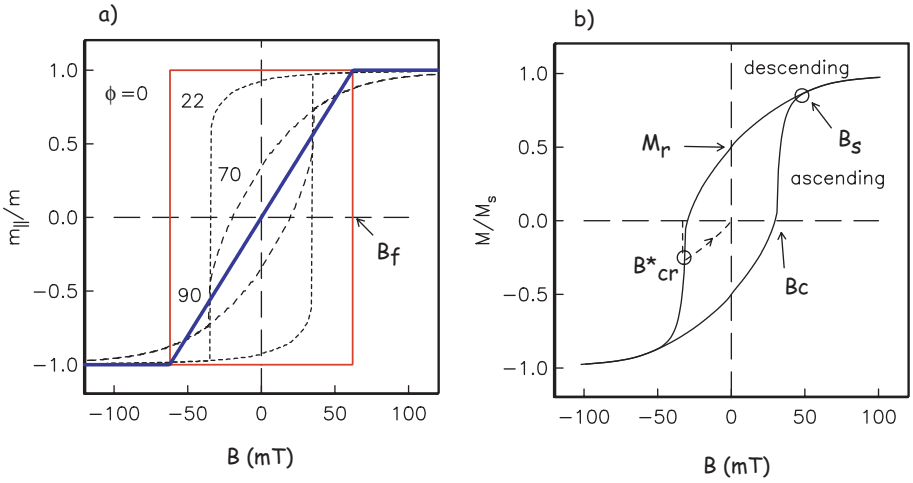

Figure 7.8: a) The component of magnetization parallel to $+B_{max}$ versus B for field applied with various angles ϕ. b) Sum of 10,000 individual curves similar to those shown in a) for ϕ drawn from a uniform distribution on a sphere. The saturation remanence M_r, bulk coercive field B_c and coercivity of remanence B^*_{cr} are indicated. (Redrawn from Tauxe et al., 1996.)

Applying fields at arbitrary angles to the easy axis results in loops of various shapes (see Figure 7.8a). As ϕ approaches 90°, the loops become thinner. Remember that the flipping fields for $\phi = 22°$ and $\phi = 70°$ are similar (see Figure 7.5) and are lower than that from $\phi = 0°$, but the flipping field for $\phi = 90°$ is infinite, so that "loop" is closed and completely reversible.

In rocks with an assemblage of randomly oriented particles with uniaxial anisotropy, we would measure the sum of all the millions of tiny individual loops. A specimen from such a rock would yield a loop similar to that shown in Figure 7.8b. If the field is first increased to $+B_{max}$, all the magnetizations are drawn into the field direction and the net magnetization is equal to the sum of all the individual magnetizations and is the *saturation magnetization* M_s. When the field is reduced to zero, the moments relax back to their individual easy axes, many of which are at a high angle to the direction of the saturating field and cancel each other out. The net remanence after saturation is termed the *saturation remanent magnetization* M_r. For a random assemblage of single domain uniaxial particles, $M_r/M_s = 0.5$. The field necessary to reduce the net moment to zero is defined as the coercive field B_c. The coercivity of remanence B_{cr} is defined as the magnetic field required to irreversibliy flip half the magnetic moments (so the net remanence after application of $-B_{cr}$ to a saturation remanence is 0). B_{cr} is always greater than or equal to B_c and the ratio B_{cr}/B_c for our random assemblage of uniaxial SD particles is 1.09 (Wohlfarth, 1958).

If one were to switch off the field at the point labeled B^*_{cr} in Figure 7.8, the magnetization would follow the dashed line and intersect the origin. For single domain grains, the dashed curve is parallel to the lower curve. So if one only measured the outer loop, one could estimate the coercivity of remanence by simply tracing the curve parallel to the lower curve (dashed line) from

Table 7.1: Predictions for randomly oriented assemblages of magnetite and titanomagnetite (from Tauxe et al., 2002).

K (Jm^{-3})	M_s (Am^{-1})	M_r/M_s	B_k (mT)	B_c (mT)
K_1=-1.3x10^4	4.8x10^5	0.87	54	10
K_1=2x10^3	1.2x10^5	0.83	34	11
$L/W = 1.3; K_u$ = 1.4 x 10^4	4.8x10^5	0.5	58	28
$L/W = 1.5; K_u$ = 1.4 x 10^4	4.8x10^5	0.5	85	41
$L/W = 2; K_u$ = 3.5 x 10^4	4.8x10^5	0.5	150	69
$L/W = \infty$; K_u = 1.4 x 10^5	4.8 x10^5	0.5	600	289

the origin to the point of intersection with the upper curve (circled in Figure 7.8). This parameter is here called B^*_{cr}. As we will learn in Lecture 8, this estimate is only valid for single domain grains.

7.3.2 Cubic anisotropy

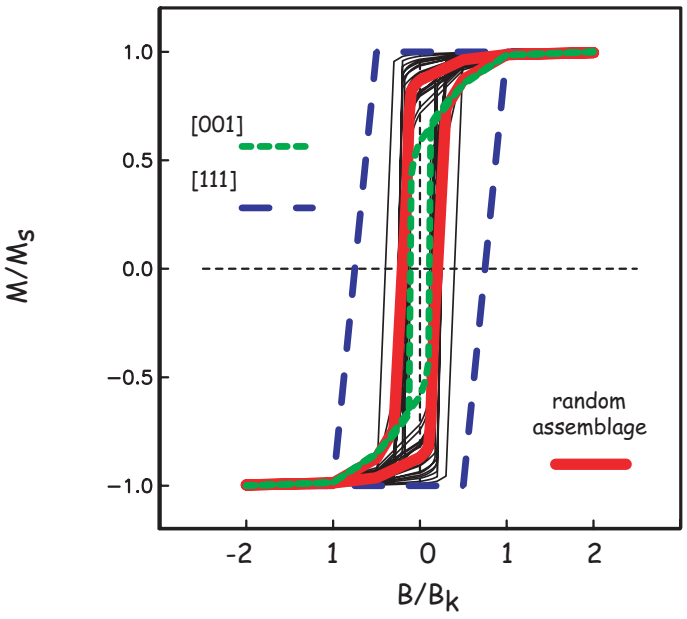

Figure 7.9: Heavy lines: theoretical behavior of cubic grans of magnetite. Dashed lines are the reponses along particular direcions. light grey lines: hysteresis response for single particles with various orientations with respect to the applied field. (Redrawn from Tauxe et al., 2002.)

In the case of equant grains of magnetite for which magnetocrystalline anisotropy dominates, there are four easy axes, instead of two as in the uniaxial case. The maximum angle ϕ between an easy axis and an applied field direction is 55°. Hence there is no individual loop that goes through the origin (see Figure 7.9). A random assemblage of particles with cubic anisotropy will therefore have a much higher saturation remanence. In fact, the theoretical ratio of M_r/M_s for such an assemblage is 0.87, as opposed to 0.5 for the uniaxial case (Joffe and Heuberger, 1974). Other theoretical predictions for hysteresis parameters are summarized in Table 7.1.

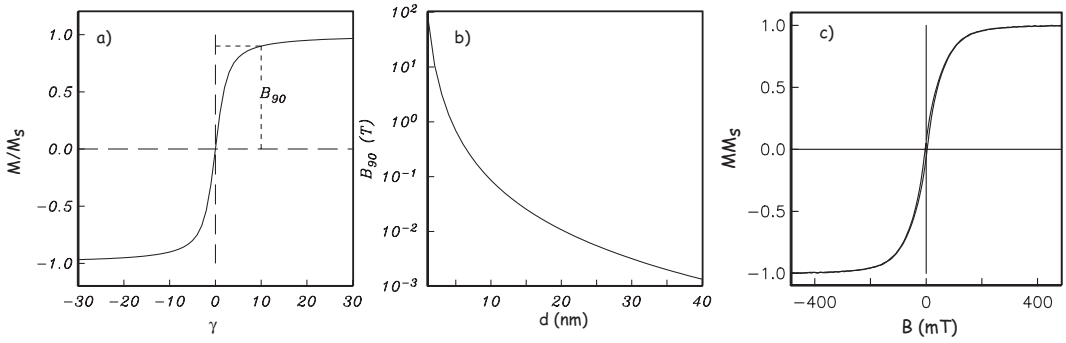

Figure 7.10: a) The contribution of SP particles with saturation magnetization M_s and cubic edge lendth d. $\gamma = BM_s d^3/kT$. There is no hysteresis. b) The field at which the magnetization reaches 90% of the maximum B_{90} is when $M_s d^3/kT \simeq 10$. (Figure redrawn from Tauxe et al., 1996.) c) Typical loop for a population of MD grains. (Data from gabbro from Troodos Ophiolite - courtesy of J.Gee).

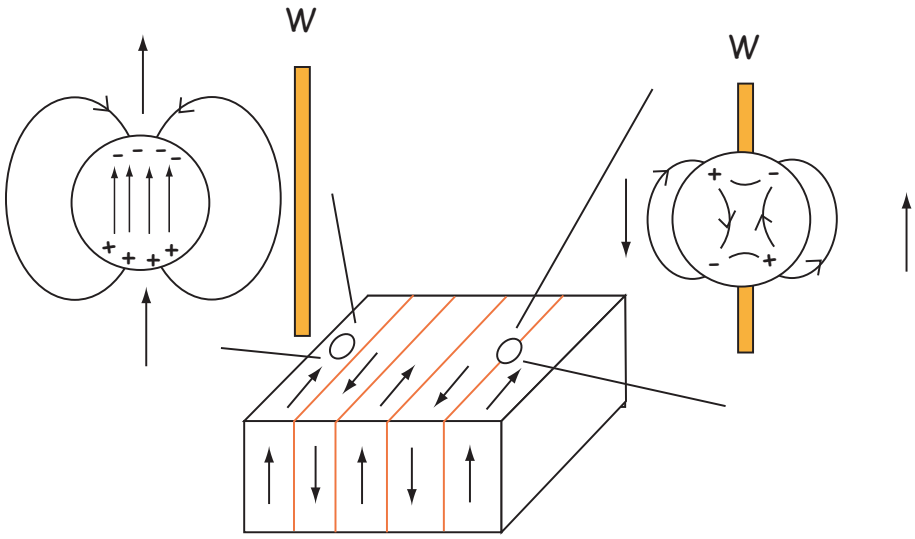

Figure 7.11: Interaction of a domain wall and a void. When the void is within a domain, free poles create a magnetic field which creates a self energy (Lecture 4). When a domain wall intersects the void, the self-energy is reduced. There are no exchange or magnetocrystalline anisotropy energy terms within the void, so the wall energy is reduced.

7.3.3 SP particles

In superparamagnetic (SP) particles, E_t is balanced by thermal energy kT. This behavior can be modelled using statistical mechanics in a manner similar to that derived for paramagnetic grains in Lecture 3 and summarized in the Appendix. In fact,

$$\frac{M}{M_s} = N(\coth \gamma - \frac{1}{\gamma}). \tag{7.5}$$

where $\gamma = \frac{M_s B v}{kT}$ and N is the number of particles of volume v.

Our end result, (Equation 7.5), is the familiar Langevin function from our discussion of paramagnetic behavior (Lecture 3); hence the term "superparamagnetic" for such particles.

The contribution of SP particles for which the Langevin function is valid with given M_s and d is shown in Figure 7.10a. The field at which the population reaches 90% saturation B_{90} occurs at $\gamma \sim 10$. Assuming particles of magnetite ($M_s = 4.8$ x 10^5 A/m) and room temperature ($T = 300°$K), B_{90} can be evaluated as a function of d (see Figure 7.10b). Because of its inverse cubic dependence on d, B_{90} rises sharply with decreasing d and is hundreds of tesla for particles a few nanometers in size, approaching paramagnetic values. The maximum size for SP behavior is rather controversial at the moment, but Tauxe et al. (1996) argue that it is $\sim$ 20 nm.

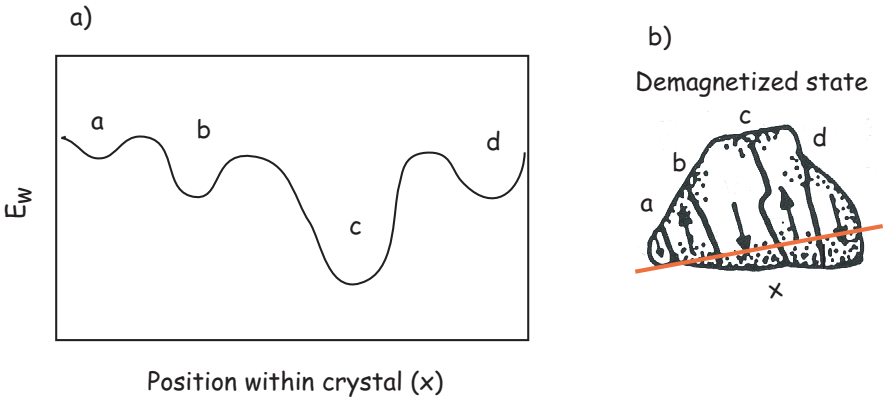

Figure 7.12: a) Schematic view of wall energy across a transect of a multi-domain grain. b) Placement of domain walls in the demagnetized state. (Domain observations from Halgedahl and Fuller, 1983.)

7.3.4 MD particles

Moving domain walls around is much easier than flipping the magnetization of an entire particle coherently. The reason for this is the same as the reason that it is easier to move a rug by lifting up a small wrinkle and pushing that through the rug, than to drag the whole rug by the same amount. Because of the greater ease of changing magnetic moments in MD grains, they have lower coercive fields and saturation remanence is also much lower than for uniformly magnetized particles (see Figure 7.10c). For grains large enough to have many walls (say a few microns), we predict that the grains would have no stability and the loop would be nearly indistinguishable from an SP loop. Yet some large grains have rather large coercivities and remanence ratios. The principle mechanism invoked to explain the unexpected stability of some grains is that wall energy is not uniform through-out the grain; some places have substantially lower energies than others and walls get "stuck" in these local energy minima (LEMs).

There are several possible causes of variability in wall energy within a magnetic grain, for example, voids, lattice dislocations, stress, etc. The effect of voids is perhaps the easiest to visualize, so we will consider voids as an example of why wall energy varies as a function of position within the grain. We show a particle with lamellar domain structure and several voids in Figure 7.11. When the void occurs within a uniformly magnetized domain (left of figure), the void sets up a demagnetizing field as a result of the free poles on the surface of the void. There is therefore, a self-energy associated with the void. When the void is traversed by a wall, the free pole area is reduced,

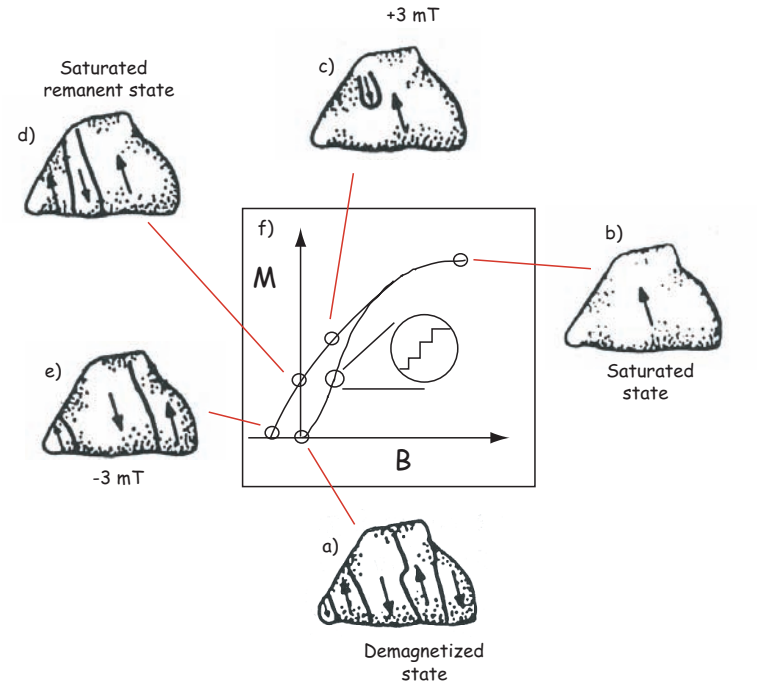

Figure 7.13: Schematic view of the magnetization process in MD grain shown in previous figure. a) Demagnetized state, b) in the presence of a saturating field, c) field lowered to +3 mT, d) remanent state, e) backfield of -3 mT, f) resulting loop. Inset shows detail of domain walls moving by small increments called Barkhausen jumps. (Domain wall observations from Halgedahl and Fuller, 1983; schematic loop after O'Reilly, 1984.)

reducing the demagnetizing field and the associated self-energy. Therefore, the energy of the void is reduced by having a wall bisect it. Furthermore, the energy of the wall is also reduced, because the area of the wall in which magnetization vectors are tormented by exchange and magnetocrystalline energies is reduced. The wall gets a "free" spot if it bisects a void. The wall energy E_w therefore is lower as a result of the void.

In Figure 7.12, we show a sketch of a hypothetical transect of E_w across a particle. There are four LEMs labelled a-d. Domain walls will distribute themselves through out the grain in order to minimize the net magnetization of the grain and also to try to take advantage of LEMs in wall energy.

Domain walls move in response to external magnetic fields (see Figure 7.13). Starting in the demagnetized state (Figure 7.13a), we apply a magnetic field that increases to saturation (Figure 7.13b). As the field increases, the domain walls move in sudden jerks as each successive local wall energy high is overcome. This process, known as *Barkhausen jumps*, leads to the stair-step like increases in magnetization (shown in the inset of Figure 7.13). At saturation, all the walls have been flushed out of the crystal and it is uniformly magnetized. When the field decreases again, to say +3 mT (Figure 7.13c), domain walls begin to nucleate, but because the energy of nucleation is larger than the energy of denucleation, the grain is not as effective in cancelling out the net magnetization, hence there is a net saturation remanence (Figure 7.13d). The walls migrate around as a magnetic field is applied in the opposite direction (Figure 7.13e) until there is no net

magnetization). The difference in nucleation and denucleation energies was called on by Halgedahl and Fuller (1983) to explain the high stability observed in some large magnetic grains.

7.4 Non-uniform magnetizations

Magnetite particles whose remanence states are in a "vortex" structure (see Lecture 4) probably flip using what has been called a "curling" mode. In order to flip its magnetic moment, the particle forms vortices which can zip through the particle. The hysteresis behavior of these particles can be modelled numerically (e.g. Tauxe et al., 2002). Examples of simulations of uniformly distributed assemblages are shown in Figure 7.14.

In Figure 7.14a we show the results from equant particles with widths of about 90 nm. The thin lines are individual loops for a given orientation of the applied field with respect to the crystallographic axes and the average loop is the heavy line. The loop from a uniform assemblage of such particles has a remanence ratio (M_r/M_s) of 0.63 and a coercive field of 14 mT. As mentioned previously, the expected values (Table 7.1) are 0.87 and 10 mT respectively for uniformly magnetized equant (CSD) particles of magnetite, so this flower state assemblage has a magnetization that is "harder". The lower M_r/M_s ratio stems from the fact that the particles are not at saturation.

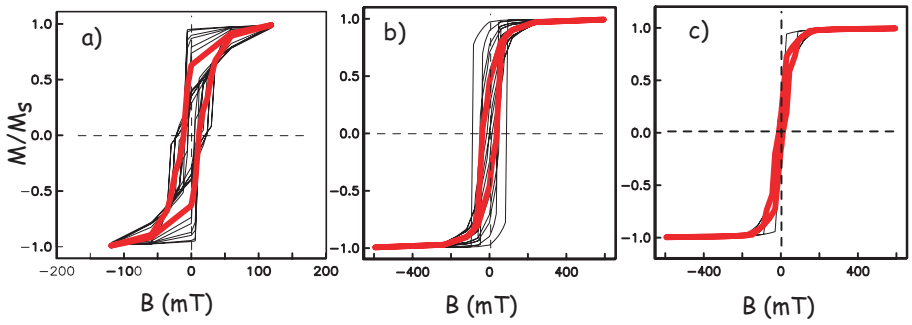

Figure 7.14: Simulated loops for assemblages of randomly oriented particles. a) Simulation of a 90 nm cubic particle. Thin lines are representative examples for various orientations of **B** with respect to the crystallographic axes. Heavy line is the average loop for a random assemblage of particles. b) Same as a) but for a 70x140 nm parallelopiped. c) Same as a) but for a 115 nm cube. Figure from Tauxe et al., 2002.

In Figure 7.14b we show a similar set of curves for an assemblage of 70 nm particles with a/b ratios of 2. The remanence ratio of this assemblage is 0.46 and the coercive field is ∼38 mT as compared to 0.5 and 69 mT (Table 7.1). These uniaxial, flower state particles therefore have lower coercive fields than expected from a random assemblage of SD grains.

A third example of an assemblage of particles is shown in Figure 7.14c. This is for an assemblage of 115 nm (vortex state) equant particles. The average loop has a squareness of 0.16 and coercive field of 10 mT. Particles with characteristic vortex remanence states therfore have lower coercive fields than SD particles, but higher than a truly MD particle. They also have remanence ratios that are in between SD and MD particles.

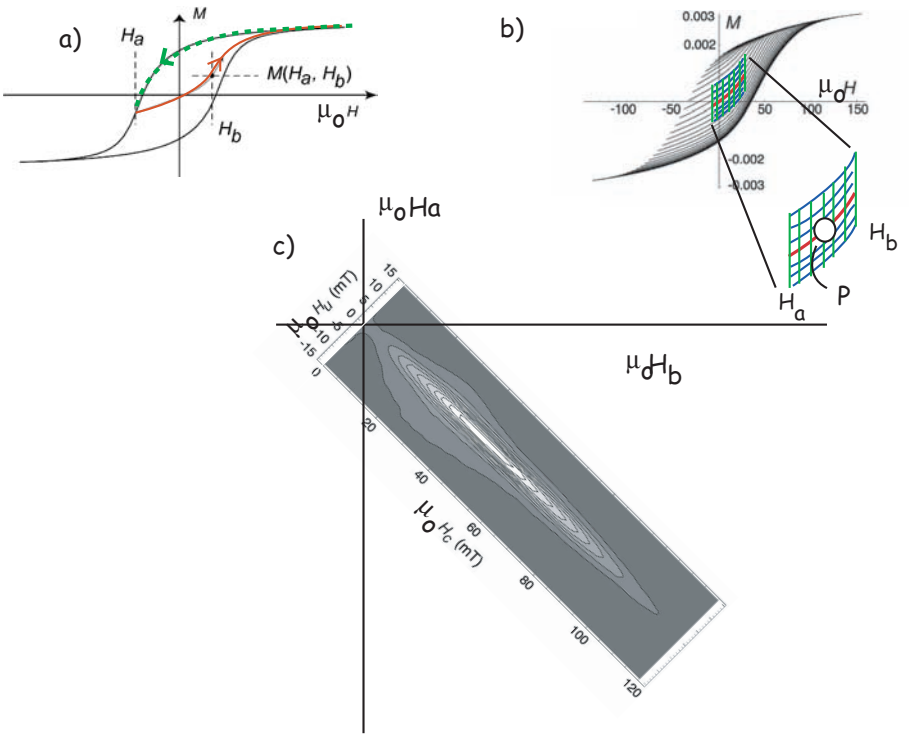

Figure 7.15: a) Dashed line is the descending magnetization curve taken from a saturating field to some field H_a. Red line is the first order reversal curve (FORC) from H_a returning to saturation. At any field $H_b > H_a$ there is a value for the magnetization $M(H_a, H_b)$. b) A series of FORCs for a single domain assemblage of particles. At any point "P" there are a set of related curves making a 7x7 grid. A polynomial surface is fit to these data is estimated. c) A contour plot of the mixed second derivative of the polynomial surface evaluated for points H_a, H_b. (Redrawn from Pike et al., Phys. Earth Planet. Int., 126, 11-25. 2001). Note: all Hs are actually $\mu_o H$.

7.5 First Order Reversal Curves

Hysteresis loops can yield a tremendous amount of information yet much of this is lost by simply estimating the set of parameters $M_r, M_s, B_{cr}, B_c, \chi_i, \chi_{hf}$, etc.. Pike et al. (e.g., 1999) popularized the method of Mayergoyz (1986) or using so-called *First Order Reversal Curves* or FORCs to represent hysteresis data. In the FORC experiment, a sample is subjected to a saturating field, as in most hysteresis experiments. The field is lowered to some field H_a, then increased again through some value H_b to saturation (see Figure 7.15a). [It is unfortunate that the FORC terminology has chosen to use H_a, yet routinely neglects the necessary μ_o to render these field values in tesla...] The magnetization curve between H_a and H_b is a "FORC". A series of FORCs (see Figure 7.15b) are generated to the desired resolution.

To transform FORC data into some useful form, they are gridded as in the inset in Figure 7.15c. In this example, we take a curve (in red) with its three neighbors on either side (in green), for a smoothing factor of $SF = 3$. The data in the box are fit with a polynomial surface of the form:

$$a_1 + a_2 H_a + a_3 H_a^2 + a_4 H_b + a_5 H_b^2 + a_6 H_a H_b$$

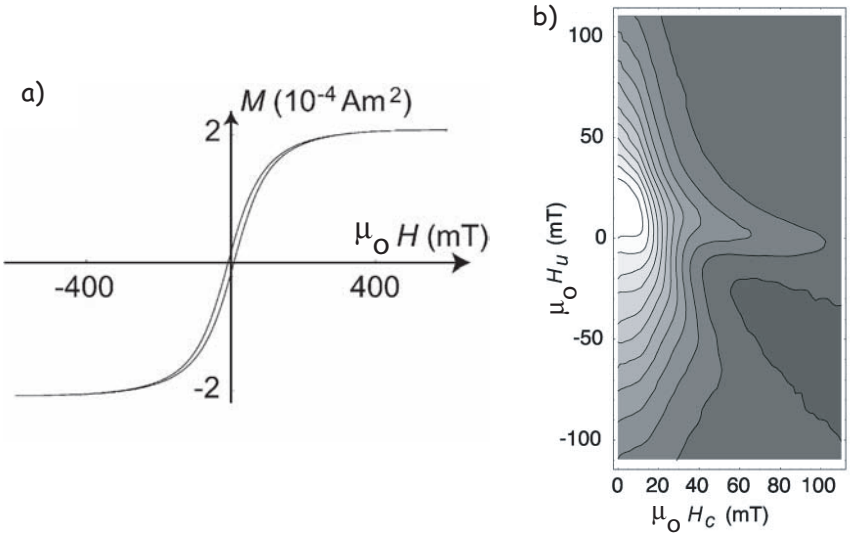

Figure 7.16: a) Hysteresis loop for a large, stressed gain of magnetite prior to annealing. b) FORC diagram from same. (Redrawn from Pike et al., 2001).

where the a_i are fitted coefficients. The coefficient $-a_6(H_a, H_b)$ is contoured as in the Figure 7.15b and is a good approximation for the second derivative of the polynomial surface at P (Figure 7.15b). A FORC diagram is the contour plot rotated such that $H_c = (H_b - H_a)/2$ and $H_u = (H_a + H_b)/2$. Please note that because $H_a < H_b$, data are only possible for positive H_c.

Imagine we travel down the descending magnetization curve (dashed line in Figure 7.15a) to a particular field $\mu_o H_a$ less than the smallest flipping field in the assemblage. If the particles are single domain, the behavior is reversible and the first FORC will travel back up the descending curve. It is only when $|\mu_o H_a|$ exceeds the flipping field of some of the particles that the FORC will trace a new curve on the inside of the hysteresis loop. In the simple single domain, non-interacting, uniaxial magnetite case, the FORC density in the quadrants where H_a and H_b are of the same sign must be zero. Indeed, FORC densities will only be non-zero for the range of flipping fields because these are the bounds of the flipping field distribution. So the diagram in Figure 7.15c is nearly that of an ideal uniaxial SD distribution.

Consider now the case in which a particle has domain walls. Walls can move much more easily than flipping the moment of an entire grain coherently. In fact, they begin to move in small jumps (from LEM to LEM) as soon as the applied field changes. If a wall nucleates while the field is decreasing and the field is then ramped back up, the magnetization curve will not be reversible, even though the field never changed sign or approached the flipping field for coherent rotation. The resulting FORC for such behavior would have much of the action in the region where H_a is positive. When transformed to H_u and H_c, the diagram will have the highest densities for small H_c but over a range of $\pm H_u$ as shown in Figure 7.16.

7.5.1 Which FORC should you use?

FORC diagrams take hours to create while a single hysteresis loop takes minutes. In many cases the the most interesting thing one learns from FORC diagrams is the degree to which there is

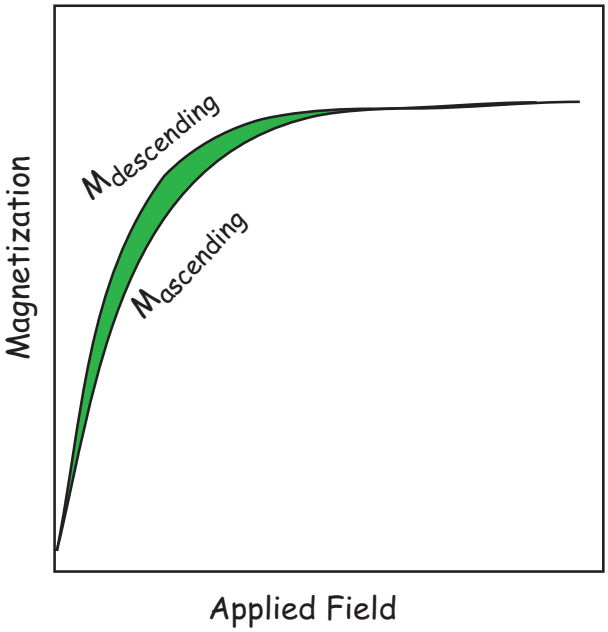

Figure 7.17: Illustration of a Zero FORC (ZFORC) whereby the descending loop from satruation is terminated at zero field and the field is then ramped back up to saturation. The transient hysteresis (TH) of Fabian (2003) is the shaded area between the two curves.

irreversible behavior when the field is reduced to zero then ramped back up to saturation (see Figure 7.17). Such irreversible behavior in what Yu and Tauxe (2004) call the "Zero FORC" or ZFORC can arise from particle interactions, domain wall jumps or from the formation and destruction of vortex structures in the magnetic grains.

Fabian (2003) defined a parameter called "transient hysteresis" which is the area between the ascending and descending loops of a ZFORC (shaded area in Figure 7.17). This is defined as:

$$TH = \sum_{0}^{B_s} [M_{descending} - M_{ascending}] \cdot \Delta B.$$

where ΔH is the field increment used in the hysteresis measurement. When normalized by M_s, TH has units of B (tesla).

Transient hysteresis is thought to result from self demagnetization, for example shifting of domain walls or the formation and destruction of vortex structures. An example of what might be causing transient hysteresis at the macro scale is shown for micromagnetic modelling of a single particle in Figure 7.18 (Yu and Tauxe, 2004). The ZFORC starts and ends at saturation. On the descending loop, a vortex structure suddenly forms, at the point on the hysteresis loop labelled a), sharply reducing the magnetization. The magnetization state just before the jump is shown as snapshot labelled "descending branch". The vortex remains along the ascending branch until much higher fields (see snapshot labelled "ascending branch"). The irreversible behavior of millions of particles with different sizes and shapes leads to the total transient hysteresis of the macro specimen. In general, Tauxe and Yu (2004) showed that the larger the particle, the greater the transient hysteresis, until truly multi-domain behavior essentially closed the loop, precluding the

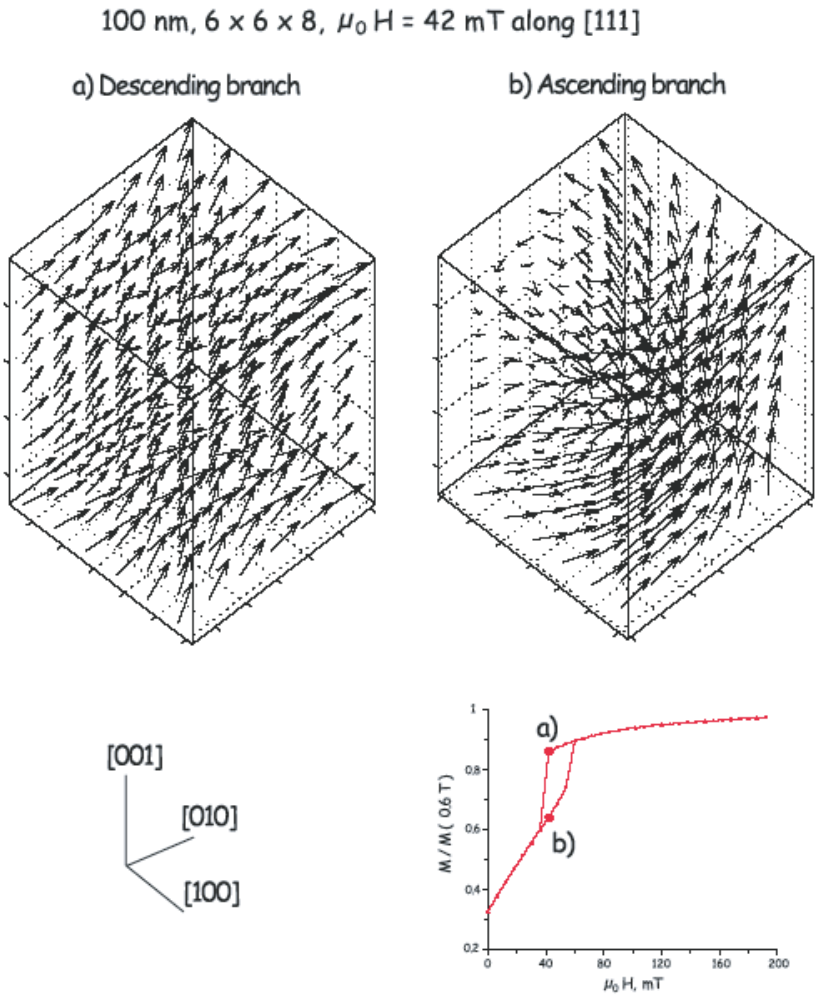

Figure 7.18: Example of source of transient hysteresis from micromagnetic modelling of a 100 nm particle undergoing a ZFORC experiment. (Figure from Yu and Tauxe, 2004.)

observation of TH (or of a FORC diagram for that matter).

7.6 A glimpse at particle interaction

Much of the character of hysteresis loops is frequently attributed to interaction between particles, something that is extremely difficult to model and up until recently impossible to observe. A new technique for imaging of both the composition and the magnetization of particles on a nanoscale (e.g., Harrison et al. 2002) allows a glimpse at the magnetization structure of tiny, interacting particles. In Figure 7.19, we show an example of the mapping of iron and titanium (top panel) and the magnetic structure inferred from "off-axis electron holography" from Harrison et al. (2002). The figure shows both uniform magnetization and vortex structures within particles and super vortex structures from magnetostratic interaction fields between particles.

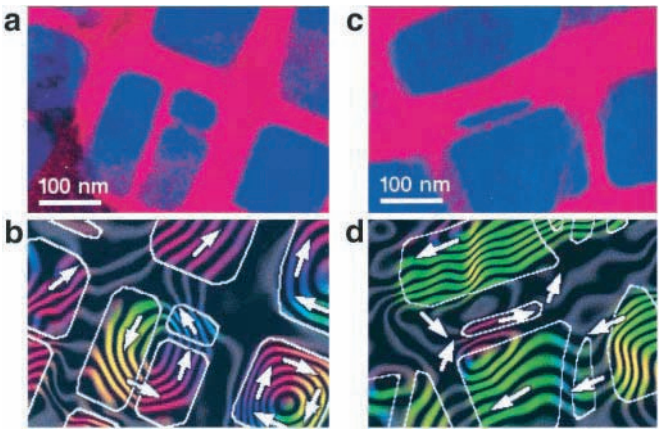

Figure 7.19: Top panel: chemical maps with iron in blue and titanium in red. These define the lamellar intergrowths of magnetite/ulvöspinel. Bottom panel: Associated magnetic microstructure. The arrows show the direction of magnetization inferred from off axis electron holography. [Figure from Harrison et al. 2002.]

Appendix

A Superparamagnetism

The derivation of superparamagnetism follows closely that of paramagnetism whereby the probability of finding a magnetization vector an angle α away from the direction of the applied field is give by:

$$n(\alpha)d\alpha = 2\pi n_o e^{(\frac{M_s Bv \cos\alpha}{kT})} \sin\alpha d\alpha. \tag{A1}$$

The total magnetization contributed by the N moments is:

$$\frac{M}{M_s} = \int_0^\pi \cos\alpha n(\alpha) d\alpha. \tag{A2}$$

Combining (A1) and (A2) we get

$$\frac{M}{M_s} = N\frac{\int_0^\pi n(\alpha)\cos\alpha d\alpha}{\int_0^\pi n(\alpha)d\alpha}$$

$$= N\frac{\int_o^\pi e^{(M_s Bv\cos\alpha)/kT}\cos\alpha\sin\alpha d\alpha}{\int_o^\pi e^{(M_s Bv\cos\alpha)/kT}\sin\alpha d\alpha}.$$

By substituting $M_s Bv/kT = \gamma$ and $\cos\alpha = x$, we write

$$\frac{M}{M_s} = N\frac{\int_1^{-1} e^{\gamma x} x dx}{\int_1^{-1} e^{\gamma x} dx} = N(\frac{e^\gamma + e^{-\gamma}}{e^\gamma - e^{-\gamma}} - \frac{1}{\gamma}) \tag{A3}$$

and finally

$$\frac{M}{M_s} = N(\coth\gamma - \frac{1}{\gamma}). \tag{A4}$$

where $\gamma = \frac{M_s Bv}{kT}$ and N is the number of particles of volume v.

Bibliography

Butler, R. F. (1992), *Paleomagnetism: Magnetic Domains to Geologic Terranes*, Blackwell Scientific Publications.

Fabian, K. (2003), 'Some additional parameters to estimate domain state from isothermal magnetization measurements', *Earth and Planetary Science Letters* **213**(3-4), 337–345.

Halgedahl, S. & Fuller, M. (1983), 'The dependence of magnetic domain structure upon magnetization state with emphasis upon nucleation as a mechanism for pseudo-single domain behavior', *J. Geophys. Res.* **88**, 6505–6522.

Joffe, I. & Heuberger, R. (1974), 'Hysteresis properties of distributions of cubic single-domain ferromagnetic particles', *Phil. Mag.* **314**, 1051–1059.

Mayergoyz, I. (1986), 'Mathematical models of hysteresis', *IEEE Trans. Magn.* **MAG-22**, 603–608.

O'Reilly, W. (1984), *Rock and Mineral Magnetism*, Blackie.

Pike, C. R., Roberts, A. P., Dekkers, M. J. & Verosub, K. L. (2001), 'An investigation of multidomain hysteresis mechanisms using FORC diagrams', *Physics of The Earth and Planetary Interiors* **126**(1-2), 11–25.

Pike, C., Roberts, A. & Verosub, K. (1999), 'Characterizing interactions in fine magnetic particle systems using first order reversal curves', *J. Appl. Phys.* **85**, 6660–6667.

Stoner, E, C. & Wohlfarth, W. P. (1948), 'A mechanism of magnetic hysteresis in heterogeneous alloys', *Phil. Trans. Roy. Soc. Lond.* **A240**, 599–642.

Tauxe, L., Bertram, H. & Seberino, C. (2002), 'Physical interpretation of hysteresis loops: Micromagnetic modelling of fine particle magnetite', *Geochem., Geophys., Geosyst.* **3**, DOI 10.1029/2001GC000280.

Tauxe, L., Mullender, T. A. T. & Pick, T. (1996), 'Potbellies, wasp-waists, and superparamagnetism in magnetic hysteresis', *Jour. Geophys. Res.* **101**, 571–583.

Wohlfarth, E. P. (1958), 'Relations between different modes of acquisition of the remanent magnetisation of ferromagnetic particles', *J.of App. Phys.* **29**, 595–596.

Yu, Y. & Tauxe, L. (2004), 'On the use of magnetic transient hysteresis in paleomagnetism for granulometry', *Geochem., Geophys., Geosyst.* **6**, Q01H14; doi: 10.1029/2004GC000839.

Lectures in Paleomagnetism - DRAFT

Lisa Tauxe
Suggested Citation:
Lisa Tauxe, "Lectures in Paleomagnetism", 2005, Essayo Press,
http://repositories.cdlib.org/sio/library/8

April 3, 2005

Chapter 8

Applied Rock (Environmental) Magnetism

Suggested Reading

For background:
Chapter 1: Maher, B and Thompson, R., 1999.
Chapter 4: Evans and Heller 2003

8.1 Introduction

There is a lively field within paleomagnetism that attempts to exploit the dependence of rock magnetic parameters on concentration, grain size and mineralogy for the purpose of gleaning information about past (and present) environments. Applications in applied rock magnetism *(environmental magnetism)* run from detection of industrial pollution to characterizing climatic change across major climatic events to constraining rainfall variations across Asia during the Quaternary. In this lecture we will review the basic tool-kit used by environmental magnetists and illustrate various applications with examples.

8.2 Applied rock magnetism toolkit

There are four basic methodologies involved in most applied rock magnetism studies: imaging of magnetic separates, hysteresis parameter estimation, thermomagnetic measurements (including Curie Temperature determination and low temperature measurements) and anhysteretic remanence (ARM) measurements. Imaging is done using optical, scanning electron and transmission electron microscopes (see e.g., Figure 8.1a) on magnetic separates, or thin sections. Hysteresis measurements (including magnetic susceptibility) are made on vibrating sample magnetometers (VSMs), alternating gradient force magnetometers (AGFMs: see Lecture 7), and susceptibility meters (Figure 8.1b) of various sorts. These measurements can be done as a function of frequency or temperature. Thermomagnetic measurements are made on a "Curie Balance" (Figure 8.1c) which measures saturation magnetization as a function of temperature. ARMs are measured using an instrument that applies a large, alternating field (an AF demagntetizer) in the presence of a small DC bias field (see Lecture 5).

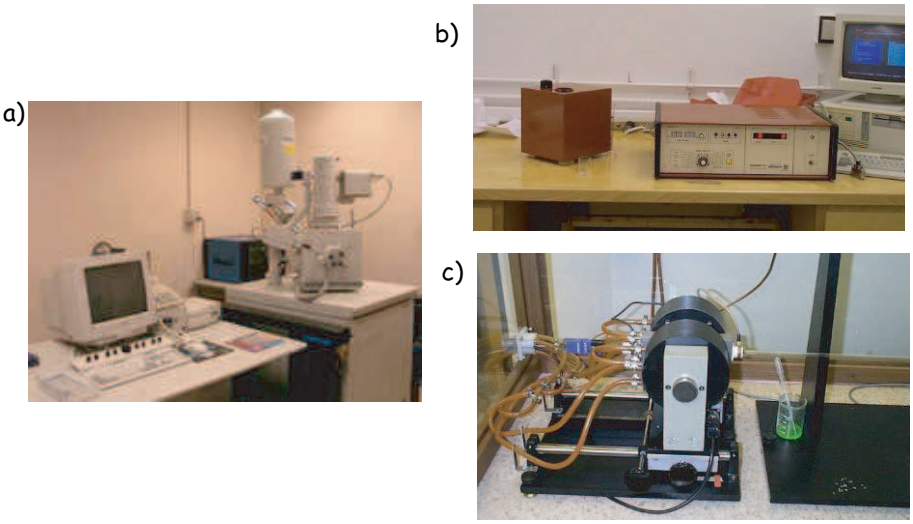

Figure 8.1: Some of the workhorse instruments of the practicing environmental magnetist. a) A scanning electron microscope. b) A susceptibility meter. c) A curie balance.

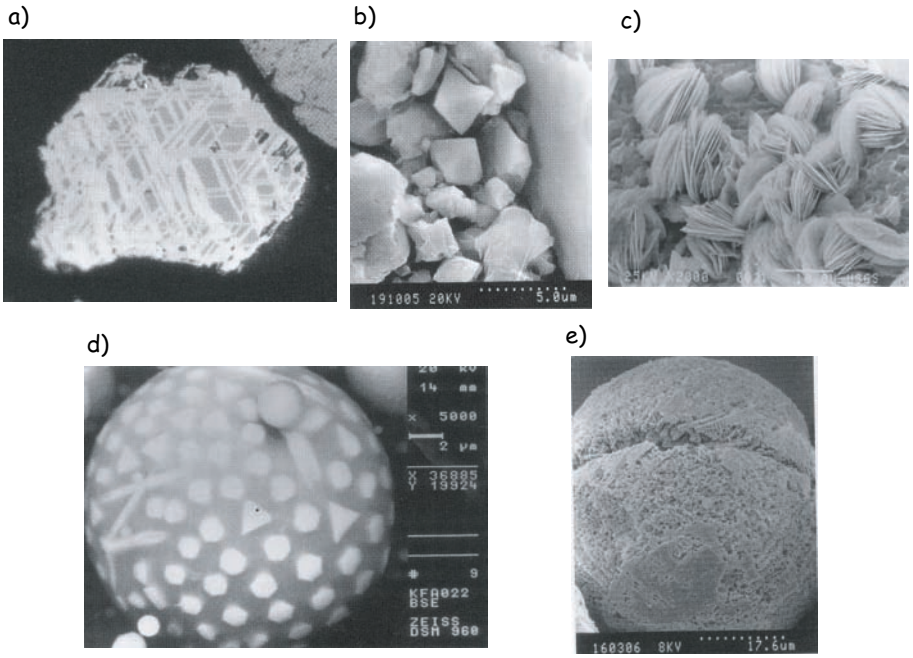

Figure 8.2: Images of magnetic phases from Maher and Thompson (1999) . a) 300 μm titanomagnetite grain of igneous origen showing high temperature exsolution lamellae b) Detrital and aeolian (titano)magnetites from Chinese Loess. (from Maher and Thompson, 1999). c) Hematite rosettes on a smectite surface. d) Backscatter SEM image of fly-ash spherule. The bright grains are iron rich particles embedded in a silicate matrix. e) Silicate spherule with dendrites of Fe-rich material of cosmic origin, showing characteristic pitting of the surface.

8.2.1 Images

Images of magnetic phases are used to constrain the origin of the magnetic phases. Igneous (Figure 8.2a), detrital or aeolian (Figure 8.2b), authigenic (Figure 8.2c), biogenic (Lecture 6), anthropogenic (Figure 8.2d) and cosmic (Figure 8.2e) sources all have distinctive ear-marks, so actually looking at the particles in question can provide invaluable information.

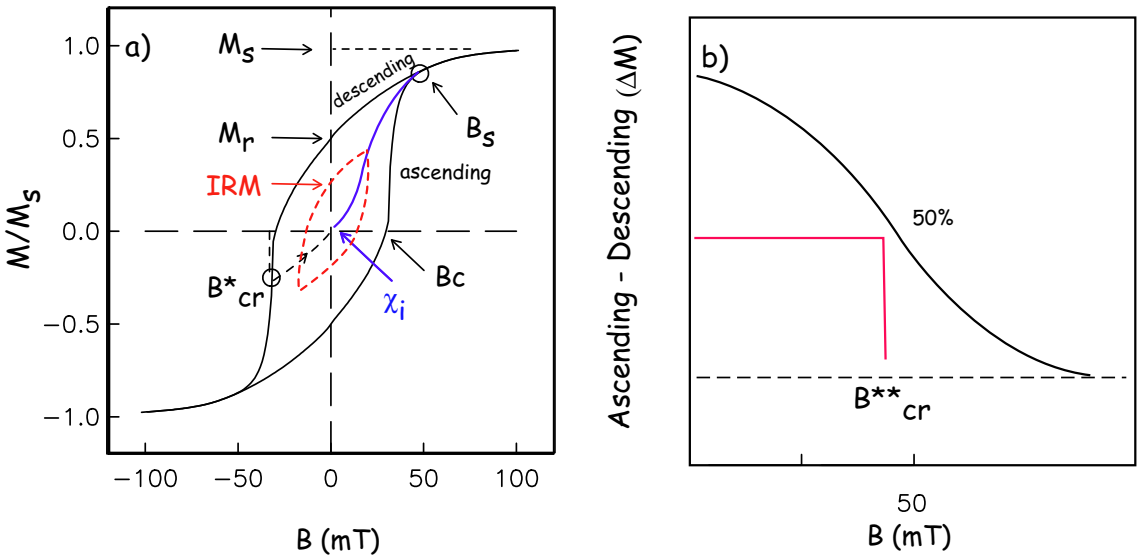

Figure 8.3: Definition of various hysteresis parameters.

8.2.2 Hysteresis parameter estimation

Hysteresis behavior is strongly controlled by mineralogy and grain size, hence hysteresis loops have the potential to help constrain the makeup of a given rock specimen. The hysteresis loop of a given sample will be the sum of all the curves generated by the individual grains. Each population of grains with a consistent coercivity spectrum will leave its imprint on the resulting loop.

We have already encountered hysteresis loops in Lecture 7 and many of the associated parameters that characterize them. There are a few more, however, that are useful in environmental magnetism (see Figure 8.3).

The slope relating magnetization and applied (low) fields is called the initial magnetic susceptibility (χ_i) (see Lectures 1 and 3). This is a reversible measurement and if the field is low enough, the magnetization will return to its initial state when the field is turned off.

Because the response to an external field is greatly enhance if a particle is superparamagnetic, SP grains are hugely more susceptible than an equivalently sized SD grain. The definition of whether a given grain is SP or not depends on the time scale of observation, so a grain can be SP over a long period (and come into equilibrium with the applied field) but be SD over a shorter time scale (and have only a sluggish response to a small applied field). Therefore χ_i is strongly frequency dependent (as well as being strongly temperature dependent). Some instruments allow the measurement of χ_i at various frequencies allowing the definition of the so-called frequency

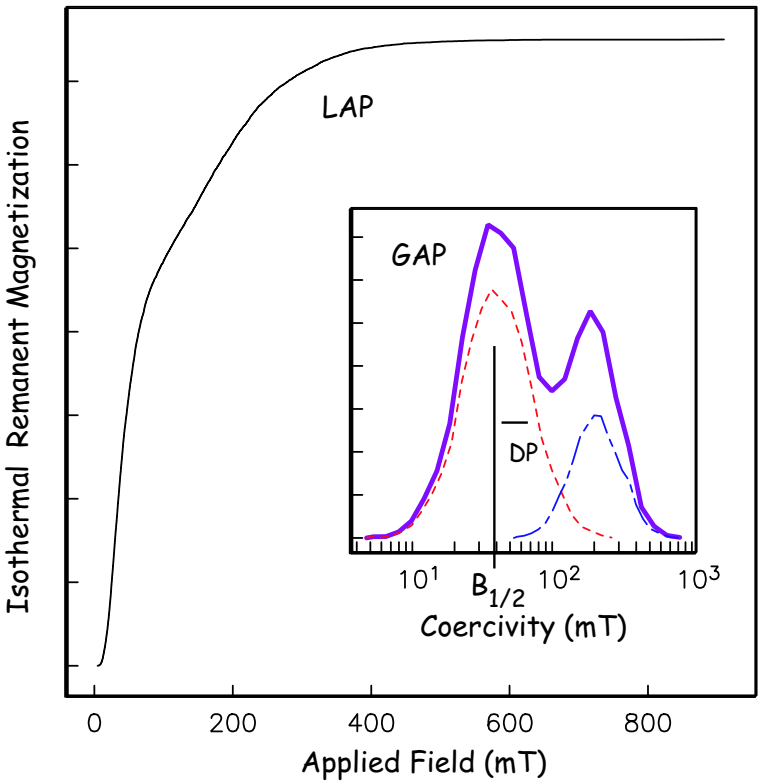

Figure 8.4: Theoretical curve for the acquisition of IRM with two magnetic components with different coercivfity spectra (see insert). The acquisition curve can be differentiated to get the heavy solid line in the insert and then decomposed into the different components assuming some distribution of coercivity (in this case log-normal). The main plot is a "linear acquisition plot" (LAP) and the heavy solid line in the inset is a "gradient of acquisition plot" (GAP) in the terminology of Kruiver et al. (2001). $B_{1/2}$ and DP are the fields required to magnetize half the population and the "dispersion parameter" of Robertson and France (1994). Note that $B_{1/2}$ is the same as B'_{cr} if there is only one population of coercivities.

dependent susceptibility or χ_{fd}. This is often used to estimate the contribution of SP particles to the total susceptibility.

As the applied magnetic field increases, individual particles will reach their flipping fields, or undergo some other irreversible reorganization of spin states (rearranging domain walls, etc.). Saturation magnetization (M_s) is the magnetization measured in the presence of a saturating field (B_s). This measurement must often be "corrected" for the contribution of paramagnetic minerals whose *high field susceptibility* χ_{hf} must be subtracted. Fortunately, paramagnetic behavior is linear up to several tesla so can usually be estimated and removed. If we subtract the high field susceptibility (which is only the paramagnetic contribution) from the initial susceptibility, we can estimate the contribution of the ferrimagnetic (*sensu lato*) particles or χ_{ferri}.

Susceptibility can also be measured as a function of the orientation of the specimen with respect to the applied magnetic field. If the susceptibility is independent of orientation, it is said to be isotropic. Anisotropic orientations of magnetic minerals can lead to an anisotropic magnetic susceptibility response which in turn can be interpreted in terms of preferred orientation of magnetic

phases. This topic will be addressed in later lectures.

The portion of the hysteresis loop that is recorded while the field is ramping up is called the *ascending* loop and the return portion recorded as the field is ramping down is the *descending* loop. Once the field is high enough, irreversible changes in the magnetization of the sample take place and the magnetization will no longer return to its initial state after the field is switched off; it displays hysteresis (see Lecture 7). The magnetization thus acquired is an IRM (see Lecture 5). The remanence remaining after application of a saturating field was termed saturation remanence M_r in Lecture 7 (also known as M_{rs} or M_{sr} in the literature). It is also synonymous with the saturation IRM (sIRM).

As mentioned in Lecture 5, the coercive field (B_c) is that field required to reduce the net magnetization to zero and the bulk coercivity of remanence (B_{cr}) is the field necessary to flip half the magnetic moments (so when the field is turned off, the remanence is reduced to zero). Two ways of estimating B_{cr} were described in Lecture 5 (B_{cr} and B'_{cr}. A third way is the intersection method described in Lecture 7 ($B*_{cr}$). A fourth way is the ΔM method illustrated in Figure 8.3b whereby the difference between the ascending and descending loops (ΔM) from Figure 8.3a is plotted versus applied field. The field at which the value of ΔM is 50% of the maximum is here called $B**_{cr}$.

Robertson and France (1994) suggested that if populations of magnetic materials have generally log-normally distributed coercivity spectra and if the IRM is the linear sum of all the contributing grains, then an IRM acquisition curve could be "unmixed" into the contributing components. The basic idea is illustrated in Figure 8.4 whereby two components each with log normally distributed coercivity spectra (see dashed and dashed-dotted lines in the inset) create the IRM acquisition curve shown. Thus by obtaining a very well determined IRM acquisition plot (the "linear acquisition plot" or LAP in Figure 8.4 using the terminology of Kruiver et al., 2001), one could first differentiate it to get the "gradient acquisition plot" or GAP using the terminology of Kruiver et al., 2001 (heavy solid line in the inset to Figure 8.4). This then can be "unmixed" to get the parameters of the contributing components such as the mean and standard deviation of the log-normal distribution (called $B_{1/2}$ and DP respectively by Robertson and France, 1999). Note that $B_{1/2}$ is synonymous with B_{cr} if there is only one population of coercivities. Also, other forms of magnetic remanence (e.g., ARM), demagnetization as well as acquisition, and other distributions are also possible as are fancier methods of inversion (see e.g., Egli 2003).

8.2.3 Combining thermal and isothermal information for rock magnetic characterization

Another very useful technique for characterizing the magnetic mineralogy in a sample is the Lowrie 3D IRM technique (Lowrie, 1990). Some important magnetic phases in geological materials (Table 1; Lecture6) are magnetite (maximum blocking temperature of ~580°C, maximum coercivity of about 0.3 T), hematite (maximum blocking temperature of ~ 675°C and maximum coercivity much larger than 5 T), goethite (maximum blocking temperature of ~ 125°C and maximum coercivity of much larger than 5 T), and various sulfides. The relative importance of these minerals in bulk samples can be constrained by a simple trick that exploits both differences in coercivity and unblocking temperature (Lowrie, 1990).

The Lowrie "3D IRM test" proceeds as follows:

- Apply an IRM along three orthogonal directions in three different fields. The first field, applied along $\mathbf{X}_1$, should be sufficient to saturate all the minerals within the sample

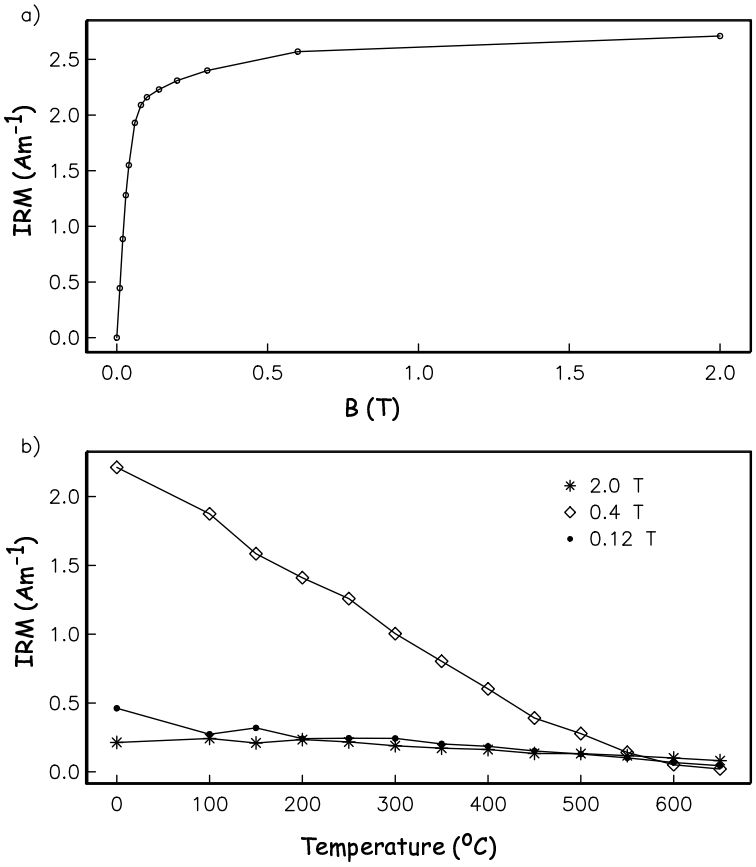

Figure 8.5: a) Acquisition of IRM (M_r). After applying a field of 2 T, the sample was subjected to two additional IRMs: 0.4 T and 0.12 T along orthogonal axes. b) Thermal demagnetization of a 3-axis IRM. Each component is plotted separately.

and is usually the largest field achievable in the laboratory (say 2 T). The second field, applied along $\mathbf{X}_2$, should be sufficient to saturate magnetite, but not to realign high coercivity phases, such as goethite or fine-grained hematite (say 0.4 T). The third IRM, applied along $\mathbf{X}_3$, should target low coercivity minerals and the field chosen is typically something like 0.12 T.

• The composite magnetization can be characterized by determining the blocking temperature spectra for each component. This is done by thermally demagnetizing the sample and plotting the magnitude of the three cartesian components (x_1, x_2, x_3) versus demagnetizing temperature.

An example of 3D IRM data are shown in Figure 8.5. The curve is dominated by a mineral with a maximum blocking temperature of between 550° and 600°C and has a coercivity less than 0.4 T, but greater than 0.12 T. These properties are typical of magnetite (Table 1; Lecture 6). There is a small fraction of a high coercivity (>0.4 T) mineral with a maximum unblocking temperature > 650°C, which is consistent with the presence of hematite (Table 1; Lecture 6).

IRM and ARM acquisition and demagnetization curves could be a rich source of information about the magnetic phases in rocks. However, these are extremely time consuming to measure

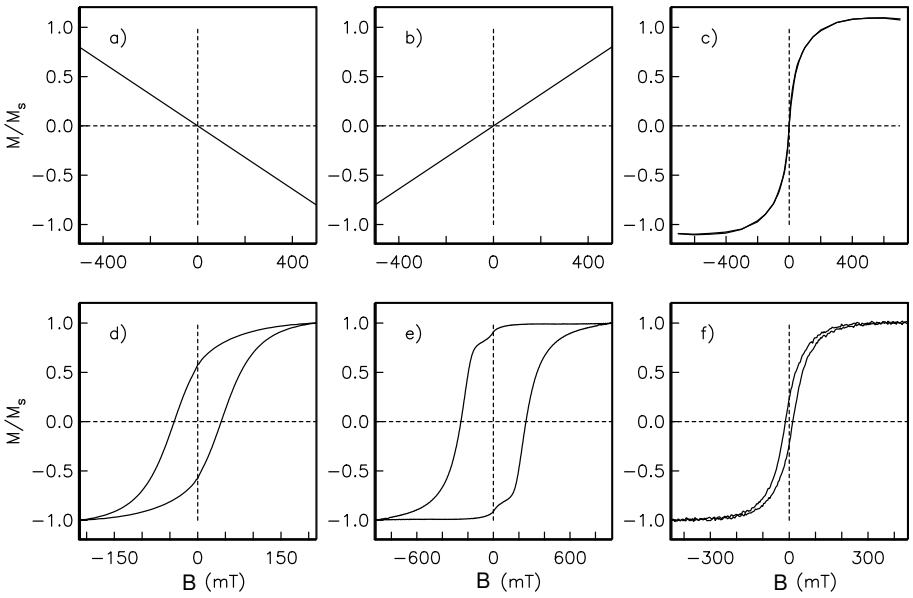

Figure 8.6: Hysteresis loops of end-member behaviors: a) diamagnetic, b) paramagnetic, c) superparamagnetic (data for submarine basaltic glass), d) uniaxial, single domain, e) magnetocrystalline, single domain, f) "pseudo-single domain".

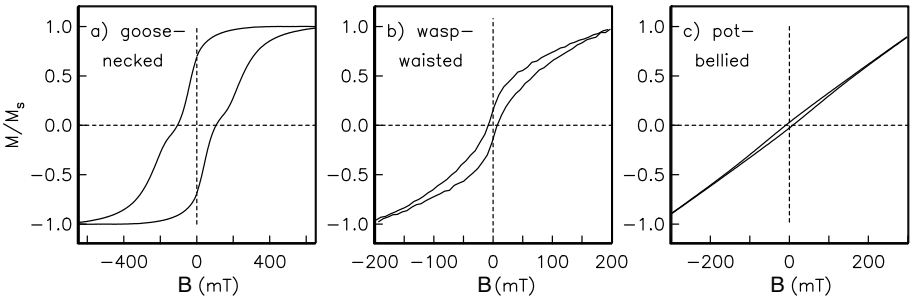

Figure 8.7: Hysteresis behavior of various mixtures: a) magnetite, and hematite, b) SD/SP magnetite (data from Tauxe et al. 1996), c) another example of SD/SP magnetite.

taking hours for each one. Hysteresis loops on the other hand are quick, taking about 10 minutes to measure the outer loop. In principle, the same information could be had from hysteresis loops as in the IRM acquisition curves.

Hysteresis loops, like IRM acquisition curves are the sum of all the contributing particles in the sample. There are several basic types of loops which are recognized the "building blocks" of the hysteresis loops we measure on geological materials. We illustrate some of the building blocks of possible hysteresis loops in Figure 8.6. Figure 8.6a shows the negative slope typical of diamagnetic material such as carbonate or quartz, while Figure 8.6b shows a paramagnetic slope. Such slopes are common when the sample has little ferromagnetic material and is rich in iron-bearing phases such as biotite or clay minerals.

When grain sizes are very small, a sample can display superparamagnetic "hysteresis" behavior (Figure 8.6c). The SP curve follows a Langevin function $L(a)$ (see Lecture 7) where a is $M_s vB/kT$,

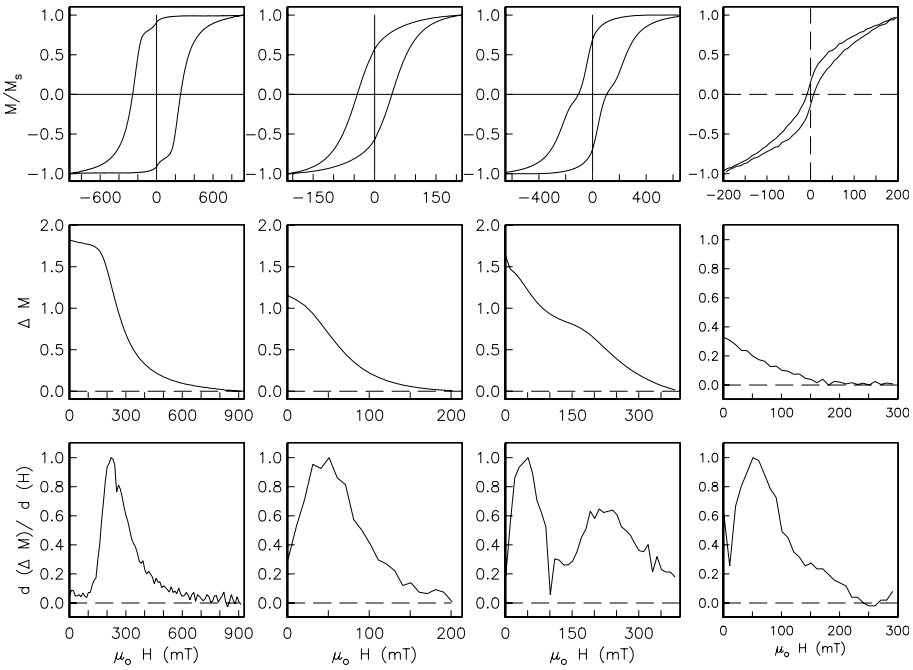

Figure 8.8: Top panels: hysteresis curves, middle panels: ΔM curves and bottom panels: $d\Delta M/dH$ curves. From the left to right: hematite, SD magnetite, hematite plus magnetite, and SD plus SP magnetite.

but integrates over the distribution of v in the sample.

Above some critical volume, grains will have relaxation times that are sufficient to retain a stable remanence (Lecture 5). As discussed in Lecture 7, populations of randomly oriented stable grains can produce hysteresis loops with a variety of shapes, depending on the origin of magnetic anisotropy and domain state. We show loops from samples that illustrate representative styles of hysteresis behavior in Figure 8.6d-f. Figure 8.6d shows a loop characteristic of samples whose remanence stems from SD magnetite with uniaxial anisotropy. In Figure 8.6e, we show data from specular hematite whose anisotropy is magnetocrystalline in origin (hexagonal within the basal plane). Note the very high M_r/M_s ratio of nearly one. Finally, we show a loop that has lower M_r/M_s ratios than single domain, yet some stability. Loops of this type have been characterized as *pseudo-single domain* PSD (Figure 8.6f). We now know that PSD behavior is typical of vortex remanence state particles.

In the messy reality of geological materials, we often encounter mixtures of several magnetic phases and/or domain states. Such mixtures can lead to distorted loops, such as those shown in Figure 8.7. In Figure 8.7a, we show a mixture of hematite plus SD-magnetite. The loop is distorted in a manner that we refer to as *goose-necked*. Another commonly observed mixture is SD plus SP magnetite which can result in loops that are either *wasp-waisted* (see Figure 8.7b) or *pot-bellied* (see Figure 8.7c).

Considering the loops shown in Figure 8.7, we immediately notice that there are two distinct causes of loop distortion: mixing two phases with different coercivities and mixing SD and SP domain states. We differentiate the two types of distortion as "goose-necked" and "wasp-waisted" (see Figure 8.7) because they look different and they mean different things.

Jackson et al. (1990) suggested that the ΔM curve (see Figure 8.3) could be differentiated to reveal different coercivity spectra contained in the hysteresis loop. The ΔM curve and its derivitive ($d\Delta M/dH$) are sensitive only to the remanence carrying phases, and not, for example, to the SP fraction, we can use these curves to distinguish the two sources of distortion. In Figure 8.8, we show several representative loops, along with the ΔM and $d\Delta M/dH$ curves. Distortion resulting from two phases with different coercivities (e.g., hematite plus magnetite or two distinct grain sizes of the same mineral) results in a "two humped" $d\Delta M/dH$ curve, whereas wasp-waisting which results from mixtures of SD + SP populations have only one "hump".

Jackson et al. (1990) also suggested a way to deal with noisy data using Fourier smoothing. This treatment is described in the appendix.

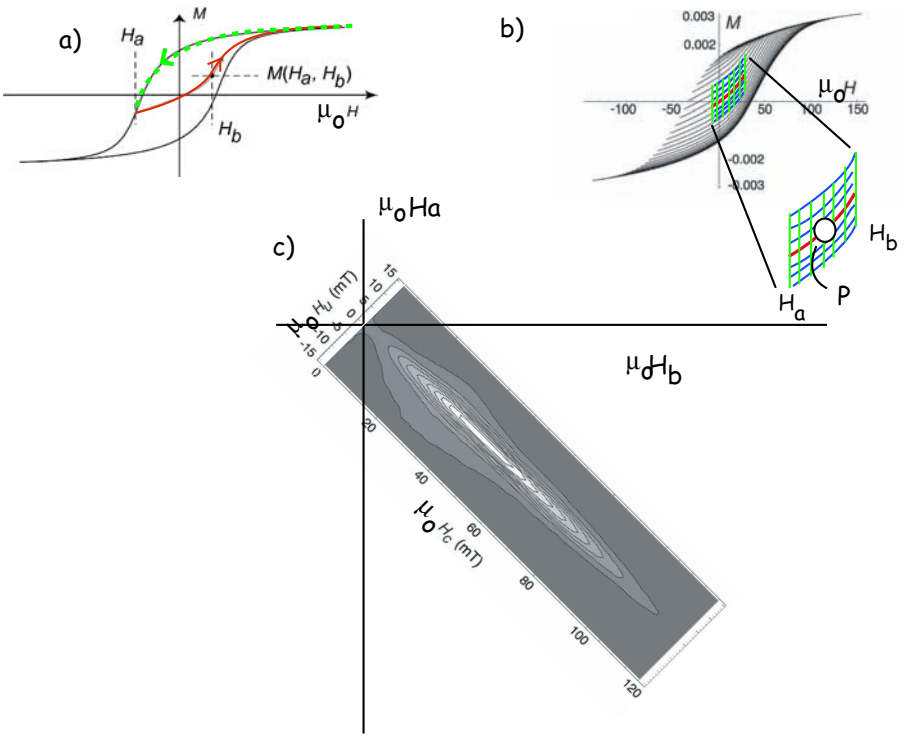

Figure 8.9: a) Dashed line is the descending magnetization curve taken from a saturating field to some field H_a. Red line is the first order reversal curve (FORC) from H_a returning to saturation. At any field $H_b > H_a$ there is a value for the magnetization $M(H_a, H_b)$. b) A series of FORCs for a single domain assemblage of particles. At any point "P" there are a set of related curves making a 7x7 grid. A polynomial surface is fit to these data is estimated. c) A contour plot of the mixed second derivative of the polynomial surface evaluated for points H_a, H_b. (Redrawn from Pike et al., Phys. Earth Planet. Int., 126, 11-25. 2001). Note: all Hs are actually $\mu_o H$.

Hysteresis loops can yield a tremendous amount of information yet much of this is lost by simply estimating the set of parameters $M_r, M_s, B_{cr}, B_c, \chi_i, \chi_{hf}$, etc.. Pike et al. (e.g., 1999) popularized the method of Mayergoyz (1986) or using so-called *First Order Reversal Curves* or FORCs to represent hysteresis data. In the FORC experiment, a sample is subjected to a saturating field, as in most hysteresis experiments. The field is lowered to some field H_a, then increased again through some value H_b to saturation (see Figure 8.9a). [It is unfortunate that the FORC terminology has

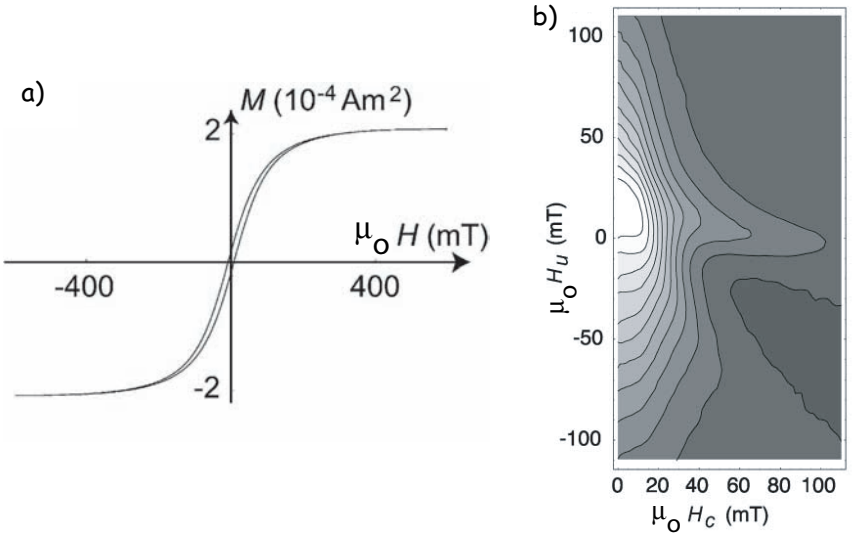

Figure 8.10: a) Hysteresis loop for a large, stressed gain of magnetite prior to annealing. b) FORC diagram from same. (Redrawn from Pike et al., 2001).

chosen to use H_a, yet routinely neglects the necessary μ_o to render these field values in tesla...] The magnetization curve between H_a and H_b is a "FORC". A series of FORCs (see Figure 8.9b) are generated to the desired resolution.

To transform FORC data into some useful form, they are gridded as in the inset in Figure 8.9c. In this example, we take a curve (in red) with its three neighbors on either side (in green), for a smoothing factor of $SF = 3$. The data in the box are fit with a polynomial surface of the form:

$$a_1 + a_2 H_a + a_3 H_a^2 + a_4 H_b + a_5 H_b^2 + a_6 H_a H_b$$

where the a_i are fitted coefficients. The coefficient $-a_6(H_a, H_b)$ is contoured as in the Figure 8.9b and is a good approximation for the second derivative of the polynomial surface at P (Figure 8.9b). A FORC diagram is the contour plot rotated such that $H_c = (H_b - H_a)/2$ and $H_u = (H_a + H_b)/2$. Please note that because $H_a < H_b$, data are only possible for positive H_c.

To interpret these diagrams in a meaningful way, let us return to Lecture 7. Imagine we travel down the descending magnetization curve (dashed line in Figure 8.9a) to a particular field $\mu_o H_a$ less than the smallest flipping field in the assemblage. If the particles are single domain, the behavior is reversible and the first FORC will travel back up the descending curve. It is only when $|\mu_o H_a|$ exceeds the flipping field of some of the particles that the FORC will trace a new curve on the inside of the hysteresis loop. In the simple single domain, non-interacting, uniaxial magnetite case, the FORC density in the quadrants where H_a and H_b are of the same sign must be zero. Indeed, FORC densities will only be non-zero for the range of flipping fields because these are the bounds of the flipping field distribution. So the diagram in Figure 8.9c is nearly that of an ideal uniaxial SD distribution.

Consider now the case in which a particle has domain walls. Walls can move much more easily than flipping the moment of an entire grain coherently. In fact, as we discussed in Lecture 7, they begin to move in small jumps (from LEM to LEM) as soon as the applied field changes. If a wall

nucleates while the field is decreasing and the field is then ramped back up, the magnetization curve will not be reversible, even though the field never changed sign or approached the flipping field for coherent rotation. The resulting FORC for such behavior would have much of the action in the region where H_a is positive. When transformed to H_u and H_c, the diagram will have the highest densities for small H_c but over a range of $\pm H_u$ as shown in Figure 8.10.

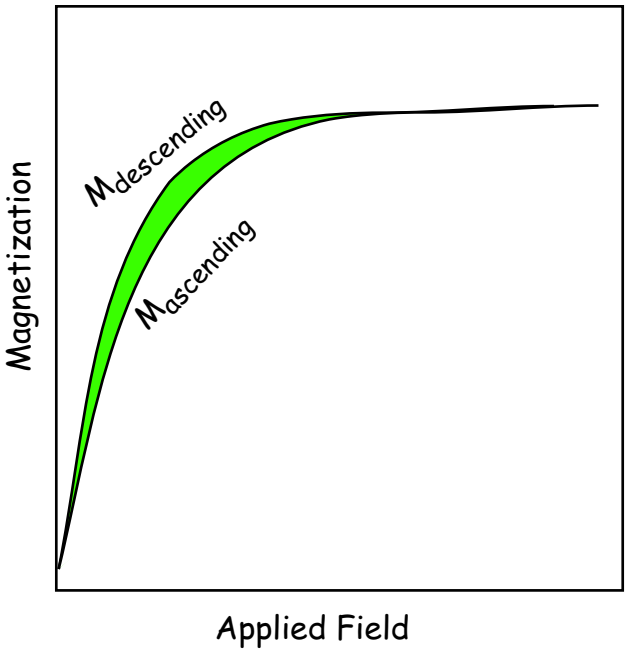

Figure 8.11: Illustration of a Zero FORC (ZFORC) whereby the descending loop from satruation is terminated at zero field and the field is then ramped back up to saturation. The transient hysteresis (TH) of Fabian (2003) is the shaded area between the two curves.

8.2.4 Which FORC should you use?

FORC diagrams take hours to create while a single hysteresis loop takes minutes. In many cases the the most interesting thing one learns from FORC diagrams is the degree to which there is irreversible behavior when the field is reduced to zero then ramped back up to saturation (see Figure 8.11). Such irreversible behavior in what Yu and Tauxe (2004) call the "Zero FORC" or ZFORC can arise from particle interactions, domain wall jumps or from the formation and destruction of vortex structures in the magnetic grains.

Fabian (2003) defined a parameter called "transient hysteresis" which is the area between the ascending and descending loops of a ZFORC (shaded area in Figure 8.11). This is defined as:

$$TH = \sum_{0}^{B_s} [M_{descending} - M_{ascending}] \cdot \Delta B.$$

where ΔH is the field increment used in the hysteresis measurement. When normalized by M_s, TH has units of B (tesla).

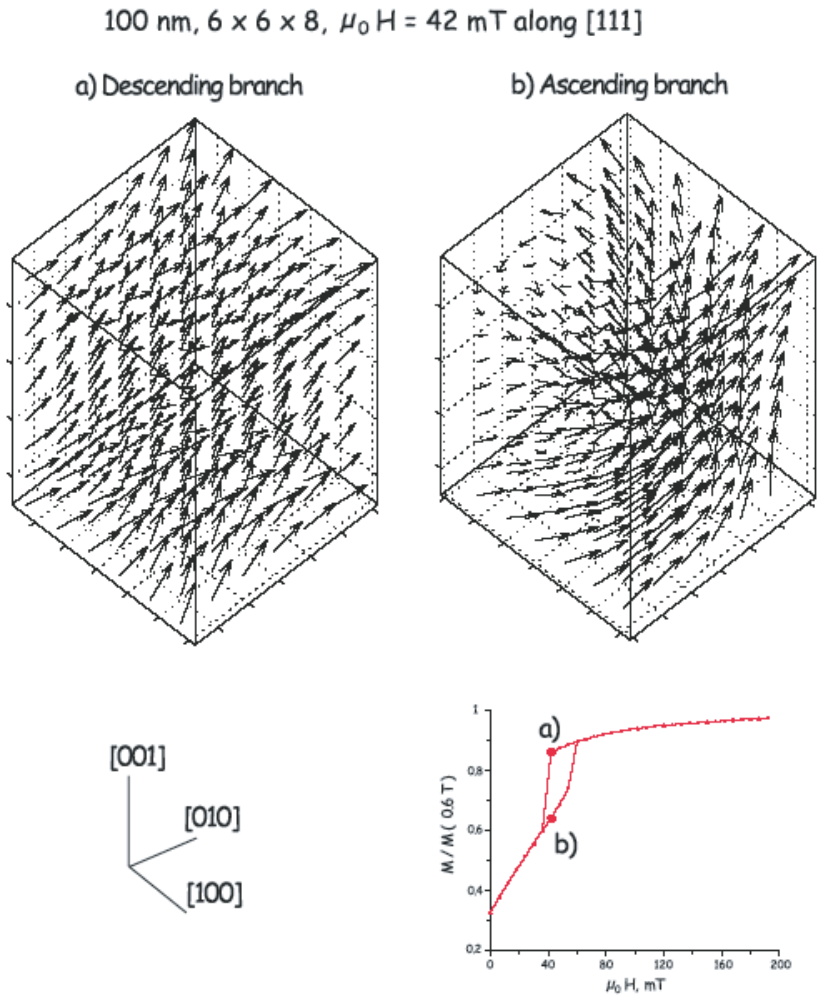

Figure 8.12: Example of source of transient hysteresis from micromagnetic modelling of a 100 nm particle undergoing a ZFORC experiment. (Figure from Yu and Tauxe, 2004.)

Transient hysteresis is thought to result from self demagnetization, for example shifting of domain walls or the formation and destruction of vortex structures. An example of what might be causing transient hysteresis at the macro scale is shown for micromagnetic modelling of a single particle in Figure 8.12 (Yu and Tauxe, 2004). The ZFORC starts and ends at saturation. On the descending loop, a vortex structure suddenly forms, at the point on the hysteresis loop labelled a), sharply reducing the magnetization. The magnetization state just before the jump is shown as snapshot labelled "descending branch". The vortex remains along the ascending branch until much higher fields (see snapshot labelled "ascending branch"). The irreversible behavior of millions of particles with different sizes and shapes leads to the total transient hysteresis of the macro specimen. In general, Tauxe and Yu (2004) showed that the larger the particle, the greater the transient hysteresis, until truly multi-domain behavior essentially closed the loop, precluding the observation of TH (or of a FORC diagram for that matter).

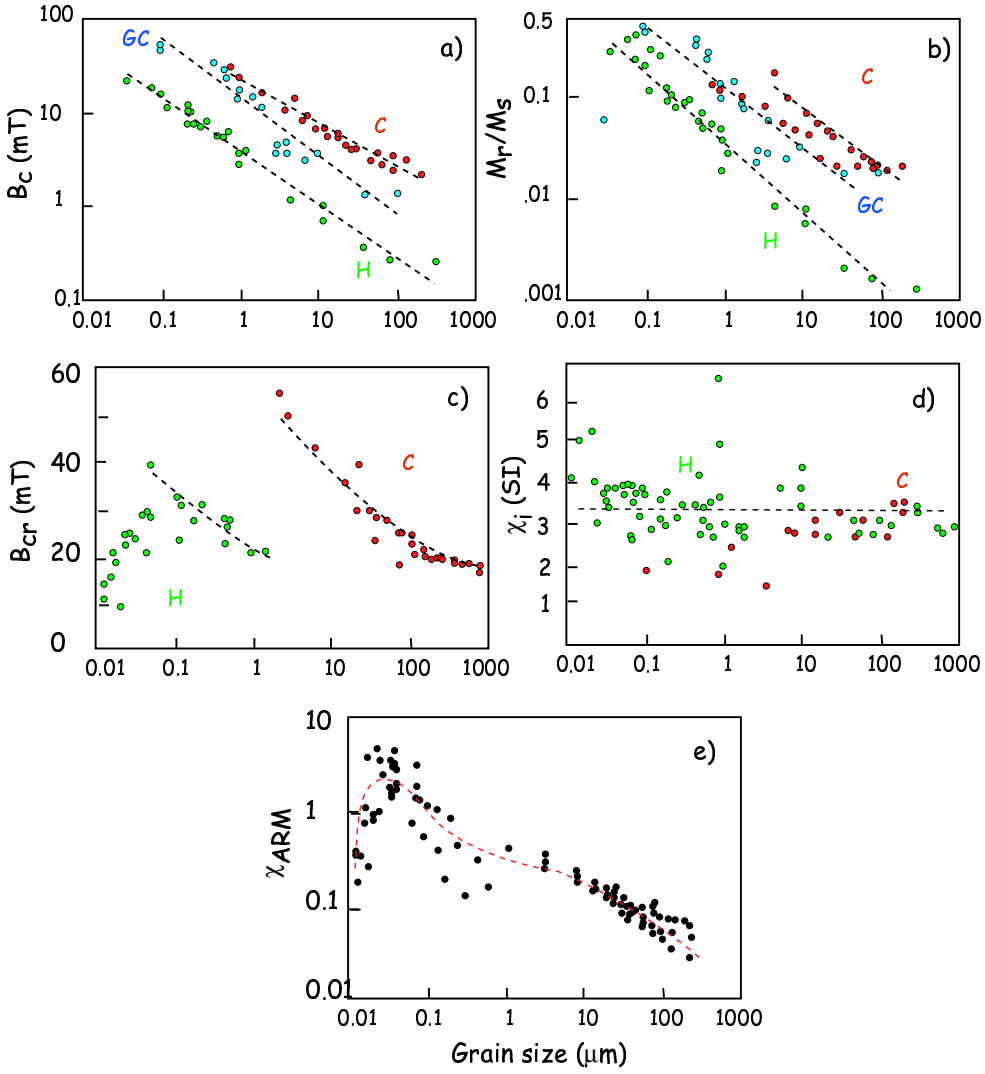

Figure 8.13: Grain size dependence in hysteresis parameters. Crushed grains (red) indicated by "C", glass ceramic grains (blue) indicated by CG; Hydrothermal grains (green) indicated by "H". a) Variation of coercive force (B_c). b) Variation of M_r/M_s. c) Variation of coercivity of remanence B_{cr}. (Data compiled by Hunt et al., 1995.) d) Variation of susceptibility with grain size. (Data compiled by Heider et al., 1996.) e) Variation in ARM with grain size. (Data of Dunlop and Argyle, 1997.)

8.3 Trends in hysteresis parameters with particle dimensions.

One holy grail of applied rock magnetism is a diagnostic set of measurements that will yield unambiguous grain size information. To this end, large amounts of hysteresis data have been collected on a variety of minerals that have been graded according to size and mode of formation. The most complete set of data are available for magnetite, as this is the most abundant magnetic phase in the world. There are three sources for magnetite typically used in these experiments: natural crystals that have been crushed and seived into grain size populatins, crystals that were grown by a glass ceramic technique and crystals grown from hydrothermal solution. In Figure 8.13a-c we show a compilation of grain size dependence of coercive force, remanence ratio, coercivity of remanence respectively. There is a profound dependence not only on grain size, but on mode of formation as well. Crushed particles tend to have much higher coercivities and remanence ratios than grown crystals, presumably because of the increased dislocation density which stabilizes domain walls in much the same manner as do voids. These abnormally high values disappear to a large extent when the particles are annealed at high temperature - a procedure which allows the dislocations to "relax" away.

The behavior of initial magnetic susceptibility is shown in Figure 8.13d. There is no strong trend with grain size over the entire range of grain sizes from single domain to multi-domain magnetite. Susceptibility is predicted to be sensitive to the SD/SP domain state transition, however, because in SP particles, the magnetization is unconstrained by magnetocrystalline or shape anisotropy energies, hence has a larger response to an applied field by a factor of $\ln(C\tau)$. Taking C to be $10^{10}s^{-1}$ and τ to be order 100 s, we find a factor of ~ 28 enhancement of magnetic susceptibility for SP grains over an SD grain of the same volume. This is the basis for using frequency dependence to detect the contribution of SP grains to a population. Because SP behavior depends on the time scale of observation, particles may behave SP at lower frequencies and not at higher frequencies. Because τ is exponentially sensitive to temperature $\chi(T)$ often yields much more information than $\chi(f)$.

Grain size trends in ARM are shown in Figure 8.13e. This trend is very poorly constrained because ARM is also a strong function of concentration and the method by which the particles were prepared. Some (e.g. Banerjee et al., 1981) have suggested that the ratio of ARM (normalized by the DC field applied to get the so-called ARM susceptibility or χ_{ARM} to χ could be used to determine grain size in magnetite, but there are substantial practicle difficulties with this method, unless a great deal is known about concentration, origin of the minerals and magnetic mineralogy.

8.4 Parameter ratios

There is a bewildering array of parameter ratios that are in popular use in the applied rock and mineral magnetism literature: $M_r/M_s, B_{cr}/B_c, ARM/\chi, ARM/M_r, M_r/\chi, IRM(x)/M_r$. The ratios M_r/M_s and B_{cr}/B_c are sensitive to remanence state (SP, SD, flower, vortex, MD) and the source of magetic anisotropy (cubic, uniaxial, stress), hence reveal something about grain size and shape. For this reason Day et al., (1977) began plotting these ratios on a diagram that has since been called the "Day" plot (see e.g., Figure 8.14).

Day plots are divided into regions of supposedly SD, "PSD" and MD behavior using some theoretical bounds as guides (see Lecture 7). The designation PSD stands for *pseudo-single domain* and has M_r/M_s ratios in between those characteristic of SD behavior (0.5 or higher) and MD (.05

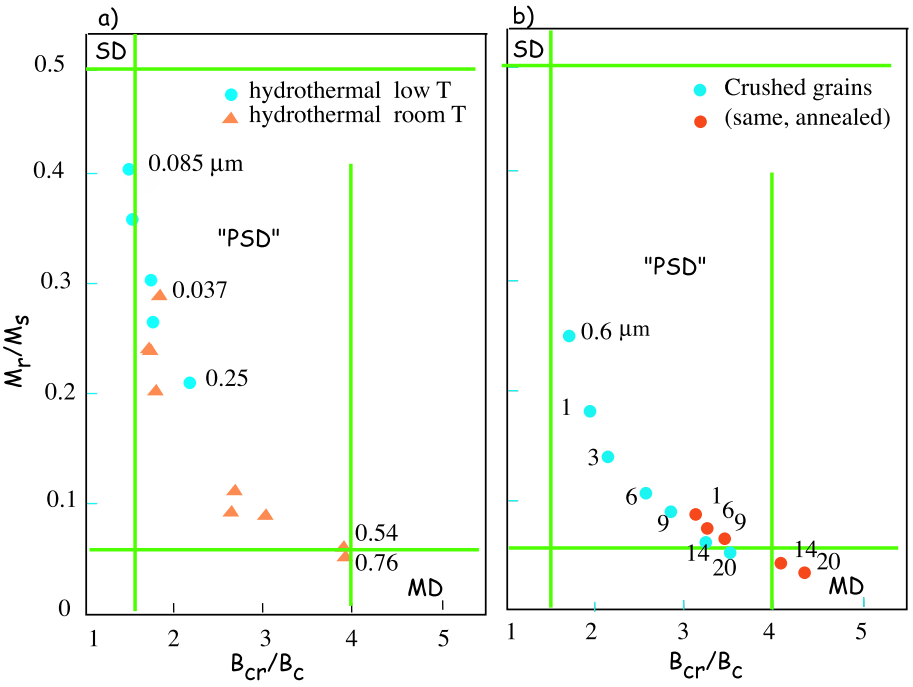

Figure 8.14: Day plot of hysteresis ratios versus grain size and mode of sample preparation. (Redrawn from Dunlop, 2002.)

or lower). In practice nearly all geological materials plot in the PSD box so the usefulness of the Day plot is limited.

Tauxe et al., (2002; see Figure 8.15) suggested that instead of the Day plot, M_r/M_s could be plotted against B_c. This type of plot has been characterized to some extent using micromagnetic modeling techniques to aide in the interpretation of hysteresis data in terms of domain state and origin of magnetic anisotropy energy.

Ratios involving ARM and χ can be complicated because both of these parameters have ratio complicated behaviors themselves. ARM is a strong function of concentration and not monotonic with grain size. χ is a "garbage can" parameter that reflects everything in the sample to some extent. Under certain uncomplicated conditions, both of these parameters can be quite useful, but care should be exercised in their interpretation.

Ratios of a lower back-field IRM (IRM(-x)) to saturation IRM (M_r or sIRM), the so-called *S-ratio*, can be used to quantify the ratio of hard (magnetized at saturation) to soft (remagnetized in the back field direction) minerals in a sample. IRM is less affected by particle interactions so behaves more linearly with concentration.

8.5 Applications

Rock magnetic parameters are relatively quick and easy to measure, compared to geochemical, sedimentological and paleontological data. When used judiciously, they can be enormously helpful in constraining a wide variety of climatic and environmental changes. There are two basic types of plots of the rock and mineral magnetic parameters discussed in this lecture: bi-plots and depth

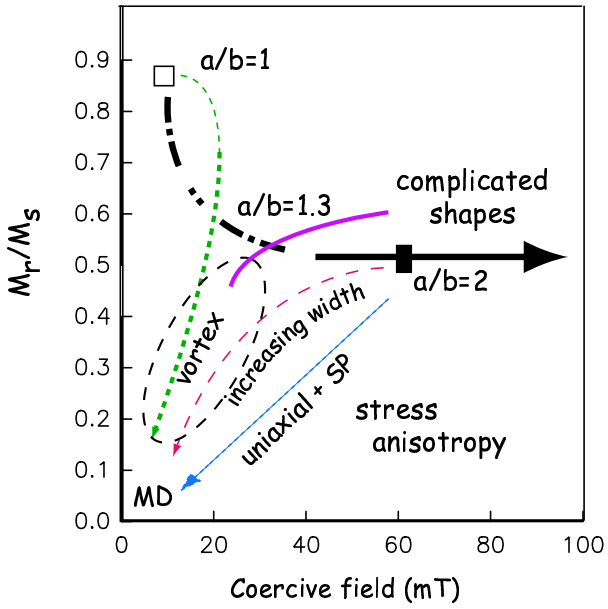

Figure 8.15: Interpretive diagram of M_r/M_s versus coercive field. The open square is the theoretical location of an assemblage of magnetite particles with cubic anisotropy. As the particle grows in length (the length to width ratio a/b approaches 1.5), the simulations plot follow the dash-dot trend. Assemblages with longer SD particles will follow the uniaxial trend indicated by the solid black arrow. SP-Uniaxial numerical simulations (SPUNS) predict the trend indicated by the blue dotted line (Tauxe et al., 1996). Assemblages with larger particle widths of equant grains follow the green dotted line; those of elongate particles follow the red dashed line. As particles become large enough for to be in the vortex remanent state, they plot in the region labelled "PSD". More complicated shapes, such as intersecting rods can give M_r/M_s ratios above 0.5, yet have enormously high stability (region labelled complicated shapes. As these particles grow, their hysteresis data trend along the solid purple line. (From Tauxe et al., 2002.)

plots. Bi-plots, for example ARM versus χ have been in use since Banerjee et al. (1981) first proposed their use (see e.g., Figure 8.16). Biplots can be useful for detecting changes in grain size, concentration, mineralogy, etc. If for example, the data in a plot of M_r verus χ plot on a line, it may be appropriate to interpret the dominant control on the rock magnetic parameters as changes in concentration alone.

Depth plots are useful for core correlation, variations in concentration, mineralogy and grain size as a function of depth. An example of a paleoceanographic application of rock magnetism from Hartl et al. (1995) is illustrated in Figures 8.17 and 8.18. Trends in isotopes and carbonate are shown in Figure 8.17. These indicate a major change in the environment at the end of the Eocene.

IRM and χ were measured as well. The pronounced changes in carbon isotopes appeared to be mirrored in the rock magnetic variations. It was tempting to attribute these variations to be simply related to the complimentary changes in % $CaCO_3$ because both IRM and χ are approximately linear functions of concentration. However, a look at the bi-plot of IRM versus χ (Figure 8.18) shows a more complicated and interesting picture. If the variations in these parameters were only caused by changes in concentration, the bi-plot would show a straight line. Instead, the data plot

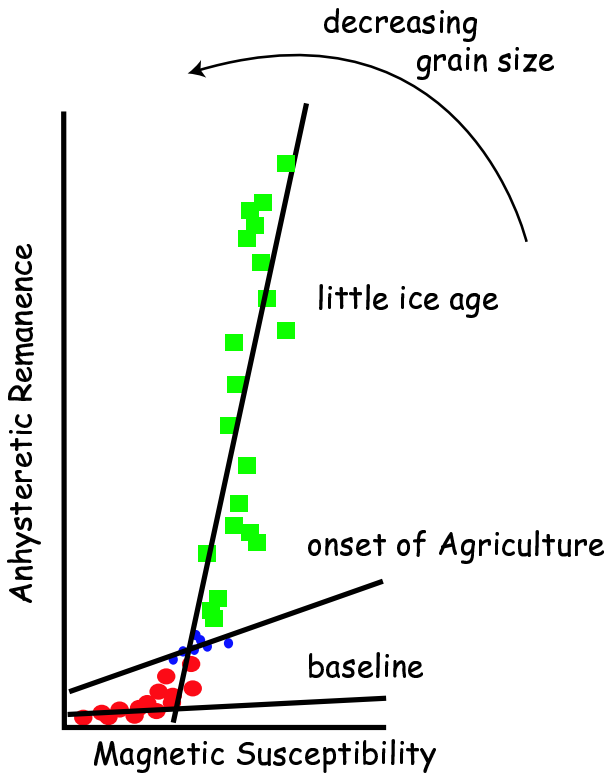

Figure 8.16: Plot of ARM versus magnetic susceptibility for a core from Minnesota. The different slopes are correlated with major climatic and anthropogenic events during the Holocene. (Redrawn from Banerjee et al., 1981).

along two lines with the Eocene data having a different slope and an overall larger constribution to χ than the Oligocene group. As mentioned earlier in the lecture, χ is a very strong function of the fraction of superparamagnetic grains to the population and Hartl et al. (1995) argue that there is a shift in grain size associated with the Eocene Oligocene boundary, with a greater fraction of SP grains in the Eocene than in the Oligocene. A change in magnetic grain size can be the result of changes in the pore water chemistry resulting from changes in organic carbon delivery. This mechanism is consistent with the carbon isotopic variations shown in Figure 8.17.

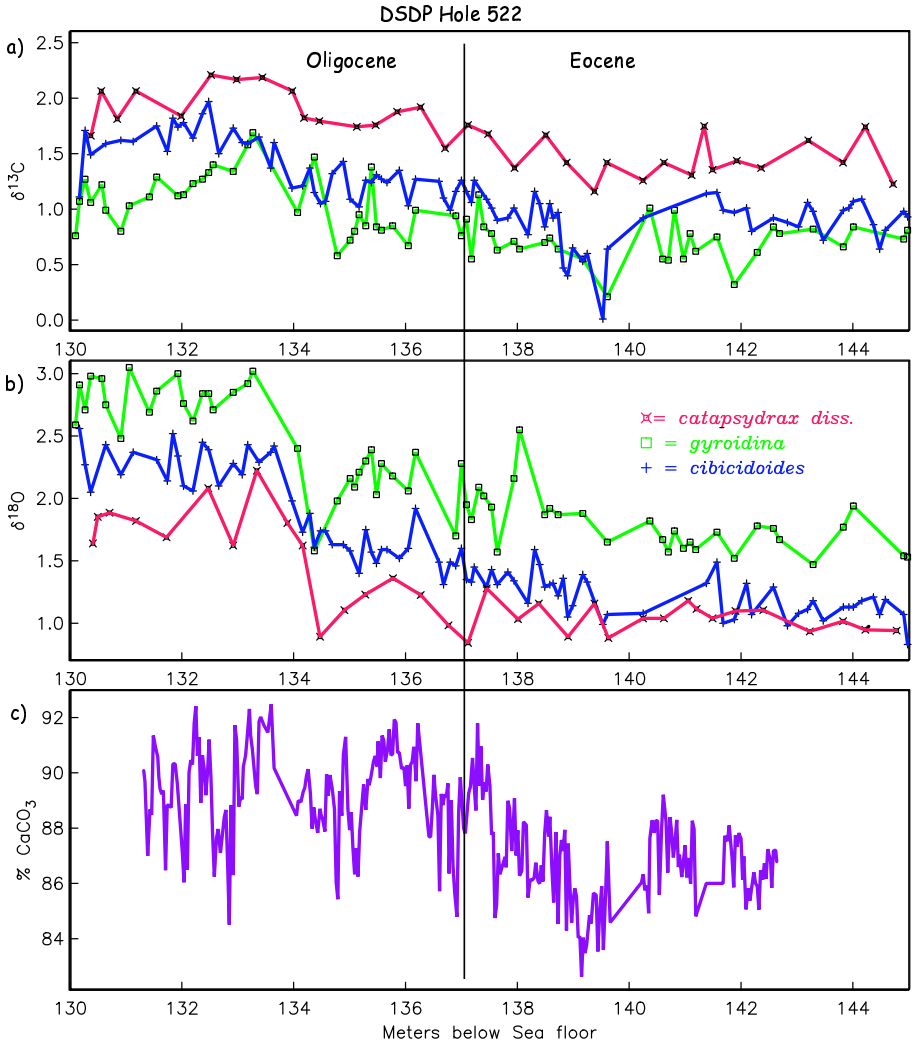

Figure 8.17: a) δ^{13}C and b) δ^{18}O isotopic variations of benthic and planktonic foraminifera from Site 522. c) Variations in percent calcium carbonate . The Eocene Oligocene boundary is defined as the last occurrence of *Hantkenina spp.* at 137 meters below sea floor. Figure redrawn from Hartl et al. (1995).

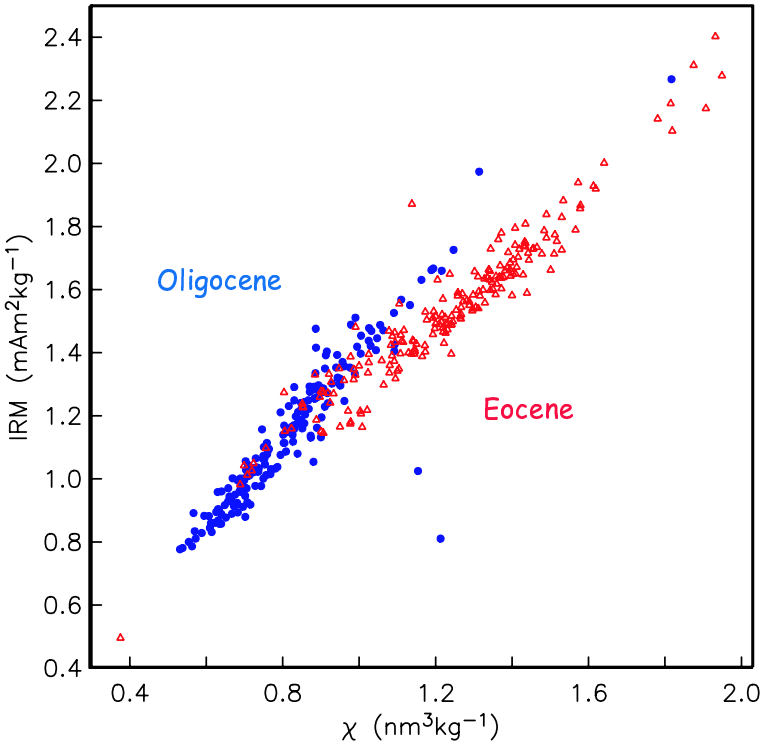

Figure 8.18: Saturation IRM versus magnetic susceptibility χ for Hole 522 across the Eocene/Oligocene boundary. The Eocene group (red triangles) plots along a line of lower IRM/χ compared to the Oligocene group (blue circles).

Appendix

A Fourier analysis of hysteresis loops

In practice, hysteresis measurements may yield rather noisy data. Jackson et al. [1990] suggested that noisy hysteresis data could be filtered using a Fourier transform. The advantages of Fourier smoothing are that the calculated hysteresis parameters are less sensitive to noise and that the ΔM and $d\Delta M/dH$ curves are more readily interpreted.

The steps involved in Fourier smoothing of hysteresis loops are as follows (see Figure A1):

- First, the contribution of paramagnetic and diamagnetic phases must be removed. Figure A1a shows some typical data from carbonate rich sediments. These samples have a strong diamagnetic (negative high field slope) contribution. We remove the diamagnetic contribution by calculating a best-fit line using linear regression for the data at high fields (after the ferromagnetic phases have reached saturation) and removing its contribution by subtraction (see Figure A1b).

- In order to ensure uniformity of data treatment, Jackson et al. [1990] recommend truncating the data at some fixed percentage of M_s (after slope adjustment). We truncate the data at 99.9% of M_s in Figure A1b.

- A Fourier transform requires data with a single y value for every x value and hysteresis data, as normally plotted are not suitable. The loops can be mapped into a suitable form for Fourier analysis by transforming the field values into radians, as shown in Figure A1c. The unfolded loop starts at the point when the descending curve intersects the y axis (M_r). From $H = 0 \rightarrow -H_{\max}$, H is mapped linearly to radians ($H' = 0 \rightarrow \pi/2$). From $H = -H_{\max} \rightarrow 0$, H is mapped to $H' = \pi/2 \rightarrow \pi$. From $H = 0 \rightarrow +H_{\max}$, we map H to $H' = \pi \rightarrow 3\pi/2$, and finally, for $H = +H_{\max} \rightarrow 0$, H is converted to $H' = 3\pi/2 \rightarrow 2\pi$.

- The "unfolded" data can then be subjected to a Fourier Transform as described by Jackson et al. [1990]. The data can be smoothed by retaining only a specified number of terms (see Figure A1d). Finally, hysteresis parameters can be calculated from the reconstituted loop and ΔM and $d\Delta M/dH$ curves can be plotted (see Figure A1e-f).

A. FOURIER ANALYSIS OF HYSTERESIS LOOPS

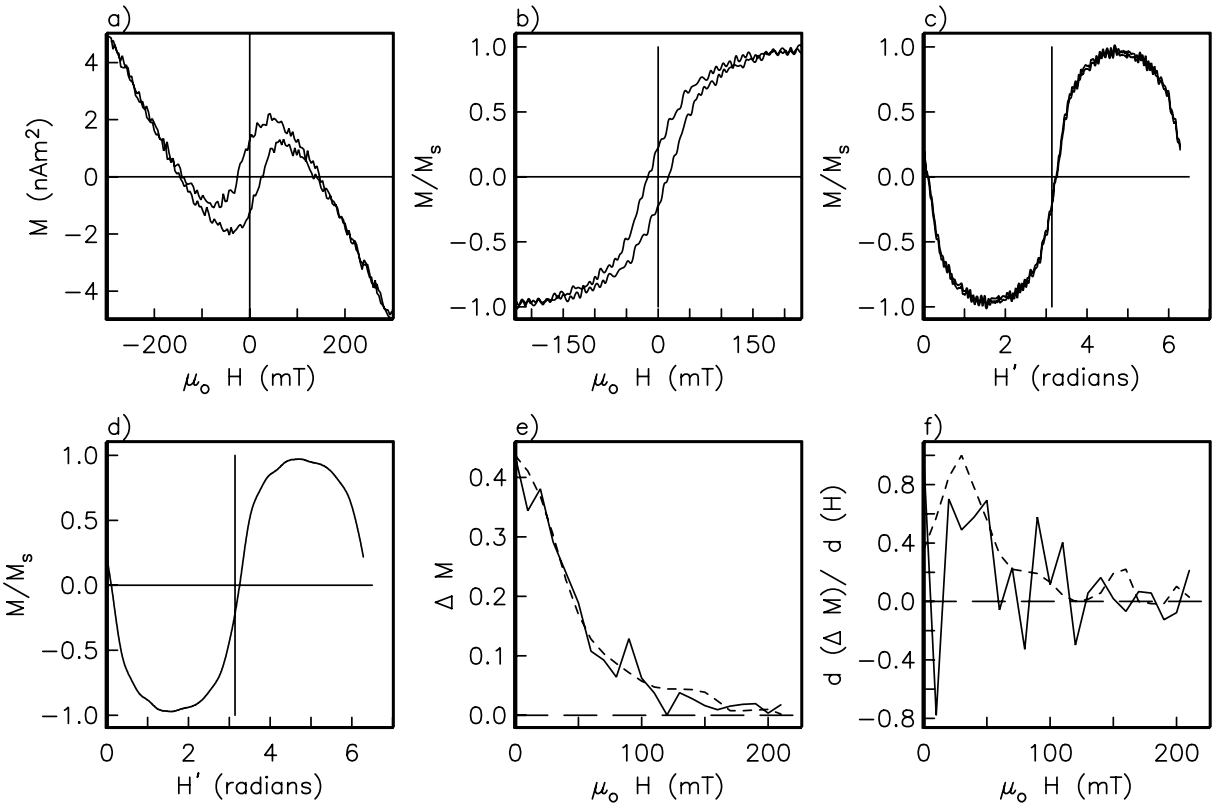

Figure A1: Steps in Fourier smoothing: a) the original data - note the negative high field slope from the diamagnetic contribution of carbonate, b) data with the high field slope removed and truncated to 99.9% of the maximum value of M, c) data from b) "unfolded" into radians, d) data from c) smoothed by using the first 15 terms of Fourier series, e) comparison of ΔM curve using original data (solid line) and smoothed data (dashed line), f) comparison of the $d\Delta M/dH$ curve using the original data (solid line) and smoothed data (dashed line).

Bibliography

Banerjee, S. K., King, J. & Marvin, J. (1981), 'A rapid method for magnetic granulometry with applications to environmental studies', *Geophys. Res. Lett.* **8**, 333–336.

Day, R., Fuller, M. D. & Schmidt, V. A. (1977), 'Hysteresis properties of titanomagnetites: grain size and composition dependence', *Phys. Earth Planet. Inter.* **13**, 260–266.

Dunlop, D. (2002), 'Theory and application of the day plot (m_{rs}/m_s versus h_{cr}/h_c) 2. application to data for rocks, sediments, and soils', *J. Geophys. Res* **107**, doi:10.1029/2001JB000487.

Dunlop, D. & Argyle, K. (1997), 'Thermoremanence, anhysteretic remanence and susceptibility of submicron magnetites: Nonlinear field dependence and variation with grain size', *J. Geophys. Res* **102**, 20199–20210.

Egli, R. (2003), 'Analysis of the field dependence of remanent magnetization curves', *Journal of Geophysical Research-Solid Earth* **108**(B2).

Evans, M. & Heller, F. (2003), *Environmental Magnetism: Principles and Applications of Enviromagnetics*, Academic Press.

Fabian, K. (2003), 'Some additional parameters to estimate domain state from isothermal magnetization measurements', *Earth and Planetary Science Letters* **213**(3-4), 337–345.

Hartl, P., Tauxe, L. & Herbert, T. (1995), 'Eartliest oligocene increase in south atlantic productivity as interpreted from "rock magnetics" at dsdp site 522', *Paleoceanography* **10**, 311–325.

Heider, F., Zitzelsberger, A. & Fabian, K. (1996), 'Magnetic susceptibility and remanent coercive force in grown magnetite crystals from 0.1 μm to 6mm', *Phys. Earth Planet. Inter.* **93**, 239–256.

Hunt, C. P., Moskowitz, B. M. & Banerjee, S. K. (1995), 'Rock physics and phase relations, a handbook of physical constants', pp. 189–204.

Jackson, M., Worm, H. U. & Banerjee, S. K. (1990), 'Fourier analysis of digital hysteresis data: rock magnetic applications', *Phys. Earth Planet. Inter.* **65**, 78–87.

Kruiver, P. P., Dekkers, M. J. & Heslop, D. (2001), 'Quantification of magnetic coercivity components by the analysis of acquisition curves of isothermal remanent magnetisation', *Earth and Planetary Science Letters* **189**(3-4), 269–276.

Lowrie, W. (1990), 'Identification of ferromagnetic minerals in a rock by coercivity and unblocking temperature properties', *Geophys. Res. Lett.* **17**, 159–162.

Maher, B. A. & Thompson, R., eds (1999), *Quaternary Climates, Environments and Magnetism*, Cambridge University Press.

Mayergoyz, I. (1986), 'Mathematical models of hysteresis', *IEEE Trans. Magn.* **MAG-22**, 603–608.

Pike, C. R., Roberts, A. P., Dekkers, M. J. & Verosub, K. L. (2001), 'An investigation of multi-domain hysteresis mechanisms using forc diagrams', *Physics of The Earth and Planetary Interiors* **126**(1-2), 11–25.

Pike, C., Roberts, A. & Verosub, K. (1999), 'Characterizing interactions in fine magnetic particle systems using first order reversal curves', *J. Appl. Phys.* **85**, 6660–6667.

Robertson, D. J. & France, D. E. (1994), 'Discrimination of remanence-carrying minerals in mixtures, using isothermal remanent magnetisation acquisition curves', *Physics of The Earth and Planetary Interiors* **82**(3-4), 223–234.

Tauxe, L., Bertram, H. & Seberino, C. (2002), 'Physical interpretation of hysteresis loops: Micromagnetic modelling of fine particle magnetite', *Geochem., Geophys., Geosyst.* **3**, DOI 10.1029/2001GC000280.

Tauxe, L., Mullender, T. A. T. & Pick, T. (1996), 'Potbellies, wasp-waists, and superparamagnetism in magnetic hysteresis', *Jour. Geophys. Res.* **101**, 571–583.

Yu, Y. & Tauxe, L. (2004), 'On the use of magnetic transient hysteresis in paleomagnetism for granulometry', *Geochem., Geophys., Geosyst.* **6**, Q01H14; doi: 10.1029/2004GC000839.

Lectures in Paleomagnetism, 2005
by Lisa Tauxe

Citation:
http://earthref.org/MAGIC/books/Tauxe/2005/

June 3, 2005

Chapter 9

Getting a paleomagnetic direction

Suggested Reading

For background:
Chapter 4: Butler (1992)
To learn more:
Chapters 8, 9: Collinson (1983)

9.1 Introduction

As discussed in Lecture 5, rocks become magnetized in a variety of ways. Both igneous and sedimentary rocks can be affected by chemical change, thereby acquiring a secondary magnetization. Many magnetic materials are affected by viscous remanent magnetization. The various components of magnetization sum together to constitute the NRM which is the "raw" remanence of the sample after extraction. The goal of paleomagnetic laboratory work is to isolate the various components of remanence and to ascribe origin, age and reliability to these components. But before the laboratory work can begin, samples must be collected. Sampling strategy is crucial to a successful study. We will briefly describe techniques for sampling, methods of orientation and overall philosophy. We will then turn to an overview of some of the more useful field and laboratory techniques that wind up with an estimate of a paleomagnetic direction.

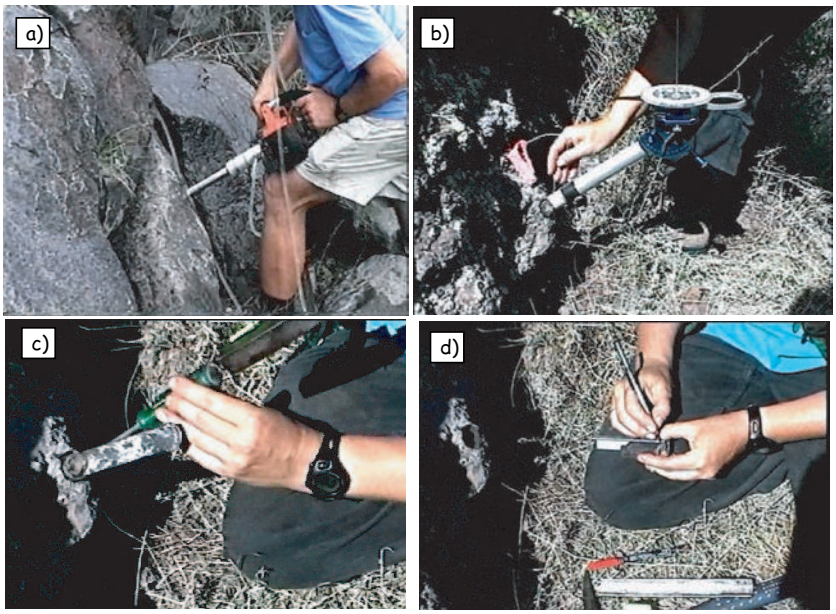

Figure 9.1: Sampling technique with a water-cooled drill: a) drill the sample, b) insert a non-magnetic slotted tube with an adjustable platform around the sample. Rotate the slot to the top of the sample and note the azimuth and plunge of the drill direction (into the outcrop) with a sun and/or magnetic compass and inclinometer. Mark the sample through the slot with a brass or copper wire. c) Extract the sample. d) Make a permanent arrow on the side of the sample in the direction of drill and label the sample with the sample name. Make a note of the name and orientation of the arrow in a field notebook.

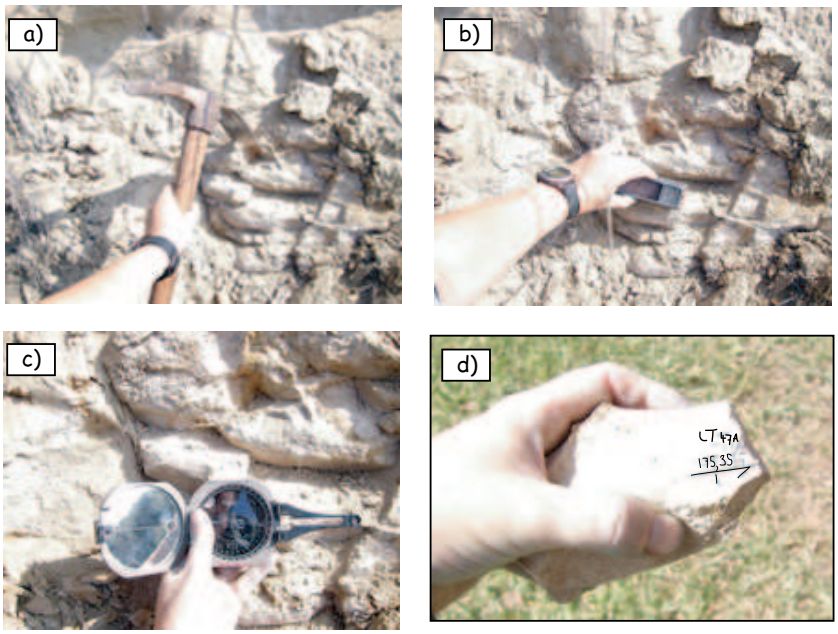

Figure 9.2: Hand sampling technique for soft sediment: a) dig down to fresh material, b) rasp off a flat surface, c) mark the strike and dip on the sample, d) extract the sample and label it.

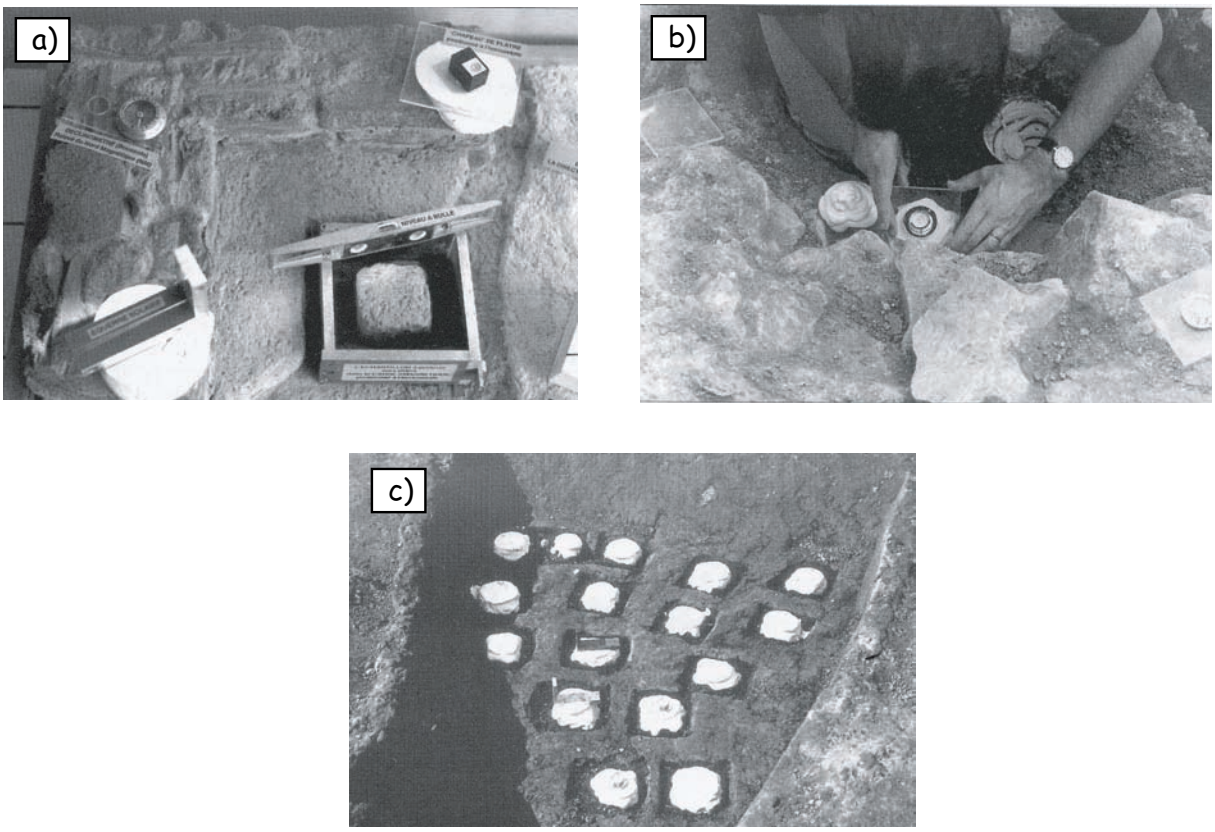

Figure 9.3: Sampling technique for oriented archeological materials. a) cut out a large sample from, for example, a baked hearth. b) cover the sample with non-magnetic plaster of paris. While the plaster of paris is still wet, place a piece of plexiglass on it and orient it such that it is horizontal using a bubble level. c) The direction to magnetic north can be inscribed on the horizontal surface, after the plaster is dry. [Picture from Evin et al. 1998]

9.2 Paleomagnetic sampling

There are several goals in sampling rock units. One is to average out the errors involved in the sampling process itself. Another is to assess the reliability of the recording medium. In addition, we often wish to average the scatter caused by secular variation of the geomagnetic field in order to estimate the time-averaged paleomagnetic field direction representative of the time that the rock unit acquired its magnetization.

The objectives of averaging recording and sampling "noise" are achieved by taking a number N of individually oriented *samples* from a single unit (called a *site*). Samples should be taken such that they represent a single time horizon, that is, they are from a single cooling unit or the same sedimentary horizon. The most careful sample orientation procedure has an uncertainty of several degrees. Precision is gained proportional to $\sqrt{N}$, so to improve the precision, multiple individually oriented samples are required. The number of samples taken should be tailored to the particular project at hand. If one wishes to know polarity, perhaps three samples would be sufficient (these would be taken primarily to assess "recording noise"). If, on the other hand, one wished to make

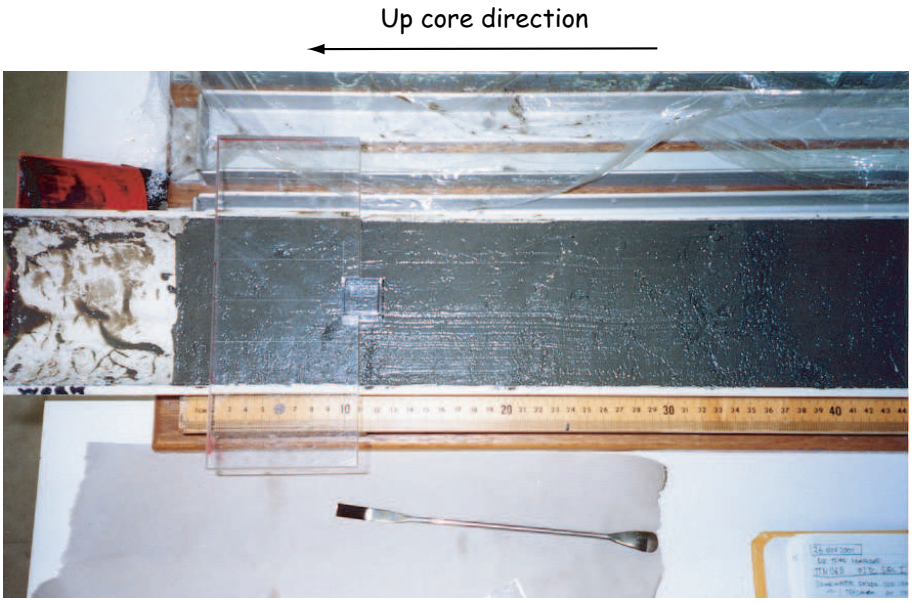

Figure 9.4: Sampling of a sediment core. A plastic cube with a hole in it to let the air escape is pressed into the split surface of a core. The orientation arrow points "up core". After extraction, a label with the sample name is put on. Figure from Kurt Schwehr's web site.

inferences about secular variation of the geomagnetic field, more samples would be necessary to suppress sampling noise.

Some applications in paleomagnetism require that the secular variation of the geomagnetic field (the paleomagnetic "noise") be averaged in order to determine the time-averaged field direction. The geomagnetic field varies with time constants ranging from milliseconds to millions of years. It is a reasonable first order approximation to assume that, when averaged over, say, 100,000 years, the geomagnetic field is similar to that of a geocentric axial dipole (equivalent to the field that would be produced by a bar magnet at the center of the Earth, aligned with the spin axis; see Lecture 2). Thus, when a time-averaged field direction is required, enough sites can be sampled to span sufficient time to achieve this goal. A good rule of thumb is about a hundred sites (each with nine to ten samples), spanning 100,000 years.

Samples can be taken using a gasoline or electric powered drill, as "hand samples" or as "sub-samples" from a piston core. The samples must be oriented before they are removed. There are many ways to orient samples and possible conventions are shown in Figures 9.1, 9.2, 9.3, and 9.4.

If a magnetic compass is used to orient samples in the field. The preferred practice is to set the compass declination to zero. Then, in post-processing, the measured azimuth must be adjusted by the local magnetic declination, which can be calculated from the known reference field (IGRF or DGRF; see Lecture 2). The plunge of the sample can also be gotten using an inclinometer (either with a Pomeroy orientation device as shown in Figure 9.1 or with some other inclinometer, such as that on a Brunton Compass.)

Sometimes large local magnetic anomalies, for example from a strongly magnetized rock unit, can lead to a bias in the magnetic direction that is not compensated for by the IGRF magnetic declination. In such cases, some other means of sample orientation is required. One relatively straightforward way is to use a sun compass. Calculation of a direction using a sun compass is

more involved than for magnetic compass, however. A dial with a vertical needle (a "gnomon") is placed on the horizontal platform shown in Figure 9.5. The angle (α) that the sun's shadow makes with the drilling direction is noted as well as the exact time of sampling and the location of the sampling site. With this information and the aid of the Astronomical Almanac or a simple algorithm (see Appendix), it is possible to calculate the desired direction to reasonable accuracy (the biggest cause of uncertainty is actually reading the shadow angle!).

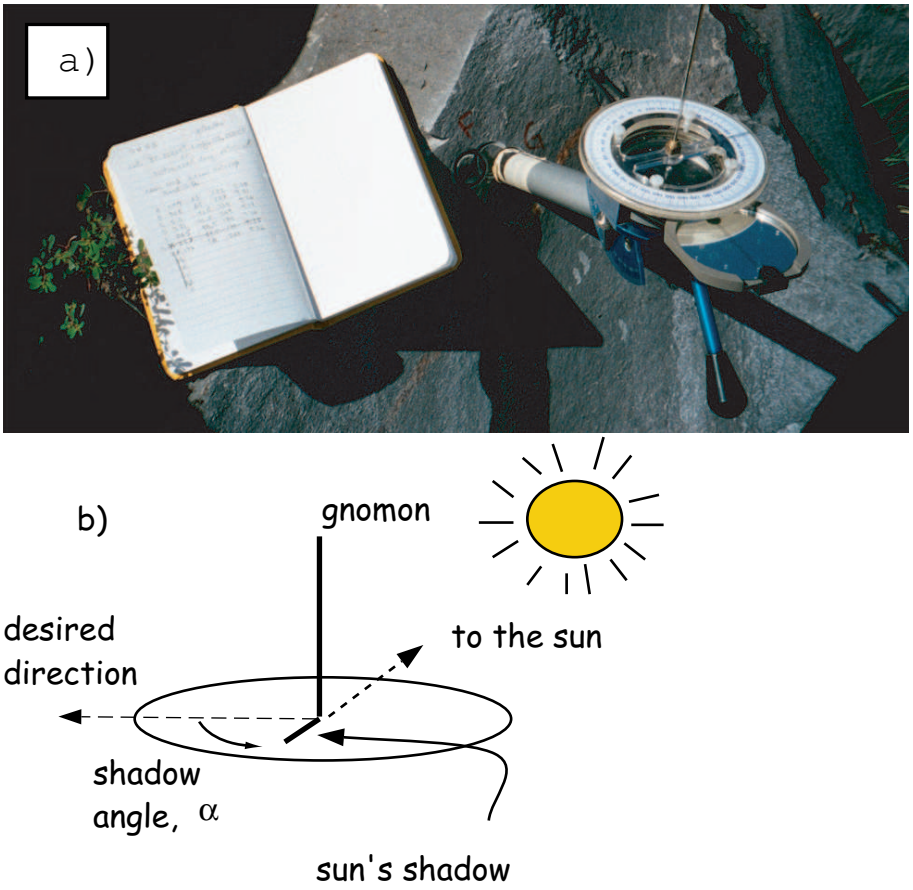

Figure 9.5: a) Pomeroy orientation device in use as a sun compass. b) Schematic of the principles of sun compass orientation.

A new technique, developed by Cathy Constable and Frank Vernon at Scripps Institution of Oceanography (see Figure 9.6) uses differential Global Positioning System (GPS) technology to determine azimuth of a baseline. Two GPS receivers are attached to either end of a one meter non-magnetic rigid base. The location and azimuth of the baseline can be computed from the signals detected by the two receivers. The orientation of the baseline is transferred to the paleomagnetic samples using a laser mounted on the base which is focused on a prism attached to the orientation device used to orient the paleomagnetic samples. The orientations derived by the differential GPS are nearly identical to those obtained by a sun compass, although it takes at least an additional half hour and is rather awkward to transport. Nonetheless, achieving sun-compass accuracy in orientations when the sun is unlikely to be readily available is a major break through for high latitude paleomagnetic field procedures.

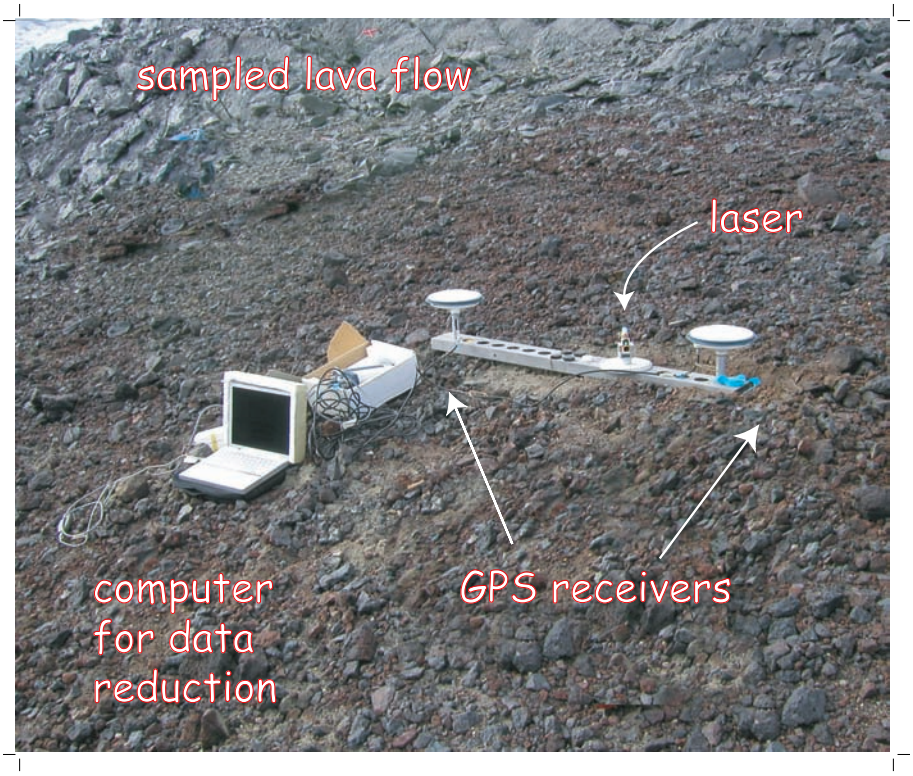

Figure 9.6: Differential GPS system for orienting paleomagnetic samples in polar regions. Photo taken during sampling trip to the foothills of the Royal Society Ranges in Antarctica, Jan. 2004.

9.3 Changing coordinate systems

Samples are brought to the laboratory and trimmed into standard sizes and shapes (see Figure 9.7). These sub-samples are called *paleomagnetic specimens*. Data often must be transformed from the sample coordinate system into, for example, geographic coordinates. This can be done graphically with a stereonet or by means of matrix manipulation. We outline the latter method in the Appendix.

9.4 Measurement of magnetic remanence

We measure the magnetic remanence of paleomagnetic samples in a *magnetometer*, of which there are various types. The cheapest and most readily available are *spinner magnetometers* so named because they spin the sample to create a fluctuating electromotive force (emf). The emf is proportional to the magnetization and can be determined relative to the three axes defined by the sample coordinate system. The magnetization along a given axis is measured by detecting the voltages induced by the spinning magnetic moment within a set of pick-up coils.

Another popular way to measure the magnetization of a sample is to use a *cryogenic magnetometer* (see Figure 9.8). These magnetometers operate using so-called *superconducting quantum interference devices* (SQUIDs). In a SQUID, the flux of an inserted sample is opposed by a current in a loop of superconducting wire. The superconducting loop is constructed with a *weak link* which stops superconducting at some very low current density, corresponding to some very small quantum

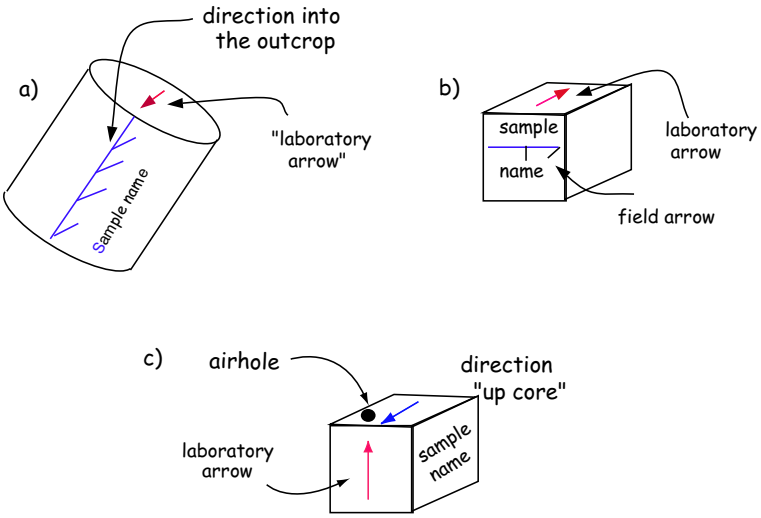

Figure 9.7: Various types of possible sample shapes and orientation conventions. a) A one inch slice from a drilled core. b) A cube of sediment sanded from a hand sample. c) A sample from a piston core.

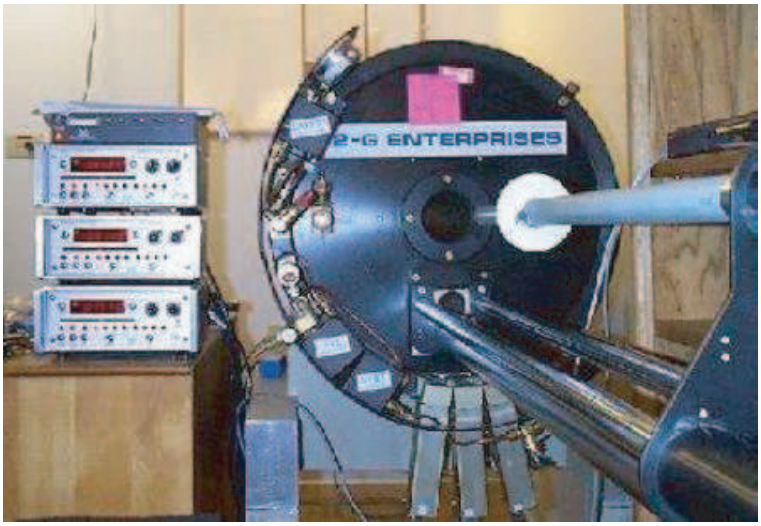

Figure 9.8: a) Cryogenic magnetometer. The sample is inserted into the opening of the shields. There are three SQUIDS that detec the magnetic moment which is read off the three electronic boxes to the left. b) Spinner magnetometer. The sample is inserted into the opening in a cup. It spins around, generating an electromagnetic force which is detected with a circular fluxgate. Two components are measured at a time.

of flux. Thus the flux within the loop can change by discrete quanta. Each incremental change is counted and the total flux is proportional to the magnetization along the axis of the SQUID. Cryogenic magnetometers are much faster and more sensitive than spinner magnetometers, but they cost much more to buy and to operate.

Magnetometers are used to measure the three components of the magnetization necessary to

define a vector (e.g., x_1, x_2, x_3). These data can be converted to the more common form of D, I and M by methods described in Lecture 2.

9.5 Demagnetization techniques

Anyone who has dealt with magnets (including magnetic tape, credit cards, and magnets) knows that they are delicate and likely to demagnetize or change their magnetic properties if abused by heat or stress. Cassette tapes left on the dashboard of the car in the hot sun never sound the same. Credit cards that have been through the dryer may lead to acute embarrassment at the check-out counter. Magnets that have been dropped, do not work as well afterwards. It is not difficult to imagine that rocks that have been left in the hot sun or buried deep in the crust (not to mention altered by diagenesis or bashed with hammers, drills, pick axes, etc.), may not have their original magnetic vectors completely intact. Because rocks often contain millions of tiny magnets, it is possible that some (or all) of these have become realigned, or that they grew since the rock formed. In many cases, there are still grains that carry the original remanent vector, but there are often populations of grains that have acquired new components of magnetization.

Through geologic time, certain grains may acquire sufficient energy to overcome the magnetic anisotropy energy and change their direction of magnetization (Lecture 5). In this way, rocks can acquire a viscous magnetization in the direction of the ambient field. Because the grains that carry the viscous magnetization necessarily have lower magnetic anisotropy energies (they are "softer", magnetically speaking), we expect their contribution to be more easily randomized than the more stable ("harder") grains carrying the ancient remanent magnetization.

There are several laboratory techniques that are available for separating various components of magnetization. Paleomagnetists rely on the relationship of relaxation time, coercivity, and temperature in order to remove (*demagnetize*) low stability remanence components. The fundamental principle that underlies demagnetization techniques is that the lower the relaxation time τ, the more likely the grain will carry a secondary magnetization. The basis for *alternating field* (AF) demagnetization is that components with short relaxation times also have low coercivities. The basis for *thermal* demagnetization is that these grains also have low blocking temperatures.

In AF demagnetization (see Figure 9.9a), an oscillating field is applied to a paleomagnetic sample in a null magnetic field environment. All the grain moments with coercivities below the peak AF will track the field. These entrained moments will become stuck as the peak field gradually decays below the coercivities of individual grains. Assuming that there is a range of coercivities in the sample, the low stability grains will be stuck half along one direction of the AF and half along the other direction; the net contribution to the remanence will be zero. In practice, we demagnetize samples sequentially along three orthogonal axes, or while "tumbling" the sample around three axes during demagnetization.

Thermal demagnetization (see Figure 9.9b) exploits the relationship of relaxation time and temperature. There will be a temperature below the curie temperature at which the relaxation time is a few hundred seconds. When heated to this temperature, grains with relaxation times this short will be in equilibrium with the field. This is the *unblocking temperature*. If the external field is zero, then there will be no net magnetization. Lowering the temperature back to room temperature will result in the relaxation times growing exponentially until these moments are once again fixed. In this way, the contribution of lower stability grains to the NRM can be randomized. Alternatively, if there is a DC field applied during cooling, the grains whose unblocking temperatures has been

a)

b)

Figure 9.9: a) Alternating field demagnetizer. The sample is placed within the coil inside the tubular shield. An alternating field is generated with a specified peak intensity. This decays away, randomizing all magnetic moments that are softer than the peak field that have a component parallel to the applied field direction. The procedure is repeated along all three axis. A small DC field can applied along the direction of the coils to produce an ARM. b) Thermal demagnetizer. Samples are placed in boats inside a non-inductively wound oven that is inside the tubular shields. The ovens are heated to a specified temperature and allowed to cool either in zero field or in a laboratory controlled DC field produced by a coil inside the shield. This either demagnetizes or remagnetizes all grains with blocking temperatures lower than the specified temperature.

exceeded will be realigned in the new field direction; they will have acquired a partial thermal remanent magnetization (pTRM).

We sketch the principles of progressive demagnetization in Figure 9.10. Initially, the NRM is the sum of two components carried by populations with different coercivities. The distributions of coercivities are shown in the histograms to the left in Figure 9.10. Two components of magnetization are shown as heavy lines in the plots to the right. In these examples, the two components are orthogonal. The sum of the two components at the start (the NRM) is shown as a + on the vector plots to the right. After the first AF demagnetization step, the contribution of the lowest coercivity grains has been erased and the remanence vector moves to the position of the first dot away from the +. Increasing the AF gradually eats away at the remanence vectors (shown as dashed arrows and dots in the plots to the right) which eventually approach the origin.

There are four different sets of coercivity spectra shown in Figure 9.10, each with a distinctive behavior during demagnetization. If the two coercivity fractions are completely distinct, the two components are clearly defined (Figure 9.10a) by the progressive demagnetization. If there is some overlap in the coercivity distribution of the components the resulting demagnetization diagram is curved (Figure 9.10b). If the two components completely overlap, both components are removed simultaneously and an apparently single component demagnetization diagram may result (Figure 9.10c). It is also possible for one coercivity spectrum to include another as shown in Figure 9.10d. Such cases result in "S" shaped demagnetization curves. Because complete overlap actually happens in "real" rocks, it is desirable to perform both AF and thermal demagnetization. If the two components overlap completely in coercivity, they might not have overlapping blocking

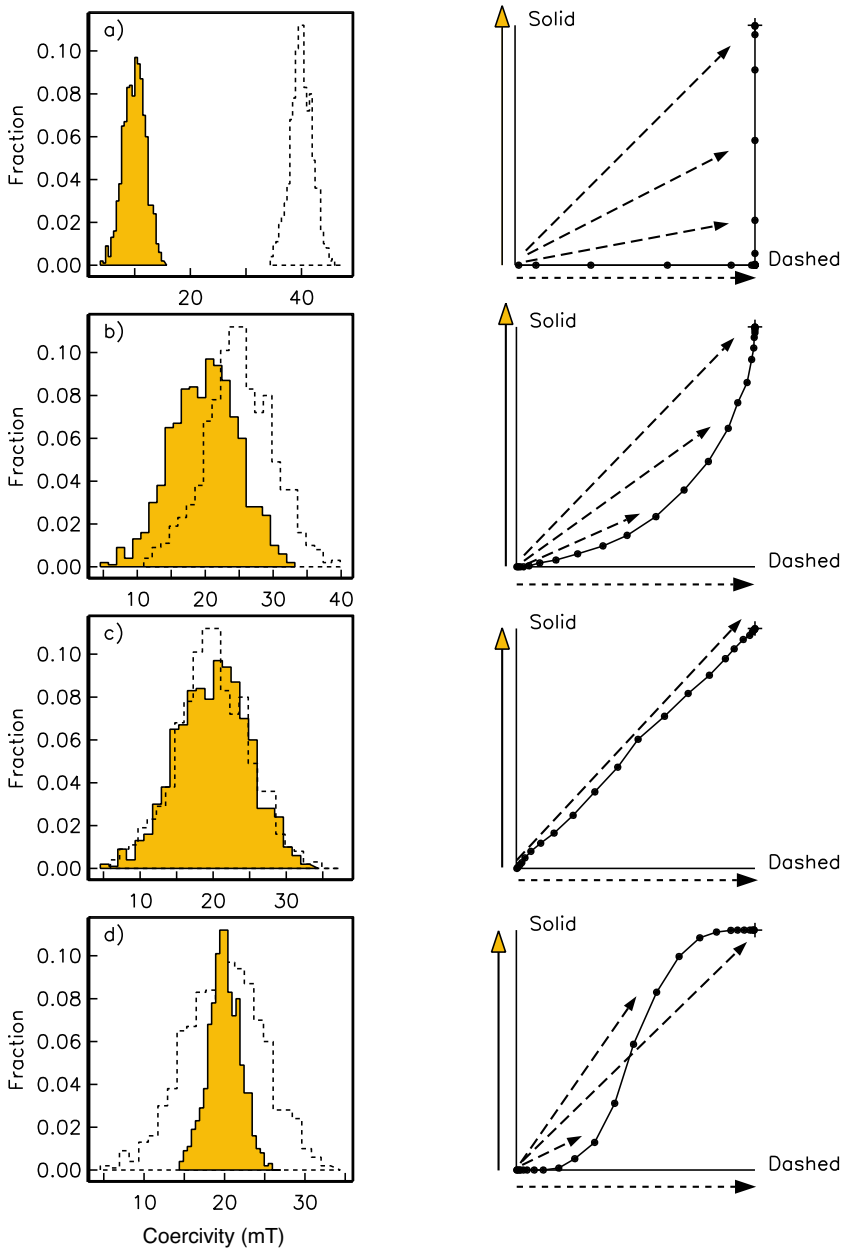

Figure 9.10: Principle of progressive demagnetization. Specimens with two components of magnetization (shown by heavy arrows on the right hand side), with discrete coercivities (plotted as histograms to the left). The original "NRM" is the sum of the two magnetic components and is shown as the + in the diagrams to the right. Successive demagnetization steps remove the component with coercivities lower than the peak field, and the NRM vector changes as a result. a) The two distributions of coercivity are completely separate. b) The two distributions partially overlap resulting in simultaneous removal of both components. c) The two distributions completely overlap. d) One distribution envelopes the other.

temperature distributions and vice versa. It is unlikely that samples from the same lithology will all have identical overlapping distributions, so multiple samples can provide clues to the possibility of completely overlapped directions in a given sample.

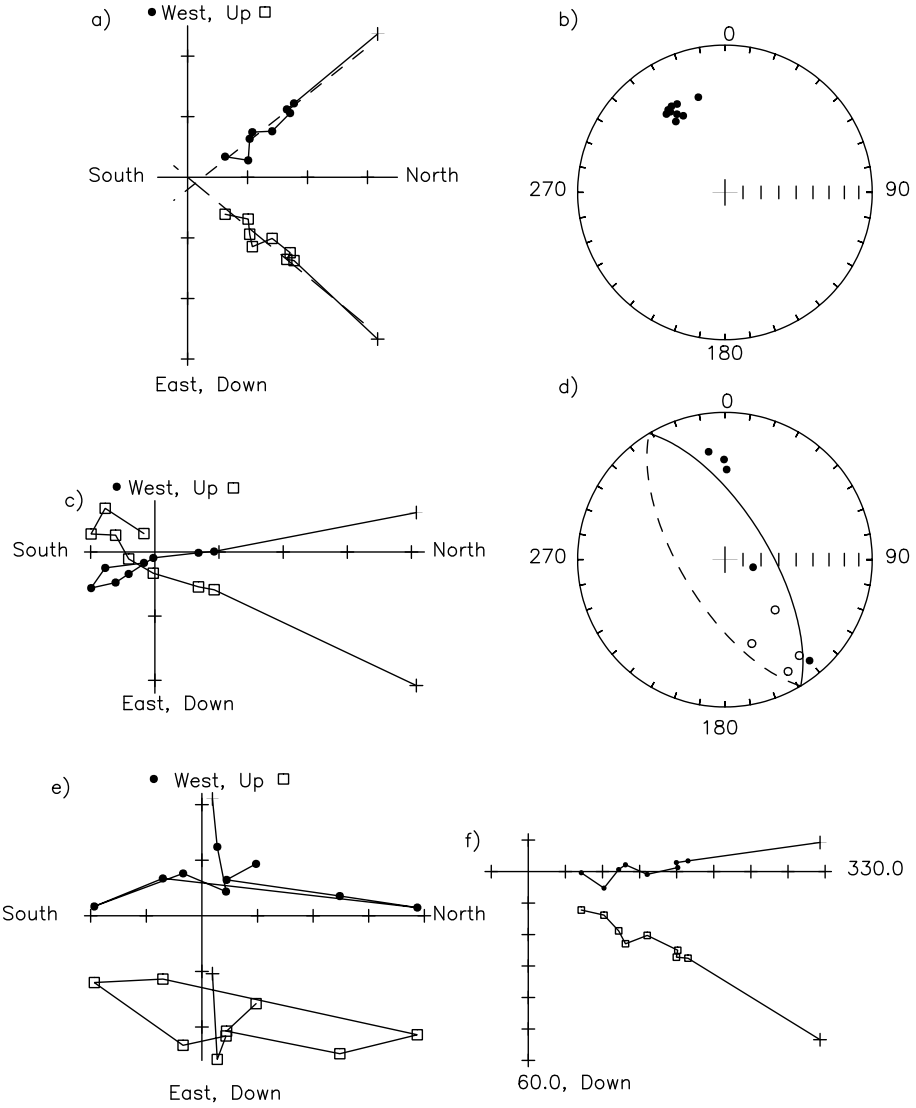

Figure 9.11: a) Orthogonal projection of data plotted with North on the horizontal axis. A single component of magnetization is present (see text). The horizontal projection is plotted with solid symbols and the vertical (North-down) component is plotted with open squares. The best-fit line through the data, as calculated by principal component analysis, is shown as a dashed line. b) Same data as in a), but plotted on an equal area projection. Solid (open) symbols are projections onto the lower (upper) hemisphere. c) Sample with two components that have overlapping stabilities. d) Same data as in c), but in an equal area projection. The trace of the best-fitting plane is shown, with a solid (dashed) line being a projection onto the lower (upper) hemisphere. e) Example of a complicated multi-component sample. f) Data from a) replotted with the horizontal axis along 330° instead of with respect to North.

9.6 Estimating a direction from demagnetization data

Now we will consider briefly the issue of what to do with the demagnetization data in terms of display and estimating a best-fit direction for various components.

The standard practice in demagnetization is to measure the NRM and then to subject the sample to a series of demagnetization steps of increasing severity using the equipment described earlier in the lecture. The magnetization of the sample is measured after each step. During demagnetization, the remanent magnetization vector will change until the most stable component has been isolated, at which point the vector decays in a straight line to the origin. This final component is called the *characteristic remanent magnetization* or ChRM.

Visualizing demagnetization data is a three-dimensional problem and therefore difficult to plot on paper. Paleomagnetists often rely on a set of two projections of the vectors, one on the horizontal plane and one on the vertical plane. These are variously called Zijderveld diagrams (Zijderveld [1967]), orthogonal projections, or vector end-point diagrams.

In orthogonal projections, the North component (x_1) is plotted versus East (x_2) (solid symbols) in one projection, and North (x_1) is replotted versus Down (x_3) (open symbols) in another projection. Here, paleomagnetic convention differs from the usual x-y plotting convention because x_2 and x_3 are on the $-y$ axis. The paleomagnetic conventions make sense if one visualizes the diagram as a map view for the solid symbols and a vertical projection for the open symbols. It may be advantageous to plot North on the vertical axis and East positive to the right. In this case the vertical projection is East versus Down. This projection is useful if the magnetization is more East-West than North-South. In fact, the horizontal axis can be any direction within the horizontal plane.

In Figure 9.11, we show three general types of demagnetization behavior. In Figure 9.11a-b, the sample has a North-Northwest and downward directed NRM (plotted as +'s). The direction does not change during demagnetization and the NRM is a single vector. The directional data are also plotted on the equal area net to the right (Figure 9.11b) and fall in the NW quadrant of the lower hemisphere. The sample in Figure 9.11c shows a progressive change in direction from a North-Northwest and downward directed component to a South-Southeast and upward direction. The vector continuously changes direction to the end and no final "clean" direction has been confidently isolated. These data are plotted on an equal area projection to the right (Figure 9.11d) along with the trace of the best-fitting plane (a great circle). The most stable component probably lies somewhere near the best-fitting plane.

In Figure 9.11e, we show what is informally known as a "spaghetti" diagram. The NRM switches from direction to direction, with little coherence from step to step. Such data are difficult to interpret and are usually thrown out.

Some people choose to plot the pairs of points (x_1, x_2) versus (H, x_3) where H is the horizontal projection of the vector given by $\sqrt{x_1^2 + x_2^2}$. In this projection, which is sometimes called a *component plot*, the two axes do not correspond to the same vector from point to point. Instead, the coordinate system changes with every demagnetization step because H almost always changes direction, even if only slightly. Plotting H versus x_3 is therefore a confusing and misleading practice. The primary rationale for doing so is because, in the traditional orthogonal projection, the vertical component reveals only an apparent inclination. If something close to true inclination is desired, then, instead of plotting H and x_3, one can simply rotate the horizontal axes of the orthogonal plot such that it closely parallels the desired declination (Figure 9.11f).

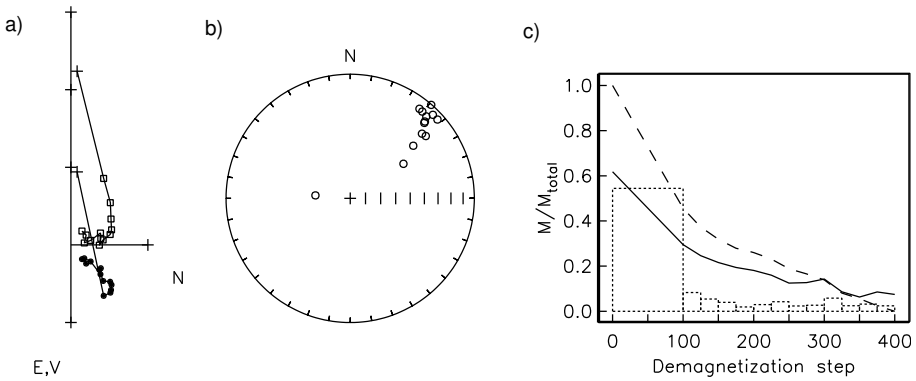

Figure 9.12: a) Specimen with strongly overlapping remanence components, in an orthogonal projection. b) Same data as in a) plotted on an equal area projection. c) Decay of NRM intensity during the demagnetization procedure (solid line). The dashed line is the decay of the vector difference sum. Boxes represent the intensity removed after each step.

9.7 Vector difference sum

An equal area projection may be the most useful way to present demagnetization data from a sample with several strongly overlapping remanence components (such as in Figures 9.11c-d and 9.12). In order to represent the vector nature of paleomagnetic data, it is necessary to plot intensity information. Intensity can be plotted versus demagnetization step in an *intensity decay curve* (Figure 9.12c). However, if there are several components with different directions, the intensity decay curve cannot be used to determine, say, the blocking temperature spectrum, because it is the vector sum of the two components. It is therefore advantageous to consider the decay curve of the *vector difference sum* (VDS.) The VDS "straightens out" the various components by summing up the vector differences at each demagnetization step, so the total magnetization is plotted, as opposed to the resultant (see Figure 9.12).

9.8 Best-fit lines and planes

Orthogonal vector projections aid in identification of the various remanence components in a sample. Demagnetization data are usually treated using what is known as *principal component analysis* (Kirschvink [1980]). What comes out of the analysis is a best-fit line through straight-line, single component data as in Figure 9.11a,b or a best-fit planes or great circle through multi-component data as in Figure 9.11c,d, and the "maximum angle of deviation" (MAD) for each of these. The details of the analysis are given in the Appendix.

9.9 Field strategies

In addition to establishing that a given rock unit retains a consistent magnetization, it is also of interest to establish when this magnetization was acquired. Arguments concerning the age of magnetic remanence can be built on indirect petrographic evidence as to the relative ages of various magnetic minerals, or by evidence based on geometric relationships in the field. There are two key field tests that require special sampling strategies: the fold test and the conglomerate test.

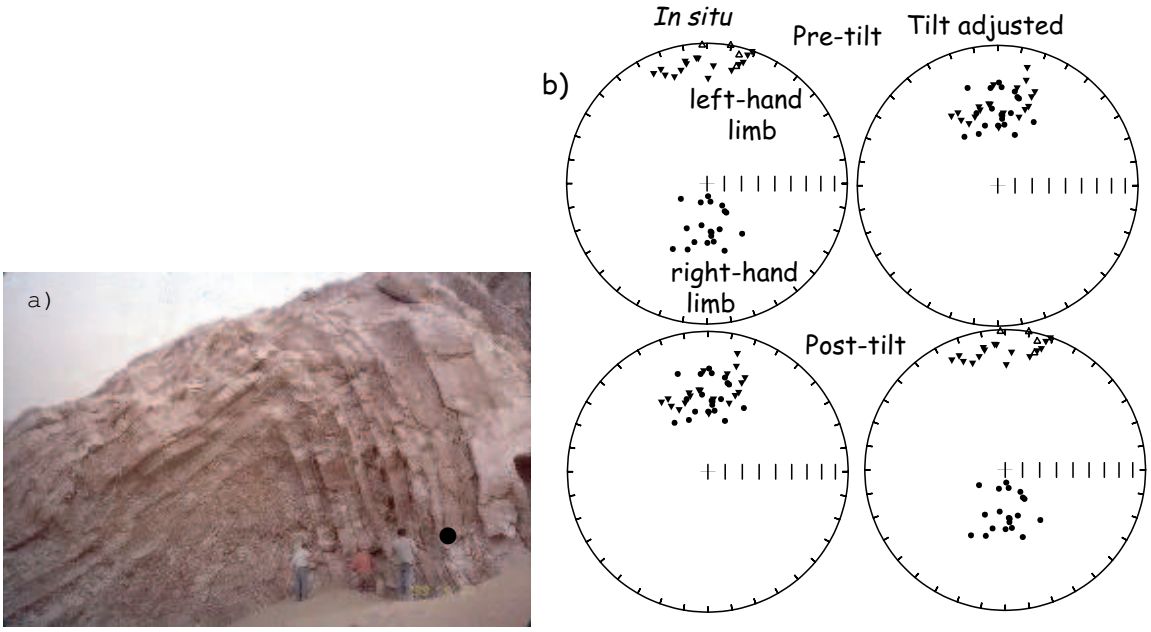

Figure 9.13: Sampling units with different bedding attitudes in the "fold test". a) Example of folded beds. (Picture from Dupont-Nivet et al., 2002.) b) Hypothetical paleomagnetic directions are shown on equal area projections before and after adjusting for bedding tilt. Top pair represents the case in which the grouping of paleomagnetic directions is improved after adjusting for tilt which would argue for a pre-tilt acquisition of remanence. Lower pair represents a post-tilt acquisition of remanence in which the grouping is worse after restoring beds to the horizontal position.

The *fold test* relies on the tilting or folding of the target geological material. If, for example, one wanted to establish the antiquity of a particular set of directions, one could deliberately sample units of like lithology, with different present attitudes (Figure 9.13). If the recovered directions are more tightly grouped before adjusting for tilt (as in the lower left panel), then the magnetization is likely to have been acquired after tilting. On the other hand, if directions become better grouped in the tilt adjusted coordinates (see upper right panel), one has an argument in favor of a pre-tilt age of the magnetization. Methods for quantifying the tightness of grouping in various coordinate systems will be discussed in later lectures.

In the *conglomerate test*, lithologies that are desirable for paleomagnetic purposes must be found in a conglomerate bed (Figure 9.14). In this rare and happy circumstance, we can sample them and show that: 1) the rock magnetic behavior is the same for the conglomerate samples as for those being used in the paleomagnetic study, 2) the directions of the studied lithology are well grouped, (Figure 9.14) and 3) the directions from the conglomerate clasts are randomly oriented (see Figure 9.14). If the directions of the clasts are not randomly distributed (Figure 9.14), then presumably the conglomerate clasts (and, by inference, the paleomagnetic samples from the studied lithology as well) were magnetized after deposition of the conglomerate. We will discuss statistical methods for deciding if a set of directions is random in later lectures.

The *baked contact test* is illustrated in Figure 9.15. It is similar to the conglomerate test in that we seek to determine whether the lithology in question has undergone pervasive secondary overprinting. When an igneous body intrudes into an existing *host rock*, it heats (or bakes) the

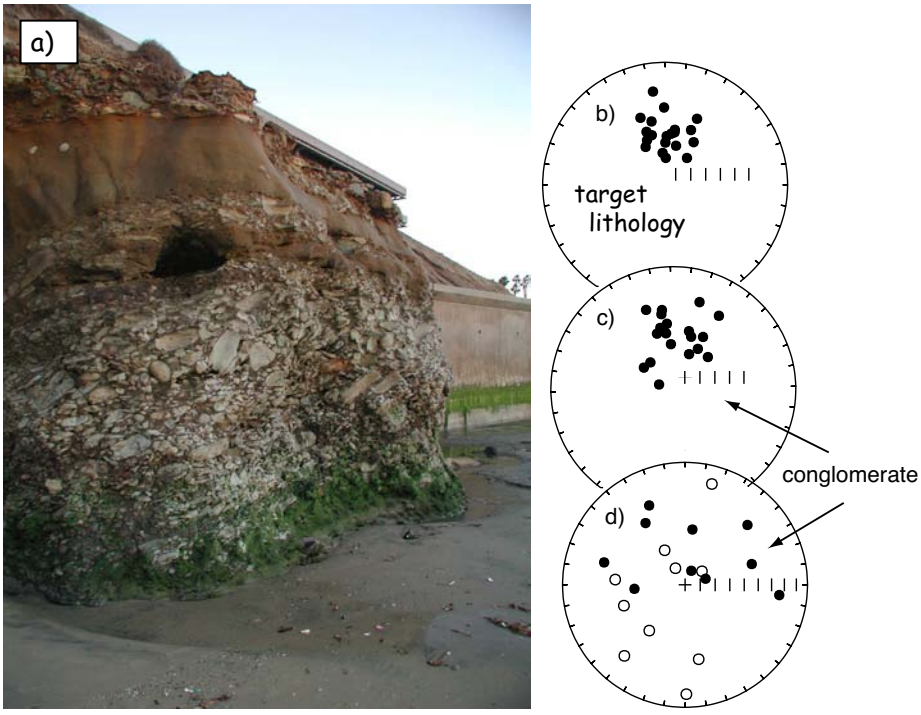

Figure 9.14: The paleomagnetic conglomerate test. a) The target lithology was involved in a catastrophic event leading to incorporation into a conglomerate bed. Samples are taken from individual clasts. The directions of samples from the target lithology are shown in b) indicating that it is relatively homogeneously magnetized. c) dirctions from the conglomerate clasts are also homogeneously magnetized; the magnetization must post-date formation of the conglomerate. In a positive conglomerate test d), the magnetization vectors of samples from the conglomerate clasts are random.

contact zone to above the Curie temperature of the host rock. The baked contact immediately adjacent to the intrusion should therefore have the same remanence direction as the intrusive unit. This magnetization may be in an entirely different direction from the pre-existing host rock. The maximum temperature reached in the baked zone decreases away from the intrusion and remagnetization is not complete. Thus the NRM directions of the baked zone gradually change from that of the intrusion to that of the host rock. Such a condition would argue against pervasive overprinting in the host rock that post-dated the intrusion, and the age of the intrusion would provide an upper bound on the age of remanence in the host rock.

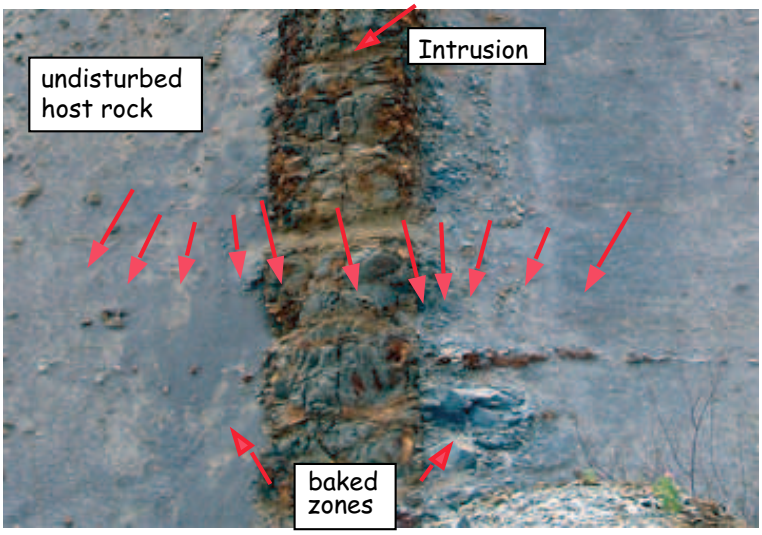

Figure 9.15: The baked contact test. In a positive test, zones baked by the intrusion are remagnetized and have directions that grade from that of the intrusion to that of the host rock. If all the material is homogeneously magnetized, then the age of the intrusion places an upper bound on the age of magnetization.

Appendix

A Directions using a sun compass

Referring to Figure 9.5, we see that the azimuth of the desired direction is the direction of the of the shadow plus the shadow angle α. The declination of the shadow itself is 180° from the direction toward the sun. In Figure A1, the problem of calculating declination from sun compass information is set up as a spherical trigonometry problem, similar to those introduced in Lecture 2 and its appendix. The declination of the shadow direction β', is given by 180 - β. We also know the latitude of the sampling location L (λ_L). We need to calculate the latitude of S (the point on the Earth's surface where the sun is directly overhead), and the local hour angle H.

Knowing the time of observation (in Universal Time), the position of S ($\lambda_s = \delta, \phi_s$ in Figure A1) can be calculated with reasonable precision (to within 0.01°) for the period of time between 1950 and 2050 using the procedure recommended in the 1996 Astronomical Almanac:

- First, calculate the Julian Day J. Then, calculate the fraction of the day in Universal Time U. Finally, calculate the parameter d which is the number of days from J2000 by:

$$d = J - 2451545 + U.$$

- The mean longitude of the sun (ϕ_s), corrected for aberration, can be estimated in degrees by:

$$\phi_s = 280.461 + 0.9856474d.$$

- The mean anomaly $g = 357.528 + 0.9856003d$ (in degrees).
- Put ϕ_s and g in the range $0 \rightarrow 360°$.
- The longitude of the ecliptic is given by $\phi_E = \phi_s + 1.915 \sin g + 0.020 \sin 2g$ (in degrees).
- The obliquity of the ecliptic is given by $\epsilon = 23.439 - 0.0000004d$.
- Calculate the right ascension (A) by:

$$A = \phi_E - ft \sin 2\phi_E + (f/2)t^2 \sin 4\phi_E,$$

where $f = 180/\pi$ and $t = \tan^2\epsilon/2$.

- The so-called "declination" of the sun (δ in Figure A1 which should not be confused with the magnetic declination D), which we will use as the latitude λ_s, is given by:

$$\delta = \sin^{-1}(\sin\epsilon \sin\phi_e).$$

- Finally, the equation of time in degrees is given by $E = 4(\phi_s - A)$.

We can now calculate the Greenwich Hour Angle GHA from the Universal Time U (in minutes) by $GHA = (U + E)/4 + 180$. The local hour angle (H in Figure A1) is $GHA + \phi_L$. We calculate β using the laws of spherical trigonometry (see Appendix to Lecture 2). First we calculate θ by the Law of Cosines (remembering that the cosine of the colatitude equals the sine of the latitude):

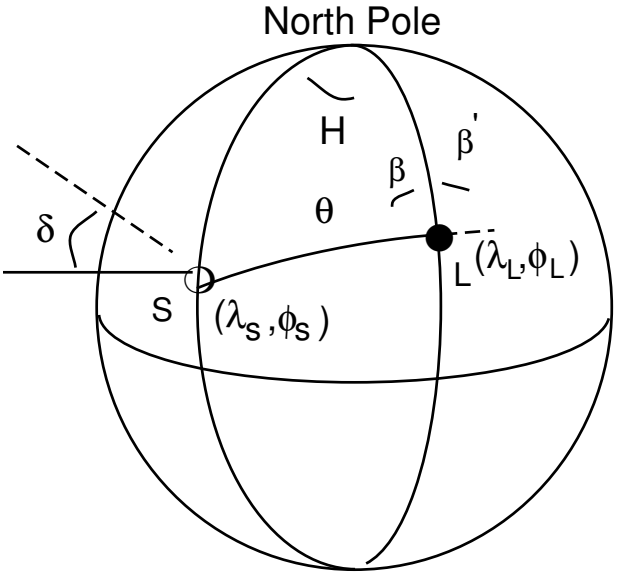

Figure A1: Calculation of the azimuth of the shadow direction (β') relative to true North, using a sun compass. L is the site location (at λ_L, ϕ_L), S is the position on the Earth where the sun is directly overhead (λ_S, ϕ_S).

$$\cos\theta = \sin\lambda_L \sin\lambda_s + \cos\lambda_L \cos, \lambda_s \cos H$$

and finally using the Law of Sines:

$$\sin\beta = (\cos\lambda_s \sin H)/\sin\theta.$$

If $\lambda_s < \lambda_L$, then the required angle is the shadow direction β', given by: $\beta' = 180 - \beta$. The azimuth of the desired direction in Figure 9.5 is β' plus the measured shadow angle α.

B Transformation of coordinates

The sample coordinate system is defined by a right-hand rule where the thumb ($\mathbf{X}_1$) is directed parallel to an arrow marked on the sample, the index finger ($\mathbf{X}_2$) is in the same plane but at right angles and clockwise to $\mathbf{X}_1$ and the middle finger ($\mathbf{X}_3$) is perpendicular to the other two (Figure B1a). The transformation of coordinates (x_i) from the $\mathbf{X}_i$ axes to the coordinates in the desired $\mathbf{X}'$ coordinate system (x'_i) is done by $x'_i = a_{ij}x_j$, or:

$$\begin{pmatrix} x'_1 \\ x'_2 \\ x'_3 \end{pmatrix} = \begin{pmatrix} a_{11} & a_{12} & a_{13} \\ a_{21} & a_{22} & a_{23} \\ a_{31} & a_{32} & a_{33} \end{pmatrix} \begin{pmatrix} x_1 \\ x_2 \\ x_3 \end{pmatrix}, \tag{B1}$$

where the a_{ij} are the *direction cosines* (the cosines of the angles between the different axes), where the subscript i refers to the new coordinate system $\mathbf{X}'$ and the subscript j refers to the old $\mathbf{X}$ coordinates. Thus, a_{12} is the cosine of the angle between $\mathbf{X}'_1$ and $\mathbf{X}_2$. The various a_{ij} can be calculated using spherical trigonometry (Lecture 2). For example, a_{11} for the general case depicted

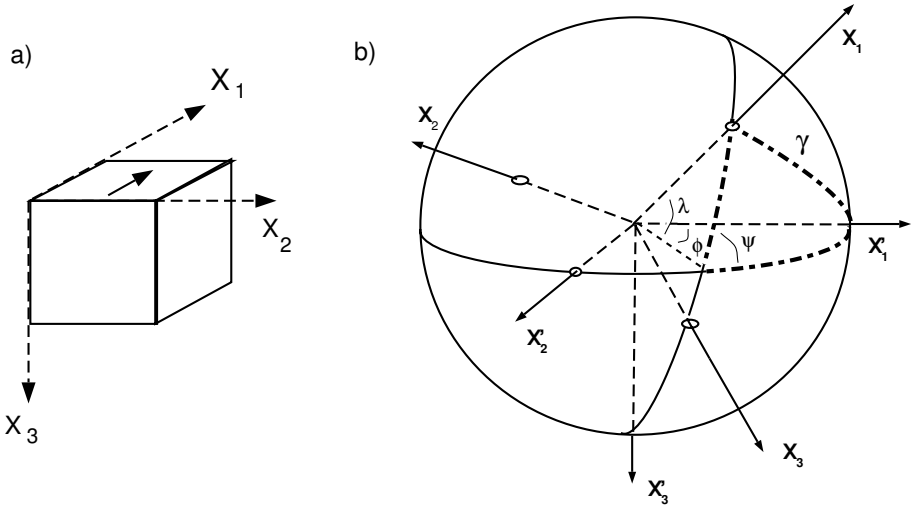

Figure B1: a) Sample coordinate system. b) Trigonometric relations between two cartesian coordinate systems, $\mathbf{X}_i$ and $\mathbf{X}'_i$. λ, ϕ, ψ are all known and the angles between the various axes can be calculated using spherical trigonometry. For example, the angle γ between $\mathbf{X}_1$ and $\mathbf{X}'_1$ forms one side of the triangle shown by dash-dot lines. Thus, $\cos\gamma = \cos\lambda\cos\phi + \sin\lambda\sin\phi\cos\psi$.

in Figure B1 is $\cos\alpha$, which is given by the Law of Cosines (Lecture 2) by using appropriate values, or:

$$\cos\alpha = \cos\lambda\cos\phi + \sin\lambda\sin\phi\cos\psi.$$

The other a_{ij} can be calculated in a similar manner. In the case of most coordinate system rotations used in paleomagnetism, X_2 is in the same plane as X'_1 and X'_2 (and is horizontal) so $\psi = 90°$. This problem is much simpler. The directions cosines for the case where $\psi = 90$ are:

$$a = \begin{pmatrix} \cos\lambda\cos\phi & -\sin\phi & -\sin\lambda\cos\phi \\ \cos\lambda\sin\phi & \cos\phi & -\sin\lambda\sin\phi \\ \sin\lambda & 0 & \cos\lambda \end{pmatrix}. \tag{B2}$$

The new coordinates can be obtained from equation B1, as follows:

$$\begin{aligned} x'_1 &= a_{11}x_1 + a_{12}x_2 + a_{13}x_3 \\ x'_2 &= a_{21}x_1 + a_{22}x_2 + a_{23}x_3 \\ x'_3 &= a_{31}x_1 + a_{32}x_2 + a_{33}x_3. \end{aligned} \tag{B3}$$

The declination and inclination can be calculated by inserting these values in the equations in Lecture 2 and its appendix. In practice, there are two transformations that are routinely made in paleomagnetism. Magnetizations are measured in sample coordinates. First, they must then be rotated into geographic coordinates. For this, the azimuth and plunge of the sample $\mathbf{X}_1$ axis can be used for ϕ and λ, respectively in equations B2 and B3. Second, samples are often taken from geologic units that are no longer in the same position as when they were magnetized; they are tilted. If paleo-horizontal can be recognized, for example, from quasi-horizontal laminations in sedimentary rocks, the orientation of the bedding plane can be measured as *strike* and *dip*, or as dip and *dip direction*. The strike is the direction of a horizontal line within the bedding plane and the

dip is the angle that the plane makes with the horizontal. Our convention is that dip is measured to the "right" of the strike direction. If the direction cosines relating the dip and dip direction to the geographic coordinate systems are plugged in for the a_{ij}, the data can be transformed into so-called *tilt adjusted* coordinates using equation B3.

C Principal Component Analysis

A sequence of data points which form a single component are equally weighted. The D, I, and M data are converted to corresponding x values (see Lecture 2). Then we calculate the coordinates of the "center of mass" ($\bar{x}$) of the data points:

$$\bar{x}_1 = \frac{1}{N}(\sum_1^N x_{1i}); \quad \bar{x}_2 = \frac{1}{N}(\sum_1^N x_{2i}); \quad \bar{x}_3 = \frac{1}{N}(\sum_1^N x_{3i}), \tag{C1}$$

where N is the number of data points involved. We then transform the origin of the data cluster to the center of mass:

$$x'_{1i} = x_{1i} - \bar{x}_1; \quad x'_{2i} = x_{2i} - \bar{x}_2; \quad x'_{3i} = x_{3i} - \bar{x}_3, \tag{C2}$$

where x'_i are the transformed coordinates.

C1 The orientation tensor and eigenvector analysis

The *orientation tensor* $\mathbf{T}$ (Scheidegger [1965]) (also known as the matrix of sums of squares and products), is extremely useful in paleomagnetism:

$$\mathbf{T} = \begin{pmatrix} \sum x'_{1i}x'_{1i} & \sum x'_{1i}x_{2i} & \sum x'_{1i}x'_{3i} \\ \sum x'_{1i}x'_{2i} & \sum x'_{2i}x'_{2i} & \sum x'_{2i}x'_{3i} \\ \sum x'_{1i}x'_{3i} & \sum x'_{2i}x'_{3i} & \sum x'_{3i}x'_{3i} \end{pmatrix}. \tag{C3}$$

$\mathbf{T}$ is a 3 x 3 matrix, where only six of the nine elements are independent. It is constructed in some coordinate system, such as the geographic or sample coordinate system. Usually, none of the six independent elements are zero. There exists, however, a coordinate system along which the "off-axis" terms are zero and the axes of this coordinate system are called the *eigenvectors* of the matrix. The three elements of $\mathbf{T}$ in the eigenvector coordinate system are called *eigenvalues*. In terms of linear algebra, this idea can be expressed as:

$$\mathbf{TV} = \tau\mathbf{V}, \tag{C4}$$

where $\mathbf{V}$ is the matrix containing three *eigenvectors* and τ is the diagonal matrix containing three *eigenvalues*. Equation C4 is only true if:

$$\det|\mathbf{T} - \tau| = 0. \tag{C5}$$

If equation C5 is expanded, we have a third degree polynomial whose roots (τ) are the eigenvalues:

$$(T_{11} - \tau)[(T_{22} - \tau)(T_{33} - \tau) - T_{23}^2] -$$

$$T_{12}[T_{12}(T_{33}-\tau)-T_{13}T_{23}]+T_{13}[T_{13}T_{23}-T_{13}(T_{22}-\tau)]=0.$$

The three possible values of τ (τ_1, τ_2, τ_3) can be found with iteration and determination. In practice, there are many programs for calculating τ. My personal favorite is the Numerical Module for Python (see many free web sites, especially Scientific Python (SciPy) for hints. Please note that the conventions adopted here are to scale the τ's such that they sum to one; the largest eigenvalue is termed τ_1 and corresponds to the eigenvector $\mathbf{V}_1$.

C2 Principal components of the orientation matrix

Inserting the values for the transformed components calculated in equation C2 into $\mathbf{T}$ gives the covariance matrix for the demagnetization data. The direction of the axis associated with the greatest scatter in the data (the principal eigenvector $\mathbf{V}_1$) corresponds to a best-fit line through the data. This is usually taken to be the direction of the component in question. This direction also corresponds to the axis around which the "moment of inertia" is least. The eigenvalues of $\mathbf{T}$ are the variances associated with each eigenvector. Thus the standard deviations are $\sigma_i = \sqrt{\tau_i}$. The so-called *maximum angular deviation* or MAD of Kirschvink [1980] is defined as:

$$MAD = \tan^{-1}(\sqrt{(\sigma_2^2+\sigma_3^2)}/\sigma_1). \quad \text{(C6)}$$

If no unique principal direction can be isolated (as for the sample in Figure 9.11c-d), the eigenvector $\mathbf{V}_3$ associated with the least eigenvalue τ_3 can be taken as the pole to the best-fit plane wherein the component of interest must lie. Kirschvink [1980] also defines a MAD angle for the plane as:

$$MAD_{\text{plane}} = \tan^{-1}\sqrt{\tau_3/\tau_2+\tau_3/\tau_1}.$$

Bibliography

Butler, R. F. (1992), *Paleomagnetism: Magnetic Domains to Geologic Terranes*, Blackwell Scientific Publications.

Collinson, D. W. (1983), 'Methods in Rock Magnetism and Paleomagnetism'.

Dupont-Nivet, G., Guo, Z., Butler, R. & Jia, C. (2002), 'Discordant paleomagnetic direction in Miocene rocks from the central Tarim Basin: evidence for local deformation and inclination shallowing', *Earth Planet. Sci. Lett.* **199**, 473–482.

Evin, K., Lambert, G.-N., Langouët, L., Lanos, P. & Oberlin, C. (1998), *La datation en laboratororie*, Editions Errance, Paris.

Kirschvink, J. L. (1980), 'The least-squares line and plane and the analysis of paleomagnetic data', *Geophys. Jour. Roy. Astron. Soc.* **62**, 699–718.

Scheidegger, A. E. (1965), 'On the statistics of the orientation of bedding planes, grain axes, and similar sedimentological data', *U.S. Geo. Surv. Prof. Pap.* **525-C**, 164–167.

Zijderveld, J. D. A., ed. (1967), *A.C. demagnetization of rocks: analysis of results*, Methods in Paleomagnetism, Chapman and Hall.

Lectures in Paleomagnetism, 2005
by Lisa Tauxe

Citation:
http://earthref.org/MAGIC/books/Tauxe/2005/

June 4, 2005

Chapter 10

Paleointensity

Suggested Reading

For background:
Coe et al. (1978)
http://www.angelfire.com/wa/hurben/mag.html
Tauxe (1993)
To learn more:
Chapter 8 & 15: Dunlop and Özdemir (1997)

10.1 Introduction

In Lecture 9 we discussed methods for obtaining directional data from rock samples. In principle, it is also possible to determine the intensity of ancient magnetic fields, because the primary mechanisms by which rocks become magnetized (e.g., thermal, chemical and detrital remanent magnetizations) can be approximately linearly related to the ambient field for low fields such as the Earth's (see Lecture 5), i.e.,

$$M_{NRM} = \alpha_{anc} B_{anc}$$

and

$$M_{lab} = \alpha_{lab} B_{lab}.$$

where α_{lab} and α_{anc} are constants of proportionality. If these are the same, we can divide the two and rearrange them to get:

$$B_{anc} = \frac{M_{NRM}}{M_{anc}} B_{lab}.$$

So, if the laboratory remanence has the same proportionality constant with respect to the applied field as the ancient one, the remanences were linearly related to the applied field, and the NRM is solely composed of a single component, all one need do to get the ancient field is measure the NRM, then give the rock a laboratory remanence and multiply the ratio by the lab field.

In practice, paleointensity is not so simple. The remanence acquired in the laboratory may not have the same proportionality constant as the original remanence (e.g., the sample has altered its capacity to acquire remanence or was acquired by a mechanism difficult to reproduce in the laboratory). The assumption of linearity between the remanence and the applied field may not

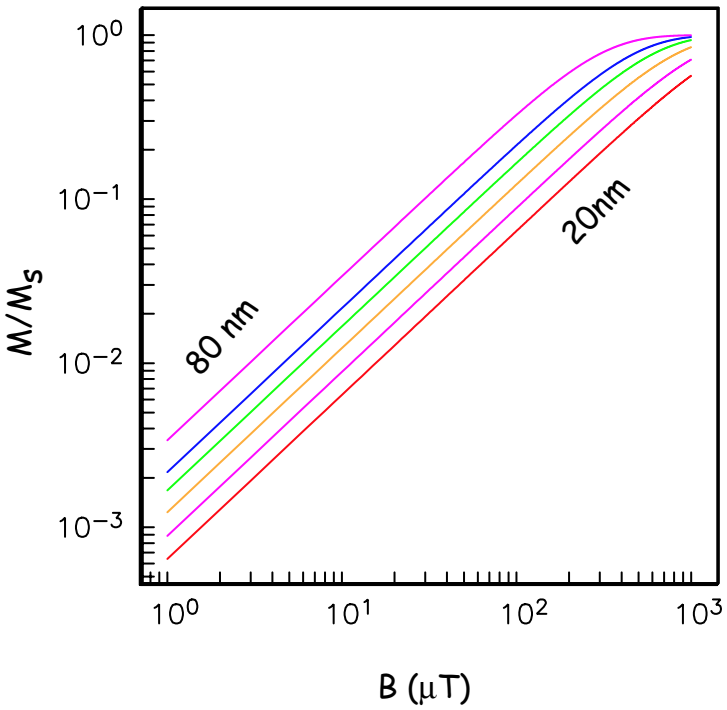

Figure 10.1: Predicted TRM expressed as a fraction of saturation for various particle sizes of magnetite. Note the nick point for which the linearity assumption fails is a strong function of particle size, but linearity holds true for fields less than a few hundred microtesla.

hold true (see e.g., numerical modelling of DRM in Lecture 5). Or, the natural remanence may have multiple components, for example, an original remanence plus a viscous one. In this lecture we will discuss the assumptions behind paleointensity estimates and outline various experimental and statistical methods in getting paleointensity data. We will start by considering thermal remanences and then address depositional ones. To my knowledge, no one has deliberately attempted paleointensity using other remanence types such as chemical or viscous remanences.

10.2 Paleointensity with thermal remanence

As we learned in Lecture 5, thermal remanences of single domain particles are expected to be linearly related to the applied field for low fields like the Earth's. Predicted TRM curves for randomly oriented populations of single domain particles ranging in size from 20 to 80 nm are plotted in Figure 10.1 (expressed as the fraction of saturation.) [Particles of magnetite larger than that will have more complicated remanent states (flower, vortex, multi-domain) and may not follow the predicted curves.] As the particle size increases, the field at which significant departures from linearity of remanence with applied field decreases. Nonetheless, the largest intensities on the Earth today (∼65 μT) are well within the linear region and one could reach several hundred microtesla before having to worry about non-linearity. Therefore the linearity assumption outlined in the introduction appears to be reasonably well founded.

The second assumption for absolute paleointensity determinations is that the laboratory and

ancient constants of linearity are the same (i.e., $\alpha_{lab} = \alpha_{anc}$). Simply measuring the NRM and giving the sample a total TRM leaves no way of verifying this assumption. Alteration of the sample during heating could change the capacity to acquire TRM and give erroneous results with no way of assessing their validity.

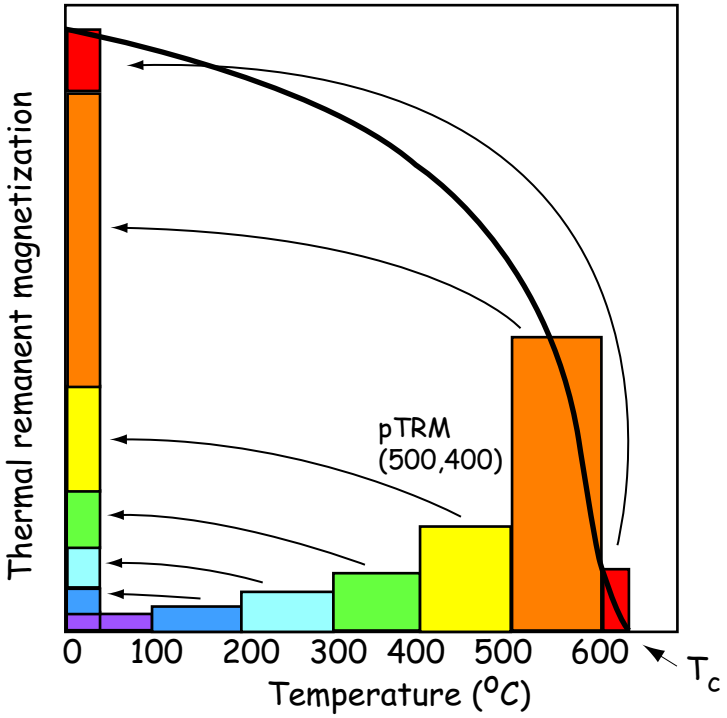

Figure 10.2: Laws of independence and additivity. pTRMs acquired by cooling between two temperature steps are independent from one another and sum together to form the total TRM.

There are several ways of checking the ability of the sample to acquire TRM in paleointensity experiments. In the following we will discuss the so-called "Thellier-Thellier" and "Shaw" methods. Other approaches attempt to prevent the alteration from occuring, for example by using microwaves to heat just the magnetic phases, leaving the rest of the sample cool. Finally, some methods attempt to normalize the remanence with IRM and avoid heating altogether. We will briefly describe each of these in turn, beginning with the Thellier-Thellier approach.

10.2.1 Thellier-Thellier type experiments

In order to detect and eliminate data after the onset of alteration, Thellier and Thellier (1959) suggested heating samples up in stages, progressively replacing the NRM with pTRMs in the hope of establishing the ratio M_{NRM}/M_{lab} prior to the onset of alteration. The so-called "Thellier-Thellier" approach is particularly powerful when lower temperature pTRM steps are repeated, to verify directly that the ability to acquire a pTRM has not changed.

The step-wise approach relies on the assumption that partial thermal remanences (pTRMs) acquired by cooling between any two temperature steps (e.g., 500° and 400°C in Figure 10.2) are independent of those acquired between any other two temperature steps. This assumption is called

the "Law of independence" of pTRMs. The approach also assumes that the total TRM is the sum of all the independent pTRMs (see Figure 10.2), an assumption called the "Law of additivity".

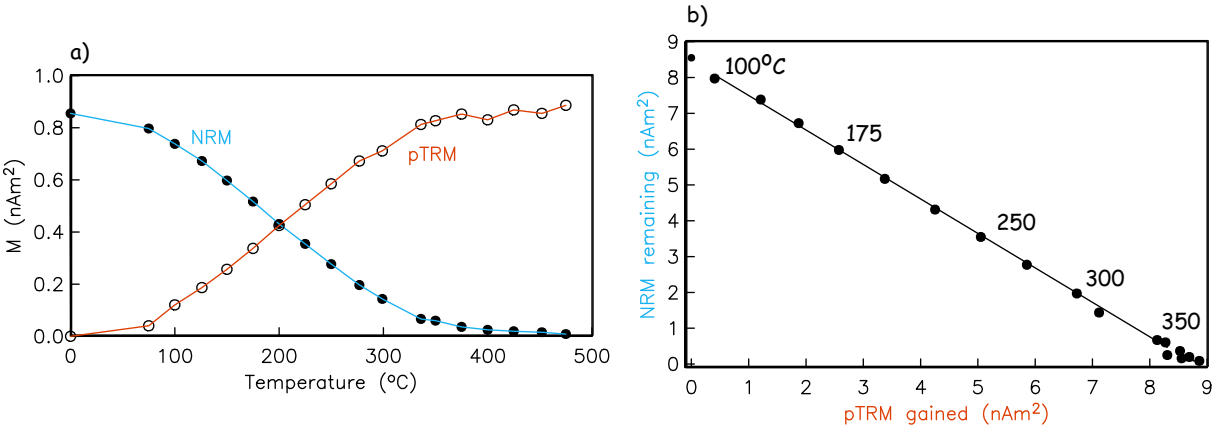

Figure 10.3: Illustration of the Thellier-Thellier method for determining absolute paleointensity. a) thermal demagnetization of NRM shown as filled circles and the laboratory acquired pTRM shown as open symbols, and b) Plot of NRM component remaining versus pTRM acquired for each temperature step.

There are several possible ways to progressively replace the NRM with a pTRM in the laboratory. In the original Thellier-Thellier method, the sample is heated to some temperature (T_1) and cooled in the laboratory field B_{lab}. After measurement of the combined remanence (what is left of the natural remanence plus the new laboratory pTRM) is:

$$M_{first} = M_{NRM} + M_{pTRM}.$$

Then the sample is heated a second time and cooled upside down (in field $-B_{lab}$). The second remanence is therefore:

$$M_{second} = M_{NRM} - M_{pTRM}.$$

Simple vector subtraction allows the determination of the NRM remaining at each temperature step and the pTRM gained (see Figure 10.3a). These are usually plotted against each other in what is usually called an "Arai plot" (Nagata et al. 1961) as in Figure 10.3b. This method implicitly assumes that a magnetization acquired by cooling from a given termperature isentirely removed by re-heating to the same temperature (i.e., $T_b = T_{ub}$. This condition is known as the Law of Reciprocity.

As magnetic shielding improved, several more sophisticated approaches were developed. In the most popular paleointensity technique (usually attributed to Coe, 1967), we substitute cooling in zero field for the first heating step allowing the direct measurement of the NRM remaining at each step. The two equations now are:

$$M_{first} = M_{NRM},$$

and

$$M_{second} = M_{NRM} + M_{pTRM}.$$

The laboratory pTRM in this "zero-field/in-field" (or ZI) method can be gotten through vector subtraction. Alternatively, the first heating and cooling can be done in the laboratory field and the second in zero field (Aitken et al., 1988), here called the "in-field/zero-field" or (IZ) method.

In all three of these approaches, lower temperature steps can be repeated to determine whether the remanence carrying capacity of the sample has changed. These steps are called the "pTRM checks". Differences between the first and second pTRMs at a given temperature indicate a change in capacity for acquiring thermal remanences and are grounds for suspicion or rejection of the data after the onset of such a change.

Despite its huge popularity and wide spread use, the double heating approach has its own drawbacks. Alteration of the ability to acquire a pTRM is not the only cause for failure of the assumption of equality of α_{lab} and α_{anc}. Recall the behavior of particles displaying transient hysteresis described in Lecture 8. Certain particles began in a saturated state but formed vortex structures as the field was lowered from saturation to zero. These vortex structures were destroyed again as the field was ramped back up. However, the field at which the vortex was destroyed was higher than the field at which it formed. One can imagine that the same thing might occur if we cooled a particle from its Curie Temperature down to zero, and then heated it back up again. Just below the Curie Temperature, the particle would be in a saturated state (because M_s is quite low and the vortex structure is just an attempt by the particle to reduce its external field). As the temperature lowers, M_s grows so at some temperature a vortex structure may form. This vortex may well remain stable to higher temperatures by analogy to the transient hysteresis phenomenon.

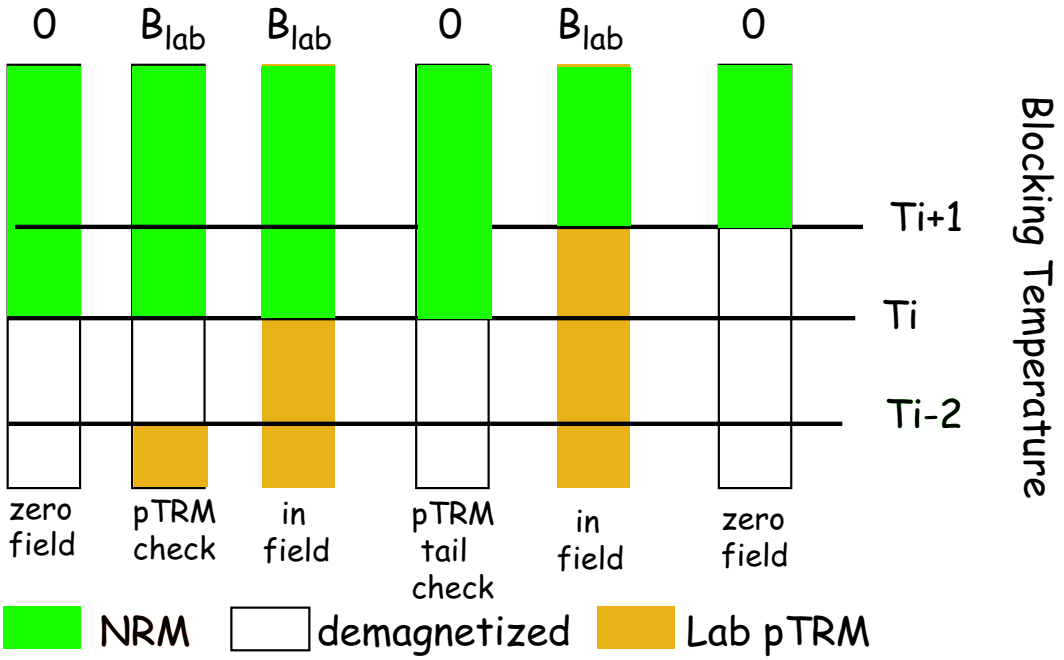

Figure 10.4: The IZZI protocol (see text). [Figure drawn in collaboration with Agnes Genevey.]

If the particle is large enough to have domain walls in its remanent state, then the scenario would be that the particle begins at saturation at just below its Curie Temperature as before. As the temperature is lowered, at some temperature domain walls will begin to form. The remanent state will have some net moment because the domain walls are distributed such that there is

incomplete cancellation leaving a small net remenence, proportional to the applied field for moderate field strengths. As the temperature ramps up again, they will "walk around" within the particle seeking to minimize the magnetostatic energy. The domain walls will not be destroyed again until temperatures very near the Curie Temperature.

The fact that blocking and unblocking of remanence occurs at different temperatures for particles with vortex or domain wall structures means that a pTRM acquired at a given temperature will not be destroyed at the same temperature. This means that $\alpha_{lab} \neq \alpha_{anc}$ and the experiment will give curved Arai plots (see Dunlop and Özdemir, 1997 for a more complete discussion). If any portion of the NRM/TRM data are used, instead of the entire temperature spectrum, the result will be biassed. For example, the lower temperature portion might be selected on the grounds that the higher temperature portion is affected by alteration or the higher temperature portion might be selected on the grounds that the lower temperature potion is affected by VRM. Both of these interpretations would be wrong.

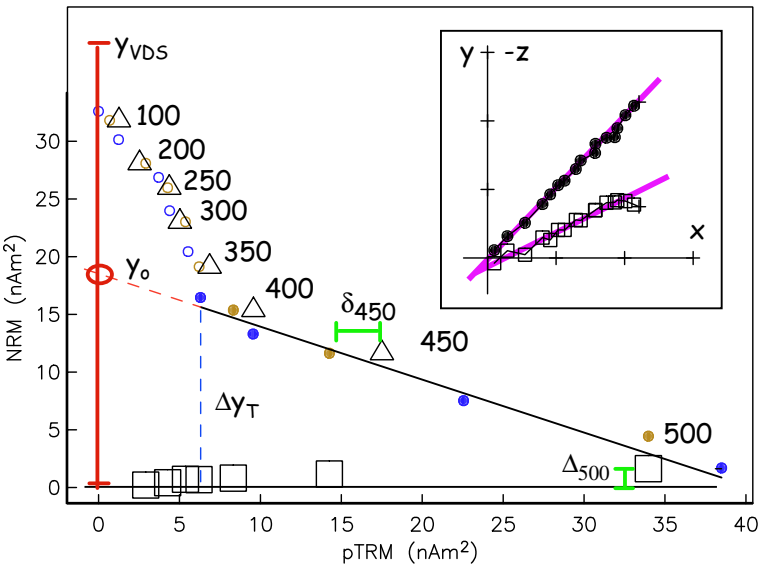

Figure 10.5: Data from an IZZI experiment. Circles are the pTRM gained at a particular temperature step versus the NRM remaining. Solid symbols are those included in the slope calculation. Blue (darker) symbols are the infield-zerofield steps (IZt) and the brown (lighter) symbols are the zerofield-infield steps (ZI). The triangles are the pTRM checks and the squares are the pTRM tail checks. The difference between the pTRM check and the original measurement is δ_i as shown by the horizontal bar labeled δ_{450}. The difference between the first NRM measurement and the repeated one (the pTRM tail check) is shown by the vertical bar labelled Δ_{500}. The vector difference sum (VDS; Lecture 9) is the sum of all the NRM components (tall vertical bar labelled VDS). The NRM fraction is shown by the vertical dashed bar. The insets are the vector components (x, y, z) of the zero field steps. The solid symbols are (x, y) pairs and the open symbols are (x, z) pairs. The specimen was unoriented with respect to geographic coordinates. The laboratory field was applied along the z-axis in the in-field steps. [Redrawn from Tauxe and Staudigel (2004).]

In order to detect inequality of blocking and unblocking and the presence of high temperature pTRM tails, two embellishments to the Thellier-Thellier type experiment have been proposed. In the first modification, a second zero field step is inserted after the in field step in the IZ method.

This so-called "pTRM-tail check" (e.g., Riisager and Riisager 2001) assesses whether the pTRM gained in the laboratory at a given temperature is completely removed by re-heating to the same temperature. If not, the sample is said to have a pTRM tail, which is a consequence of an inequality of the unblocking temperature T_{ub} and the original blocking temperature T_b in violation of the law of reciprocity and grounds for rejection. The second modification is to alternate between the IZ methods and the ZI methods (the so-called "IZZI" method of Yu et al., 2004, see Figure 10.4). This method is also extremely sensitive to the presence of pTRM tails and obviates the need for the pTRM-tail check step. An example of a complete IZZI experiment is shown in Figure 10.5.

A well done paleointensity experiment allows us to calculate a number of parameters to quantify the data reliability. Many of these are listed in the Appendix. Paleointensity parameters are designed to test 1) whether the NRM was a single component magnetization, 2) whether alteration occurred during laboratory re-heating, and 3) whether blocking and unblocking were reciprocal. They also provide measures of over-all quality (scatter about the best-fit line, distribution of temperature steps, fraction of the NRM, etc. of a given experiment. Examples of a variety of typical experiments are shown in Figure 10.6.

There are several other violations of the fundamental assumptions that require additional tests and/or corrections in the paleointensity experiment besides alteration or failure of the law of reciprocity. For example, if the sample is anisotropic with respect to the acquisition of thermal remanence, the anisotropy tensor must be determined and the intensity corrected (e.g, Fox and Aitken, 1980). Moreover, because the approach to equilibrium is a function of time, slower cooling results in a larger TRM; hence differences in cooling rate between the original remanence acquisition and that acquired in the laboratory will lead to erroneous results (e.g., Halgedahl et al., 1980). The detection and correction for anisotropy will be the subject of a later lecture. Compensating for differences in cooling rate is relatively straight forward if the original cooling rate is known and the samples behave according to single domain theory (see, e.g., Figure 10.7 for a simple graphical correction method). Alternatively, one could take an empirical approach in which the rock is allowed to acquire a pTRM in under varying cooling rates, an approach useful for cooling rates of up to a day or two.

10.2.2 Use of ARM to detect alteration

The previous section was devoted to Thellier-Thellier style experiments in which alteration of the ability of a sample to acquire pTRM changes during laboratory heating is detected. In this section we will consider an alternative approach, long in use in paleointensity studies. In the so-called "Shaw method" (e.g., Shaw, 1974) we measure the NRM, then progressively demagnetize it with alternating fields to establish the coercivity spectrum of the sample prior to heating. The sample is then given an ARM (which is thought to be analogous to the original TRM). This ARM is also progressively demagnetized. Then the sample is given a total TRM, which is AF demagnetized as well. Finally, the sample is given a second ARM and demagnetized for a final time. If the first and second ARMs do not have the same coercivity spectrum, the sample has altered and the NRM/TRM ratio is suspect. Some have suggested that the ratio of the first ARM to the second be used to "correct" the NRM/TRM ratio (e.g., Rolph and Shaw, 1985).

The primary reasons stated for using the Shaw method are 1) that it is faster and 2) that because the sample is only heated once (albeit to a high temperature), alteration is minimized. The first rationale is no longer very persuasive because modern thermal ovens have very high capacities (e.g., we can heat up to 60 samples at once at SIO) and the Thellier-Thellier method is certainly not

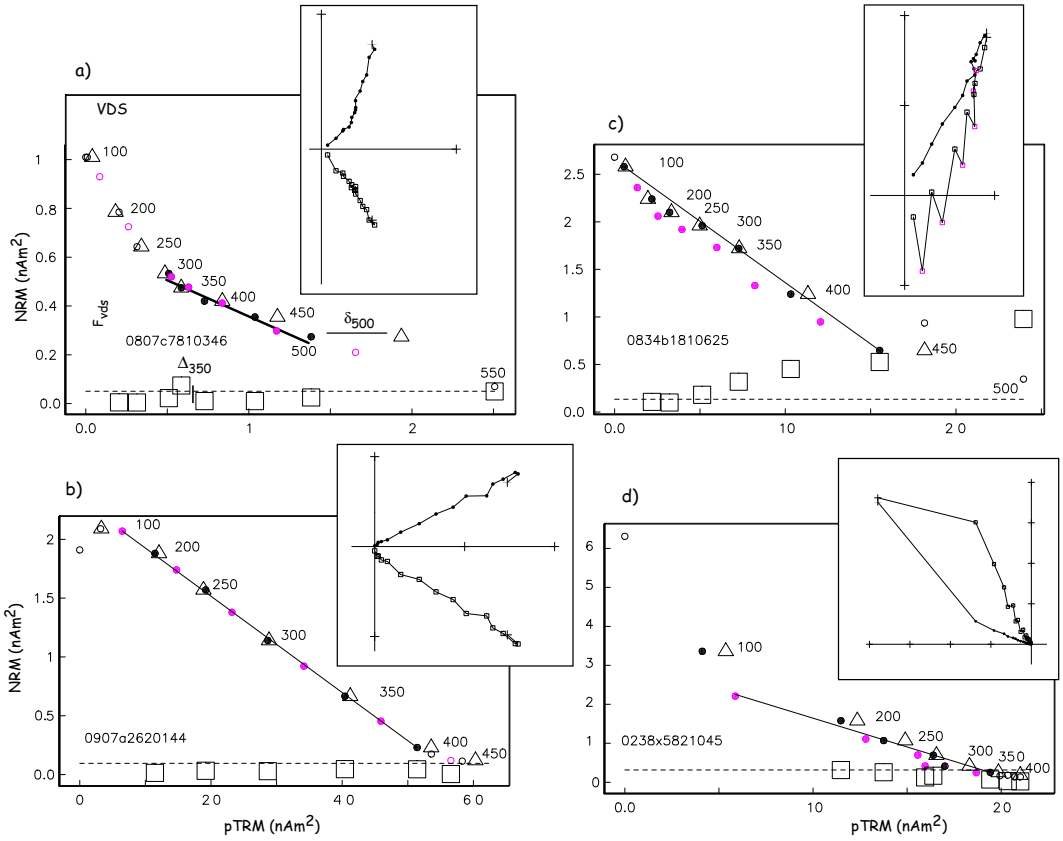

Figure 10.6: Examples of paleointensity data (symbols same as in Figure 10.5). a) Sample showing curved Arai plot, and two component vector-end point diagrams suggestive of a low-Temperature viscous component (note how the pTRM tail checks are near zero and the IZ and ZI data are not zig-zagged as would be the case for pTRM tails.) b) Example of nearly ideal behavior. c) Example of zig-zagging indicative of failure of reciprocity of blocking and unblocking. d) Example of so-so data. [Figure from Tauxe, in press.]

slower than the Shaw method on a per sample basis any more. The second rationale may have some validity, but if alteration does occur, it is difficult or at least inadvisable to use the data because the unaltered part can not be extracted from the altered part.

10.2.3 Use of microwaves for thermal excitation

Up until now we have not concerned ourselves with HOW the magnetic moment of a particular grain flips its moment. In Lecture 5 we mention "thermal energy" and leave it at that. But how does thermal energy do the trick?

Instead of electronic spins being simply aligned with some minimum energy direction (aligned with the field, or along some easy axis), we alluded to random thermal fluctuations. An external magnetic field generates a torque (Lecture 3) on the electronic spins, and in isolation, a magnetic moment will respond to the torque in a manner similar in some respects to the way a spinning top responds to gravity: the magnetic moment will precess about the applied field direction, spiraling

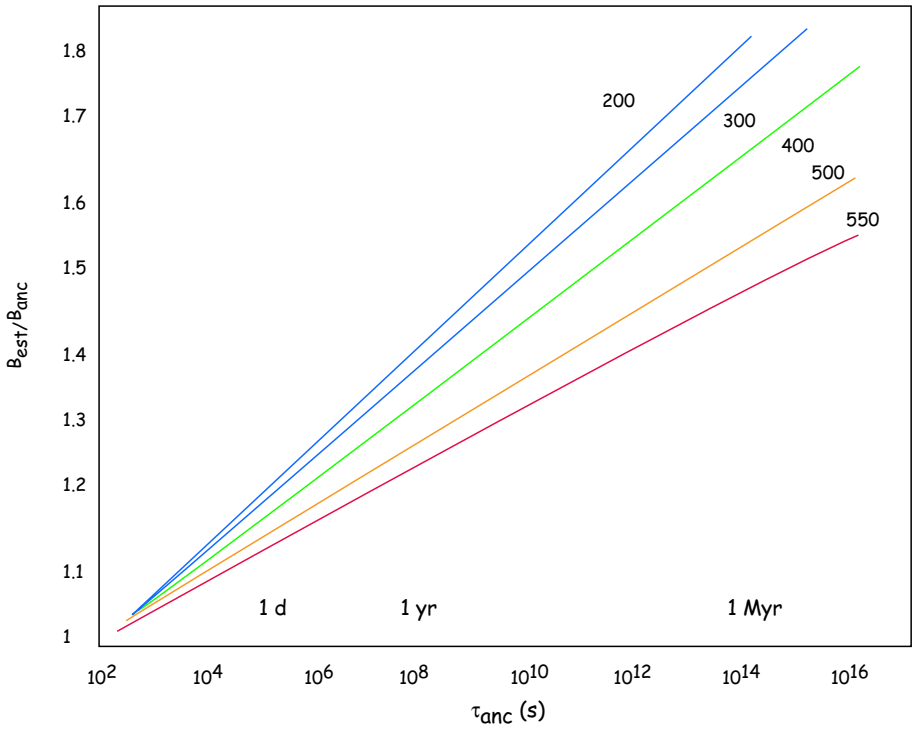

Figure 10.7: Ratio of estimated field intensity B_{est} to ancient field intensity B_{anc} versus the original relaxation time τ_{anc} (related to cooling rate) and blocking temperature (numbers ranging from 200 to 550°C). If a particle fraction of the remanence has a blocking temperature of 400°C and took a year to cool originally, a laboratory experiment with a cooling time of a few hundred seconds will overestimate the field by approximately 30%. [Redrawn from Selkin et al., 2000.]

in and come to a rest parallel to it (Figure 10.8a). Because of the strong exchange coupling (Lecture 4) in magnetic phases, spins tend to be aligned parallel (or antiparallel) to one another and the spiralling is done in a coordinated fashion, with neighboring spins as parallel as possible to one another (Figure 10.8b). This phenomenon is known as a "spin wave".

Raising the temperature of a body transmits energy (via "phonons") to the electronic spins, increasing the amplitude of the spin waves. This magnetic energy is quantized in "magnons". In the traditional Thellier-Thellier experiment, the entire sample is heated and the spin waves are excited to the point that some may flip their moments as described in Lecture 5 and the preceding section.

As in most kitchens, there are two ways of heating things up: the conventional oven and the microwave oven. In the microwave oven, molecules with certain vibrational frequencies (e.g., water) are excited by microwaves. These heat up, passing their heat on to the rest of the pizza (or whatever). If the right microwave frequency is chosen, ferromagnetic particles can also be excited directly, inviting the possibility of heating only the magnetic phases, leaving the matrix alone (e.g., Walton et al., 1993). The rationale for developing this method is to reduce the degree of alteration

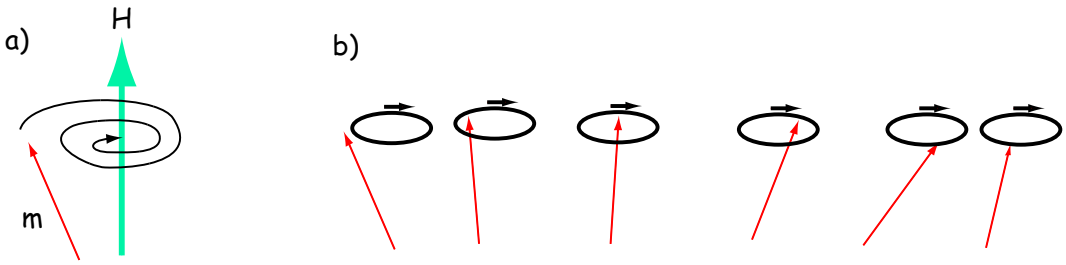

Figure 10.8: a) response of a magnetic moment to the torque of an applied field for isolated moments. b) Response of coupled moments to a perturbation. Neighboring spins produce an effect known as "spin waves".

experienced by the sample because the matrix often remains relatively cool, while the ferromagnetic particles themselves get hot. [The magnons get converted to phonons, thereby transferring the heat from the magnetic particle to the matrix encouraging alteration, but there may be ways of reducing this tendency (see Walton 2004).]

The same issues of alteration, reciprocity and cooling rate differences arise in the microwave approach as in the thermal approach. Ideally, the same experimental protocol could be carried out with microwave ovens as with thermal ovens. In practice, however, it has proved quite difficult to repeat the same internal temperature making double (or even quadruple) heatings problematic although great progress toward this end has been made recently (e.g., Böhnel et al., 2003.) However, it is likely that the issues of reciprocity of blocking and unblocking in the original (thermally blocked) and the laboratory (microwave unblocked) and differences in the rate of blocking and unblocking will remain a problem for some time as they have for thermally blocked remanences. Nonetheless, if alteration can be prevented by this method, it is worth pursuing until all the bugs have been worked out.

10.2.4 Use of IRM normalization

Sometimes it is difficult or impossible to heat samples because they will alter in the atmosphere of the lab, or the material is too precious to subject to heating experiements (e.g., lunar samples and perhaps some archeological artifacts). Looking again at Figure 10.1 suggests an alternative for order of magnitude guesstimates for paleointensity without heating at all. TRM normalized by a saturation remanence (IRM) is linearly related to the applied field, for single domain remanences in fields up to some value depending on mineralogy.

Cisowski and Fuller (1986) advocated the use of IRM normalization of the NRMs of lunar samples to estimate paleointensity. They argued that, especially when both remanences were partially demagnetized using alternating field demagnetization, the NRM:IRM ratio gave order of magnitude constraints on absolute paleointensity and reasonable relative paleointensity estimates. Their argument is based on mono-mineralic suites of rocks with uniform grain size. They further argue that multi-domain contributions can be eliminated by the AF demagnetization.

As can be seen by examining Figure 10.1, at best only order of magnitude estimates for absolute paleointensity are possible. The mono-mineralic and uniform grain size constraints make even this unlikely. Finally, the behavior of multi-domain TRMs and IRMs do not behave similarly under AF demagnetization, the former being much more stable than the latter. Nonetheless, if magnetic uni-

formity can be established, it may in fact be useful for establishing relative paleointensity estimates as is done routinely in sedimentary paleointensity studies (see next section). However, the caveats concerning single component remanences are still valid and perhaps complete AF demagnetization of the NRM would be better than a single "blanket" demagnetization step.

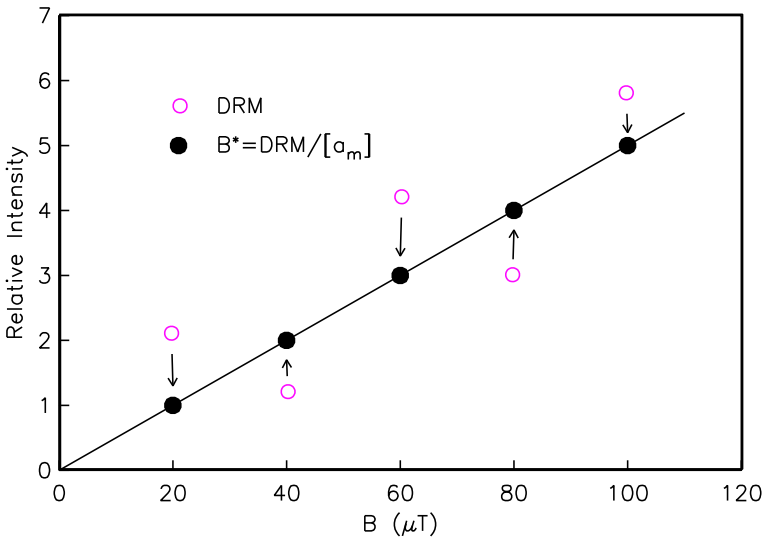

Figure 10.9: Principles of relative paleointensity. The original DRM is plotted as open symbols. It is a function not only of the applied field, but also of the magnetic activity $[a_m]$ of the sample. When normalized by $[a_m]$ (dots), the DRM is a linear function of applied field B.

10.3 Paleointensity with DRMs

The principle on which paleointensity studies in sedimentary rocks rests is that DRM is linearly related to the magnitude of the applied field **B**. We learned in Lecture 5 that this is unlikely to be universally true, yet it is the foundation of all relative paleointensity studies published to date. Forgetting for the moment that non-linear behavior may in fact be frequently obeyed in nature, we will proceed with a discussion of paleointensity in sediments making the assumption of linearity.

Following from the introductory discussion of paleointensity in general, we require a laboratory redeposition experiment that duplicates the natural remanence acquisition process in order to be able to determine absolute paleointensity in sediments. The problem with sedimentary paleointensity data is that laboratory conditions can rarely (if ever) achieve this. Assuming that the remanence is not chemical but depositional in origin, the intensity of remanence is still a complicated function of applied field, magnetic mineralogy, concentration, and even chemistry of the water column.

Under the ideal conditions depicted in Figure 10.9, the initial DRM of a set of samples deposited under a range of magnetic field intensities (B) is shown as open circles. The relationship is not linear because each sample has a different response to the applied field (here called magnetic activity $[a_m]$) as a result of differences in the amount of magnetic material, magnetic mineralogy, etc. For example, samples with a higher concentration of magnetic material will have a higher DRM. If $[a_m]$ can be successfully approximated, for example, by bulk remanences such as IRM or ARM, or

by bulk magnetic susceptibility χ_b (Lectures 5 and 8), then a normalized DRM (shown as dots in Figure 10.9) will reflect at least the relative intensity of the applied field.

Our theoretical understanding of DRM is much less developed than for TRM (Lecture 5). Because of the lack of a firm theoretical foundation for DRM, there is no simple method for determining the appropriate normalization parameter. In Lectures 5 and 8 we considered a variety of theoretical aspects of DRM and various parameters potentially useful for normalization. Many proxies have been proposed ranging from normalization by bulk magnetic properties such as ARM, IRM, or χ. Perhaps the most robust of these uses a step-wise demagnetization/remagnetization approach similar to the Thellier-Thellier method for thermal remanences, using either a TRM or an ARM as the laboratory remanence (Tauxe et al. 1995). One can imagine that even more sophisticated normalization techniques could be devised by targeting particular coercivity fractions discovered by the IRM component diagrams discussed in Lecture 8.

How can sedimentary relative paleointensity data be judged? Here are some thoughts:

1. The natural remanence must be carried by a detrital phase of high magnetic stability. Furthermore, the portion of the natural remanent vector used for paleointensity should be a single, well defined component of magnetization. The nature of the NRM can be checked with progressive demagnetization using AF and thermal techniques. Supplementary information from hysteresis and rock magnetic experiments can also be useful.

2. The detrital remanence must be an excellent recorder of the geomagnetic field, exhibit no inclination error and if both polarities are present the two populations should be antipodal. The associated directional data must therefore be plotted on equal area projections whenever they are available.

3. Large changes in concentration (more than about an order of magnitude) and any change in magnetic mineralogy or grain size should be avoided. These changes can be detected with the use of bi-plots of, for example, IRM and χ (see Lecture 8). Such bi-plots should be linear, with low scatter.

4. The relative paleointensity estimates that are coherent with bulk rock magnetic parameters should be treated with caution. Coherence can be assessed using standard spectral techniques.

5. Records from a given region should be coherent within the limits of a common time scale. Whenever possible duplicate records should be obtained and compared.

6. For a relative paleointensity record to have the maximum utility, it should have an independent time scale. Many deep sea sediment records are calibrated using oxygen isotopic curves or magnetostratigraphic age constraints (or both). Lake sediments are more difficult to date and rely for the most part on radiocarbon ages.

Appendix

A Absolute paleointensity parameter estimation

1. We can calculate the best-fit line (and its maximum angle of deviation - MAD) for the component used for paleointensity using the technique described in Lecture 9. The angle between the component (shown as the heavy purple line in the inset to Figure 10.5 and the origin is the Deviation ANGle (DANG).

2. We can calculate the best-fit slope (b) for the data on the NRM-pTRM plot and its the standard error σ (York, 1966; Coe et al. 1978). The procedure for calculating the best-fit slope, which is the best estimate for the paleofield, is given as follows:

   • Take the N data points that span two temperature steps T_1 and T_2, the best-fit slope b relating the NRM (y_i) and the pTRM (x_i) data in a least squares sense (taking into account variations in both x and y is given by:

$$b = -\sqrt{\frac{\sum_i (y_i - \bar{y})^2}{\sum_i (x_i - \bar{x})^2}}, \tag{A1}$$

   where $\bar{y}$ is the average of all y values and $\bar{x}$ is the average of all x values.

   • The y-intercept (y_o; see Figure 10.5) is given by $\bar{y} - b\bar{x}$.

   • The standard error of the slope σ is:

$$\sigma_b = \sqrt{\frac{2\sum_i (y_i - \bar{y})^2 - 2b\sum_i (x_i - \bar{x})(y_i - \bar{y})}{(N-2)\sum_i (x_i - \bar{x})^2}}. \tag{A2}$$

3. The parameter $\beta = \sigma/|b|$ is a measure of the uncertainty in the slope caused by the scatter in the data about the best-fit line.

4. The remanence fraction, f, was defined by Coe et al. (1978) as:

$$f = \Delta y_T / y_o,$$

   where Δy_T is the length of the NRM/TRM segment used in the slope calculation (see Figure 10.5.

5. The "gap factor" g penalizes uneven distribution of data points and is:

$$g = 1 - \bar{\Delta}\bar{y}/\Delta y_T,$$

   where $\bar{\Delta}\bar{y}$ is given by :

$$\bar{\Delta}\bar{y} = \frac{1}{\Delta y_T} \sum_{i=1}^{i=N-1} \Delta y_i^2$$

   and is the weighted mean of he gaps Δy_i between the N data points along the selected segment. As data spacing becomes less uniform, g decreases.

6. The Coe quality index q combines the standard error of the slope, the NRM fraction and the gap factors by:

$$q = \beta f g$$

7. Because f as defined by Coe et al. (1978) does not reflect the fraction of the total remanence, only the fraction of the remanence component used in the slope calculation, Tauxe and Staudigel (2004) proposed the parameter f_{vds} which is calculated as:

$$f_{vds} = \Delta y_T / y_{vds}$$

,

where y_{vds} is the vector difference sum of the entire NRM (see Figure 10.5 and Lecture 9). This parameter becomes small, if the remanence is multi-component, whereas the original f is blind to multi-component remanences.

8. Failure of a pTRM check is an indication of either poor reproducibility (usually accompanied by large scatter) or of irreversible changes in the ferromagnetic minerals in the specimen. We calculate the difference between the two in-field measurements for a given pTRM check as δ_i (see Figure 10.5). We calculate the sum of the δ_i and normalize it by the pTRM acquired by cooling from the maximum temperature step used in the slope calculation to room temperature. This parameter, expressed as a percentage, is called the Difference RATion Sum or DRATS.

9. The assumption that the blocking and unblocking temperatures for a given pTRM are equivalent may not always be true for multi-domain (MD) particles. The absolute value of the difference between the original NRM measured at a given temperature step (vertical component of the circles in Figure 10.5 and the second zero field step (known as the pTRM tail check) results from some of the pTRM imparted in the laboratory at T_i having unblocking temperatures that are different from T_i. The absolute value of these differences (Δ_i) are plotted as squares in Figure 10.5. The Maximum Difference, normalized by the VDS of the NRM and expressed as a percentage is the parameter MD.

10. In certain specimens, the IZZI protocol leads to rather interesting behavior, described in detail by Yu et al. (2004). The data with pTRM checks (associated with triangles) are the zerofield-infield (ZI) steps (lighter circles) and the intervening steps are the infield-zerofield (IZ) steps (darker circles). Alternating the two results in a "zigzag" in some specimens (barely discernible in Figure 10.5). Yu and Tauxe (2005) defined a parameter Z that quantifies the "zigzagging":

$$Z = \sum_{0}^{T_c} |(b_i - \bar{b})(r_i)$$

where b is the slope of the best fit line through all the selected points and b_i is the slope between two adjacent temperature steps. r_i is the pTRM fraction acquired by cooling from T_i to room temperature, normalized by the total TRM.

Bibliography

Aitken, M. J., Allsop, A. L., Bussell, G. D. & Winter, M. B. (1988), 'Determination of the intensity of the Earth's magnetic field during archeological times: reliability of the Thellier technique', *Rev. Geophys.* **26**, 3–12.

Bohnel, H., Biggin, A. J., Walton, D., Shaw, J. & Share, J. A. (2003), 'Microwave palaeointensities from a recent Mexican lava flow, baked sediments and reheated pottery', *Earth and Planetary Science Letters* **214**(1-2), 221–236.

Cisowski, S. & Fuller, M. (1986), Lunar paleointensities via the IRM(s) normalization method and the early magnetic history of the moon, *in* W. Hartmann, R. Phillips & G. Taylor, eds, 'The Origin of the Moon', Lunar and Planetary Science Institute, Houston, pp. 411–424.

Coe, R. S. (1967), 'The determination of paleo-intensities of the Earth's magnetic field with emphasis on mechanisms which could cause non-ideal behavior in Thellier's method', *J. Geomag. Geoelectr.* **19**, 157–178.

Coe, R. S., Grommé, S. & Mankinen, E. A. (1978), 'Geomagnetic paleointensities from radiocarbon-dated lava flows on Hawaii and the question of the Pacific nondipole low', *J. Geophys. Res.* **83**, 1740–1756.

Dunlop, D. & Ozdemir, O. (1997), *Rock Magnetism: Fundamentals and Frontiers*, Cambridge University Press.

Fox, J. M. W. & Aitken, M. J. (1980), 'Cooling-rate dependence of thermoremanent magnetization', *Nature* **283**, 462–463.

Halgedahl, S. & Fuller, M. (1980), 'Magnetic domain observations of nucleation processes in fine particles of intermediate titanomagnetite', *Nature* **288**, 70–72.

Nagata, T. (1961), 'Rock Magnetism'.

Riisager, P. & Riisager, J. (2001), 'Detecting multidomain magnetic grains in Thellier palaeointensity experiments', *Phys. Earth Planet. Inter.* **125**(1-4), 111–117.

Rolph, T. C. & Shaw, J. (1985), 'A new method of palaeofield magnitude correction for thermally altered samples and its application to Lower Carboniferous lavas', *Geophys. J. R. astr. Soc.* **80**, 773–781.

Selkin, P., Gee, J., Tauxe, L., Meurer, W. & Newell, A. (2000), 'The effect of remanence anisotropy on paleointensity estimates: A case study from the Archean Stillwater complex', *Earth Planet. Sci. Lett.* **182**, 403–416.

Shaw, J. (1974), 'A new method of determining the magnitude of the paleomanetic field application to 5 historic lavas and five archeological samples', *Geophys. J. R. astr. Soc.* **39**, 133–141.

Tauxe, L. (1993), 'Sedimentary records of relative paleointensity of the geomagnetic field: theory and practice', *Rev. Geophys.* **31**, 319–354.

Tauxe, L. (in press), 'Long term trends in paleointensity: The contribution of DSDP/ODP submarine basaltic glass collections', *Phys. Earth Planet. Int.* .

Tauxe, L. & Staudigel, H. (2004), 'Strength of the geomagnetic field in the Cretaceous Normal Superchron: New data from submarine basaltic glass of the Troodos Ophiolite', *Geochemistry, Geophysics, Geosystems* **5**(2), Q02H06, doi:10.1029/2003GC000635.

Thellier, E. & Thellier, O. (1959), 'Sur l'intensité du champ magnétique terrestre dans le passé historique et géologique', *Ann. Geophys.* **15**, 285–378.

Walton, D. (2004), 'Avoiding mineral alteration during microwave magnetization', *Geophys. Res. Lett.* **31**, L03606, doi:10.1029/2003GL019011.

Walton, D., Share, J., Rolph, T. C. & Shaw, J. (1993), 'Microwave Magnetisation', *Geophys. Res. Lett.* **20**, 109–111.

York, D. (1966), 'Least-squares fitting of a straight line', *Can. Jour. Phys.* **44**, 1079–1086.

Yu, Y. & Tauxe, L. (2005), 'Testing the IZZI protocol of geomagnetic field intensity determination', *Geochem., Geophys., Geosyst.* **in press**.

Yu, Y., Tauxe, L. & Genevey, A. (2004), 'Toward an optimal geomagnetic field intensity determination technique', *Geochemistry, Geophysics, Geosystems* **5**(2), Q02H07, doi:10.1029/2003GC000630.

Lectures in Paleomagnetism, 2005
by Lisa Tauxe

Citation:
http://earthref.org/MAGIC/books/Tauxe/2005/

June 8, 2005

Chapter 11

Fisher statistics for paleomagnetic directions

Suggested Reading

Background:
Chapters 1-5: Taylor (1982)
Chapter 6: Butler (1992)
To learn more:
Chapters 2-5: Fisher et al. (1987)

11.1 Introduction

In the previous few lectures we learned about routine paleomagnetic sampling and laboratory procedures. Once paleomagnetic directions have been obtained after stepwise demagnetization, principal component analysis, etc., one may wish to interpret them in terms of ancient geomagnetic field directions. To do this, there must be some way of calculating mean vectors and of quantifying the confidence intervals. But before we can understand the statistics of vectors we need some idea about statistics in general.

11.2 Statistics of scalars

The starting point for most statistical discussions is the so-called "normal" distribution, or "Gaussian" distribution. Let's say that we made 1000 measurements of some parameter, say bed thickness in a particular sedimentary formation in centimeters. We plot these in histogram form in Figure 11.1a.

A normal distribution can be characterized by two parameters, the mean (μ) and the variance σ^2. How to estimate the parameters of the underlying distribution is the art of statistics. We all know that the arithmetic mean of a batch of data $\bar{x}$ drawn from a normal distribution is calculated by:

$$\bar{x} = \frac{1}{N}\sum_{i=1}^{N} x_i.$$

The mean estimated from the data shown in Figure 11.1 is 10.09. If we had measured an infinite number of bed thicknesses, we would have gotten the bell curve shown in the figure and calculated a mean of 10.

The "spread" in the data is characterized by the variance σ^2. Variance for normal distributions can be estimated by the parameter s^2:

$$s^2 = \frac{1}{N-1}\sum_{i=1}^{N}(x_i - \bar{x})^2.$$

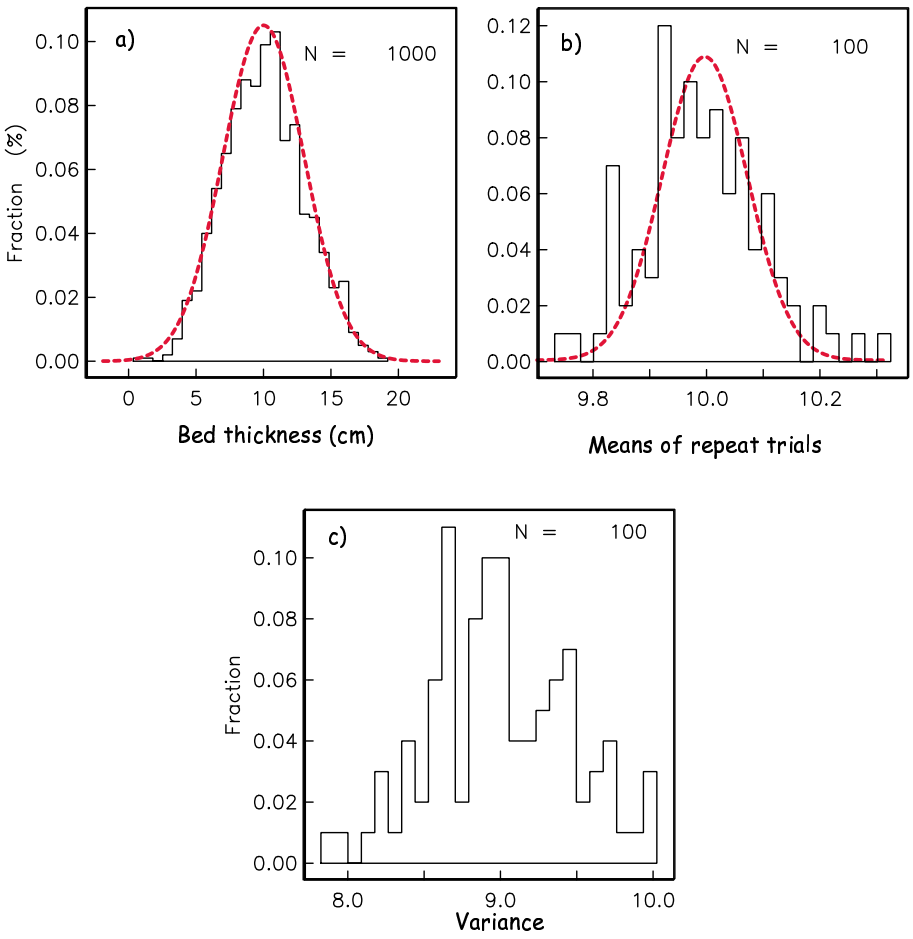

Figure 11.1: a) Histogram of 1000 measurements of bed thickness in some sedimentary formation. Also shown is the smooth curve of a normal distribution with a mean of 10 and a standard deviation of 3. b) Histogram of the means from 100 repeated sets of 1000 measurements from the same sedimentary formation. The distribution of the means is much tighter. c) Histogram of the variances (s^2) from the same set of experiments as in b). The distribution of variances is not bell shaped; it is χ^2.

In order to get the units right on the uncertainty in the mean (cm - not cm^2), we have to take the square root of s^2. The parameter s gives an estimate of the standard deviation σ and is the bounds around the mean that includes 63% of the values. The 95% confidence bounds are given by

$1.96s$ (this is what a "2-σ error" is), and should include 95% of the means. The bell curve shown in Figure 11.1 has a σ (standard deviation) of 3, while the s is 2.97.

If you repeat the bed measuring experiment a few times, you will never get exactly the same measurements in the different trials. The mean and standard deviations measured for each trial then are "sample" means and standard deviations. If you plotted up all those sample means, you would get another normal distribution whose mean should be pretty close to the true mean, but with a much more narrow standard deviation. In Figure 11.1b we plot a histogram of means from 100 such trials of 1000 measurements each drawn from the same distribution of $\mu = 10, \sigma = 3$. In general, we expect the standard deviation of the means (or "standard error of the mean" s_m) to be related to s by

$$s_m = \frac{s}{\sqrt{N_{trials}}}$$

What if we were to plot up a histogram of the estimated variances as in Figure 11.1c? Are these also normally distributed? The answer is no, because variance is a squared parameter relative to the original units. In fact, the distribution of variance estimates from normal distibutions is expected to be "chi-squared" (χ^2). The width of the χ^2 distribution is also governed by how many measurements were made. The so-called "number of degrees of freedon" ν is given by the number of measurements made minus the number of measurements required to make the estimate, so ν for our case is $N - 1$. Therefore we expect the variance estimates to follow a χ^2 distribution with $N - 1$ degrees of freedom of χ^2_ν.

We often wish to consider ratios of variances (for example to decide if the data are more scattered in one data set relative to another). In order to do this, we must know what ratio would be expected from data sets drawn from the same distributions. Ratios of such variances follow a so-called F distribution with ν_1 and ν_2 degrees of freedom for the two data sets. This is denoted $F[\nu_1, \nu_2]$. Thus if the ratio f, given by:

$$f = \frac{s_1^2}{s_2^2}$$

is greater than the 5% critical value of $F[\nu_1, \nu_2]$ (check in the F-table in the Appendix), the hypothesis that the two variances are the same can be rejected at the 95% level of confidence.

11.3 Statistics of vectors

We turn now to the trickier problem of sets of measured vectors. We will consider the case in which all vectors are assumed to have a length of one, i.e., these are unit vectors. Unit vectors are just "directions".

Consider the various sets of directions plotted as equal area projections (see Lecture 2) in Figure 11.2. These are all measurements of a single, vertical direction, but with varying degrees of precision. It would be handy to be able to calculate a mean direction for the data sets and to quantify the precision of the measurements.

The average inclination, calculated as the arithmetic mean of the inclinations, will obviously not be vertical. We will see, however, that the vector mean of the directions of each data set is actually nearly vertical as it should be. In the following, we will demonstrate the proper way to calculate mean directions and confidence regions for directional data that are distributed in the manner shown in Figure 11.2. We will also briefly describe several useful statistical tests that are popular in the paleomagnetic literature.

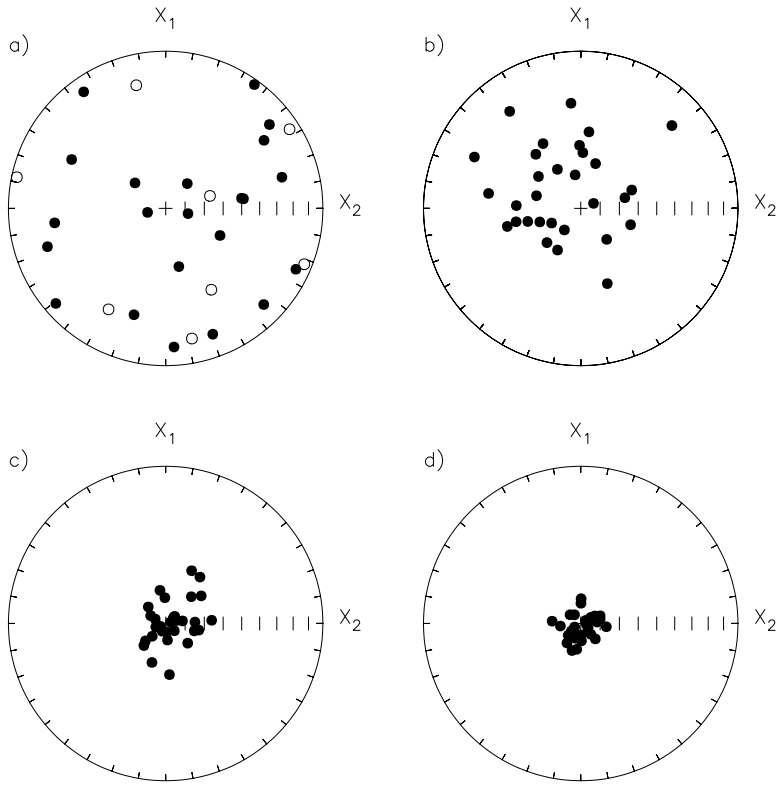

Figure 11.2: Four hypothetical data sets with decreasing scatter: a) is nearly uniformly distributed on the sphere, whereas d) is fairly well clustered. All data sets were drawn from Fisher distributions with vertical true directions.

Paleomagnetic directional data are subject to a number of factors that lead to scatter. These include:

1. uncertainty in the measurement caused by instrument noise or sample alignment errors,
2. uncertainties in sample orientation,
3. uncertainty in the orientation of the sampled rock unit,
4. variations among samples in the degree of removal of a secondary component,
5. uncertainty caused by the process of magnetization,
6. secular variation of the Earth's magnetic field, and
7. lightning strikes.

Some of these sources of scatter (e.g., items 1, 2 and perhaps 6 above) lead to a symmetric distribution about a mean direction. Other sources of scatter contribute to distributions that are wider in one direction than another. For example, in the extreme case, item four leads to a girdle distribution whereby directions are smeared along a great circle. In order to calculate mean directions with confidence limits, paleomagnetists rely heavily on the special statistics known as *Fisher statistics* (Fisher, 1953), which were developed for assessing dispersion of unit vectors on a sphere. In most instances, paleomagnetists assume a Fisher distribution for their data because the statistical treatment allows calculation of confidence intervals, comparison of mean directions, comparison of scatter, etc.

11.4 Parameter estimation

The Fisher probability density function (Fisher, 1953) is given by:

$$F = \frac{\kappa}{4\pi \sinh \kappa} \exp(\kappa \cos \alpha), \tag{11.1}$$

where α is the angle between the unit vector and the true direction and κ is a precision parameter such that as $\kappa \rightarrow \infty$, dispersion goes to zero.

Because the intensity of the magnetization has little to do with the validity of the measurement (except for very weak magnetizations), it is customary to assign unit length to all directions. The mean direction is calculated by first converting the individual directions (D_i, I_i) to cartesian coordinates (x_1, x_2, x_3) by the methods given in Lecture 2. The length of the resultant vector, R, is given by:

$$R^2 = (\sum_i x_{1i})^2 + (\sum_i x_{2i})^2 + (\sum_i x_{3i})^2, \tag{11.2}$$

and the cartesian coordinates of the mean direction are given by:

$$\bar{x}_1 = \frac{1}{R}(\sum_i x_{1i}); \quad \bar{x}_2 = \frac{1}{R}(\sum_i x_{2i}); \quad \bar{x}_3 = \frac{1}{R}(\sum_i x_{3i}). \tag{11.3}$$

The cartesian coordinates can, of course, be converted back to geomagnetic elements $(\bar{D}, \bar{I})$ by the familiar method described in Lecture 2.

The precision parameter for the Fisher distribution, κ, is estimated by

$$\kappa \simeq k = \frac{N-1}{N-R} \tag{11.4}$$

(where N is the number of data points). Using this estimate of κ, we estimate the circle of 95% confidence ($p = 0.05$) about the mean, α_{95}, by:

$$\alpha_{95} = \cos^{-1}[1 - \frac{N-R}{R}[(\frac{1}{p})^{\frac{1}{(N-1)}} - 1]]. \tag{11.5}$$

In the classic paleomagnetic literature, α_{95} was further approximated by:

$$\alpha'_{95} \simeq \frac{140}{\sqrt{kN}},$$

which is reliable for k larger than about 25 (see Tauxe et al., 1991).

Another useful parameter (introduced by Irving, 1964) is the so-called *circular standard deviation* (CSD), also sometimes called the angular standard deviation), which is approximated by:

$$CSD \simeq \frac{81}{\sqrt{k}},$$

which is the circle containing ~66% of the data.

If directions are converted to VGPs as outlined in Lecture 2, the transformation distorts a rotationally symmetric set of data into an elliptical distribution. The associated α_{95} may no longer be appropriate. Cox and Doell (1960) suggested the following for 95% confidence regions in VGPs. Ironically, it is more likely that the VGPs are spherically symmetric implying that most sets of directions are not!

$$dm = \alpha_{95}\frac{\cos\lambda}{\cos\bar{I}}$$

$$dp = \frac{1}{2}\alpha_{95}(1 + 3\sin^2\lambda), \tag{11.6}$$

where dm is the uncertainty in the paleomeridian (longitude), dp is the uncertainty in the paleoparallel (latitude), and λ is the site paleolatitude.

Two examples of Fisher distributions, one with a large degree of scatter (κ=5) and one that is relatively tightly clustered (κ=50) are shown in Figure 11.3. Also shown are the Fisher mean directions and α_{95}s for each data set.

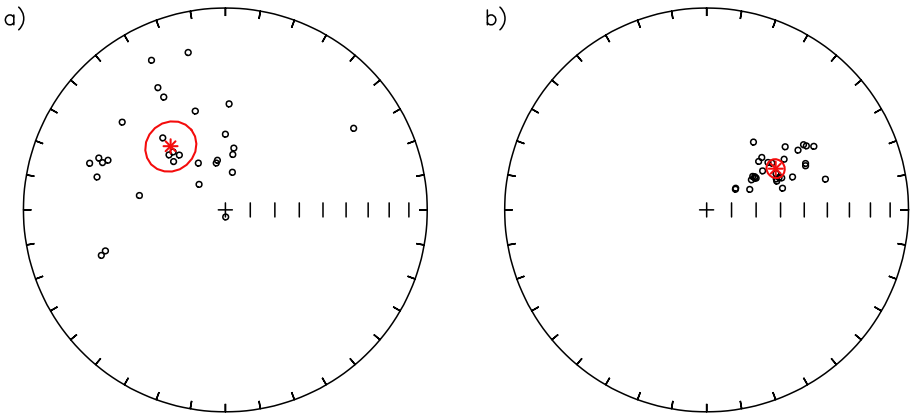

Figure 11.3: Two Fisher distributions: a) $\kappa = 5$, b) $\kappa = 50$. Mean directions are shown as asterisks, and α_{95}s as ellipses.

The Fisher distribution allows us to ask a number of questions about paleomagnetic data sets, such as:

1. Is a given set of directions random? This is the question that we ask when we perform a conglomerate test (Lecture 9).

2. Is the mean direction of a given (Fisherian) data set different from some known direction? This question comes up when we compare a given data set with, for example, the directions of the present or GAD field.

3. Are two (Fisherian) data sets different from each other? For example, are the normal directions and the antipodes of the reversed directions the same for a given data set?

4. If a given site has some samples that allow only the calculation of a best-fit plane and not a directed line, what is the site mean direction that combines the best-fit lines and planes (see Lecture 9)?

In the following discussion, we will briefly summarize ways of addressing these issues using Fisher techniques.

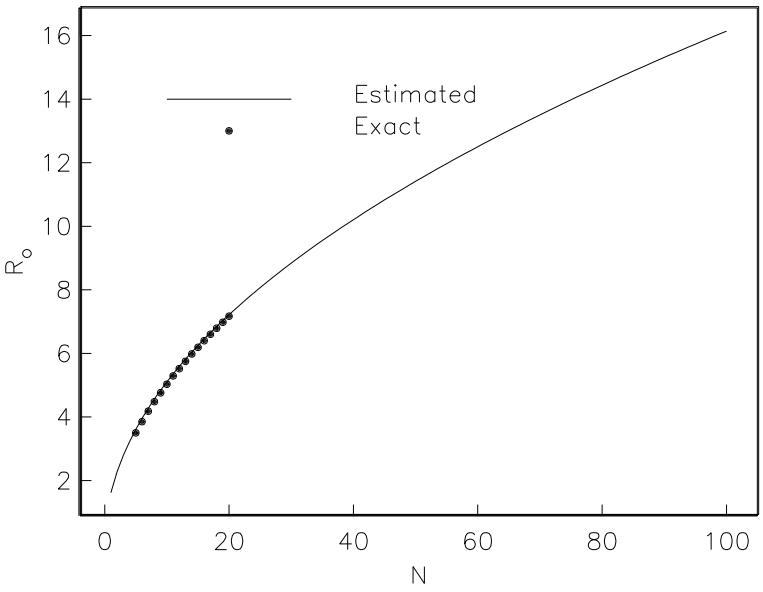

Figure 11.4: Values of R_o calculated by Equation 11.7 (line) and exactly (dots) for 95% level of confidence. Exact data are from Watson (1956).

11.5 Watson's test for randomness

Watson [1956] demonstrated how to test a given directional data set for randomness. His test relies on the calculation of R given by Equation 11.2. Because R is the length of the resultant vector, randomly directed vectors will have small values of R, while, for less scattered directions, R will approach N. Watson (1956) defined a parameter R_o that can be used for testing the randomness of a given data set. If the value of R exceeds R_o, the null hypothesis of total randomness can be rejected at a specified level of confidence. If R is less than R_o, randomness cannot be rejected. Watson calculated the value of R_o for a range of N for the 95% and 99% confidence levels. Watson (1956) also showed how to estimate R_o by:

$$R_o = \sqrt{7.815 \cdot N/3}. \tag{11.7}$$

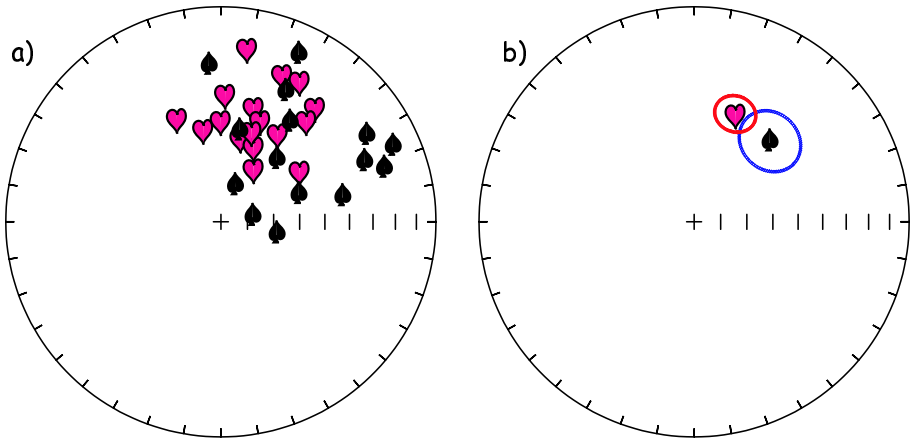

Figure 11.5: a) Equal area projections of declinations and inclinations of two hypothetical data sets. b) Fisher means and circles of confidence from the data sets in a).

We plot R_o versus N in Figure 11.4 using both the exact method (dots) and the estimation given by Equation 11.7. The estimation works well for $N > 10$, but is somewhat biased for smaller data sets. The critical values of R for $5 < N < 20$ from Watson (1956) are listed for convenience in Table D2.

The test for randomness is particularly useful for determining if, for example, the directions from a given site are randomly oriented (the data for the site should therefore be thrown out). Also, one can determine if directions from conglomerate clasts are randomly oriented in the conglomerate test (see Lecture 9).

11.6 Comparing known and estimated directions

The calculation of confidence regions for paleomagnetic data is largely motivated by a need to compare estimated directions with either a known direction (for example, the present field) or another estimated direction (for example, that expected for a particular paleopole, the present field or a GAD field). Comparison of a paleomagnetic data set with a given direction is straightforward using Fisher statistics. If the known test direction lies outside the confidence interval computed for the estimated direction, then the estimated and known directions are different at the specified confidence level.

11.7 Comparing two estimated directions

The case in which we are comparing two Fisher distributions can also be relatively straight forward. If the two confidence circles do not overlap, the two directions are different at the specified level of certainty. When one confidence region includes the mean of the other set of directions, the difference in directions is not significant.

The situtation becomes a little more tricky when the data sets are as shown in Figure 11.5a. The Fisher statistics for the two data sets are:

i	symbol	$\bar{D}$	$\bar{I}$	N	R	k	α_{95}
1	spades	43.3	47.1	20	17.9077	9.1	11.5
2	hearts	20.9	45.3	20	19.0908	20.9	7.3

As shown in the equal area projection in Figure 11.5b, the two α_{95}s overlap, but neither includes the mean of the other. This sort of "grey zone" case has been addressed by many workers. A particularly useful parameter (V_w) was proposed by Watson (1983; see Appendix for details).

V_w was posed as a test statistic that increases with increasing difference between the mean directions of the two data sets. Thus, the null hypothesis that two data sets have a common mean direction can be rejected if V_w exceeds some critical value which can be determined through what is called *Monte Carlo simulation*. The technique gets its name from famous gambling locale because we use randomly drawn samples ("cards") from specified distributions ("decks") to see what can be expected from chance. What we want to know is the probabilty that two data sets (hands of cards?) drawn from the same underlying distribution would have a given V_w statistic just from chance.

We proceed as follows:

1. Calculate the V_w statistic for the data sets. [The V_w for the two data sets shown in Figure 11.5a is 8.5.]

2. In order to determine the critical value for V_w, we draw two Fisher distributed data sets with dispersions of k_1 and k_2 and N_1, N_2, but having a common direction. You can try this "by hand", with the program **fisher** from the **pmag** distribution of programs (downloadable at sorcerer.ucsd.edu/software).

3. The calculate V_w for these simulated data sets.

4. Repeat the simulation some large number of times (say 1000). This defines the distribution of V_ws that you would get from chance by "sampling" a distributions with the same direction.

5. Sort the V_ws in order of increasing size. The critical value of V_w at the 95% level of confidence is the 950^{th} simulated V_w.

The V_ws simulated for two distributions with the same κ and N as our example data sets but drawn from distributions with the same mean are plotted in a histogram in Figure 11.6 with the bounds containing the lowermost 95% of the 1000 simulations shown as a dashed line. The value of 8.5, calculated for the data set is shown as a heavy vertical line and is clearly larger than 95% of the simulated populations which gives a critical value of 6.2. This simulation therefore supports the suggestion that the two data sets do not have a common mean at the 95% level of confidence.

This test can be applied to the two polarities in a given data collection to see if the they are antipodal. In this case, one would take the antipodes of one of the data sets before calculating V_w. This test is a Fisherian form of the *reversals test*.

11.8 Combining vectors and great circles

Consider the demagnetization data shown in Figure 11.7 for demagnetization data of various specimens from a certain site. The data from sample *tst1a* seem to reach some well defined direction and hover there. A mean direction for the last few demagnetization steps can be calculated using Fisher

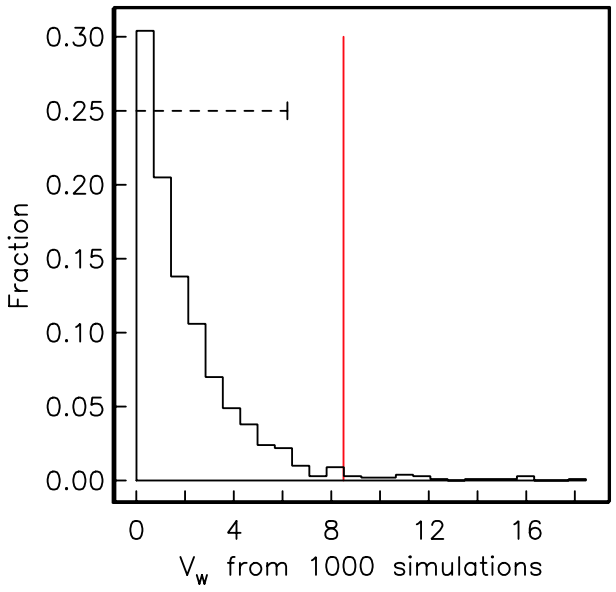

Figure 11.6: Distribution of V_w for simulated Fisher distributions with the same N and κ as the two shown in Figure 11.5. The dashed line includes the smalleds 95% of the V_ws calculated for the simulations. The heavy vertical line is the V_w calculated for the two data sets. According to this test, the two data sets do not have a common mean.

statistics. We can calculate a best-fit line from the data for sample *tst1b* (Figure 11.7b) using the principal component method of Kirschvink [1980] as outlined in Lecture 9. The data from *tst1c* track along a great circle path and can be used to calculate the pole to the best-fit plane calculated as in Lecture 9. McFadden and McElhinny (1988) described a method for estimating the mean direction and the α_{95} from sites that mix planes (great circles on an equal area projection) and directed lines (see Appendix). The key to their method is to find the direction within each plane that gives the tightest grouping of directions. Then "regular" fisher statistics can be applied.

11.9 Inclination only data

A different problem arises when only the inclination data are available as in the case of unoriented drill cores. Cores can be drilled and arrive at the surface in short, unoriented pieces. Specimens taken from such core material will be oriented with respect to the vertical, but the declination data are unknown. It is often desirable to estimate the true Fisher inclination of data set having only inclination data, but how to do this is not obvious. Consider the data in Figure 11.8. The true Fisher mean declination and inclination are shown by the asterisk. If we had only the inclination data and calculated a gaussian mean ($< I >$), the estimate would be too shallow as pointed out earlier.

Several investigators have addressed the issue of inclination-only data. McFadden and Reid (1982) developed a maximum likelihood estimate for the true inclination which works reasonably well. Their approach is outlined in the Appendix.

By comparing inclinations estimated using the McFadden-Reid technique with those calculated using the full vector data, it is clear that the method breaks down at high inclinations and high

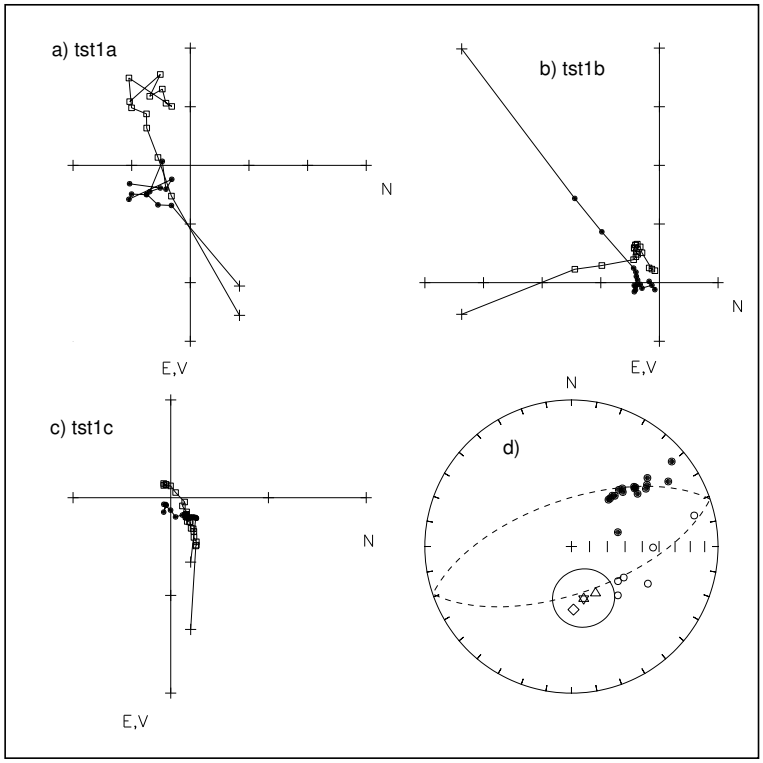

Figure 11.7: Examples of demagnetization data from a site whose mean is partially constrained by a great circle. The samples a)*tst1a*, b)*tst1b* and c) *tst1c* which are sibling samples from the same reversely magnetized site. The demagnetization data are plotted as orthogonal projections. The directional data from *tst1c* do not define a single component, but describe a great circle as shown in d). The sample *tst1b* allows calculation of a principal component whose direction is plotted as a diamond in d). Specimen *tst1a* has data that do not converge to the origin. A mean direction was calculated for this sample by standard Fisher statistics and is plotted as a triangle in d. The best-fit great circle and two directed lines allow a mean (star) and associated α_{95} to be calculated using the method of McFadden and McElhinny (1988).

scatter. It is also inappropriate for data sets that are not Fisher distributed!

11.10 Is a given data set Fisher distributed?

Clearly, the Fisher distribution allows powerful tests and this power lies behind the popularity of paleomagnetism in solving geologic problems. The problem is that these tests require that the data be Fisher distributed. How can we tell if a particular data set is Fisher distributed? What do we do if the data are not Fisher distributed? These questions are addressed in the rest of the lecture.

Let us now consider how to determine whether a given data set is Fisher distributed. There are actually many ways of doing this. There is a rather complete discussion of the problem in Fisher et al. (1987) and if you really want a complete treatment try the supplemental reading list. The quantile-quantile (Q-Q) method described by Fisher et al. (1987) is fairly intuitive and works well. We outline it briefly in the following.

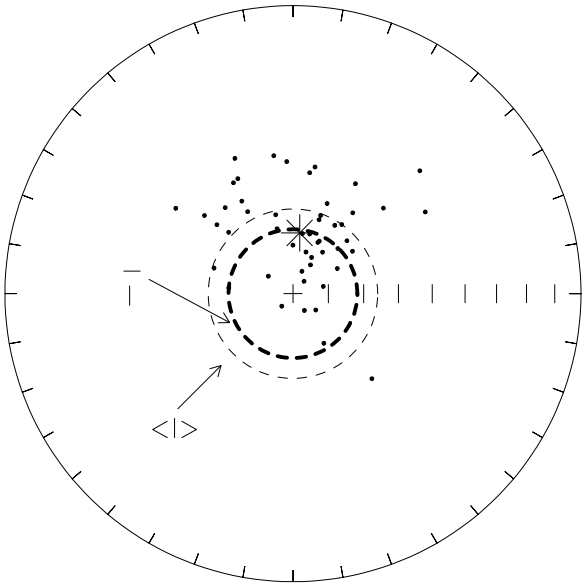

Figure 11.8: Directions drawn from a Fisher distribution with a near vertical true mean direction. The Fisher mean direction from the sample is shown by a asterisk. The Gaussian average inclination ($< I >$) is shallower than the Fisher mean $\bar{I}$.

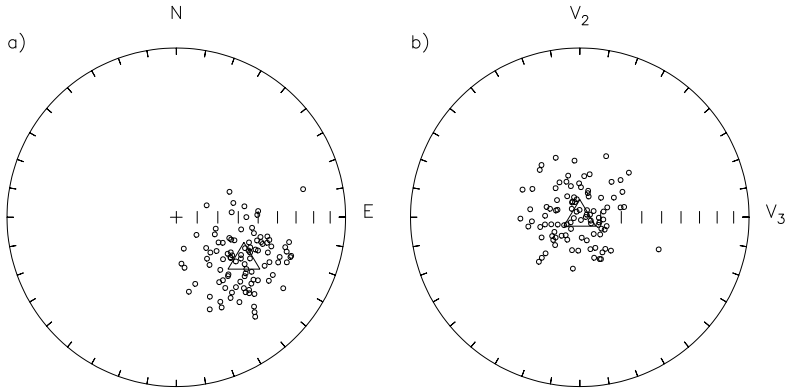

Figure 11.9: Transformation of coordinates from a) geographic to b)"data" coordinates. The direction of the principal eigenvector $\mathbf{V}_1$ is shown by the triangle in both plots.

11.10. IS A GIVEN DATA SET FISHER DISTRIBUTED?

The idea behind the Q-Q method is to exploit the fact that declinations in a Fisher distribution, when viewed along the mean, are spread around the clock evenly - there is a uniform distribution of declinations. Also, the inclinations (or rather the co-inclinations) are clustered close to the mean and the frequency dies off exponentially away from the mean direction.

Therefore, the first step in testing for Fisher-ness is to transpose the data such that the mean is the center of the distribution. You can think of this as rotating your head around to peer down the mean direction. On an equal area projection, the center of the diagram is the mean. In order to do this transformation, we first calculate the orientation matrix $\mathbf{T}$ of the data and the associated eigenvectors $\mathbf{V}_i$ and eigenvalues τ_i (Appendix to Lecture 9 - in case you haven't read it yet, do so NOW). Substituting the direction cosines relating the geographic coordinate system $\mathbf{X}$ to the coordinate system defined by $\mathbf{V}$, the eigenvectors, where $\mathbf{X}$ is the "old" and $\mathbf{V}$ is the "new" set of axes, we can transform the coordinate system for a set of data from "geographic" coordinates (Figure 11.9a) where the vertical axis is the center of the diagram, to the "data" coordinate system, (Figure 11.9b) where the principal eigenvector ($\mathbf{V}_1$) lies at the center of the diagram, after transformation into "data" coordinates.

Equation 11.1 for the Fisher distribution function suggests that declinations are symmetrically distributed about the mean. In "data" coordinates, this means that the declinations are uniformly distributed from $0 \rightarrow 360°$. Furthermore, the probability P of finding a direction of α away from the mean is exponential:

$$P = F \sin\alpha = \frac{\kappa}{4\pi \sinh\kappa} \exp(\kappa \cos\alpha) \sin\alpha. \tag{11.8}$$

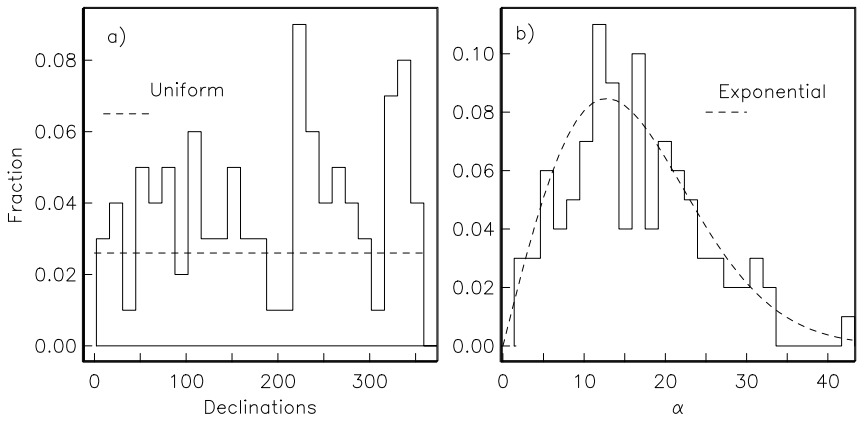

Figure 11.10: a) Declinations and b) co-inclinations (α) from Figure 11.9. Also shown are behaviors expected for D and I from a Fisher distribution, i.e., declinations are uniformly distributed while co-inclinations are exponentially distributed.

Let us compare the data from Figure 11.9 to the expected distributions for a Fisher distribution with $\kappa = 20$ (Figure 11.10). The data were generated using the program **fisher** which relies on the method outlined by Fisher et al. (1987), that draws directions from a Fisher distribution with a specified κ. We used a κ of 20, and it should come as no surprise that the data fit the expected distribution rather well. But how well is "well" and how can we tell when a data set *fails* to be fit

by a Fisher distribution?

We wish to test whether the declinations are uniformly distributed and whether the inclinations are exponentially distributed as required by the Fisher distribution. Plots such as those shown in Figure 11.10 are not as helpful for this purpose as a plot known as a *Quantile-Quantile* (Q-Q) plot (see Fisher et al., 1987). In a Q-Q plot, the data are graphed against the value expected from a particular distribution. Data compatible with the chosen distribution plot along a line. The procedure for accomplishing this is given in the Appendix. In Figure 11.11a, we plot the declinations from Figure 11.9 (in data coordinates) against the values calculated assuming a uniform distribution and in Figure 11.11b, we plot the co-inclinations against those calculated using an exponential distribution. As expected, the data plot along lines and neither of the test statistics M_u nor M_e (see Appendix) exceed the critical values.

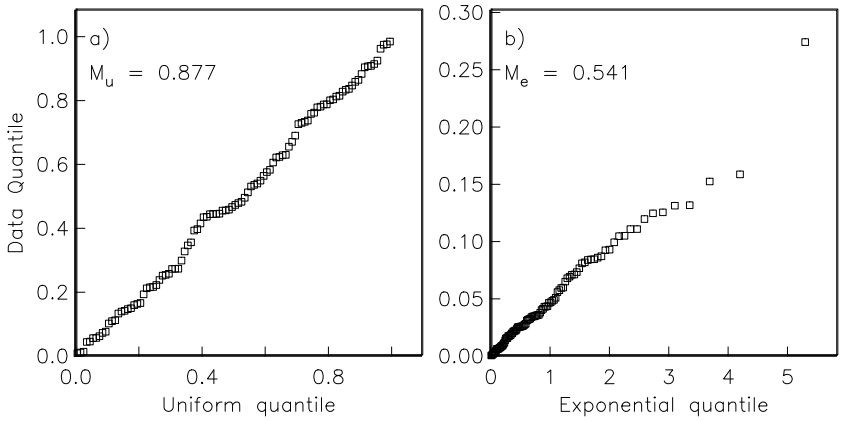

Figure 11.11: a) Quantile-quantile plot of declinations (in data coordinates) from Figure 9 plotted against an assumed uniform distribution. b) Same for inclinations plotted against an assumed exponential distribution. The data are Fisher distributed.

Appendix

A Calculation of Watson's V_w

1. Calculate R_i, and k_i where $i = 1, 2$ for the two data sets with N_1, N_2 samples using Equations 11.2 and 11.4.
2. Calculate $\bar{x}_{ij}$ (where $j = 1, 3$ for the three axes) using Equation 11.3.
3. Calculate $\bar{X}_{ij} = R_i \bar{x}_{ij}$.
4. Find the weighted means for the two data sets:

$$\hat{X}_j = \sum_i^2 k_j \bar{X}_{ij}$$

5. Calculate the weighted overall resultant vector R_w by

$$R_w = (\hat{X}^2 + \hat{Y}^2 + \hat{Z}^2)^{\frac{1}{2}},$$

and the weighted sum S_w by,

$$S_w = \sum_i^2 k_i R_i.$$

6. Finally, Watson's V_w is defined as

$$V_w = 2(S_w - R_w).$$

B Combining lines and planes

1. Calculate M directed lines (2 in our case) and N great circles (1 in our case) using principal component analysis (see Lecture 9) or Fisher statistics.
2. Assume that the primary direction of magnetization for the samples with great circles lies somewhere along the great circle path (i.e., within the plane).
3. Assume that the set of M directed lines and N unknown directions are drawn from a Fisher distribution.
4. Iteratively search along the great circle paths for directions that maximize the resultant vector R for the $M + N$ directions.
5. Having found the set of N directions that lie along their respective great circles, estimate the mean direction using Equation 11.3 and κ as:

$$k = \frac{2M + N - 2}{2(M + N - R)},$$

The cone of 95% confidence about the mean is given by:

$$\cos \alpha_{95} = 1 - \frac{N' - 1}{kR}, [(\frac{1}{p})^{1/(N'-1)} - 1],$$

where $N' = M + N/2$ and $p = .02$

C Inclination only calculation

We wish to estimate the co-inclination ($\alpha = 90 - I$) of N Fisher distributed data (α_i), the declinations of which are unknown. We define the estimated value of α to be $\hat{\alpha}$. McFadden and Reid showed that $\hat{\alpha}$ is the solution of:

$$N \cos \hat{\alpha} + (\sin^2 \hat{\alpha} - \cos^2 \hat{\alpha}) \sum \cos \alpha_i - 2 \sin \hat{\alpha} \cos \hat{\alpha} \sum \alpha_i = 0,$$

which can be solved numerically.

They further define two parameters S and C as:

$$S = \sum \sin(\hat{\alpha} - \alpha_i),$$

$$C = \sum \cos(\hat{\alpha} - \alpha_i).$$

An unbiassed approximation for the Fisher parameter κ, k is given by:

$$k = \frac{N-1}{2(N-C)}.$$

The unbiased estimate $\hat{I}$ of the true inclination is:

$$\hat{I} = 90 - \hat{\alpha} + \frac{S}{C}.$$

Finally, the α_{95} is estimated by:

$$\cos\alpha_{95} = 1 - \frac{1}{2}(\frac{S}{C})^2 - \frac{f}{2Ck},$$

where f is the critical value taken from the F distribution (see Table A-1) with 1 and (N-1) degrees of freedom.

D Quantile-Quantile plots

In order to do this, we proceed as follows (Figure D1):

1. Sort the variable of interest ζ_i into ascending order so that ζ_1 is the smallest and ζ_N is the largest.

2. If the data are represented by the underlying density function as in Figure D1a, then the ζ_i's divide the curve into $(N+1)$ areas, A_i, the average value of which is $a = 1/(N+1)$. If we assume a form for the density function of ζ_i, we can calculate numbers z_i, that divide the theoretical distribution into areas a_i each having an area a (see Figure D1b).

3. An approximate test for whether the data ζ_i are fit by a given distribution is to plot the pairs of points (ζ_i, z_i), as shown in Figure D1c. If the assumed distribution is appropriate, the data will plot as a straight line.

4. The density function P is the distribution function F times the area, as mentioned before. The z_i are calculated as follows:

$$F(z_i) = (i - \tfrac{1}{2})/n, \text{where } i = 1, \ldots, n, \tag{D1}$$

so that:

$$z_i = F^{-1}((i - \tfrac{1}{2})/n), \text{where } i = 1, \ldots, n, \tag{D2}$$

and where F^{-1} is the inverse function to F. If the data are uniformly distributed (and constrained to lie between 0 and 1), then both $F(x)$ and $F^{-1}(x) = x$. For an exponential distribution $F(x) = 1 - e^{-x}$ and $F^{-1}(x) = -\ln(1-x)$.

D. QUANTILE-QUANTILE PLOTS

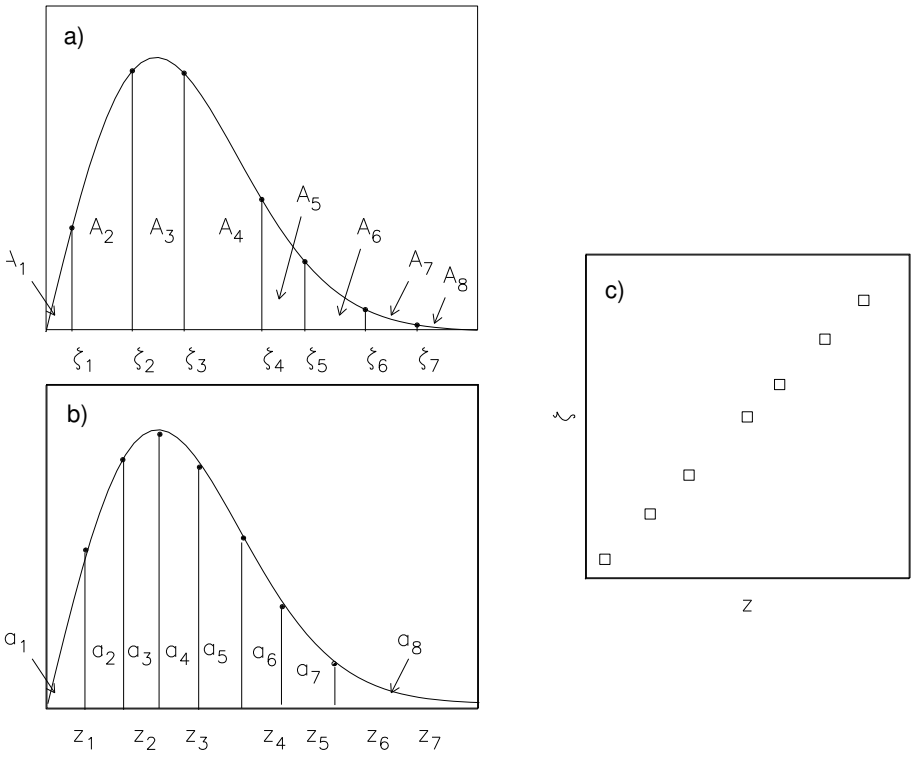

Figure D1: a) Illustration of how the sorted data ζ_i divide the density curve into areas A_i with an average area of $1/(N+1)$. b) The values of z_i which divide the density function into equal areas $a_i = 1/(N+1)$. c) Q-Q plot of z and ζ.

5. Finally, we can calculate parameters M_u and M_e which, when compared to critical values, allow rejection of the hypotheses of uniform and exponential distributions, respectively. To do this, we first calculate:

$$D_N^+ = \text{maximum}[\frac{i}{N} - F(x)], \tag{D3}$$

and

$$D_N^- = \text{maximum}[F(x) - \frac{(i-1)}{N}]. \tag{D4}$$

For a uniform distribution $F(x) = x$, so M_u is calculated by first calculating D_N^+ as the maximum of $[i/N - \zeta_i]$ and D_N^- as the maximum of $[\zeta_i - (i-1)/N]$. M_u is $D_N^+ + D_N^-$. A value of $M_u > 1.207$ (see Fisher et al., 1987) can be grounds for rejecting the hypothesis of uniformity at the 95% level of certainty. Similarly, $D_N^+ D_N^-$ can be calculated for the inclination (using $\zeta_i = 90 - I_i$) as the maximum of $[i/N - (1 - e^{-\zeta_i})]$ and maximum of $[(1 - e^{-\zeta_i}) - (i-1)/N]$ respectively. $M_e = D_N^+ + D_N^-$. Values larger than 1.094 allow rejection of the exponential hypothesis. If either M_u or M_e exceed the critical values, the hypothesis of a Fisher distribution can be rejected.

Table D1: F-Tables for ν degrees of freedom.

ν	1	2	3	4	5	6	7	8	9
1	161.45	199.50	215.71	224.58	230.16	233.99	236.77	238.88	240.54
2	18.51	19	19.16	19.25	19.3	19.33	19.35	19.37	19.38
3	10.13	9.55	9.28	9.12	9.01	8.94	8.89	8.85	8.81
4	7.71	6.94	6.59	6.39	6.26	6.16	6.09	6.04	6
5	6.61	5.79	5.41	5.19	5.05	4.95	4.88	4.82	4.77
6	5.99	5.14	4.76	4.53	4.39	4.28	4.21	4.15	4.1
7	5.59	4.74	4.35	4.12	3.97	3.87	3.79	3.73	3.68
8	5.32	4.46	4.07	3.84	3.69	3.58	3.5	3.44	3.39
9	5.12	4.26	3.86	3.63	3.48	3.37	3.29	3.23	3.18
10	4.96	4.1	3.71	3.48	3.33	3.22	3.14	3.07	3.02
11	4.84	3.98	3.59	3.36	3.2	3.09	3.01	2.95	2.9
12	4.75	3.89	3.49	3.26	3.11	3	2.91	2.85	2.8
13	4.67	3.81	3.41	3.18	3.03	2.92	2.83	2.77	2.71
14	4.6	3.74	3.34	3.11	2.96	2.85	2.76	2.7	2.65
15	4.54	3.68	3.29	3.06	2.9	2.79	2.71	2.64	2.59
16	4.49	3.63	3.24	3.01	2.85	2.74	2.66	2.59	2.54
17	4.45	3.59	3.2	2.96	2.81	2.7	2.61	2.55	2.49
18	4.41	3.55	3.16	2.93	2.77	2.66	2.58	2.51	2.46
19	4.38	3.52	3.13	2.9	2.74	2.63	2.54	2.48	2.42
20	4.35	3.49	3.1	2.87	2.71	2.6	2.51	2.45	2.39
21	4.32	3.47	3.07	2.84	2.68	2.57	2.49	2.42	2.37
22	4.3	3.44	3.05	2.82	2.66	2.55	2.46	2.4	2.34
23	4.28	3.42	3.03	2.8	2.64	2.53	2.44	2.37	2.32
24	4.26	3.4	3.01	2.78	2.62	2.51	2.42	2.36	2.3
25	4.24	3.39	2.99	2.76	2.6	2.49	2.4	2.34	2.28
26	4.23	3.37	2.98	2.74	2.59	2.47	2.39	2.32	2.27
27	4.21	3.35	2.96	2.73	2.57	2.46	2.37	2.31	2.25
28	4.2	3.34	2.95	2.71	2.56	2.45	2.36	2.29	2.24
29	4.18	3.33	2.93	2.7	2.55	2.43	2.35	2.28	2.22
30	4.17	3.32	2.92	2.69	2.53	2.42	2.33	2.27	2.21
40	4.08	3.23	2.84	2.61	2.45	2.34	2.25	2.18	2.12
60	4	3.15	2.76	2.53	2.37	2.25	2.17	2.1	2.04
120	3.92	3.07	2.68	2.45	2.29	2.18	2.09	2.02	1.96

Table 1 - continued.

ν	10	12	15	24	30	40	60	120	Inf
1	241.88	243.90	245.95	249.05	250.1	251.14	252.2	253.25	254.32
2	19.4	19.41	19.43	19.45	19.46	19.47	19.48	19.49	19.5
3	8.79	8.74	8.7	8.64	8.62	8.59	8.57	8.55	8.53
4	5.96	5.91	5.86	5.77	5.75	5.72	5.69	5.66	5.63
5	4.74	4.68	4.62	4.53	4.5	4.46	4.43	4.4	4.37
6	4.06	4	3.94	3.84	3.81	3.77	3.74	3.7	3.67
7	3.64	3.57	3.51	3.41	3.38	3.34	3.3	3.27	3.23
8	3.35	3.28	3.22	3.12	3.08	3.04	3.01	2.97	2.93
9	3.14	3.07	3.01	2.9	2.86	2.83	2.79	2.75	2.71
10	2.98	2.91	2.85	2.74	2.7	2.66	2.62	2.58	2.54
11	2.85	2.79	2.72	2.61	2.57	2.53	2.49	2.45	2.4
12	2.75	2.69	2.62	2.51	2.47	2.43	2.38	2.34	2.3
13	2.67	2.6	2.53	2.42	2.38	2.34	2.3	2.25	2.21
14	2.6	2.53	2.46	2.35	2.31	2.27	2.22	2.18	2.13
15	2.54	2.48	2.4	2.29	2.25	2.2	2.16	2.11	2.07
16	2.49	2.42	2.35	2.24	2.19	2.15	2.11	2.06	2.01
17	2.45	2.38	2.31	2.19	2.15	2.1	2.06	2.01	1.96
18	2.41	2.34	2.27	2.15	2.11	2.06	2.02	1.97	1.92
19	2.38	2.31	2.23	2.11	2.07	2.03	1.98	1.93	1.88
20	2.35	2.28	2.2	2.08	2.04	1.99	1.95	1.9	1.84
21	2.32	2.25	2.18	2.05	2.01	1.96	1.92	1.87	1.81
22	2.3	2.23	2.15	2.03	1.98	1.94	1.89	1.84	1.78
23	2.27	2.2	2.13	2.01	1.96	1.91	1.86	1.81	1.76
24	2.25	2.18	2.11	1.98	1.94	1.89	1.84	1.79	1.73
25	2.24	2.16	2.09	1.96	1.92	1.87	1.82	1.77	1.71
26	2.22	2.15	2.07	1.95	1.9	1.85	1.8	1.75	1.69
27	2.2	2.13	2.06	1.93	1.88	1.84	1.79	1.73	1.67
28	2.19	2.12	2.04	1.91	1.87	1.82	1.77	1.71	1.65
29	2.18	2.1	2.03	1.9	1.85	1.81	1.75	1.7	1.64
30	2.16	2.09	2.01	1.89	1.84	1.79	1.74	1.68	1.62
40	2.08	2	1.92	1.79	1.74	1.69	1.64	1.58	1.51
60	1.99	1.92	1.84	1.7	1.65	1.59	1.53	1.47	1.39
120	1.91	1.83	1.75	1.61	1.55	1.5	1.43	1.35	1.25

Table D2: Critical values of R_o for a random distribution [Watson, 1956.]

N	95%	99%	N	95%	99%
5	3.50	4.02	13	5.75	6.84
6	3.85	4.48	14	5.98	7.11
7	4.18	4.89	15	6.19	7.36
8	4.48	5.26	16	6.40	7.60
9	4.76	5.61	17	6.60	7.84
10	5.03	5.94	18	6.79	8.08
11	5.29	6.25	19	6.98	8.33
12	5.52	6.55	20	7.17	8.55

Bibliography

Butler, R. F. (1992), *Paleomagnetism: Magnetic Domains to Geologic Terranes*, Blackwell Scientific Publications.

Cox, A. & Doell, R. (1960), 'Review of Paleomagnetism', *Geol. Soc. Amer. Bull.* **71**, 645–768.

Fisher, N. I., Lewis, T. & Embleton, B. J. J. (1987), 'Statistical Analysis of Spherical Data'.

Fisher, R. A. (1953), 'Dispersion on a sphere', *Proc. Roy. Soc. London, Ser. A* **217**, 295–305.

Irving, E. (1964), *Paleomagnetism and Its Application to Geological and Geophysical Problems*, John Wiley and Sons, In.c.

Kirschvink, J. L. (1980), 'The least-squares line and plane and the analysis of paleomagnetic data', *Geophys. Jour. Roy. Astron. Soc.* **62**, 699–718.

McFadden, P. L. & McElhinny, M. W. (1988), 'The combined analysis of remagnetization circles and direct observations in paleomagnetism', *Earth Planet. Sci. Lett.* **87**, 161–172.

McFadden, P. L. & Reid, A. B. (1982), 'Analysis of paleomagnetic inclination data', *Geophys. J.R. Astr. Soc.* **69**, 307–319.

Tauxe, L., Kylstra, N. & Constable, C. (1991), 'Bootstrap statistics for paleomagnetic data', *Jour. Geophys. Res.* **96**, 11723–11740.

Taylor, J. (1982), *An Introduction to Error Analysis: The Study of Uncertainties in Physical Measurements*, University Science Books, Mill Valley, CA.

Watson, G. (1983), 'Large sample theory of the Langevin distributions', *J. Stat. Plann. Inference* **8**, 245–256.

Watson, G. S. (1956), 'A test for randomness of directions', *Mon. Not. Roy. Astron. Soc. Geophys. Supp* **7**, 160–161.

Lectures in Paleomagnetism, 2005
by Lisa Tauxe

Citation:
http://earthref.org/MAGIC/books/Tauxe/2005/

June 8, 2005

Chapter 12

Beyond Fisher statistics

Suggested Reading

For background:
Chapter 1: Borradaile (2003)
Efron, B. and Tibshirani (1982)
Tauxe, L. et al. (1990)
To learn more:
Chapters 2-5: Fisher, et al. (1987)

12.1 Introduction

Paleomagnetists have depended since the 1950's on the special statistical framework developed by Fisher (1953) for the analysis of unit vector data. The power and flexibility of a variety of tools based on Fisher statistics enables quantification of parameters such as the degree of rotation of a crustal block, or whether the geomagnetic field really averages to a geocentric axial dipole independent of polarity. These tools, however, require that the paleomagnetic data belong to a particular parametric distribution - the Fisher distribution.

In many important situations, the Fisher distribution fails to represent paleomagnetic data adequately. To begin with, it is likely that the geomagnetic field itself produces directions that are far from Fisher distributed (Creer et al., 1959). Collections of paleomagnetic directions from the last five million years from around the globe (e.g., McElhinny and McFadden, 1997) suggest that data from equatorial regions (Figure 12.1a) are in fact significantly elongate while those from high latitudes are more symmetric (Figure 12.1c).

The failure of the Fisher model for directional data sets makes sense if the geomagnetic field is essentially controlled by a geocentric axial dipole with "noise" added by other terms, a topic we will cover in more detail in later lectures. Such models generate spherically symmetric distributions of the VGPs. When converted to equivalent directions are more elongate as the observation site approaches the equator (see Figure 12.1b,c). Because VGPs that are farther from the pole are associated with weaker field strengths in collections of paleomagnetic data and in many models of the field, the Fisher assumption of unit vector length over emphasizes the importance of the "outliers" and leads to mean inclinations that are shallower than the true mean (see e.g., Creer, 1983).

Another example of the inadequacy of the Fisher distribution is the fact that the magnetic field

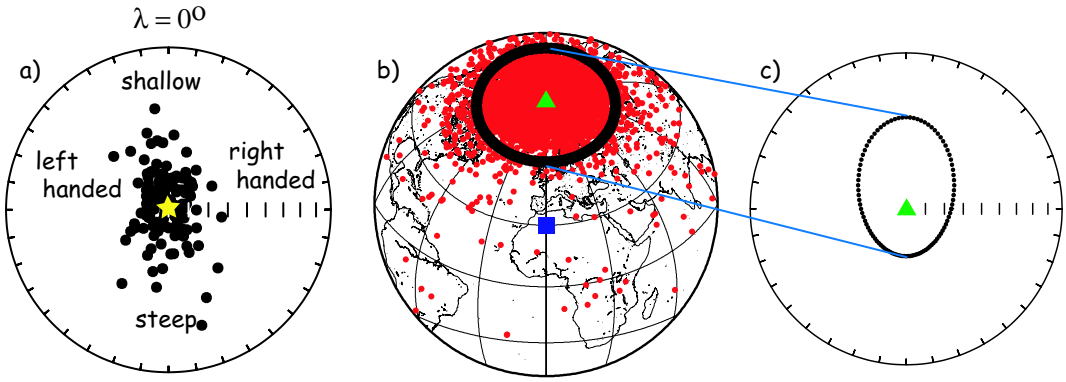

Figure 12.1: a) Paleomagnetic directions from the PSVRL database (see McElhinny and McFadden (1997)) compiled for latitude band 0-5° (N&S). Antipodes of reverse directions are used. Directions rotated to the expected direction (star: $D = 0°, I = 0°$) using the D', I' transformation in Lecture 2. Directions in the upper (lower) half of the diagram are shallower (steeper) than expected and those to the right (left) are right-handed (left-handed). b) VGPs from geomagnetic vectors evaluated from the statistical field model of Tauxe and Kent (2004) at 30°N (site of observation shown as square). The geographic pole is shown as a triangle. A set of VGP positions at 60° N are shown as the black ring. c) Directions observed at the site of observation [square in b)] converted from black ring of VGPs in a) which correspond to the VGP positions at 60°N. These directions have been projected along expected direction at site of observation (triangle). Note that a circularly symmetric ring about the geographic pole gives an asymmetric distribution of directions with a shallow bias. [Figures from Tauxe and Kent, 2004.]

exists in two stable polarity states. Because the Fisher distribution allows only uni-modal data, bi-polar data must be separated into separate modes or one mode must be "flipped" to the antipode prior to calculating a mean. Furthermore, remanence vectors composed of several components tend to form streaked distributions. Similarly, structural complications (e.g., folding) can lead to streaked distributions of directional data.

Thus, non-Fisherian data are a fact of paleomagnetic life. The Fisher-based tests can frequently be inappropriate and could result in flawed interpretations. In Lecture 11 we learned the basics of Fisher statistics and how to test data sets against a Fisher model. In this lecture, we will discuss what to do when Fisher statistics fail. We will begin with essentially parametric approaches that treat certain types of non-fisherican data. We then turn to the use of non-parametric methods such as the bootstrap and jackknife in paleomagnetic applications.

12.2 Non-fisherian approaches to paleomagnetic vectors

12.2.1 The Kent Distribution

The D', I' data from equatorial sampling sites from the last five million years shown in Figure 12.1a have a more elliptical distribution than the symmetrical distribution required for a Fisherian data set. To treat such data, it is probably inappropriate to use a Fisher confidence ellipse and a distribution that allows data with elliptical directional dispersion would be better. The elliptical

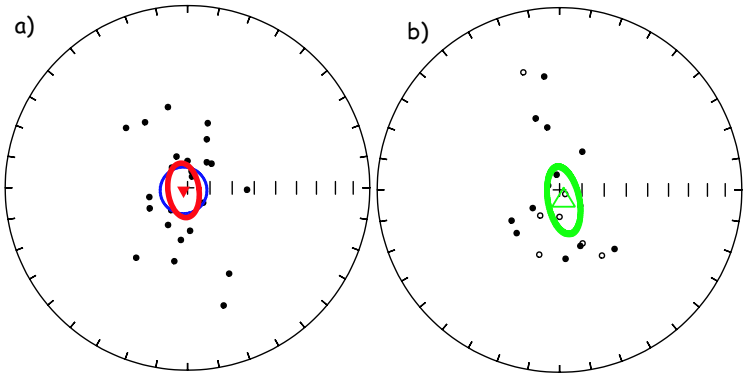

Figure 12.2: A subset of data from Figure 12.1a plotted with the Fisher circle of confidence (light blue line) and the Kent 95% confidence ellipse (heavy red line).

analogue of the Fisher distribution is the Kent distribution (Kent, 1982) and is given by:

$$F = c(\kappa, \beta)^{-1} \exp\left(\kappa \cos\alpha + \beta \sin^2\alpha \cos 2\phi\right)$$

where α is the angle between a given direction and the true mean direction (estimated by the fisher mean (see Lecture 11), and ϕ is an angle in the plane perpendicular to the true direction with $\phi = 0$ parallel to the major eignevector $\mathbf{V}_2$ in that plane. κ is a concentration parameter similar to the Fisher κ and β is the "ovalness" parameter. $c(\kappa, \beta)$ is a complicated function of κ and β. When β is zero, the Kent distribution reduces to a Fisher distribution. Details of the calculation of Kent 95% confidence ellipse are given in the Appendix.

If we were to collect data from the equatorial region, we might well obtain a set of directions such as those shown in Figure 12.1b. AThe Fisher α_{95} circle of confidence for this data set is shown as the light blue line and the Kent ellipse as the heavy red line. The Kent ellipse clearly represents the the distribution of data better than the Fisher α_{95}, being elongate in the same sense as the data themselves.

12.2.2 The Bingham distribution

The Kent distribution has the advantage that it can deal with elliptical data sets while the Fisher distribution cannot. However, many paleomagnetic data sets are also bi-modal and the Kent and Fisher distributions can only deal with data sets with a single polarity. It was precisely for treating bimodal, elliptical data that the Bingham distribution was developed (Bingham, 1974). The Bingham distribution is given by:

$$F = \frac{1}{4\pi d(k_1, k_2)} \exp\left(k_1 \cos^2\phi + k_2 \sin^2\phi\right) \sin^2\alpha$$

where α and ϕ are as in the Kent distribution, k_1, k_2 are concentration parameters ($k_1 < k_2 < 0$) and $d(k_1, k_2)$ is a constant of normalization. Values for k_1, k_2 can be estimated by numerical integration and can be converted into 95% confidence ellipses, the details of which are given in the Appendix. In a nut shell, the $\mathbf{V}_1$ eigenvector of the orientation matrix (associated with the largest eigenvalue, see Lecture 9) is the mean direction and the 95% confidence ellipse semi-axes are proportional to

the intermediate and minimum eigenvalues. The Bingham mean therefore is not necessarily the same as the Fisher or Kent mean. If we take each vector end-point to be a mass, the Bingham mean is the axis about which the moment of inertia would be least. The Fisher mean is somewhat different, in that it is the vector sum of unit vectors. The Bingham mean is less effected by outliers than the Fisher mean, lying closer to the center of mass of data points.

The principle drawback of the Bingham distribution is that because the orientation matrix uses the entire data set (normal and reverse) the two modes are assumed to be antipodal and to share the same distribution parameters. The question of whether normal and reverse data sets are antipodal and have the same dispersion is in fact a question we may wish to ask! One could separate the two modes prior to calculation of the Bingham ellipse, but then the rationale for using the Bingham distribution is lost.

12.2.3 The Bingham-Le Goff approximation

Estimating the parameters for the Bingham ellipse exactly is computationally taxing and all of the available "canned" programs use the look up table of Mardia and Zemloch (1977; see Appendix). Le Goff et al. (1992) suggested some approximations which may be valid for concentrated distributions. They also introduced the concept of weighting results according to some reliability criteria. For the general case, however, it seems preferable to use the exact Kent (1982) ellipses on uni-modal data sets. These could of course be weighted if such weighting is desired.

12.2.4 The bi-Gaussian Distribution

Until now we have continued the Fisher assumption of unit vectors. As already mentioned, neglect of the vector strength can lead to bias. Love and Constable (2003) began the hard work of incorporating intensity information into the parameter estimation problem. Their method can handle bi-modal spherical Gaussian data such as those shown in Figure 12.3. Estimation of the Love parameters are beyond the scope of these lecture notes. Moreover, many data sets are not spherically symmetric as already noted and the Love and Constable (2003) approach must be generalized to elliptical, more "blade-like" data sets than the "cotton balls" currently treatable.

12.3 The simple bootstrap

As we have mentioned, "real" data may be pathological in several respects including bi-modal and elliptically distributed data. Neither the Kent nor the Bingham statistical methods have the test for common mean so critical to paleomagnetic studies. Moreover, none of the methods we have described so far can provide confidence ellipses for an off-center mean direction as is likely to occur in records of the geomagnetic field (see Figure 12.1c). Finally, data may be overprinted or contain the record of a paleomagnetic transition, resulting in "streaked" or non-antipodal mean directions, conditions that make the conventional methods inappropriate. In this section we will discuss alternative methods for estimating confidence bounds which is sufficiently flexible to accomodate all of these short comings, provided the data set is large enough.

In Figure 12.4a we show a fairly typical "not great" paleomagnetic data set. The data are elliptical, bi-modal and one has the suspicion that the normal and reverse modes may be neither antipodal nor share the same concentration or ovalness parameters. Clearly some non-parametric approach would be desirable. The approach for characterizing uncertainties for vectors we will take

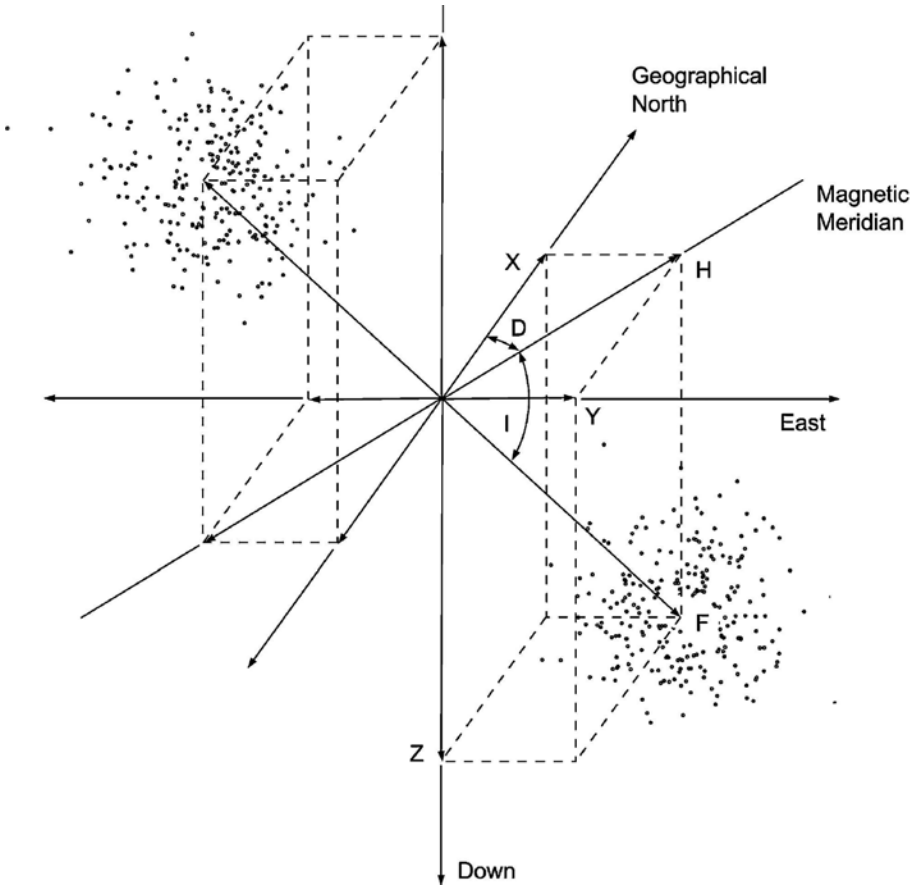

Figure 12.3: A bi-gaussian set of vectors suitable for treatment using the method of Love and Constable (2003). [Figure from Love and Constable, 2003.]

here is based on a technique known as the statistical *bootstrap*. As we shall see, the bootstrap has the flexibility to allow us to treat awkward data sets like that shown in Figure 12.4a.

The principles of the bootstrap are giving in the Appendix. In essence, the parameter of interest (say, the mean vector) is calculated from many resampled data sets, whose data points are selected at random from the original data. The bootstrapped estimates "map out" the likely distribution of the parameter, allowing estimation of confidence regions. Before we extend the bootstrap from the scalar treatment in the appendix to vectors, it is important to point out that with the bootstrap, it is assumed that the underlying distribution is represented by the data, demanding that the data sets be rather large. Moreover, the bootstrap estimates are only asymptotically true, meaning that a large number of bootstrap calculations are required for the confidence intervals to be valid. It's a good thing we have fast computers with huge hard-drives.

There are a variety of ways we can use the bootstrap to estimate confidence regions for paleomagnetic data. We will start with the most "Fisher" like approach of taking unit vectors of a single polarity. Then we will accommodate dual polarity data sets and develop analogous tests to those so useful for Fisher distributions.

To do a simple bootstrap on a data set with only one polarity (say the normal data in Figure 12.4a, we first randomly draw N data points from the data shown in Figure 12.4a. Each set

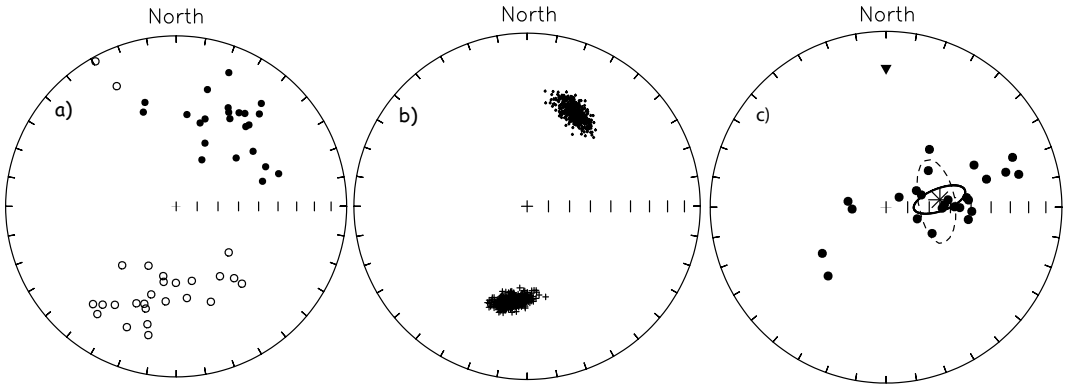

Figure 12.4: Hypothetical non-Fisherian data set. Normal and reversed polarity data that are not symmetrically distributed. Filled (open) circles plot on the lower (upper) hemisphere. b) Equal area projection of 500 bootstrapped means for para-data sets drawn from the data shown in a) Tiny circles (plusses) are lower (upper) hemisphere projections from the normal (reversed) polarity mode of each para-data set. c) Normal polarity data from a) transformed into VGPs and plotted in polar equal area projection. The dashed ellipse is obtained from VGP transformation of α_{95}, while the solid ellipse is determined by a bootstrap.

of N data points is a "para-data set" (also known as a "pseudo-sample"). We then calculate a Fisher mean of the para-data set (one little circle in Figure 12.4b. This resampling procedure can be repeated many times. We show 500 such bootstrapped means in Figure 12.4b.

Now we can estimate the region of 95% confidence for the bootstrapped means. A non-parametric approach would be to draw a contour enclosing 95% of the bootstrapped means. In many applications, paleomagnetists desire a more compact way of expressing confidence regions (for example, to list them in a table) and this necessitates some parametric assumptions about the distribution of the means. For this limited purpose, approximate 95% confidence regions can be estimated by noting the elliptical distribution of the bootstrapped means and by assuming that they are Kent (1982) distributed.

When paleomagnetic data are bimodal, as in Figure 12.4a, we can proceed in one of two ways. We could just calculate the principle eigenvector of the orientation matrix ($\mathbf{V}_1$) as in Bingham statistics of each bootstrapped para-data set or we can separate the data into two modes and calculate Fisher means for each mode separately (as in Figure 12.4b).

To separate the data into normal and reverse sub-sets, we first calculate the orientation matrix and its principal eigenvector $\mathbf{V}_1$. By transforming the data set into the coordinates of $\mathbf{V}_1$ (see appendix to Lecture 2), the transformed inclinations could be used to assign polarity in an automated and unbiased way; positive inclinations belong to one mode and negative inclinations to the other. After separation, Fisher means can be calculated for each mode separately. Alternatively, if a more robust estimate of the "average" direction is desired, one could calculate the principal eigenvector $\mathbf{V}_1$ of each mode, which is less sensitive to the presence of outliers.

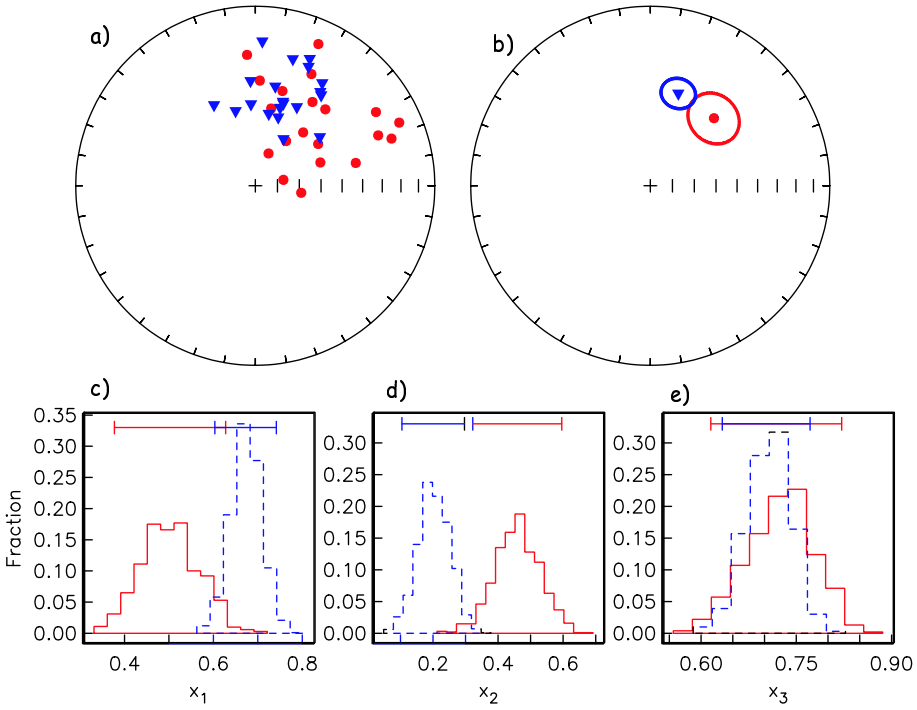

Figure 12.5: The bootstrap test for a common mean. a) Equal-area projections of two data sets two simulated Fisherian data sets (triangles and circles) each with κ of 20. b) Means and α_{95}s of data sets shown in a). c) Histograms of x_1 components of the bootstrapped means from 500 para-data sets. Also shown are the bounds for each data set that include 95% of the components. The confidence intervals for the different data sets overlap. d) Same as c) but for the x_2 component. The confidence intervals do not overlap. e) same as d) but for the x_3 component.

12.4 The parametric bootstrap

The bootstrap just described is a "simple" or "naive" bootstrap in that no distribution is assumed for the data. We did assume, however, that all the uncertainty inherent in the data is reflected in the data distribution. If the data set is smaller than about $N = 20$, this leads to uncertainty ellipses that are too small (Tauxe et al., 1991). Many paleomagnetic data sets are smaller than this, yet they are demonstrably non-Fisherian. Luckily, if we are able to assume some parametric form for data from e.g., a given site, we can perform a superior technique which is known as the *parametric bootstrap*. As applied here, we assume that each site with N_s samples is Fisher distributed (in principle, a testable assumption). Then, after random selection of a particular site for inclusion in the para-data set, we draw N_s new directions from a Fisher distribution with the same mean direction, κ and N. From these, we then calculate a substitute mean direction, and use that in the para-data set. Otherwise, we follow the same procedure as before.

For large data sets ($N > 25$), the parametric and simple bootstraps yield very similar confidence ellipses. For smaller data sets, the parametric ellipses are larger, and are probably more realistic.

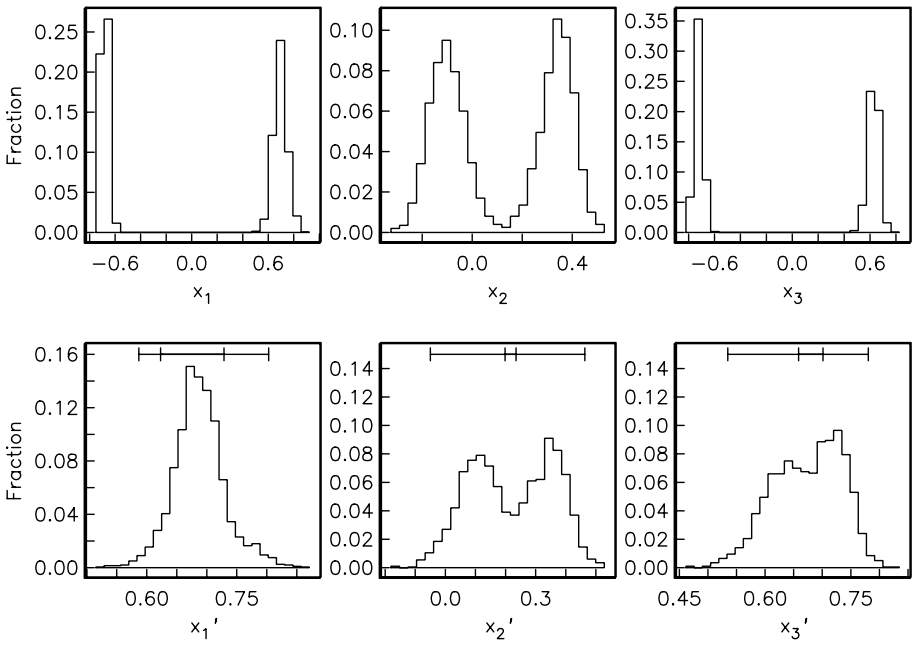

Figure 12.6: Histograms of cartesian coordinates of means of para-data sets drawn from the data shown in Figure 12.4a. In the lower plots, the reversed polarity mode has been flipped to the antipode (x_i'). The intervals containing 95% of each set of components are drawn (see last two figures). Because the confidence bounds from the two data sets overlap in all three components, the means of the reverse and normal modes cannot be distinguished at the 95% level of confidence; they pass the bootstrap reversals test.

12.5 Application to VGPs

We stated earlier that the transformation of Fisher distributed directional data to VGPs can cause a distortion from rotationally symmetric data to elliptically distributed data. To illustrate what happens if data are distributed as in our hypothetical normal data set, we calculate VGPs in Figure 12.4a, the ellipse described by dp, dm (Lecture 11), and our bootstrap confidence ellipses. The VGPs are plotted in Figure 12.4c and the dp, dm is shown as a dotted line. Because the declinations are smeared and the dp must point towards the site (shown as a triangle), the long axis of the so-called 95% confidence regions is perpendicular to the actual data distribution. The 95% confidence ellipse, calculated using the bootstrap, is shown as a solid line. The bootstrapped confidence ellipse gives a better sense of the uncertainty and follows the trend in the data.

12.6 When are two data sets distinct?

The test for a common mean addresses the question "can the means of two data sets be discriminated from one another?" Another way of putting it is, "If a set of bootstrap means is examined, are there two distinct groups or is there just one?" We explore these ideas by considering the same Fisherian data sets we used in Lecture 11 for the Watson's V_w test. In Figure 12.5 we show two data sets (triangles and circles), each drawn from distributions with a κ of 20. The mean direction of each lies outside the confidence region of the other and the but the V_w test of Watson has a value

of 11.7 with a critical value of 6.3, hence they fail the test for a common mean.

In order to develop a bootstrap test analagous to the V_w test for use on non-Fisherian data sets, we first convert a set of bootstrapped mean directions to to cartesian coordinates. Histograms of the cartesian coordinates of the bootstrap means (Figure 12.5c-e) are distinct in the x_2 component, confirming that the two means can be distinguished at the 95% confidence level.

12.7 Application to the "reversals test"

The so-called *reversals test* in paleomagnetism constitutes a test for a common mean for two modes, one of which has been "flipped" to its antipode. We apply our bootstrap test for common mean to the data shown in Figure 12.4. The histograms of the cartesian coordinates of the bootstrapped means are shown in Figure 12.6. There are two "humps" in the bootstrap test. However, the confidence intervals for the normal and reverse antipodes overlap, thereby suggesting that the two means cannot be distinguished at the 95% level of confidence. Thus, the data in Figure 12.4 pass the bootstrap reversals test.

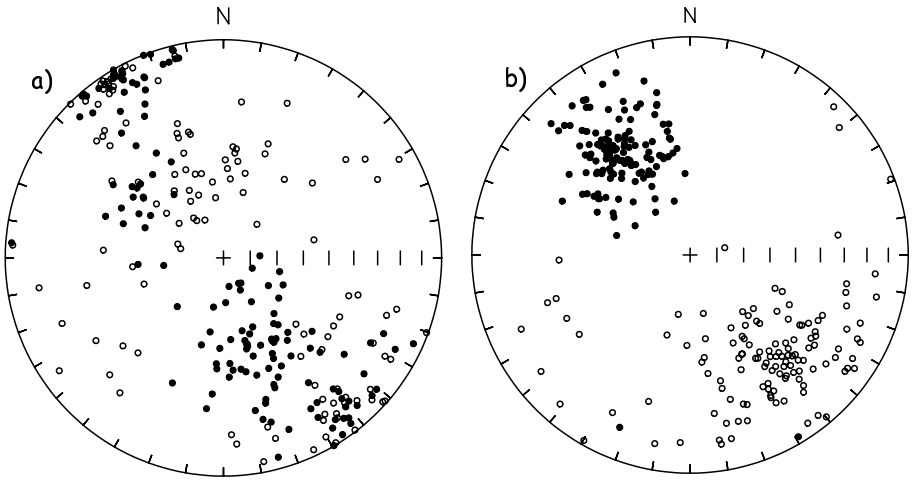

Figure 12.7: a) Equal area projection of a set of directions in geographic coordinates. The data are streaked in a girdle distribution and the polarity of many data points is ambiguous. b) Data from a) after 100% adjusting for tilt. Polarities are more readily identifiable. [Redrawn from Tauxe and Watson, 1994.]

12.8 Application to the fold test

A final test is extremely useful in paleomagnetism: the fold test (Lecture 9). One of the key components in paleomagnetic studies is to determine the coordinate system (geographic, tilt adjusted or somewhere in between) for which the directional data are most tightly clustered. If a rock has moved from its original position, was it magnetized in the original, in the present or in some other position? Moreover, is simple rotation about strike an appropriate method to restore the beds to their original positions? In the classic fold test as first proposed by Graham (1949), the directions of magnetization of a deformed rock unit are assumed to be most closely parallel in the

orientation in which the magnetization was acquired. Therefore, if a rock has retained an original magnetization through a subsequent folding or tilting event, the magnetic directions may cluster most tightly after they have been rotated back to their original positions. This of course is NOT true for elongate data such as those shown in Figure 12.1a.

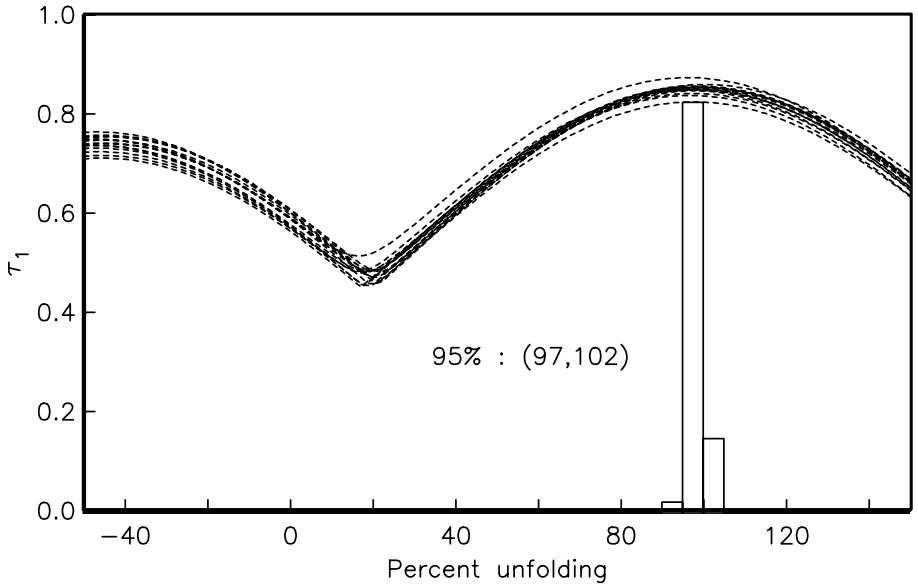

Figure 12.8: The largest eigenvalues τ_1 of the orientation matrices from representative para-data sets drawn from Figure 12.6. The directions are adjusted for tilt incrementally from -50% to 150%. The largest value of τ_1 occurs near 100% in all of the para-data sets. Histogram is of 500 maxima of τ_1 and the calculated 95% confidence interval. These data "pass" the bootstrap fold test. [Redrawn from Tauxe and Watson, 1994.]

The fold test appears at first glance to be simple, but it is not. The primary problem is that paleomagnetic vectors are never perfectly parallel. The scattered nature of the data means that a statistical test is necessary to determine whether clustering is "significantly" better in one orientation or another.

In Lecture 11 we suggested that variances could be compared using an F-test, so it was long the practice in paleomagnetism to compare estimated precisions before and after tilt adjustment (McElhinny, 1964). The ratio of the two estimates of κ were compared with those listed in statistical "F" tables (see Appendix to Lecture 11). Ratios higher than the "F" value for a given N were deemed to constitute a significant increase in concentration after adjusting for tilt, thus representing a positive fold test. This test can be done on the back of an envelope and is still in frequent use.

Although its simplicity is a great strength, there are several problems with the classical fold test. First, the geomagnetic field has two preferred states and is not perfectly dipolar. Directions observed in paleomagnetic samples are therefore not only scattered but are often of two polarities. Second, the magnetic directions may be most tightly clustered somewhere other than in "geographic" or 100% tilt adjusted coordinates. Finally, structual "corrections" are not perfectly known. Not only are the bedding orientations themselves often difficult to measure accurately, but detection of complications such as plunging folds, and multiple phases of tilting requires extensive field work.

12.8. APPLICATION TO THE FOLD TEST

It is nearly impossible to assess rotation about the vertical axis on the basis of field relations alone, as it results in no visible effect on the dip of the beds themselves. Because of this uncertainty, we might reasonably ask whether if the data are actually most tightly clustered at, say 90% tilt adjusted (as opposed to 100%), does this constitute a "failed" fold test.

We consider first the problem of dual polarity. We plot a data set in geographic coordinates in Figure 12.7a and in tilt adjusted coordinates in Figure 12.7b. The polarity is ambiguous and the calculation of κ necessitates using the tilt adjusted data to identify the polarity of the samples. The classic fold test requires calculation of κ which can only be done with data of a single polarity. Obviously, fold tests that rely on κ will not be straightforward with data such as these.

An alternative approach is based on the orientation matrix. In the orientation matrix, polarity does not play a role and the "tightness" of grouping is reflected in the relative magnitudes of the eigenvalues (τ). As the data become more tightly grouped, the variance along the principal axis grows and those along the other axes shrink. Thus, examination of the behavior of τ_1 during unfolding would reveal the point at which the tightest grouping is achieved, without knowledge of polarity.

Suppose we find that the degree of unfolding required to produce the maximum in τ_1 is 98%. Is this a positive fold test suggesting a pre-folding remanence or is the difference between 98% and 100% significant? For this we call on the familiar bootstrap. Numerous para-data sets can be drawn. We can then calculate the eigenparameters of the orientation matrix for a range of percent unfolding. Some examples of the behavior of τ_1 during tilt adjustment of representative para-data sets drawn from the data in Figure 12.7a are shown in Figure 12.8. Figure 12.8 is a histogram of maxima of τ_1 from 500 para-data sets. These are sorted and the 95% confidence interval for the degree of unfolding required to produce the tightest grouping (the highest τ_1) is thus constrained to lie between 97 and 102%.

The data from Figure 12.7a are shown after 100% tilt adjustment in Figure 12.7b. The tilt adjusted data are not only better grouped, but now the polarities of most samples can be readily determined. An advantage of the bootstrap approach is the fact that the data do not need prior editing to split them into normal and reversed polarity groups, which is a particularly onerous task for the data considered here.

For small data sets, we could of course employ a parametric bootstrap, whereby para-data sets are generated by first randomly selecting a site for inclusion, then by drawing a substitute direction from a Fisher distribution having the same D, I, N, and κ.

Appendix

A Estimation of Kent 95% confidence ellipse

Kent parameters are calculated by rotating unimodal directions x into the data coordinates x' by the transformation:

$$x' = \mathbf{\Gamma}^T x, \tag{A1}$$

where $\mathbf{\Gamma} = (\gamma_\mathbf{1}, \gamma_\mathbf{2}, \gamma_\mathbf{3})$, and the columns of $\mathbf{\Gamma}$ are called the constrained eigenvectors of $\mathbf{T}$. The vector $\gamma_\mathbf{1}$ is parallel to the Fisher mean of the data, whereas $\gamma_\mathbf{2}$ and $\gamma_\mathbf{3}$ (the major and minor axes) diagonalize $\mathbf{T}$ as much as possible subject to being constrained by $\gamma_\mathbf{1}$ (see Kent (1982), but note that his x_1 corresponds to x_3 in conventional paleomagnetic notation). The following parameters may then be computed

$$\begin{array}{c} \hat{\mu} = N^{-1}\sum_k {x_{k1}}' \\ \hat{\sigma}_2^2 = N^{-1}\sum_k ({x_{k2}}')^2 \\ \hat{\sigma}_3^2 = N^{-1}\sum_k ({x_{k3}}')^2. \end{array} \tag{A2}$$

As defined here, $\hat{\mu} = R/N$ (R is closely approximated by the equation for R in Lecture 11). Also to good approximation, $\hat{\sigma}_2^2 = \tau_2$, and $\hat{\sigma}_3^2 = \tau_3$, where τ_i are the eigenvalues of the orientation matrix. The semi-angles ζ_{95} and η_{95} subtended by the major and minor axes of the 95% confidence ellipse are given by:

$$\zeta_{95} = \sin^{-1}(\sigma_2\sqrt{g}), \quad \eta_{95} = \sin^{-1}(\sigma_3\sqrt{g}), \tag{A3}$$

where $g = -2\ \ln(0.05)/(N\hat{\mu}^2)$.

The tensor $\mathbf{\Gamma}$ is, to a good approximation, equivalent to $\mathbf{V}$, the eigenvectors of the orientation matrix. Therefore, the eigenvectors of the orientation matrix $\mathbf{V}$ give a good estimate for the directions of the semi-angles by:

$$\begin{array}{l} D_\zeta = \tan^{-1}(v_{22}/v_{12}), I_\zeta = \sin^{-1}v_{32}, \\ D_\eta = \tan^{-1}(v_{23}/v_{13}), I_\eta = \sin^{-1}v_{33}, \end{array} \tag{A4}$$

where for example the x_2 component of the smallest eigenvector $\mathbf{V}_3$ is denoted v_{23}.

B Estimation of Bingham 95% confidence parameters

The Bingham distribution is given by:

$$F = \frac{1}{4\pi d(k_1, k_2)} \exp\left(k_1 \cos^2\phi + k_2 \sin^2\phi\right) \sin^2\alpha$$

where α and ϕ are as in the Kent distribution, k_1, k_2 are concentration parameters ($k_1 < k_2 < 0$) and $d(k_1, k_2)$ is a constant of normalization given by:

$$d(k_1, k_2) = \frac{1}{4\pi} \int_0^{2\pi} \int_0^{\pi} \exp\left(\left(k_1 \cos^2\phi + k_2 \sin^2\phi\right) \sin^2\theta\right) \sin\theta d\theta\phi.$$

To estimate the axes of the Bingham confidence ellipse, we first calculate the eigenparameters of the orientation matrix as for Kent parameters and described in the Appendix to Lecture 9.

Note that through-out these lecture notes τ_i are the eigenvalues and $\mathbf{V}_i$ are the eigenvectors. The principle eigenvector $\mathbf{V}_1$ of the orientation matrix is associated with the largest eigenvalue τ_1. In Bingham (1974), ω_1 is the τ_3 and ω_3 is τ_1. In Bingham statistics, the $\mathbf{V}_1$ direction is taken as the mean - it is not always parallel to the Fisher mean of a unimodal set of directions.

The maximum likelihood estimates of k_1, k_2, the concentration parameters are gotten by first maximizing the log likelihood function:

$$F = -N \log(4\pi) - N \log d(k_1, k_2) + k_1\omega_1 + k_2\omega_2.$$

These are listed for convenience in Table B1 as calculated by Mardia and Zemroch (1977). Once these are estimated, the semi-axes of the 95% confidence ellipse around the mean direction $\mathbf{V}_1$ are given by:

$$\epsilon_{ij}^2 = \chi_p^2(\nu)\sigma_{ij}^2,$$

where $\chi_p^2(\nu) = 5.99$ is the χ^2 value for significance ($p = .05$ for 95% confidence) with $\nu = 2$ degrees of freedom and

$$\sigma_{ij}^2 = \frac{1}{2N(\omega_i - \omega_j)(k_i - k_j)}$$

.

Bingham (1974) set $k_3 = 0$, so the semi axes of the confidence ellipse about the principle direction $\mathbf{V}_1$, associated with ω_3, are therefore:

$$\epsilon_{32} = \frac{1.22}{-k_2 N(\omega_3 - \omega_2)}$$

and

$$\epsilon_{31} = \frac{1.22}{-k_1 N(\omega_3 - \omega_1)}.$$

Because $k_1 < k_2 < 0$, the semi-axes are positive numbers. Please note that we use the corrected version of Tanaka (1999) as opposed to the more oft quoted but erroneous treatment of Onstott (1980) in this appendix. Note also that the N is required for σ because we have normalized the ωs to sum to unity for consistency with other eigenvalue problems in this set of lecture notes. The N is missing in the treatment of Tanaka (1999) presumably because the eigenvalues sum to N. Finally, note that these values of ϵ are in radians and must be converted to degrees for most applications.

C The statistical bootstrap

In Figure B1, we illustrate the essentials of the statistical bootstrap. We will develop the technique using data drawn from a normal distribution. First, we generate a synthetic data set by drawing 500 data points from a normal distribution with a mean $\bar{x}$ of 10 and a standard deviation σ of 2. The synthetic data are plotted as a histogram in Figure B1a. In Figure B1b we plot the data as a Q-Q plot against the z_i expected for a normal distribution (see Abramowitz and Stegun (1970).

In order to calculate the appropriate values for z_i assuming a normal distribution:

1. For $i = 1 \rightarrow N$, calculate $p = \frac{i}{N+1}$.

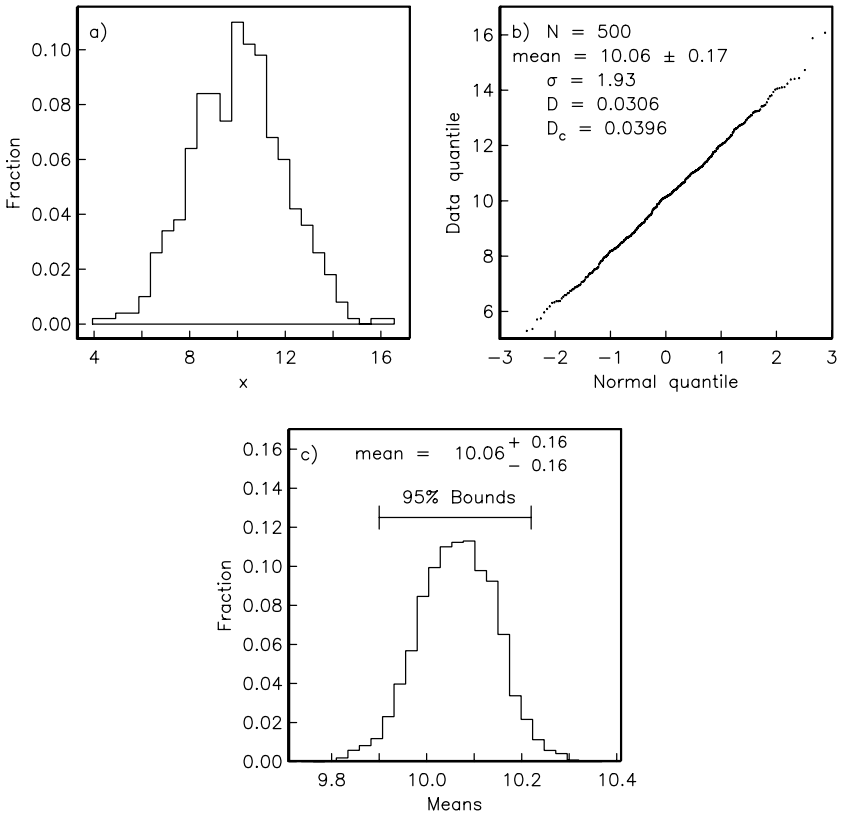

Figure B1: Bootstrapping applied to a normal distribution. a) 500 data points are drawn from a Gaussian distribution with mean of 10 and a standard deviation of 2. b) Q-Q plot of data in a). The 95% confidence interval for the mean is given by Gauss statistics as ± 0.17. 10,000 new (para) data sets are generated by randomly drawing N data points from the original data set shown in a). c) A histogram of the means from all the para-data sets. 95% of the means fall within the interval $10.06^{+0.16}_{-0.16}$, hence the bootstrap confidence interval is similar to that calculated with Gaussian statistics.

2. If $p > 0.5$, then $q = 1 - p$; if $p < 0.5$, then $q = p$.

3. Calculate the following for all $p \neq 0.5$:

$$t = \sqrt{-2\ln^{-1}(q)},$$

and

$$u = t - \frac{(a_1 + a_2 t_+ a_3 t^2)}{(1 + a_4 t + a_5 t^2 + a_6 t^3)},$$

where $a_1 = 2.515517, a_2 = 0.802853, a_3 = 0.010328, a_4 = 1.432788, a_5 = 0.189269, a_6 = 0.001388$.

4. If $p > 0.5$, then $z_i = u$; if $p < 0.5$, then $p = -u$.

5. If $p = 0.5$, then $z_i = 0$.

The values of z_i calculated in this way for the simulated Gaussian distribution are plotted as the "normal quantile" data in Figure B1b.

The simulated data fall along a line in Figure B1b which suggests that they are normally distributed (as one would hope). To test this in a more quantitative way, we can calculate D_N^+ and D_N^- as follows:

1. Calculate the mean $\bar{x}$ and standard deviation σ for the data.

2. Then calculate:
$$p = \frac{x_i - \bar{x}}{\sqrt{2}\sigma},$$
and
$$q = \frac{1}{1 + 0.3275911|x|}.$$

3. Substitute q into the following expression (function 7.1.26 from Abramowitz and Stegun (1970):
$$\mathrm{erf}(q) = 1 - e^{-p^2}[a_1 q + a_2 q^2 + a_3 q^3 + a_4 q^4 + a_5 q^5],$$
where $a_1 = 0.254829592, a_2 = -0.284496736, a_3 = 1.421413741,$ and $a_5 = 1.061405429$.

4. Change the sign of $\mathrm{erf}(q)$ such that it has the same sign as q.

5. Substitute $F(x) = 0.5(1 + \mathrm{erf}(q))$ into Equations D3 and D4 in the Appendix to Lecture 11 for D_N^+ and D_N^- respectively. The Kolmogorov-Smirnov parameter D (e.g., Fisher et al., 1987) is the larger of D_N^+ or D_N^-.

6. The null hypothesis that a given data set is normally distributed can be rejected at the 95% level of confidence if D exceeds a critical value D_c given by $0.886/\sqrt{N}$.

Applying the foregoing to the data in Figure B1a yields a D value of 0.0306. Because $N = 500$, the critical value of D, D_c at the 95% confidence level is 0.0396. Happily, our program has produced a set of 500 numbers for which the null hypothesis of a normal distribution has not been rejected. The mean is about 10 and the standard deviation is 1.9. The usual Gaussian statistics allow us to estimate a 95% confidence interval for the mean as $\pm 1.96\sigma/\sqrt{N}$ or ± 0.17.

The mean of the synthetic dataset is about 10 and the standard deviation is 1.9. The usual Gaussian statistics allow us to estimate a 95% confidence interval for the mean as $\pm 1.96\sigma/\sqrt{N}$ or ± 0.17.

In order to estimate a confidence interval for the mean using the bootstrap, we first randomly draw a list of N data by selecting data points from the original data set. Some data points will be used more than once and others will not be used at all. We then calculate the mean of the "para-data set". We repeat the procedure of drawing para-data sets and calculating the mean many times (say 10,000 times). A histogram of the "bootstrapped" means is plotted in Figure B1c. If these are sorted such that the first mean is the lowest and the last mean is the highest, the 95%

of the means are between the 250^{th} and the $9{,}750^{th}$ mean. These therefore are the 95% confidence bounds because we are approximately 95% confident that the true mean lies between these limits. The 95% confidence interval calculated for the data in Figure B1 by bootstrap is about $\pm$ 0.16 which is nearly the same as that calculated the Gaussian way. However, the bootstrap required orders of magnitude more calculations than the Gaussian method, hence it is ill-advised to perform a bootstrap calculation when a parametric one will do. Nonetheless, if the data are not Gaussian, the bootstrap provides a means of calculating confidence intervals when there is no quick and easy way. Furthermore, with a modern computer, the time required to calculate the bootstrap illustrated in Figure B1 was virtually imperceptible.

Bibliography

Abramowitz, M. & Stegun, I. A. (1970), 'Handbook of Mathematical Functions'.

Bingham, C. (1974), 'An antipodally symmetric distribution on the sphere', *Ann. Statist.* **2**, 1201–1225.

Borradaile, G. J. (2003), *Statistics of Earth Science Data: Their Distribution in Time, Space, and Orientation*, Springer, Berlin.

Creer, K., Irving, E. & Nairn (1959), 'Paleomagnetism of the Great Whin Sill', *Geophys. J. Int.* **2**, 306–323.

Creer, K. M. (1983), 'Computer synthesis of geomagnetic paleosecular variations', *Nature* **304**, 695–699.

Efron, B. (1982), 'The Jackknife, the Bootstrap and Other Resampling Plans'.

Fisher, N. I., Lewis, T. & Embleton, B. J. J. (1987), 'Statistical Analysis of Spherical Data'.

Graham, J. W. (1949), 'The stability and significance of magnetism in sedimentary rocks', *Jour. Geophys. Res.* **54**, 131–167.

Kent, J. T. (1982), 'The Fisher-Bingham distribution on the sphere', *J. R. Statist. Soc. B.* **44**, 71–80.

Le Goff, M., Henry, B. & Daly, L. (1992), 'Practical method for drawing a VGP path', *Phys. Earth Planet. Inter.* **70**, 201–204.

Love, J. & Constable, C. G. (2003), 'Gaussian statistics for paleomagnetic vectors', *Geophys. J. Int.* **152**, 515–565.

Mardia, K. V. & Zemrock, P. J. (1977), 'Table of maximum likelihood estimates for the Bingham distribution', *J. Statist. Comput. Simul.* **6**, 29–34.

McElhinny, M. W. (1964), 'Statistical significance of the fold test in paleomagnetism', *Geophys. Jour. R. astro. Soc.* **8**, 338–340.

McElhinny, M. W. & McFadden, P. L. (1997), 'Palaeosecular variation over the past 5 Myr based on a new generalized database', *Geophys. J. Int.* **131**(2), 240–252.

Onstott, T. C. (1980), 'Application of the Bingham Distribution Function in paleomagnetic studies', *J. Geophys. Res.* **85**, 1500–1510.

Tanaka, H. (1999), 'Circular asymmetry of the paleomagnetic directions observed at low latitude volcanic sites', *Earth Planets Space* **51**, 1279–1286.

Tauxe, L., Constable, C. G., Stokking, L. B. & Badgley, C. (1990), 'The use of anisotropy to determine the origin of characteristic remanence in the Siwalik red beds of northern Pakistan', *Jour. Geophys. Res.* **95**, 4391–4404.

Tauxe, L. & Kent, D. V. (2004), A simplified statistical model for the geomagnetic field and the detection of shallow bias in paleomagnetic inclinations: Was the ancient magnetic field dipolar?, *in* e. a. Channell, J.E.T., ed., 'Timescales of the Paleomagnetic field', Vol. 145, American Geophysical Union, Washington, D.C., pp. 101–116.

Tauxe, L., Kylstra, N. & Constable, C. (1991), 'Bootstrap statistics for paleomagnetic data', *Jour. Geophys. Res.* **96**, 11723–11740.

Tauxe, L. & Watson, G. S. (1994), 'The fold test: an eigen analysis approach', *Earth Planet. Sci. Lett.* **122**, 331–341.

Lectures in Paleomagnetism, 2005
by Lisa Tauxe

Citation:
http://earthref.org/MAGIC/books/Tauxe/2005/

June 8, 2005

Chapter 13

Paleomagnetic tensors

Suggested Reading

For background:
Part II: Means (1976)
Tarling and Hrouda (1993)
Chapter 2: Collinson (1983)
To learn more:
Chapters 5 and 6: Tauxe (1998)

13.1 Introduction

In the previous several lectures we have been concerned with magnetic vectors. Higher dimensional magnetic tensors are also tremendously useful in geological studies and have found wide use in studies involving sedimentary, igneous and metamorphic rocks. Such data have applications in determining such varied parameters as paleocurrent directions, degree of paleosol maturity, directions of magma injection, tectonic strain, etc. The most frequently used magnetic tensors are the anisotropy of magnetic susceptibility (AMS) and the anisotropy of anhysteretic remanence (AARM) tensors, although TRM, DRM and IRM anisotropy are also measured from time to time. We will begin by describing the measurement of magnetic susceptibility and how the AMS tensor is determined. Then we will extend the discussion to the anisotropy of remanences.

13.2 Measurement of magnetic susceptibility

The concept of magnetic susceptibility was first introduced in Lecture 1. It is usually taken as the ratio of the induced magnetization to an inducing magnetic field or M_I/H. In practice, many laboratories use equipment that works on the principle illlustrated in Figure 13.1 whereby an alternating current is driven through the coil on the right inducing a current in the coil on the left. This alternating current generates a small alternating field (generally less than 1 mT) along the axis of the coil. When a sample is placed in the coil, the alternating current induces an alternating magnetic field in the sample. This causes an offset in the alternating current in the coil on the right which is proportional to the induced magnetization. After calibration, this offset can then be cast in terms of magnetic susceptibility. If the sample is placed in the solinoid in different orientations (e.g., those in Figure 13.1d), the anisotropy of the magnetic susceptibility can be determined.

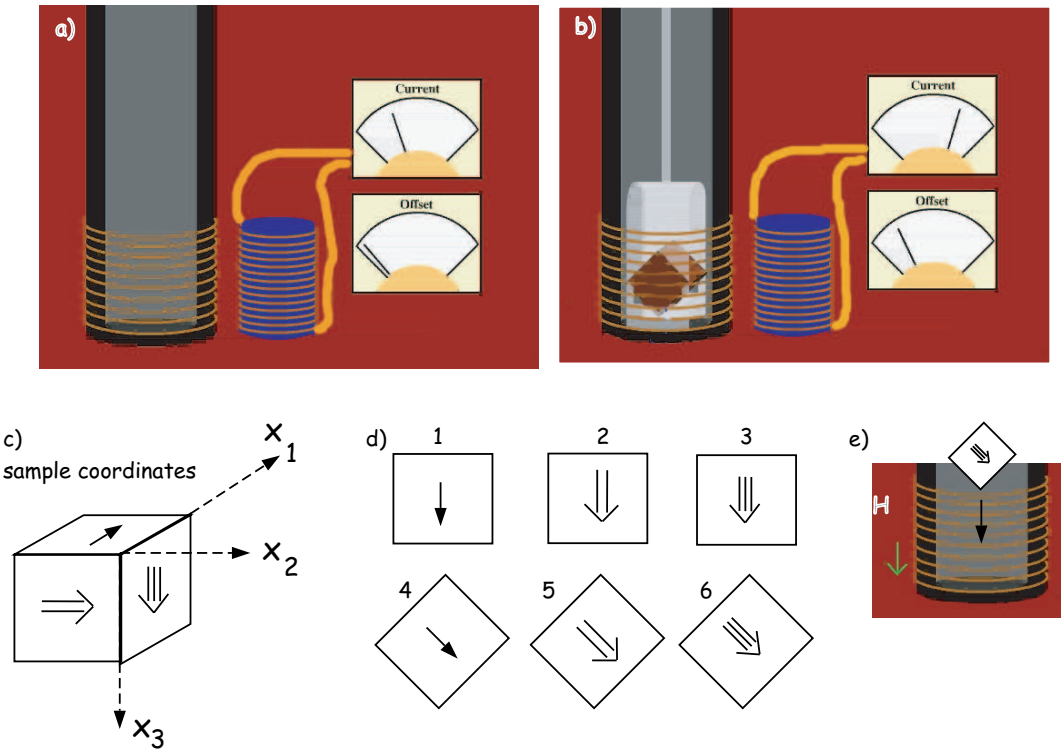

Figure 13.1: Measuring magnetic susceptibility. a) An alternating current applied in the coil on the right induces a current in the left-hand coil. This induces a magnetization in the sample shown in b), which in turn offsets the current in the coil to the right. The offset is proportional to the magnetic susceptibility of the sample. [Figure modified from Genevieve Tauxe, http://magician.ucsd.edu/Lab_tour/movs/isosuscp.mov.] c) Definition of sample coordinates. d) Scheme for measuring six elements of **K**. d) The sample is placed in the different orientations in the coil as in e) with alternating field **H**.

Before we launch into a detailed discussion of AMS data it is worth thinking briefly about what controls magnetic susceptibility and what the data might mean. At an atomic level, magnetic susceptibility results from the response of electronic orbits and/or unpaired spins to an applied field (Lecture 3). The diamagnetic response (orbits) is extremely weak and unless a specimen is nearly pure carbonate or quartz, it can be neglected. The paramagnetic response of, say, biotite, is much stronger, but if there is any appreciable ferromagnetic material in the specimen, the response will be dominated by that.

In highly magnetic minerals such as magnetite, the susceptibility is dominated by the shape anisotropy. For a uniformly magnetized particle (e.g., small SD magnetite), the maximum susceptibility is at a high angle to the easy axis, because the moments are already at saturation along the easy direction. So we have the somewhat paradoxical result that uniformly magnetized particles have maximum susceptibilities along the short axis of elongate grains. For vortex remanent state, or multi-domain particles and perhaps for strongly flowered grains, this would not be the case and the maximum susceptibility is along the particle length. Another perhaps non-intuitive behavior is for superparamagnetic particles whose response is quite large (some 25 times larger than a sin-

gle domain particle of the same size!). Chains of particles may also have non-intuitively obvious magnetic responses because of interparticle interaction.

Ferromagnetic phases can occur as discrete grains in rocks or as inclusions within other mineral phases. Often the magnetic phases in silicate hosts like plagioclase are crystallographically aligned. The AMS response can therefore be controlled by the alignment of the host minerals, by the alignment of interacting chains of magnetic particles or by the alignment of the discrete magnetic grains in the rock. Therefore care must be exercised in the interpretation of AMS results.

The relationship between a small applied magnetic field vector **H** and the induced magnetization vector **M** until now has been taken as a scalar. However, if the magnetic response of the specimen depends on the orientation of the applied field (i.e., it is anisotropic) it can often be approximated by a small set of linear equations. Components of the induced magnetization in a given coordinate system ($\mathbf{M}_i$) whose axes are denoted by $\mathbf{X}_1, \mathbf{X}_2$, and $\mathbf{X}_3$ (see Figure 13.1c) are related to the components of the applied field along the sample axes $\mathbf{H}_i$ (see Lecture 2) by the following linear equations:

$$\begin{aligned} M_1 &= \chi_{11}H_1 + \chi_{12}H_2 + \chi_{13}H_3 \\ M_2 &= \chi_{21}H_1 + \chi_{22}H_2 + \chi_{23}H_3 \\ M_3 &= \chi_{31}H_1 + \chi_{32}H_2 + \chi_{33}H_3, \end{aligned} \tag{13.1}$$

where χ_{ij} are coefficients of magnetic susceptibility.

13.3 Treatment of anisotropy data

The linear relationship between the two vectors can be cast as a second-order tensor. The coefficients χ_{ij} are the elements of a second-order, symmetric tensor, known as the *anisotropy of magnetic susceptibility (AMS) tensor* χ. The set of Equations 13.1 can be rewritten in subscript notation as:

$$M_i = \chi_{ij}H_j. \tag{13.2}$$

Because $\chi_{ij} = \chi_{ji}$, the susceptibility tensor χ defines a symmetric, second-order tensor that has 6 independent matrix elements. For convenience we define a related column matrix **s** having six elements that are related to the elements of χ by:

$$\begin{aligned} s_1 &= \chi_{11} \\ s_2 &= \chi_{22} \\ s_3 &= \chi_{33} \\ s_4 &= \chi_{12} = \chi_{21} \\ s_5 &= \chi_{23} = \chi_{32} \\ s_6 &= \chi_{13} = \chi_{31}. \end{aligned} \tag{13.3}$$

In practice, only s_1, s_2, and s_3 can be measured directly, the terms s_4 to s_6 are only indirectly determined. In the simplest experiment,, there are six measured values of susceptibility K_i. These are determined in six sample positions, for example, as shown in Figure 13.1d. Measurement in position 1 gives $K_1 = s_1$. Similarly, in position 2, we measure $K_2 = s_2$, and in position 3, we get $K_3 = s_3$. But, $K_4 = \frac{1}{2}(s_1 + s_2) + s_4$, $K_5 = \frac{1}{2}(s_2 + s_3) + s_5$, and $K_6 = \frac{1}{2}(s_1 + s_3) + s_6$. From this we see that the elements of **s** are related to the matrix of measurements **K** in subscript notation by:

$$K_i = A_{ij}s_j, \tag{13.4}$$

where **A** depends on the experimental design and is called the *design matrix*. The measurement scheme shown in Figure 13.1, has the design matrix:

$$\mathbf{A} = \begin{pmatrix} 1 & 0 & 0 & 0 & 0 & 0 \\ 0 & 1 & 0 & 0 & 0 & 0 \\ 0 & 0 & 1 & 0 & 0 & 0 \\ .5 & .5 & 0 & 1 & 0 & 0 \\ 0 & .5 & .5 & 0 & 1 & 0 \\ .5 & 0 & .5 & 0 & 0 & 1 \end{pmatrix}. \tag{13.5}$$

Although there are six measurements and six unknowns, the elements of **s** are overdetermined, because the diagonal measurements depend on three parameters. In order to calculate the best-fit values $\bar{\mathbf{s}}$ for **s**, we can use linear algebra:

$$\bar{\mathbf{s}} = (\mathbf{A}^T\mathbf{A})^{-1}\mathbf{A}^T\mathbf{K} \quad \text{or} \quad \bar{\mathbf{s}} = \mathbf{B}\mathbf{K}, \tag{13.6}$$

where $\mathbf{A}^T$ is the transpose of **A**. The elements of **B** for the scheme shown in Figure 13.1 are readily determined as:

$$\mathbf{B} = \begin{pmatrix} 1 & 0 & 0 & 0 & 0 & 0 \\ 0 & 1 & 0 & 0 & 0 & 0 \\ 0 & 0 & 1 & 0 & 0 & 0 \\ -.5 & -.5 & 0 & 1 & 0 & 0 \\ 0 & -.5 & -.5 & 0 & 1 & 0 \\ -.5 & 0 & -.5 & 0 & 0 & 1 \end{pmatrix}. \tag{13.7}$$

In the special case in which **A** is a square matrix (as in Equation 13.5), $(\mathbf{A}^T\mathbf{A})^{-1}\mathbf{A}^T$ reduces to $\mathbf{A}^{-1}$ (i.e. $\mathbf{B} = \mathbf{A}^{-1}$).

There exists one coordinate system **V** (whose axes are the eigenvectors of χ: $\mathbf{V}_1$, $\mathbf{V}_2$, $\mathbf{V}_3$) in which the off-axis terms of χ are zero (see Appendix C of Lecture 9). In this special coordinate system:

$$\begin{aligned} M_1 &= s_1 H_1 = \chi_{11} H_1 \propto \tau_1 H_1 \\ M_2 &= s_2 H_2 = \chi_{22} H_1 \propto \tau_2 H_2 \\ M_3 &= s_3 H_3 = \chi_{33} H_3 \propto \tau_3 H_3. \end{aligned} \tag{13.8}$$

The eigenvalues τ_1, τ_2 and τ_3 correspond to the maximum, intermediate, and minimum susceptibility, respectively. These are the susceptibilities along the principal, major and minor eigenvectors $\mathbf{V}_1$, $\mathbf{V}_2$, and $\mathbf{V}_3$, respectively. Scaling χ by its trace yields values for τ that sum to unity. [Note that $\mathbf{V}_1, \mathbf{V}_2$ and $\mathbf{V}_3$ are sometimes referred to as K_{max}, K_{int}, and K_{min}, respectively in the literature.]

When the coordinate system of the susceptibility data is defined by the eigenvectors, then the components of magnetization M_i satisfy the following:

$$\frac{M_1^2}{\tau_1^2} + \frac{M_2^2}{\tau_2^2} + \frac{M_3^2}{\tau_3^2} = 1. \tag{13.9}$$

The surface described by Equation 13.9 illustrated in Figure 13.2b traces an ellipsoid termed the *magnitude ellipsoid* by Nye (1957) whose semi-axes are directed along **V** and have lengths that are proportional to the τ_i. We will refer to this ellipsoid in the following as the anisotropy of magnetic susceptibilty (AMS) ellipsoid. Because it is possible to have negative eigenvalues making the magnitude ellipsoid difficult to visualize, some workers prefer the representation quadric, which

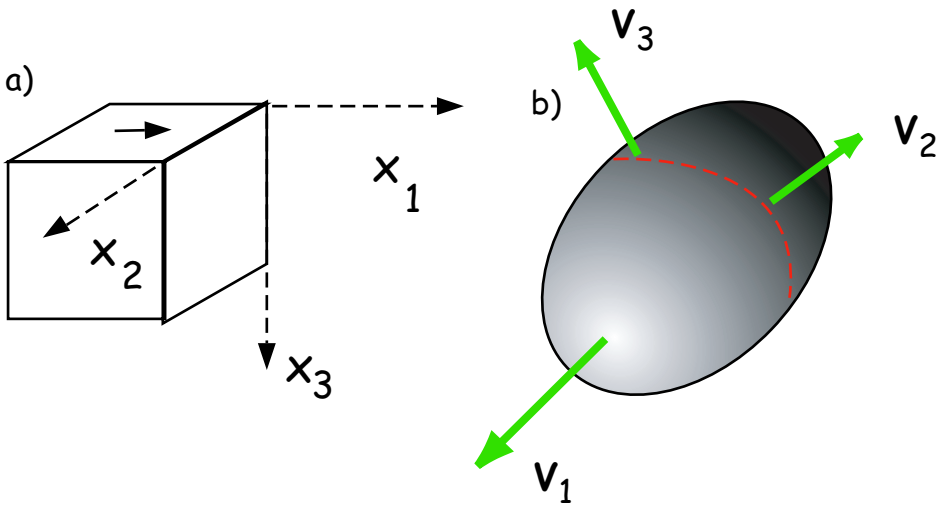

Figure 13.2: a) Arbitrary coordinate system of a specimen. b) The magnitude ellipsoid of of the AMS. Its coordinate system is defined by the eigenvectors $\mathbf{V}_1$ and $\mathbf{V}_2$. The lengths along the eigenvectors of the ellipsoid surface are related to the eigenvalues (see text).

has a less direct relationship to the eigenvalues. In the case of negative eigenvalues (say for a carbonate dominated system), it is also possible to simply offset the eigenvalues by some DC offset to ensure positivity.

Many publications list AMS data in terms of the eigenvalues and eigenvectors, collectively referred to as eigenparameters so it is handy to have a way to transform eigenparameters back into matrix elements. This can be done using tricks from linear algebra:

$$\chi = \mathbf{V}\tau\mathbf{V}^T, \tag{13.10}$$

where $\mathbf{V}^T$ is the transpose of $\mathbf{V}$. [Note that several (maybe even three) decimal places are required to do this inversion in a satisfactory fashion, yet almost no one reports to this degree of precision and the tensor elements you get back out may be very different than those that went in if there is insufficient precision.]

The eigenparameters of the susceptibility tensor are related to the statistical alignment of dia-, para-, and/or ferromagnetic phases within the rock and the AMS ellipsoid can be used to describe the magnetic fabric of the rock. Much of the interpretation of AMS data in the literature revolves around an assessment of directions of principal axes and relative magnitudes of the eigenvalues.

There is a bewildering variety of conventions for describing the relationships among the three eigenvalues (see, Table 13.1 for a partial list). A practical initial classification scheme can be made with the following rules: when ($\tau_1 \simeq \tau_2 \simeq \tau_3$), the shape is a sphere; when ($\tau_1 \simeq \tau_2 > \tau_3$), it is oblate. The shape is prolate when ($\tau_1 > \tau_2 \simeq \tau_3$), and, finally, the anisotropy ellipsoid is triaxial when ($\tau_1 > \tau_2 > \tau_3$). Because there are nearly always three distinct values of τ, it is a statistical problem to decide whether the eigenvalues from a given data set are significantly different from one another.

Making only six measurements allows calculation of the eigenparameters, but gives no constraints for their uncertainties. We would like to ask questions such as the following:

1) Is a particular axis parallel to some direction? Is $\mathbf{V}_3$ vertical as might be expected for a primary sedimentary fabric? Is $\mathbf{V}_1$ parallel to some lineation such as elongated vesicles in volcanic dikes, or deformed ooids in strained rocks?

2) Are two sets of eigenvectors distinct? Are data from two sides of a dike margin imbricated, allowing interpretation of flow direction? Has progressive strain rotated the rock fabrics?

3) What is the shape of the AMS ellipsoid? Are the eigenvalues distinct? Is the fabric oblate, as for consolidated, undeformed sedimentary rocks? Does the shape change as a result of progressive deformation in metamorphic rocks?

In order to address questions such as these, we need some sort of confidence intervals for the eigenparameters; hence we need to make multiple measurements and we need a means of translating the measurements into uncertainties in AMS data. The principles of error analysis for anisotropy measurements were originally laid out by Hext (1963), and were later fleshed out by Jelinek (1976, 1978). These are analytical approaches. Constable and Tauxe (1990) took an entirely different approach using a bootstrap. We will begin with the Hext (1963) method which serves as the foundation for all modern AMS statistical analysis.

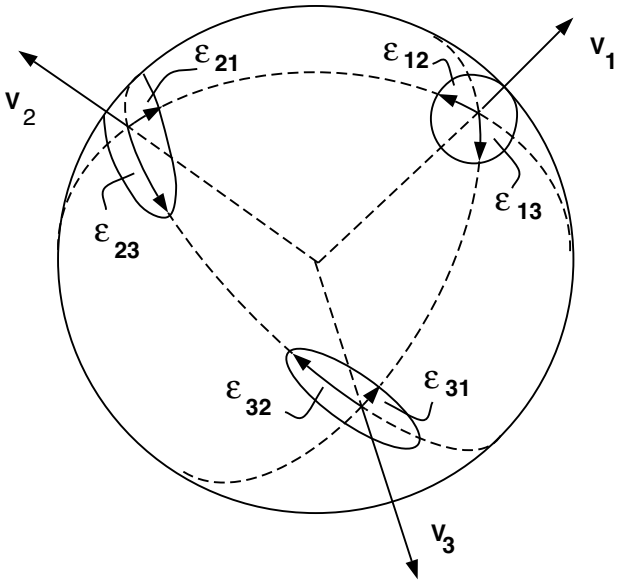

Figure 13.3: Relationship of the uncertainty ellipses (calculated by Hext statistics for AMS data) to the principal axes. The major and minor semi-axes of the uncertainty ellipses are oriented along the axes defined by the eigenvectors.

13.4 Hext Statistics

According to Hext (1963), each measurement K_i has an unknown measurement "error":

$$K_i = A_{ij} s_j + \delta_i. \tag{13.11}$$

The residual sum of squares S_o is:

$$S_o = \sum_i \delta_i^2, \tag{13.12}$$

and the estimated variance is:

$$\sigma^2 = S_o/n_f. \tag{13.13}$$

n_f is the number of degrees of freedom, given by $N_{meas} - 6$ where N_{meas} is the number of measurements and six is the number of measurements required to determine the susceptibility tensor.

There are many measurement schemes in common usage with as few as six (for which of course σ^2 is undefined) and as many as several hundred. The scheme of Jelinek (1976), has the number of measurements $N_{meas} = 15$, and is described in detail in the Appendix as it is currently perhaps the most widely used.

Each measurement system has an associated design matrix from which the **B** matrix can be determined. That for the 15 measurement scheme can be found in the Appendix. Once the **B** matrix is set up, we can calculate the best-fit values for **s**:

$$\bar{s}_i = B_{ij} K_j. \tag{13.14}$$

The best-fit values for **K** ($\bar{\mathbf{K}}$) can then be calculated by substituting the right **A** matrix (see e.g., Appendix):

$$\bar{K}_i = A_{ij} \bar{s}_j.$$

Now we can calculate the δ_i by:

$$\delta_i = K_i - \bar{K}_i, \tag{13.15}$$

and S_o is given by Equation 13.12.

Assuming that the uncertainties in **K** (the δ_i) have zero mean, and that they are uncorrelated, normally distributed, and small (so that the products of uncertainties can be neglected), Hext (1963) proposed that approximate 95% confidence ellipses for the eigenvectors (see Figure 13.3) can be calculated as described in the Appendix.

We turn now to the problem of calculating confidence intervals for the eigenvalues. In practice, there will almost always be three distinct values of τ returned from an eigenvalue calculation. But, when are these values statistically distinct? First, one might ask if the ellipsoid is significantly different from a sphere. Hext statistics allows calculation of F statistics and comparison with values in F tables (Appendix to Lecture 11); in this way one can test if the data are isotropic (F) ($\tau_1 = \tau_2 = \tau_3$), if $\tau_1 = \tau_2$ (F_{12}), or if $\tau_2 = \tau_3$ (F_{23}). Calculation of the F statistics is given in the Appendix. F values below the critical values do not allow rejection of the hypothesis of isotropy or rotational symmetry, respectively.

13.5 Anisotropy of magnetic remanence

Magnetic susceptibility is in many ways like color in that many things contribute and often it is as difficult to interpret. Magnetic remanence is a much more targeted parameter because only ferromagnetic particles contribute to it and certain remanences are sensitive to only particular minerals or grain sizes. Hence anisotropy of magnetic remanence can be a more subtle instrument than AMS. Furthermore, certain applications such as paleointensity, paleodirectional determinations or correction of inclination error may require the anisotropy of the TRM or DRM to be taken into

account. For example, paleointensity on pot sherds or other anisotropic specimens must be corrected for specimen's anisotropy (e.g., Aitken et al. 1981) and the inclination "error" of DRM (see Lecture 5) can be corrected using information from ARM anisotropy (e.g., Jackson et al. 1991).

ARM is often considered analogous to TRM. Its acquisition is mathematically identical, relying instead on variations in applied field as opposed to temperature as a blocking mechanism (see Lecture 5). It is far more convenient to give a sample an ARM than a TRM in the laboratory, so ARM and ARM anisotropy are frequently substituted for the analogous TRM. Of course, the two are NOT identical and proper care should be taken to ensure that the appropriate remanence is used for the particular purpose. Nonetheless, anisotropy of ARM (AARM) is a useful measurement and we describe first how AARM is determined in the SIO laboratory. There are slight experimental differences between AARM and ATRM which will be noted.

13.5.1 Anisotropy of ARM and TRM

Prior to acquisition of the laboratory remanence, the specimen should be in a fully demagnetized state which is measured as a baseline. Then one applies an ARM in at least three directions (say positions 1, 2 and 3 in Figure 13.1d). Generally, from six to 15 orientations for the ARM are used to get a reasonable estimate of the uncertainties. Between each position, the specimen should be demagnetized along the axis of the subsequent ARM. This measurement is substracted from the subsequent ARM by vector subtraction. Each ARM step (after subtraction of the baseline) gives three orthogonal remanence components (K_{ij}^R). Please note that it is possible to give ARMs in the presence of different AF fields from very high (presumably a total ARM) to lower (giving a partial ARM of pARM). The DC field is also variable, but should be in the region where the (p)ARM is linearly related to the DC field.

The main difference between AARM and ATRM in procedure is that the demagnetization step is not required in TRM. Instead, the sample is simply placed in each direction without the intervening baseline step.

The equation for anisotropy of magnetic remanence that is analogous to Equation 13.1 is $M_i = \chi_{ij}^R H_j$ where χ^R are the coefficients for the remanent anisotropy. These can be reduced to the elements of $\mathbf{s}$ by multiplying by the appropriate $\mathbf{B}$ matrix, depending on the number and orientation of positions used in the experiment. Because each measurement yields information along three axes, the design matrix has three times as many elements as for the AMS experiment with the same number of measurements. For example, for a six position experiment, the design matrix is 18 x 6 instead of 6x6. After determining $\mathbf{s}$, the other Hext parameters can be determined as before, using $n_f = 3N_{meas} - 6$.

13.5.2 Anisotropy of DRM

We learned in Lecture 5 that the inclination of DRM is often too shallow and that it follows the tangent function:

$$\tan I_o = f \tan I_f, \tag{13.16}$$

where I_o and I_f are the observed DRM inclination and the applied field inclination respectively (King, 1955). The parameter f is the "flattening factor".

Jackson et al. (1991) restate the relationship of the DRM (M_d) to the applied field $\mathbf{H}$ as:

$$M_d = \mathbf{k_d H}$$

where $\mathbf{k_d}$ is the DRM tensor. The eigenvalues of the $\mathbf{k_d}$ matrix are here referred to as κ_{d_i} where κ_{d_1} is here taken as the largest for consistency with the rest of these Lecture Notes. Jackson et al. (1991) demonstrated that the flattening factor f is equivalent to the ratio $\kappa_{d_3}/\kappa_{d_1}$. Therefore the trick to correcting flattened inclinations is to estimate $\mathbf{k_d}$.

There could be several ways of estimating the DRM tensor in the lab: directly, by redeposition or indirectly, by measuring the anisotropy of a proxy remanence (say ARM). Redeposition is in practice quite problematic because it is rarely possible to recreate the original depositional conditions of grain size, water chemistry, particle flux, turbulence and so on that might play a role in determining the anisotropy tensor. The proxy approach is straightforward in the lab, but difficult to tie directly to the DRM anisotropy. What is required is a laboratory remanence that closely targets the same spectrum of coercivities as that carrying the DRM. By AF demagnetizing the NRM and an ARM or a pARM it can be shown that the (p)ARM often satisfies this requirement (see e.g., Levi and Banerjee 1976). From this, Jackson et al. (1991) argue that the ARM tensor is the best proxy remanence for the DRM.

The relationship between the ARM and DRM anisotropy tensors is not straightforward. Jackson et al. (1991) consider the complexity of the processes that align and misalign particle long-axes, including the external magnetic field, gravitational, compactional, electrostatic, surface tension and Van der Waal's forces. The result of all of these is only a slight net alignment (as discussed in Lecture 5). Under certain circumstances including post-depositional compaction and syn-depositional effect of elongate particles landing on the sediment/water interface, there can be preferential alignment in the horizontal plane leading to inclination shallowing.

In order to tie the AARM tensor to the DRM anisotropy tensor, we need to determine the orientations of the particle long axes as well as the effects of individual particle anisotropies. This latter results from the fact that individual particles are not ordinarily at saturation being generally (except for very small grains or grains of low magnetization materials) non-uniformly magnetized themselves (e.g., vortex remanence state). The rationale is that because AARM reflects the variations in the capacity for carrying remanence in the detrital particles, that AARM can be used to determine the anisotropy of DRM, if the ARM anisotropy of the detrital particles themselves can be determined. The details of how this are done in practice is summarized in the Appendix.

13.6 When are data suitable for Hext statistics?

The assumptions for using the techniques outlined in the foregoing are that the uncertainties in the measurements have zero mean, are normally distributed, and are small. While measurement error using modern equipment is likely to be quite small, data from a collection of samples often do not conform to these restrictive assumptions. In particular, the δ values are often large.

Constable and Tauxe (1990) showed that, in general, δs from AMS data calculated for multiple samples (that must be normalized by their trace) will not generally be normally distributed. Hence, data incorporating multiple samples are often not amenable to Hext statistics. A bootstrap for paleomagnetic tensors is described in the next section. In the rest of the lecture, we will continue our discussion of anistropy and paleomagnetic tensors with a brief discussion of remanence anisotropy.

13.7 Bootstrap confidence ellipses

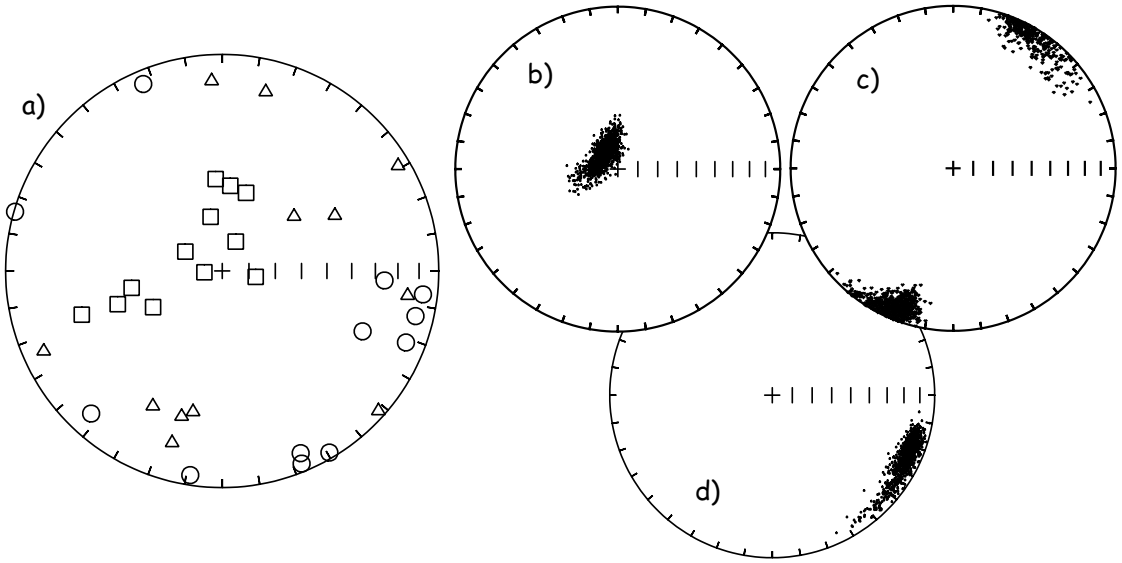

Figure 13.4: a) Lower hemisphere projection of directions of $\mathbf{V}_1$ (squares), $\mathbf{V}_2$ (triangles), and $\mathbf{V}_3$ (circles) from the margin of a volcanic dike in the Troodos Ophiolite. b) Equal area projection of principal eigenvectors ($\mathbf{V}_1$) of 500 para-data sets drawn from the data in a). c) Same as b) for the major eigenvectors ($\mathbf{V}_2$). d) Same as b) for the minor eigenvectors ($\mathbf{V}_3$).

The eigenvector data in Figure 13.4a were obtained by analyzing numerous individually oriented samples from one of the quenched margins of a dike in the Troodos Ophiolite on Cyprus. We plot the eigenvectors on an equal area net using the lower hemisphere projection and follow the convention that the $\mathbf{V}_1$s are squares, $\mathbf{V}_2$s are triangles, and $\mathbf{V}_3$s are circles. The data are rather typical for those obtained from a single homogeneous body of rock in that the δ distributions that are neither normally distributed, nor small.

Constable and Tauxe (1990) developed a bootstrap for anisotropy data which is similar to that introduced in Lecture 12 for vectors. As in Lecture 12, we first take a number of randomly selected para-data sets of the data from those shown in Figure 13.4a. The eigenparameters of the bootstrapped average $\bar{s}$ matrices are then calculated. Such bootstrapped eigenvectors are shown in the equal area projections in Figure 13.4(b-d).

A non-parametric confidence region for the bootstrapped distributions shown in Figure 13.4b-d could be drawn as a contour line enclosing 95% of the bootstrapped eigenvectors. Because it is often useful to characterize the average uncertainties with a few parameters (for example, to put them in a data table), we can proceed as with the unit vectors and assume some sort of distribution for the eigenvectors, for example, the Kent distribution from Lecture 12). However, for most of the questions outlined at the beginning of the lecture, it is preferrable to assess directly the 95% confidence bounds on the parameter of interest.

By analogy with the bootstrap for unit vectors and the fold test, we can also perform parametric bootstraps. There are two flavors of these. The first flavor, the *sample parametric bootstrap*, proceeds as follows: After randomly selecting a particular sample for inclusion, each element of $\mathbf{s}$ is replaced by a simulated element drawn from a normal distribution having the σ as calculated for

the sample data. This Monte Carlo type simulation assumes that the measurement uncertainties are normally distributed, which is likely to be the case. If instrument noise is significant, then the sample parametric bootstrap is an important tool.

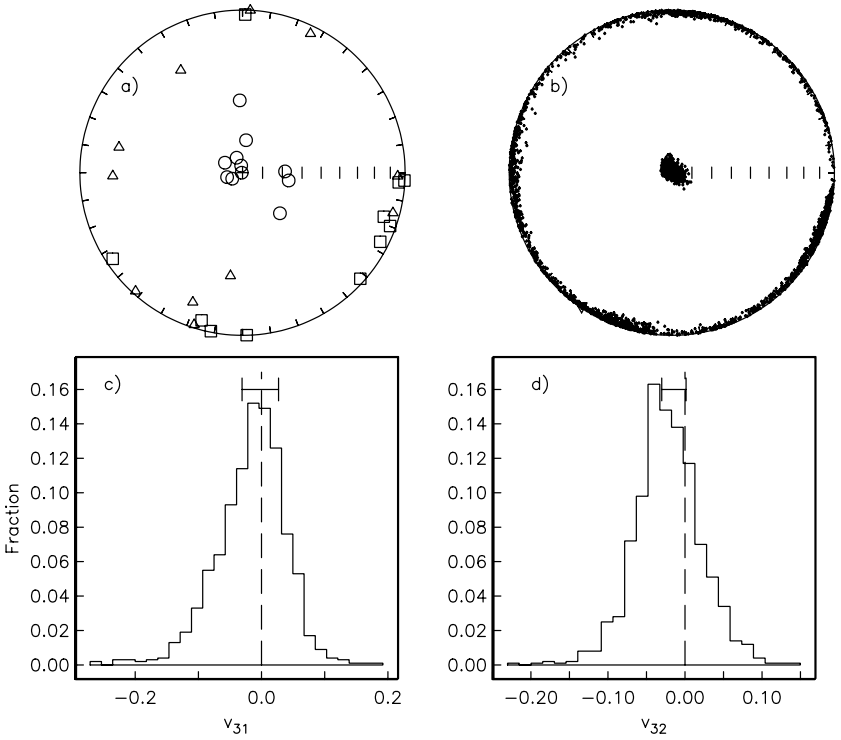

Figure 13.5: a) AMS data from Cretaceous carbonate limestones in Italy (the Scaglia Bianca Formation) in tilt adjusted coordinates. a) Lower hemisphere projections of the principal $\mathbf{V}_1$ (squares), major $\mathbf{V}_2$ (triangles), and minor $\mathbf{V}_3$ (circles) eigenvectors. b) Bootstrapped eigenvectors from para-data sets of the data in a). c) Histogram of the v_{31} components of $\mathbf{V}_3$ from b) with bounds containing 95% of the components. The zero value expected from a vertical direction is shown as a dashed line. d) same as c) but for the v_{32} component. Since both v_{31} and v_{32} are indistinguishable from zero, $\mathbf{V}_3$ is vertical at the 95% level of confidence.

Because the δ_i data from homogeneous rock bodies are often normally distributed, we can also perform a parametric bootstrap at the level of the site (the *site parametric bootstrap*). This is done by drawing para-data sets as before, but replacing individual elements of $\mathbf{s}$ with simulated data drawn from normal distributions with Σ calculated from the data for an entire site. This procedure goes a long way toward calculating realistic confidence intervals from sites with too few samples.

Speaking of "too few samples", we emphasize that bootstrapped confidence ellipses are only asymptotically correct, relying on the assumption that the full statistical variability is represented in the data set. It is inadvisable to rely on bootstrapped uncertainties with fewer than about 20 specimens as they will be too small. If it is possible to perform a parametric bootstrap (i.e., the δs are normally distributed), then perhaps as few as six samples can be done. Borradaile (2003) states incorrectly that the bootstrap is preferable for small sample sizes, this being only true if a parametric bootstrap can be performed.

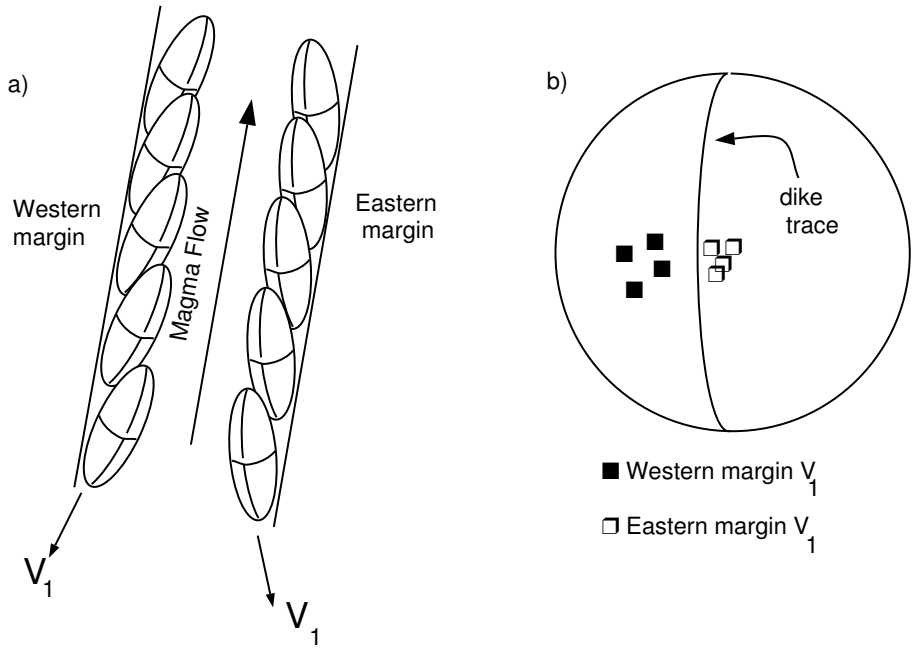

Figure 13.6: Principles of AMS for interpretation of flow directions in dikes (see Knight and Walker, 1988.)

13.8 Comparing mean eigenvectors with other axes

We can now consider whether a particular axis is distinct from a given direction or another eigenvector. For example, we may wish to know if a given data set from a series of sediments has a vertical minor eigenvector as would be expected for a primary sedimentary fabric. In Figure 13.5a we show AMS data from samples taken from the Scaglia Bianca Formation (Cretaceous white limestones) in the Umbrian Alps of Italy. They have been rotated into tilt adjusted coordinates; hence the bedding pole is vertical. Instead of plotting the 95% confidence ellipses, which all require unnecessary parametric assumptions, we show the bootstrap eigenvectors in Figure 13.5b. The smear of points certainly covers the vertical direction, consistent with a vertical direction for $\mathbf{V}_3$. To make the test at a given level of confidence (say 95%), we can employ the method developed for unit vectors in which the eigenvector of choice (here $\mathbf{V}_3$) is converted to cartesian coordinates and sorted. Then the bootstrapped 95% confidence bounds can be directly compared with the expected value. For a direction to be vertical, both the x_1 and x_2 components must be indistinguishable from zero. We plot v_{31} and v_{32} as histograms, with the 95% confidence bounds shown above in Figure 13.5. The expected value of zero is shown by dashed lines. Because zero is included within the confidence intervals, these data have a direction of $\mathbf{V}_3$ that cannot be distinguished from vertical at the 95% level of confidence.

Another question that often arises is whether eigenvectors from two sets of AMS data can be distinguished from one another. For example, are the $\mathbf{V}_1$ directions from data sets collected from two margins of a dike different from one another and on opposite sides of the dike plane as expected from anisotropy controlled by crystal imbrication.

The principles by which flow directions can be determined in volcanic dikes were laid out by

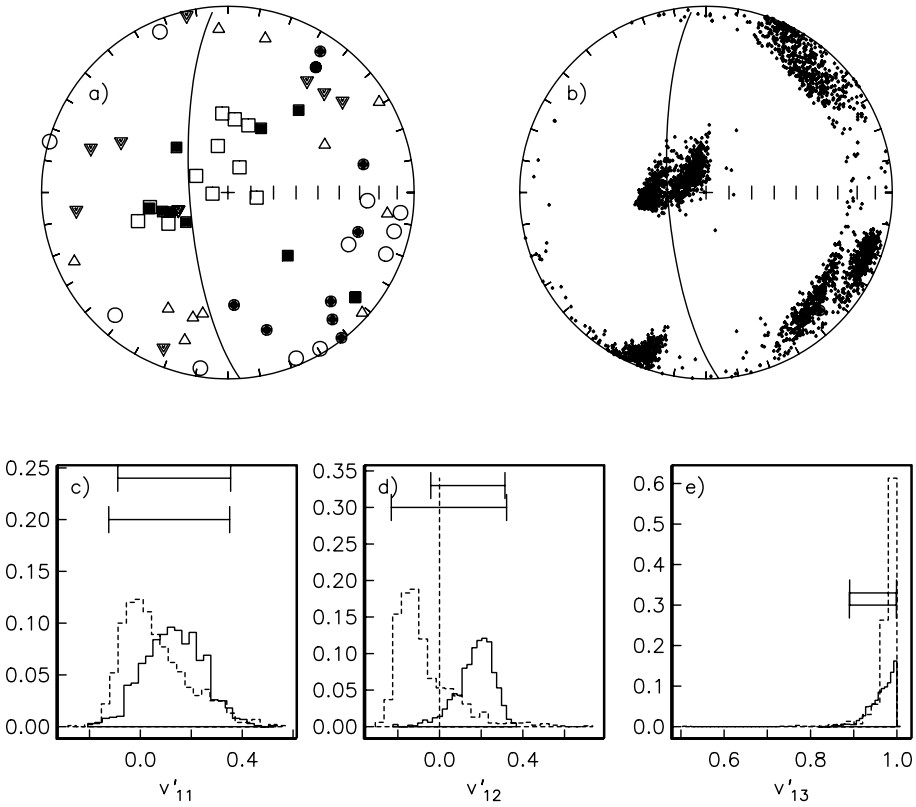

Figure 13.7: AMS data obtained from samples from the margins of a nearly vertical dike in the Troodos Ophiolite. a) Equal area projection of principal (squares), major (triangles), and minor (circles) eigenvectors. Data from the Eastern (Western) margins are shown as open (solid) symbols. The dike trace is shown as a great circle. b) Bootstrapped eigenvectors from the data shown in a). c) Histogram of cartesian coordinates v'_{11} of the bootstrapped principal eigenvectors. These have been rotated into "dike coordinates" (see text). d) Same as c) but for v'_{12}. The dike plane (dashed line) is centered with respect to the $\mathbf{X}_2$ direction. The v_{12} componenent from neither margin is distinct from the dike plane or from each other, based on the 95% confidence bounds drawn above the histograms. e) Same as c) but for v'_{13}.

Knight and Walker (1988). While the magma is flowing in the dike, elongate particles become imbricated against the chilled margins (see Figure 13.6). Opaque phases such as magnetite are often observed to be distributed along the fabric of the silicate phases (see Hargraves, 1991). The principal eigenvectors arising from such a *distribution anisotropy* parallel the fabric of the silicates. In Figure 13.6b, we show that in the ideal case, the $\mathbf{V}_1$ directions from the two margins are distinct and fall on either side of the dike trace. Because the convention is to plot AMS data in lower hemisphere projections, the fact that the western margin data plot on the western side, and the eastern margin data plot on the eastern side suggests that the flow was upward. Thus, the AMS data from chilled margins of dikes can give not only a lineation, but a well constrained direction of magma flow.

In Figure 13.7a, we show the eigenvectors of AMS data from samples obtained from both quenched margins of a nearly vertical north-south trending dike in the Troodos Ophiolite in Cyprus.

The bootstrapped eigenvectors are shown in Figure 13.7b. In order to address the problem of whether the $\mathbf{V}_1$s are distinct from the dike plane, we first rotate them into *dike coordinates* (whereby the dike pole is parallel to X_2 and direction of dip is parallel to X_3). Then the question of whether the $\mathbf{V}_1$ direction is distinct reduces to whether the v_{12} components can be distinguished from zero (the dike plane). In Figure 13.7c, we show the histogram of the cartesian components of $\mathbf{V}_1$ and the 95% confidence intervals of the two data sets. As we can see from the overlapping confidence bounds, the data are neither distinct from the dike margin, nor from each other.

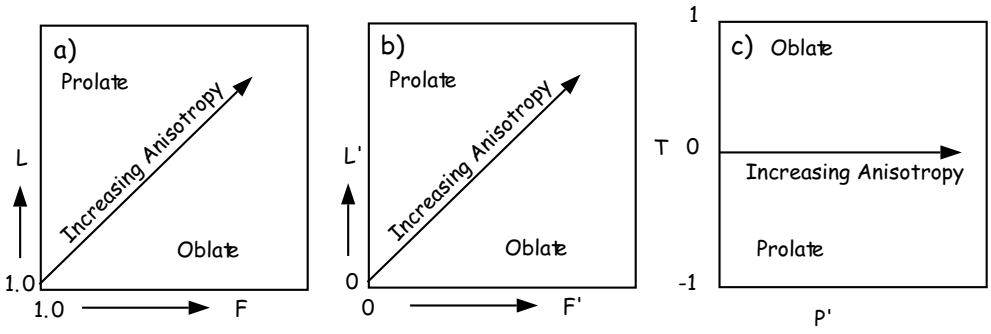

Figure 13.8: Properties of various AMS diagrams: a) Flinn, b) Ramsay and c) Jelinek.

13.9 Shape

There are innumerable ways of plotting and characterizing shapes of AMS ellipsoids in the literature. We will focus here on a few and discuss how bootstrapping could be helpful in providing a means for discriminating differences in data sets and so on. We list some popular so-called "shape parameters" in Table 14.1.

Many researchers use the "total anisotropy" parameter of Owens (1974). This has the uncomfortable property of ranging up to 300%; hence, we prefer the parameter called here the % anisotropy of Tauxe et al. (1990) as this ranges from 0 - 100%. The so-called "corrected anisotropy" of Jelinek (1981) has several definitions in the literature (compare for example Borradaile (1988) with Jelinek (1981); we have used the original definition of Jelinek (1981).

With the plethora of parameters comes a host of plotting conventions. We will consider five types of plots here: histogram of bootstrapped eigenvalues, the Flinn diagram (F versus L) after Flinn (1962], the Ramsay diagram (F' versus L') after Ramsay (1967), the Jelinek diagram (P' versus T) after Jelinek (1981), and the ternary projection (see Woodcock, 1977 and Tauxe et al., 1990). The Flinn, Ramsay, and Jelinek diagrams are shown in Figure 13.8 and the ternary projection is shown in Figure 13.10.

The Flinn and Ramsay diagrams are very similar, but the Ramsay plot has the advantage of having a zero minimum as opposed to starting at 1.0 as in the Flinn diagram. Both are essentially polar plots, with radial trajectories indicating increasing anisotropy. Shape is reflected in the angle, with "oblate" shapes above the line and "prolate" shapes below.

It is important to remember that, in fact, only points along the plot axes themselves are truly oblate or prolate and that all the area of the plot is in the "triaxial" region. Because of statistical uncertainties, samples that plot in this region may fail the F_{12} or F_{23} tests of Hext and be classifiable

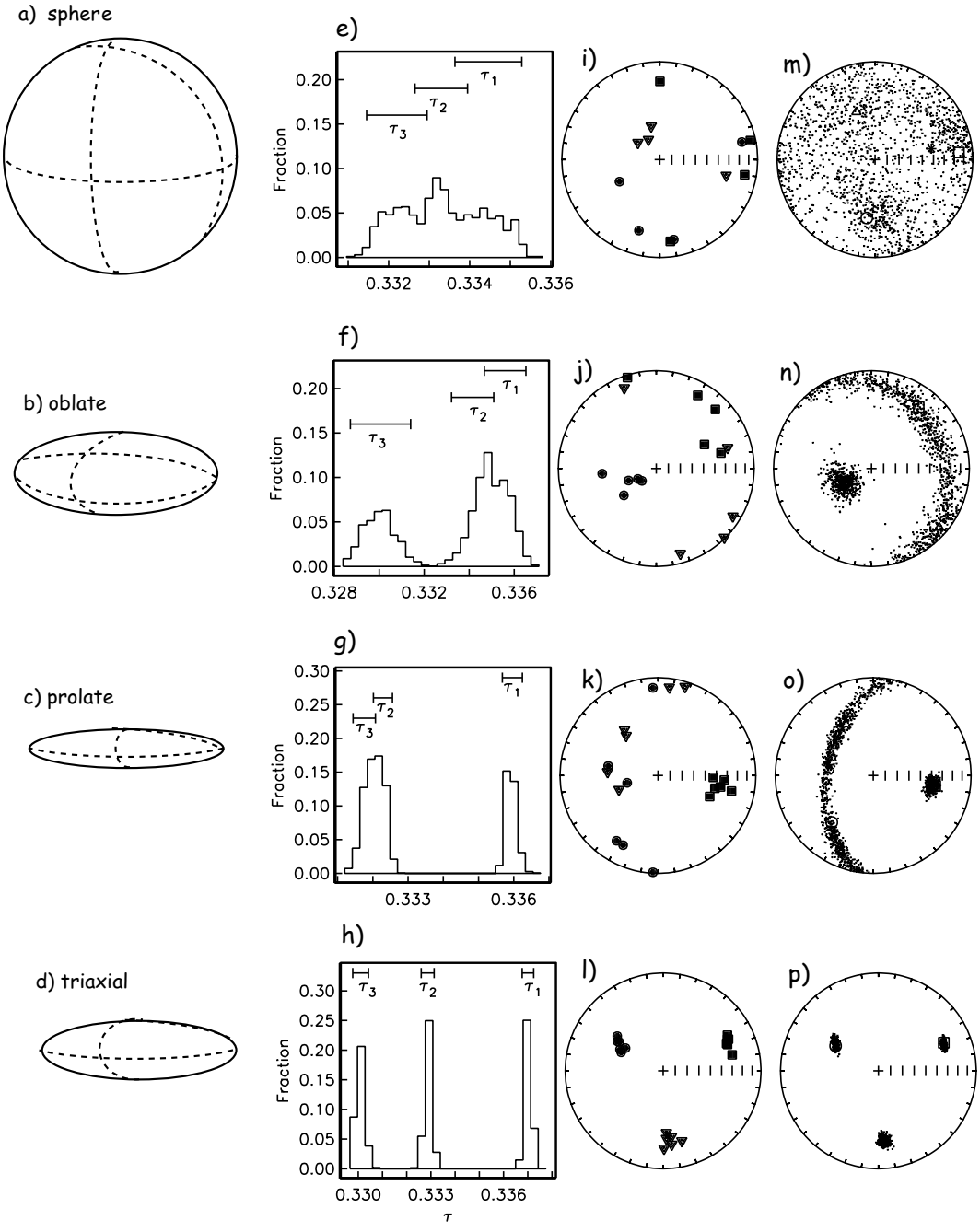

Figure 13.9: Determination shape of AMS ellipsoids using the bootstrap. a)-d) Magnitude ellipsoids. e)-h) Histograms of the bootstrapped eigenvalues associated with the eigenvectors plotted in i)-l) (same conventions as in Figure 5). The bounds containing 95% of each eigenvalue are shown above the histograms. m)-p) Bootstrapped eigenvectors.

as "oblate" or "prolate". In general, however, only a narrow zone near the axes can be considered oblate or prolate, so these terms are often used loosely.

The Jelinek diagram is more cartesian in nature than the Flinn or Ramsay plots. "Corrected" anisotropy increases along the horizontal axis and shape reflected in the vertical axis. There is no real advantage to using the highly derived P' and T parameters over the Ramsay or Flinn plots. Nonetheless they are quite popular (Tarling and Hrouda, 1993).

In the ternary projection, there are actually three axes (see Figure 13.10a). The projection can be plotted as a normal X-Y plot by using the E' and R parameters listed in Table 1 (see Figure 13.10b).

In none of the various types of plots just discussed are the horizontal and vertical axes independent of one another, but all the diagrams reflect the essence of the ellipsoid shape. Unlike the histogram with bootstrap confidence intervals, it is not possible to determine whether the various eigenvalues or ratios thereof can be distinguished from one another in a statistical sense.

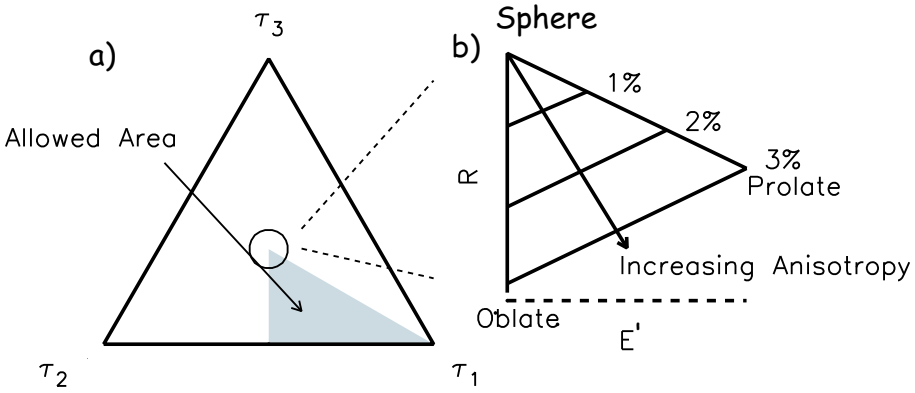

Figure 13.10: Properties of the Ternary diagram: a) there are three axes with limits of τ_1, τ_2, τ_3. Because of the constraint that $\tau_1 > \tau_2 > \tau_3$, only the shaded region is allowed. This is bounded at the top by a sphere when all three eigenvalues are equal, to the bottom left by a disk and to the bottom right by a needle. Geological materials generally have a low degree of anisotropy and plot close to the sphere. This region is enlarged in b) which illustrates how the ternary projection can be plotted as E' versus R and how shape (oblate, prolate, sphere) and percent anisotropy appear on the diagram.

All discussions of the "shape" of the AMS ellipsoid revolve around the relationships between the various eigenvalues. The first question to consider is whether these can be distinguished in a statistical sense. The Hext version of linear perturbation analysis has the ability to check for significance of the anisotropy (using the F parameters). However, the approximations involved in the Hext method make it inappropriate for most data sets involving more than one sample. Bootstrapping allows for testing the significance of the differences in eigenvalues and the less restrictive assumptions allow bootstrap tests to be applied more widely.

The simplest means of determining whether two sets of eigenvalues are distinct from one another requires the assumption that the bootstrapped eigenvalues are normally distributed. Here we calculate the standard deviations of the populations of eigenvalues. While the eigenvalues may often satisfy the requirement of normal distribution, they equally often may not. Hence, we desire a less restrictive way of deciding whether eigenvalues are distinct.

13.9. SHAPE

One alternative way of checking whether eigenvalues can be discriminated is quite similar to the bootstrap test for common mean described in Lecture 12. In Figure 13.9a-d, we sketch the four shape categories defined in the beginning of the chapter. The eigenvectors calculated for samples from four sites are shown in Figure 13.9i-l. Bootstrapped eigenvectors are shown in Figure 13.9m-p. Histograms of the associated bootstrapped eigenvalues are shown in Figure 13.9e-h. There are three "humps" in all of the histograms, but the 95% confidence bounds provide a means for quantifying the shape tests defined earlier.

In Figure 13.9a, we illustrate the behavior of data from an AMS ellipsoid that is essentially spherical in shape. The three eigenvalues plotted in the histogram (Figure 13.9e) have overlapping confidence intervals, hence they are indistinguishable. The corresponding bootstrapped eigenvectors shown in Figure 13.9m plot in a cloud with no preferred orientations.

In Figure 13.9b we show data characteristic of an oblate ellipsoid. The smallest eigenvalue is distinct from the other two in Figure 13.9f, but the 95% confidence bounds of τ_2 overlap those of τ_1. The $\mathbf{V}_3$ eigenvector is consequently reasonably well defined, but the distribution of bootstrapped $\mathbf{V}_2$ and $\mathbf{V}_1$ form a girdle distribution (Figure 13.9n).

The data from a prolate ellipsoid (see Figure 13.9c) have a distinct τ_1 distribution (Figure 13.9g), while τ_2 and τ_3 are clumped together. The $\mathbf{V}_1$ directions are nicely defined, but the $\mathbf{V}_2$ and $\mathbf{V}_3$ directions are smeared in a girdle (Figure 13.9o)).

Finally, the triaxial case is shown in Figure 13.9d. All three eigenvalues are distinct (Figure 13.9h) and the corresponding eigenvectors well grouped (Figure 13.9p).

There is no "right" way to plot eigenvalue data. Each application requires careful thought as to what is actually being tested. What do you want to know? The histogram method illustrated in Figure 13.9 is most appropriate for classifying shape characteristics of a relatively homogeneous set of samples. However, it may not be ideal for examining trends in behavior among samples or data sets. For example, one may wish to show the progressive change in shape and degree of anisotropy as a function of metamorphism. In such a case, one of the other plots (Flinn, Ramsay, Jelinek, or ternary) may serve better. Or one may wish to examine temporal trends in shape, for example the progressive change in sedimentary fabric with depth. In this case, plots of eigenvalues versus stratigraphic position may be the most useful way of looking at the data.

Table 13.1: Assorted anisotropy parameters.

Parameter (Reference)	Equation
Bulk Susceptibility (see text)	$\chi_b = (s_1 + s_2 + s_3)/3$
Normalized eigenvalues (see text)	$\tau_1 + \tau_2 + \tau_3 = 1$
Log eigenvalues (Jelinek, 1981)	$\eta_1 = \ln \tau_1; \eta_2 = \ln \tau_2; \eta_3 = \ln \tau_3$
Log mean susceptibility (Jelinek, 1981)	$\bar{\eta} = (\eta_1 + \eta_2 + \eta_3)/3$
Magnitude of Anisotropy:	
% Anisotropy (Tauxe et al. , 1990)	$\%h = 100(\tau_1 - \tau_3)$
"Total" Anisotropy (Owens, 1974)	$A = (s_1 - s_3)/\chi_b$
Anisotropy Degree (Nagata, 1961)	$P = \tau_1/\tau_3$
"Corrected" Anisotropy (Jelinek, 1981)	$P' = \exp\sqrt{2[(\eta_1 - \bar{\eta})^2 + (\eta_2 - \bar{\eta})^2 + (\eta_3 - \bar{\eta})^2]}$
Shape:	
Shape Factor (Jelinek, 1981])	$T = (2\eta_2 - \eta_1 - \eta_3)/(\eta_1 - \eta_3)$
Lineation (Balsley and Buddington, 1960)	$L = \tau_1/\tau_2$
Foliation (Stacey et al., 1960)	$F = \tau_2/\tau_3$
log Lineation (Woodcock, 1977)	$L' = \ln(L)$
log Foliation (Woodcock, 1977)	$F' = \ln(F)$
Elongation (Tauxe, 1998)	$E' = \tau_1 + .5\tau_3$
Roundness (Tauxe, 1998)	$R = \sin(60)\tau_3$

Appendix

A The 15 measurement protocol

The Jelinek (1976) 15 measurement scheme is illustrated in Figure A1. This is the procedure recommended in the manual distributed with the popular Kappabridge susceptiblity instruments. In the 15 measurement case shown in Figure A1, the design matrix is:

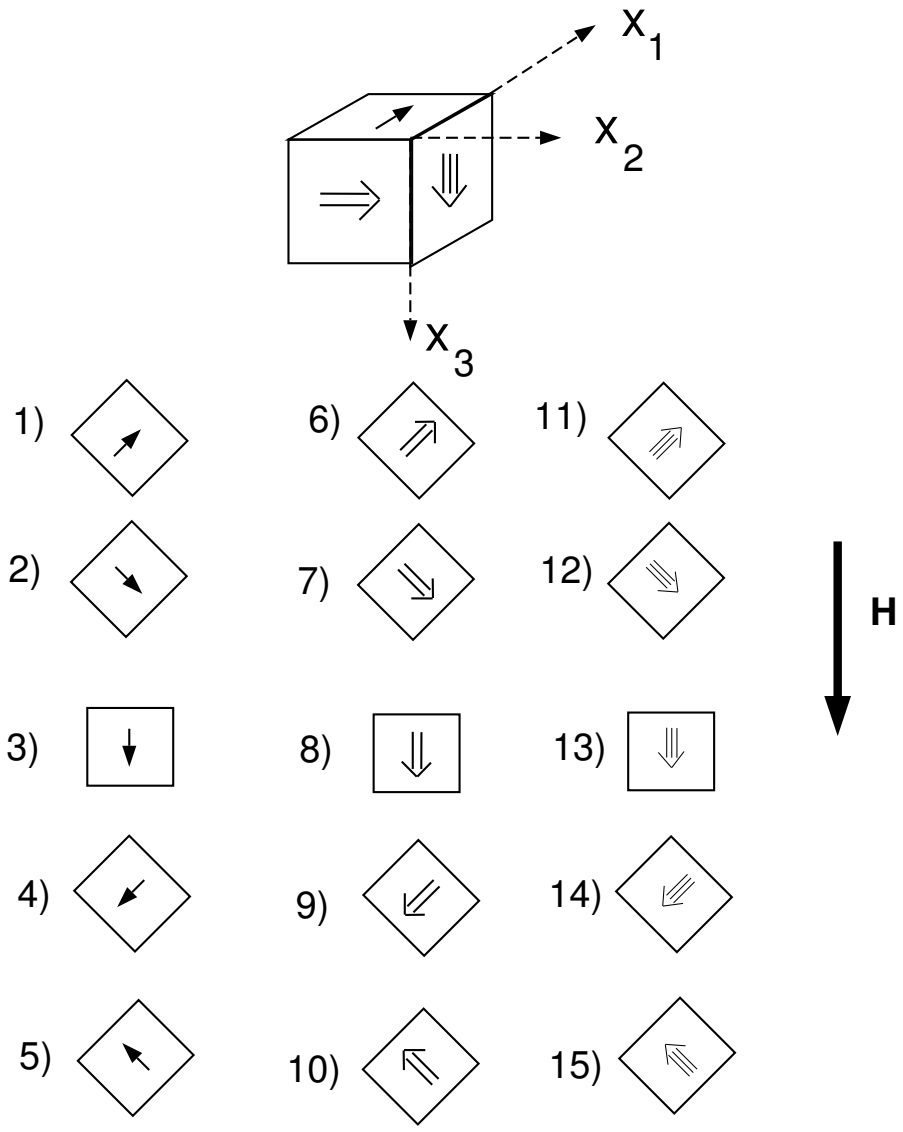

Figure A1: The 15 position scheme of Jelinek (1976) for measuring the AMS of a sample.

$$\mathbf{A} = \begin{pmatrix} .5 & .5 & 0 & -1 & 0 & 0 \\ .5 & .5 & 0 & 1 & 0 & 0 \\ 1 & 0 & 0 & 0 & 0 & 0 \\ .5 & .5 & 0 & -1 & 0 & 0 \\ .5 & .5 & 0 & 1 & 0 & 0 \\ 0 & .5 & .5 & 0 & -1 & 0 \\ 0 & .5 & .5 & 0 & 1 & 0 \\ 0 & 1 & 0 & 0 & 0 & 0 \\ 0 & .5 & .5 & 0 & -1 & 0 \\ 0 & .5 & .5 & 0 & 1 & 0 \\ .5 & 0 & .5 & 0 & 0 & -1 \\ .5 & 0 & .5 & 0 & 0 & 1 \\ 0 & 0 & 1 & 0 & 0 & 0 \\ .5 & 0 & .5 & 0 & 0 & -1 \\ .5 & 0 & .5 & 0 & 0 & 1 \end{pmatrix}, \tag{A1}$$

and $\mathbf{B} = \frac{1}{20}\times$

$$\begin{pmatrix} 3 & 3 & 8 & 3 & 3 & -2 & -2 & -2 & -2 & -2 & 3 & 3 & -2 & 3 & 3 \\ 3 & 3 & -2 & 3 & 3 & 3 & 3 & 8 & 3 & 3 & -2 & -2 & -2 & -2 & -2 \\ -2 & -2 & -2 & -2 & -2 & 3 & 3 & -2 & 3 & 3 & 3 & 3 & 8 & 3 & 3 \\ -5 & 5 & 0 & -5 & 5 & 0 & 0 & 0 & 0 & 0 & 0 & 0 & 0 & 0 & 0 \\ 0 & 0 & 0 & 0 & 0 & -5 & 5 & 0 & -5 & 5 & 0 & 0 & 0 & 0 & 0 \\ 0 & 0 & 0 & 0 & 0 & 0 & 0 & 0 & 0 & 0 & -5 & 5 & 0 & -5 & 5 \end{pmatrix}. \tag{A2}$$

B Hext confidence ellipses

The Hext (1963) confidence ellipses shown in Figure 13.3 are calculated as follows:

1. We assume that the uncertainties in the eigenvectors are in a plane that is tangent to the unit sphere. We further assume that they belong to a two-dimensional normal distribution with semi-axes that are aligned along the $\mathbf{V}_i$. The ellipse with semi-axes ϵ_{ij} that outline a 95% confidence region in this plane is then projected onto the sphere (Figure 13.3).

2. Calculate the matrices $\bar{\mathbf{s}}$, $\bar{\mathbf{K}}$, and the δ_i from the measured values of $\mathbf{K}$.

3. Calculate the eigenvectors $\mathbf{V}$ and eigenvalues τ of $\bar{\mathbf{s}}$.

4. Calculate σ by Equations 13.12 and 13.13.

5. The confidence regions are outlined by ellipses along semi-axes ϵ_{ij} aligned with the eigenvectors. The i subscripts refer to the axis on which the ellipse is attached and the j subscripts refer to the axis to which it points. Thus, ϵ_{12} is the semi-axis that defines the confidence region of $\mathbf{V}_1$ directed toward $\mathbf{V}_2$ (Figure 13.3).

   The three unique semi-angles of the confidence ellipses ϵ_{ij} are calculated by:

$$\begin{aligned} \epsilon_{12} &= \tan^{-1}[f\sigma/2(\tau_1-\tau_2)] \\ \epsilon_{23} &= \tan^{-1}[f\sigma/2(\tau_2-\tau_3)] \\ \epsilon_{13} &= \tan^{-1}[f\sigma/2(\tau_1-\tau_3)] \\ \epsilon_{21} &= \epsilon_{12} \\ \epsilon_{32} &= \epsilon_{23} \\ \epsilon_{31} &= \epsilon_{13}, \end{aligned} \tag{B1}$$

where

$$f = \sqrt{2(F_{(2,n_f);(1-p)})},$$

and where $F_{(2,n_f)}$ is the value from the F table (see Table D1 of Lecture 11), with 2 and n_f degrees of freedom, at the p probability level. The value of $F_{(2,n_f)}$ for $N_{meas} = 15$ measurements ($n_f = 9$) at the 95% level of confidence ($p = .05$) is 4.26 and so $f = 2.92$.

C Hext F statistics for significance of eigenvalue ratios

Because of the mindless precision of modern computers, there are always three different eigenvalues returned by subroutines for eigenparameter calculation. But, these may not be significantly different from one another. In order to test for significance, Hext (1963) developed three F statistics: F for significance of overall anisotropy, F_{12} for significant difference between the maximum and intermediate eigenvalues (are the data oblate?) and F_{23} for significant difference between the intermediate and minimum eigenvalues (are the data prolate?). (If all three are positive, the data are triaxial). The F statistics are calculated as follows:

$$\begin{aligned} F &= 0.4(\tau_1^2+\tau_2^2+\tau_3^2-3\chi_b^2)/\sigma^2 \\ F_{12} &= 0.5((\tau_1-\tau_2)/\sigma)^2 \\ F_{23} &= 0.5((\tau_2-\tau_3)/\sigma)^2, \end{aligned} \tag{C1}$$

where the bulk susceptibility χ_b is given by:

$$\chi_b = (\bar{s}_1+\bar{s}_2+\bar{s}_3)/3. \tag{C2}$$

The critical value for F (see F Table in the appendix to Lecture 9) is 3.4817 for 95% confidence (for F_{12} and F_{23}, it is 4.2565).

D Correction of inclination error with AARM

The magnitude of ARM is here denoted M_a. The particle anisotropy is denoted a and is defined as the and is given by:

$$a = [\frac{M_{a_{||}}}{M_{a_\perp}}]_{particle} \tag{D1}$$

where $M_{a_{||}}$ and $M_{a_\perp}$ are the magnitudes of the ARM acquired parallel to and perpendicular to the detrital particle long axis respectively. The normalized eigenvalues of the ARM tensor (q_i) are defined as:

$$q_i = \frac{M_{a_i}}{M_a}.$$

Stephenson et al. (1986) defined an orientation distribution function for the preferred alignment of particle long axes whose eigenvalues are given by κ_i where $\kappa_1 > \kappa_2 > \kappa_3$ as usual. Jackson et al. (1991) collect together the two sources of anisotropy (alignment of particle long axes and individual particle anisotropies) as:

$$\kappa_i = \frac{q_i(a+2)-1}{(a-1)}. \tag{D2}$$

Assuming that the DRM anisotropy is identical to the orientation distribution function of particle long axes we can combine and rearrange Equations 13.16 and D2 to get the relationship between the flattening factor f and the ARM anisotropy:

$$f = \frac{q_3(a+2)-1}{q_1(a+2)-1}$$

From the forgoing, measuring the AARM tensor yields the values for q, but determining values for a are more problematic. Vaughn et al. (2005) describe a technique whereby magnetic particles are separated from the matrix, then allowed to dry in an epoxy matrix in the presence of a magnetic field sufficient to fully align the long axes of the magnetic particles (say 50 mT). The AARM parallel to and perpendicular to the axis of alignment therefore gives a by Equation D1.

Bibliography

Aitken, M., Alcock, P., G.D., B. & Shaw, C. (1981), 'Archaeomagnetic determination of the past geomagnetic intensity using ancient ceramics: allowance for anisotropy', *Archaeometry* **23**, 53–64.

Balsley, J. R. & Buddington, A. F. (1960), 'Magnetic susceptibility anisotropy and fabric of some Adirondack granites and orthogneisses', *Amer. Jour. Sci.* **258A**, 6–20.

Borradaile, G. J. (1988), 'Magnetic susceptibility, petrofabrics and strain', *Tectonophysics* **156**, 1–20.

Borradaile, G. J. (2003), *Statistics of Earth Science Data: Their Distribution in Time, Space, and Orientation*, Springer, Berlin.

Collinson, D. W. (1983), 'Methods in Rock Magnetism and Paleomagnetism'.

Constable, C. & Tauxe, L. (1990), 'The bootstrap for magnetic susceptibility tensors', *J. Geophys. Res.* **95**, 8383–8395.

Flinn, D. (1962), 'On folding during three-dimensional progressive deformation', *Geol. Soc. London Quart. Jour.* **118**, 385–433.

Hargraves, R. B. (1991), 'Distribution anisotropy: the cause of AMS in igneous rocks?', *Geophys. Res. Lett.* **18**, 2193–2196.

Hext, G. R. (1963), 'The estimation of second-order tensors, with related tests and designs', *Biometrika* **50**, 353–357.

Jackson, M. J., Banerjee, S. K., Marvin, J. A., Lu, R. & Gruber, W. (1991), 'Detrital remanence, inclination errors and anhysteretic remanence anisotropy: quantitative model and experimental results', *Geophys. J. Int.* **104**, 95–103.

Jelinek, V. (1976), 'The statistical theory of measuring anisotropy of magnetic susceptibility ofrocks and its application', *unpublished.* .

Jelinek, V. (1978), 'Statistical processing of anisotropy of magnetic susceptibility measured on groups of specimens', *Studia Geophys. et geol.* **22**, 50–62.

Jelinek, V. (1981), 'Characterization to the magnetic fabric of rocks', *Tectonophys.* **79**, 63–67.

King, R. F. (1955), 'The remanent magnetism of artificially deposited sediments', *Mon. Nat. Roy. astr. Soc., Geophys. Suppl.* **7**, 115–134.

Knight, M. D. & Walker, G. P. L. (1988), 'Magma flow directions in dikes ofteh Koolau Comples, Oahu, determined from magnetic fabric studies', *Jour. Geophys. Res.* **93**, 4301–4319.

Levi, S. & Banerjee, S. K. (1976), 'On the possibility of obtaining relative paleointensities fromlake sediments', *Earth Planet. Sci. Lett.* **29**, 219–226.

Means, W. (1976), *Stress and Strain: Basic Concepts of Continuum Mechanics for Geologists*, Springer-Verlag.

Nagata, T. (1961), 'Rock Magnetism'.

Nye, J. F. (1957), 'Physical Properties of Crystals'.

Owens, W. H. (1974), 'Mathematical model studies on factors affecting the magnetic anisotropy of deformed rocks', *Tectonophys.* **24**, 115–131.

Ramsay, J. G. (1967), 'Folding and fracturing of rocks'.

Stacey, F. D., Joplin, G. & Lindsay, J. (1960), 'Magnetic anisotropy and fabric of some foliated rocks from S.E. Australia', *Geophysica Pura Appl.* **47**, 30–40.

Stephenson, A., Sadikern, S. & Potter, D. K. (1986), 'A theoretical and experimental comparison of the susceptibility and remanence in rocks and minerals', *Geophys. J. R. astr. Soc.* **84**, 185–200.

Tarling, D. H. & Hrouda, F. (1993), 'The Magnetic Anisotropy of Rocks'.

Tauxe, L. (1998), *Paleomagnetic Principles and Practice*, Kluwer Academic Publishers, Dordrecht.

Tauxe, L., Constable, C. G., Stokking, L. B. & Badgley, C. (1990), 'The use of anisotropy to determine the origin of characteristic remanence in the Siwalik red beds of northern Pakistan', *Jour. Geophys. Res.* **95**, 4391–4404.

Vaughn, J., Kodama, K. P. & Smith, D. (2005), 'Correction of inclination shallowing and its tectonic implications: The Cretaceous Perforada Formation, Baja California', *Earth Planet. Sci. Lett.* **232**, 72–82.

Woodcock, N. H. (1977), 'Specification of fabric shapes using an eigenvalue method', *Geol. Soc. Amer. Bull.* **88**, 1231–1236.

Lectures in Paleomagnetism, 2005
by Lisa Tauxe

Citation:
http://earthref.org/MAGIC/books/Tauxe/2005/

June 12, 2005

Chapter 14

The ancient geomagnetic field

Suggested Reading

For background:
Chapters 1 and 7: Butler (1992)
Lecture 2: this lecture series
To learn more:
Chapters 1, 2.4, 4, 6.4: Merrill et al. (1996)

14.1 Motivation for study of the behavior of the Earth's magnetic field

The magnetic field is one component of the highly complex Earth system. It interacts with the atmosphere, the biosphere, the deep mantle and even the inner core. It also has the useful property of pointing roughly North (or South). Records of the Earth's magnetic field play a role in many aspects of Earth Science; hence some knowledge of how it behaves is important to all Earth scientists. The following is a partial list of reasons to study the geomagnetic field

- Atmospheric interaction

Radioactive forms of carbon, beryllium and chlorine are produced in the atmosphere by cosmic ray bombardment. The decay of these isotopes is used for dating purposes in a wide variety of disciplines. There are large variations in ages predicted from tree ring, varve or ice layer counting or U/Th dating and those estimated by radiocarbon dating (see Figure 14.1). Some of these variations could be caused by changes in the carbon balance between the atmosphere and the deep ocean (which is a reservoir of old carbon) and some could be caused by changes in magnetic field strength. Because the magnetic field shields the atmosphere to a large extent from cosmic rays, changes in the intensity of the magnetic field result in changes in production, hence are a key parameter in deriving accurate age information. To date, there is rather poor agreement between the variations in radiocarbon production predicted using changes in paleointensity of the geomagnetic field (see, e.g., Figure 14.1.) Either the field variations are not known, the relationship between those variations and radiocarbon production is not known or the actual variations in production are not known because of unconstrained reservoir effects (or any combination of these factors).

- Biospheric interaction

Some living forms make magnetic crystals (Lecture 6). In the case of magnetotactic bacteria, these tiny magnets are used for physical orientation. In some cases, animals may use magnetic field

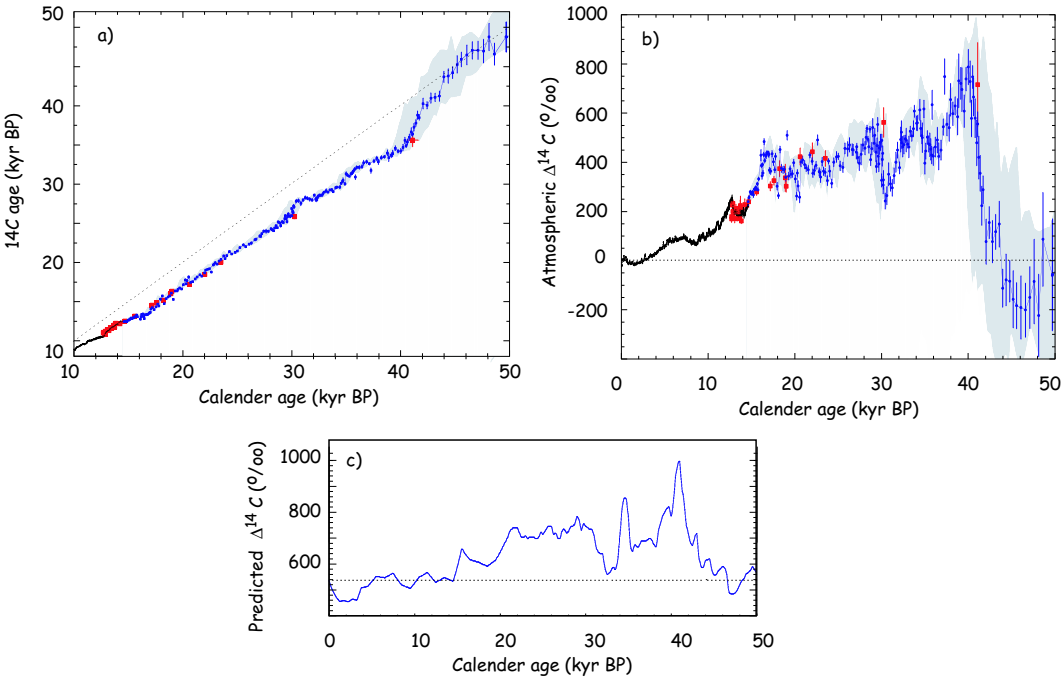

Figure 14.1: a) Radiocarbon calibration data from from Cariaco ODP Leg 165, Holes 1002D and 1002E (blue circles), plotted versus calendar age assigned by correlation of detailed paleoclimate records to the Greenland Ice Core GISP2. The thin black line is high-resolution radiocarbon calibration data from tree rings joined at 12 cal. ka B.P. to the varve counting chronology. Red squares are paired ^{14}C-U/Th dates from corals. Light gray shading represents the uncertainties in the Cariaco calibraion. The radiocarbon dates are too young, falling well below the dashed line of 1:1 correlation. b) Compilation of data interpreted as production rate changes in radiocarbon (Δ^{14}C) versus calender age. (symbols same as in a). c) Predicted variation of Δ^{14}C from the geomagnetic field intensity variations from sediments of the north Atlantic (Laj et al., 2002) using the model of Masarik and Beer (1999). [Figure modified from Hughen et al., 2004.]

lines for navigation.

- Deep mantle interaction

Studies of seismic waves have demonstrated large variations in seismic velocity near the core mantle boundary. There appears to be an annulus of faster velocities surrounding the Pacific ocean which may reflect the influence of cold subducted slabs. The geomagnetic field is generated by convection in the outer core. This convection could be a strong function of the thermal gradient at the top of the core. Temperature variations therefore could conceivably have an effect on the geomagnetic field (e.g., Glatzmaier et al., 1999). Is there any evidence for this? Are there any changes in the magnetic field as a function of long term changes in the CMB?

- Inner core interaction

Numerical simulations of the magnetic field predicted that the process of generation of the magnetic field interacted with the inner core in such a way as to make it spin faster than the rest of the Earth (Glatzmaier and Roberts, 1996). The effect has been sought in seismic data (e.g., Song and Richards, 1996), although its existence is still a matter of debate.

• Tectonic and Geological applications

Paleomagnetic data often are a critical component of stratigraphic and tectonic investigations because they provide temporal and paleogeographic constraints unavailable by any other method. Therefore, it is useful to know what sorts of data can be expected from records of the geomagnetic field, as oppose to geological modification through overprinting or post-formation rotation. It is also useful to know how long one must average the observations to achieve a reasonable estimate of the time averaged field (TAF) and whether or not it can be approximated by a GAD model.

•The sky is falling!

Hulot et al. (2002) were among the first to point out the fact that the Earth's magnetic field has dropped in intensity over the last two decades. This observation, combined with the fact that the reverse flux patches on the core mantle boundary appear to be growing lead to speculation that the geomagnetic field might be starting to reverse its polarity. What is the likelihood that this will happen? What does the field do when it is about to reverse? What is the average intensity of the field and how frequently does it do what it is doing now without reversing?

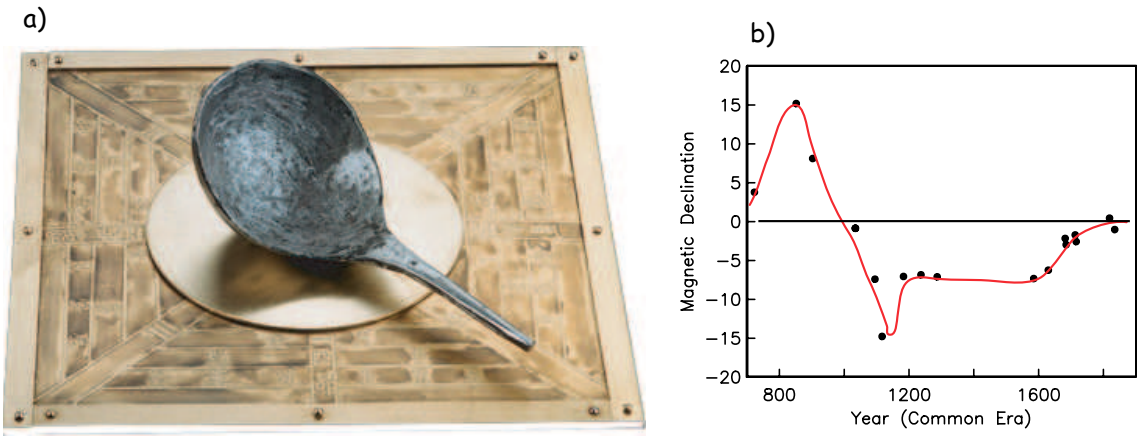

Figure 14.2: a) A reconstruction of the south pointing spoon (*shao*) used by the Chinese in the second century BCE. b) Measurements of magnetic declination made in China from 720 CE to 1829. [Compiled by Smith and Needham, 1967.]

In order to answer some of the questions just raised, we need measurements of the geomagnetic field. The geomagnetic field changes on frequencies of 10s of microseconds (radio waves) to millions and perhaps billions of years. Direct observations contribute to our knowledge of field behavior up to the order of 100s of years, but on longer times scales we need to use paleomagnetic and archeomagnetic techniques. We will first review what is known from historical measurements of the geomagnetic field. Then we will turn to what we can glean from "accidental records" made by archeological and geological materials.

14.2 Historical measurements of the Earth's Magnetic field

The magnetic properties of lodestone were already well known by at least several centuries BCE. Legend has it that a boy in ancient Greece discovered the magnetic properties of lodestone that he found near the city of Magnesia. The earliest compass dates from the second century BCE. Lodestone spoons (see Figure 14.2a) were placed on bronze plates, often decorated with images of

the Big Dipper and other heavenly images. These "south pointers" were apparently used primarily for prognostication, geomancy and Feng Shui. It was not until sometime in the late 14th Century that compasses were used for sea-going navigation in China.

That the magnetic field changes was apparently first discovered in China around 720 CE when the astronomer Yi-Xing measured magnetic declination (see Figure 14.2b). The compass did not arrive in Europe until some time in the 12^{th} century, but the idea of declination did not accompany it. The deviation of magnetic north from true north was not rediscovered until the early 1400s. Europeans began to make systematic measurements of declination in the early 1500s. Magnetic inclination was discovered in the mid-1500s in Europe.

Gilbert (1600) noted variations in field strength with latitude based on the sluggishness or rapidity with which a compass settled on the magnetic direction. Magnetic intensity was first measured quantitatively in the late 1700s by French scientist Robert de Paul, although all records were lost in a ship wreck. The expedition sent to search for the lost ship made several measurements, using the period of oscillation T of a vertical dip needle with magnetic moment m and moment of inertia I. These are related to B by:

$$T = 2\pi\sqrt{\frac{I}{mB}}.$$

These measurements supported Gilbert's hunch that the intensity of the field increases away from the equator.

The internal origin of the magnetic field was discovered by Gilbert in 1546 who made a systematic study of the magnets and the the Earth's magnetic field, published in 1600. While aware of deviations of magnetic declination from true north, Gilbert thought that the field was unchanging in time. It wasn't until Gellibrand, in 1634, compared declination measurements made in London over a period of some 50 years and concluded that the geomagnetic field changes. Thus Europeans discovered secular variation of the magnetic field in 1634, over a millenium after the Chinese.

Scientific exploration at sea began with the expeditions of the Pink Paramore under Caption Edmond Halley (1698-1701). Halley published the first geomagnetic chart in 1702 (see Figure 14.3). He noticed that some geomagnetic features appeared to be moving to the west, a phenomenon known as *westward drift*. compare for example the "line of no variation" in Figure 14.3 with the line of zero declination in Figure 2.5 in Lecture 2. It has moved significantly to the west in the equatorial and southern Atlantic realms.

Gauss provided the mathematical framework we use today to deal with geomagnetic data when he invented the spherical harmonic expression for the geomagnetic potential field (see Lecture 2). The first such analysis (done in 1838) was based on 84 data points evaluated on an evenly spaced grid from isomagnetic charts of the magnetic field elements available at the time.

Fastforwarding to our own millenium, we find researchers still poring over these centuries old measurements. Bloxham, Gubbins, Jackson and colleagues are mining the maritime records of early European sea-faring merchants. These ship's logs contain a huge treasure trove of measurements of declination and sometimes inclination since the 16th century (see e.g., Jackson et al., 2000). The intensity of the radial component of the magnetic field inferred for the core mantle boundary at two time intervals is shown in Figure 14.4. Compare Figure 14.4b with Figure 2.5a in Lecture 2 which is the intensity of the magnetic field observed at the surface. There are more so-called "flux patches" (the spots of higher intensity) in Figure 14.4b because the field was evaluated closer to the source (the core), but the general pattern is similar. The field for 1600, however, was somewhat

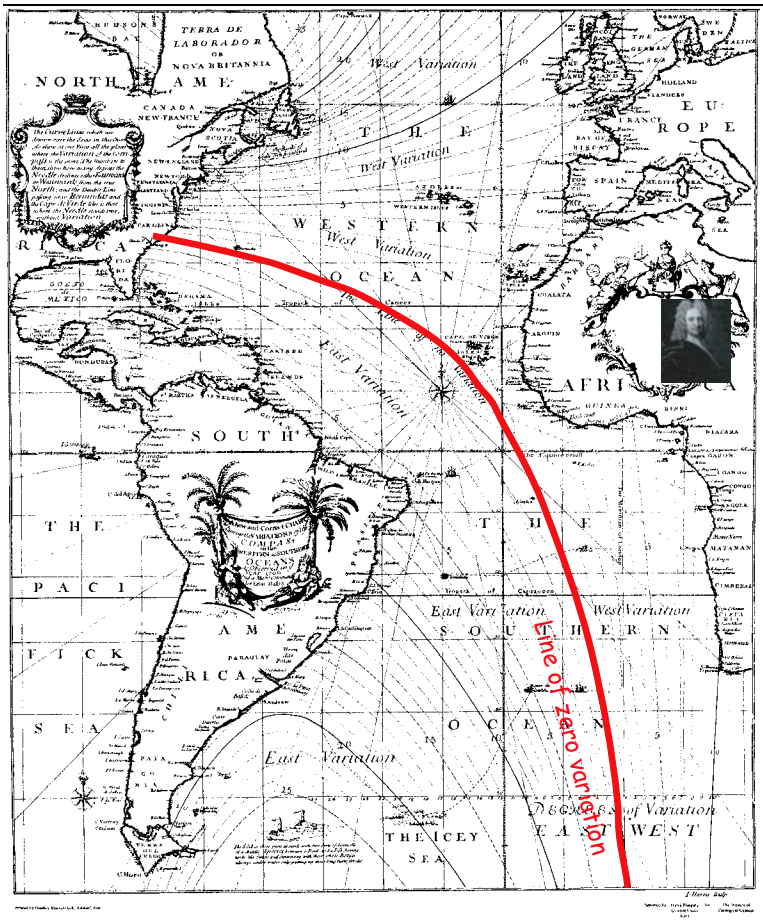

Figure 14.3: Chart of magnetic declination from Halley, (To make observations on the magneticall needle etc.: the Voyages of the Pink Paramore under captain Edmond halley, FRS: 1698-1701) published in 1702.

different. The number and positions of the flux patches has changed substantially since then. Some flux patches, in particular the prominant patch that is now over Africa, have drifted westward from the Indian ocean, a phenomenon largely responsible for "westward drift".

As already mentioned, observatory measurements of the intensity of the magnetic field are only available since the mid-19th century. These show that the large changes in declination and inclination were also accompanied by even more dramatic changes in field strength. We plot the intensity of the field evaluated from the **gufm1** model of Jackson et al. (2000) for San Diego, CA, in Figure 14.4c. If the field continues on its recent trajectory, it will reach zero by the year 2500.

14.3 The archeo- and paleomagnetic record of geomagnetic field behavior

Historical observations quickly run out as we go back in time. Prior to 720 CE there are no surviving human measurements. Yet the average field based on the historical measurements (e.g., Jackson

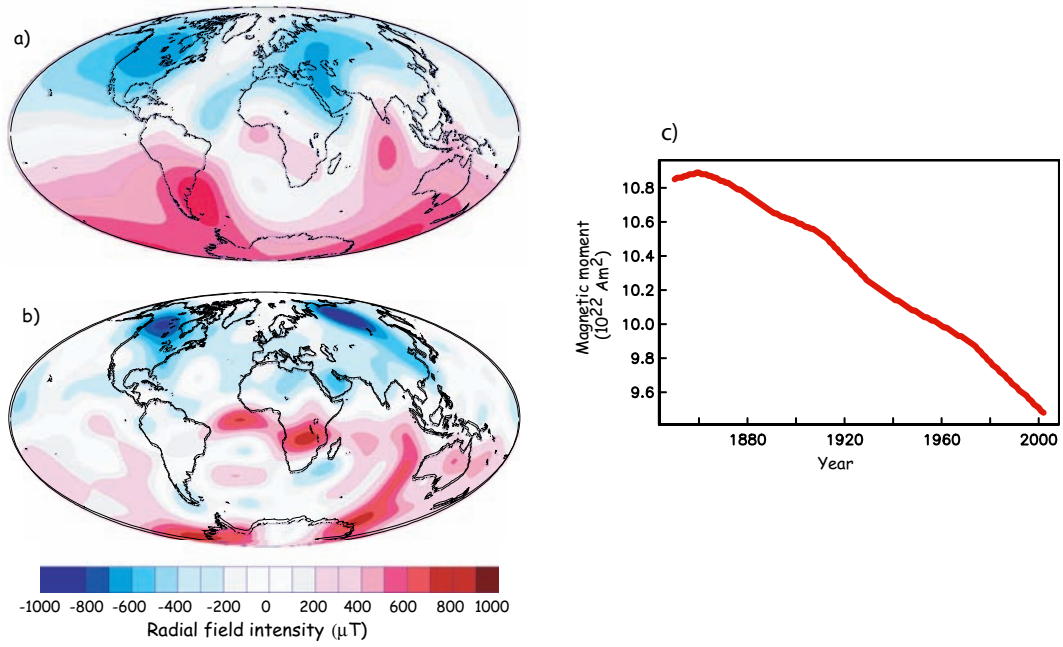

Figure 14.4: Maps of the intensity of the radial magnetic field at the core mantle boundary. b) Deduced from the secular variation measurements compiled by Jackson et al., (2000) for 1600. b) Map from the IGRF of 1990. c) Magnetic intensity in San Diego, CA evaluated from the **gufm1** model.

et al., 2000) is anything but GAD. To see how observations of the magnetic field such as westward drift, quasi-stationary flux lobes and the degree of "GADness" change through time, we must turn to rock and archeological materials to give us a picture of the ancient geomagnetic field.

14.3.1 Pioneers in paleomagnetism

Strongly magnetized rocks (as opposed to the mineral lodestone) had been noticed during the 1700s because of their effect on compass needles, but the fact that certain rocks were magnetized in the direction of the Earth's field was discovered by Delesse in 1849 and Melloni in 1853. Folgerhaiter extended the study of fossil magnetizations to the magnetic properties of baked archeological materials in 1899. Naturally baked material (heated by lava flows) was studies by David (1904) and Brunhes (1906). In the course of their investigations, they discovered materials that were magnetized in a direction opposite to the Earth's field. This first application of the baked contact test led to speculation that the Earth's field had reversed its polarity in the past.

Mercanton (1926) argued that the field had reversed based on the fact that reversely magnetized rocks were found all over the world. Matuyama (1929) further supported the argument by demonstrating that all the reversely magnetized rocks in Japan were older than the overlying normally magnetized rocks. It was not until the combined use of paleomagnetism and K-Ar dating allowed researchers in the U.S. and Australia (e.g., Cox et al., 1963) to demonstrate the global synchrony of polarity intervals that the scientific community embraced the notion of polarity reversals.

Sedimentary materials were first used for the investigation of secular variation by Johnson et al. (1948) who measured samples from varved lakes in New England. Mackereth developed a

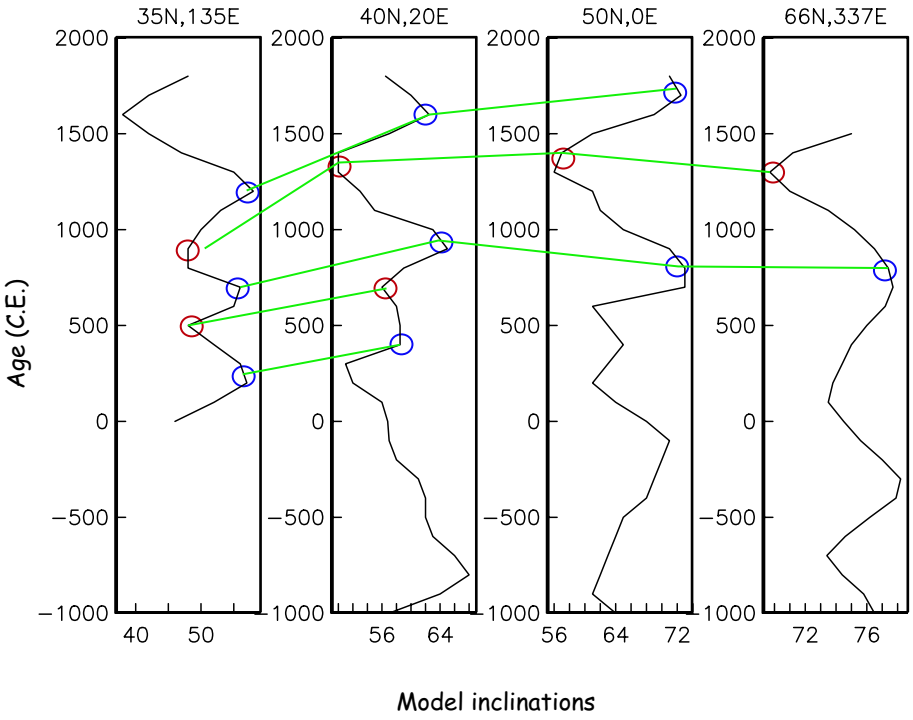

Figure 14.5: Inclinations evaluated at 100 year intervals from the PSVMOD1.0 of Constable et al. (2000) for selected records. These are plotted from West to East. Maxima and minima are noted. Westward drift would imply that these features would "rise" to the right.

pneumatic for coring device for use in lakes in 1958, opening the way for studies of the detailed time variations of the magnetic field.

14.3.2 The last few millenia

Constable et al. (2000) assembled a data set of 24 time series of directional data from archeomagnetic and lake sediment sources evaluated at 100 year intervals (PSVMOD1.0). We plot examples of several of the inclination records from West to East in Figure 14.5. The most recent attempt at spherical harmonic modelling of archeomagnetic, marine and lake sedimentary data is that of Korte and Constable (2005) who have pressed back 7000 year and have included intensity data in their modelling efforts.

14.3.3 Westward drift

We mentioned that early workers measuring the secular variation of declination noticed that certain features appeared to move west with time. A careful look at the data shows that this tendency as a subtle, probably only locally observed effect. Yukutake (1967) collected together the data available at the time and marked the occurrences of maxima and minima in both declination and inclination. Some of these are marked on Figure 14.5 as examples. Yukutake then plotted these maxima and minima as a function of age and longitude of the observation site. The data appeared to suggest that the features moved westward at a rate of about a half a degree per year. This would

mean that the maxima and minima on Figure 14.5 would rise to the right as they sort of do, but the data are rather unconvincing.

14.3.4 The more distant past

For more distant times in the past, we look at records from one place over time. In Figure 14.6, we see an example of one such record, obtained from dry lake sediments exposed along the shores of Mono Lake. The geomagnetic field oscillated around the GAD direction with an amplitude of some 30° over an interval of some 9 meters (the age is debated, but recent estimates place the record at approximately 38-41 ka; Kent et al., 2002) On rare occasions, the field departs drastically from what can be considered normal of secular variation and executes what is known as a *geomagnetic excursion*. The definition of a geomagnetic excursion is usually magnetic records in which the VGPs are more than 45° away from the average pole for that time and place. The convention is to name the excursion after the place where it was first observed, so this would be the "Mono Lake excursion", if it is distict from the "Laschamp excursion" discovered in volcanics near Laschamp, France.

Excursions are thought to be accompanied by a decreases in paleointensity (DIPs) (a paleointensity low). For this reason, some recent studies have identified "excursions" based on the occurence of paleointensity lows (see Figure 14.7), but this is strictly speaking incorrect.

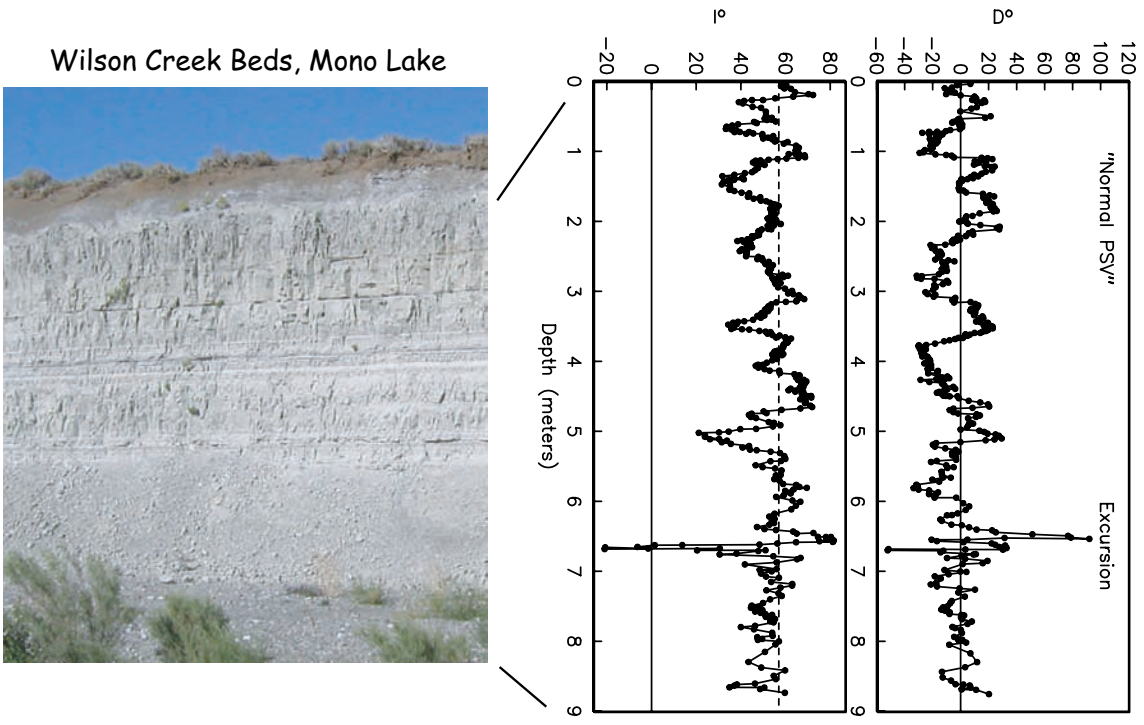

Figure 14.6: Paleosecular variation of the magnetic field (D and I) observed in the Wilson Creek section north of Mono Lake. The inclination expected from an geocentric axial dipole is shown as a dashed line. The declination is expected to be zero. The so-called "Mono Lake" excursion is marked. The data are from Lund et al. (1988) and represent some 23 kyr of time.

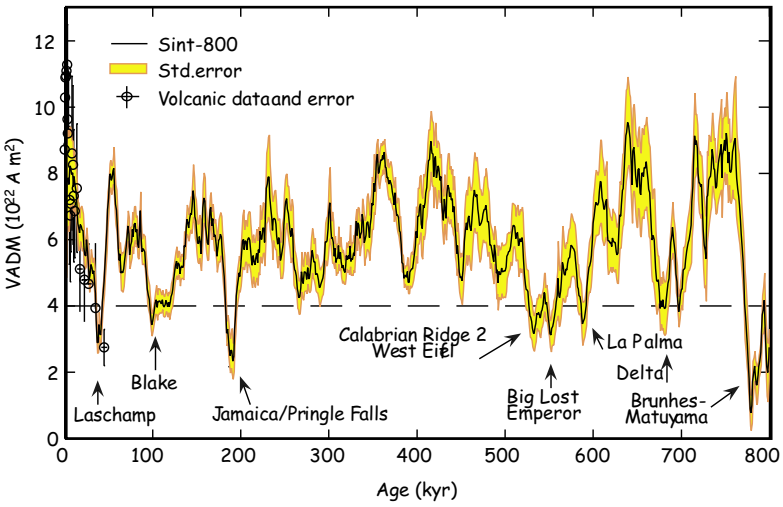

Figure 14.7: Stack of relative paleointensity records from deep sea sediments. [Figure modified from Guyodo and Valet, 1999.]

When viewed over sufficient time, the geomagnetic field reverses its polarity, by which we mean that the sign of the axial dipole term (g_1^0) changes. An example of a so-called *polarity reversal* is shown in Figure 14.8a (Clement and Kent, 1984). The intensity of the magnetic field appears to drop to approximately 10% of its average value and the directions migrate from one pole to the other over a period of several thousand years. When the polarity is the same as the present polarity it is said to be *normal*. When it is in the opposite state, it is said to be *reverse*. The duration of the reversal process also appears to be a function of latitude (Clement, 2004).

The details of what happens during a polarity reversal are still rather unclear because they occur so quickly, geologically speaking. Some high resolution sedimentary records are like that shown in Figure 14.8 whereby there is an orderly progression from one polarity to the other. However, a polarity transition captured by rapidly erupted lava flows records a more complex picture (see Figure 14.8b). There are a few conclusions we can draw however: 1) they occur quickly and 2) they are always associated with low geomagnetic intensities (see Figure 14.9a).

A more controversial observation about directions in extrema was first pointed out by Clement (1991): when mapped to VGP positions, they plot in preferred paths (see Figure 14.9b). These paths are seen in most data sets, but can be made to disappear when certain criteria are applied (e.g., Prévot and Camps, 1993). The intriguing thing about the paths is that they appear to coincide with the shear velocity anomalies (see Figure 14.9c). Whether or not the paths exist has been debated ever since. However, recent work by Love (1999) seems to support the preferred path hypothesis.

On average, the field spends about half its time in each polarity state, and only a tiny fraction (1-2%) of the time in an intermediate state. Rocks of both polarities have been documented from early in the Earth's history (at least since the late Archean, see Strik et al. 2003), although the frequency of reversal has changed considerably through time (see Opdyke and Channell, 1996 and Merrill et al., 1996).

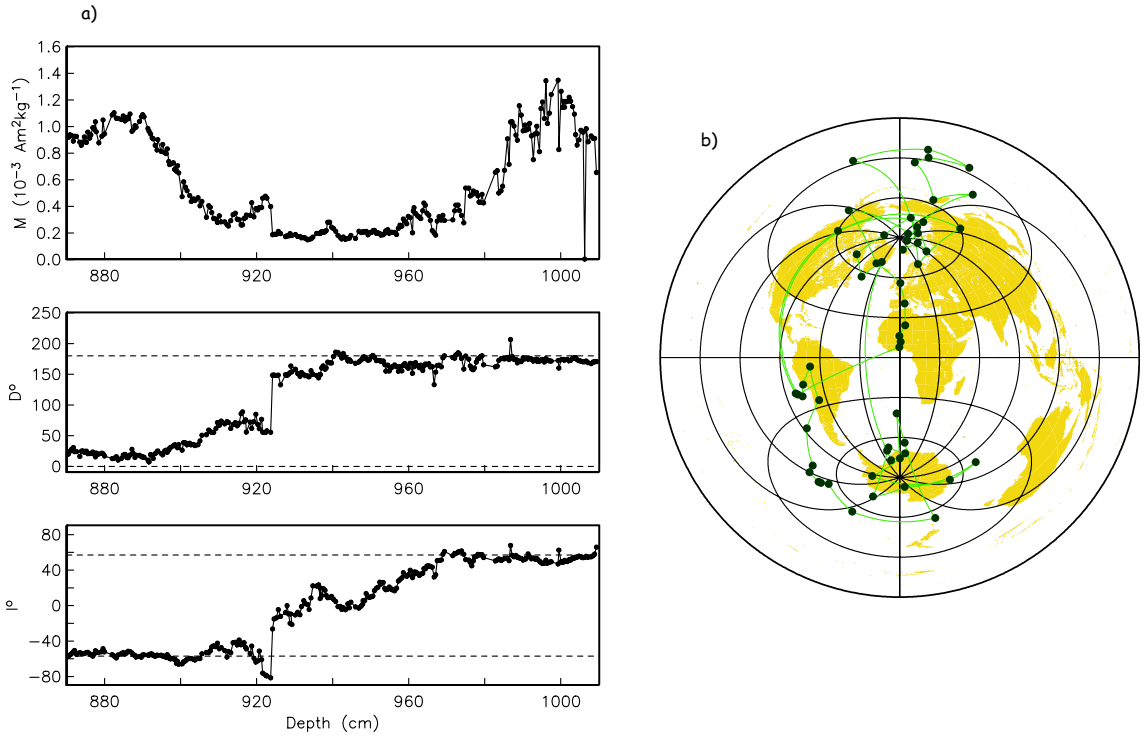

Figure 14.8: a) The lower Jaramillo geomagnetic polarity reversal as recorded in deep sea sediments from core RC14-14. Inclinations and declinations expected from a normal and reverse GAD field are shown as dashed lines. [Data from Clement and Kent, 1984]. b) Record of polarity transition recorded at Steens Mountain. [Data from Camps et al., 1999.]

14.4 Geomagnetic polarity time scale - a first look

A list of dates of past geomagnetic polarity reversals is known as a *geomagnetic polarity time scale* (GPTS). How the time scale is calibrated is discussed in the next lecture. For now we will just take it as a given. In Figure 14.10 we show the polarity history from the marine magnetic anomaly template. The details of the history of reversals for times older than the oldest sea floor magnetic anomaly record (about 160 Ma) are sketchy, but will eventually be documented using sedimentary records of the magnetic field (see e.g., Kent and Olsen, 1999).

Examination of the reversal history shown in Figure 14.10 suggests that reversals occur at apparently random intervals without a predictable pattern. Furthermore, the frequency of reversals appears to change (see for example, Constable, 2003). Above the polarity history in Figure 14.10, we plot the number of reversals in four million year intervals as a histogram. The reversal frequency is relatively high in the interval 124-150 Ma, but appears to drop gradually to zero at the beginning of the so-called Cretaceous Normal Superchron (CNS), a period of some 40 m.y. in which no (or very few) reversals occurred. Since the end of the CNS at about 84 Ma, the frequency of reversals has increased to the present average rate of about four per million years.

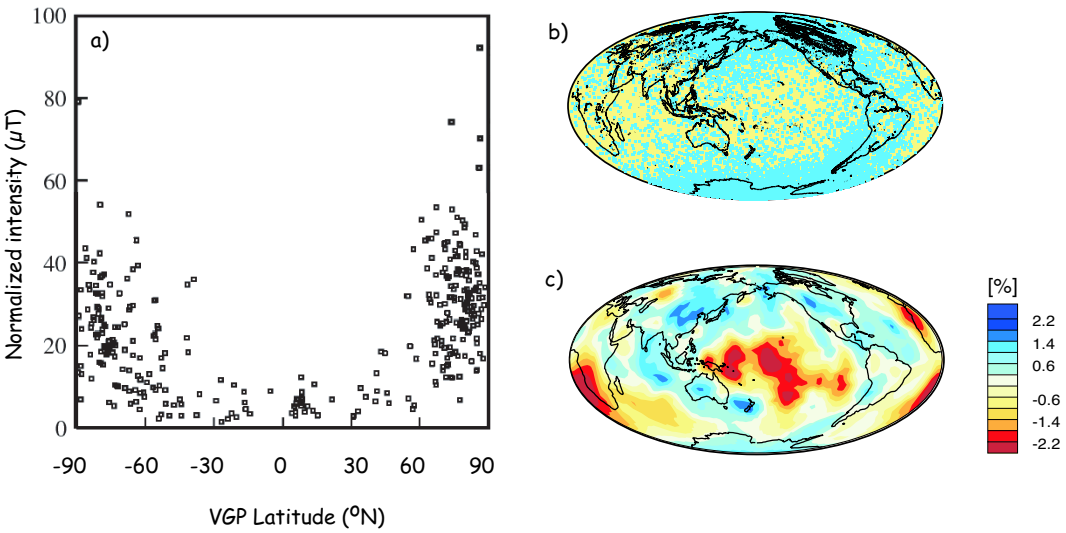

Figure 14.9: a) Normalized intensity (see Love, 2000) versus VGP latitude. As is seen in every data set of its kind, intermediate (transitional or excursional) directions (low VGP latitudes) are associated with low paleointensities. b) Plot of transitional VGPs from the TRANS data base. No selection criteria were applied. c) Shear wave velocity SB448 model from Masters et al. (2000) evaluated at 2770 km (core mantle boundary region). There is a fast (cold) ring around the Pacific, presumably from the influence of subducted slabs.

14.5 The time averaged field

It now seems possible to determine full scale spherical harmonic models as a function of time back thousands of years. Beyond a certain limit, however, there simply are not enough data with sufficient age control and spatial density to go back very far in time in this sort of fashion. The approach for longer time scales has been to look at the average magnetic field. There has therefore been a large effort over the past decade or so to bring together data for the purpose of evaluating the time averaged field.

The last five million years has been a recent focus because of the reduced effects of plate motion (e.g., Johnson and Constable, 1997). Data from lava flows from all over the world have been compiled into various databases and analyzed from a variety of view points. It was recently realized that the data had been compiled using less than optimum criteria and that many more data of higher overall quality may be required for a robust TAF model to be produced. Data from the new TAF project are only just becoming available. In the mean time, I show a plot of the TAF model of Hatakayama and Kono (2002) in Figure 14.11. Although the field is not perfectly GAD, the flux lobes seen in the historical field are nearly erased. The remaining non-dipole features may be artifacts of bad data.

It is worthwhile mentioning at this point that one of the primary assumptions in many paleomagnetic studies is that the magnetic field, when averaged over sufficient time, averages to that of a GAD field. This means that if VGPs are averaged from units spanning enough time to average out secular variation, the mean pole is coincident with the spin axis. Such a pole is called a *paleomagnetic pole*. As continents move, they carry with them rock units that retain a record of the spin axis

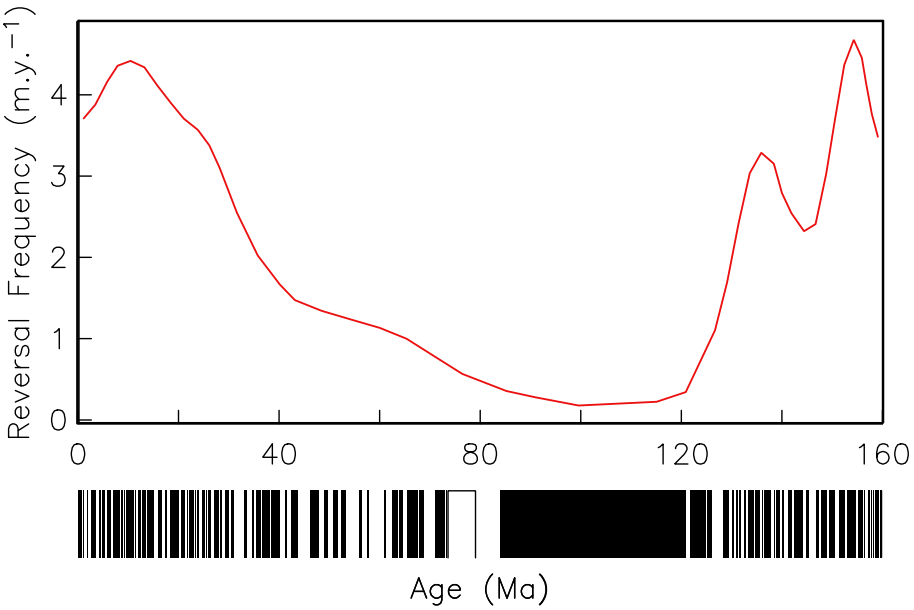

Figure 14.10: Barcode: The Geomagnetic Polarity Time Scale (GPTS) for the last 150 Ma (Berggren et al., 1995; Gradstein et al., 1995). Line traces the reversal frequency (number of reversals in a four million year interval) estimated by Constable (2003).

in the continental reference frame, so these poles tend to form swaths called *apparent polar wander paths* or APWPs. We will learn more about APWPs in later lectures. What is interesting to note now is that how much time is required to average out secular variation is not really known, but is more than 400 years and less than 5 million. Most text books claim that 10^4 - 10^5 years is sufficient (e.g., Butler, 1992). Also poorly defined is the minimum number of sampling sites required for a "good" average. Butler (1992) recommend at least ten, while ranging from ten while (Tauxe et al., 2003) suggest that approximately 100 sites are required to fully sample secular variation.

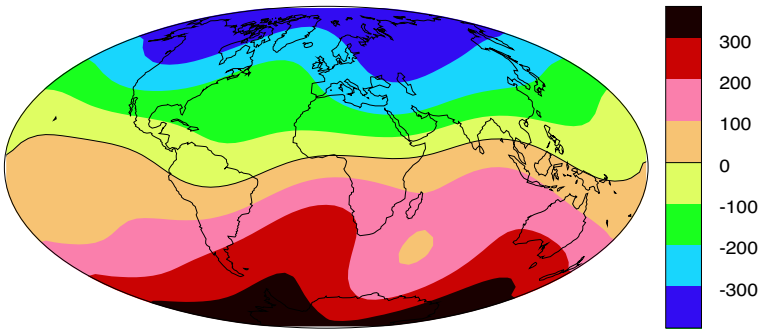

Figure 14.11: Time averaged radial magnetic field evaluated at the core mantle boundary. [Data from Hatakeyama and Kono. 2002.]

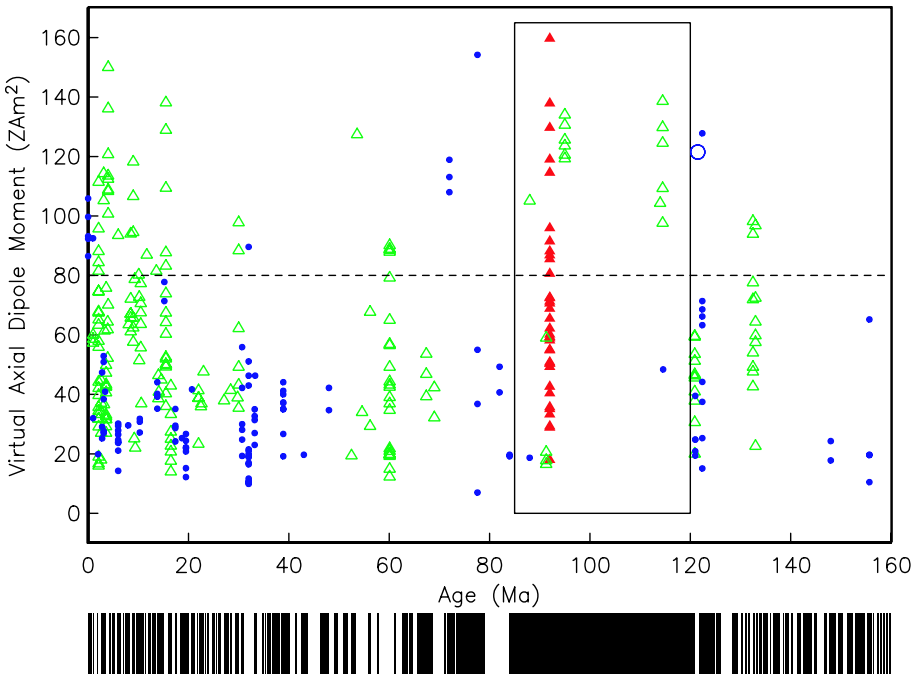

Figure 14.12: Summary of VADM data versus age compiled by Tauxe (in press). Green triangles are from lava flows. Red triangles arebasaltic glass data from the Troodos ophiolite. Dots are the DSDP/ODP submarine basaltic glasses. The present field is the dotted line. The thin solid line is the average dipole moment calculated assuming a log-normal distribution of the glass data. At the bottom is the Geomagnetic Polarity Time scale. [Figure from Tauxe, in press.]

14.6 Long term changes in paleointensity

As well as retaining a record of the direction of the magnetic field when cooled from high temperature,the magnetization in a rock has an intensity that is also a function of field magnitude. It is sometimes possible to estimate the magnitude of the Earth's field from geological samples. We plot a compilation of such data since the Jurassic in Figure 14.12, from Tauxe (in press). Early compilations suggested that much of the Mesozoic had a rather low field intensity (the *Mesozoic dipole low* of Prévot et al. (1990) with an apparent average intensity of about 25% of the present field which is ~ 80 ZAm^2. The compilation of high quality paleointensity data by Tauxe (in press) shows that the Cenozoic also had a predominantly low field, suggesting that the Mesozoic "dipole low" is probably the most common state of the geomagnetic field, with anomalously high values occurring in the latter part of the Cretaceous and early Cenozoic and during the last few thousand years.

14.7 Statistical models of paleosecular variation

From studies of the time averaged field it seems that, at least for the last five million years, the field has been dominantly that of a geocentric axial dipole (GAD). At any particular instant in time, however, there will be significant deviations owing to the non-axial dipole contributions. This,

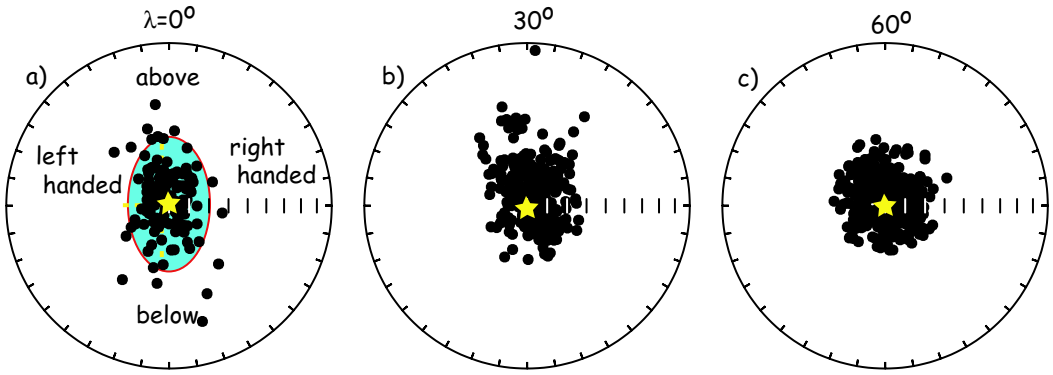

Figure 14.13: a) Paleomagnetic directions from the PSVRL database (see McElhinny and McFadden, 1997) compiled for latitude band 0-5° (N&S). Antipodes of reverse directions are used. The expected direction is at the star at the center of the equal area projection. Directions in the upper (lower) half are above (below) those expected and those to the right (left) are right-handed (left-handed). The red ellipse illustrates the elongation E of the directional data where E is the ratio of the eigenvalues along the maximum and minimum axes (here vertical and E-W respectively). b) Same as a) but for 25-35° (N&S) latitude band. c) Same as a) but for 55-65° (N&S) latitude band.

combined with distortions in the recording process (some of which were discussed in Lecture 5) and decreasing preservation of rocks with increasing age makes evaluating the GAD hypothesis increasingly difficult as we go back in time.

There has been considerable effort in collecting the data relevant to describing the statistical character of the geomagnetic field over time. Selected results from one such collection (that of McElhinny and McFadden, 1997; MM97) are shown in Figure 14.13. Directions from lava flows less than five million years old from particular latitudinal bands are plotted with respect to the expected GAD direction at that particular latitude (D', I' from Lecture 2).

Several things are worth mentioning about the data in Figure 14.13. First, it appears that the equatorial data are more elongate than those from higher latitudes (something we mentioned in Lecture 11). The elongation parameter E can be used to quantify this and is the τ_2/τ_3 ratio where τ_i are the eigenvalues of the orientation matrix (see Appendix C of Lecture 9). Secondly, the scatter in the directional data seems to go down with increasing latitude. The MM97 database culls data with VGP latitudes at an arbitrary angle away from the poles which results in a rather peculiar distribution of directions for the high latitude sites (Figure 14.13c). Third, when the directions are converted to VGP latitudes the scatter increases with increasing latitude.

VGP scatter is quantified by the parameter S (e.g., Cox 1969), defined as:

$$S^2 = (N-1)^{-1} \sum_{i=1}^{N} (\Delta_i)^2$$

where N is the number of observations and Δ is the angle between the i^{th} VGP and the spin axis. S' is the scatter calculated using the VGP collections that were culled of low latitude VGPs and this parameter is shown for the MM97 dataset in Figure 14.13d.

Most early modeling efforts by the paleomagnetic community went toward explaining the scatter in VGPs with latitude. This is but one of the many interesting and useful observations about the

statisitical behavior of the magnetic field and it would be wonderful if we had a way of predicting for a given latitude the full vector distributions expected from the geomagnetic field. To find a "full service" statistical paleosecular variation model, we begin with the work of Constable and Parker; hereafter CP88).

The CP88 statistical paleosecular variation model assumes that the time varying geomagnetic field acts as "Giant Gaussian Process" (GGP) whereby the gauss coefficients (see Lecture 2) g_l^m, h_l^m (except for the axial dipolar term, g_1^0 and in some models also the axial quadrupole term g_2^0) have zero mean. The standard deviations (see Figure 14.14a) are a function of degree l and a fitted parameter α (as in Figure 14.14b), and follow the formula:

$$\sigma_l^2 = \frac{(c/a)^2 l \alpha^2}{(l+1)(2l+1)} \tag{14.1}$$

where c/a is the ratio of the core radius to that of Earth (0.57). Many data sets show a persistent offset in equatorial inclinations at least in reverse polarity data sets, consistent with a small non-zero mean axial quadrupolar term ($\bar{g}_2^0$). We are ignoring this effect here because it is in all studies a small term.

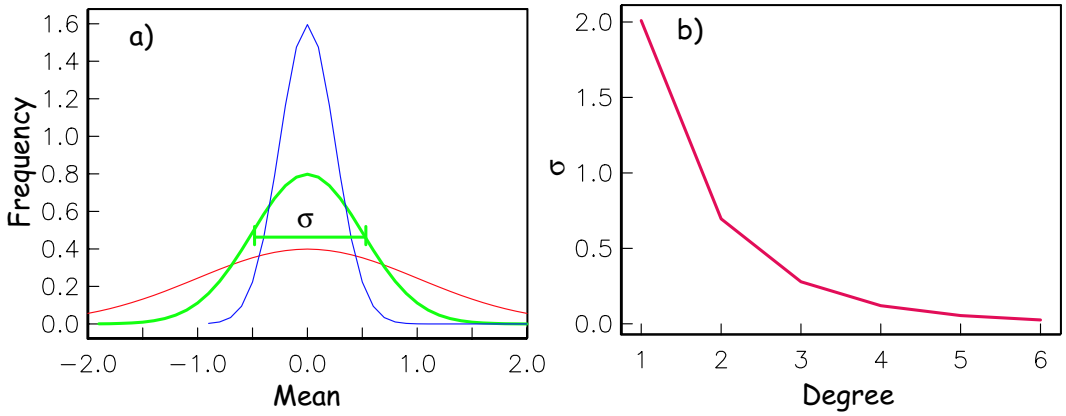

Figure 14.14: a) Illustration of a normal distribution with varying standard deviations. b) Variation of standard deviation σ as a function of spherical harmonic degree l in the CP88 model.

Once the average dipole moment $\bar{g}_1^0$, its standard deviation σ_1^0 and α are fixed, realizations of field models can be created by drawing the gauss coefficients from their respective gaussian distributions. Geomagnetic vectors can then be calculated for any given location using the usual transformation from the geomagnetic potential equation to geomagnetic elements (see Lecture 2).

The principal drawback of the CP88 model is that it fails to fit the observed scatter in the paleomagnetic data with latitude. Most of the subsequent variations on this theme attempted to address the VGP scatter problem by introducing more fitted parameters, losing the elegant simplicity of the CP88 model.

The most recent model of the statistical paleosecular variation genre is the TK03.GAD model of Tauxe and Kent (2004). Like CP88, TK03.GAD has only three parameters: $\bar{g}_1^0$ (set to fit a recent estimate for the long term average intensity of the axial dipole as in Figure 14.12), α as defined in CP88, but fit to the more recent compilation of directional data of McElhinny and McFadden (1997) and a new paramter β which is the ratio of the asymmetric ($l+m$ odd) to the symmetric ($l+m$ even) gauss coefficients for a given l. We show the variation in σ with degree for

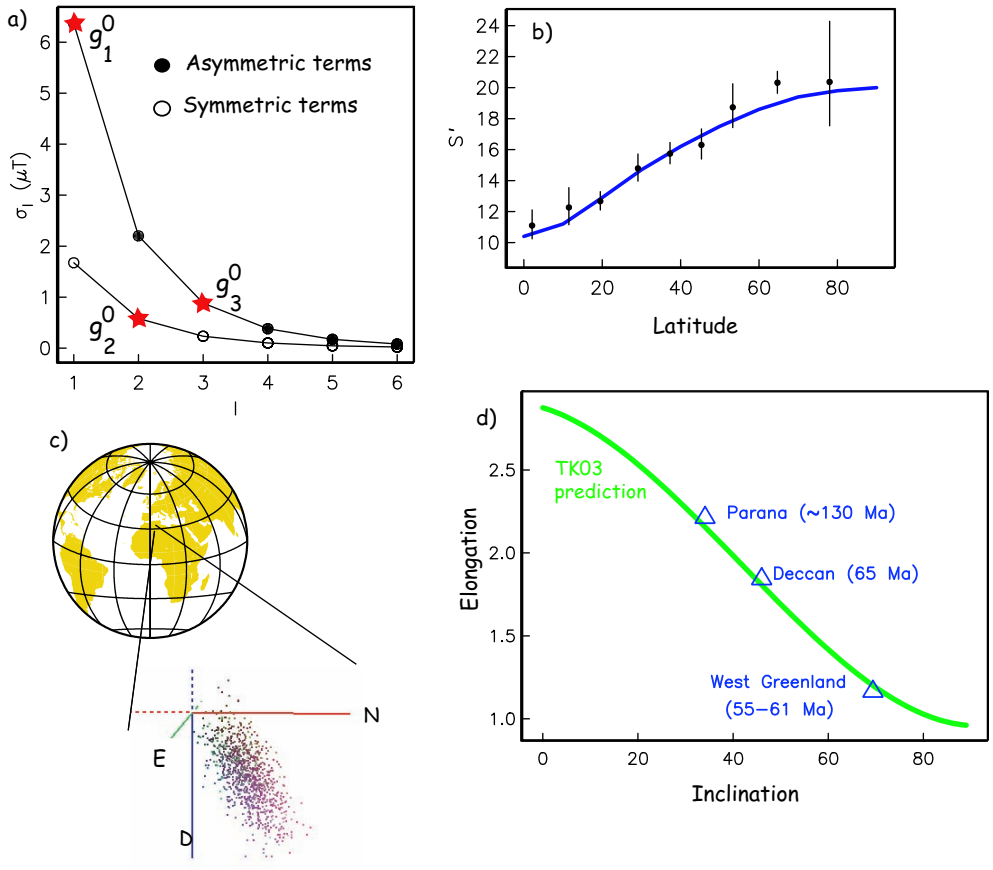

Figure 14.15: a) Variation of the standard deviation σ_l as a function of harmonic degree l for asymmetric and symmetric terms for the statistical field model TK03.GAD. All terms have zero mean except the axial dipole term. b) Estimated behavior of S' from the data compilation of McElhinny and McFadden (1997) (circles). Blue line is the predicted variation of S' from the TK03.GAD model of Tauxe and Kent (2004). c) 1000 vector endpoints from realizations of model TK03.GAD at 30°N. d) Elongation versus inclination predicted from the TK03.GAD model. Triangles are data from large igneous provinces back through time.

the two families (asymmetric and symmetric) in Fig. 14.15a. The term β allows a much improved fit to the paleomagnetic observations while the model retains the simplicity of the CP88 model (see Figure 14.15b).

In Fig. 14.15c we show the vector end points calculated from 1000 realizations of the model at 30°N. The distribution of these vectors predicts what would be observed at that latitude if we had a large number of observations of the geomagnetic field or its paleomagnetic proxies.

Models like TK03 can predict the distribution of geomagnetic field vectors at any location. These, then, can be compared with the observed paleomagnetic data in order to assess whether the data are consistent with the field model. The TK03 model was designed to predict values for S in agreement with those observed in the PSVRL database (see Figure 14.15b), but there are other attributes of the field that can be predicted as well. For example, while inclination can be calculated from the simple dipole formula (see Lecture 2) for any latitude, the elongation of the directions

(e.g., Figure 14.13a) requires a statistical field model. In fact, because elongation goes down with increasing latitude, while inclination goes up, there is a unique elongation inclination pair that is consistent with a given statistical field model. The elongation/inclination trend calculated from the TK03.GAD model is shown in Figure 14.15d.

Data from the last five million years fit the model predictions as it was designed to do, but the model can be tested through time by calculating the elongation/inclination pair for data sets of any age. The requirements are that the data are referenced to paleo-horizontal, that the directions represent the ancient geomagnetic field (they are not biased by overprinting, inclination error, etc.), and that there be a sufficient number to represent the statistical variability of the ancient geomagnetic field. There are not many data sets that satisfy these requirements. Three data sets from ancient large igneous provinces, however do: the Deccan Traps in India (Vandamme et al., 1991), the West Greenland volcanic province (Riisager et al., 2003) and the Paraná Basalts (Ernesto et al., 1999). The elongation/inclination pairs from these three data sets are plotted on Figure 14.15d for comparison with the model predictions. It appears that the TK03.GAD model can be used as a guide to the geomagnetic field behavior for at least the last 130 million years.

Bibliography

Berggren, W., Kent, D., Swisher III, C. & Aubry, M.-P. (1995), A Revised Cenozoic Gochronology and Chronostratigraphy, *in* W. Berggren, D. Kent, M.-P. Aubry & J. Hardenbol, eds, 'Geochronology Time Scales and global Stratigraphic Correlation', SEPM, Tulsa, Oklahoma, pp. 129–212.

Brunhes, B. (1906), 'Recherches sur le direction d'aimantation des roches volcaniques', *J. Phys.* **5**, 705–724.

Clement, B. M. (1991), 'Geographical distribution of transitional VGPs: evidence for non-zonal equatorial symmetry during the Matuyama-Brunhes geomagnetic reversal', *Earth Planet. Sci. Lett.* **104**, 48–58.

Clement, B. M. (2004), 'Dependence of the duration of geomagnetic polarity reversals on site latitude', *Nature* **428**(6983), 637–640.

Clement, B. M. & Kent, D. V. (1984), 'A detailed record of the Lower Jaramillo polarity transition from a southern hemisphere, deep-sea sediment core', *Jour. Geophys. Res.* **89**, 1049–1058.

Constable, C. G. (2003), Geomagnetic reversals: rates, timescales, preferred paths, statistical models and simulations, *in* C. Jones, A. Soward & K. Zhang, eds, 'Earth's Core and Lower Mantle', The Fluid Mechanics of Astrophysics and Geophysics, Taylor and Francis, London.

Constable, C. G., Johnson, C. L. & Lund, S. P. (2000), 'Global geomagnetic field models for the past 3000 years: transient or permanent flux lobes?', *Phil Trans Roy Soc London, Series A* **358**(1768), 991–1008.

Constable, C. & Parker, R. L. (1988), 'Statistics of the geomagnetic secular variation for the past 5 m.y.', *J. Geophys. Res.* **93**, 11569–11581.

Cox, A. (1969), 'Research note: Confidence limits for the precision parameter, K', *Geophys. J. Roy. Astron. Soc* **17**, 545–549.

Cox, A. V., Doell, R. R. & Dalrymple, G. B. (1963), 'Geomagnetic polarity epochs and Pleistocene geochronometry', *Nature* **198**, 1049–1051.

David, P. (1904), 'Sur la stabilité de la direction d'aimantation dan auelques rochess volcaniques', *C. R. Acad Sci. Paris* **138**, 41–42.

Glatzmaier, G. A., Coe, R. S., Hongre, L. & Roberts, P. H. (1999), 'The role of the Earth's mantle in controlling the frequency of geomagnetic reversals', *Nature* **401**(6756), 885–890.

Glatzmaier, G. & Roberts, P. (1996), 'Rotation and magnetism of Earth's inner core', *Science* **274**, 1887–1891.

Gradstein, F., Agterberg, F., Ogg, J., Hardenbol, J., Van Veen, P., Thierry, J. & Huang, Z. (1995), A Triassic, Jurassic and Cretaceous time scale, *in* W. Berggren, D. Kent, M.-P. Aubry & J. Hardenbol, eds, 'Geochronology Time Scales and global Stratigraphic Correlation', SEPM, Tulsa, Oklahoma, pp. 95–126.

Guyodo, Y. & Valet, J. P. (1999), 'Global changes in intensity of the Earth's magnetic field during the past 800 kyr', *Nature* **399**(6733), 249–252.

Hatakeyama, T. & Kono, M. (2002), 'Geomagnetic field model for the last 5 My: time-averaged field and secular variation', *Phys. Earth Planet. Int.* **133**, 181–215.

Hughen, K., Lehman, S., Southon, J., Overpeck, J., Marchal, O., Herring, C. & Turnbull, J. (2004), 'C-14 activity and global carbon cycle changes over the past 50,000 years', *Science* **303**(5655), 202–207.

Hulot, G., Eymin, C., Langlais, B., Mandea, M. & Olsen, N. (2002), 'Small-scale structure of the geodynamo inferred from Oersted and Magsat satellite data', *Nature* **416**, 620–623.

Jackson, A., Jonkers, A. R. T. & Walker, M. R. (2000), 'Four centuries of geomagnetic secular variation from historical records', *Phil Trans Roy Soc London, Series A* **358**(1768), 957–990.

Johnson, C. & Constable, C. (1997), 'The time averged geomagnetic field: global and regional biases for 0-5 Ma', *Geophys. J. Int.* **131**, 643–666.

Johnson, E. A., Murphy, T. & Torreson, O. W. (1948), 'Pre-history of the Earth's magnetic field', *Terr. Magn. atmos. Elect.* **53**, 349–372.

Kent, D., Hemming, S. & Turrin, B. (2002), 'Laschamp excursion at Mono Lake?', *Earth Planet. Sci. Lett.* **197**, 151–164.

Kent, D. V. & Olsen, P. (1999), 'Astronomically tuned geomagnetic polarity time scale for the Late Triassic', *Jour. Geophys. Res.* **104**, 12831–12841.

Korte, M. & Constable, C. (2005), 'Continuous geomagnetic field models for the past 7 millennia: 2. CALS7K', *Geochem., Geophys., Geosyst.* **6**, Q02H16: DOI 10.1029/2004GC000801.

Laj, C., Kissel, C., Mazaud, A., Michel, E., Muscheler, R. & Beer, J. (2002), 'Geomagnetic field intensity, North Atlantic Deep Water circulation and atmospheric Δ^{14}C during the last 50 kyr', *Earth Planet. Sci. Lett.* **200**, 177–190.

Love, J. (1999), 'Reversals and excursions', *A & G* **40**, 6.14–6.19.

Lund, S. P., Liddicoat, J., Lajoie, T. L. K. & Henyey, T. L. (1988), 'Paleomagnetic evidence for long-term (10^4 year) memory and periodic behavior in the Earth's core dynamo process', *Geophys. Res. Lett.* **15**, 1101–1104.

Masarik, J. & Beer, J. (1999), 'Simulation of particle fluxes and cosmogenic nuclide production in the Earth's atmosphere', *J. Geophys. Res* **104**, 12099–12110.

BIBLIOGRAPHY

Masters, G., Laske, G., Bolton, H. & Dziewonski, A. M. (2000), The Relative Behavior of Shear Velocity, Bulk Sound Speed, and Compressional Velocity in the Mantle: Implications for Chemical and Thermal Structure, *in* S. Karato, R. Forte, G. Liebermann, G. Masters & L. Stixrude, eds, 'Earth's Deep Interior', Vol. 117 of *AGU Monograph*, American Geophysical Union, Washington, D.C.

Matuyama, M. (1929), 'On the direction of magnetisation of basalt in Japan, Tyosen and Manchuria', *Proc. Imp. Acad. Jap.* **5**, 203–205.

McElhinny, M. W. & McFadden, P. L. (1997), 'Palaeosecular variation over the past 5 Myr based on a new generalized database', *Geophys. J. Int.* **131**(2), 240–252.

Mercanton, P. (1926), 'Inversion de l'inclinaison magnétique terrestre aux ages géologique', *Terr. Magn. Atmosph. Elec* **31**, 187–190.

Merrill, R. T., McElhinny, M. W. & McFadden, P. L. (1996), *The Magnetic Field of the Earth: Paleomagnetism, the Core, and the Deep Mantle*, Academic Press.

Opdyke, N. D. & Channell, J. E. T. (1996), *Magnetic Stratigraphy*, Academic Press.

Prévot, M. & Camps, P. (1993), 'Absence of preferred longitude sectors for poles form volcanic records of geomagnetic reversals', *Nature* **366**, 53–57.

Prévot, M., Derder, M. E. M., McWilliams, M. & Thompson, J. (1990), 'Intensity of the Earth's magnetic field: evidence for a Mesozoic dipole low', *Earth Planet. Sci. Lett.* **97**, 129–139.

Selkin, P. & Tauxe, L. (2000), 'Long-term variations in paleointensity', *Phil. Trans. Roy. Soc. Lond.* **358**, 1065–1088.

Smith, P. J. (1967), 'The intensity of the ancient geomagnetic field: a review and analysis', *Geophys. J.R. astr. Soc.* **12**, 321–362.

Song, X. & Richards, P. G. (1996), 'Seismological evidence for differential rotation of the Earth's inner core', *Nature* **382**, 221–224.

Strik, G., Blake, T. S., Zegers, T. E., White, S. H. & Langereis, C. G. (2003), 'Palaeomagnetism of flood basalts in the Pilbara Craton, Western Australia: Late Archaean continental drift and the oldest known reversal of the geomagnetic field', *J. Geophys. Res* **108**, doi:10.1029/2003JB002475.

Tauxe, L. (2005), 'Inclination flattening and the geocentric axial dipole hypothesis', *Earth Planet. Sci. Lett.* **233**, 247–261.

Tauxe, L. (in press), 'Long term trends in paleointensity: The contribution of DSDP/ODP submarine basaltic glass collections', *Phys. Earth Planet. Int.* .

Tauxe, L., Constable, C., Johnson, C., Miller, W. & Staudigel, H. (2003), 'Paleomagnetism of the Southwestern U.S.A. recorded by 0-5 Ma igneous rocks', *Geochem., Geophys., Geosyst.* p. DOI 10.1029/2002GC000343.

Tauxe, L. & Kent, D. V. (2004), A simplified statistical model for the geomagnetic field and the detection of shallow bias in paleomagnetic inclinations: Was the ancient magnetic field dipolar?, *in* e. a. Channell, J.E.T., ed., 'Timescales of the Paleomagnetic field', Vol. 145, American Geophysical Union, Washington, D.C., pp. 101–116.

Yukutake, T. (1967), 'The westward drift of the Earth's magnetic field in historic times', *J. Geomag. Geoelectr.* **19**, 103–116.

Lectures in Paleomagnetism, 2005
by Lisa Tauxe

Citation:
http://earthref.org/MAGIC/books/Tauxe/2005/

June 16, 2005

Chapter 15

The GPTS and magnetostratigraphy

Suggested Reading

For background:
Chapter 9: Butler (1992)
Chapters 4 & 5: McElhinny and McFadden (2000)
To learn more:
Opdyke and Channell (1996)
Oreskes (2001)
Glen (1982)
http://www.stratigraphy.org/
Gradstein et al., 2004

15.1 Introduction

The geological time scale is a list of ordered events placed in a temporal/spatial context. Time (see Figure 15.1) is broken into Eons (e.g., Phanerozoic, Proterozoic), Eras (e.g., Mesozoic, Cenozoic), Periods (e.g., Cretaceus, Paleogene), Series (e.g, Oligocene, Miocene) and Stages (e.g, Messinian, Zanclean). The fundamental unit, the stage is ideally defined by its base at a particular place and many such "Global Standard Section and Points", or GSSPs have been identified. Numerical ages are attached to these stage boundaries by a variety of methods. Some methods have explicit numerical age control (e.g., from the predictable decay of radioactive isotopes or variations in climate caused by the relationship of the Earth and the sun), while others have only relative age information (e.g., the progressive change of fossil assemblages, or the identification of contemporaneous events in the geological record). Almost always numerical ages are estimated by correlation, interpolation, and/or extrapolation. As such, the geological time scale is a work in constant revision. The most recent is that of Gradstein et al. (2004), which will probably be the standard for about a decade.

One of the important tools in assembling the geological time scale is the geomagnetic polarity time scale (GPTS). Identification of a particular polarity reversal allows direct correlation of isochronous events between continental and marine sequences, between northern and southern hemispheres and between the Pacific and Atlantic realms. Apart from the identification of unique ash layers or the very rare geochemical tracers like an iridium spike, there is no better way to tie together the stratigraphic record. In this lecture we will review how the modern GPTS was constructed and will briefly consider some applications of the GPTS to geological problems.

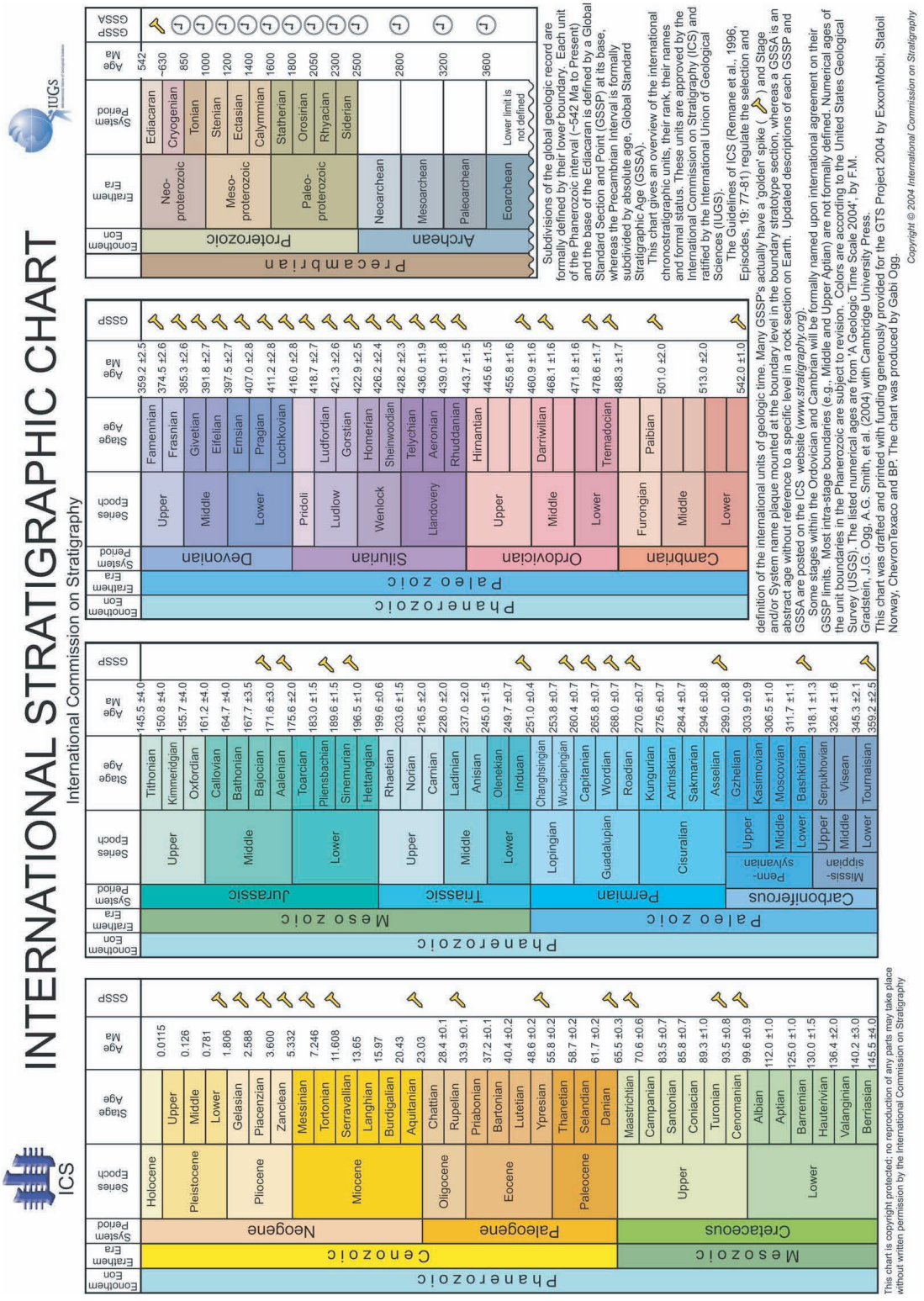

Figure 15.1: The International Stratigraphic Chart. (See interactive version at: http://www.stratigraphy.org/.)

15.2 Early efforts in defining the GPTS

We learned in Lecture 14 that early workers discovered reversely magnetized rocks in the early 20^{th} century, and some suspected that there was a globally synchronous pattern of polarity reversals (e.g., Matuyama, 1929). However, it was not until combined studies of both age (using the newly developed age dating technique using the decay of radioactive potassium to argon) and polarity (from globally distributed lava flows) that the first Geomagnetic Polarity Time Scales (GPTS) began to take shape (Figure 15.2; see e.g., Cox et al., 1963, 1964).

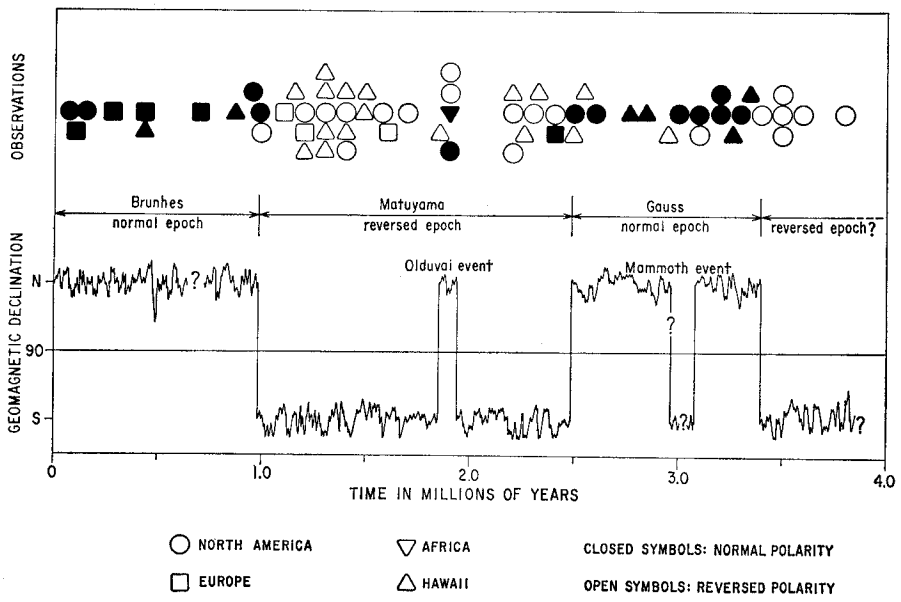

Figure 15.2: Magnetic polarities from volcanic units plotted against age as determined by the potassium-argon method. The first three long intervals were named after famous geomagnetists. [Figure from rom Cox et al., 1964].

Cox et al. (1964) broke the polarity sequence into times of dominantly normal polarity (i.e., the field vector more or less parallel to today's field) and times of dominantly reverse polarity (i.e., the field vector more or less antipodal to today's field). They called these time units "Epochs" (note that they are now known as *Chrons*). The first three were named after some major players in geomagnetism: B. Brunhes (who first discovered reversely magnetized rocks), M. Matuyama (who first saw that the reversely magnetized rocks were older than the normal ones), and F. Gauss (who worked out the first geomagnetic field model). A fourth was later named after W. Gilbert (who first realized that the Earth itself was a magnet). Cox et al. (1964) also recognized the existence of shorter intervals which they called "Events" (e.g., the Olduvai and Mammoth events in Figure 15.2; note that events are now known as *sub-chrons*). These shorter intervals are traditionally named after the place where they were first documented.

Time scales constructed in the manner of Cox and colleagues based on discrete polarity, date pairs are necessarily limited by the uncertainty in the dating of young basalts. In the early 60's this uncertainty exceeded the average duration of polarity intervals for times prior to about five million years (except for the very long intervals of a single polarity like the Permian "Kiaman" interval which lasted over 50 million years).

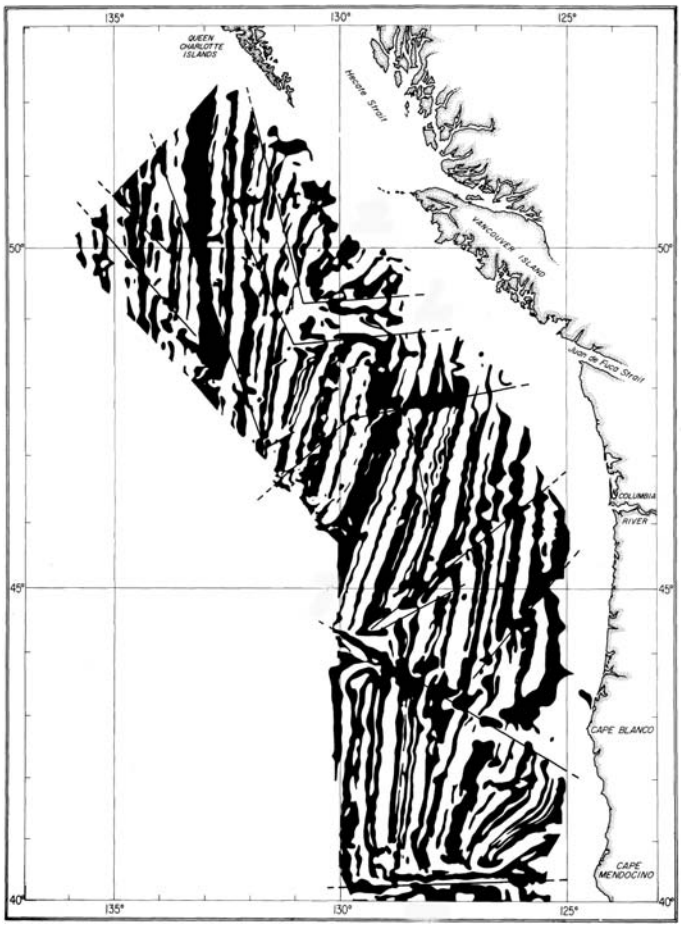

Figure 15.3: Map of the pattern of magnetic anomalies off northwestern North America. [Modified from Mason and Raff, 1961.]

Shortly after the publication of Cox et al. (1963) and McDougall and Tarling (1963), which essentially laid to rest doubts about the validity of geomagnetic reversals and sketched the rudiments of the first GPTS, Vine and Matthews (1963) put ideas about polarity reversals and the bizarre "magnetic stripes" in marine magnetic anomaly data (Figure 15.3; e.g., Mason and Raff, 1961) together as strong proof of sea floor spreading. The realization that the marine magnetic anomalies were a record of polarity history meant that the template for the pattern of reversals could be extended far beyond the resolution of the K-Ar method (see Figure 15.4, e.g., Pitman and Heirtzler 1966). It was not long before such a template for paleomagnetic reversals based on magnetic anomalies (numbering 1 to 31) was proposed. By assigning an age of 0 Ma to the ridge crest, an age of 3.35 Ma to the of the Gauss/Gilbert boundary (stars in Figure 15.4) and assuming constant spreading for the South Atlantic anomaly sequence, Heirtzler et al. (1968) produced a GPTS that extended to about 80 Ma. The age of anomaly 31 was estimated to be about 71.5 Ma. The truly astounding thing is that the currently accepted age for anomaly 31 is about 68 Ma (e.g., Cande and Kent, 1995) a difference of only a few percent!

In a parallel effort to the marine magnetic anomaly work, several groups were investigating the magnetic stratigraphy of deep sea sediment cores (e.g., Harrison, 1966 and Opdyke et al. 1966). In

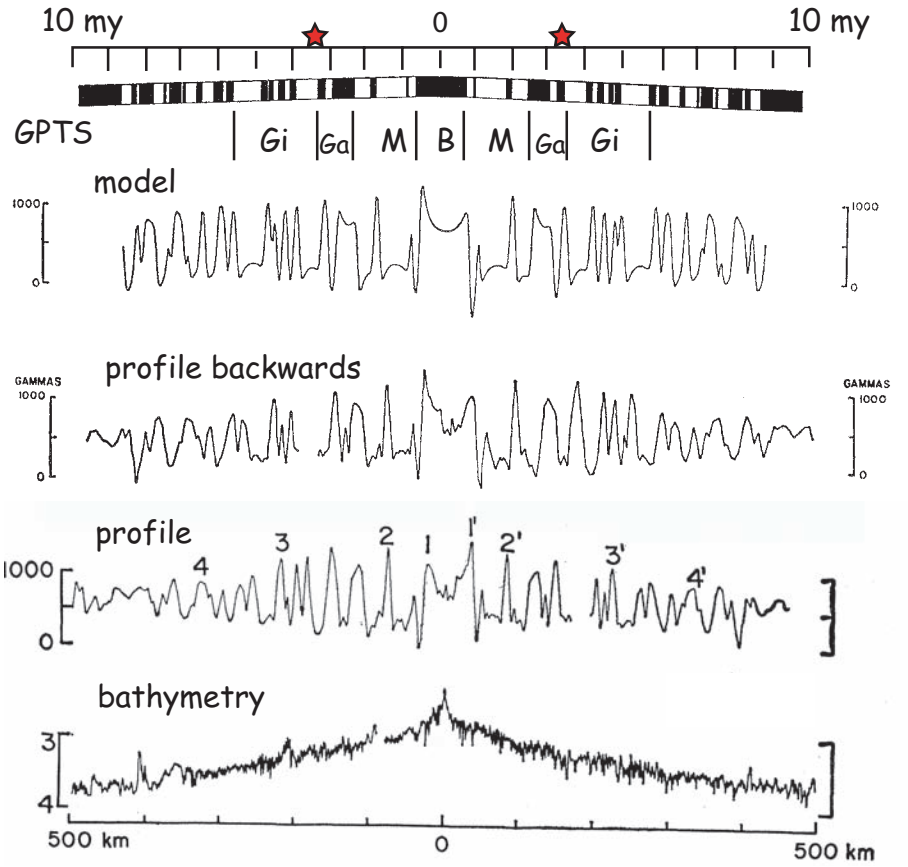

Figure 15.4: A profile of bathymetry (bottom panel) and magnetic anomalies (labelled "profile") obtained from the East Pacific Rise (Eltanin 19 profile, also known as "the magic profile".) The magnetic anomaly profile, flipped east-to-west is replotted above (labelled "profile backwards"). Assuming a magnetization of a 500 m thick section of oceanic crust (black and white pattern above), a model for the predicted anomalies could be generated (labelled "model"). Above is the inferred time scale. The position of the Gauss/Gilbert boundary is marked by stars. [Adapted from Pitman and Heirtzler, 1966.]

Figure 15.5 we show the record of inclination versus depth of Opdyke et al., (1966) obtained from a core taken off the coast of Antarctica. Upwardly pointing (negative) inclinations are normal and positive inclinations are reversely magnetized. This polarity pattern was correlated to the currently available time scale which included the new "event" known as the Jaramillo (Doell and Dalrymple, 1966) and revised age estimates for the "epoch" boundaries.

The polarity sequence from magnetostratigraphic records was extended back into the Miocene by Opdyke et al. (1974, see Figure 15.6). The epochs, defined by the magnetostratigraphy could not easily be correlated to the anomaly data shown in Figure 15.4 and the two numbering schemes (anomaly numbers and epoch numbers) remained separate until the correlation between the two was deemed sufficiently robust.

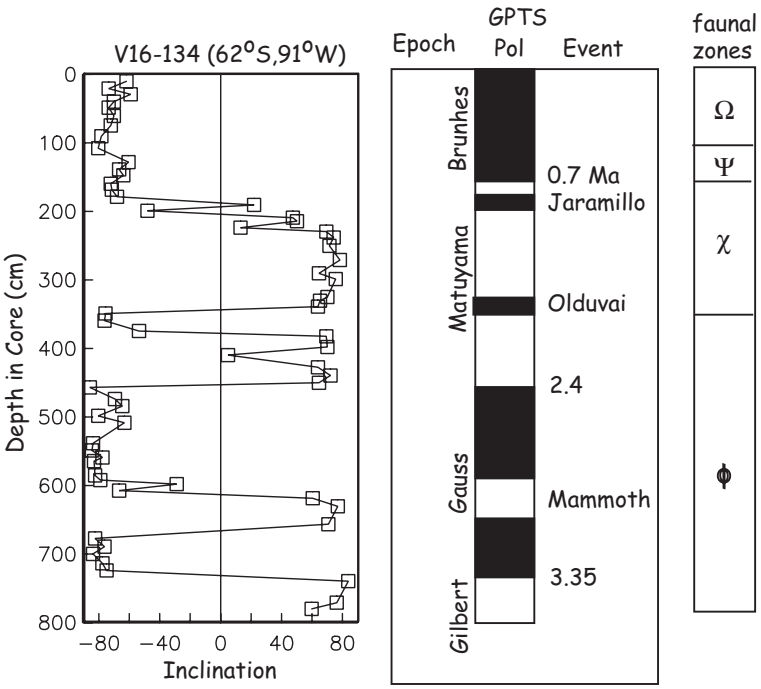

Figure 15.5: left: Inclinations from core V16-134 plotted against depth. middle: The GPTS as it was known in 1966. Faunal zones of the southern ocean identified within the core. [Adapted from Opdyke et al., 1966.]

15.2.1 A note about terminology

The Epoch/Event terminology was changed to Chron/sub-chron in 1979 by international agreement (Anonymous, 1979). Along with chrons and sub-chrons, the international subcommission defined "superchrons". Cande and Kent (1992) later defined "cryptochrons". Superchrons are extremely long polarity intervals, such as the Kiaman (also known as the Permo-Carbaniferous Reverse Superchron or PCRS) which lasted from 298 to 265 Ma (Gradstein et al., 2004) and the Cretaceous Normal Superchron (CNS: 84-125 Ma in Gradstein et al., 2004) Cryptochrons are "tiny wiggles" in the marine magnetic anomaly record that are too short to be unequivocally interpreted as full reversals (i.e., shorter than about 30 kyr). Some of these may be related to geomagnetic "excursions" (see Lecture 14.)

In an attempt to rationalize the Neogene chron (event) terminology (which numbered chrons from 5-22) and the anomaly terminology (running from 1 to about 6C), Cande and Kent (1992) broke the time scale into chrons and sub-chrons based on the anomaly numbering scheme distinguishing chrons from anomalies with the letter "C". Because the anomaly numbering system only had 34 anomalies from the end of the CNS to the present, many more subdivisions were required, particularly in the very "busy" interval between Anomalies 5 and 6. These anomalies are denoted 5' 5A, 5AA, 5AB and the like, so the present Neogene GPTS is a nightmare of chron and sub-chron names like C4n.1r or C5ADr where the "n"s and "r"s refer to polarity and the .1s refer to sub-chrons within chrons (e.g, C4n). For a complete listing of the GPTS since the CNS, please refer to the Appendix.

15.2.2 The addition of biostratigraphy

An interesting aspect to the magnetostratigraphic work typified by Opdyke et al. (1966) was the identification of biostratigraphic zones (Ω to ϕ in Figure 15.5) based on faunal assemblages in the core. These zones are therefore tied directly to the magnetostratigraphic record. The addition of biostratigraphy to the GPTS problem brought new possibilities for the calibration of the time scale in that certain boundaries could be dated by radioisotopic means using datable layers (e.g., ash beds) within stratigraphic sections. If a particular well dated biostratigraphic horizon could be tied to the magnetostratigraphic record, then the associated numerical ages could be attached to the GPTS. Exploiting this possibility, LaBrecque et al. (1977) used the magnetostratigraphic record in Italian carbonates (e.g., Alvarez et al., 1977) which tied the Cretaceous/Tertiary (K/T) boundary to a reverse polarity zone between two normal polarity intervals correlated with marine magnetic anomalies 29 and 30. The accepted age for the K/T boundary at the time was 65 Ma (van Hinte, 1976) which is virtually identical to the currently accepted age of 65.5± 0.3 Ma (Gradstein et al., 2004), so ages for the anomalies numbered 1-34 could be estimated by interpolation and extrapolation. Note that anomaly 14 is now thought to be a cryptochron (S. Cande, pers. comm.) and has not been included as a numbered anomlay in timescales since LaBrecque et al., 1977.)

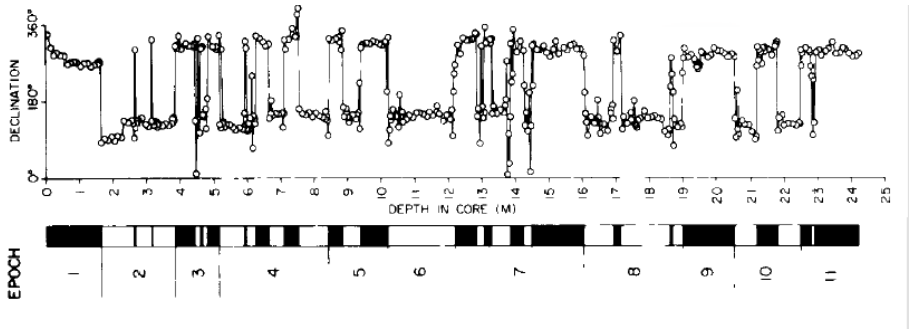

Figure 15.6: Declinations from deep-sea piston core RC12-65 from the equatorial Pacific Ocean (using an arbitrary zero line because the cores were not oriented). The epoch system of magnetostratigrahic nomenclature was extended back to Epoch 11 in this core and to Epoch 19 in companion cores. [Figure from Opdyke et al., 1974].

15.2.3 Astrochronology

Until 1990, the GPTS was dated using numerical ages based on the decay of radioactive elements (largely the K/Ar method). An alternative approach to dating of stratigraphic sequences long in use is based on the climatically induced changes in lithology or stable isotopic records in sediments that are caused by variations in the Earth's orbit around the sun. The relationship of the Earth's orbit to the sun results in changes in the amount and latitudinal distribution of solar radiation (so-called "insolation") reaching the Earth as a function of time. According to the *Milankovitch hypothesis* (e.g., Hays et al. 1976), changes in insolation at high northern latitudes vary with periodicities reflecting precession (with a beat of around 21 kyr), obliquity ($\sim$ 40 kyr) and eccentricity ($\sim$ 100 kyr). These cahnges in insolation resulted in measurable changes in the chemistry of the oceans and atmospheres and left an indelible mark on the lithostratigraphy (e.g., variations in carbonate) and the isotopic ratios of oxygen (the light isotope ^{16}O gets preferentially incorporated into glacial ice at

high latitudes, leaving the oceans richer in ^{18}O.) Because the precession, obliquity and eccentricity of Earth's orbit can be robustly predicted as a function of age at least for several million years (and perhaps even 10s of millions of years), identification of these patterns in the stratigraphic record allow numerical ages to be attached to the sedimentary sequence. This is a method known as "astrochronology". Starting with Shackleton (1990) and Hilgen et al. (1991), astrochronology has been applied to the GPTS (see e.g., Figure 15.7).

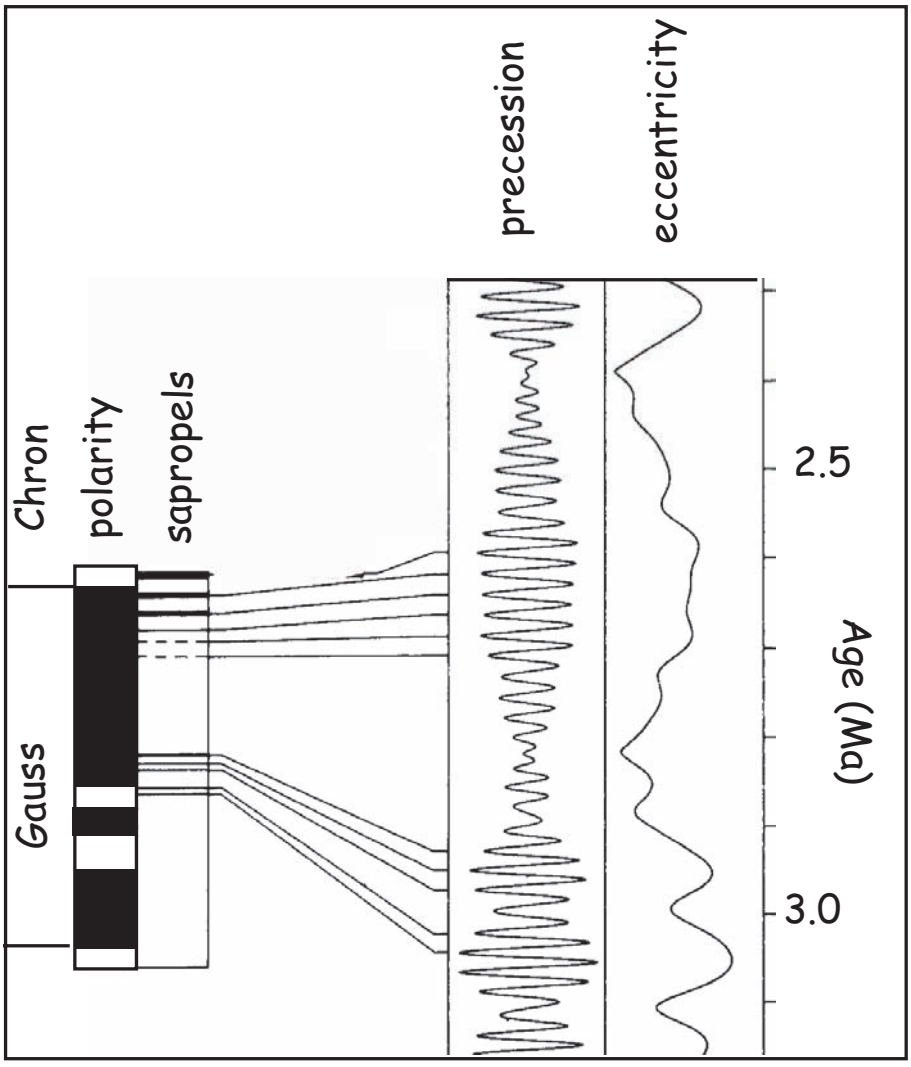

Figure 15.7: Illustration of the "astrochronology" dating method. The sequence of polarity intervals and climatically induced sapropel layers is correlated to the GPTS (left) and the orbital cycles (right). The numerical ages from the orbital cycles can then be tranferred to the GPTS. [Adapted from Hilgen et al., 1991.]

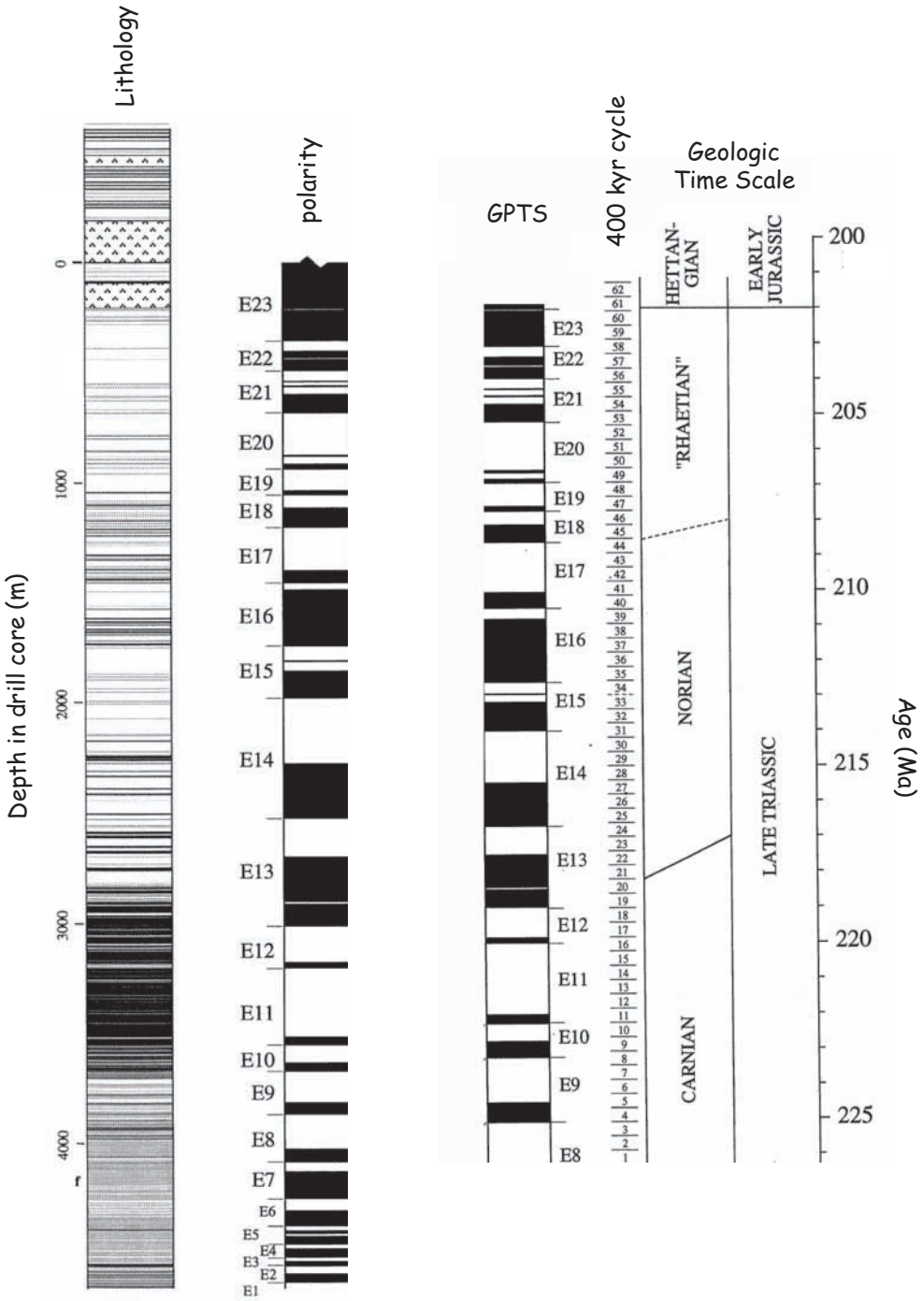

Figure 15.8: Left: Lithostratigraphic and magnetostratigraphic pattern derived from overlapping drill cores into the Newark Basin. Right: Interpretation for the GPTS based on astrochronology and correlation to the Geological Time Scale. [Adapted from Kent et al., 1995 and Kent and Olson, 1999.]

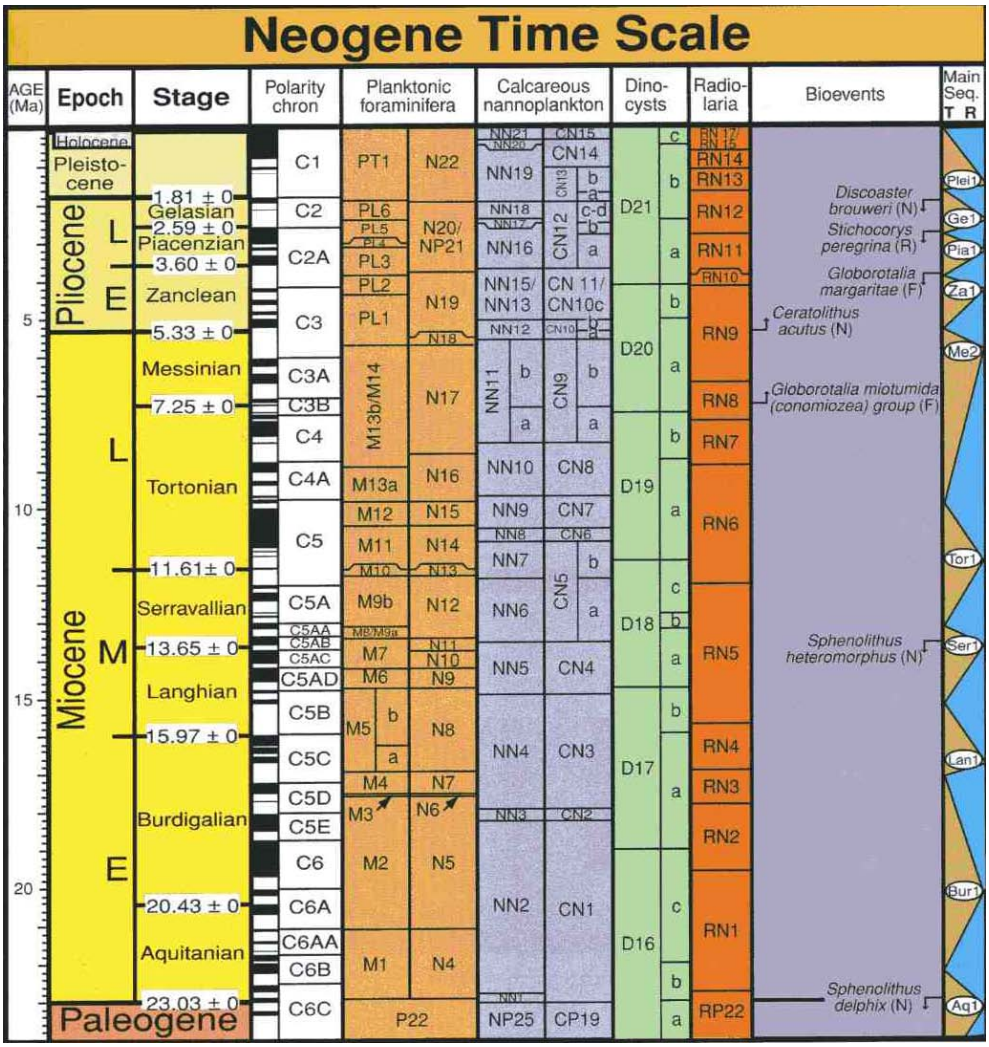

Figure 15.9: The Neogene of the Geological Time Scale. [Figure from Gradstein et al., 2004.]

15.2.4 The Mesozoic and beyond

By the early 70s the large scale structure of the marine magnetic anomalies had been sketched out. There was a young set numbered 1-34 which terminated in a vast expanse of oceanic crust with no correlatable anomalies known as the "Cretaceous Quiet Zone" or CQZ. The Cretaceous Quiet Zone is well established as being a period of time with very few (or no!) reversals. The CQZ is synonymous with the Cretaceous Normal Superchron, or CNS and extends from the middle of the middle of the Santonian ($\sim$ 84 Ma) to the middle of the Aptian stage ($\sim$ 125 Ma). On the old end of the CQZ was another set of anomalies, known as the "M-sequence" (e.g., Larson and Heirtzler, 1972). These extend from M0 (which bounds the old end of the CQZ) to M25 based on marine magnetic anomalies.

Because the oldest sea floor is about 180 Ma and the oldest marine magnetic anomaly sequence is very poorly expressed (it is known as the "Jurassic Quiet Zone"), polarity intervals older than

about M25 are defined using various magnetostratigraphic sections obtained from land exposures. The M-squence of polarity intervals was extended to about M39 using sections from Spain and Poland. The M-sequence has now been fairly firmly tied to geological stages and thereby calibrated in terms of numerical ages (see e.g., Gradstein et al., 2004).

As we go back farther in time, the GPTS necessarily becomes more sketchy. What is required is long sequences of stratigraphic sections with few gaps and reasonably constant sediment accumulation rates. Such sequences are difficult to identify and piece together so the GPTS will only slowly be completed.

One very long part of the GPTS in the middle to late Triassic is, however, quite well known. Using a series of drill cores with overlapping sections, Kent et al. (1995) defined a set of polarity intervals labelled E1 to E23 (see Figure 15.8). Kent and Olson (1999) interpreted lithologic cycles within sections as 400 kyr climatic cycles and calibrated their composite depth scale to time. Their resulting time scale is shown to the right in Figure 15.8.

Painstakingly acquired overlapping stratigraphic sections will be the basis for future extensions of the GPTS. Stay tuned - this is very much a work in progress and is advancing rapidly.

15.3 Current Status of the Geological Time Scale.

For reference, we include the dates of the most recent GPTS in the Appendix. As an example of the detailed correlations between the polarity time scale and various biological time scales, we show the Neogene portion from Gradstein et al. (2004) in Figure 15.9. For details, the reader is referred to the original reference. Please note that the time scale is a consensus document that balances a tremendous amount of information from a variety of sources. As such, it is subject to change, although not change should not be frequent or drastic.

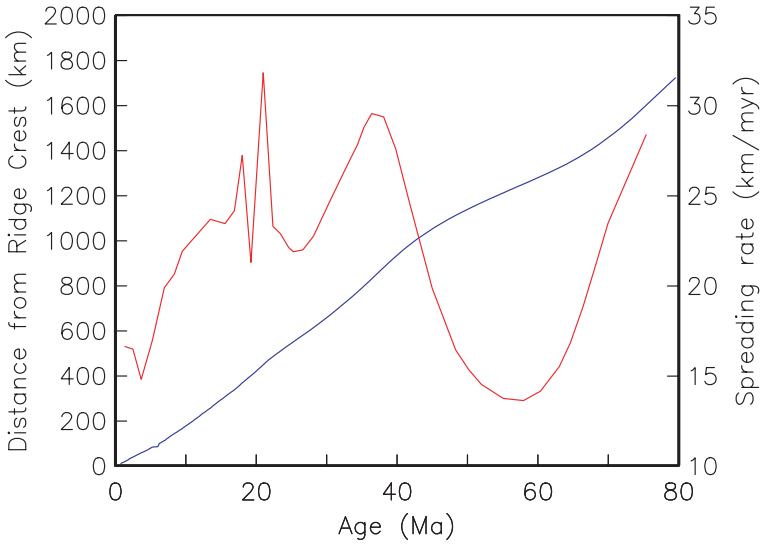

Figure 15.10: Plot of distance from the ridge crest in the South Atlantic versus age using the GPTS of Gradstein et al., (2004). The differential of this curve gives instantaneous spreading rate.

15.4 Applications

15.4.1 Dating geological sequences

An important application of the fact that the geomagnetic field undergoes frequent reversals, whose ages are fairly well known, at least for the last hundred million years or so, is to use the GPTS as a dating tool for stratigraphic sequences. The pattern of polarity zones is determined by measuring the magnetization of samples taken from the stratigraphic section. If the polarity zones in the so-called *magnetostratigraphy* can be unambiguously correlated to the GPTS, they constitute a precise temporal framework for sedimentary or volcanic sequences. Such records have proved invaluable for correlating stratigraphic information on a global basis and are the primary means for calibrating the Cenozoic fossil record with respect to time. Furthermore, knowing the ages of polarity reversals allows the calculation of rates of processes such as sea-floor spreading, sediment accumulation, extinctions and speciation and provide independent verification of orbital calculations.

Sedimentation is not always a continuous process in many environments and a stratigraphic section may have gaps of significant duration. Also, the magnetic recording process of the rock may be unreliable over all or part of the section. Furthermore, incomplete sampling may give a polarity log that is undersamples. For these reasons, there must be ways of establishing the reliability of a given polarity sequence and the robustness of a given correlation. For a more complete discussion of the subject of magnetostratigraphy, the reader is referred to the comprehensive book by Opdyke and Channell (1996) entitled *Magnetic Stratigraphy*. Briefly, the elements of a good magnetostratigraphic study include the following points.

- It must be established that a single component of magnetization can be (and has been) isolated by stepwise demagetization. To demonstrate this, examples of demagnetization data should be shown (see Lecture 9). There must also be a clear discussion of how directions were determined for each sample.

- Geological materials are not always perfect recorders of the geomagnetic field. It often happens that a given stratigraphic horizon has no consistent magnetization. Multiple samples per horizon (say three to five separately oriented samples) with coherent directions (i.e., non-random by tests such as those discussed in Lecture 11) indicate that the magnetization at a given level is reproducible. While it is not always possible to take multiple samples (for example from limited drill core material), it is alway desirable and certainly should be done whenever possible.

- The directional data must fall into two clearly separated groups that are identifiable as either normal or reverse polarity. If fully oriented samples have been taken, the data can be plotted on an equal area projection (see Appendix to Lecture 2) and/or subjected to the reversals test (Lectures 11 and 12). Often drill cores are not azimuthally oriented, and the paleomagnetic inclination is the only indicator of polarity. In this case, one can plot histograms of the inclination and establish that the two polarities (positive and negative) have discrete "humps" at the values expected for the site (paleo)latitude.

- The average direction should be compared with the reference field (the GAD field; see Lecture 2), and the expected direction based on the age of the formation for the sampling location. This can be done on an equal area projection, or in cartesian coordinates (e.g., using Fisher statistics or a bootstrap as described in Lectures 11 and 12).

- Field tests (such as the fold test or conglomerate test as described in Lecture 9) that compare the age of magnetization relative to the rock formation are desirable.
- An independent estimate of the approximate age of the sequence is necessary. The better the age constraints, the more confident we can be in a given interpretation.
- The magnetostratigraphic pattern should match the polarity time scale. Few polarity zones should be ignored either in the section or in the time scale. Ideally, each polarity zone should be based on multiple sites in the section.

15.4.2 Measuring rates

One very useful application of the GPTS is to infer rates of for example spreading, sediment accumulation, etc. We illustrate this approach in Figure 15.10. Distance from the ridge crest of each identified anomaly is plotted against age. The previous standard GPTS based on the work of Cande and Kent (1992) built smooth changes in spreading rate into the GPTS itself. The Gradstein et al. (2004) time scale does not have this constraint for the Neogene, because much of it was calibrated using astrochronological methods. As a result there are sharp changes in spreading rate implied, which may be artifacts of the method of calibration. It may therefore be preferable to calibrate the time scale using some balance between astrochronology, smooth variations in spreading rate and radioisotopic methods.

15.4.3 Tracing of magnetic isochrons

Most magnetostratigraphic applications involve determination of a magnetostratigraphy through a stratigraphic sequence of sediments. Because polarity transitions occur relatively rapidly, the horizon bounding two polarity zones may represent an almost isochronous level. It is therefore possible to use magnetostratigraphy in a lateral sense, in order to delineate isochronous horizons within a given package of sediments (Behrensmeyer and Tauxe. 1982). In Figure 15.11, we show the application of magnetostratigraphy for tracing isochrons in a series of stratigraphic sections. The small sand body (darker gray) labeled "A" appears to have removed the normal polarity zone seen in sequences on the right of the figure either by erosion or because of unsuitable paleomagnetic properties of sand. Sand bodies B and C appear to represent quasi-isochronous horizons.

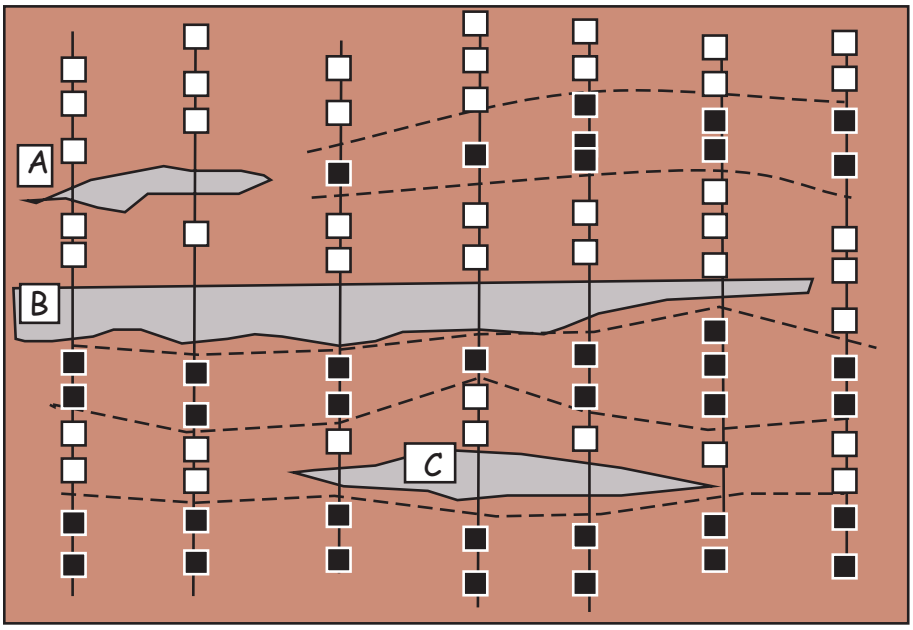

Figure 15.11: Application of magnetostratigraphic techniques for delineating isochronous horizons in a series of stratigraphic sections. The polarities of sampling sites are shown by open (reverse) and solid (normal) symbols. The light shading indicates silts, while the darker shaded units (labelled A-C) represent sand bodies, which were not suitable for paleomagnetic analysis in this example. The inferred isochrons (horizons that separate polarity zones) are shown as heavy dashed lines.

Appendix

Table A1: Geomagnetic polarity time scale of Gradstein et al. (2004).

Chron	sub-Chron	Dist. of old end from SA ridge (km)	Age of base (Ma)	alternate names
C1	C1n	12.14	0.781	Brunhes
	C1r.1	15.37	0.988	Matuyama
	C1r.1n	16.39	1.072	Jaramillo
	C1r.3r	27.8	1.778	
C2	C2n	31.51	1.945	Olduvai
	C2r.1r	35.04	2.128	
	C2r.1n	35.57	2.1482	Reunion
	C2r.2r	41.75	2.581	
C2A	C2An.1n	49.44	3.032	Gauss
	C2An.1r	50.7	3.116	Kaena
	C2An.2n	52.31	3.207	
	C2An.2r	54.1	3.33	Mammoth
	C2An.3n	58.03	3.596	
	C2Ar	66.44	4.187	Gilbert
C3	C3n.1n	68.23	4.3	
	C3n.1r	70.56	4.493	
	Cn.2n	73.56	4.631	
	C3n.2r	76.76	4.799	
	C3n.3n	78.26	4.896	
	C3n.3r	80.4	4.997	
	C3n.4n	84.68	5.235	
	C3r	86.87	6.033	
C3A	C3An.1n	101.42	6.252	
	C3An.1r	103.92	6.436	
	C3An.2n	109.6	6.733	
	C3Ar	116.7	7.14	
C3B	C3Bn	119.74	7.212	
	C3Br.1r	120.62	7.251	
	C3Br.1n	121.3	7.285	
	C3Br.2r	124.68	7.454	
	C3Br.2n	125.35	7.489	
	C3Br.3r	126.48	7.528	
C4	C4n.1n	129.08	7.642	
	C4n.1r	130.83	7.695	
	C4n.2n	139.37	8.108	
	C4r.1r	142.49	8.254	
	C4r.1n	143.15	8.3	
	C4r.2r	152.32	8.769	

Chron	sub-Chron	Dist. of old end	Age of base (Ma)
C4A	C4An	159.16	9.098
	C4Ar.1r	163.49	9.312
	C4Ar.1n	165.16	9.409
	C4Ar.2r	171	9.656
	C4Ar.2n	172.34	9.717
	C4A.3r	174.47	9.779
C5	C5n.1n	177.49	9.934
	C5n.1r	178.38	9.987
	C5n.2n	201.13	11.04
	C5r.1r	203.44	11.118
	C5r.1n	204.51	11.154
	C5r.2r	213.04	11.554
	C5r.2n	214.28	12
	C5r.3r	223.52	12.014
C5A	C5An.1n	226.81	12.116
	C5An.1r	229.23	12.207
	C5An.2n	234.25	12.415
	C5Ar.1r	240.65	12.73
	C5Ar.1n	241.35	12.765
	C5Ar.2r	242.9	12.82
	C5Ar.2n	243.94	12.878
	C5Ar.3r	247.92	13.015
C5AA	C5AAn	251.38	13.183
	C5AAr	255.19	13.369
C5AB	C5ABn	260.03	13.605
	C5ABr	264.53	13.734
C5AC	C5ACn	273.28	14.095
	C5ACr	275.66	14.194
C5AD	C5ADn	285.8	14.581
	C5ADr	290.17	14.784
C5B	C5Bn.1n	292.24	14.877
	C5Bn.1r	295.63	15.032
	C5Bn.2n	298.45	15.16
	C5Br	318.39	15.974
C5C	C5Cn.1n	324.87	16.268
	C5Cn.1r	325.65	16.303
	C5Cn.2n	329.38	16.472
	C5Cn.2r	330.95	16.543
	C5Cn.3n	334.88	16.721
	C5Cr	347.64	17.235

Chron	sub-Chron	Dist. of old end	Age of base (Ma)
C5D	C5Dn	355.45	17.533
	C5Dr	360.88	17.717
	C5Dr.1n	361.55	17.74
	C5Dr.2r	370.87	18.056
C5E	C5En	382.45	18.524
	C5Er	388.64	18.748
C6	C6n	413.88	20
	C6r	422.93	20.04
C6A	C6An.1n	427.81	20.213
	C6An.1r	434.18	20.439
	C6An.2n	441.85	20.709
	C6Ar	452.46	21.083
C6AA	C6AAn	454.63	21.159
	C6AAr.1r	461.59	21.403
	C6AAr.1n	463.92	21.483
	C6AAr.1n	468.97	21.659
	C6AAr.2r	469.79	21.688
	C6AAr.2n	472.08	21.767
	C6AAr.3r	475.99	21.936
C6B	C6Bn.1n	477.29	21.992
	C6Bn.2n	483.7	22.268
	C6Br	490.61	22.564
C6C	C6Cn.1n	495.05	22.754
	C6Cn.1r	498.54	22.902
	C6Cn.2n	501.55	23.03
	C6Cn.2r	506.47	23.249
	C6Cn.3n	509.41	23.375
	C6Cr	524.64	24.044
C7	C7n.1n	525.92	24.102
	C7n.1r	527.29	24.163
	C7n.2n	536.04	24.556
	C7r	543.97	24.915
C7A	C7An	547.82	25.091
	C7Ar	552.3	25.295
C8	C8n.1n	555.55	25.444
	C8n.1r	556.6	25.492
	C8n.2n	571.04	26.154
	C8r	583.3	26.714

Chron	sub-Chron	Dist. of old end	Age of base (Ma)
C9	C9n	607.96	27.826
	C9 r	616.12	28.186
C10	C10n.1n	622.16	28.45
	C10n.1r	623.9	28.525
	C10n.2n	628.29	28.715
	C10r	645.65	29.451
C11	C11n.1n	652.56	29.74
	C11n.1r	655.31	29.853
	C11n.2n	664.15	30.217
	C11r	674.26	30.627
C12	C12n	686.5	31.116
	C12r	742.63	33.266
C13	C13n	755.44	33.738
	C13r	784.4	34.782
C15	C15n	791.78	35.043
	C15r	802.15	35.404
C16	C16n.1n	806.87	35.567
	C16n.1r	810.93	35.707
	C16n.2n	827.67	36.276
	C16r	834.68	36.512
C17	C17n.1n	856.19	37.235
	C17n.1r	859.46	37.345
	C17n.2n	865.54	37.549
	C17n.2r	867.33	37.61
	C17n.3n	872.1	37.771
	C17r	879.83	38.032
C18	C18n.1n	907.31	38.975
	C18n.1r	909.21	39.041
	C18n.2n	921.21	39.464
	C18r	947.96	40.439
C19	C19n	954.12	40.671
	C19r	977.65	41.59
C20	C20n	1006.06	42.774
	C20r	1060.24	45.346

Chron	sub-Chron	Dist. of old end	Age of base (Ma)
C21	C21n	1094.71	47.235
	C21r	1117.55	48.599
C22	C22n	1130.78	49.427
	C22r	1150.83	50.73
C23	C23n.1n	1153.9	50.932
	C23n.1r	1155.75	51.057
	C23n.2n	1168.2	51.901
	C23r	1178.96	52.648
C24	C24n.1n	1184.03	53.004
	C24n.1r	1185.61	53.116
	C24n.2n	1186.34	53.167
	C24n.2r	1188.05	53.286
	C24n.3n	1195.35	53.808
	C24r	1234.51	56.665
C25	C25n	1241.5	57.18
	C25r	1257.81	58.379
C26	C26n	1262.74	58.737
	C26r	1303.81	61.65
C27	C27n	1308.7	61.983
	C27r	1325.71	63.104
C28	C28n	1341.99	64.128
	C28r	1347.03	64.432
C29	C29n	1358.66	65.118
	C29r	1371.84	65.861
C30	C30n	1407.22	67.696
	C30r	1409.56	67.809
C31	C31n	1429.14	68.732
	C31r	1481.12	70.961
C32	C32n.1n	1487.68	71.225
	C32n.1r	1493.94	71.474
	C32n.2n	1531.81	72.929
	C32r.1r	1539.94	73.231
	C32r.1n	1542.32	73.318
	C32r.2r	1549.41	73.577
C33	C33n	1723.76	79.543
	C33r	1862.32	84
CNS	C34n	125.0	

Bibliography

Alvarez, W., Arthur, M. A., Fischer, A. G., Lowrie, W., Napoleone, G., Premoli-Silva, I. & Roggenthen, W. M. (1977), 'Type section for the Late Cretaceous-Paleocene reversal time scale', *Geol. Soc. Amer. Bull.* **88**, 383–389.

Anonymous (1979), 'Magnetostratigraphic polarity units- a supplementary chapter of the ISSC International stratigraphic guide', *Geology* **7**, 578–583.

Behrensmeyer, A. K. & Tauxe, L. (1982), 'Isochronous fluvial systems in Miocene deposits of Northern Pakistan', *Sedimentology* **29**, 331–352.

Butler, R. F. (1992), *Paleomagnetism: Magnetic Domains to Geologic Terranes*, Blackwell Scientific Publications.

Cande, S. C. & Kent, D. V. (1992), 'A new geomagnetic polarity time scale for the late Cretaceous and Cenozoic', *Jour. Geophys. Res.* **97**, 13917–13951.

Cande, S. C. & Kent, D. V. (1995), 'Revised calibration of the geomagnetic polarity timescale for the late Cretaceous and Cenozoic', *J. Geophys. Res* **100**, 6093–6095.

Cox, A., Doell, R. R. & Dalrymple, G. B. (1964), 'Reversals of the Earth's magnetic field', *Science* **144**, 1537–1543.

Cox, A. V., Doell, R. R. & Dalrymple, G. B. (1963), 'Geomagnetic polarity epochs and Pleistocene geochronometry', *Nature* **198**, 1049–1051.

Doell, R. & Dalrymple, G. (1966), 'Geomagnetic polarity epochs: A new polarity event and the age of the Brunhes-Matuyama boundary', *Science* **152**, 1060–1061.

Glen, W. (1982), 'The Road to Jaramillo'.

Gradstein, F., Ogg, J. & Smith, A.G., e. (2004), *Geologic Time Scale 2004*, Cambridge University Press, Cambridge.

Harrison, C. G. A. (1966), 'The paleomagnetism of deep sea sediments', *Jour. Geophys. Res.* **71**, 3033–3043.

Hays, J. D., Imbrie, J. & Shackleton, N. J. (1976), 'Variations in the Earth's orbit: pacemaker of the ice ages', *Science* **194**, 1121–1132.

Heirtzler, J. R., Dickson, G. O., Herron, E. M., Pitman, W. C. I. & LePichon, X. (1968), 'Marine magnetic anomalies geomagnetic field reversals, and motions of the ocean floor and continents', *Jour. Geophys. Res.* **73**, 2119–2136.

Hilgen, F. J. (1991), 'Astronomical calibration of Gauss to Matuyama sapropels in the Mediterranean and implication for the Geomagnetic Polarity Time Scale', *Earth Planet. Sci. Lett.* **104**, 226–244.

Kent, D. V. & Olsen, P. (1999), 'Astronomically tuned geomagnetic polarity time scale for the Late Triassic', *Jour. Geophys. Res.* **104**, 12831–12841.

Kent, D. V., Olsen, P. E. & Witte, W. K. (1995), 'Late Triassic-earliest Jurassic geomagnetic polarity sequence and paleolatitudes from drill cores in the Newark rift basin, eastern North America', *Jour. Geophys. Res.* **100**, 14965–14998.

LaBrecque, J. L., Kent, D. V. & Cande, S. C. (1977), 'Revised magnetic polarity time scale for Late Cretaceous and Cenozoic time', *Geology* **5**, 330–335.

Larson, R. L. & Pitman, W. C. I. (1972), 'World-wide correlation of Mesozoic magnetic anomalies, and its implications', *Geol. Soc. Amer. Bull.* **83**, 3645–3662.

Mason, R. & Raff, A. (1961), 'Magnetic survey off the west coast of North America, 32 degrees N. latitude to 42 degrees N. latitude', *Geol. Soc. Amer. bull.* **72**, 1259–1265.

Matuyama, M. (1929), 'On the direction of magnetisation of basalt in Japan, Tyosen and Manchuria', *Proc. Imp. Acad. Jap.* **5**, 203–205.

McDougall, I. & D.H., T. (1963), 'Dating reversals of the Earth's magnetic fields', *Nature* **198**, 1012–1013.

McElhinny, M. & McFadden, P. (2000), *Paleomagnetism: Continents and Oceans*, Academic Press.

Opdyke, N. D. & Channell, J. E. T. (1996), *Magnetic Stratigraphy*, Academic Press.

Opdyke, N. D., Glass, B., Hays, J. D. & Foster, J. (1966), 'Paleomagnetic study of Antarctic deep-sea cores', *Science* **154**, 345–357.

Oreskes, N. (2001), *Plate Tectonics: An insider's history of the modern theory of the Earth*, Westview Press, Boulder, CO.

Shackleton, N. J., Berger, A. & Peltier, W. R. (1990), 'An alternative astronomical calibration of the lower Pleistocene timescale based on ODP Site 677', *Trans. Roy. Soc. Edinburgh: Earth Sciences* **81**, 251–261.

van Hinte, J. (1976), 'A Cretaceous time scale', *Am. Assoc. Petroleum Geologists Bull.* **60**, 498–516.

Vine, F. J. & Matthews, D. H. (1963), 'Magnetic anomalies over oceanic ridges', *Nature* **199**, 947–949.

Lectures in Paleomagnetism - DRAFT

Lisa Tauxe
Suggested Citation:
Lisa Tauxe, "Lectures in Paleomagnetism", 2005, Essayo Press,
http://repositories.cdlib.org/sio/library/8

May 20, 2005

Chapter 16

Apparent Polar Wander Paths and tectonic applications

Suggested Supplemental Reading

For background:
Chapters 10 and 11: Butler (1992)
McElhinny and McFadden (2000)
To learn more:
Besse and Courtillot (2002)
http://www.scotese.com/

16.1 Introduction

No course in paleomagnetism would be complete without a lecture on apparent polar wander and tectonic applications of paleomagnetism. So what is apparent polar wander? The simplicity of the notion of a centered dipole giving rise to an observed direction at a given location on the surface of the Earth led to the definition of an equivalent pole position (the VGP of Lecture 2). In Lecture 14 we mentioned that averages of a number of VGPs sufficient to "average out" secular variation are known as paleomagnetic poles. When these are plotted on a map, they tend to "wander away" from the spin axis with increasing age of the rock unit sampled (e.g, Hospers, 1955; Irving, 1958). Data from a single continent can not distinguish between the wandering of the north pole (true polar wander) and the wandering of the continents (apparent polar wander). But data from multiple continents and a firm belief in the essential dipolar nature of the geomagnetic field (dating back to 1600!), convinced paleomagnetists in the 50s of the reality of continental drift. In this lecture we will consider how apparant polar wander paths for the various continents can be constructed and briefly discuss a few tectonic applications.

16.2 Some terminology

Before we dive into the details of paleomagnetic poles and the construction of Apparent Polar Wander Paths (APWPs), we need to review some basic terminology and establish working definitions for various terms in paleomagnetism. These are: specimen, sample, site, and the various poles.

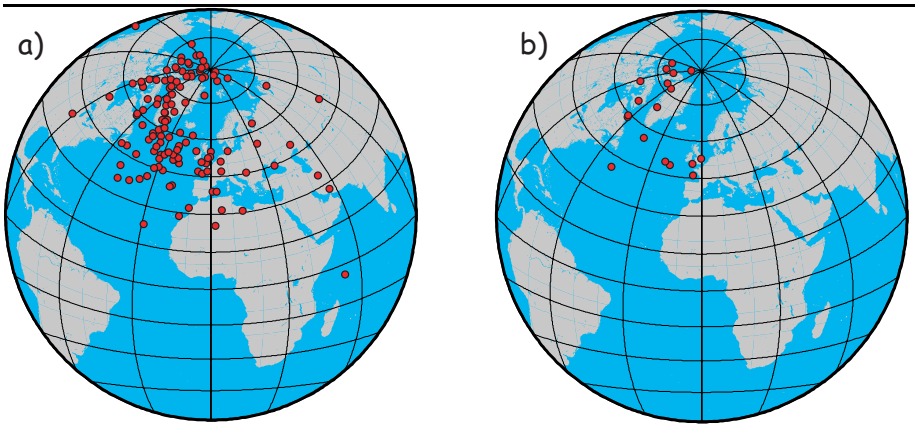

Figure 16.1: Paleomagnetic poles from Australia for the last 200 Ma from GPMDB. a) No selection criteria. b) The selection criteria of BC02.

These terms are used in different ways by different authors; for the purpose of this lecture series, we will use them in the following way:

Term	Definition
Specimen	Something that gets measured.
Sample	Something that gets taken either in the field or sub-sampling of a core, pot sherd, or other object. Samples can be prepared into for measurement as one or more specimens.
Site	A group of samples expected to be homogeneous with respect to the property to be measured (e.g., a single lava flow or a single sedimentary horizon).
VGP	The mapping of a direction from a spot reading of the geomagnetic field to an equivalent pole (see Lecture 2).
Paleomagnetic pole	An average of a number of VGPs sufficient to average out secular variation. Can also be the mapping of an average of a number of directions to the equivalent pole (see Lecture 14).

16.3 Paleomagnetic poles and apparent polar wander

There have been nearly 7000 paleomagnetic poles published since 1925. These range in age from the Archean to quite recent and in quality from excellent to highly questionable. Paleomagnetic poles have been assembled into the Global Paleomagnetic Database (GPMDB), a version of which is available for downloading at the the National Geophysical Data Center (NGDC) repository:

http://www.ngdc.noaa.gov/seg/geomag/paleo.shtml

As an example of the process of constructing APWPs, we will follow the work of Besse and Courtillot (2002) (hereafter BC02) who recently updated the apparent polar wander paths for the major continents for the last 200 Myr. We begin with the plot of all the paleomagnetic poles (regardless of quality) compiled in the GPMB for Australia for the last 200 Myr in Figure 16.1. These poles form a smear that extends in a broad arc away from the spin axis sown the Atlantic and then into Europe and Africa, although there are also isolated poles that are quite far away

from the general trend.

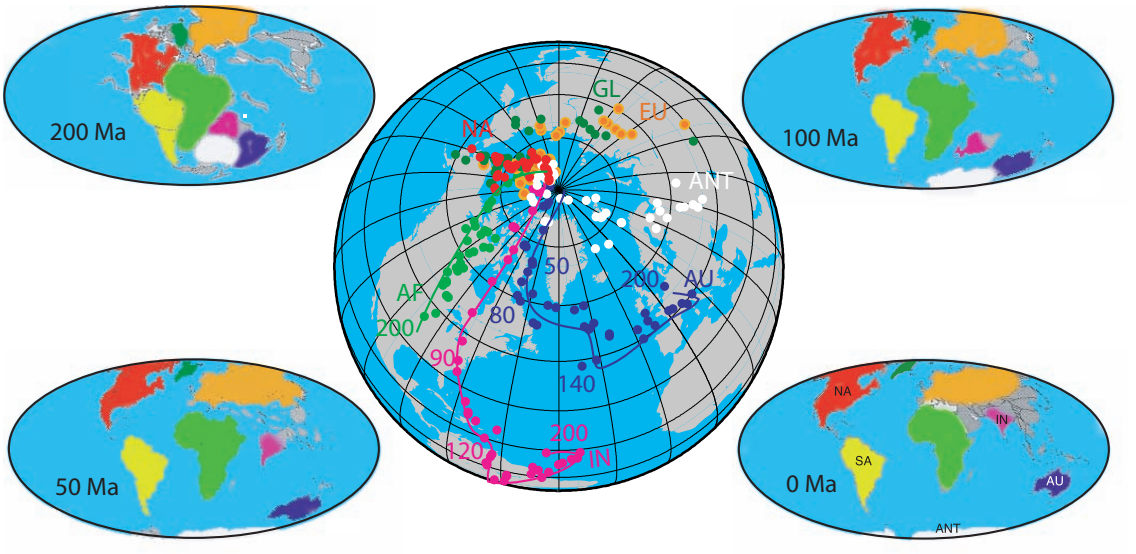

Figure 16.2: Maps of continental reconstructions for 200, 100, 50 and 0 Ma. The central map is of the apparant polar wander paths for the various continents for the last 200 million years, evaluated at five million year intervals. [Reconstructions from www.scotese.com and APWPs of Besse and Courtillot, 2002.]

Picking out the meaningful poles from the published data is the art of paleomagnetism. We have been building a tool kit for dealing with this problem throughout these lecture notes. There is some agreement in what constitutes a "good" pole among various workers. The basic selection criteria used by most workers are based those summarized by Van der Voo (1990). The "Voo Criteria" are:

1. The age of the formation must be known rather accurately. In the Voo criteria, the age should be known to within a half of period (see Lecture 15) or within a numerical age of $\pm$ 4% for Phanerozoic data. For Precambrian rocks, the age should be known to within $\pm$ 4 % or 40 Myr, whichever is smaller. BC02 demanded age uncertainties of $\pm$ 15 Myr.

2. In order to average errors in orientation of the samples and scatter caused by secular variation, there must be a sufficient number of individually oriented samples from enough sites. What constitutes "sufficient" and "enough" here is somewhat subjective and a matter of debate. The Voo Criteria recommend a minimum of 24 discrete samples of the geomagnetic field having a $\kappa > 10$. Some authors also compare scatter within and between sites in order to assess whether secular variation has been sufficiently sampled, but this relies on many assumptions as to what the magnitude of secular variation was (see Lecture 14). Butler (1992) suggested using the scatter of VGPs (S in Lecture 14) to decide whether secular variation has been averaged out or whether there is excess scatter in the data set. BC02 used only poles with at least six sites and 36 samples, each site having a 95% confidence interval less than 10° in the Cenozoic and 15° in the Mesozoic.

3. It must be demonstrated that a coherent characteristic remanence component has been iso-

lated by the demagnetization procedure. McElhinny and McFadden (2000) attempt to standardize the description of the demagnetization status of a dataset using a demagnetization code (DC) (see Table 16.1). BC02 use only poles with a DC of at least 2.

4. The age of the magnetization relative to the age of the rock should be constrained using field tests (fold test, conglomerate test, baked contact test, see Lecture 9). BC02 reject poles that fail a fold test or a reversals test.

5. There should be agreement in the pole position from units of similar age from a broad region and adequate knowledge of any structural corrections necessary. BC02 reject poles from "mobile regions", or incorporate data from regions that have undergone only vertical axis rotation by using inclination only data (see Lecture 13).

6. Both polarities should be represented and the two data sets should be antipodal.

7. Pole positions should not fall on a younger part of the pole path or on the present field direction. Such poles should be viewed with suspicion.

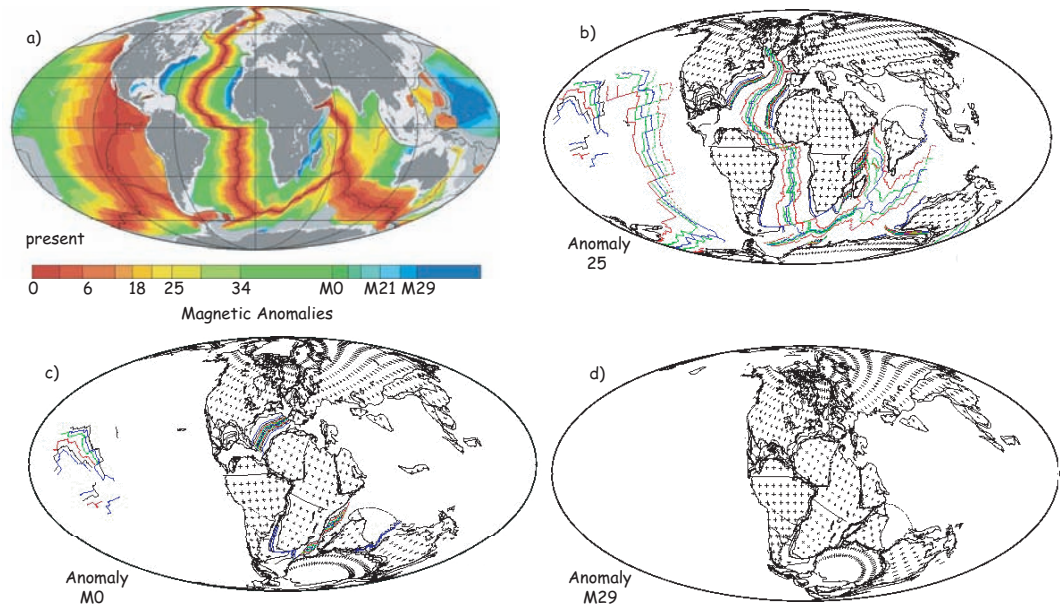

Figure 16.3: a) Position of the major anomalies and inferred age of the sea floor. [Figure modified from http://www.geosci.usyd.edu.au/research/marinegeophysics/Resprojects/ and Müller et al. (19997).] b-d) Reconstructions based on fitting of matching magnetic anomalies for selected times. [Figures from http://gdcinfo.agg.nrcan.gc.ca/app/utig_report_e.html and Royer et al. (1992).]

In the Voo criteria, each pole gets a point for every criterion that it passes. The sum of the points is the quality factor Q which ranges from 0 to 7. It is not expected that every pole satisfy all seven criteria (very few would!). Most authors use poles with $Q > 2$. BC02 on the other hand use critieria 1-5 (must have all of them) but do not require 6 or 7.

Table 16.1: Demagnetization Codes (DC) summarized by McElhinny and McFadden (2000).

DC	Description
0	Only NRM values reported. No evidence for demagnetization.
1	Only NRM values reported. Demagnetization on pilot specimens suggest stability.
2	Demagnetization at a single step on all specimens. No demagnetograms shown.
3	Demagnetograms shown that justify demagnetization procedure chosen.
4	Principal component analysis (PCA) carried out from analysis of Zijderveld diagrams. (see Lecture 9)
5	Magnetic vectors isolated using two or more demagnetization methods with PCA. e.g., thermal and AF demagnetization (see Lecture 9).

Of the 137 poles from Australia in the GPMDB plotted in Figure 16.1a, only 18 meet the BC02 criteria (see Figure 16.1b). These form a sparse track which would be the basis for the Apparent Polar Wander Path (APWP) for Australia. A similar story plays out on all the major continental blocks, so the pole paths for the continents are not very well constrained using this approach. This is why most authors use less stringent demands on their poles. However, BC02 had a plan. They argue that if the rotation parameters between continents are well known as a function of age, then poles from one continent can be transferred to the coordinate system of another. In fact, all the poles could be transferred to a single continent and used to compose a single "master" apparent polar wander path. This master path could then be re-exported back to the contributing continents. This plan works in principle if the correct poles of rotation are used, hence the demands for accurate age control of the individual paleomagnetic poles.

BC02 argue that the poles of rotation among the seven continents of Africa, Antarctica, Australia, India, North America, South America and Europe are well enough known for the last 180 Myr or so. The basis for their optimism is the fact that the magnetic anomaly patterns in the intervening oceans have been carefully mapped (see, e.g., Figure 16.3) The finite rotation poles that "roll up" the sea floor, superimposing magnetic anomalies on opposite sides of the ridge crest, can be used to transform paleomagnetic poles from one continent to another (see Appendix for details). The exported (synthetic) APWPs for the seven continents are shown in Figure 16.2.

The BC02 approach works well for the last 180 Myr or so. Prior to that, however, the rotation parameters are not as well constrained, independent of the paleomagnetic data themselves. Both the quality and quantity of the available poles decline with increasing age. The assumptions of the GAD hypothesis and amount and style of secular variation become increasingly problematic. Furthermore, most continents are composed of separate blocks whose relationships in ancient times are unknown or poorly known. An exception to this is supercontinents like Gondwana or its precursor Pangea, for which it is possible to combine data from different parts of the supercontinent with some confidence.

McElhinny and McFadden (2000) summarize the data from major continental blocks for the Phanerozoic and construct APWP using data with $Q > 2$. They claim that the APWP for Australia (see Figure 16.4a) is the best determined of all the continents. The portion from the present to about 200 Ma is similar (although of course not as detailed) as that of BC02 (blue dots in Figure 16.2. Beyond that the poles are sparse and the path is very jerky leading to the suspicion that it is somewhat aliased.

Because Australia was once part of Gondwana and the reconstruction of Gondwana is rather

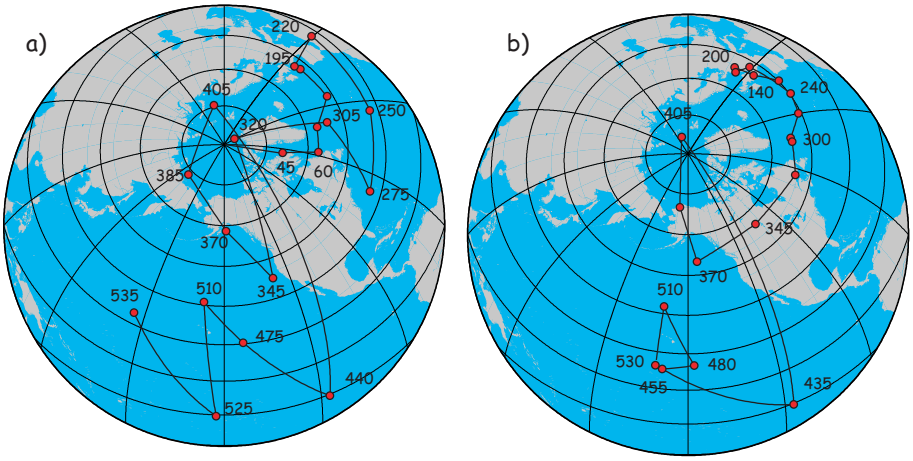

Figure 16.4: The Australian APWP for the Phanerozoic. a) Australian poles only (Table 6.14 of McElhinny and McFadden, 2000). b) Composite Gondwana path exported to Australia. [Table 7.3 of McElhinny and McFadden, 2000, rotated to Australian coordinates (see text).]

straight-forward, a similar approach to building a composite Gondwana APWP has long been taken by paleomagnetists. This was done by McElhinny and McFadden (2000) using the rotation parameters of Lottes and Rowley (1990) to transfer the Gondwana poles to NW African coordinates. Their composite APWP for Gondwana, rotated back to Austraian coordinates (using a finite rotation pole of 28.1S, 66.8W and -52.1° (clockwise) is plotted in Figure 16.4b. Some of the jerkiness of the Australian poles only plot has been removed, but more work is still needed.

16.4 Plate Reconstructions

One of the first uses of paleomagnetic data was as a test of the idea of *continental drift* (e.g., Wegener, 1915). Data from one continent, for example the data from Australia in Figure 16.1 could be interpreted to indicate either motion of the continent with respect to a fixed geomagnetic pole, or motion of the geomagnetic pole with respect to a fixed continent. To test the hypothesis of continental drift, data from at least two continents are required.

The synthetic APWPs from BC02 are not suitable for testing continental drift because that hypothesis (in the form of sea-floor spreading) is a built-in assumption. Data from each continent separately are required, as is some reconstruction not based on the idea of sea floor spreading (e.g., the fit of the continental shelves). Such APWPs can in fact be used to test particular reconstructions as we will show using data from the North America and Europe.

In Figure 16.5, we plot the data compiled by van der Voo (1990) for North America and Europe which meet his minimum standards of reliability (i.e., $Q > 2$). In Figure 16.5a, the poles are plotted with respect to present-day coordinates: the poles clearly fall on two separate tracks. This indicates that either the field was not at all dipolar, or that the two continents have moved, not only with respect to the geomagnetic pole, but also with respect to each other.

Many people who have contemplated the globe have had the desire to fit North and South America against Europe and Africa by closing the Atlantic Ocean. One such attempt, known as the *Bullard fit* (Bullard et al., 1965), fits the continents together using misfit of a particular

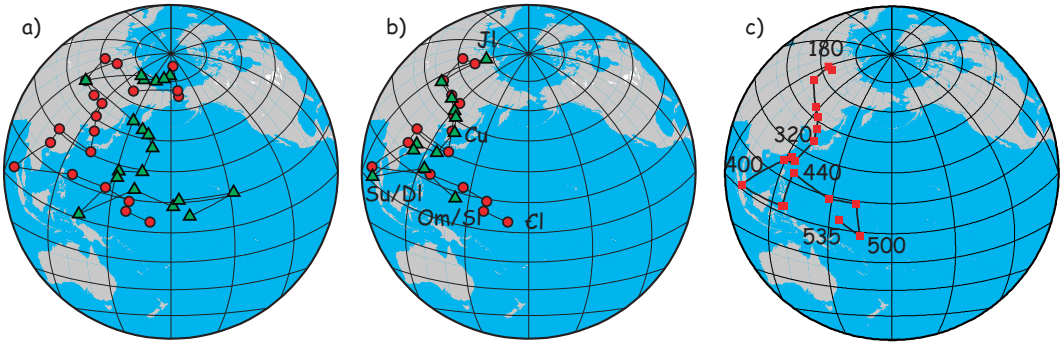

Figure 16.5: Poles from North America (circles) and Europe (triangles). (Data from van der Voo, 1990.) a) in present day coordinates. b) after rotation of Europe to close the Atlantic Ocean using the so-called "Bullard" fit (Bullard, 1965). c) APWP made by combining all the data from Laurentia and Europe in a master curve, in North American coordinates. [Poles from McElhinny and McFadden, 2000.]

contour on the continental shelves as the primary criterion. Following van der Voo (1990) (and many before him), we rotate the European poles, using the Bullard fit, into North American coordinates in Figure 16.5b. After closing the Atlantic, the curves overlap rather well, and, if the ages of the poles are also taken into account, the match is convincing. The agreement provides strong support of the continental drift hypothesis and also of the Bullard fit. Other reconstructions could be tested for a superior fit (see McElhinny and McFadden, 2000). Finally, combining poles from Europe and North America to create a master Laurussia curve and transferring it to North American coordinates yields the track shown in Figure 16.5c.

Please note that longitude of the reconstructions is not constrained, so the continents could be at any longitude and still have poles that fit identically. Some reconstructions of Pangea take advantage of this fact in order to accommodate overlap among continental masses in the early Mesozoic (see e.g., Irving, 1977).

16.5 Discordant poles and displaced terranes

Regions with paleomagnetic directions that are significantly different from the direction expected from the appropriate reference pole of the APWP may have rotated or translated from their original positions as an independent entity (a tectonostratigraphic terrane of *microplate*). As workers began investigations in the western parts of North America, it soon became apparent that many of the poles were well off the beaten track for the rest of North America (see, e.g., Irving, 1979). To illustrate this, we plot the data from North America that meet minimum van der Voo standards ($Q > 2$). The poles from "cratonic" North America (from van der Voo, 1993) are plotted as circles in Figure 16.6. Also shown as triangles is a small selection of so-called *discordant poles* (from van der Voo, 1981). What is immediately obvious is that the discordant poles do not fall anywhere near the APWP. Most are from western North America and indicate some clockwise rotations (the poles are rotated to the right of the expected poles). When taking into account the age of the formations, many also seem to have directions that are too shallow, which suggests possible northward transport of 1000's of kilometers. The validity and meaning of these discordant

directions is still under debate, but it is obvious that most of the western Cordillera is not *in situ*.

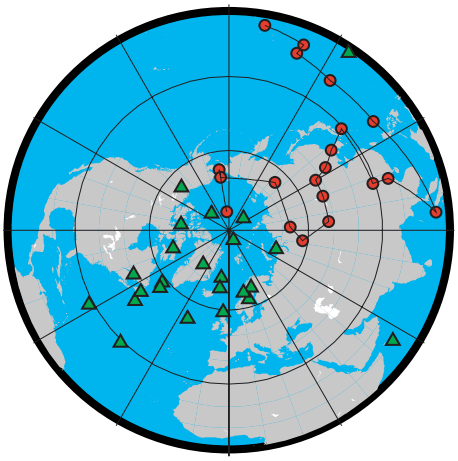

Figure 16.6: Circles are "reliable" poles from cratonic North America. (Data from van der Voo, 1990). So-called "discordant poles" from western North America are plotted as triangles (data from van der Voo, 1981).

16.6 Testing GAD

One of the most useful assumptions in paleomagnetism is that the geomagnetic field is on average closely approximated by a geocentric axial dipole (GAD). As discussed in Lecture 14, the GAD hypothesis has been found to be true for at least the last 5 million years with the largest non-GAD contribution to the spherical harmonic expansion generally being of the order of 5%. For the more ancient past, it is difficult to test the GAD (or any other field) hypothesis owing to plate motions, accumulating problems of overprinting, and difficulty in reconstructing paleo-horizontal. Although most paleomagnetic studies make the implicit assumption of a GAD field, several recent studies have called the essential GAD nature of the ancient field into question. These studies fall into two groups: those that use reference poles and plate tectonic reconstructions to predict directions (e.g., Si and van der Voo, 2001) and those that compare observed statistical distributions of directions to those predicted by different field models (e.g., Kent and Smethurst, 1998). The inescapable conclusion from these and other studies is that there is often a strong bias toward shallow inclinations and many studies have called on non-dipole field contributions, in particular large (up to 20%) average axial octupole (g_3^0)contributions (see Lectures 2 and 14). We will explore these ideas in the rest of this lecture.

16.6.1 Predicted directions and the Asian inclination anomaly

Earlier in the lecture, we discussed the BC02 APWPs for the major continents. These can be used to predict directions for a given time and place using the spherical trigonometric tricks covered in the Appendix to Lecture 2. Despite the general success of the BC02 APWPs for predicting directions, comparison of predicted directions with those observed in many data sets from red beds in Central Asia led many authors to the conclusion that the GAD hypothesis failed. We show an

example of such a data set in Figure 16.7, although it is atypical in that there are an unusually large number of directions. These have a mean of $\bar{D} = 356.1°$, $\bar{I}$ =43.7°. Assuming that the location of the study (presently located at 39.5°N, 94.7°E) has been fixed to the European coordinate system and taking the 20 Myr pole for Europe from BC02 (81.4°N, 149.7°E), the inclination is predicted to be 63° (see dashed line in Figure 16.7). These sediments are typical of Asian sedimentary units in having an inclination relative to the predicted values that is some 20° too shallow.

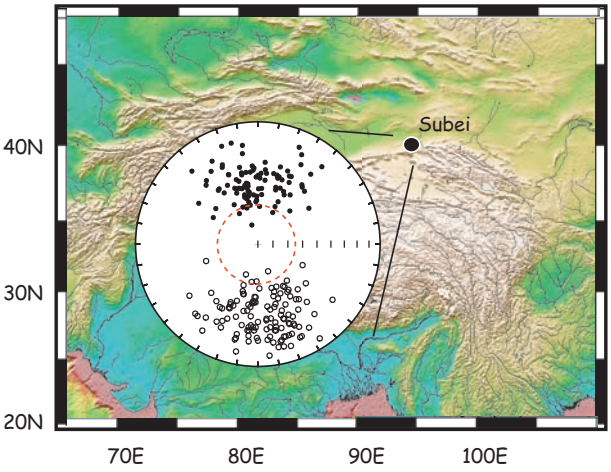

Figure 16.7: Paleomagnetic directions of Oligo-Miocene redbeds from Asia in equal area projection (stratigraphic coordinates). [Redrawn from Tauxe and Kent, 2004; data from Gilder et al., 2001.]

From Lecture 14 we know that paleomagnetic directions from the last five million years are, if anything, elongate in the North-South plane. However, the data in Figure 16.7 are distinctly elongate east-west. Tauxe and Kent (2004) pointed out that sedimentary inclination flattening not only results directions that are too shallow, but also whose N-S elongations are reduced in favor of elongations that are more east-west. This effect is shown in Figure 16.8 whereby Figure 16.8a is an equal area projection of 100 realizations of the TK03.GAD model evaluated at 30°N latitude (see Lecture 14). Figure 16.8b are the same directions but put through the flattening formula $\tan I_o = f \tan I_f$ (see Lecture 5) with a value for f of 0.6 and Figure 16.8c is the same but for $f = 0.4$.

The "elongation-inclination" (E/I) method of detecting and correcting inclination shallowing of Tauxe and Kent (2004) simply "unflattens" observed directional data sets using the inverse of the flattening formula and values for f ranging from 1 (no unflattening) to 0.3. At each unflattening step, they calculate inclination and elongation (τ_2/τ_3 of the orientation matrix, see Lecture 9) and plot these as in Figure 16.9a. In Figure 16.9b, elongation is plotted against inclination to form a curve. We know from Lecture 14 that elongation decreases from the equator to the pole, while inclination increases; A best-fit polynomial through the inclination - elongation data from model TK03.GAD is: $E = 2.88 - 0.0087I - .0005I^2$ shown as dashed line in Figure 16.9b. There is a unique pair of elongation and inclination that is consistent with the TK03.GAD field model (circled in Figure 16.9b) with an inclination of 64°.

To obtain confidence bounds on the "corrected" inclination, the E/I method performs a bootstrap. E/I curves from twenty such bootstrapped data sets are shown as thin lines in Figure 16.9b. A histogram of 1000 crossing points of bootstrap curves with the model elongation-inclination line

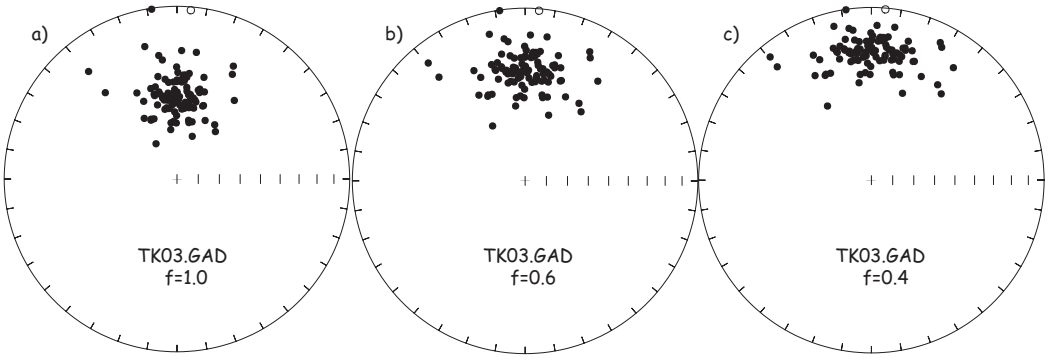

Figure 16.8: a) 100 realizations from the TK03.GAD statistical field model evaluated at 30°N. b) Same as a) flattened with an $f = 0.6$. c) Same as b) but with $f = 0.4$.

are plotted in Figure 16.9d. The mode of the bootstrapped crossings is at an inclination of 63° with 95% of the crossings falling between 56 and 69°, consistent with that predicted by the BC02 path for stable Europe.

Tan et al. (2003) performed the AARM correction (see Lecture 13) on the Tarim red beds and found an identical correction factor. Hence AARM correction (which is labor intensive in the lab) and EI correction (which is labor intensive in the field) give similar results. Both methods strongly suggest that inclination shallowing in the Asian red beds is indeed caused by sedimentary inclination shallowing of the type described in Lecture 5.

16.6.2 The "Statistical distribution" method and the Paleozoic/Pre-Cambrian geomagnetic field

The "statisitcal distribution method" of Evans (1976) for characterizing the time averaged ancient geomagnetic field requires no *a priori* assumptions about the structure of the ancient geomagnetic field. It relies instead on a large data set spanning sufficient time for the plates to have moved over the surface of the globe. The frequency of inclinations can be compared with that expected from some arbitrary magnetic field, e.g., a GAD field. It assumes that enough paleomagnetic sites have been sampled with sufficient spatial and temporal coverage that the entire ancient geomagnetic field will have been represented. Kent and Smethust (1998; KS98) employed the method on data extracted from the GPMDB data base. We follow their approach here using the compilation of paleomagnetic pole positions contained in GPMDBv.3.1. We have excluded only data that the authors themselves disavowed and separated the data by age (Cenozoic [0-65], Mesozoic [65-250 Ma], Paleozoic [250-550], PreCambrian [550-3500]). In order to overcome sampling biases in which certain areas at certain times are over represented in the database, Evans (1976) and KS98 bin the data by age and geographic area. We repeat the analysis of KS98 for the Cenozoic data set in Figure 16.10. The sampling sites are shown in Figure 16.10a and the frequency plots are in Figure 16.10b. The data appear to be consistent with a dominantly GAD field as was found by previous studies.

When KS98 (Kent & Smethurst 1998) examined the data from the Paleozoic and Pre-Cambrian, however, they found a strikingly different pattern as shown in Figure 16.10d. They concluded

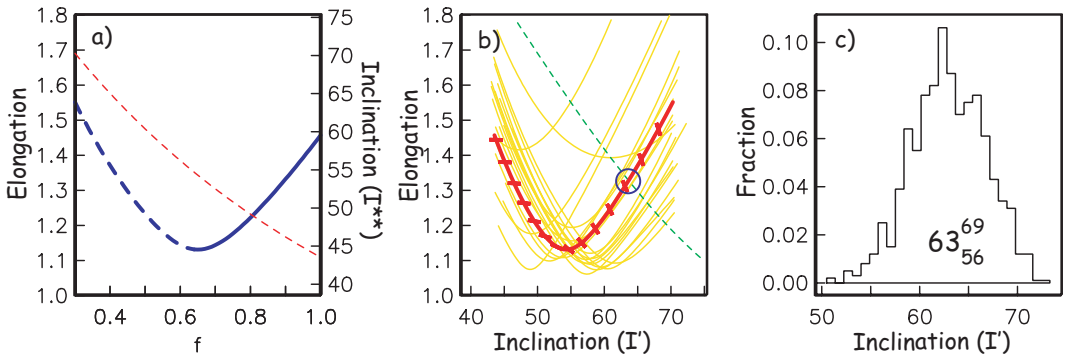

Figure 16.9: a) Plot of elongation (heavy solid and dashed line) and inclination (dashed) as a function of unflattening by the parameter f. Elongation is E-W (N-S) when heavy line is solid (dashed) b) Plot of elongation versus inclination for the data in a) (solid) and for the TK03.GAD model (dashed). Also shown are results from 20 bootstrapped datasets. The crossing points represents the inclination/elongation pair most consistent with the TK03.GAD model. c) Histogram of crossing points from 1000 bootstrapped datasets. The most frequent inclination (63°) is exactly that predicted from the Besse and Courtillot (2002) European APWP. The 95% confidence bounds on this estimate are 56-69°. [Figure modified from Tauxe and Kent, 2004.]

that the frequency distribution of Paleozoic and Pre-Cambrian inclination data are severely biased toward shallower directions and are not consistent with a GAD model.

KS98 (Kent & Smethurst 1998) discussed several possible causes of the bias: inclination "error" in sediments, non-random plate motion, and non-GAD fields, in particular, a time averaged geomagnetic field with a large ($\sim 20\%$) octupolar (g_3^0) contribution. In order to address the issue of sedimentary bias, KS98 separated the data into those of sedimentary origin and those of so-called "crystalline" origin, mostly extrusive and intrusive igneous rocks as shown in Figure 16.10c. Both types of rocks yield highly biased frequency plots.

The frequency distribution expected for sedimentary rocks exhibiting "inclination error" can be estimated by using the inclination error formula as before. We show the expected distribution of inclinations from such a process (using $f = 0.5$) in Figure 16.10d as the long dashed line. The sedimentary data (short dashed line) are quite consistent with this prediction. This result should come as no surprise perhaps because the overwhelming majority of the data come from so-called "red beds" with detrital hematite as a dominant carrier of remanence.

Because "crystalline" rocks do not suffer from depositional inclination error, the fact that they too were biased shallow was taken as support that the shallow bias was not solely the result of a sedimentary artifact. KS98 (Kent & Smethurst 1998) drew the conclusion that either the field was indeed biased with a large octupolar contribution, or that the continents had not drifted randomly, but had preferentially been near the equator.

There is another possibility. In the Paleozoic and the Pre-Cambrian, it is likely that most rock units have experienced some degree of tilting. For intrusive rocks, the amount of tilting could be unconstrained. Extrusives, however, generally have initial dips within some 30° of horizontal, depending on the type of volcano. Therefore, paleo-horizontal in even the extrusive units would not necessarily be known to better than 30° unless they are intercalated with sediments whose paleo-horizontal is much better constrained. The distribution of inclinations becomes increasingly

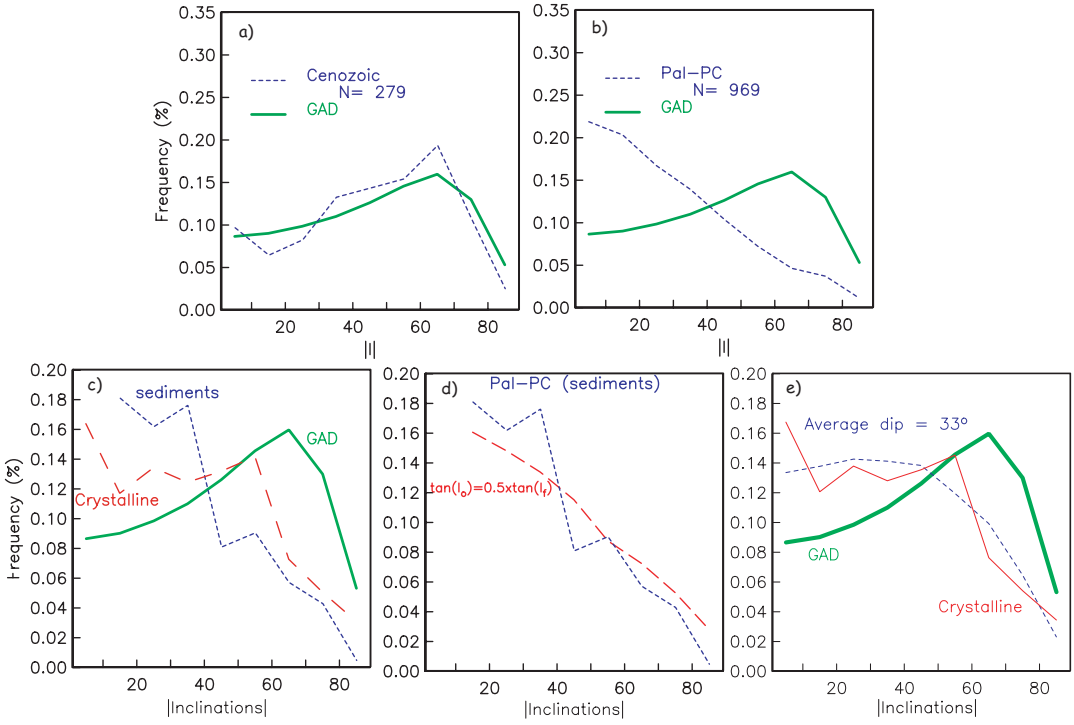

Figure 16.10: a) Frequency of inclinations. Dashed line is (binned) Cenozoic results. Solid line is expectation from GAD c) same as a) for Paleozoic-Precambrian results. b) Same as a) but for Paleozoic-Precambrian results. c) Same as b) but sediments shown as short dashed line and crystalline rocks shown as long dashed line. Also shown is the trend expected from GAD. d) same as c) but for sediments only. Also shown is trend expected GAD inclinations transformed by the inclination error formula. e) same as d) but for crystalline rocks. Also shown is the trend expected from random tilting of a GAD distribution of directions with an average dip of 33°.

skewed toward shallow directions as the amount of average tilting increases. In fact, it is perhaps surprising that simulations show that uncorrected tilt has a similar effect on the distribution of inclinations as the addition of a non-zero axial octupole.

The relevance to the structure of the ancient geomagnetic field of poorly constrained tilting is shown in Figure 16.10e in which we plot the frequency distribution obtained by tilting observations derived from the 1995 IGRF by random amounts with an average tilt of 33° and that obtained from the crystalline rocks in the database. Such tilts are not unexpected from a collection of Paleozoic/Pre-Cambrian intrusives and extrusives. We find that the poorly constrained tilt hypothesis explains the observations as well as the introduction of a large axial octupole contribution.

16.7 Concluding remarks

And so we return to where we started at the beginning of this course with an assumption that the geomagnetic field is essentially that of a centered dipole. There is no compelling evidence that the field has operated in a vastly different way in ancient times, apart from the puzzling change

in reversal frequency. We are getting better at all aspects of paleomagnetic research from better designed field programs to better laboratory analyses to more sophisticated data analysis. There remains much to be done. Enjoy.

Appendix

A Method for rotating paleomagnetic poles using finite rotation poles

The following is based on the procedure described in Box 7.3 of Cox and Hart (1986). Given the coordinates of the paleomagnetic pole P_p with latitude λ_p, longitude ϕ_p the finite rotation pole P_f with latitude λ_f, longitude ϕ_f, the way to transform coordinates is as follows (you should also review Appendix A4 of Lecture 1 and Lecture 2).

Convert the latitudes and longitudes to cartesian coordinates by:

$$P_1 = \cos\phi\cos\lambda, P_2 = \sin\phi\cos\lambda, P_3 = \sin\lambda$$

where P is the pole of interest.

Set up the rotation matrix R as:

$$\begin{aligned}
R_{11} &= P_{f1}P_{f1}(1-\cos\Omega)+\cos\Omega \\
R_{12} &= P_{f1}P_{f2}(1-\cos\Omega)-P_{f3}\sin\Omega \\
R_{13} &= P_{f1}P_{f3}(1-\cos\Omega)+P_{f2}\sin\Omega \\
R_{21} &= P_{f2}P_{f1}(1-\cos\Omega)+P_{f3}\sin\Omega \\
R_{22} &= P_{f2}P_{f2}(1-\cos\Omega)+\cos\Omega \\
R_{23} &= P_{f2}P_{f3}(1-\cos\Omega)-P_{f1}\sin\Omega \\
R_{31} &= P_{f3}P_{f1}(1-\cos\Omega)-P_{f2}\sin\Omega \\
R_{32} &= P_{f3}P_{f2}(1-\cos\Omega)+P_{f1}\sin\Omega \\
R_{33} &= P_{f3}P_{f3}(1-\cos\Omega)+\cos\Omega
\end{aligned}$$

The coordinates of the transformed pole (P_t) are:

$$\begin{aligned}
P_{t1} &= R_{11}P_{p1}+R_{12}P_{p2}+R_{13}P_{p3} \\
P_{t2} &= R_{21}P_{p1}+R_{22}P_{p2}+R_{23}P_{p3} \\
P_{t3} &= R_{31}P_{p1}+R_{32}P_{p2}+R_{33}P_{p3}
\end{aligned}$$

which can be converted back into latitude and longitude in the usual way (see Lecture 2).

Bibliography

Besse, J. & Courtillot, V. (2002), 'Apparent and true polar wander and the geometry of the geomagnetic field over the last 200 myr', *J. Geophys. Res* **107**, doi:10.1029/2000JB000050.

Bullard, E. C., Everett, J. E. & Smith, A. G. (1965), 'A symposium on continential drit - iv. the fit of the continents around the atlantic', *Phil. Trans. Roy. Soc.* **258**, 41–51.

Butler, R. F. (1992), *Paleomagnetism: Magnetic Domains to Geologic Terranes*, Blackwell Scientific Publications.

Cox, A. & Hart, R. (1986), *Plate Tectonics: How it Works*, Blackwell Scientific, Oxfort.

Evans, M. (1976), 'Test of the dipolar natrue of the geomagneitc field throughout phanerozoic time', *Nature* **262**, 676–677.

Hospers, J. (1955), 'Rock magnetism and polar wandering', *J. Geol.* **63**, 59–74.

Irving, E. (1958), 'Paleogeographic reconstruction from paleomagnetism', *Geophys. Jour. Roy. astr. Soc.* **1**, 224–237.

Irving, E. (1977), 'Drift of the major continental blocks since the devonian', *Nature* **270**, 304.

Irving, E. (1979), 'Paleopoles and paleolatitudes of north america and speculations about displaced terrains', *Can. J. Earth Sci.* **16**, 669–694.

Kent, D. & Smethurst, M. (1998), 'Shallow bias of paleomagnetic inclinations in the paleozoic and precambrian', *Earth Planet. Sci. Lett.* **160**, 391–402.

Lottes, A. & Rowley, D. (1990), Early and late permian reconstructions of pangaea, *in* W. McKerro & C. Scotese, eds, 'Paleozoic Paleogeogrpahy and Biogeography', Vol. 12, Geol. Soc. London Meme, pp. 383–395.

McElhinny, M. & McFadden, P. (2000), *Paleomagnetism: Continents and Oceans*, Academic Press.

Mueller, R., Roest, W., Royer, J., Gahagan, L. & Sclater, J. G. (1997), 'A digital age map of the ocean floor'.

Royer, J., Mueller, R., Gahagan, L., Lawver, L., Mayes, C., Nuernberg, D. & Sclater, J. G. (1992), 'A global isochron chart', *Univ. Texas Inst. Geophys. Tech. Rept.* **117**.

Si, J. & Van der Voo, R. (2001), 'Too-low magnetic inclinations in central asia: an indication of a long-term tertiary non-dipole field?', *Terra Nova* **13**, 471–478.

Tan, X. D., Kodama, K. P., Chen, H. L., Fang, D. J., Sun, D. J. & Li, Y. A. (2003), 'Paleomagnetism and magnetic anisotropy of cretaceous red beds from the tarim basin, northwest china: Evidence for a rock magnetic cause of anomalously shallow paleomagnetic inclinations from central asia', *Journal of Geophysical Research-Solid Earth* **108**(B2).

Tauxe, L. & Kent, D. V. (2004), A simplified statistical model for the geomagnetic field and the detection of shallow bias in paleomagnetic inclinations: Was the ancient magnetic field dipolar?, *in* e. a. Channell, J.E.T., ed., 'Timescales of the Paleomagnetic field', Vol. 145, American Geophysical Union, Washington, D.C., pp. 101–116.

Voo, R. V. d. (1981), 'Paleomagnetism of north america-a brief review', *Paleoreconstruction of the Continents, Geodynamic Series Amer. Geophys.* **2**, 159–176.

Voo, R. V. d. (1990), 'Phanerozoic paleomagnetic poles from europe and north-america and comparisons with continental reconstructions', *Rev. of Geophysics* **28**, 167–206.

Wegener, A. (1915), *Die Entstehung der Kontinente*.